BOUNDARY ELEMENT TECHNIQUES FOR THE INFILTRATION OF DUAL-SCALE POROUS MEDIA IN THE PROCESSING OF COMPOSITES MATERIALS

A dissertation submitted by

Iván David Patiño Arcila

In partial fulfillment of the requirements for the Degree of

Doctor en Ingeniería

Área de Nuevos Materiales

Principal Supervisor:

César Nieto Londoño, PhD.

Advisors:

Prof. Henry Power, PhD.

Whady F. Flórez Escobar, PhD.

Universidad Pontificia Bolivariana

Escuela de Ingeniería

Doctorado en Ingeniería

Medellín

2017

UNIVERSIDAD PONTIFICIA BOLIVARIANA
DOCTORADO EN INGENIERÍA
ACTA DE JURADOS

En la fecha, los suscritos asistimos a la Presentación Pública de la Tesis Doctoral, donde el estudiante del Doctorado en Ingeniería, Magister:

IVÁN DAVID PATIÑO ARCILA

Sustentó su tesis:

"BOUNDARY ELEMENTS TECHNIQUES FOR THE INFILTRATION OF DUAL-SCALE POROUS MEDIA IN THE PROCCESING OF COMPOSITE MATERIALS"

Elaborada como requisito para optar al título de DOCTOR EN INGENIERÍA, trabajo que habíamos examinado previamente a la sesión. Oída la presentación y sustentación acordamos la siguiente calificación (señale con una X):

Aprobado	Reprobado
X	

Distinción:

Ninguna	Magna Cum Laude	Summa Cum Laude	Cum Laude
		X	

Justificación:

LOS TRES JURADOS ESTIMAMOS QUE EL TRABAJO ES SOBRESALIENTE, EXEDE LOS ALCANCES INICIALMENTE PLANTEADOS Y PRESENTA RESULTADOS NO REPORTADOS EN LA LITERATURA Y QUE ABREN EL CAMINO A NUEVAS LINEAS DE INVESTIGACION.

LUIZ WROBEL.
Jurado: Dr. Luiz Wrobel

JULIÁN SIERRA PÉREZ.
Jurado: Dr. Julián Sierra Pérez

Jurado: Dr. Iván Darío López Gómez

Director: Dr. Cesar Nieto Londoño

Medellín, 10 de agosto de 2017

Para Liliana, la coautora espiritual y silenciosa del presente trabajo.

AGRADECIMIENTOS

La elaboración de la presente Tesis Doctoral se debe a la ayuda brindada por una gran cantidad de personas. Quiero agradecer a mi Director Principal, Dr. César Nieto Londoño, por su apoyo académico y administrativo continuo durante todo este proceso, al igual que a mi Asesor, Dr. Whady Flórez Escobar, por su disposición permanente de colaborarme. Quiero hacer un especial reconocimiento a la ayuda brindada por mi otro Asesor, Profesor Henry Power, quien desafortunadamente falleció unos meses después de concluir este trabajo; su contribución a la elaboración de la presente tesis es invaluable y sus enseñanzas académicas aún más. También agradezco al Dr. Luis Javier Cruz Riaño, la primera persona que depositó su entera confianza en mí para enrolarme por este arduo camino de la investigación académica.

En el plano personal, agradezco el apoyo de mi familia. A los miembros que se fueron y a los que aún me acompañan, un sincero agradecimiento por su comprensión y por su apoyo desinteresado. Especial agradecimiento a mis padres Iván y María Eugenia, a mi hermano Ricardo, a mi tía Marina y a mi gran abuela Carlina, de quien Dios solicitó su presencia meses después de concluir este trabajo.

El agradecimiento a Claudia Liliana Bedoya merece un punto aparte. Su tesón, paciencia, cordura, coraje, fortaleza espiritual y, ante todo, su amor desinteresado, han sembrado una base firme en el hogar sobre la cual todo es posible edificar (hasta una Tesis Doctoral laureada Summa Cum Laude). Te amo mi Papu.

Y sobre todo, Gracias a Dios.

TABLE OF CONTENT

LIST OF FIGURES viii

LIST OF TABLES xv

ABSTRACT 1

1. PRELIMINARIES. 2

1.1 Introduction 2

1.2 Problem statement and justification 5

1.3 Literature Review 9

1.3.1 General concepts 9

1.3.2 Single-scale porous media 10

1.3.3 Dual-scale fibrous reinforcements 15

1.3.4 Numerical techniques to track the fluid front 26

1.3.5 Influence of voids on the mechanical properties of composites materials 30

1.4 Objectives 34

1.5 Methodology 34

2. THEORETICAL BACKGROUND 37

2.1 Liquid Composites Molding 37

2.2 Modeling of dual-scale fibrous reinforcements 40

2.2.1 Governing equations of porous media 40

2.2.2 Governing equations for dual-scale porous media at mesoscopic scale 44

2.2.3 Governing equations for dual-scale porous media at macroscopic scale 45

2.3 Permeability and capillary 47

2.4 Boundary Element Techniques 52

2.4.1 Green identities and reciprocal relation 52

2.4.2 Boundary integral formulations 54

3. VOID FORMATION IN DUAL-SCALE FIBROUS REINFORCEMENTS BASED ON THE STOKES-DARCY FORMULATION 58

3.1 Introduction 58

3.2 Governing equations, boundary and matching conditions 62

3.3 Integral equation formulations and numerical techniques 67

3.4 Results and discussion 72

3.4.1 Validation of the BEM code for Stokes-Darcy problems 72

3.4.2 Comparison with CV/FAN approach. 76

3.4.3 Influence of processing, geometric and material variables on the void formation. 83

3.4.4 Analysis of capillary-driven and pressure-driven flow fields 95

3.5 Conclusions 110

4. VOID FORMATION IN DUAL-SCALE FIBROUS REINFORCEMENTS BASED ON THE STOKES-BRINKMAN FORMULATION 113

4.1 Introduction 113

4.2 Governing equations, matching conditions and boundary conditions 118

4.3 Integral equation formulations and numerical techniques 121

4.4 Results and discussion 125

4.4.1 Validation and comparison of the BEM approaches for Stokes-Brinkman problems. 125

4.4.2 Simulation data and void characterization 136

4.4.3 Comparison between Stokes-Darcy and Stokes-Brinkman approaches 138

4.4.4 Influence of matching conditions on the void formation for the Stokes-Brinkman approach. 148

4.4.5 Influence of RUC compaction on void formation 159

4.5 Conclusions 164

5. DYNAMIC VOID EVOLUTION IN DUAL-SCALE FIBROUS REINFORCEMENTS USING THE STOKES-DARCY FORMULATION 167

5.1 Introduction 167

5.2 Mathematical model and numerical techniques 171
5.3 Results 172
5.3.1 Stokes-Darcy approach for filling of tows assuming fully filled channels 172
5.3.2 Dynamic evolution of intra-tow void 187
5.4 Conclusions 204
6. MULTISCALE FILLING SIMULATIONS IN DUAL-SCALE FIBROUS REINFORCEMENTS 207
6.1 Introduction 207
6.2 Governing equations, boundary conditions and matching conditions 212
6.3 Integral equation formulations and numerical techniques. 213
6.4 Methodology for calculation of the sink function, S_g 215
6.5 Results and discussion 220
6.5.1 Analysis of saturation in mesoscopic simulations 220
6.5.2 Calculation of the sink function 228
6.5.3 Calculation of effective unsaturated permeability and gap permeability from BEM simulations. 245
6.5.4 Macroscopic unidirectional simulations 253
6.6 Conclusions 264
7. CONCLUDING REMARKS, CONTRIBUTIONS AND FUTURE WORKS. 268
Appendix A. 279
Appendix B. 283
Appendix C. 286
References 293

LIST OF FIGURES

Figure 1 Type of filling problems in dual-scale porous media, a) Macroscopic problem, b) Mesoscopic problem-Simultaneous impregnation, c) Mesoscopic problem-Fully filled channel. 4
Figure 2 Microphotography of fibrous reinforcements, a) Single-scale fibrous reinforcement, b) Dual-scale fibrous reinforcement..... 10
Figure 3 Triangular finite elements grid with hexagonal control volumes in the FEM/CV conforming technique. 12
Figure 4 Representation of void formation in dual-scale fibrous reinforcements. a) Microvoids inside the bundles, b) Macrovoids in the gaps. Source: Park and Lee [83] 16
Figure 5 Main physical assumptions of filling of dual-scale fibrous reinforcements. a) Case 1: Simultaneous impregnation of bundles and channels , b) Case 2: Channels completely filled before any impregnation takes place inside the bundles, c) Approach 3: Channels and bundles completely filled of liquid..... 21
Figure 6 Direct Euler integration technique. 26
Figure 7 Typical situations requiring special conditions in the characteristic equations method. a) Slope discontinuities, b) Expanding corners. 27
Figure 8 Fast marching and level set method for interface advancement. a) Fast Marching. b) Level Set. Source: Sethian [57] 28
Figure 9 Volume of fluid techniques. 29
Figure 10 General stages of LCM . a) Preforming of fibers (Optional), b) Fiber positioning, c) Compaction, d) Resin injection, e) Resin curing, f) Demolding and finishing. 39
Figure 11 General scheme of a Representative Unit Cell (RUC). 40
Figure 12 RUC's with the same porosity modeled with different laws (Darcy and Brinkman)..... 45
Figure 13 Balance of forces in the interface liquid-gas in open channels..... 50
Figure 14 Balance of forces in the interface liquid-gas in capillary tubes..... 51
Figure 15 Scheme of capillary impregnation of longitudinal bundles. 66
Figure 16 Scheme of coupled problem Stokes-Darcy with analytical solution. 72
Figure 17 Convergence of BEM solution for Stokes-Darcy problem. a) For the pressure, varying K_1/K_2. b) For the horizontal velocity, varying K_1/K_2.c) For the pressure, varying γ. d) For the horizontal velocity, varying γ. 74
Figure 18 Execution time vs. Mesh-size for Stokes-Darcy problem. 75

Figure 19 Comparison between analytical and BEM solution taking h=5×10^{-2}, K_1/K_2=10 and γ=1.29. a) Contour plots of pressure. b) Streamlines. 76
Figure 20 Mode I of the RUC configuration used in Jinlian et al. 78
Figure 21 Comparison of filling instants between BEM and CV/FAN simulations. 81
Figure 22 Stages of the filling of the RUC. 83
Figure 23 Scheme of the problem of filling of the RUC at constant flow rate. 86
Figure 24 Simulations for the parametric study using Stokes-Darcy. 89
Figure 25 Plot of Void Content vs. C_a^*. a) BEM simulations (Author), b) Experimental results of Kang, Lee & Hahn [25] c) Experimental results of Leclerc & Ruiz [77] 91
Figure 26 Detail of zones of void formation for C_a^*=1.21. 92
Figure 27 Inlet pressure vs.Time for $C_a^*=6.03\times10^{-2}$. a) Total filling, b) Before the flow reaches the weft. 97
Figure 28 Capillary pressure at the flow front for $C_a^*=6.03\times10^{-2}$, a) Before flow reaches the weft, b) After flow reaches the weft. 97
Figure 29 Inlet pressure vs. Time for C_a^*=1.21. a) Total filling, b) Before flow reaches the weft. 98
Figure 30 Capillary pressure at the flow front for C_a^*=1.21. a) Before flow reaches the weft, b) After flow reaches the weft. 98
Figure 31 Inlet velocity profiles for $C_a^*=6.03\times10^{-2}$ at several time instants. 99
Figure 32 Inlet velocity profiles for C_a^*=1.21 at several time instants. 100
Figure 33 Inlet flow rate distribution in the time for $C_a^*=6.03\times10^{-2}$. 101
Figure 34 Inlet flow rate distribution in the time for C_a^*=1.21 101
Figure 35 Velocity field for $C_a^*=6.03\times10^{-2}$ before the flow reaches the weft. 104
Figure 36 Velocity field for $C_a^*=6.03\times10^{-2}$ after the flow reaches the weft 106
Figure 37 Velocity field for C_a^*=1.21 before the flow reaches de the weft 108
Figure 38 Velocity field for C_a^*=1.21 after the flow reaches de the weft 110
Figure 39 Scheme of RUC for the problem of simultaneous filling using the Stokes-Brinkman formulation. 118
Figure 40 Scheme of problems of Brinkman admitting analytical solutions. a) Only Brinkman. b) Coupled Stokes-Brinkman. 125
Figure 41 Plot of convergence for Brinkman problem of Fig 40a. a) χ^2=[0.1,1], b) χ^2=[1,10], c) $\chi^2=[1\times10^2,1\times10^3]$ (DR-BEM), d) $\chi^2=1\times10^2$ (BEM-ISO). 126

Figure 42 Graphical comparison between analytical and numerical solutions for Brinkman problem of Fig.40a with h=5.00×10^{-2}. 127
Figure 43 Plot of convergence for Stokes-Brinkman problem of Fig. 40b. a) χ^2=1×10^3 (BEM-ISO) b) χ^2=1×10^2 (BEM-ISO), c) χ^2=18 (BEM-ISO), d) χ^2=1×10^4 (DR-BEM), e) χ^2=1×10^3 (DR-BEM) , f) χ^2=1×10^2 (DR-BEM), g) χ^2=18 (DR-BEM). 130
Figure 44 Graphical comparison between analytical and numerical solutions for Stokes-Brinkman problem of Fig. 40b with h=5.00×10^{-2}. a) χ^2=1×10^4, b) χ^2=1×10^3, c) χ^2=1×10^2, d) χ^2=18. 132
Figure 45 Velocity profiles for coupled Stokes-Brinkman problem at several mesh sizes. a) BEM/DR-BEM approach (Author). b) FEM approach [20] 135
Figure 46 Scheme of void characterization 138
Figure 47 Comparison of void formation between Stokes-Brinkman with β=1.24 and Stokes-Darcy with γ=1.27, for C_{cap}=1×10^{-2} 141
Figure 48 Detail of void formation for Stokes-Darcy and Stokes-Brinkman formulations and C_{cap}=1×10^{-2}. a) First weft (Stokes-Brinkman, β=1.24), b) First weft (Stokes-Darcy, γ=1.27), c) Second weft (Stokes-Brinkman, β=1.24), d) Second weft (Stokes-Darcy, γ=1.27) 143
Figure 49 Total fillings of RUC's in S-D and S-B for C_{cap}=1×10^{-1} and C_{cap}=5×10^{-1},a) C_{cap}=1×10^{-1} (Stokes-Brinkman, β=1.24), b) C_{cap}=1×10^{-1} (Stokes-Darcy, γ=1.27), c) C_{cap}=5×10^{-1} (Stokes-Brinkman, β=1.24), d) C_{cap}=5×10^{-1} (Stokes-Darcy, γ=1.27) 145
Figure 50 Detail of void formation for C_{cap}=1×10^{-1} in Stokes-Brinkman approach with β=1.24 . a) First weft, b) Second weft 145
Figure 51 Saturation curves for S-D and S-B formulations.a) Comparisson Stokes-Brinkman with β=1.24 vs. Stokes-Darcy with γ=1.27, b) Stokes-Darcy for C_{cap}=1×10^{-1} 147
Figure 52 Total fillings of RUC's for Stokes-Brinkman with β=0.7. a) C_{cap}=1×10^{-2}, b) C_{cap}=1×10^{-1}, c) C_{cap}=5×10^{-1} 150
Figure 53 Optical microscopic images of voids formed inside bundles, a) Cigar-shaped bubbles, b) Elliptical bubbles, c) Almost circular bubbles. Source: Hamidi et al [170] 151
Figure 54 Total filling of the RUC for the continuous-stress condition and C_{cap}=1×10^{-2} 152
Figure 55 . Comparison of saturation curves for continuous and jump stress conditions and C_{cap}=1×10^{-2} 155
Figure 56 Velocity vectors for jump-stress and continuous-stress conditions along the interface channel-tows. a) Velocity vectors for jump-stress, b) Velocity vectors for continuous-stress, c) Velocity vectors for interface channel-warp (Jump-stress), d) Velocity vectors for interface

channel-warp (Continuous-stress), e) Velocity vectors for interface channel-weft (Jump-stress), f) Velocity vectors for interface channel-weft (Continuous-stress). 157
Figure 57 Interfacial velocity profiles for continuous-stress and jump-stress conditions. a) Velocity profiles for interface channel-warp, b) Velocity profiles for interface channel-weft 158
Figure 58 Typical compaction curve of fibrous reinforcements 159
Figure 59 Total fillings of compacted RUC's for Stokes-Brinkman with β=1.24. a) $C_{cap}=1\times10^{-2}$, b) $C_{cap}=1\times10^{-1}$, c) $C_{cap}=5\times10^{-1}$ 161
Figure 60 Influence of RUC compaction on fluid front positions. a) Influence of inter-tow distance on fluid front positions according to Yang et al [22] b) Comparison between the minimum fluid front positions in the warps of C-D and R-D (Author) 162
Figure 61 Scheme of the mesoscopic problem assuming full-filled channels 173
Figure 62 Instants of tow filling with the traditional approach. a) Warps and weft unsaturated, b) Total saturation of warps, c) Total saturation of the RUC 175
Figure 63 Instants of tows filling with the current Stokes-Darcy approach assuming full air compressibility. a) Warps and weft unsaturated, b) Total saturation of warps, c) Instant of end of compression and onset of void mobilization, d) Motion towards right extreme of the weft, e) Detail of Figure 63d, f) Arrival of bubble to right extreme of the weft and onset of void migration, g) Detail of Figure 63f, h) Stage 1 of void migration, i) Stage 2 of void migration, j) Stage 3 of void migration (until bubble is in the neighborhood of the RUC's edge), k) Detail of void migration ... 180
Figure 64 Velocity field and streamlines when bubble is compressing. a) Velocity field and streamlines for the channel domain, b) Detail 1 of Fig. 64a, c) Detail 2 of Fig. 64a, d) Velocity field for the weft domain, e) Detail 1 of Fig. 64d, f) Detail 2 of Fig. 64d, g) Detail 3 of Fig. 64d, h) Streamlines for the weft domain 184
Figure 65 Velocity field and streamlines when bubble is partially escaping. a) Velocity field and streamlines for the channel domain, b) Detail of Fig. 65a, c) Velocity field and streamlines for the weft domain, d) Detail 1 of Fig. 65c, e) Detail 2 of Fig. 65c, f) Detail 3 of Fig. 65c, g) Detail 4 of Fig. 65c 187
Figure 66 Plot of Unsaturated Volume vs. t/t_{inj} for several inlet flow rates. Source: Guorichon et al [5] 189
Figure 67 Instants of air migration from the tows towards the channel for the Case 1 (Reported values of P_{air}, r_1 and $\langle S_g^v \rangle_{norm}$ in each figure correspond to the last bubble front). a) $t/t_{total}=0.112$, b) $t/t_{total}=0.476$, c) $t/t_{total}=0.765$, d) $t/t_{total}=0.922$, e) $t/t_{total}=1.0$ 192

Figure 68 Relationship between the void velocity in channel, $\langle u_v \rangle$ and the resin velocity, $\langle u_g \rangle^g$. Source: Park et al. [79] 192
Figure 69 Behavior of r_1 and $\langle S_g^v \rangle_{norm}$ in the time for the Case 1. a) Plot r_1 vs. t/t_{total} for Case 1, b) Plot of $\langle S_g^v \rangle_{norm}$ vs. t / t_{total} for Case 1 193
Figure 70 Instants of air migration from the tows towards the channel for Case 2, λ=16mN/m (Reported values of P_{air}, r_1 and $\langle S_g^v \rangle_{norm}$ in each figure correspond to the last bubble front). a) From t / t_{total} =0 to t / t_{total} =0.325, b) From t/ t_{total} =0.363 to t/ t_{total} =0.423, c) From t/ t_{total} =0.504 to t/ t_{total} =0.692, d) From t/ t_{total} =0.764 to t/ t_{total} =1.0 196
Figure 71 Behavior of r_1 and $\langle S_g^v \rangle_{norm}$ in the time for the Case 2, λ=16 mN/m. a) Plot r_1 vs. t/t_{total}, b) Plot of $\langle S_g^v \rangle_{norm}$ vs. t/t_{total} 197
Figure 72 Representation of not void migration for λ=20mN/m, $\langle P_g \rangle^g$=102kPa and $\Delta P/\Delta x = 5.83 \times 10^3$ kPa/m 198
Figure 73 Effect of increment of the pressure gradient, $\Delta P/\Delta x$, on the void migration. a) Small compression of the bubble, b) Displacement and expansion of the bubble, c) Expansion of the bubble, d) Contraction and splitting of the bubble (From darker to lighter line). 200
Figure 74 Process of stepwise void elimination. a) Initial splitting, b) Second stage of compression, c) Second stage of mobilization towards the right extreme of the weft, d) Second stage of void migration, e) Second migration and subsequent splitting, f) Third stage of compression (red lines and red arrow) and subsequent mobilization towards the right extreme of the weft (green lines and green arrow), g) Third stage of void migration, h) Third migration and subsequent splitting, i) Comparison between the initial (green line) and the final (red line) bubble inside the weft after three splittings. 202
Figure 75 Effect of increment of average pressure, $\langle P_g \rangle^g$, on the void migration. a) Bubble contraction, b) Bubble displacement, c) Migration of the bubble 204
Figure 76 Typical pressure profiles in unidirectional injections for dual-scale fibrous reinforcements. a) Linear-Concave, b) Linear-Convex, c) Linear-Convex-Concave. Source: Park et al [83] 218
Figure 77 Comparison of saturation curves obtained by the classical methodology. a) RUC geometry of Wang and Grove [225], b) RUC geometry of Tan [12], c) RUC geometry of this work, d) Saturation curve of Wang and Grove [225], e) Saturation curve of [12], f) Curve S_t vs. τ of this work 223
Figure 78 Influence of the total saturation, S_t, on the inlet velocity profile 224

Figure 79 Difference between the inlet and outlet velocities for several values of S_t 225
Figure 80 Influence of S_t on $(\langle u_g \rangle^g)^*$ 225
Figure 81 Influence of $\langle P_g \rangle^g$ on the inlet and outlet velocities. a) Low saturation (S_t=0.235), b) Medium saturation (S_t=0.554), c) High saturation (S_t=0.893). 226
Figure 82 Influence of $\langle P_g \rangle^g$ on $(\langle u_g \rangle^g)^*$ for several values of S_t and $\Delta P/\Delta x$=5.83×10^3 kPa/m 227
Figure 83 Influence of the pressure gradient on $(\langle u_g \rangle^g)^*$ 227
Figure 84 Influence of $\langle P_g \rangle^g$ and $\Delta P/\Delta x$ on the saturation curve S_t vs. t^* 231
Figure 85 Plots of S_t vs τ using the proposed methodology, a) For λ<1 (Partial or total air dissolution), b) λ=1 (Full air compressibility) 233
Figure 86 Influence of vacuum pressure on the equilibrium time and equilibrium saturation..... 234
Figure 87 Plot of t_{eq} vs. $T' = \mu / |P_{vac} - \langle P_g \rangle^g|$ 235
Figure 88 Plots of the regression model for S_t^{eq}. a) Plots of S_t^{eq} vs. $|P_{vac}|$ for several values of $\langle P_g \rangle^g$, b) Plot of slope, m, vs $\langle P_g \rangle^g$, c) Plot of intercept ,b, vs $\langle P_g \rangle^g$, d) Verification of the regression model of S_t^{eq} vs $\langle P_g \rangle^g$ with P_{vac}=-75kPa 236
Figure 89 Comparison between direct and indirect procedures for the calculation of S_g..... 237
Figure 90 Comparison between fitting models of the sink term, S_g. a) Original fit model for λ=1, $\langle P_g \rangle^g$=202kPa and P_{vac}=-75kPa, b) Original fit model for λ=0.5, $\langle P_g \rangle^g$=162kPa and P_{vac}=-25kPa, c) Original fit model in the work of Wang and Grove [225], d) Improved fit model for λ=1, $\langle P_g \rangle^g$=202kPa and P_{vac}=-75kPa, e) Improved fit model for λ=0.5, $\langle P_g \rangle^g$=162kPa and P_{vac}=-25kPa. . 239
Figure 91 Plots to find the fitting coefficients of the sink function, S_g, for λ=1. a) A_1 vs $\langle P_g \rangle^g$ for several values of P_{vac}, b) b_1 vs $|P_{vac}|$, c) A_1 vs $|P_{vac} - \langle P_g \rangle^g|$, d) A_2 vs $\langle P_g \rangle^g$ for several values of P_{vac}, e) m_2 vs $|P_{vac}|$, f) b_2 vs $|P_{vac}|$, g) A_3 vs $\langle P_g \rangle^g$ for several values of P_{vac}, h) A_3 vs $|P_{vac} - \langle P_g \rangle^g|$, i) A_4 vs $|P_{vac} - \langle P_g \rangle^g|$ 244
Figure 92 Influence of $\langle P_g \rangle^g$ and $\Delta P/\Delta x$ on K_g and K_{eff}. a) Plot of K_g vs. $\langle P_g \rangle^g$ for several values of $\Delta P/\Delta x$, b) Curves K_{eff} vs S_t for several values of $\Delta P/\Delta x$ and $\langle P_g \rangle^g$, ε_t=0.15, c) Curves K_{eff} vs S_t for several values of $\Delta P/\Delta x$ and $\langle P_g \rangle^g$, ε_t=0.46..... 247
Figure 93 Influence of the tow porosity, ε_t, on the curve of K_{eff} vs S_t 248
Figure 94 Influence of weft geometry on the gap permeability, K_g. a) Influence of aspect ratio of the weft on the gap permeability, b) Influence of the gap porosity on the gap permeability 252
Figure 95 Influence of weft geometry on the effective permeability, K_{eff}. a) Influence of the weft aspect ratio on the curve of K_{eff} vs S_t, b) Influence of the gap porosity on the curve of K_{eff} vs S_t. 252

Figure 96 Scheme of unidirectional filling of dual-scale fibrous reinforcements in molds. Source: Zhou, Alms and Advani [101] 254
Figure 97 Plots of convergence for the solution of macroscopic unidirectional filling using the present DR-BEM scheme, a) L^2 relative error norm vs Mesh-size for the fluid front positions, b) Relative error, E, vs. Mesh-size for the length of the partially saturated region. 255
Figure 98 Comparison between the analytical and DR-BEM non-dimensional fluid front positions for macroscopic unidirectional injections at constant pressure. 256
Figure 99 Curves of saturation for *Serie 1*, a) Coincidence of curves having the same air entrapment parameter, λ, when λ<1 , b) Influence of the air entrapment parameter, λ, and injection pressure, P_{inj} 259
Figure 100 Curves of saturation for *Serie 2*, a) Coincidence of curves having the same air entrapment parameter, λ, when λ<1, b) Influence of the air entrapment parameter, λ, and vacuum pressure, P_{vac} 260
Figure 101 Curves of saturation for *Serie 3*, a) Coincidence of curves having the same air entrapment parameter when λ<1, b) Influence of the air entrapment parameter, λ, and injection flow rate, Q_{inj} 262
Figure 102 Pressure profiles for unidirectional fillings of dual-scale fibrous reinforcements, a) Constant pressure regime (Figure 99a, λ=0), b) Constant flow rate regime (Figure 101a, λ=0)..... 264

Figure A1 Scheme of EIS transformation 279

Figure C 1 Scheme of tracking of the fluid front 287
Figure C 2 Plots of C_{CFL} vs. C_a^* 288
Figure C 3 Plots of C_{CFL} vs. C_{cap} 288

LIST OF TABLES

Table 1 Differences and contributions of the present work regarding previous works. 7
Table 2 Summary of works of modeling and simulation in dual-scale fibrous reinforcements (1) .. 22
Table 3 Summary of works of modeling and simulation in dual-scale fibrous reinforcements (2) .. 24
Table 4 Assessment of accuracy of the BEM algorithm for Stokes-Darcy problem 73
Table 5 Variation of the final void size with the anisotropy degree, K_1 / K_2 82
Table 6 Simulation data for the reference case *(Serie 1)* in Stokes-Darcy formulation 88
Table 7 Void characterization of all simulations of parametric study Stokes-Darcy (Note: for $C_a^*=6.03\times10^{-2}$ no void formation was obtained) 88
Table 8 Data to run the simulations of Brinkman problem of Fig 40a 126
Table 9 Data to run the simulations of Stokes-Brinkman problem of Fig 40b 128
Table 10. Characteristics of meshes and L^2 relative error norms of BEM/DR-BEM solution 133
Table 11 Simulation data for the reference case (*Serie 1*) in Stokes-Brinkman formulation 138
Table 12 Characterization of final voids for S-B with β=1.24 and S-D with γ=1.27 146
Table 13 Influence of β and C_{cap} on the void size 151
Table 14 Influence of β and C_{cap} on the void shape. 151
Table 15 Influence of compaction and C_{cap} on the void size. 164
Table 16 Influence of compaction and C_{cap} on the void shape. 164
Table 17 Simulations data for comparison between the classical and the present approach for tows filling assuming full filled channels 174
Table 18 Data of simulations of tows filling with the classical methodology 222
Table 19 Filling times obtained from BEM simulations with the classical methodology 222
Table 20 Ratio $\langle|\tilde{u}_g|\rangle^g / \langle u_g\rangle^g$ for filling instants of Fig. 63a-j. 227
Table 21 Series of simulations for the determination of the sink function, S_g 229
Table 22 Fitting coefficients of the regression model for S_g 244
Table 23 Values of m_ψ and b_ψ for the fitting coefficients when λ<1. 244
Table 24 Additional simulations to study the influence of ε_t and the weft geometry on K_g and K_{eff} 248
Table 25 Influence of the tow porosity, ε_t, on $\langle\hat{u}_l\rangle$ for two levels of total saturation, S_t. 251
Table 26 Data for comparison between the analytical and DR-BEM results of macroscopic unidirectional simulations. 255

Table 27 Data of macroscopic unidirectional simulations considering the lumped function for the sink term, S_g..... 257

ABSTRACT

Boundary Element Techniques are implemented in the simulation of the impregnation phenomenon of dual-scale porous media used in the processing of composites materials at both mesoscopic (filling of Representative Unitary Cells) and macroscopic scales (filling of cavities). Three kinds of problems are considered: 1) Simultaneous filling of channels and bundles to study the void formation in Representative Unitary Cells (RUC´s) at constant inlet pressure and constant inlet flow rate regimes, based on the Stokes-Darcy (S-D) and Stokes-Brinkman (S-B) formulations, 2) Filling of bundles considering fully filled channels, based on the Stokes-Darcy formulation, to study the dynamic evolution of voids (compression, motion, migration and splitting), to determine sink functions that account for the partial saturation effects and to analyse the influence of the saturation level on the effective unsaturated permeability, 3) Unidirectional filling of cavities considering the partial saturation effects by means of a lumped strategy, based on an Equivalent Darcy formulation. All numerical codes are validated with classical coupled problems free fluid-porous media and the moving boundary simulations are compared with numerical and experimental results previously reported in the literature. The first kind of problem is tackled in Chapters 3 and 4, where tracking algorithms that generate the exact fluid front shape are developed, as well as a flow-direction dependent model for the capillary pressure. According to the numerical results, the size and shape of the voids are influenced by some processing, material and geometric variables, as well as by the formulation type (S-D and S-B), matching conditions and RUC compaction. On the other hand, Chapter 5 deals with part of the second problem abovementioned. Numerical results show that the dynamic evolution of intra-tow voids is highly influenced by the mechanical pressure, capillary properties and pressure gradient, which is in agreement with previous experimental works. Finally, part of the second problem and the whole third problem are deemed in Chapter 6, where multi-scale filling simulations are performed using a lumped strategy. In this chapter, lumped sink functions in terms of several volume-averaged variables are found by running several filling simulations at mesoscopic scale and using fitting models. Those functions are then used in the macroscopic equations to account for the influence of the sink effect in the behavior of the global saturation, global pressure and time evolution of the fluid front position, obtaining some results that are in agreement with previous works.

1. PRELIMINARIES.

1.1 Introduction

The phenomenon of infiltration of fluids into porous structures has a wide range of applications, from the permeation of underground soils by water and the extraction and filtration of oil, passing through the processing of advanced composites materials, to the impregnation of biological systems by several sorts of liquids. For instance, in the particular case of the processing of composites materials, some specific applications could be mentioned, namely, the filling of cavities and void formation in fibrous reinforcements, which are key issues in the manufacturing of parts by Liquid Composite Molding (LCM) processes, the infiltration of high conductivity phase-change fluids into foams for the development of thermal energy storage composites (TES), the fabrication of pre-impregnated rigid cores for thermal and/or acoustic insulation, among other applications.

According to the different orders of permeability that are present at the mesoscopic scale of a porous medium, such medium can be classified into single-scale or dual-scale porous medium. In a single scale porous medium, there is only one scale of permeability in the Representative Unit Cell (RUC); conversely, a dual-scale porous medium comprises two scales of permeability, which can be different each other by several orders of magnitude. In some specific situations, the macroscopic behavior of a dual-scale porous medium could be approximated to the one of an equivalent single-scale medium considering the macroscopic permeability in the modeling of the infiltration phenomenon; however, in other cases, the imbalances of flow that take place inside the RUC due to the dissimilar permeabilities of different sub-domains have a strong influence on the macroscopic behavior of the flow. For instance, in the particular case of fibrous reinforcements employed in LCM processes, a very low tow porosity and a very small space between the tows inside the RUC leads to a behavior analogous to a single-scale porous medium, contrary to what happens when the tow porosity is intermediate to high and/or the size of the gaps between the tows is significant [1], [2], where the flow imbalances inside the RUC have an important influence on the macroscopic behavior of the flow.

The phenomenon of filling of dual-scale porous media can be divided into two main problems: the filling of a Representative Unit Cell (RUC) having a specific architecture and

regions of different permeabilities (Figure 1 b-c) [3]–[10] and the filling of cavities at macroscopic scale taking into account the effects produced by the imbalances of flow inside the RUC's (mesoscopic scale) (Figure 1a) [5], [8], [11]–[14]. The FEM/CV technique is, by far, the most used in the simulations of both kinds of problems, as it is shown in the Literature Review of the present work. BEM-based and mesh-free techniques have been used in similar problems, but most of the works using these kinds of techniques have not considered the anisotropy of the porous bodies inside the RUC and the moving boundaries (fluid fronts), being those cases the most common in the processing of composites because they replicate the real conditions of manufacturing of parts. Regarding the works that consider the influence of the saturation level on the macroscopic filling of cavities and make use of BEM-based techniques, it is important to mention that most of them have assumed that the permeability can be represented in terms of the saturation level by known constitutive models [15]–[18]; this approach could be appropriate for the infiltration of certain types of porous media for which several experimental relationships permeability-saturation have been previously established (like the retention curves for soil-water systems), but it is not applicable for other types of porous media like the ones treated in the present work. Thus, the influence of the saturation on the effective unsaturated permeability needs to be determined from the mesoscopic simulations because no constitutive relationships are known a priori for dual-scale fibrous reinforcements used in composites.

Summarizing, the simulation of the infiltration of dual-scale porous media in the processing of composites materials poses several physical challenges. From the point of view of the mesoscopic simulations *(simulations of RUC filling)*, there are many applications where the anisotropic nature of the porous bodies and the moving-boundary character of the problem cannot be omitted, which implies an additional complexity in the problem; besides, due to the non-static character of the problem *(moving-boundary)*, both the capillary pressure in the fluid front and the mass transfer between subdomains of different permeabilities need to be considered. From the point of view of the macroscopic simulations *(simulations of filling of porous cavities)*, the main challenge lies in the consideration of the influence of the partial saturation that takes place inside the RUC's (which is caused by the dual-scale nature of the porous medium) on the global impregnation of the cavity, taking into account

that constitutive equations permeability-saturation are not well-defined for dual-scale fibrous reinforcements.

In view of the aforementioned aspects, the present research is addressed to the application of Boundary Element Techniques in the simulation of the impregnation phenomena in dual-scale fibrous reinforcements used in the processing of composite materials. After an extensive literature review, it could be concluded that these techniques have not been implemented yet for this particular application. In general, three kind of problems are considered here: 1) Simultaneous filling of channels and tows, Figure 1b, to study the void formation in RUC's at constant inlet pressure and constant inlet flow rate regimes, based on the Stokes-Darcy and Stokes-Brinkman formulations, 2) Filling of bundles considering full filled channels, Figure 1c, based on the Stokes-Darcy formulation, to study the dynamic void evolution (compression, displacement, migration and breaking), to determine a sink function that accounts for the partial saturation effects and to analyse the influence of the saturation level on the effective unsaturated permeability, 3) Filling of cavities considering the partial saturation effects by mean of a lumped strategy, Figure 1c, based on an Equivalent Darcy formulation. A deeper description of each one of these problems is done in the Introduction of each chapter of the present work.

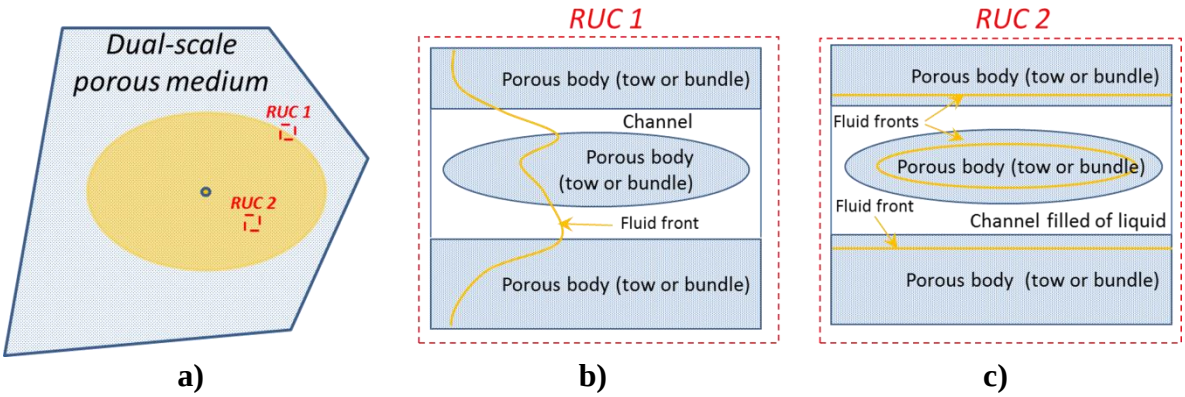

Figure 1 Type of filling problems in dual-scale porous media, a) Macroscopic problem, b) Mesoscopic problem-Simultaneous impregnation, c) Mesoscopic problem-Fully filled channel.

1.2 Problem statement and justification

The processing of composites materials is an engineering area that has aroused interest in the last thirty years in the scientific community. The development of new processing techniques and the improvement of the existing ones are tightly linked to the advancement of the simulation methods. In that area, one of the principal concerns is the dual-scale nature of some fibrous reinforcements that are used in the manufacturing of parts by Liquid Composite Molding (LCM), because such a nature supposes imbalances of flow inside the Representative Unit Cell (RUC), which, in turn, cause uncontrolled defects and could considerably affect the global behavior of the flow during the filling of cavities. Due to the increasing interest in the modeling and simulation of the filling phenomenon in dual-scale reinforcements, recent works have been developed in that subject using mainly FEM/CV or commercial FEM-based software, as it will be detailed in the Literature Review. Some works that make use of BEM techniques have been also developed for infiltration of porous media, but the partial saturation effects inside the RUC have been taken into account implicitly by using constitutive laws of permeability-saturation, which are not applicable in this case.

As it was aforementioned, the simulations of filling of dual-scale porous media applied to composites processing can be classified into two main categories: mesoscopic simulations (Figure 1b-c) and macroscopic simulations (Figure 1a). After doing a review of representative researches in that area, several open issues were identified; these issues are the focus of the present work and can be summarized in the following questions:

At the mesoscopic scale:

- What is the influence of the processing, geometric and material variables on the void formation?
- How does the injection regime (constant pressure or constant flow rate) affect the void formation?
- Do the formulation type (Stokes-Darcy or Stokes-Brinkman) and/or the interface matching conditions have any influence on the void formation?
- What is the influence of the RUC compaction on the void formation?

- How do the average pressure, pressure gradient and surface tension affect the dynamic void evolution? It is possible to remove the bubbles from the bundles towards the channel? Which variables are involved in that process?
- How does the effective unsaturated permeability behave with the saturation level, porosity of bundle and RUC geometry?

At the macroscopic scale:

- How do the vacuum pressure, air entrapment parameter and capillary pressure influence the impregnation of dual-scale porous media at macrosocopic scale? It is possible to obtain a function accounting for the partial saturation effects (sink function) that considers these parameters?
- How do the partial saturation effects influence the velocity and pressure fields at macroscopic scale?
- What is the influence of the injection regime (constant pressure or constant flow rate) on the behaviour of the global saturation?

The consideration of these problems using BEM-based computational simulations involves several numerical challenges, which are briefly mentioned in the following bullets:

- The solution of problems of coupled sub-domains with very dissimilar permeabilities usually implies ill-conditioned systems and special solvers could be required.
- The BEM solution of the anisotropic Brinkman equation is not yet a closed problem since several strategies can be implemented.
- The constant flow rate regime entails a defective boundary condition, which implies a special treatment.
- The consideration of the capillary effects in both the channels and the tows supposes others numerical challenges. Firstly, a flow direction-dependent equation for the capillary pressure in the porous media needs to be deduced here in order to avoid using experimental shape factors as done by other authors. On the other hand, the numerical errors associated to the calculation of the curvature of the channel fluid front can have a relevant influence on the calculation of the time step used to advance the moving interface when using a direct integration scheme.

- The use of a lumped strategy to tackle multiscale problems in dual-scale porous media implies the deduction of sink functions in terms of several variables, which in turn involves a considerable amount of simulations.
- The tracking of the fluid front is not a trivial problem here since several constraints shall be imposed to the time step in order to avoid physical inconsistencies or the magnification of numerical errors. Smoothing and remeshing algorithms are also required.

Some differences and contributions of the present research regarding other works in the field of composites processing can be identified in Table 1. A detailed description of these differences and contributions is done in the development of the subsequent chapters.

Table 1 Differences and contributions of the present work regarding previous works.

Type	Previous works	Present work
Numerical formulation for modelling the void formation in RUC's	Darcy- Darcy, with equivalent permeability for the channels. Navier Stokes equation modified with permeability and capillary source terms that activate in the bundles	*Stokes-Darcy and Stokes-Brinkman*
Numerical technique to solve the governing equations	Mostly *FEM/CV techniques,* which imply the use of at least one domain mesh	*BEM techniques,* where only one contour mesh is required
Numerical techniques to track the fluid front position	Mostly *VOF or Level Set,* which imply the reconstruction of the fluid front by interface capturing schemes	*Euler integration of kinematic condition and Smoothing and remeshing algorithms,* which brings a higher order accuracy of the fluid front shape
Simultaneous capillary effects in channels and bundles	Not considered to the best of the author's knowledge	Considered

Influence of the flow orientation on the capillary pressure in the bundles	It has not been considered in some works, whereas experimental shape factors have been used in others.	A flow orientation-dependent formula is deduced for the capillary pressure in the bundles.
Influence of the type of formulation, Stokes-Darcy or Stokes-Brinkman, on the void formation	Not considered before to the best of the author's knowledge	Considered
Influence of interface matching conditions channel-bundles on the void formation	Not considered before to the best of the author's knowledge	It is considered the influence of the slip coefficient for the Stokes-Darcy formulation and the jump stress coefficient for the Stokes-Brinkman formulation.
Influence of type of regime on the void formation at mesoscopic scale	Not considered before to the best of the author's knowledge	It is considered the influence of two types of regimes: Constant inlet pressure and constant inlet flow rate.
Coupling between mesoscopic and macroscopic simulations using a lumped strategy	The Sink function has been obtained in terms of the averaged pressure and the saturation degree only	The Sink function is obtained in terms of the averaged pressure, saturation degree, vacuum pressure and air entrapment parameter, considering implicitly the capillary pressure in the porous media.
Methodology to obtain the sink function	*Traditional methodology:* It is prescribed a uniform pressure in the channels. The filling of the tows depends on the prescribed pressure and on the fluid front pressure, which are assumed constant during the whole filling.	*Proposed methodology:* Prescription of a pressure gradient along the channel to be consistent with the fluid motion direction. The filling of the tows depends on the matching conditions between coupled domains, channel-bundles, and on the fluid front pressure, which varies according to the air compressibility, air dissolution and capillary pressure.

Analysis of dynamic void evolution: Compression, motion, migration and breaking	Most of works have focused in the possible paths of void migration, particularly along the channels	The present work is focused in the conditions that brings about the void migration from the bundles towards the channels and the subsequent void splitting
Study of effective properties of dual-scale fibrous reinforcements	Study of the influence of the bundle porosity and RUC geometry on the effective *saturated* permeability of dual-scale fibrous reinforcements	Study of the influence of bundle porosity and RUC geometry on the relationship between the effective *unsaturated* permeability and the saturation degree of dual-scale reinforcements

1.3 Literature Review

The following Literature Review is a compilation of the principal researches that have focused on the study of the phenomenon of infiltration in fibrous reinforcements, and some other relevant works that have dealt with similar problems, whose numerical implementations could have a potential application in this topic. Firstly, the numerical techniques that have been employed to solve the governing equations of single-scale porous media are presented and classified into three families: domain-meshing, boundary-meshing and mesh-free techniques. Afterwards, a summary of some progresses in flow modeling and simulation in dual-scale porous media to predict formation of voids and their dynamic evolution is presented. Moreover, the principal numerical techniques to track the fluid front are briefly explained as well, and finally, a concise State of the Art on the influence of the voids on the mechanical properties of composites is presented. The present Literature Review does not give details of each work, but, as the present dissertation develops, further details about some works are outlined in each chapter.

1.3.1 General concepts

In single-scale porous media, it is only considered one scale for the impregnation phenomenon; hence, it is only recognized one domain at the mesoscopic scale that includes fibers and inter-fiber spaces as a whole for flow analysis purposes (Figure 2a). On the contrary, in dual-scale porous media, the scale of permeability of the channels or gaps is

from one up to several orders of magnitude larger than the scale of permeability of the tows or bundles (Figure 2b); consequently, the analysis of flow shall consider both the governing equations of the channels and the bundles and the interface conditions between these domains. In general, for the channels domain, the Navier-Stokes equation can be applied, and, in the particular case of small pore Reynolds numbers, which is very common in the processing of composites, the model can be simplified to the Stokes equation [19]. For the bundles or tows, the flow can be modeled using the Brinkman or the Darcy equation [20]–[24].

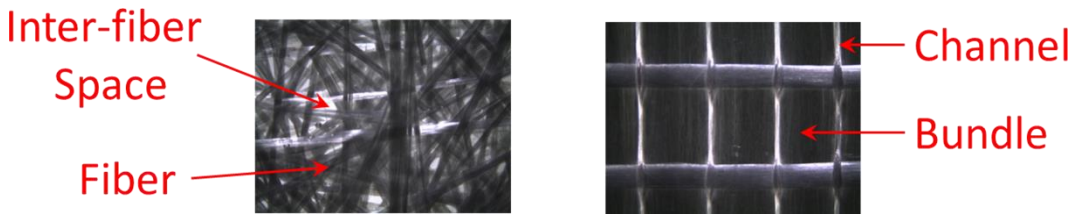

Figure 2 Microphotography of fibrous reinforcements, a) Single-scale fibrous reinforcement, b) Dual-scale fibrous reinforcement.

In dual scale porous media, they are distinguished two kinds of flows: the macroscopic flow and the microscopic flow. The macroscopic or principal flow takes places in the channels and the corresponding permeability is the macroscopic or gap permeability (the permeability after assuming that the bundles are impermeable). The microscopic flow takes place inside the bundles and it is driven by both mechanical and capillary pressure. The permeability associated to this impregnation is known as microscopic or tow permeability [25]. The unbalance between those flows entails several consequences: at the mesoscopic level, this unbalance is responsible for the formation of voids by mechanical entrapment of air; at the macroscopic level, it could originate changes in the behavior of some macroscopic variables due to the arising of sink and source terms in the governing equations [26], [27].

1.3.2 Single-scale porous media

Some representative works of filling simulation in single-scale porous media are presented because they constitute the base of the works of simulation in dual-scale fibrous reinforcements.

***Domain-meshing techniques*.**

Finite Difference Method (FDM) was one of the first employed for simulating the filling of fibrous reinforcements in the processing of composites [28], [29]. It is an adequate method in two-dimensional geometries with very regular boundaries, but it turns problematic as the geometric complexity augments; therefore, it is not usable in many industrial applications. Pure finite element methodologies have been also developed, but they do not enforced mass conservation on the boundaries between adjacent elements. For instance, a methodology based on an alternate form of the mass conservation equation in terms of a fill factor and including temporal variations was proposed in [30]. This methodology implies the simultaneous transient solution of the fill factors and the pressure field, which demands additional computational costs regarding other finite element-based techniques, where a quasi-steady approach is considered, as is the case of FEM/CV techniques.

The FEM/CV schemes are widely used in filling simulations of fibrous reinforcements. The principal argument of the FEM/CV schemes is to solve the governing equations for the pressure field by using the finite element method and to track the fluid front by considering filling factors in control volumes [31], [32]. There are two remarkable types of FEM/CV schemes, which are the base of the principal commercial software for filling of parts in composites: FEM/CV conforming and FEM/CV non-conforming.

The FEM/CV conforming scheme was initially implemented at the beginning of nineties in [33], [34]. In this scheme, since the mass conservation is not locally preserved at the element level, a control volume, CV, should be assigned to each node of the FEM grid to enforce a mass flux balance. In the two-dimensional case, the triangular finite elements with hexagonal control volumes is the most common mesh configuration; the hexagons are conformed from the centroids of the FE triangles and from the midpoints of the edges, as it is shown in the Figure 3. The general steps of this scheme are the next ones [35]:

- The control volumes (CV's) are generated from the finite element grid, and the porous volume of each CV shall be computed.
- At the beginning of the simulation, the CV's contiguous to the inlet ports are considered completely saturated. In the subsequent time instants, the saturated region is determined from the filling factors of the CV's.

- Using the boundary conditions, the pressure is calculated in the nodes of the finite element mesh corresponding to the saturated domain. The resultant system is modified with the intention to annul the pressure in empty or partially filled CV's in order to impose zero pressure condition in the fluid front [36].
- Once the pressure is computed in all finite element nodes, pressure gradients can be approximated using a finite difference scheme and the velocity is then calculated by Darcy law. This velocity is discontinuous in the boundaries of the elements, which originates the necessity to use CV's for imposing a local mass balance [36].
- The net flow in a CV is computed from the contributions of the associated finite elements, taking into account the normal components of the velocities to the edges of each CV.
- The time increment is chosen in such a way that at least one CV becomes fully saturated. If longer increments are used, a violation of the principle of mass conservation occurs, and for shorter times, the fluid front position could not be significantly affected [33].
- Once the time increment is determined, the filling factor in all control volumes can be updated and the fluid front position is established by mean of interface capturing schemes.
- The steps are repeated until the cavity is completely filled.

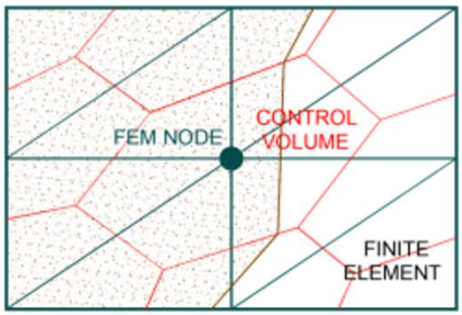

Figure 3 Triangular finite elements grid with hexagonal control volumes in the FEM/CV conforming technique.

The FEM/CV conforming scheme is the base of the commercial software LIMS^{TM}, developed in the University of Delaware. Some important complex simulations of filling of parts using this software can be found elsewhere [37]–[39].

Alternatively to FEM/CV conforming, a single local mass conservative CV scheme has been implemented for the filling of fibrous reinforcements [3]. This scheme uses non-structured CV elements with generalized Finite Differences to evaluate the fluxes in terms of linear polynomial interpolation of the pressure field; no auxiliary elements in the mesh are required, but the convergence rate decreases regarding the one of the FEM/CV conforming. On the other hand, the FEM/CV non-conforming scheme has a similar convergence rate to the FEM/CV conforming and no auxiliary CV's are required since the Finite Elements operate also as Control Volumes [40]. In this scheme, the filling factor is related with the level of saturation of the finite elements and the interpolation functions of the pressure are selected in such a way that the continuity of velocities on the boundaries of the elements is achieved at expenses of obtaining discontinuous pressures with exception of the midpoints [40], [41]. It has been demonstrated that FEM/CV non-conforming algorithms converge faster than FEM/CV conforming ones if the mesh size is properly selected [42]. Software PAM-RTM^{TM}, developed in the École Polytechnique of Montréal, works using the FEM/CV non-conforming scheme. Some representative works using this software have been developed in [41], [43], [44].

Boundary-meshing techniques.

Specific researches about simulations of LCM processes using boundary-meshing methods are not as extensive as the ones done by domain-meshing techniques. However, a considerable amount of similar elliptic problems of heat transfer, groundwater infiltration and elastic response of anisotropic materials have been modeled by the former kinds of techniques, and some authors have applied those procedures to the simulation of the filling phenomenon in LCM processes [45]–[48]. The boundary element method (BEM) has been applied to the simulation of the infiltration of fiber reinforced preforms in [45], [46], [48]–[53]; in some works, it has been found that mass unbalances could arise depending on the number of nodes lying on the boundaries [52]–[54].

BEM techniques for homogeneous porous media .

A second order elliptic problem in homogenous porous media was tackled by Clements [55], [56] using BEM and the resulting integral formulation was applied next to the

infiltration of single-scale reinforced preforms in [46], where the level set method proposed by Sethian [57] was employed to track the fluid front in isotropic media. A similar research was executed in [58] for homogeneous anisotropic preforms using the quasi-isotropic equivalent system (EIS) proposed by Adams, Russell and Refenbeld [59], by mean of which the anisotropic domain can be transformed into an isotropic one and the Laplace equation emerges in the transformed domain.

BEM techniques for heterogeneous porous media.

The change of the porosity in porous media causes the modification of all volume-averaged properties. In the case of the filling phenomenon of fiber reinforced preforms, the main property is the permeability. When spatial heterogeneities appear, a domain integral also appears in the integral formulation of the problem and the handling of that domain integral is just what distinguishes one numerical scheme from another one.

If the porous medium is isotropic and stepwise homogeneous, the multi-zone BEM formulation employed in [60] can be used. In this formulation, they are considered localized homogeneous zones and compatibility equations are applied between these zones. If the medium is isotropic and the permeability varies in the space as a known function, the domain integral can be divided into small homogeneous sub-domain integrals that can be solved by numerical methods; this procedure was used for the simulation of the infiltration of water into underground beds [61] and its principal disadvantages is specifically the discretization of the domain. One remarkable work focused on the simulation of the RTM process with heterogeneous preforms was developed using the BEM and the perturbation techniques of Rangoni [62] to deal with the domain integral [45]; in that work, the transformed potential is expanded by mean of perturbation series, being the major disadvantage of this scheme the robustness added by those series. One of the most common methods to deal with the domain integral is the Dual Reciprocity Boundary Element Method (DR-BEM) proposed by Partridge, Brebbia and Wrobel [63] and employed in [64] for simulating the groundwater infiltration of isotropic media applied to civil constructions.

With respect to anisotropic and heterogeneous porous media, two main ways to tackle second order elliptic problems by BEM are identified: 1) to develop generalized fundamental solutions that annul the domain integral [65], [66], where a forced function is

introduced in place of the Dirac delta function in the singularly forced equation, and 2) to use fundamental solutions of homogeneous media and treat the resulting domain integral by the DR-BEM [67], [68]. The assessment of the approximation functions used in the DR-BEM for this kind of problems can be found in Zhang and Zhu [69] and Partridge [70]. Recent works using DR-BEM for filling of cavities in the RTM process can be found in [53], [71].

Mesh-free techniques.

One meshfree technique that has been used in the simulation of the filling of single-scale porous media is the Method of the Natural Elements (NEM) [47], [72], where some trial and test functions are constructed using natural neighbor interpolants and those interpolants are built on the basis of the Voronoi tessellation and computed numerically by using the Delaunay triangulation. Among the different possibilities, the NEM allows extracting the shape of the saturated domain and the position of the moving interface by employing a cloud of nodes only [73]. The NEM is an attractive numerical alternative, because of its ability to integrate transport equations and its meshfree character.

1.3.3 Dual-scale fibrous reinforcements

Macro-voids and micro-voids formation.

As it was mentioned before, in dual-scale fibrous reinforcements, the difference between the micro-flow and macro-flow can be significant. This difference can lead to formation of voids by mechanical entrapment of air; voids formed inside the bundles are named micro-voids (Figure 4a) and voids in the channels are known as macro-voids (Figure 4b). In general, a high velocity of the injected liquid with respect to the capillary velocity inside the bundles leads to the formation of micro-voids, and a low velocity, to formation of macro-voids [74], as it is illustrated in the Figure 4a,b. The complexity of the simulations in dual-scale fibrous reinforcements lies in the consideration of two domains with different scales of permeability. In the channels, the flow is driven by viscous forces; in the tows, additional capillary forces shall be considered because of the small hydraulic diameter of the pores [75]. A term has been proposed in [76] to establish a relationship between the

capillary and viscous forces and it is called the modified capillary number, C_a^*, which is defined later. Some simulations have sought to find the optimum value of C_a^* that better produces a balance between both forces in order to minimize the void formation [44], [77]–[82].

a) **b)**

Figure 4 Representation of void formation in dual-scale fibrous reinforcements. a) Microvoids inside the bundles, b) Macrovoids in the gaps. Source: Park and Lee [83]

In general, the filling simulations of dual scale fibrous reinforcements have been focused mainly on the following problems: 1) simulation of void formation and fluid front imbalances at mesoscopic scale, 2) simulation of totally saturated RUC´s to determine effective properties, 3) simulation of compression and transport of bubbles, 4) simulation of the influence of the sink effect on the behavior of volume-averaged variables.

Void formation and fluid front imbalances.

Regarding the *simulation of void formation and fluid front imbalances at the mesoscopic scale*, several works have been developed for some fabrics. For example, some simulations were made in [3] for two kind of positioning of warps and wefts using the Finite Volume Method to solve the governing equations and the FAN technique (Flow Analysis Network) to advance the fluid front, considering that the trapped air behaved like an ideal gas. It was analyzed the influence of the fiber stacking and of the anisotropy ratio of permeability on the final void content inside the transverse bundle. Two important conclusions were accomplished: as the anisotropy ratio of permeability is larger, the size of the final void increases, and a higher void content is obtained for the positioning Weft-Warp-Warp-Weft than for the positioning Weft-Warp-Weft-Warp. Other relevant works were presented in [25] and [4]. In the first one [25], it was established a ratio among the time for the liquid inside the transverse bundle and the time for the liquid in the channels to traverse the

transverse bundle width, and they were established theoretical relationships between this ratio and the percentage and size of the voids for several values of C_a^*. In the second work [4], the model proposed in the former research was used to develop a real-time simulation control method in order to reduce the formation of microvoids at the end of the transverse bundles. In both works, the FEM/CV conforming scheme was used.

Afterwards, the influence of the global porosity of the RUC in the void formation inside the transverse tow was studied in [5], [84], as well as the critical pressure for the remotion of the microvoids, using the FEM/CV conforming method. This numerical method was also employed in [81] to study the influence of C_a^* and the tow porosity on the final void content. The authors found an optimal value for C_a^* that determines the transition between macrovoids and microvoids, in which the void content is the smallest possible. The influence of the combination between the Reynolds number, R_e, and the modified capillary number, C_a^*, on the final void content of the RUC was studied in [80] considering the Navier Stokes equation modified with source terms that activate only in the bundles to consider the permeability and capillary. In that work, an optimum capillary number, C_a^*, for each value of R_e, was achieved. An optimal processing window for Reynolds numbers of order $\mathcal{O}(2)$ and capillary numbers of order $\mathcal{O}(-3)$ was found. On the other hand, the simulation of unidirectional flow considering circular tows and radial coordinates was tackled in [22] using the Finite Volume method for the solution of the governing equations and the Volume of Fluid (VOF) to advance the interface. The authors studied the effect of the following variables in the fluid front positions: filling velocity, resin viscosity, inter-tow dimension and intra-tow dimension.

Calculation of the effective permeability.

In the simulation of dual-scale fibrous reinforcements, *problems where both the tows and the channels are assumed to be totally saturated with liquid* have been also considered. The main objective of that kind of simulations is to calculate the effective permeability and determine the influence of some geometric variables in such property. For instance, FEM was used in [20] to simulate single-tow and tow-tow arrangements under prescribed pressure gradients, using the Stokes-Brinkman approach; in that work, it was studied the influence of the fiber volume fraction, aspect ratio of tows, tow permeability and degree of

compaction on the effective permeabilities in the main directions. A similar research was carried out in [85], in which the influence of the type of stress matching condition on the effective permeabilities of 3D fibrous reinforcements was analyzed, finding an irrelevant influence for low porosities.

Compression and transport of bubbles.

The modeling and simulation of *compression and transport of bubbles* have also gained interest in the field of composites processing. The bubble compresses as a result of the pressure surrounding the tow and of the capillary pressure; on the other hand, the bubble transport can occur mainly by two mechanisms: dissolution of gas molecules of the trapped air into the liquid and the mechanical mobilization of the bubbles pursuing different paths. Both the bubble compression and transport have been studied in [5], [86], [87]. In some researches, the dissolution of the air into the liquid has been implicitly considered in the air pressure by introducing a lumped function that accounts for the fraction of escaped air, λ, in terms of the relative fluid front position, ξ_f, which is defined as $\xi_f = r_f/r_o$, with r_f and r_o as the current and initial fluid front positions inside the tow [11], [88].

The *void mobilization* is another phenomenon that deserves particular attention, because during the injection it is likely to reach velocities that bring about high drag forces that, in turn, exceed the interfacial forces, leading to the displacement of voids. This displacement implies that there is a way to eliminate residual voids even when the void formation by entrapment of air is difficult to avoid. The void mobilization can take place along several paths: in spaces between the monofilaments of the fiber tows, from the tows towards the channels and along the channels between the tows. An important work considering the former path was presented in [89], in which the transportation of very low viscosity drops across an array of cylinders, imitating the void migration in an array of fibers, was considered. One paramount conclusion of that work is that the length of the bubbles could help to its mobility, because larger pressure gradients are reached as the bubble is larger and this helps to surpass the capillary forces. The motion of bubbles along the inter-bundle channels or gaps of biaxial non-crimped fabrics was studied in [90]. By means of a permeability network model and the Monte Carlo method, the authors concluded that the paths of bubble migration in the channels depends significantly on the position of the

threads joining the tows and on the number of fibers crossing the channels, and that the bubbles tends to move in the direction of the tows. In that work, it was also studied in detail the relationship between the local pressure gradient, the local gap size and the probability of free-bubble motion, bubble trapping and bubble splitting. The level set method was used to track the fluid front. In a subsequent work, the same authors built a 3D numerical model to study the creation and mobilization of voids in non-crimped fabrics and considered both the intra-tow and inter-tow voids movement [78]. The authors concluded that the movement of intra-tow voids (microvoids) is much slower than the movement of inter-tow voids (macrovoids). Finally, the motion of macrovoids was also considered in [4], where it was introduced a phenomenological factor, F_u, relating the liquid velocity, $\langle u_g \rangle^g$, and the void velocity, $\langle u_v \rangle$; according to that work, $\langle u_v \rangle$ is a piecewise continuous function of $\langle u_g \rangle^g$, with an inflection point corresponding to the critical liquid velocity for the onset of void mobilization, $\langle u_g^{crit} \rangle^g$, which is the value of $\langle u_g \rangle^g$ from which the void migrates along the channels.

Simulations at macroscopic scale considering the sink effect.

The problem of *macroscopic simulations makes reference to the filling of cavities influenced by the sink effect*, which in turn refers to the delayed absorption of the resin into the tows with respect to the filling of the channels. In order to consider the sink effect on the macroscopic fillings, a sink term, S_g, is considered in the macroscopic continuity equation. In [91], it was considered that the sink term, S_g, depends mainly on the pressure surrounding the tow, $\langle P_g \rangle^g$, and on the tow saturation, S_t, and they were established sink functions, $S_g(S_t, \langle P_g \rangle^g)$, for several simple tow geometries. Some simulations using the sink functions, $S_g(S_t, \langle P_g \rangle^g)$, were conducted in [13], where the principal contribution was the addition of 'slave' elements into the original FEM/CV mesh with the objective to deem the tow saturation in those elements. In this modified FEM/CV scheme, the porous volume of the fiber tows in the CV is represented by adding a one dimensional bar, with the same porous volume of the tows, to the master node of the CV. The simulation is run as usual in the FEM/CV conforming scheme, but two fill factors shall be distinguished for each CV: the fill factor in the modified CV represents the saturation of the gaps and the fill factor in

the ‘slave’ bar, the saturation of the tows. This scheme has been used in [11], [25] and interesting results of pressure profiles have been acquired from the simulations; nevertheless, as it is recognized in [83], neither the capillary pressure, nor the air compressibility and air solubility are taken into account using this modified scheme. A two phase flow model for the prediction of saturation in dual-scale fibrous reinforcements, which considers these three factors, was recently published [92], [93], obtaining good agreement with experimental observations.

Alternative forms of the volume-averaged governing equations for partially saturated flow in dual-scale fibrous reinforcements were established for isothermal flows in [6] and for non-isothermal reactive flows in [7]; these equations were stated for two sub-domains: the channels and the tows. The dynamic interaction among both sub-domains was considered by introducing a new quantity called the interfacial kinetic effect tensor, which includes the effects of the liquid absorption by the tows and the presence of slippage on the interface channels-tows. These equations were simplified later in [10] under certain assumptions with the purpose to make them tractable for LCM processes. Then, the FEM/CV conforming method was applied to solve those simplified governing equations at both macroscopic and mesoscopic scales, in order to simulate the filling phenomenon in woven fabrics [8], [14]. Three outstanding and interrelated researches deserve special attention in this regard. In [14] it was studied the influence of the sink effect on the position of the global fluid front. In that work, it was employed an iterative-corrected strategy, namely, the fluid flow in the tows is solved at the mesoscopic scale supposing a uniform pressure in the surrounding channels, the velocity field in the channel-tow interfaces is computed using Darcy’s law and the sink term, S_g, is then calculated using that velocity field. Afterwards, the pressure field at the macroscopic scale is calculated considering the sink term, S_g, and it is compared with the values supposed as boundary conditions at the mesoscopic scale, to be corrected until both pressure fields are similar. This research was extended to the non-isothermal and reactive cases. In the processing of composites, the non-isothermal case happens when the resin and/or the mold are heated. This situation was simulated in [8], where the influence of the sink effect on the global temperature profile for several time instants was analyzed. On the other hand, the reactive case refers to the consideration of

the resin curing during the filling of the cavity. The influence of the sink effect on the global degree of cure profile was studied in [94].

Summary of works of modeling and simulation in dual-scale fibrous reinforcements.

To conclude the present section, the aforementioned works about dual-scale fibrous reinforcements and some others are classified in the Table 2 and Table 3 in accordance with: the main physical assumption of filling according to Figure 5, the phenomena and/or properties that were analyzed, the variables that were considered, the dimension of the problem and the numerical techniques used for the simulation.

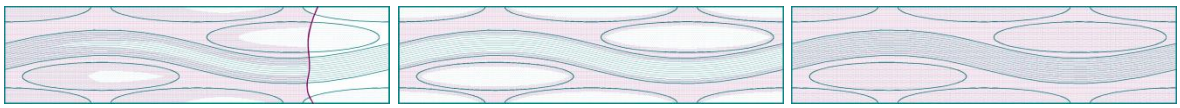

a) **b)** **c)**

Figure 5 Main physical assumptions of filling of dual-scale fibrous reinforcements. a) Case 1: Simultaneous impregnation of bundles and channels , b) Case 2: Channels completely filled before any impregnation takes place inside the bundles, c) Approach 3: Channels and bundles completely filled with liquid.

Table 2 Summary of works of modeling and simulation in dual-scale fibrous reinforcements (1)

Ref	Assumption	Phenomena and/or properties analyzed												
		Flow imbalance	Macrovoid formation	Microvoid formation	Remotion of voids	Effective permeability	Compressibility of voids	Void dissolution	Void motion space between fibers	Void motion from tows to channels	Void motion along channels	Sink effect	Non-isothermal	Reactive
Jinlian, Yi, and Xueming [3]	1			x			x							
Koo, Il, and Hahn [25]	1		x	x										
Gourichon et al [5]	2				x					x				
Schell et al [81]	2						x							
DeValve and Pitchumani [80]	1	x	x	x			x							
Hwang and Advani [20]	3					x								
Tan and Pillai, [85]	3					x								
Lundström [86]	2						x	x						
J. M. Lawrence, Neacsu, and Advani [11]	2						x	x						
Kang and Kolleing [89]	3								x					
Frishfelds, Lundström, Jakovics[90], [95]	1										x			
Lundström, Frishfelds, Jakovics [78]	1									x	x			
Lee, Il Lee, and Kang [4]	1				x						x			
Pillai and Advani [91]	2											x		
Simacek Advani [13]	2											x		
Pillai [6], [7]	2											x	x	x

Ref	Assumption	Phenomena and/or properties analyzed												
		Flow imbalance	**Macrovoid formation**	**Microvoid formation**	**Remotion of voids**	**Effective permeability**	**Compressibility of voids**	**Void dissolution**	**Void motion space between fibers**	**Void motion from tows to channels**	**Void motion in channels**	**Sink effect**	**Non-isothermal**	**Reactive**
Tan and Pillai [14]	2											x		
Tan and Pillai (2) [8]	2											x	x	
Tan and Pillai (3)[94]	2											x	x	x
Foley and Gillespie [87]	1	x												
Gangloff, Hwang , Suresh [96]	3										x			
Di Fratta et al [97]	2-3					x						x		
Tahir, Hallströmand Åkermo [98]	3					x								
Cender, Simacek, Advani [99]	2											x		
Haji, Saouab, Nawab [100]	2-3					x						x		
Gascón et al [92], [93]	2							x	x			x		
Zhou, Alms and Advani [101]	2											x		
Zhou et al. [102]	2											x		
Shou, Ye and Fan [24]	3					x								
Shou et al [23]	3					x								
Patiño et al [103]	1	x		x			x							
Patiño et al [104]	1	x		x			x							

Table 3 Summary of works of modeling and simulation in dual-scale fibrous reinforcements (2)

Ref	Numerical techniques	Variable considered													Dimension
		Fiber stacking	Tow size and geometry	Anisotropy ratio	Fiber fraction of tows	RUC porosity	Viscous vs. Capillary forces	Reynolds number	Matching conditions	Critical velocity of void remotion	Global pressure	Tempera ture	Cure degree	Global saturation	
Jinlian, Yi, and Xueming [3]	CV-FAN	x		x											2D
Koo, Il, and Hahn [25]	Na							x							2D
Gourichon et al [5]	FEM/CV -VOF					x	x								2D
Schell et al [81]	FEM/CV -VOF				x			x							2D
DeValve and Pitchumani [80]	Ansys-Fluent							x	x						3D
Hwang and Advani [20]	FEM-VOF	x			x	x				x					2D
Tan and Pillai, [85]	FEM-VOF									x					3D
Lundström [86]	na				x										2D
J. M. Lawrence, Neacsu, and Advani [11]	FEM/CV -VOF				x						x			x	2D
Kang and Kolleing [89]	na				x			x							2D
Frishfelds, Lundström, Jakovics[90], [95]	Monte Carlo-Level Set	x	x					x			x				2D
Lundström, Frishfelds, Jakovics [78]	Monte Carlos-Level Set	x	x					x			x				3D
Lee, Il Lee, and Kang [4]	na						x	x							2D
Pillai and Advani [91]	na										x			x	2D
Simacek Advani [13]	FEM/CV - VOF										x			x	2D
Pillai [6], [7]	na											x	x	x	3D

Ref	Numerical techniques	Phenomena and/or properties analyzed													Dimension
		Fiber stacking	Tow size and geometry	Anisotropy ratio	Fiber fraction of tows	RUC porosity	Viscous vs. Capillary forces	Reynolds number	Matching conditions	Critical velocity of void remotion	Global pressure	Tempera ture	Cure degree	Global saturation	
Tan and Pillai [14]	FEM/CV - VOF										x			x	3D
Tan and Pillai (2) [8]	FEM/CV - VOF										x	x		x	3D
Tan and Pillai (3)[94]	na										x	x	x	x	3D
Foley and Gillespie [87]	FEM-VOF	x	x			x									2D
Gangloff, Hwang , Suresh [96]	FEM/CV Comsol				x				x	x					2D
Di Fratta et al [97]	na					x					x				2D
Tahir, Hallströmand Åkermo [98]	ANSYS Fluent		x		x	x									2D
Cender, Simacek, Advani [99]	na				x	x									2D
Haji, Saouab, Nawab [100]	FLOW 3D/VOF				x										3D
Gascón et al [92], [93]	na													x	2D
Zhou, Alms and Advani [101]	na										x			x	2D
Zhou et al. [102]	na										x			x	2D
Shou, Ye and Fan [24]	na				x				x						2D
Shou et al [23]	Na								x						2D
Patiño et al [103]	BEM/Marker particle		x	x	x	x	x								2D
Patiño et al [104]	DR-BEM/Marker particle						x		x						2D

1.3.4 Numerical techniques to track the fluid front

The numerical techniques mentioned above deal with the solution of the pressure field equation and the velocities in the fluid front. Regarding the techniques to track the moving boundary, four of them can be emphasized here: the direct Euler integration, the volume of fluid, the characteristic equation technique, and the fast marching and level set techniques.

In the direct Euler integration (Figure 6), the advancement of any node in the boundary is computed once the normal velocity is known, with the finite difference schemes as the most used. The main disadvantages of this technique are: the numerical instabilities arising when two or more nodes in the boundary become very close among them, the possibility of crossing of points during the advancement of the fluid front and the difficulties to deal with encountered flows. This method is used in the present work and the problems associated to its implementation are dealt by mean of remeshing and smoothing algorithms and imposing several constraints to the time step, as it is detailed later.

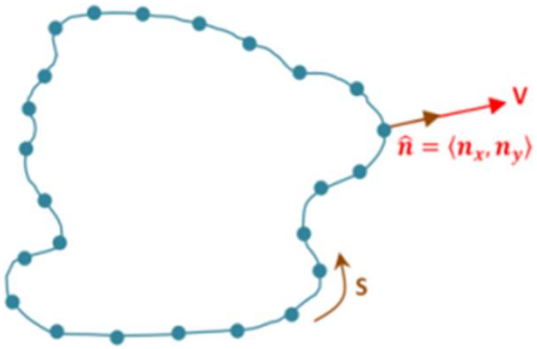

Figure 6 Direct Euler integration technique.

The base of the characteristic equations technique is the transformation of the PDE that describes the motion of the fluid front into an ordinary differential equation. According to this technique, the vertical fluid front position can be described by a Hamilton-Jacobi equation [105], whose corresponding characteristic equations are used to track the moving boundary. In some parts of the fluid front, slope discontinuities are present and the characteristic equations have not solution (Figure 7a). In those particular cases jump conditions are applied to compute the velocity components in the discontinuities [105]. Other particular situations with this technique are the expanding corners, where there are

infinite ways to connect the nodes that surge from the displacement of the fluid front (Figure 7b); the entropy condition is applied in this situation. As the last conditions, there are other special conditions associated with this technique that make it difficult to implement.

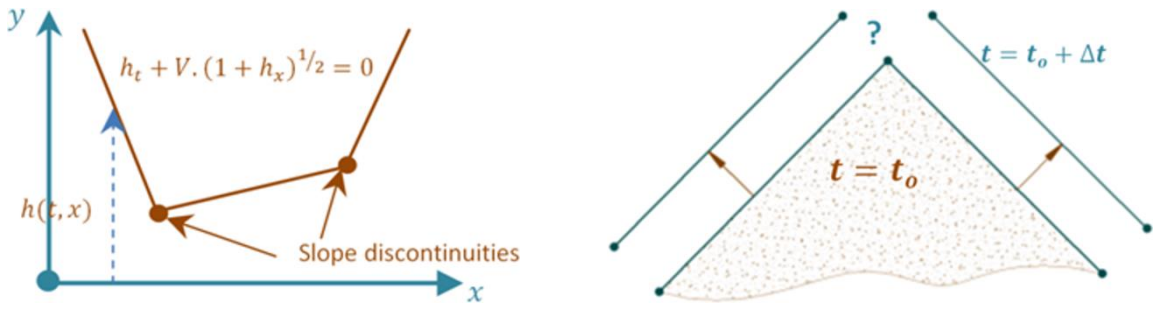

a) **b)**

Figure 7 Typical situations requiring special conditions in the characteristic equations method. a) Slope discontinuities, b) Expanding corners.

The fast marching method, level set method and combinations among them are interesting techniques for capturing the motion of interfaces; they were originally proposed by Sethian [57]. Their application in the fluid front tracking of filling simulations in LCM have been increasing for both single-scale [46], [50], [58], [106] and dual-scale preforms [78].

The fast marching method is a boundary value formulation in terms of a function $T(\vec{x})$ that describes the arrival time of the fluid front to a given point $\vec{x}$; the solution surface for $T(\vec{x})$ can be obtained by solving the Eikonal equation [107]. The position of the fluid front, Γ(t), in a determined time instant, t, can be described as: $\Gamma(t) = \{\vec{x}\epsilon\Omega / T(\vec{x}) = t\}$ (Figure 8a). The Fast marching method is suitable for flows that always move exclusively positive or negative to the boundary (surface is exclusively contracting or expanding, but not both ones in a same problem), because a single crossing time is permitted at each grid point [57].

The level set method is an initial value formulation, where a signed distance function, $\emptyset(\vec{x}, t)$, representing the distance of any point $\vec{x}$ to the interface Γ(t) is considered [57]. This distance function is zero at the moving interface and can be calculated by solving a pure advection equation. The position of the fluid front, Γ(t), in a determined time, t, using the Level Set is described as: $\Gamma(t) = \{\vec{x}\epsilon\Omega / \emptyset(\vec{x}, t) = 0\}$ (Figure 8b). The main advantage of the Level Set over the Fast Marching method is that the extended velocity can be both

positive and negative, which means that this method can describe both expanding and contracting surfaces in a same problem.

The calculation of the extended velocity function has been deeply discussed because it is a key factor in the correct implementation of both methods [107], [108]. A mixed approach that have shown an acceptable efficiency in many problems consists on using the Fast Marching method to compute the extended velocity function of an interface that is being tracked by the Level Set method. Both the Fast Marching and the Level Set Method require the use of specific solvers for hyperbolic equations. Two schemes are commonly found in the literature [109], [110]: the Euler scheme and the Third order Runge-Kutta variation decreasing scheme (TVD).

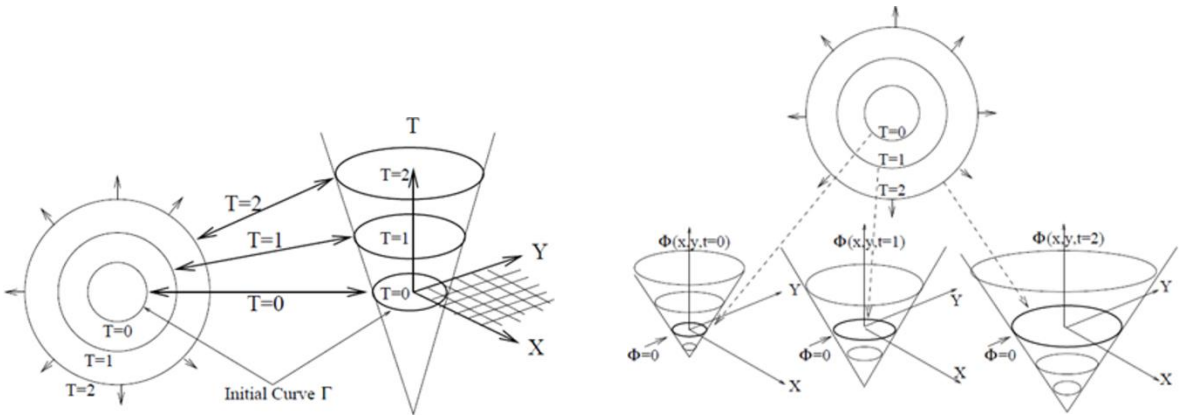

Figure 8 Fast marching and level set method for interface advancement. a) Fast Marching. b) Level Set. Source: Sethian [57]

Finally, the volume of fluid techniques (VOF) are the most used for tracking the fluid front when FEM or CV are used to compute the pressure field and the normal velocities [3], [8], [22], [33], [40], [80], [94], [111]. In these techniques, a fluid volume fraction, f_v, is assigned to each control volume or element, with $f_v = 1$ corresponding to the liquid phase and $f_v = 0$ to the gas phase, while the fluid front is located in the region where $0 < f_v < 1$ (Figure 9). The fluid volume fraction, f_v, can be determined by the solution of a pure advection transport equation (hyperbolic problem), which can be numerically instable due to the appearance of smooth shock profiles, requiring the use of specific solvers [22], [80], [111]. Another less rigorous but useful form to determine f_v is to consider the local mass balance at the control volumes or elements; in that case, f_v is also called the fill factor and accounts for the amount of liquid entering a control volume (conforming) or element (non-

conforming) per unit volume [3], [8], [14], [33], [40]. Once the values of f_v in the control volumes or elements of the fluid front are known, interface capturing schemes are implemented to reconstruct the approximated fluid front shape, being one of the most applied the Flow Analysis Network (FAN) [3], [112], [113].

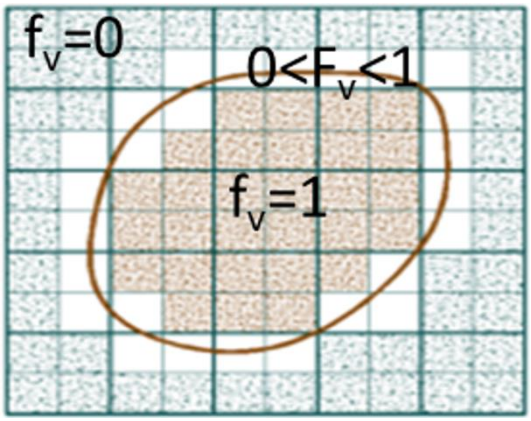

Figure 9 Volume of fluid techniques.

The VOF techniques apply to mesh-fix approaches, where only one mesh is considered for the whole domain (saturated and non-saturated). On the contrary, in the mesh-moving approaches, only the saturated domain is meshed and the original mesh elements could evolve in size and shape (Lagrangian) or the mesh can be updated continuously (Eulerian) as the filling takes place [36]. In the mesh-moving approaches the mesh have element nodes corresponding exactly to the moving interface, allowing in this way the direct application of the interface dynamic condition. However, the computational cost of the mesh-moving Eulerian approaches could be considerably higher regarding the mesh-fix approaches since domain remeshing is required as the fluid front progresses, whereas, for the mesh-moving Lagrangian approaches, the original mesh could become significantly distorted and/or coarse as the filling occurs.

1.3.5 Influence of voids on the mechanical properties of composites materials

The study of void formation in dual-scale fibrous reinforcements used in the processing of composites materials is encouraged by several reasons. One of the most important is the high influence of the voids on the mechanical performance of the composites. Even though the present work is not aimed to simulate the mechanical response of fiber reinforced composites with the presence of induced voids, some works illustrating this are briefly presented in this subsection.

In general, the study of the influence of the voids in the mechanical response of composite materials can be addressed by using analytical models, experimental tests and/or numerical simulations. Many authors agree about the low influence of the voids on the tensile properties of unidirectional, cross ply and woven fabric composites made with conventional reinforcements (like glass and carbon) when subjected to low strain rates [114]–[120]. However, for non-conventional composites or medium to high strain rate regimes, different results can be found in the literature. For instance, in Protz et al. [119], non-crimp fabric glass/epoxy composites were manufactured using Vacuum Assisted Resin Transfer Molding (VARTM) and different void contents were obtained (between 0.02% and 4.53%) by modifying the processing conditions. The authors studied the influence of the void content on the tensile strength at several strain rates, namely, $\dot{\varepsilon} = [4 \times 10^{-4}, 4 \times 10^{-3}, 4 \times 10^{-2}, 4 \times 10^{-1}, 4{,}40]s^{-1}$, concluding that this influence can be disregarded when the strain rate is below $\dot{\varepsilon} = 4 \times 10^{-1}s^{-1}$, whereas for $\dot{\varepsilon} = 4\ s^{-1}$ the decrease of the tensile strength with the void content is important and for the highest strain rate considered, $\dot{\varepsilon} = 40\ s^{-1}$, this reduction is even more significant, which allows inferring that the tensile strength is more sensitive to the void content as the strain rate is higher. The influence of the voids on the mechanical properties of unidirectional flax fiber reinforced composites was experimentally investigated by Li [120], finding that the tensile strength, tensile modulus and ILSS are more sensitive to the void content in those kinds of composites than in glass and carbon reinforced composites. The influence of the void location was also studied in that work, concluding that the fracture modes of the composites are considerably affected by voids located inside the flax yarns, whereas the ILSS is highly influenced by voids located between the yarns. Conversely to glass and carbon reinforced composites, the presence of voids at the fiber/matrix interface leads to the decrease of the tensile strength.

Several authors are in agreement about the reduction of the interlaminar shear strength (ILSS) with the void content after a critical void content has been reached [114], [118], [121]–[124]. In Costa et al [121], the behavior of this property with the void content in carbon fiber reinforced composites considering two resin systems, epoxy and bismalemide, was studied, obtaining for both resin systems a similar critical void content (0.9%). Similarly, Jeong [122] and Guo et al [114] also reported the existence of a critical void content for the reduction of the ILSS, which is 1.11% for unidirectional carbon/epoxy laminates according to [114], and 0.8% for woven fabric graphite/epoxy and 1.0% for woven fabric graphite/polyimide laminates according to [122]. In DeAlmeida and Neto [123], a fracture criterion based on the Mar-Lin equation was proposed and used to define an acceptable void level according to the reduction of the ILSS.

The influence of the voids on the flexural properties of composites has been widely studied as well. According to Guo [114], the concept of critical void content is also applicable to flexural properties, i.e., when a critical threshold is exceeded, the void content has a detrimental effect on the flexural properties. For void contents from 0.5 to 3.5%, Liu et al [115] concluded that the tensile modulus is practically insensitive to the void content, contrarily to the flexural modulus that decreases with such a content. The reduction of the flexural modulus, E_f, and flexural strength, S_f, with the void content was also reported by Hagstrand et al [116] in unidirectional glass/polypropylene composites beams, where a reduction of around 1.5% in those properties for each 1% increase in the void content was obtained. However, the authors also emphasized that the increase of the void content leads to the increase of the beam dimension and, consequently, of the moment of inertia, I, which in turn could bring about the increase of the bending rigidity, $E_f I$, when the void content is below 14%.

The influence of voids on the fatigue resistance of composites has been studied as well. For instance, Bureau and Denault [124] manufactured continuous glass/polypropylene composites under different processing conditions of temperature, holding time, cooling rate and pressure to obtain laminates with different void contents. Several samples were obtained to carry out tensile, three-points bending and short beam shear tests, as well as flexural fatigue tests, finding that the behavior of the fatigue S-N curves is influenced by the void content by two reasons. The first one is that the fatigue strength coefficient is

directly proportional to the flexural strength, which decreases with the void content; the second one is that the fatigue strength exponent is inversely proportional to the ILSS, which decreases with the void content too. In a similar fashion, the flexural fatigue performance of unidirectional fiber reinforced composites produced by vacuum bag with void contents between 0.5% and 6% was studied by Chambers et al. [125]. According to the authors, in general, the void content affects the initiation and propagation of flaws, and consequently, the flexural fatigue performance. However, authors posed that the void content can be considered as a very simplistic variable to describe the influence of the voids on the fatigue life of the composites. For a same void content, different void sizes and locations could be expected, and these factors (void size and location) are strongly linked to the fatigue performance. The results of Chambers et al. [125] suggested the existence of the critical void size (void area>0.03mm^2) above which the influence of the voids on the flexural fatigue life is more significant. The authors also concluded that voids located at the midplane of the laminate have a more important influence on the fatigue life.

According to Zhang [126], the impact resistance could be also affected by the void content. Impact tests in carbon/epoxy laminates with three porosity levels were conducted by the authors, finding that, for the same impact energy, the dent depth and damage area significantly increases with the void content, whereas the Tensile Strength After Impact (TAI) slightly decreases.

The computational mechanics has noticeably contributed to the comprehension of the interaction between the voids and the mechanical response of the composite. Finite Element Analyses (FEA) of Representative Unitary Cells (RUC´s) with induced voids and being subjected to normal and shear loadings were performed by Huang and Talreja [117] with the purpose to determine the relationship between the void characteristics and the effective elastic constants. The FEA model was validated using a problem that admits analytical solution based on the theory of Mori-Tanaka, and then it was used to carry out a parametric study. According to the numerical results, the void content has an important effect on the out-of-plane modulus, whereas the in-plane moduli are less significant affected. For a constant void content, the void shape also influences the properties, with the flat voids having a positive effect on the in-plane moduli, but a negative one on the out-of-plane stiffness, and the long voids reducing the out-of-plane modulus, but having a negligible

effect on the in-plane stiffness. On the other hand, the effect of voids on the fracture behavior of woven fabric composites was numerically studied by Ricota et al. [127]. The beam-on-elastic-foundation theory was modified by the authors to account for the transverse shear effect and material orthotropy, and the resulting model was used to calculate the Mode I Strain Energy Release Rate (SERR) in a double cantilever beam (DCB) with the voids placed ahead of the crack tip. Two-dimensional finite element analyses were carried out to validate the analytical model. The influence of the size, shape and location of voids on the SERR was investigated, concluding that the increase of the void size and the decrease of the distance between the void and the crack tip for all kinds of voids considered, as well as the increase of the void aspect ratio for elongated voids, lead to the increase of the SERR.

Finite Element Analyses (FEA) of the mechanical response of RUC's with different fiber volume fractions and void contents were also conducted by Dong [118] considering the properties of carbon/epoxy composites. The influence of the void content on the properties of laminae and laminates was studied, finding that the transverse properties of laminae (transverse modulus, in-plane shear modulus, transverse tensile strength, transverse compressive strength and in-plane shear strength) are significantly affected by the void content, as well as it is the ILSS of the laminate. The influence of the void content on the longitudinal modulus and longitudinal strength of the laminae is almost insignificant, confirming previous results. Regarding the effective tensile strength and effective modulus of the laminate, the critical void content from which these properties reduce depends on the stacking sequence. As reasonable, for laminates conformed with plies predominantly oriented along or in a direction close to the loading axis, the reduction of the mentioned properties with the void content could not be significant.

1.4 Objectives

General objective.

Implement BEM techniques in the simulation of the impregnation phenomena of dual-scale porous media used in the processing of composites materials.

Specific objectives.

- Analyze the influence of processing, material and geometric variables on the void formation by mechanical entrapment of air, by mean of the simulation of simultaneous filling of RUC's.
- Analyze the influence of the type of formulation for coupled problems free fluid-porous media (Stokes-Darcy and Stokes-Brinkman) and of the interface matching conditions on the void formation process, by mean of the simulation of simultaneous filling of RUC's.
- Devise a new methodology to determine the influence of macroscopic parameters on the saturation rate of the bundles during the RUC filling, and, in this way, determine sink functions to be used in macroscopic problems (filling of cavities).
- Determine the influence of the RUC geometry on the relationship between the effective unsaturated permeability and the saturation degree, by mean of filling simulations assuming full filled channels.
- Study the critical conditions associated to the compressibility, motion, migration and splitting of the bubbles formed in the bundles, by mean of filling simulations assuming full filled channels.
- Analyze the influence of processing parameters in the filling of cavities considering the partial saturation of the RUC's (sink effect) at both constant pressure and constant flow rate regimes.

1.5 Methodology

The present work is developed in six main stages. The first two stages correspond to Chapters 1 and 2, respectively. In the present Chapter 1, the problem statement, literature review, objectives and methodology are presented, whereas in the Chapter 2 the theoretical background supporting this work is summarized.

The third stage tackles the simulation of simultaneous filling of channels and bundles inside the RUC using two formulations, Stokes-Darcy and Stokes-Brinkman. This stage is aimed to study the influence of processing, geometric and material variables, as well as the influence of the formulation type (Stokes-Darcy and Stokes-Brinkman) and interface matching conditions on the size, shape and location of voids formed by mechanical entrapment of air at mesoscopic scale. In this stage two types of numerical codes are developed: codes to solve the governing equations and codes to track the fluid front. Regarding to the first kind of codes, BEM-based algorithms for Stokes-Darcy and Stokes-Brinkman problems are developed, and the validation of such algorithms is done with classical problems admitting analytical solutions. Once the validation has been done, the codes are implemented in moving-boundary problems applied to the processing of composites and results are compared with previous works. This stage is developed in Chapters 3 and 4.

In the fourth stage it is considered the impregnation of bundles inside the RUC when the channel is totally filled with liquid using the Stokes-Darcy formulation. The goals of this stage can be summarized as follow: 1) study the dynamic evolution of voids formed inside the transverse bundle, considering the processes of compression, motion, migration and splitting, 2) devise a new methodology for determining a sink function in terms of macroscopic parameters in order to conduct macroscopic simulations in the following stage, 3) determine the influence of the RUC geometry on the curves of effective unsaturated permeability against saturation degree. The Stokes-Darcy code developed in the Stage 3 is adapted to the particular problems of this fourth stage, where considerable amount of simulations are required with the purpose to deduce sink functions from the fit model that describes the behaviour of the saturation rate in terms of several macroscopic variables. This stage is developed in Chapters 5 and part of Chapter 6.

The stage 5 is devoted to the unidirectional filling of cavities taking into account the partial saturation of the RUC's using an Equivalent Darcy formulation. The main purpose of this stage is to analyse the influence of the inlet pressure, inlet flow rate, vacuum pressure and air entrapment parameter on the behaviour of the global saturation in dual scale fibrous reinforcements. The sink functions obtained in *Stage 4* are used to deal with the multiscale coupling between the macroscopic and mesoscopic fillings by means of a lumped strategy.

A DR-BEM code for the solution of Poisson type equations with non-linear terms is developed. This code is validated with an analytical solution of a simple macroscopic problem at constant inlet pressure regime. The assessment of the ability of the sink functions to predict physically consistent macroscopic results is done by comparing the numerical pressure profile with previous experimental works. This stage is developed in the last part of Chapter 6. In the last stage, Chapter 7 presents the concluding remarks, contributions and future works.

2. THEORETICAL BACKGROUND

In the present section some general concepts and equations supporting this research are succinctly presented, but the specific conceptual, mathematical and numerical frameworks of each topic are presented in the next chapters for sake of clarity. Firstly, the general description of Liquid Composites Molding (LCM) processes is done, identifying the principal stages and advantages of these processes. Then, the deduction of the governing laws of dual-scale fibrous reinforcements from the volume-averaging method is briefly presented in order to identify the physical considerations that lead to the Darcy and Brinkman equations in its different forms at mesoscopic and macroscopic scale. The principal kinds of permeabilities found in scientific literature and the general formulae for the calculation of the capillary pressure in open channels and porous media are exposed thereupon and, finally, the deduction of the boundary integral formulations for the Laplace and Stokes equation is concisely shown. Some concepts and equations presented here are repeated in the following chapters to make easier the reading.

2.1 Liquid Composites Molding

The processing techniques of composites materials can be grouped into two families: open molding techniques and closed molding techniques. In the first ones, the part is manufactured in a one-side mold, while in the second ones, mold and counter-mold are required. Examples of open molding techniques are [128]: hand lay up, spray up, filament winding, vacuum bagging, centrifugation, among others. On the other hand, in the family of closed molding techniques, the Liquid Composites Molding (LCM) techniques can be highlighted. In the LCM techniques, the dried fibrous reinforcements, which can be previously preformed by mean of binders, heat and/or radiation (Figure 10a), are positioned into a cavity (Figure 10b) and then they are compacted by the counter-mold (Figure 10c); these reinforcements assume the shape of the cavity and are deformed, according to their drapeability, due to the compaction pressure (Figure 10b-c); then, a pressure-driven and/or vacuum-driven resin flow is injected to fill the void spaces, process in which the capillary pressure and/or gravity can play an important role (Figure 10d). Subsequently, the total resin curing takes place (Figure 10e), the part is removed from the mold and finishing operations could be required (Figure 10f). Both the injected resin and the molds can be

heated to facilitate the processes of impregnation, compaction and curing. The most common LCM techniques are [129]: Resin Transfer Molding (RTM), Vacuum Assisted Resin Transfer Molding (VARTM), Structural Reaction Injection Molding (S-RIM), Co-Injection Resin Transfer Molding (CIRTM), Seemann's Composites Resin Infusion Molding (SCRIM), RTM light, Compresion Resin Transfer Molding (CRTM) and Resin Infusion between Double Flexible Tooling (RIDFT). The LCM techniques are massively used in many industrial sectors: aerospace, aeronautical, military, transport, construction, naval, sport equipment, safety, alternative energies, among others. The massive acceptance of LCM techniques in the industry is supported by the advantages of these techniques with respect to other ones, some of which are briefly mentioned in the following bullets:

- The dimensional control of the parts is very good.
- The surface finishing of the pieces is excellent.
- These techniques allow using many kinds of high-performance fibrous reinforcements and resins not usable in other processes.
- High fiber contents can be reached with these techniques, which imply parts with better mechanical properties.
- These techniques allow controlling the void formation and remotion by modifying material, geometric and processing parameters that are more complicated or even not possible to control in other techniques.
- The manufacturing speed is faster than in other techniques, as the open molding techniques for example.
- These techniques allow incorporating different kinds of fibrous reinforcements at several orientations to obtain pieces with mechanical properties fitted to almost any application.
- Almost any kind of cores can be used in the manufacturing of parts with these techniques, allowing in this way the fabrication of lightweight structures, thermal, acoustic and electric insulated panels, impact-resistant arrangements, among others.
- These techniques are environmentally friendly since the styrene emissions are manageable and the waste of material is lower with respect to other techniques.

- Flexibility in the geometrical design is one of the most important features of these techniques, that is, parts of complex geometries can be obtained because the addition of inserts and the integration of several complex cavities are allowable with LCM.

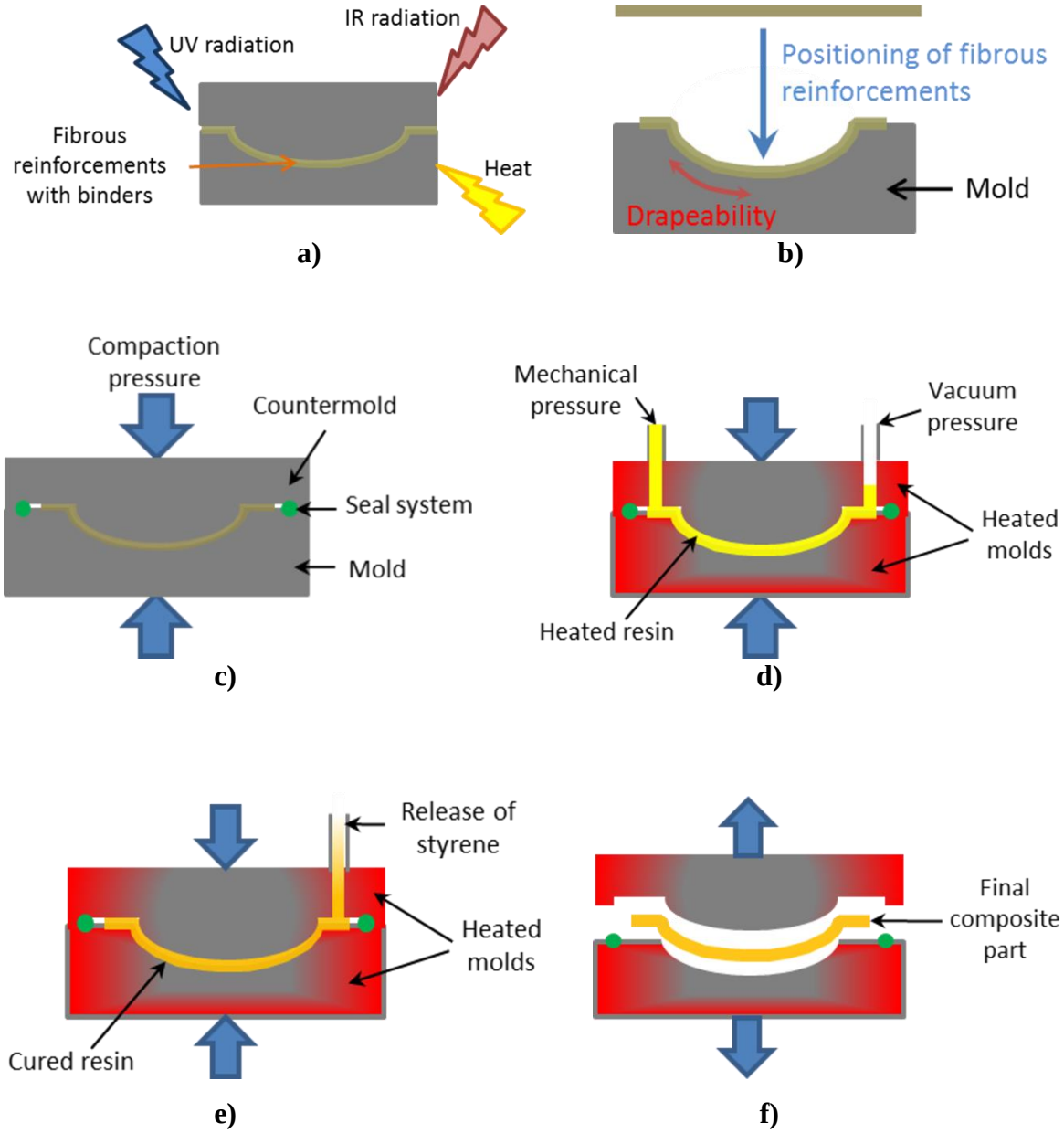

Figure 10 General stages of LCM . a) Preforming of fibers (Optional), b) Fiber positioning, c) Compaction, d) Resin injection, e) Resin curing, f) Demolding and finishing.

2.2 Modeling of dual-scale fibrous reinforcements

2.2.1 Governing equations of porous media

Volume-averaged quantities.

In a porous medium, a Representative Unit Cell (RUC), named also Representative Elementary Volume (REV), is a portion of the space associated to each point, Q, that is used to describe the volume-averaged properties of the medium, as shown in Figure 11. The RUC shall be large enough to average out the local variations of the properties under certain scales constraints, but small enough to prevent averaging out long range variations. The RUC must be much smaller than the total domain of the macroscopic problem, but bigger than the individual pores of the medium [130], as it is also shown in Figure 11, where it is observed that three phases can coexist into a RUC, namely, solid, liquid and gas.

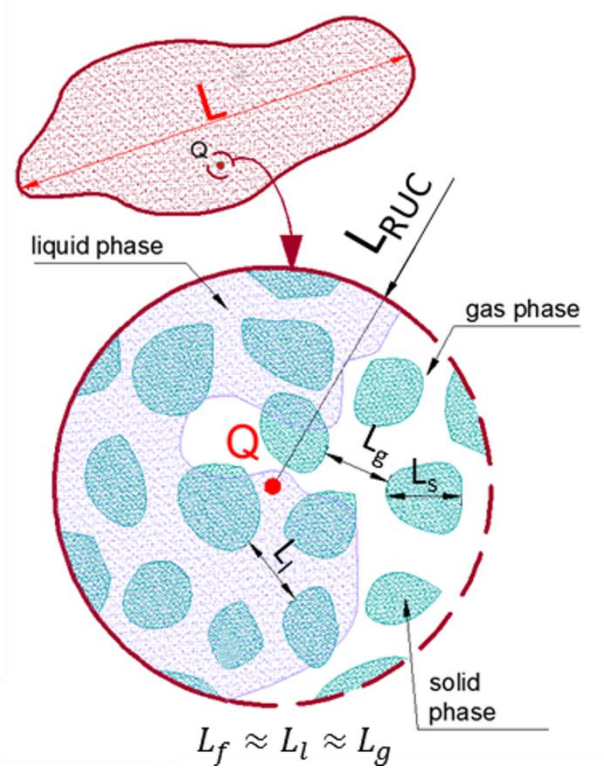

Figure 11 General scheme of a Representative Unit Cell (RUC).

The properties or physical variables of the points inside the RUC can be averaged with respect to the total RUC volume or to the volume of one phase. Therefore, three types of averages can be defined for any property or variable $B(\vec{x}, t)$ [130]:

- *Spatial average:* The average of the values of $B(\vec{x},t)$ in all points of the RUC regarding the total volume of the RUC, V_{RUC}.

$$\langle B\rangle = \frac{1}{V_{RUC}}\int_{V_{RUC}} B(\vec{x},t)d\Omega \tag{1a}$$

- *Phase average of phase β:* The average of the values of $B(\vec{x},t)$ in the points belonging to phase β regarding the total volume of the RUC, V_{RUC}.

$$\langle B_\beta\rangle = \frac{1}{V_{RUC}}\int_{V_\beta} B(\vec{x},t)dV_\beta \tag{1b}$$

- *Intrinsic phase average of phase β:* The average of the values of $B(\vec{x},t)$ in the points belonging to phase β regarding the total volume of the phase β, V_β

$$\langle B_\beta\rangle^\beta = \frac{1}{V_\beta}\int_{V_\beta} B(\vec{x},t)dV_\beta \tag{1c}$$

The relationship between $\langle B_\beta\rangle$ and $\langle B_\beta\rangle^\beta$ is as follows:

$$\langle B_\beta\rangle = \varepsilon_\beta\langle B_\beta\rangle^\beta \tag{2},$$

where $\varepsilon_\beta = V_\beta/V_{RUC}$ is the porosity of the phase β.

The following theorems are very useful in the deduction of the volume-averaged conservation equations for porous media [131]:

Theorem of phase volume-averaged gradient for scalar quantities, B_β:

$$\langle\frac{\partial B_\beta}{\partial x_i}\rangle = \frac{\partial\langle B_\beta\rangle}{\partial x_i} + \frac{1}{V_{RUC}}\int_{A_\beta} B_\beta\widehat{n_{\iota\beta}}dA_\beta \tag{3a}$$

Theorem of phase volume-averaged divergence for vector quantities, B_{i_β}:

$$\langle\frac{\partial B_{i\beta}}{\partial x_i}\rangle = \frac{\partial\langle B_{i\beta}\rangle}{\partial x_i} + \frac{1}{V_{RUC}}\int_{A_\beta} B_{i\beta}\widehat{n_{\iota\beta}}dA_\beta \tag{3b}$$

Theorem of phase volume-averaged time derivative for scalar quantities, B_β:

$$\langle\frac{\partial B_\beta}{\partial t}\rangle = \frac{\partial\langle B_\beta\rangle}{\partial t} - \frac{1}{V_{RUC}}\int_{A_\beta} B_\beta u^*_{i\,\beta}\widehat{n_{\iota\beta}}dA_\beta \tag{3c},$$

where $\widehat{n_{\iota\beta}}$ and $u^*_{i\,\beta}$ represent the "i" component of the normal vector and of the deformation velocity of the contour of the phase β, whereas A_β is the area of such contour.

Mass conservation equation.

The general form of the volume-averaged mass conservation equation for the phase β is as follows:

$$\langle\frac{\partial\rho_\beta}{\partial t}\rangle+\langle\frac{\partial\left(\rho_\beta u_{i_\beta}\right)}{\partial x_i}\rangle=0 \tag{4}$$

where ρ_β and u_{i_β} are the density and "i" component of the pointwise velocity in the phase β, respectively. If the boundaries of the phase β are not deformable, the application of theorems 3b and 3c to the terms of Eq. 4 leads to the following equation:

$$\frac{\partial\langle\rho_\beta\rangle}{\partial t}+\frac{\partial\langle\rho_\beta u_{i_\beta}\rangle}{\partial x_i}=-\frac{1}{V_{RUC}}\int_{A_\beta}\rho_\beta u_{i_\beta}\widehat{n_{i_\beta}}dA_\beta \tag{5}$$

Momentum conservation equation.

If the phase β is non-deformable, the general form of the volume-averaged momentum equation is as follows:

$$\frac{\partial\langle\rho_\beta u_{i_\beta}\rangle}{\partial t}+\langle\frac{\partial\left(\rho_\beta u_{i_\beta}u_{j_\beta}\right)}{\partial x_j}\rangle-\langle\frac{\partial\left(\sigma_{ij_\beta}\right)}{\partial x_j}\rangle-\langle\rho_\beta g_{i_\beta}\rangle=0 \tag{6}$$

where σ_{ij_β} and g_{i_β} are the pointwise Cauchy stress tensor and body acceleration, which are defined as:

$$\sigma_{ij_\beta}=-p_\beta\delta_{ij}+\mu_\beta\left(\frac{\partial u_{i_\beta}}{\partial x_j}+\frac{\partial u_{j_\beta}}{\partial x_i}\right) \tag{7a}$$

$$g_{i_\beta}=-\frac{\partial(gh)}{\partial x_i} \tag{7b}$$

where g and h stand for the gravity and height with respect to a reference system, whereas μ_β is the fluid viscosity in the phase β.

If the theorems of 3a and 3b are applied in Eq.6, the equation 7b is substituted in the resulting expression and the terms are properly associated, the following is obtained:

$$\begin{aligned}\frac{\partial\langle\rho_\beta u_{i_\beta}\rangle}{\partial t}+\frac{\partial\langle\rho_\beta u_{i_\beta}u_{j_\beta}\rangle}{\partial x_j}-\frac{\partial\langle\sigma_{ij_\beta}\rangle}{\partial x_j}+\rho_\beta\frac{\partial\langle gh\rangle}{\partial x_i}+\frac{1}{V_{RUC}}\Big[\Big(\int_{A_\beta}\rho_\beta u_{i_\beta}u_{j_\beta}\widehat{n_{j_\beta}}dA_\beta\Big)-\\ \frac{1}{\rho_\beta}.\Big(\int_{A_\beta}\sigma_{ij_\beta}\widehat{n_{j_\beta}}dA_\beta\Big)+\rho_\beta\int_{A_\beta}gh\widehat{n_{i_\beta}}dA_\beta\Big]=0\end{aligned} \tag{8}$$

Then, the substitution of the Eq.7a into 8 and the application of theorems 3a and 3b generate the next equation:

$$\frac{\partial\langle\rho_\beta u_{i_\beta}\rangle}{\partial t}+\frac{\partial\langle\rho_\beta u_{i_\beta}u_{j_\beta}\rangle}{\partial x_j}+\frac{\partial\langle p_\beta\rangle}{\partial x_j}\delta_{ij}-\mu_\beta\frac{\partial^2\langle u_{i_\beta}\rangle}{\partial x_j^2}-\mu_\beta\frac{\partial^2\langle u_{j_\beta}\rangle}{\partial x_j x_i}+\rho_\beta\frac{\partial\langle gh\rangle}{\partial x_i}+ \tag{9}$$

$$\frac{1}{V_{RUC}}\left[\left(\int_{A_\beta}\rho_\beta u_{i_\beta}u_{j_\beta}\widehat{n_{j_\beta}}dA_\beta\right)-\left(\int_{A_\beta}\sigma_{ij_\beta}\widehat{n_{j_\beta}}dA_\beta\right)+\rho_\beta\int_{A_\beta}gh\widehat{n_{i_\beta}}dA_\beta-\right.$$
$$\left.\mu_\beta\frac{\partial}{\partial x_j}\left(\int_{A_\beta}u_{i_\beta}\widehat{n_{j_\beta}}+u_{j_\beta}\widehat{n_{i_\beta}}dA_\beta\right)\right]=0$$

Considering the Eq.2, the phase-volume averaged pressure can be written as $\langle p_\beta\rangle=\varepsilon_\beta\langle p_\beta\rangle^\beta$ and the pressure gradient can be expanded as:

$$\frac{\partial\langle p_\beta\rangle}{\partial x_j}=\varepsilon_\beta\frac{\partial\langle p_\beta\rangle^\beta}{\partial x_j}+\langle p_\beta\rangle^\beta\frac{\partial\varepsilon_\beta}{\partial x_j} \tag{10}$$

By doing $B_\beta=1$ in Eq.3a, it is obtained that $\partial\langle\varepsilon_\beta\rangle/\partial x_i=-1/V_{RUC}\int_{A_\beta}\widehat{n_{i_\beta}}dA_\beta$, and Eq.10 can be written as:

$$\frac{\partial\langle p_\beta\rangle}{\partial x_j}=\varepsilon_\beta\frac{\partial\langle p_\beta\rangle^\beta}{\partial x_j}-\frac{\langle p_\beta\rangle^\beta}{V_{RUC}}\int_{A_\beta}\widehat{n_{j_\beta}}dA_\beta \tag{11}$$

From (11) in (9), applying index contraction and associating, the next equation is obtained:

$$\frac{\partial\langle\rho_\beta u_{i_\beta}\rangle}{\partial t}+\frac{\partial\langle\rho_\beta u_{i_\beta}u_{j_\beta}\rangle}{\partial x_j}+\varepsilon_\beta\frac{\partial\langle p_\beta\rangle^\beta}{\partial x_i}-\mu_\beta\frac{\partial^2\langle u_{i_\beta}\rangle}{\partial x_j^2}-\mu_\beta\frac{\partial^2\langle u_{j_\beta}\rangle}{\partial x_j x_i}+\rho_\beta\frac{\partial\langle gh\rangle}{\partial x_i}+$$
$$\frac{1}{V_{RUC}}\left[\left(\int_{A_\beta}\rho_\beta u_{i_\beta}u_{j_\beta}\widehat{n_{j_\beta}}dA_\beta\right)-\left(\int_{A_\beta}\sigma_{ij_\beta}\widehat{n_{j_\beta}}dA_\beta\right)+\rho_\beta\int_{A_\beta}gh\widehat{n_{i_\beta}}dA_\beta-\right. \tag{12}$$
$$\left.\mu_\beta\frac{\partial}{\partial x_j}\left(\int_{A_\beta}u_{i_\beta}\widehat{n_{j_\beta}}+u_{j_\beta}\widehat{n_{i_\beta}}dA_\beta\right)-\langle p_\beta\rangle^\beta\int_{A_\beta}\widehat{n_{j_\beta}}dA_\beta\right]=0$$

Under certain scales constraints, which are mentioned and applied in Chapter 6 and explained in detail in [130], the inertial effects in the porous medium can be neglected, and the firsts two terms of Eq.12 can be dropped, as well as the first integral appearing in such a equation. After some terms association, the following is obtained:

$$\varepsilon_\beta\frac{\partial\langle p_\beta\rangle^\beta}{\partial x_i}-\mu_\beta\frac{\partial^2\langle u_{i_\beta}\rangle}{\partial x_j^2}-\mu_\beta\frac{\partial^2\langle u_{j_\beta}\rangle}{\partial x_j x_i}+\rho_\beta\frac{\partial\langle gh\rangle}{\partial x_i}+\frac{1}{V_{RUC}}\left[-\left(\int_{A_\beta}\sigma_{ij_\beta}\widehat{n_{j_\beta}}dA_\beta\right)+\right.$$
$$\left.\rho_\beta\int_{A_\beta}gh\widehat{n_{i_\beta}}dA_\beta-\langle p_\beta\rangle^\beta\int_{A_\beta}\widehat{n_{j_\beta}}dA_\beta\right]-\frac{\mu_\beta}{V_{RUC}}\frac{\partial}{\partial x_j}\left(\int_{A_\beta}u_{i_\beta}\widehat{n_{j_\beta}}+u_{j_\beta}\widehat{n_{i_\beta}}dA_\beta\right)=0 \tag{13}$$

By defining the viscous drag interaction force as:

$$f_{d_i}=\frac{1}{V_{RUC}}\left[-\left(\int_{A_\beta}\sigma_{ij_\beta}\widehat{n_{j_\beta}}dA_\beta\right)+\rho_\beta\int_{A_\beta}gh\widehat{n_{i_\beta}}dA_\beta-\langle p_\beta\rangle^\beta\int_{A_\beta}\widehat{n_{j_\beta}}dA_\beta\right]=$$
$$\mu_\beta\varepsilon_\beta\left(K_{ij_\beta}\right)^{-1}\langle u_{j_\beta}\rangle \tag{14},$$

the Eq.13 is reduced to:

$$\varepsilon_\beta \frac{\partial \langle p_\beta \rangle^\beta}{\partial x_i} - \mu_\beta \frac{\partial^2 \langle u_{i_\beta} \rangle}{\partial x_j^2} - \mu_\beta \frac{\partial^2 \langle u_{j_\beta} \rangle}{\partial x_j x_i} - \rho_\beta \frac{\partial \langle gh \rangle}{\partial x_i} + \mu_\beta \varepsilon_\beta \left(K_{ij_\beta}\right)^{-1} \langle u_{j_\beta} \rangle - \frac{\mu_\beta}{V_{RUC}} \frac{\partial}{\partial x_j} \left(\int_{A_\beta} u_{i_\beta} \widehat{n_{j_\beta}} + u_{j_\beta} \widehat{n_{i_\beta}} dA_\beta \right) = 0 \quad (15)$$

where $\left(K_{ij_\beta}\right)^{-1}$ is the inverse of the permeability tensor of the phase β, K_{ij_β}.

2.2.2 Governing equations for dual-scale porous media at mesoscopic scale

At mesoscopic scale, several approaches can be identified in the literature for the flow modeling in the channels and bundles inside the RUC (See Figure 1b,c). The bundles are usually conceived as single-scale porous media containing two phases behind the fluid front: liquid *(l)* and solid *(s)* [6], [7], [12]. Considering incompressible resin, non-deformable and impenetrable fibers and neglecting gravitational effects, Eq.5 and Eq.15 for $\beta = l$ reduce to:

$$\frac{\partial \langle u_{i_l} \rangle}{\partial x_i} = 0 \quad (16a)$$

$$\varepsilon_l \frac{\partial \langle p_l \rangle^l}{\partial x_i} - \mu_l \frac{\partial^2 \langle u_{i_l} \rangle}{\partial x_j^2} + \mu_l \varepsilon_l \left(K_{ij_l}\right)^{-1} \langle u_{j_l} \rangle = 0 \quad (16b)$$

Eq. 16b is the Brinkman law that can be also written as:

$$\frac{\partial \langle p_l \rangle^l}{\partial x_i} - \mu_{eff} \frac{\partial^2 \langle u_{i_l} \rangle}{\partial x_j^2} + \mu_l \varepsilon_l \left(K_{ij_l}\right)^{-1} \langle u_{j_l} \rangle = 0 \quad (17),$$

where $\mu_{eff} = \mu_l / \varepsilon_l$ is the effective viscosity, which, theoretically, is the ratio between the real liquid viscosity and the porosity, but that can assume another values according to the matching conditions between the channels and the tows as shown in Chapter 4.

Eq.17 can reduce to the Darcy law under the following scale restrictions: $(L_{RUC}/L)^2 << 1$ and $L_{RUC} \gg L_f$ [130], where L is the characteristic length of the macroscopic saturated domain, whereas L_{RUC} and L_f are the characteristic lengths of the RUC and the fluid phase, respectively, as shown in Figure 11 ($f \equiv l$ in this case since the air is not considered). In Figure 12 two RUC's with the same fluid porosity, ε_f, are considered, with the first one satisfying the second Darcy restriction, i.e., $L_{RUC} \gg L_f$, while the second one does not. This means that the Darcy simplification is not strictly associated to the value of the porosity, ε_f, but to the pore distribution itself, with higher probability to be complied when ε_f is low. For instance, as mentioned by [6], the Darcy simplification is not possible if the RUC's

comprise the interface channel-bundle. In the present work, the flow modeling in the tows is carried out by the Darcy law in Chapter 3 and by the Brinkman law in Chapter 4.

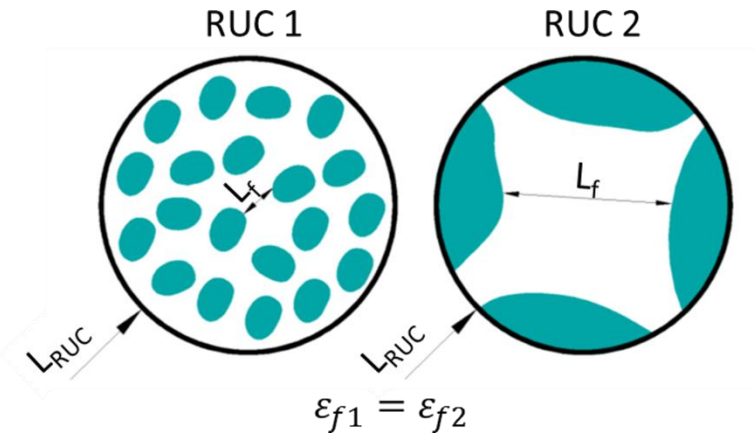

Figure 12 RUC's with the same porosity modeled with different laws (Darcy and Brinkman).

For the channels, the flow modeling can be carried out using the Navier-Stokes equation, which considerably simplifies to the Stokes equation when the channel Reynolds number is small. This is the situation considered here given the usual conditions of LCM processes. Other authors have modeled the flow in the channels using the Darcy law with an equivalent permeability [3], [25], [79]. This last approach is compared with the implemented Stokes-Darcy approach in Chapter 3.

2.2.3 Governing equations for dual-scale porous media at macroscopic scale

At macroscopic scale, two approaches to model the unsaturated filling of cavities can be mentioned. In the first one, a fluid phase (f), including both liquid (l) and gas (g), is considered, and the gas density and velocity are neglected, obtaining the following mass conservation equation from Eq. 5 for incompressible liquids:

$$\frac{\partial \varepsilon_l}{\partial t} + \frac{\partial \langle u_{i_l} \rangle}{\partial x_i} = -\frac{1}{V_{RUC}} \int_{A_f} u_{i_f} \widehat{n_{i_f}} dA_f \tag{18}$$

By defining the saturation as the ratio between the volume of the liquid and volume of the fluid phase, $s = V_l/V_f$, considering that $\varepsilon_l = V_l/V_{RUC}$ and taking into account the impermeability and non-deformability of the fibers, i.e., $u_{i_f} = 0$ in A_f, Eq.18 can be written as:

$$\varepsilon_f \frac{\partial s}{\partial t} + \frac{\partial \langle u_{i_l} \rangle}{\partial x_i} = 0 \quad (19),$$

where ε_f is the porosity of the fluid phase, which remains constant.

Doing $\beta = f$ in Eq.15, considering the mentioned assumptions, neglecting the gravitational effects and applying the Darcy scale constraints, the following momentum equation is obtained:

$$\langle u_{i_f} \rangle = -\frac{K_{ij_f}}{\mu_f} \frac{\partial \langle p_f \rangle^f}{\partial x_j} \quad (20),$$

As $\langle u_{i_f} \rangle \approx \langle u_{i_l} \rangle$ and considering that both the permeability and the capillary pressure shall be considered function of the saturation, s, Eq.20 can be substituted into Eq.19 to obtain the well-known Richards equation:

$$\varepsilon_f \frac{\partial s}{\partial t} - \frac{\partial}{\partial x_i}\left(\frac{K_{ij_f}(s)}{\mu_f} \frac{\partial \langle p_f \rangle^f(s)}{\partial x_j}\right) = 0 \quad (21),$$

where $K_{ij_f}(s)$ is also known as the effective unsaturated permeability, which is studied in Chapter 6 of this work.

The second approach for the macroscopic modeling of dual-scale porous media, which is employed in the present work, was proposed by [6]. Two phases are considered: the channels or gaps *(g)*, which are assumed to be initially filled of liquid, and bundles or tows *(t)*, which are considered initially empty (See Figure 1c). The mass conservation equation can be obtained from Eq. 5 by doing $\beta = g$, considering an incompressible fluid, assuming non-deformable tows and representing the gap-tow interface as gt*:*

$$\frac{\partial \langle u_{i_g} \rangle}{\partial x_i} = -S_g \quad (22),$$

where $S_g = -1/V_{RUC} \int_{A_{gt}} u_{i_{gt}} \widehat{n_{i_{gt}}} dA_{gt}$ is the sink term that arises in this approach considering that the tows are permeable.

On the other hand, the momentum equation is achieved from Eq.15 by doing $\beta = g$. Substituting Eq.22 in the resulting equation, neglecting gravitational effects and organizing terms, the following is obtained:

$$\frac{\partial \langle p_g \rangle^g}{\partial x_i} - \mu_{eff_g} \frac{\partial^2 \langle u_{i_g} \rangle}{\partial x_j^2} + \mu_g \left(K_{ij_g}\right)^{-1} \langle u_{j_g} \rangle - \mu_{eff_g} \frac{\partial}{\partial x_j} I_{ij} = 0 \quad (23),$$

where $\mu_{eff_g} = \mu_g/\varepsilon_g$ is the effective viscosity in the gaps or channels, while $I_{ij} = -S_g\delta_{ij} + 1/V_{RUC}\int_{A_{gt}} u_{i_{gt}}\widehat{n_{j_{gt}}} + u_{j_{gt}}\widehat{n_{i_{gt}}}dA_{gt}$ is interfacial kinetic effects tensor. According to [6], Eq.23 is the equivalent Brinkman equation for dual-scale porous media. The second term of this equation can be dropped under the same two scale restrictions abovementioned (See Figure 11 and Figure 12) applied to the gap phase; the second restriction reads $L_{RUC} \gg L_g$, with L_g as the characteristic length of the gaps. According to [6], [14], the last term of Eq.23 is likely to become important in regions where the gradient of S_g is very large, but for woven fabrics, the not consideration of this term is an initial good approximation that significantly simplifies the problem. Details about the scale restrictions that shall be complied here to use the Darcy law in the macroscopic modeling are shown Chapter 6.

2.3 Permeability and capillary

Permeability.

The permeability is the property that indicates the easiness of impregnation of fibrous reinforcements. Several kinds of permeabilities can be identified according to the approach used to study the impregnation phenomenon. The permeability obtained from experimental unidirectional or radial injections is known as the apparent permeability, K_{app}, since the mathematical model is based on the simple continuity and Darcy laws for single-scale porous media, which is not necessarily valid for dual-scale porous media where the delayed absorption of resin into the tows (sink term) shall be considered, as shown in Eq.22. Tests to determine K_{app} can be classified into two main families: saturated and unsaturated tests. In the former ones, the preform is totally filled with the injection liquid at constant flow rate, Q_{inj}, and two values of pressure, P_1 and P_2, are obtained in points separated by a distance L_{12}, in order to calculate the apparent saturated permeability, $K_{app,sat}$, as follows:

$$K_{app,sat} = -\frac{Q_{inj}}{A}\frac{\mu L_{12}}{P_2 - P_1} \quad (24),$$

where μ and A are the fluid viscosity and cross section area of the mold. On the other hand, in the unsaturated tests, which are usually conducted at constant pressure, P_{inj}, the permeability is calculated according to the fluid front positions in the time. In unidirectional

injections, the apparent unsaturated permeability can be calculated in three ways as follows [132]:

Apparent unsaturated elemental permeability:

$$K_{app,uns}^{elem} = \frac{\varepsilon\mu}{2}.\left(\frac{L_{ff}(t_{i+1})-L_{ff}(t_i)}{t_{i+1}-t_i} + \frac{L_{ff}(t_i)-L_{ff}(t_{i-1})}{t_i-t_{i-1}}\right).\left(\frac{L_{ff}(t_i)}{P_{inj}-P_{ff}}\right) \quad (25a)$$

Apparent unsaturated pointwise permeability:

$$K_{app,uns}^{point} = \frac{\varepsilon\mu.[L_{ff}(t_i)]^2}{2.t_i(P_{inj}-P_{ff})} \quad (25b)$$

Apparent unsaturated interpolated permeability:

$$K_{app,uns}^{inter} = \varepsilon\mu\frac{\sum_{i=1}^{n}\left(L_{ff}(t_i).\sqrt{t_i(P_{inj}-P_{ff})}\right)}{2\sum_{i=1}^{n}t_i(P_{inj}-P_{ff})} \quad (25c)$$

where ε and P_{ff} are the global porosity of the preform and the fluid front pressure, respectively, while $L_{ff}(t_i)$ and $L_{ff}(t_{i+1})$ represent the fluid front position in times t_i and t_{i+1}, respectively. On the other hand, in radial injections, the apparent unsaturated permeabilities in the principal directions are calculated using the following equation [133], [134]:

$${K_1}_{app,uns}^{radial} = \left[{x_{ff}}^2.\left(2ln\left(\frac{x_{ff}}{x_o}\right)-1\right)+{x_o}^2\right].\frac{\mu\varepsilon}{4(P_{inj}-P_{ff})t_i} \quad (26a)$$

$${K_2}_{app,uns}^{radial} = \left[{y_{ff}}^2.\left(2ln\left(\frac{y_{ff}}{y_o}\right)-1\right)+{y_o}^2\right].\frac{\mu\varepsilon}{4(P_{inj}-P_{ff})t_i} \quad (26b),$$

where x_{ff} and y_{ff} are the fluid front positions in the principal directions of permeability (x and y), while x_o and y_o represent the dimensions of the inlet port in the principal directions of permeability.

As the modeling of dual-scale fibrous reinforcements using the apparent permeabilities could be inaccurate, others types of theoretical and numerical models are required according to the governing laws presented in Sections 2.2.2 and 2.2.3. At mesoscopic scale (filling of RUC's), if the tows are considered as a bank of aligned circular fibers, several models can be used to compute the main tow permeabilities, K_1 and K_2 [23], [24], [102], [135], with the Gebart model [135] as one of the most accepted:

$${K_1}_{gebart} = 8R^2.\left(1-V_f\right)^3/\left(c.(V_f)^2\right) \quad (27a)$$

$$K_{2_{gebart}} = c_1\left(\sqrt{V_{f,max}/V_f} - 1\right)^{5/2} R^2 \quad (27b),$$

where $V_f = 1 - \varepsilon_t$ is the fiber volume fraction of the tow, with ε_t as the tow porosity, whereas the parameters c, c_1 and $V_{f,max}$ depends on the type of fibers arrangement.

The modeling of the filling in dual-scale fibrous reinforcements at macroscopic scale using the Richards equation, Eq.21, requires to known a relationship between the effective unsaturated permeability, $K_{eff}(s)$, and the saturation, s. For the infiltration of soils, some empirical relationships have been established [136], [137], as well as for the infiltration of non-woven preforms [138]–[140], however, for woven or cross ply fabrics, as the ones considered here, no empirical relationships between $K_{eff}(s)$ and s are known in the literature. It is important to mention that when $s = 1$, K_{eff} is called the effective saturated, absolute or intrinsic permeability, $K_{eff,sat}$, whose behavior in dual-scale fibrous reinforcement has been previously studied by several authors [20], [23], [24], [85], [98]. In the ideal case, $K_{eff,sat} = K_{app,sat}$ (Eq. 24). Another common term found in composites literature is the relative permeability, $K_r(s)$, as defined by:

$$K_r(s) = \frac{K_{eff}(s)}{K_{eff,sat}} \quad (28),$$

On the other hand, the macroscopic modeling of dual-scale fibrous reinforcements using the approach of Pillai [6], Eq.(23), implies to know the gap or channel permeability, K_g, which is not dependent on the channels saturation since it is assumed that channels are totally filled with liquid before the impregnation of the bundles occurs at any RUC. This permeability indicates the easiness of impregnation of the network conformed by the channels assuming impermeable tows and can be determined from numerical simulations at mesoscopic scale by prescribing a pressure gradient in the RUC and applying a Stokes-Darcy formulation, as done in Chapter 6. The permeability of complex cell-structures has been determined from numerical simulations in [139], [141]–[143]; in the present work, the gap permeability, K_g, is determined in Chapter 6 for a simpler RUC geometry using the BEM results.

Other type of permeability that is very common in the scientific literature is the effective permeability in the direction determined by an angle ϕ_i; this permeability can be computed in terms of the principal permeabilities, K_1 and K_2, as follows [144]:

$$K_{eff}(\phi_i) = \frac{K_1.K_2}{K_1.sen^2(\phi_i)+K_2.cos^2(\phi_i)} \quad (29),$$

where ϕ_i is the angle between the given direction vector and the major axis of permeability.

Capillary.

The capillary pressure is the pressure difference existing across the interface separating two immiscible fluids generated by the difference between the adhesive and cohesive forces. In an open channel, the expression for the capillary pressure can be obtained straightforwardly by considering a differential element of the interface, as shown in Figure 13.

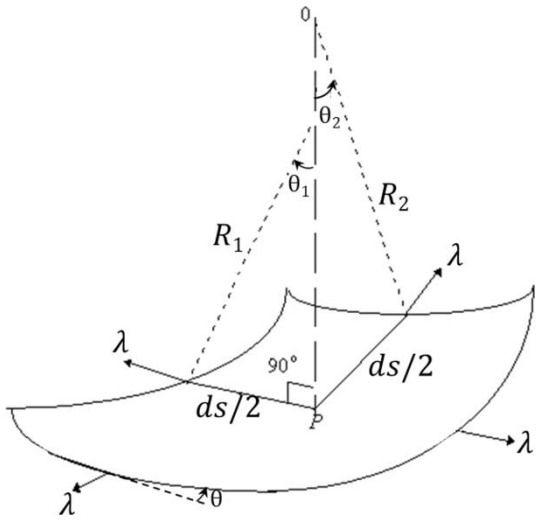

Figure 13 Balance of forces in the interface liquid-gas in open channels.

The forces equilibrium equation is as follows:

$$P_{cap}\left(ds.cos(\theta)\right)^2 = 2\left(\lambda ds.sin(\theta_1)\right) + 2\left(\lambda ds.sin(\theta_2)\right) \quad (30),$$

where λ is the surface tension in the interface liquid-gas. Considering that $cos(\theta) \approx 1$ because θ is very small and taking into account that $sin(\theta_1) = (ds/2)/R_1$ and $sin(\theta_2) = (ds/2)/R_2$, the following is obtained after solving for P_{cap} in Eq.30:

$$P_{cap} = \lambda\left(\frac{1}{R_1} + \frac{1}{R_2}\right) \quad (31),$$

or in terms of the curvatures, κ_1 and κ_2:

$$P_{cap} = \lambda(\kappa_1 + \kappa_2) \quad (32),$$

The sign of the capillary pressure in the numerical implementation depends either on the sign of the curvatures and on the orientation of the normal vector along the interface. In this work, the curvature is calculated in the wetting phase and the normals are outwardly oriented from this phase towards the non-wetting phase; hence, the sign of Eq.32 is changed in the kinematic condition applied to the channel fluid front.

In porous media, the deduction of expressions for P_{cap} is not so trivial considering that P_{cap} depends on the architecture of the porous medium and the flow orientation. In a bank of parallel fibers, when the flow goes along the fibers direction, it is supposed that the inter-fiber spaces act as capillary tubes having an equivalent capillary ratio, R_{ec}, as it can be appreciated in Figure 14.

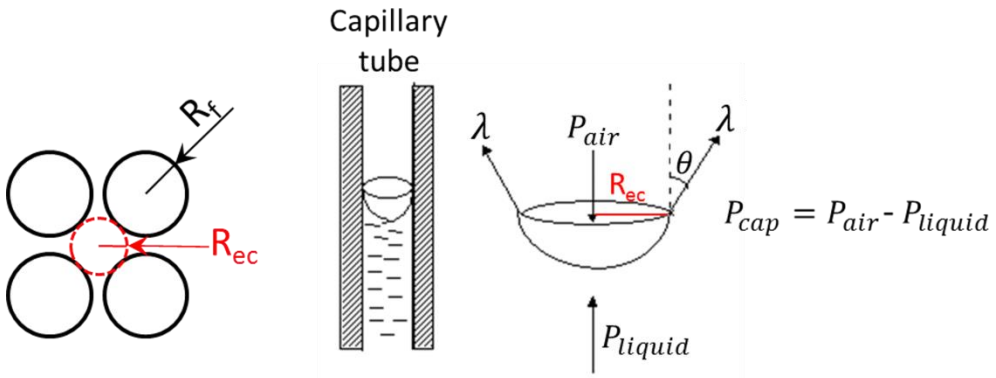

Figure 14 Balance of forces in the interface liquid-gas in capillary tubes.

The force equilibrium equation in this case is as follows:

$$P_{cap}\pi.R_{ec}^2 = 2\pi R_{ec}\lambda cos(\theta) \quad (33),$$

with θ as the contact angle. Solving for P_{cap}, the well-known Young-Laplace equation for capillary tubes is obtained:

$$P_{cap} = \frac{2\lambda cos(\theta)}{R_{ec}} \quad (34),$$

where the equivalent capillary ratio can be approximated as $R_{ec} = R_f\,\varepsilon_t/(1-\varepsilon_t)$, with R_f as the fiber radius, leading to the following expression:

$$P_{cap} = \frac{2(1-\varepsilon_t)\lambda cos(\theta)}{\varepsilon_t R_f} \quad (35)$$

In a similar fashion, it can be demonstrated that the capillary pressure for flow across a bank of aligned fibers (perpendicular to fibers) is:

$$P_{cap} = \frac{(1-\varepsilon_t)\lambda cos(\theta)}{\varepsilon_t R_f} \quad (36)$$

When the flow goes oblique to fibers, the calculation of P_{cap} has been tackled by introducing experimental shape factors in the Young Laplace equation in such a way that P_{cap} ranges between the values defined by Eqs. (35) and (36) [75], [145]–[147]. In the present thesis, a flow direction-dependent formula for the capillary pressure not incorporating empirical factors is obtained based on the work of Massodi and Pillai [148], in which a general formula for P_{cap} in terms of microstructure parameters was deduced on the basis of the energy balance principle. The expression obtained for P_{cap} is presented in Chapter 3.

It is important to remind that empirical relationships between P_{cap} and s are required for the solution of the Richards equation. This topic is out of the scope of the present work, but could be addressed in future researches using BEM simulation. The treatment of this particular issue in non-woven samples can be found in [138]–[140].

2.4 Boundary Element Techniques

The deduction of the boundary integral formulations for the Laplace and Stokes equations is briefly presented here since these formulations are used in the BEM solution of coupled Stokes-Darcy problems for isotropic porous media, being this the simplest case. The BEM formulation for the solution of coupled Stokes-Darcy problems for anisotropic porous media is presented in Chapter 3, while the DR-BEM formulation for coupled Stokes-Brinkman problems is shown Chapter 4. In Chapter 6, the DR-BEM formulation to solve multi-scale problems of partially saturated flow using a lumped strategy is presented.

2.4.1 Green identities and reciprocal relation

Laplace equation [149]

For any pair of twice differentiable functions, f and g, the following is valid:

$$\frac{\partial}{\partial x_i}\left(f\frac{\partial g}{\partial x_i}\right) = f\frac{\partial^2 g}{\partial x_i^2} + \frac{\partial f}{\partial x_i}\frac{\partial g}{\partial x_i} \quad (37),$$

which can be rewritten as follows:

$$f\frac{\partial^2 g}{\partial x_i^2} = \frac{\partial}{\partial x_i}\left(f\frac{\partial g}{\partial x_i}\right) - \frac{\partial f}{\partial x_i}\frac{\partial g}{\partial x_i} \quad (38),$$

Eq.38 is known as the *First Green Identity*. If the functions f and g are interchanged in Eq.38 and the resulting expression is subtracted from Eq.37, the *Second Green Identity* is obtained:

$$f\frac{\partial^2 g}{\partial x_i^2} - g\frac{\partial^2 f}{\partial x_i^2} = \frac{\partial}{\partial x_i}\left(f\frac{\partial g}{\partial x_i} - g\frac{\partial f}{\partial x_i}\right) \quad (39)$$

If the functions f and g satisfies the Laplace equation, the left hand side terms of Eq.(39) vanish, obtaining the reciprocal relation for the Laplace equation:

$$\frac{\partial}{\partial x_i}\left(f\frac{\partial g}{\partial x_i} - g\frac{\partial f}{\partial x_i}\right) = 0 \quad (40),$$

Stokes equation [150]

Two independent velocity fields satisfying mass conservation, u_i and u_i^*, and pressure fields, p_i and p_i^*, with corresponding stress tensors σ_{ij} and σ_{ij}^*, are considered. Similarly to Eq.37, the following is valid:

$$\frac{\partial}{\partial x_i}\left(u_j^*\sigma_{ij}\right) = u_j^*\frac{\partial \sigma_{ij}}{\partial x_i} + \frac{\partial u_j^*}{\partial x_i}\sigma_{ij} \quad (41)$$

Applying the definition of stress tensor, i.e., $\sigma_{ij} = -p\delta_{ij} + \mu\left(\partial u_i/\partial x_j + \partial u_j/\partial x_i\right)$, in the last term of the Eq.41, the following is obtained:

$$\frac{\partial}{\partial x_i}\left(u_j^*\sigma_{ij}\right) = u_j^*\frac{\partial \sigma_{ij}}{\partial x_i} - p\frac{\partial u_j^*}{\partial x_i}\delta_{ij} + \mu\frac{\partial u_j^*}{\partial x_i}\left(\frac{\partial u_i}{\partial x_j} + \frac{\partial u_j}{\partial x_i}\right) \quad (42),$$

where the second right-hand side term is dropped applying index contraction and mass conservation, i.e., $p\left(\partial u_j^*/\partial x_i\right)\delta_{ij} = p(\partial u_i^*/\partial x_i) = 0$. Reorganizing, the counterpart expression of Eq.38 is obtained as follows:

$$u_j^*\frac{\partial \sigma_{ij}}{\partial x_i} = \frac{\partial}{\partial x_i}\left(u_j^*\sigma_{ij}\right) - \mu\frac{\partial u_j^*}{\partial x_i}\left(\frac{\partial u_i}{\partial x_j} + \frac{\partial u_j}{\partial x_i}\right) \quad (43),$$

and following a similar procedure to the mentioned above for the Laplace equation, the counterpart of Eq.39 and the reciprocal relation for the Stokes equation are gotten as follows:

$$u_j^*\frac{\partial \sigma_{ij}}{\partial x_i} - u_j\frac{\partial \sigma_{ij}^*}{\partial x_i} = \frac{\partial}{\partial x_i}\left(u_j^*\sigma_{ij} - u_j\sigma_{ij}^*\right) \quad (44)$$

$$\frac{\partial}{\partial x_i}\left(u_j^*\sigma_{ij} - u_j\sigma_{ij}^*\right) = 0 \quad (45)$$

It is important to highlight that Eq.45 is valid provided that both solutions satisfied the Stokes equation.

2.4.2 Boundary integral formulations

Laplace equation [149]

The singularly forced Laplace equation in 2D is defined as:

$$\frac{\partial^2 p^*}{\partial {x_i}^2} + \delta_2\left(\vec{x} - \vec{\xi}\right) = 0 \tag{46},$$

where $\delta_2\left(\vec{x} - \vec{\xi}\right)$ is the Dirac delta function in two-dimensions, $\vec{x}$ is the field point and $\vec{\xi}$ is the source point. The function p^* satisfies the Laplace equation everywhere with exception of the point $\vec{\xi}$, where it is singular. The solution of the Eq.46 in unbounded domains is the free space Green's function and is given by:

$$p^*\left(\vec{x}, \vec{\xi}\right) = -\frac{1}{2\pi} ln(r) \tag{47},$$

with $r = \left|\vec{x} - \vec{\xi}\right|$ as the distance between the field and source point.

In the Eq.39, it is considered that $f = p$ and $g = p^*$, with p as a solution of the Laplace equation, i.e., $\partial^2 p / \partial x_i^2 = 0$. Additionally, considering that $\partial^2 p^* / \partial x_i^2 = -\delta_2\left(\vec{x} - \vec{\xi}\right)$ from Eq.46, the Eq.39 becomes:

$$-p\delta_2\left(\vec{x} - \vec{\xi}\right) = \frac{\partial}{\partial x_i}\left(p(\vec{x})\frac{\partial p^*\left(\vec{x}, \vec{\xi}\right)}{\partial x_i} - p^*\left(\vec{x}, \vec{\xi}\right)\frac{\partial p(\vec{x})}{\partial x_i}\right) \tag{48}$$

Taking the integral of Eq.48 over the domain Ω and applying the divergence theorem in the right-hand side terms, the following equation is obtained:

$$\int_\Omega \; p\delta_2\left(\vec{x} - \vec{\xi}\right)d\Omega = \int_s \; p^*\left(\vec{x}, \vec{\xi}\right)q(\vec{x})dS - \int_s \; q^*\left(\vec{x}, \vec{\xi}\right)p(\vec{x})\hat{n_i}dS \tag{49},$$

where $\hat{n_i}$ is the outward normal vector, $q^*\left(\vec{x}, \vec{\xi}\right) = \left(\partial p^*\left(\vec{x}, \vec{\xi}\right)/\partial x_i\right)\hat{n_i}$ and $q\left(\vec{x}, \vec{\xi}\right) = \left(\partial p\left(\vec{x}, \vec{\xi}\right)/\partial x_i\right)\hat{n_i}$. The first right hand side integral is the Single Layer Potential (SLP), while the second one is the Double Layer Potential (DLP). For interior and exterior points, the integral of the left hand side can be dealt using the Dirac delta properties, whereas for points lying on the boundary, the continuous and discontinuous properties of SLP and DLP needs to be considered. After solving the left hand side integral, the next expression is obtained:

$$c(\vec{\xi})p(\vec{\xi}) = \int_s \; p^*(\vec{x},\vec{\xi})q(\vec{x})dS - \int_s \; q^*(\vec{x},\vec{\xi})p(\vec{x})\hat{n}_\iota dS \qquad (50),$$

where:

$$c(\vec{\xi}) = \begin{cases} 1 \; when \; \vec{\xi} \; is \; inside \; \Omega \\ (\alpha/(2\pi)) \; \; when \; \vec{\xi} \; lies \; on \; the \; boundary \; of \; \Omega \\ 0 \; when \; \vec{\xi} \; is \; outside \; \Omega \end{cases}$$

with α as the solid angle that has a value of $\alpha = \pi$ for smooth boundaries.

Stokes equation [150]

The singularly forced Stokes equation in 2D is defined as:

$$\frac{\partial \sigma_{ij}^*}{\partial x_j} + \delta_2(\vec{x} - \vec{\xi})b_i = 0 \qquad (51),$$

or equivalently as:

$$-\frac{\partial p^*}{\partial x_i} + \mu \frac{\partial^2 u_i^*}{\partial {x_j}^2} + \delta_2(\vec{x} - \vec{\xi})b_i = 0 \qquad (52),$$

The velocity and pressure fields, u_i^* and p^*, as well as the stress tensor σ_{ij}^*, corresponding to the solution of Eqs. 51 and 52, along with the solution of mass conservation equation, are the fundamental solutions, which represent the Stokes flow solution when a point force is applied in the point $\vec{\xi}$. In Eq.51, b_i is a vector indicating the strength and magnitude of the applied force. The fundamental solutions are given by:

For the velocity:

$$u_i^*(\vec{x},\vec{\xi}) = \frac{1}{4\pi\mu} G_{ij}(\vec{x} - \vec{\xi})b_j \qquad (53a)$$

For the pressure:

$$p^*(\vec{x},\vec{\xi}) = \frac{1}{4\pi} p_j(\vec{x} - \vec{\xi})b_j \qquad (53b)$$

For the stress tensor:

$$\sigma_{ik}^*(\vec{x},\vec{\xi}) = \frac{1}{4\pi} T_{ijk}(\vec{x} - \vec{\xi})b_j \qquad (53c),$$

where $G_{ij}(\vec{x} - \vec{\xi})$, $p_j(\vec{x} - \vec{\xi})$ and $T_{ijk}(\vec{x} - \vec{\xi})$ are the Green's functions. In the case of unbounded domains (free-space), the Green's functions in 2D are as follows:

For the velocity:

$$G_{ij}\left(\vec{x}-\vec{\xi}\right)=ln\left(\frac{1}{r}\right)\delta_{ij}+\frac{\widehat{x_i}\widehat{x_j}}{r^2} \tag{54a}$$

For the pressure:

$$p_j\left(\vec{x}-\vec{\xi}\right)=2\frac{\widehat{x_j}}{r^2} \tag{54b}$$

For the stress tensor:

$$T_{ijk}\left(\vec{x}-\vec{\xi}\right)=-p_j\left(\vec{x}-\vec{\xi}\right)\delta_{ij}+\mu\left(\frac{\partial G_{ij}\left(\vec{x}-\vec{\xi}\right)}{\partial x_k}+\frac{\partial G_{kj}\left(\vec{x}-\vec{\xi}\right)}{\partial x_i}\right)=-4\frac{\widehat{x_i}\widehat{x_j}\widehat{x_k}}{r^4} \tag{54c},$$

where $\widehat{x_i}=x_i-\xi_i$ and $r=\left|\vec{x}-\vec{\xi}\right|$.

In the Eq.44, u_i^* and σ_{ij}^* are taken as the fundamental solutions defined in Eqs.53a and 53c, while u_i and σ_{ij} are considered solution of the Stokes equation. Therefore, the following is valid: $\partial\sigma_{ij}/\partial x_j=0$ and $\partial\sigma_{ij}^*/\partial x_j=-\delta_2\left(\vec{x}-\vec{\xi}\right)b_i$ from Eq.51. Taking into account the symmetry property of the stress tensor, it is also valid: $\partial\sigma_{ji}/\partial x_j=0$ and $\partial\sigma_{ji}^*/\partial x_j=-\delta_2\left(\vec{x}-\vec{\xi}\right)b_i$. As Eq.44 is scalar, it is possible to interchange indexes in the left hand side terms, i.e., $i\rightarrow j$ and $j\rightarrow i$. Besides, as the vector b_i is arbitrary, it can be set to one. These considerations lead to the following vector equation:

$$\delta_2\left(\vec{x}-\vec{\xi}\right)u_m=\frac{\partial}{\partial x_i}\left(\frac{1}{4\pi\mu}G_{jm}\left(\vec{x}-\vec{\xi}\right)\sigma_{ij}(\vec{x})-u_j(\vec{x})\frac{1}{4\pi}T_{imj}\left(\vec{x}-\vec{\xi}\right)\right) \tag{55}$$

Taking the integral of Eq.55 over the domain Ω and applying the divergence theorem in the right-hand side terms, the following equation is obtained:

$$\int_\Omega\ \delta_2\left(\vec{x}-\vec{\xi}\right)u_m\,d\Omega=\int_s\ \frac{1}{4\pi\mu}G_{jm}\left(\vec{x}-\vec{\xi}\right)\sigma_{ij}(\vec{x})\widehat{n_i}ds-\int_s\ u_j(\vec{x})\frac{1}{4\pi}T_{imj}\left(\vec{x}-\vec{\xi}\right)\widehat{n_i}ds \tag{56},$$

which can be rewritten, considering the symmetry property of the stress tensor, of the Green's functions for the velocity and of the Green's functions for the stress tensor, i.e., $\sigma_{ij}=\sigma_{ji}$, $G_{jm}=G_{mj}$, and $T_{imj}=T_{jmi}$, and relabeling indexes ($m\rightarrow i, i\rightarrow k$), as follows:

$$\int_\Omega\ \delta_2\left(\vec{x}-\vec{\xi}\right)u_i\,d\Omega=\int_s\ \frac{1}{4\pi\mu}G_{ij}\left(\vec{x}-\vec{\xi}\right)\sigma_{jk}(\vec{x})\widehat{n_k}ds-\int_s\ u_j(\vec{x})\frac{1}{4\pi}T_{jik}\left(\vec{x}-\vec{\xi}\right)\widehat{n_k}ds \tag{57}$$

Considering the definition of the traction vector, $t_j=\sigma_{jk}\widehat{n_k}$, and the following terms:

$$U_i^j(\vec{x},\vec{\xi}) = -\frac{1}{4\pi\mu} G_{ij}(\vec{x}-\vec{\xi}) \tag{58a}$$

$$K_{ij}(\vec{x},\vec{\xi}) = -\frac{1}{4\pi} T_{jik}(\vec{x}-\vec{\xi})\widehat{n_k} = \frac{1}{4\pi} T_{jik}(\vec{\xi}-\vec{x})\widehat{n_k} \tag{58b},$$

the Eq.57 can be rewritten as:

$$\int_\Omega \delta_2(\vec{x}-\vec{\xi}) u_i \, d\Omega = \int_s K_{ij}(\vec{x},\vec{\xi}) u_j(\vec{x}) \, ds - \int_s U_i^j(\vec{x},\vec{\xi}) t_j(\vec{x}) ds \tag{59}$$

with the first integral of the right hand side as the Double Layer Potential (DLP) and the second one as the Single Layer Potential (SLP). In a similar fashion as the Laplace equation, the left hand side integral can be solved using the properties of the Dirac delta function and the properties of SLP and DLP, obtaining the next expression:

$$c_{ij}(\vec{\xi}) u_j(\vec{\xi}) = \int_s K_{ij}(\vec{x},\vec{\xi}) u_j(\vec{x}) \, ds - \int_s U_i^j(\vec{x},\vec{\xi}) t_j(\vec{x}) ds \tag{60},$$

where:

$$c_{ij}(\vec{\xi}) = \begin{cases} \delta_{ij} \; when \; \vec{\xi} \; is \; inside \; \Omega \\ (\alpha/(2\pi))\delta_{ij} \; when \; \vec{\xi} \; lies \; on \; the \; boundary \; of \; \Omega \\ 0 \; when \; \vec{\xi} \; is \; outside \; \Omega \end{cases}$$

with α as the solid angle that has a value of $\alpha = \pi$ for smooth boundaries.

3. VOID FORMATION IN DUAL-SCALE FIBROUS REINFORCEMENTS BASED ON THE STOKES-DARCY FORMULATION[♠]

3.1 Introduction

In the processing of composites materials many kinds of fibrous reinforcements have two well-differentiated domains at the mesoscopic scale, channels and tows. Some authors have modeled the filling of these fibrous reinforcements considering that both flow regions are governed by the Darcy law, with the scale of permeability of the channels considerably larger than the scale of permeability of the tows [3], [4], [14], [25]. In this type of approach the low Reynolds number flow, creeping flow, inside the thin channels is approximated by the Hele-Shaw cross average flow with an equivalent permeability. By using this approximation some details of the interface process between the two media, channels and tows, are lost, allowing only mass conservation and continuity of pressure across the media. An alternative approach, and more robust, is to model the flow in the channels as a Stokes flow, and the flow in the porous tows using the Darcy law (see [19], [23], [24], [100]), with the corresponding coupling conditions between the two flow regions. This type of mathematical formulation will be used in this chapter. Besides, the solid phase is considered as non-deformable, the injected fluid is Newtonian and incompressible, inertial effects are neglected (creeping flow), the tow porosity is constant and the permeability changes according to the fibers orientation (anisotropic porous media).

The problem of simulation of the impregnation process of fibrous reinforcements at the mesoscopic scale comprises two general aspects: the solution of the coupled governing equations of the flow field and the advancement of the fluid front. The numerical simulation of both aspects has been previously considered in the literature using different numerical techniques, being one of the most popular the FEM/CV conforming technique (among others see [8], [13], [14], [33], [38]), where the Finite Element Method (FEM) is used to solve the governing equations and obtain the nodal values of the pressure field. Since this type of FEM approach does not preserve locally mass conservation at the element level, each Finite Element is internally subdivided and coupled with the neighbors'

[♠] **The results of the present chapter were published in: Iván David Patiño Arcila, Henry Power, César Nieto Londoño, Whady Felipe Flórez Escobar, "Boundary element simulation of void formation in fibrous reinforcements based on the Stokes-Darcy formulation". Published in: Switzerland, Computer Methods In Applied Mechanics And Engineering, ISSN: 0045-7825 ed:**

subdivisions to form a local Control Volume (CV), i.e., one CV for each FEM node, as it was shown in Figure 3. In each CV a filling factor, f, is evaluated from the mass flux balance and the fluid front position is determined by interface capturing schemes. Several of these schemes have been proposed in the literature; among them, the Flow Analysis Network (FAN) approach, originally proposed by Tadmor et al.[151], considers that each value of f is associated to the center node of the corresponding CV, and that the position of the fluid front is determined by a weighted average value of the distances between the neighbor CV's nodes in term of their corresponding nodal vales of f.

Alternatively to the use of a FEM/CV conforming approach, a single CV formulation allows the nodal values of the pressure field as well as the mass flux balance at each CV to be determined without the need of creating auxiliary elements for a given discretization. Since this type of approach is locally mass conservative, this is achieved at the expense of lowering the convergence rate of the numerical solution in comparison with a FEM simulation; see for instance Jinlian et al.[3], where a CV/FAN approach is used to study the mechanism of void formation during RUC filling processes. The CV formulation of Jinlian et al. [3] uses non-structured CV elements with a generalized Finite Difference (FD) approach to evaluate the surface fluxes in terms of linear polynomial interpolation of the pressure field. To keep the rate of convergence of the FEM/CV approach without the need of defining auxiliary elements for the mass flux balance, it is possible to use a nonconforming FEM formulation, which is locally mass conservative, allowing the evaluation of the filling factor, f, at each element of the FEM discretization and the corresponding position of the fluid front [40].

For the tracking of the fluid front, instead of evaluating a filling factor f by mass conservation balance at each element, it is possible to solve a pure advection transport equation defined for both phases, liquid and air, with the fluid properties (viscosity in this case) given as a weighted average in terms of the volume of fluid fraction, f_v, whose value also ranges between 0 and 1. As a hyperbolic problem, solution of f_v admits smooth shock profiles, requiring the use of specific solvers. This technique, which is usually known simply as VOF, has been previously used in the literature together with FEM and CV techniques, see for example [111] for FEM/VOF and [22] and [80] for CV/VOF simulations. Level Set formulations can be also considered for the tracking of the fluid

front, where a signed distance function, $\emptyset$, which is the solution of a pure advection transport equation, needs to be found, in such a way that in the filled region $\emptyset > 0$, in the empty region $\emptyset < 0$ and in the moving interface $\emptyset = 0$. Specific solvers need to be used as well to solve the corresponding hyperbolic problem, and particularly, it is necessary to avoid, as possible, numerical diffusion that will disperse the position of the interface. In [106] a nonconforming FEM/Level-Set approach is presented for the numerical simulation of resin transfer moulding process (RTM) in order to study race-tracking effects and macro-void formation in complex geometries.

In contrast with mesh-moving schemes, where at each time step the mesh is refined and forced to have elements nodes at the moving interface, in the above mesh-fix approaches it is not possible to impose directly the interface dynamic condition, which consists on the balance of surface forces (capillary tension). In some cases, those surface forces can be considered as volume forces that are introduced into the original momentum equation and are smoothly distributed around the fluid front [80]. Another alternative is the use of enhanced FEM interpolations, as those ones used in fracture mechanics, where the interface dynamic condition is imposed inside the elements containing the fluid front. In [106], this type of enhanced or extended FEM approach (XFEM) was adapted to the nonconforming FEM/Level-Set solution of the RTM process.

In the present chapter, the phenomenon of impregnation of the RUC is simulated by the Boundary Element Method (BEM). In contrast with the FEM/CV techniques or any other domain discretization approach, the BEM only requires the use of a mesh along the contour of each sub-domain and not the use of internal elements, which is convenient when dealing with moving boundary problems. In this approach it is also possible to implement directly the dynamic interface condition at those boundary elements belonging to the fluid front. Although the BEM technique is very popular to solve coupled Stokes-Darcy problems, to the best of the author's knowledge, this method has not been implemented yet in the simulation of void formation in fibrous reinforcements. The BEM has been previously used in the filling at the macroscopic scale considering a single-scale porous medium, see for instance [46], [50], where a level set approach is used to track the fluid front position. In our numerical scheme, a direct integration of the interface kinematic condition is used to advance the fluid front (Euler method), instead of solving an auxiliary hyperbolic problem.

In this way both interface boundary conditions at the fluid front, dynamic and kinematic, are satisfied simultaneously in the numerical solution. This tracking methodology assures a higher order accuracy of the fluid front shape when compared with the abovementioned techniques.

The free boundary nature of the present problem implies the existence of some aspects not considered in other types of coupled Stokes-Darcy flow problems:

- The flow cannot be assumed primordially unidirectional and the mass exchange between the sub-domains cannot be disregarded a priori, meaning that Saffman's simplication of the slip condition at the interface between the Stokes and Darcy flow media is not necessarily valid in the present case. Consequently, the general Beavers-Joseph slip condition needs to be considered and the tangential component of the Darcy pressure gradient, which is usually neglected by other authors [152], [153], needs to be evaluated numerically.
- Some authors have taken a constant capillary pressure for the porous medium [14], [80], [81] and others have considered the change of that pressure with the flow orientation by introducing experimental shape factors [145], [146]. In the present chapter, a general expression based on the energy balance principle that was proposed by Pillai and Massodi [148] is adapted to the particular case of a porous medium consisting on aligned micro-cylinders, in such a way that the shape factor is computed theoretically and no experimental parameters are required.
- In the simulation of dual-scale porous media for the processing of composites, the effect of capillary forces in the channel flow region, which is associated to the curvature of the moving front (See Chapter 2), is not usually considered [3], [13], [22], [80], [81]. This simplification is valid provided that the viscous forces exceed the capillary ones by several orders of magnitudes. However, when the injection pressure or flow rate leads to small modified capillary numbers, C_a^*, the capillary forces in the channel can have an important influence in the impregnation process, and they need to be taken into account in the simulation, as it is the case of the lowest value of C_a^* considered here.

In the first part of this chapter, the developed BEM code is validated with an analytical solution of a simple Stokes-Darcy coupled problem, which was developed here by using the lubrication approximation for the channel flow and the Equivalent Isotropic System

transformation (EIS) for the anisotropic porous medium. Having validated the proposed numerical scheme, two types of RUC filling problems are considered: The first one consists on the simulation at constant pressure regime of the simultaneous filling of the channels and tows that are present inside the RUC. The main objective of this simulation is to compare the obtained BEM results with those ones found by Jinlian et al.[3] with the CV/FAN approach. The second case, where a constant inlet flow rate is considered, consists on a parametric study to determine the influence of processing, geometric and material parameters on the size, shape and location of the voids formed by mechanical entrapment of air. The parameters studied in the analysis are: modified capillary number, tow porosity, width of the transverse tow, fluid penetrativity and RUC porosity. In both cases, a simplified two-dimensional geometry of the RUC is analyzed. Although a rigorous study of the impregnation process at the mesoscopic framework implies the modeling of three dimensional flows, many authors have considered 2D geometries [3], [4], [22]–[25], [81] to simplify their numerical analysis, but capturing the behavior of the main processes. The particular geometry chosen in the present chapter is the same as the one considered in [3], which is an adequate simplification of the longitudinal sections of multilayer cross-ply fabrics. Additionally, according to Jinlian et.al [3], this simplification is also suitable for multilayer woven fabrics when the configuration is Warp-Weft-Warp-Weft and the crimp degree is low.

3.2 Governing equations, boundary and matching conditions

When the Reynolds number and the permeability are small, the coupling problem between the fluid in the channel and the fluid in the porous medium can be defined by a Stokes-Darcy formulation as:

For the channel (Stokes domain):

$$\mu\left(\partial^2 u_i/\partial x_j x_j\right) - \partial p/\partial x_i = 0 \tag{61a}$$

$$\partial u_i/\partial x_i = 0 \tag{61b}$$

For the porous medium (Darcy flow in the principal directions of permeability):

$$\langle u_f\rangle_i = -(K_i/\mu).\left(\partial\langle \mathrm{p_f}\rangle^{\mathrm{f}}/\partial x_i\right) \tag{62a}$$

$$\partial\langle u_f\rangle_i/\partial x_i = 0 \tag{62b},$$

where u_i and p are the "i" component of the velocity field and the fluid pressure in the channel flow, $\langle u_f \rangle_i$ and $\langle \mathrm{p_f} \rangle^{\mathrm{f}}$ are the "i" component of the volume-averaged velocity field and volume-averaged fluid pressure at the porous space (tow), K_i is the "i" component of the anisotropic permeability and μ is the liquid viscosity, with a corresponding pore velocity given by $\langle u_f \rangle_i / \varepsilon_t$, where ε_t represents the tow porosity (for more details see [130]). From now on, the volume-averaged symbols are omitted for sake of simplicity, but it is convenient to bear in mind that both the velocity and the pressure in the porous medium are not pointwise quantities, but volume-averaged quantities instead.

The architecture of the porous medium is considered as a bank of aligned micro-cylinders, and, under this assumption, the main components of the permeability can be computed using the model proposed by Gebart [135]:

$$K_1 = 8{R_f}^2 . \left(1 - V_f\right)^3 / \left(c . (V_f)^2\right) \tag{63a}$$

$$K_2 = c_1 \left(\sqrt{V_{f,max}/V_f} - 1\right)^{5/2} {R_f}^2 \tag{63b},$$

where R_f and V_f are the fiber radius and the fiber volume fraction, respectively. The parameters c, c_1 and $V_{f,max}$ depend on the type of array. In this case, a hexagonal array is considered and these parameters are as follows:

$$c = 53 \tag{64a}$$

$$c_1 = 16 / \left(9\pi\sqrt{6}\right) \tag{64b}$$

$$V_{f,max} = \pi / \left(2\sqrt{3}\right) \tag{64c}$$

The following matching conditions between the Stokes and Darcy domains are considered:

- *Continuity of normal velocities:*

$$u_i^{(s)} \hat{n}_i = u_i^{(d)} \hat{n}_i \tag{65},$$

  with the normal vector, $\hat{n}_i$, outwardly oriented from the Stokes domain, and where "s" stands for Stokes and "d" for Darcy.

- *Jump of tangential velocities:* this condition has been widely discussed in the literature [154], [155], but the most common is the slip condition of Beavers-Joseph that reads [156], [157]:

$$\mu \left(\frac{\partial u_i}{\partial x_j} + \frac{\partial u_j}{\partial x_i}\right)^{(s)} \hat{n}_j \hat{\tau}_i = \frac{\gamma \mu}{\sqrt{tr(K)/2}} \left(u_i^{(d)} - u_i^{(s)}\right) \hat{\tau}_i \tag{66},$$

where γ is the slip coefficient, $\hat{\tau}_i$ is the tangential vector and K is the permeability tensor. The slip coefficient, γ, is usually found by mean of experiments, but when the ratio between the height of the porous medium and the square root of the permeability is very high, a good approximation for this coefficient is [158]:

$$\gamma = 1/\left(\varepsilon_t{}^{1/2}\right) \tag{67}$$

The Beavers-Joseph condition could be simplified to the Saffman condition by neglecting the Darcy velocity, $u_i^{(d)}$, in the Eq.66 [159]; the main advantage of Saffman condition is that it is expressed in terms of only variables in the Stokes domain. However, as it was pointed out by Cao *et al*. [156], Saffman's assumptions omitting the Darcian term in the Eq.66 are not applicable for all cases. Firstly, the Saffman's simplification implies unidirectional flow in straight interfaces where no mass exchange takes place between the two media, and, secondly, this approximation requires the isotropic condition of the porous medium, although some authors have implemented it successfully in non-isotropic media under periodic conditions [154], [160]. Due to the lack of strong basis to justify the applicability of such simplifications in all cases treated here, it is reasonable to take the original Beavers-Joseph condition, Eq.66.

- *Continuity of surface tractions:*

$$\hat{n}_i \sigma_{ij}^{(s)} \hat{n}_j = -p^{(d)} \tag{68}$$

where $\sigma_{ij}^{(s)}$ is the Cauchy stress tensor in the Stokes domain and $p^{(d)}$ is the pressure in the Darcy domain.

On the other hand, the boundary conditions can be classified into three types:

- *Inlet conditions:* Two different types of conditions at the inlet are considered, namely, constant pressure and constant flow rate. In the case of constant inlet pressure, the conditions are as follows:

At the Stokes domain:

$$t_1 = -\overline{p_{in}}\widehat{n_1},\ u_2 = 0 \tag{69}$$

At the Darcy domain:

$$p = \overline{p_{in}} \tag{70}$$

where t_1 is the surface traction in the horizontal direction and $\overline{p_{in}}$ stands for the prescribed inlet pressure. For the constant flow regime, the inlet boundary conditions are given by the total flow rate, $\bar{Q} = \bar{Q}^{(s)} + \bar{Q}^{(d)}$, with corresponding contributions:

At the Stokes domain:

$$\bar{Q}^{(s)} = \int_{A_{inl}^{(s)}} u_1 . dA, u_2 = 0 \quad (71)$$

At the Darcy domain:

$$\bar{Q}^{(d)} = \int_{A_{inl}^{(d)}} (-K_n/\mu)(\partial p/\partial \hat{n}) dA \quad (72),$$

where K_n is the effective permeability in the normal direction (See Eq.29), while $A_{inl}^{(s)}$ and $A_{inl}^{(d)}$ represents the total inlet areas of the Stokes and Darcy domains, respectively.

- *No-flux conditions:* they are specified at the boundaries where symmetry is defined.
- *Moving interface conditions:* Kinematic and dynamic conditions at the moving boundaries between the liquid and air phases (fluid fronts) are:

Kinematic condition:

$$dx_i/dt = u_n \hat{n}_i = (u_j . \hat{n}_j)\hat{n}_i \text{ (at the Stokes and Darcy domain)} \quad (73)$$

Dynamic condition:

$$t_i + P_{air}\hat{n}_i = P_{cap}\hat{n}_i \text{ (at the Stokes domain)} \quad (74a)$$

$$p - P_{air} = -P_{cap} \text{ (at the Darcy domain)} \quad (74b),$$

where P_{air} is the air pressure obeying the perfect gas law and P_{cap} is the capillary pressure. In the interface kinematic condition at the porous medium, the normal fluid front velocity is given by the normal component of the pore velocity as follows:

$$u_n = -[K_i/(\varepsilon_t \mu)] . (\partial p/\partial x_i)\hat{n}_i \quad (75)$$

At the interface between the Stokes flow and the air, the capillary pressure is computed as: $P_{cap} = -\lambda\kappa = -\lambda(\nabla \cdot \hat{n})$, where λ and κ are the liquid surface tension and curvatures of the moving boundaries, respectively. On the other hand, in the porous medium, the capillary pressure depends on the contact angle (θ), surface tension (λ), architecture of the porous medium and orientation of the flow with respect to the fiber axis (φ). Recently, it was proposed the following general formula to approximate the capillary pressure in porous media on the basis of the energy-balance principle [148]:

$$P_{cap} = 2(\lambda . cos(\theta)/R_{ec}) \quad (76a)$$

$$R_{ec} = 2\left(A_{int,s}/C_{int,s}\right)(\varepsilon_t/(1-\varepsilon_t)) \quad (76b),$$

where $A_{int,s}$ is the cross sectional area of the solid particles in the flow direction and $C_{int,s}$ is the wetted perimeter of the solid particles, as shown in Figure 15 for the tow architecture considered here.

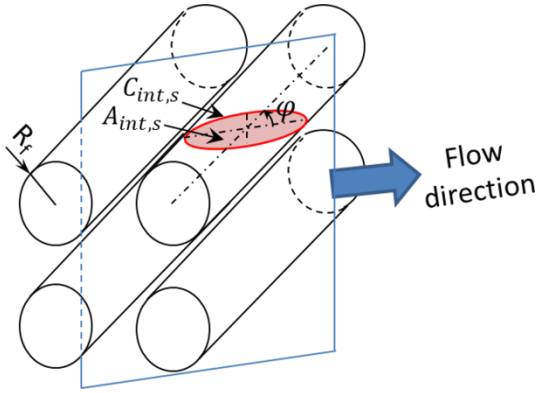

Figure 15 Scheme of capillary impregnation of longitudinal bundles.

The capillary pressure at any point of the longitudinal tow depends on the angle between the direction of the moving fluid front and the fiber axis, φ (Figure 15). If the flow infiltrates the tow in parallel or oblique direction, as shown in Figure 15, $A_{int,s}$ and $C_{int,s}$ are approximated as the sectional area and perimeter of a truncated circular cylinder using the Gauss-Kummer series for the perimeter of the resulting ellipse [161]. Therefore, for $0 \leq \varphi < \pi/2$, equations for $A_{int,s}$ and $C_{int,s}$ are as follows:

$$A_{int,s} = n_f \pi {R_f}^2 sec(\varphi) \quad (77a)$$

$$C_{int,s} = n_f \pi R_f \left(1 + sec(\varphi)\right).\left(1 + \sum_{i=1}^{\infty} \binom{1/2}{i}^2 \left(\frac{sec(\varphi)-1}{sec(\varphi)+1}\right)^{2i}\right) \quad (77b),$$

where n_f is the number of fibers inside the tows . When the flow is parallel to the fibers $(\varphi = 0)$, the Eqs. 77a and 77b reduces to the same equations employed by [145], [162]. If the impregnation occurs perpendicular to the fibers $(\varphi = \pi/2)$, the following expressions are used:

$$A_{int,s} = 2 n_f L_f R_f \quad (78a)$$

$$C_{int,s} \approx 2 n_f L_f \quad (78b),$$

where L_f represents the length of the fibers. On the other hand, for the transverse tow is assumed that the fluid front moves inward perpendicular to the fibers and the mean capillary pressure given by Neacsu et al. [163] is used:

$$P_{cap,r} = \left(\lambda/R_f\right).\left[\sin\left(\beta_{sup}+\theta\right) - \sin\left(\beta_{inf}+\theta\right)\right]/\left(\frac{5\pi}{6}(1+\eta) - 1 - \sqrt{3}/2\right) \quad (79a)$$

$$\eta = d/R_f \quad (79b)$$

$$\beta_{sup} \cong (\pi/2 - \theta) \quad (79c)$$

$$\beta_{inf} \cong (\theta - \pi/2) \quad (79d),$$

where $P_{cap,r}$ is the mean capillary pressure and d is the half-distance between fibers. The ratio η is known as the relative spacing ratio, which, for hexagonal arrays, can be computed as:

$$\eta = \sqrt{\pi/\left(2\sqrt{3}(1-\varepsilon_t)\right)} - 1 \quad (80)$$

On the other hand, it is important to point out that the mean capillary pressure in the model of Neacsu et al [163] is computed in a range between two limits of the local angular coordinate of the contact point between the meniscus and the fiber, β, taking the origin in the center of the fiber. The inferior limit appearing in Eq.79d, β_{inf}, is a negative angle corresponding to the instant when the meniscus first touches the surface of two neighboring fibers, whereas the superior limit of Eq.79c, β_{sup}, is reached when the flow is transferred to the next concentric layers of fibers. For more details, see [163].

Given the surface only mesh discretization required in the BEM employed in this work, all of the above boundary and interface conditions can be directly imposed into the corresponding surface integral representational formula of the Stokes and Darcy flows.

3.3 Integral equation formulations and numerical techniques

The boundary integral formulations for the Stokes [164] and Darcy anisotropic [56], [58], [149] equations are given in terms of the corresponding Green's integral formulae:

$$c_{ij}(\xi)u_j(\xi) = \int_S K_{ij}(\xi,y)\,u_j(y)dS_y - \int_S U_i^j(\xi,y)\,t_j(y)dS_y \quad (81)$$

$$c(\xi^e)p(\xi^e) = \int_S p^*(\xi^e,y^e)\,q(y^e)dS_{y^e} - \int_S q^*(\xi^e,y^e)\,p(y^e)dS_{y^e} \quad (82),$$

where:

$c_{ij} = (\alpha/2\pi)\delta_{ij}$, with α as the solid angle at the source point, whose value is $\alpha = \pi$ for points located over a smooth contour. For points located inside the domain, $c_{ij} = \delta_{ij}$. In a similar fashion, $c(\xi^e)$ is equal to ½ for points over a smooth surface and to 1, for points

inside the domain. On the other hand, the superscript "e" represents the Equivalent Isotropic System (EIS) that is obtained after scaling the *x* and *y* coordinates of the original system in terms of the anisotropic ratio of permeability, K_1/K_2, as it is shown in *Appendix A.*

The integral kernels in Eq.81 and Eq.82 are given in terms of the corresponding fundamental solutions, which are the following:

$$U_i^j(\xi, y) = -\frac{1}{4\pi}\left[ln\left(\frac{1}{r}\right)\delta_{ij} + \frac{(\xi_i - y_i)(\xi_j - y_j)}{r^2}\right]$$

$$K_{ij}(\xi, y) = -\frac{1}{\pi}\frac{(\xi_i - y_i)(\xi_j - y_j)(\xi_k - y_k)n_k(y)}{r^4}$$

$$p^*(\xi^e, y^e) = -\frac{1}{2\pi}\ln(r^e)$$

$$q^*(\xi^e, y^e) = -\frac{1}{2\pi(r^e)^2}\left[(y_1^e - \xi_1^e)f^e\widehat{n_i^e}(y) + (y_2^e - \xi_2^e)f^e\widehat{n_2^e}(y)\right]$$

$$f^e = \left\|(K_1/K_2)^{1/4}\widehat{n_1}, (K_2/K_1)^{1/4}\widehat{n_2}\right\|$$

$$r = |\xi - y|$$

$$r^e = |y^e - \xi^e|,$$

where ξ (ξ^e in the EIS system) and y (y^e in the EIS system) are the source and field points, respectively, with the integrals containing the fundamental solutions $U_i^j(\xi, y)$ (Stokes) and $p^*(\xi^e, y^e)$ (Darcy) corresponding to the Single Layer Potential (SLP), and those ones containing $K_{ij}(\xi, y)$ (Stokes) and $q^*(\xi^e, y^e)$ (Darcy) to the Double Layer Potential (DLP). The factor f^e comes from the transformation of the normal vectors, as shown in *Appendix A*. As it is demonstrated in *Appendix A*, the Eq.82 can be also written in the original coordinate system with fundamental solutions given by:

$$p^*(\xi, y) = -\frac{1}{2\pi}ln(r_e)$$

$$q^*(\xi, y) = \frac{K_i}{K_e}\frac{\partial p^*}{\partial y_i}(\xi, y)\widehat{n_i}(y) = -\frac{1}{2\pi(r_e)^2}\left[(y_1 - \xi_1)\widehat{n_1}(y) + (y_2 - \xi_2)\widehat{n_2}(y)\right]$$

$$r_e = \left[(K_2/K_1)^{\frac{1}{2}}(y_1 - \xi_1)^2 + (K_1/K_2)^{\frac{1}{2}}(y_2 - \xi_2)^2\right]^{1/2}$$

$$K_e = (K_1K_2)^{1/2}$$

In both the Darcy and Stokes domain, the boundary and the physical variables are discretized using quadratic isoparametric interpolation. At the corners, discontinuous shape functions with a collocation factor of $\alpha_{dis} = 2/3$ are used [165]. To compute the integrals,

standard Gaussian quadrature is used. The singularities of the integrals of the DLP are treated using the Rigid Body Motion principle [149], [150] and the singular integrals of the SLP using the Telles transformation [166]. After the discretization of the contour and variables of the problem, systems of linear algebraic equations are obtained, which can be written in matrix form as:

$$[H]^{(s)}_{2N_s\times 2N_s}\vec{u} = [G]^{(s)}_{2N_s\times 2N_s}\vec{t} \tag{83}$$

$$[H]^{(d)}_{N_d\times N_d}\vec{p} = [G]^{(d)}_{N_d\times N_d}\vec{q} \tag{84},$$

where N_s and N_d are the total number of points of the boundary in the Stokes and Darcy domains, respectively. In Eq.83, $\vec{u}$ and $\vec{t}$ are the velocity and traction vectors, respectively, whereas in Eq.84, $\vec{p}$ and $\vec{q}$ represent the pressure and normal derivative of pressure, respectively.

The matching conditions between Stokes and Darcy flows specified in Section 3.2 can be implemented directly in terms of the fluid velocities and Stokes shear stresses, using the corresponding interpolation functions. In the Beavers-Joseph slip condition, Eq.66, the only physical variable that cannot be expressed directly as a local projection of variables appearing in the integral equations, Eq.81 and Eq.82, is the Darcy velocity, $u_i^{(d)}$. However, by using the Darcy's law and approximating the pressure gradient with Lagrange interpolation functions for quadratic elements, $\mathrm{L}_j(\zeta)$, the tangential projection of the Darcy velocity can be expressed as:

$$u_i^{(d)}\hat{\tau}_i = -(K_i/\mu)(\partial\zeta/\partial x_i)\hat{\tau}_i\left(\partial \mathrm{L}_j(\zeta)/\partial\zeta\right)p_j \tag{85}$$

with $\zeta \in [-1,1]$. By imposing the boundary and matching conditions, a well-posed system of equations is obtained for the constant pressure regime, whereas for the constant flow regime an additional equation needs to be considered, as will be discussed later. In both cases, the final system of algebraic equations is solved using a Singular Value Decomposition (SVD) algorithm [167], [168]. The main reason to use a SVD solver is due to the coupling of two systems of integral equations where the resulting matrix system after discretization is composed by elements of significant differences in magnitude (ill-conditioning) and not easy to solve by a simple direct solver like Gauss elimination.

The numerical technique used to track the moving boundaries is based on a first order Euler integration of the kinematic condition, Eq.73. As an explicit time stepping-algorithm is

used, the time step needs to be restricted to small values, with magnitudes decreasing as the capillary number decreases. As the fluid penetrates the RUC, the fluid front evolves in shape and size, requiring the use of a remeshing algorithm to describe the moving front as time progresses. Besides, since in the BEM formulation of the problem two different surface integral equations are used to represent the solution, corresponding to the Stokes (channel) and Darcy (tows) flows, it is necessary that, during the time evolution, a point at the fluid front in one domain does not cross into the other domain, requiring the addition of a geometrical constrain to the time step, Δt. The details of the fluid front tracking technique implemented here can be seen in *Appendix C.*

Although quadratic isoparametric BEM elements always gives higher precision than constant or linear elements, the nodes at the edge of the quadratic elements have a slightly higher accuracy than the middle one, resulting, in our case, in similar differences on the accuracy of the predicted interface velocity at those element nodes. In the case where surface tension effect is negligible, and therefore the interface curvature is not important in the filling process, these very small differences will only affect the evolution of the moving front after a very long time. However, when surface tension effect is dominant and the interface curvature needs to be considered, these differences can affect the evolution of the interface due to the errors in the evaluation of the interface curvature. Consequently, when quadratic isoparametric BEM is implemented for the solution of moving boundary problems, it is always recommended to employ a surface smoothing algorithm after a series of time steps, recursively, to mitigate this difference in accuracy between the element nodes. The numerical details of this algorithm are also presented in *Appendix C*.

After updating the position of the fluid front, the redistribution and remeshing of the interface elements is carried out by fitting parametric cubic splines along the newly positioned interface nodes, from where the length of the interface is directly obtained by integration of the corresponding spline curves. The splines are forced to be perpendicular to the boundaries where the symmetric condition is prescribed and its slope is kept continuous in the interfaces between the subdomains (i.e. channels and bundles).

In an evolution point x^i, both the unit normal vector, $\hat{n}^i$, and the curvature, κ^i, are computed numerically using the following fourth-order lagrangian polynomial [169]:

$$\left(x_j'\right)^i = 1/6\left(x_j^{i-2} - 8x_j^{i-1} + 8x_j^{i+1} - x_j^{i+2}\right),\ j = 1,2 \tag{86}$$

$$\left(x_j''\right)^i = 1/3\left(-x_j^{i-2} + 16x_j^{i-1} - 30x_j^i + 16x_j^{i+1} - x_j^{i+2}\right),\ j = 1,2 \tag{87}$$

$$\hat{n}^i = 1/\left(\sqrt{((x_1')^i)^2 + ((x_2')^i)^2}\right).\langle (x_2')^i, -(x_1')^i\rangle \tag{88}$$

$$\kappa^i = \left[(x_1')^i(x_2'')^i - (x_2')^i(x_1'')^i\right]/\left[\left((x_1')^i\right)^2 + \left((x_2')^i\right)^2\right]^{3/2} \tag{89}$$

Once the meshes of the moving boundaries have been reconstructed at the current time step and the normal and curvatures have been computed, the BEM algorithm is used to calculate the velocity at the moving boundary and the cycle is repeated again in a quasi-static approach given the low Reynolds approximation of the problem.

The velocity and pressure fields in the two flow regions, channels and tows, are post-processing calculations that can be carried out once the systems defined by Eq.81 and Eq.82 are solved. The fluid velocity inside the channel is computed using Eq.81 with $c_{ij} = \delta_{ij}$. The integral representation for the pressure is used to compute the pressure field inside the channel [149]:

$$p(\xi) = 2\mu \int_S \Pi_{ik}(\xi, y)\, \widehat{n_k}(y) u_i(y) dS_y - \int_S p_i(\xi, y)\, t_i(y) dS_y \tag{90}$$

where $p_i(\xi, y) = -\frac{1}{2\pi r^2}(\xi_i - y_i)$ is the fundamental solution for the pressure equation and $\Pi_{ik}(\xi, y) = \frac{1}{2\pi}\left[\frac{\delta_{ik}}{r^2} - \frac{2}{r^4}(\xi_i - y_i)(\xi_k - y_k)\right]$ is the gradient of $p_i(\xi, y)$.

In the porous medium, the pressure field inside the domain is obtained from Eq.82 with $c(\xi) = 1$, while the pressure gradient is found by taking the directional derivative of Eq.82, as follows:

$$\frac{\partial p(\xi^e)}{\partial \xi_i^e} = \int_S \frac{\partial p^*(\xi^e, y^e)}{\partial \xi_i^e} q(y^e) dS_{y^e} - \int_S \frac{\partial q^*(\xi^e, y^e)}{\partial \xi_i^e} p(y^e) dS_{y^e} \tag{91}$$

The velocities in the interior points of the porous media are given by the Darcy's law, in terms of the pressure gradient, Eq.91.

3.4 Results and discussion

3.4.1 Validation of the BEM code for Stokes-Darcy problems

To verify the developed numerical code, the coupled Stokes-Darcy problem of Figure 16 that admits an analytical solution is considered. The problem is defined by two parallel domains totally saturated, with the upper one as an anisotropic homogeneous porous medium with the principal directions of permeability coinciding with the x and y axes and

$\varepsilon_t = 0.6$, and the lower domain as a thin channel. The slip coefficient given by Eq. 67 is $\gamma = 1.29$.

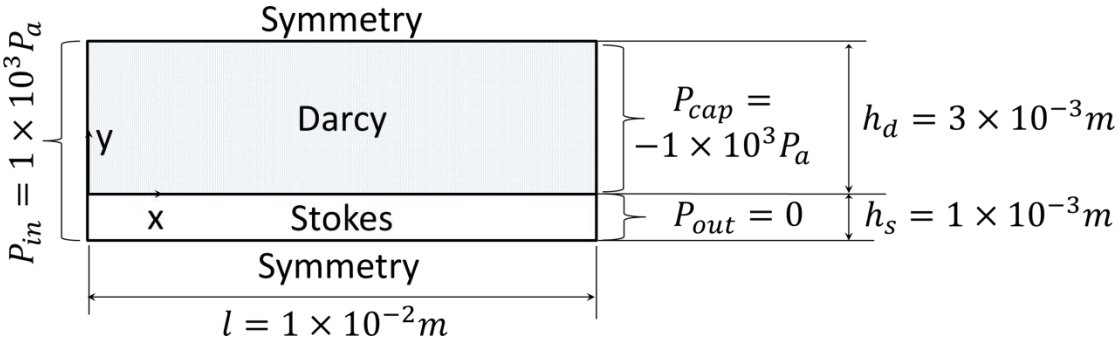

Figure 16 Scheme of coupled problem Stokes-Darcy with analytical solution.

For this particular problem, an analytical solution in terms of power series was developed here and it is detailed in the *Appendix B.* The goal of the solution is to predict the pressure and velocity fields in both the Darcy and the Stokes domain.

The L^2 relative error norms between the analytical and the BEM solutions for the pressure, p, and velocities, u_1 and u_2, are shown in the Table 4. Three factors are considered for the analysis of these errors: the mesh size (h), the anisotropic ratio (K_1/K_2), keeping constant the longitudinal permeability at $K_1 = 1 \times 10^{-10} m^2$, and the slip coefficient (γ). The mesh size is reported as $h = e/H$, where $H = h_d + h_s$ is the total height of the domain (See Figure 16) and *e* represents the size of one quadratic element. The meshgrid for the internal points is uniformly distributed and constructed from the extension of the points of the contour mesh.

According to Table 4, the maximum error for a determined mesh size is always obtained for the horizontal velocity, u_1, when $K_1/K_2 = 0.1$ and $\gamma = 0.01$, but this error decreases as the mesh is finer. In general, the refinement of the mesh leads to the reduction of the L^2 error in all situations, which means that the BEM code converges to the analytical solution; however, the order of convergence is not necessarily the same in all cases. For instance, in the Figure 17a, they are presented the power fit curves for the data of $L^2\ relative\ error\ norm\ vs. Mesh\ size$ for the pressure, considering $\gamma = 1.29$; the orders of convergence, n_c, which are the exponents of the power regression equations, are presented as well. As the anisotropic ratio, K_1/K_2, departures from one, namely, from the isotropic condition, the L^2 error increases; furthermore, the order of convergence, n_c, drops

as K_1/K_2 increases. The same plot type for the horizontal velocity is presented in the Figure 17b. In that case, the reduction of the anisotropic ratio, K_1/K_2, brings about the increase of the L^2 error and the reduction of the order of convergence. The vertical velocities, u_2, are not considered in the present convergence analysis since they are very close to zero, however, as observed in the Table 4, the accuracy corresponding to u_2 is acceptable enough in all situations. On the other hand, the influence of the slip coefficient, γ, on the accuracy and convergence of the BEM algorithm for p and u_1 is represented in Figure 17c and Figure 17d, respectively, taking $K_1/K_2 = 10$. For the pressure, this influence is insignificant (Figure 17c); conversely, in the case of the horizontal velocity, the accuracy diminishes as the slip coefficient, γ, is lower and the highest order of convergence is achieved for $\gamma = 1.29$ (Figure 17d).

Table 4 Assessment of accuracy of the BEM algorithm for Stokes-Darcy problem

Mesh size (h)	**Variable**	**L^2 relative error norms**											
		K_1/K_2=0.1			**K_1/K_2=1**			**K_1/K_2=10**			**K_1/K_2=100**		
		γ = 1.29	**γ = 0.1**	**γ = 0.01**	**γ = 1.29**	**γ = 0.1**	**γ = 0.01**	**γ = 1.29**	**γ = 0.1**	**γ = 0.01**	**γ = 1.29**	**γ = 0.1**	**γ = 0.01**
1,00 E-01	p	4.93 E-02	4.91 E-02	4.90 E-02	4.78 E-02	4.78 E-02	4.77 E-02	5.04 E-02	5.04 E-02	5.03 E-02	5.70 E-02	5.70 E-02	5.70 E-02
	u_1	1.64 E-02	9.46 E-02	1.77 E-01	1.04 E-02	5.12 E-02	1.49 E-01	9.61 E-03	4.01 E-02	1.36 E-01	9.54 E-03	3.87 E-02	1.34 E-01
	u_2	4.22 E-02	4.11 E-02	3.95 E-02	4.79 E-02	4.81 E-02	4.98 E-02	4.94 E-02	4.97 E-02	5.42 E-02	5.10 E-02	5.18 E-02	6.28 E-02
5,00 E-02	p	3.11 E-02	3.11 E-02	3.10 E-02	3.07 E-02	3.07 E-02	3.07 E-02	3.33 E-02	3.34 E-02	3.34 E-02	4.24 E-02	4.24 E-02	4.24 E-02
	u_1	1.15 E-02	6.85 E-02	1.26 E-01	6.51 E-03	3.72 E-02	1.07 E-01	5.65 E-03	2.91 E-02	9.76 E-02	5.60 E-03	2.81 E-02	9.62 E-02
	u_2	4.20 E-02	4.09 E-02	3.95 E-02	4.77 E-02	4.79 E-02	4.92 E-02	4.92 E-02	4.92 E-02	4.96 E-02	5.02 E-02	5.03 E-02	5.27 E-02
3,33 E-02	p	2.43 E-02	2.42 E-02	2.43 E-02	2.38 E-02	2.38 E-02	2.39 E-02	2.61 E-02	2.61 E-02	2.61 E-02	3.37 E-02	3.37 E-02	3.37 E-02
	u_1	9.88 E-03	5.96 E-02	1.09 E-01	5.26 E-03	3.24 E-02	9.26 E-02	4.39 E-03	2.54 E-02	8.48 E-02	4.39 E-03	2.45 E-02	8.36 E-02
	u_2	4.16 E-02	4.02 E-02	3.78 E-02	4.73 E-02	4.72 E-02	4.71 E-02	4.91 E-02	4.91 E-02	4.93 E-02	4.99 E-02	5.00 E-02	5.09 E-02

2,50 E-02	p	2.01 E-02	2.00 E-02	2.00 E-02	1.96 E-02	1.97 E-02	1.97 E-02	2.18 E-02	2.19 E-02	2.19 E-02	2.97 E-02	2.97 E-02	2.97 E-02
	u_1	8.46 E-03	5.11 E-02	9.30 E-02	4.44 E-03	2.78 E-02	7.91 E-02	3.65 E-03	2.18 E-02	7.25 E-02	3.72 E-03	2.10 E-02	7.14 E-02
	u_2	3.63 E-02	3.41 E-02	3.13 E-02	4.44 E-02	4.35 E-02	3.99 E-02	4.90 E-02	4.91 E-02	4.92 E-02	4.98 E-02	4.98 E-02	5.01 E-02

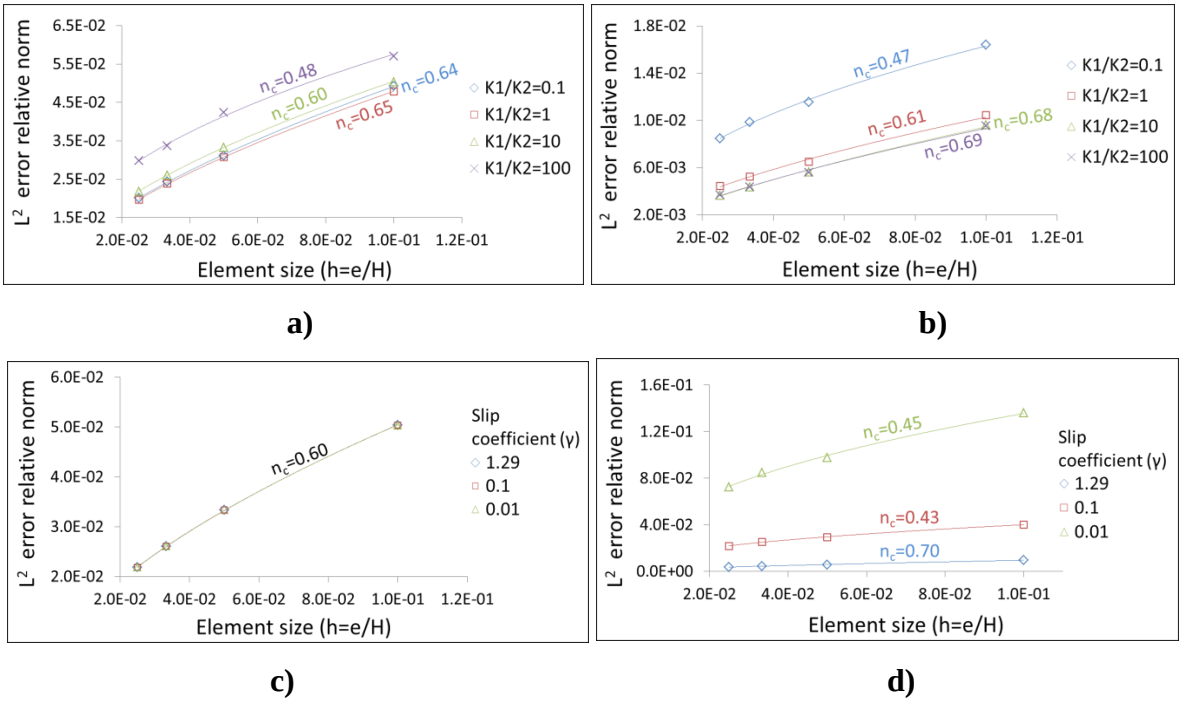

Figure 17 Convergence of BEM solution for Stokes-Darcy problem. a) For the pressure, varying K_1/K_2. b) For the horizontal velocity, varying K_1/K_2.c) For the pressure, varying γ. d) For the horizontal velocity, varying γ.

In the present chapter, the slip coefficients that are used in the free-boundary simulations are calculated using the Eq.67 and have an order of magnitude of $\mathcal{O}(0)$. Considering the results achieved for $\gamma = 1.29$ in the Table 4, it is expected to obtain an acceptable accuracy for those free-boundary simulations, even for the coarser mesh evaluated here, i.e., $h = 1 \times 10^{-1}$. In order to define the adequate mesh size for the free-boundary simulations, both the L^2 relative error norms and the execution times need to be considered. The CPU times for all mesh sizes considered here, with an Intel Pentium 2.1 GHz and 2GB of memory, are shown in the Figure 18. Primarily, it is important to mention that the increments of the elapsed time with the mesh refinement for the free-boundary problems of

the next sub-sections will be larger than the ones appreciated in the Figure 18, because the refinement of the mesh inexorably entails lower time intervals, Δt, for the advancement of the moving boundaries due to the CFL condition and to the restrictions for Δt described in the *Appendix C*. Therefore, it is convenient to evaluate, using the present results, the improvement of the accuracy in light of the raise of the execution time. For example, taking $\gamma = 1.29$, if the mesh size is reduced from $h = 1 \times 10^{-1}$ to $h = 5 \times 10^{-2}$, the average relative reduction of the L^2 error is 33.7% for the pressure and 32.3% for the horizontal velocity, at the expense of an increment in the CPU time of 6.49 times; in that case, the refinement of the mesh could be justified. Conversely, to change the mesh-size from $h = 1 \times 10^{-1}$ to $h = 3.3 \times 10^{-2}$ could be considered impractical because it would imply an increment of the CPU time of 23.40 times to reduce the error in 48.2 % for the pressure and 54.3 % for the horizontal velocity. Taking this in mind, the mesh-size is taken as $h = 5 \times 10^{-2}$ in the free-boundary simulations, where the mesh is fine enough to allow approximating the fluid front shape by parametric cubic splines adequately *(Appendix C.)*, but not too much fine in order to obtain reasonable execution times. In the Figure 19a,b, the BEM contour plots of the pressure and the streamlines, for $K_1/K_2 = 10$, $\gamma = 1.29$ and the selected mesh-size ($h = 5 \times 10^{-2}$), are compared with the analytical solution, obtaining a satisfactory agreement.

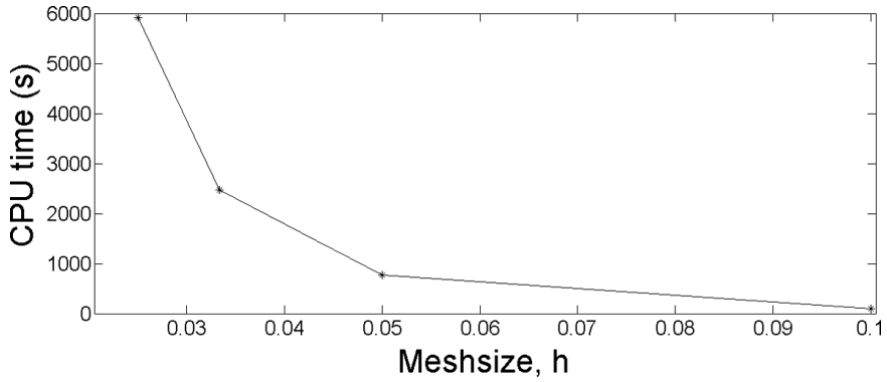

Figure 18 Execution time vs. Mesh-size for Stokes-Darcy problem.

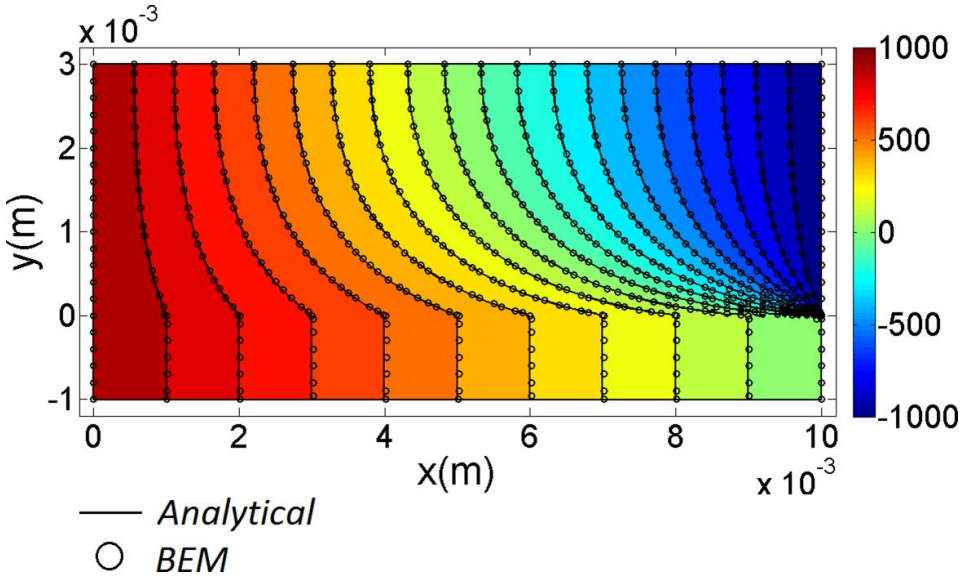

a)

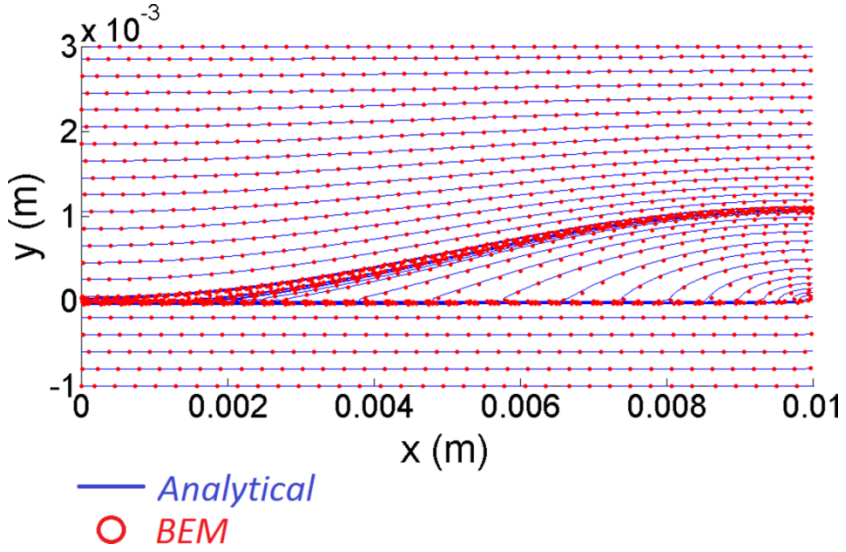

b)

Figure 19 Comparison between analytical and BEM solution taking $h=5\times10^{-2}$, $K_1/K_2=10$ and $\gamma=1.29$. a) Contour plots of pressure. b) Streamlines.

3.4.2 Comparison with CV/FAN approach.

Problem statement.

In the particular case of fabrics used as reinforcements in composite materials, with the flow moving in the warp direction, the RUC has three distinguishable domains: channels, longitudinal bundles (warps) and transverse bundles (wefts). When a simultaneous filling

takes place inside the RUC, the flow is driven by a combination of viscous, capillary and gravity forces, and the imbalances between the flow in the channels and the flow in the porous media (warps and wefts) lead to the formation of voids by entrapment of air. This sub-section is devoted to the description of the filling stages of the RUC until the void formation and to the comparison between the present BEM results and previous CV/FAN solutions in order to establish the influence of the mathematical model, numerical techniques and matching conditions used in both simulations.

Two modes of RUC for multilayer woven fabrics were considered by Jinlian et al. [3]. The Mode I consists on a simultaneous stacking of warps and wefts and it is the one considered here because of its geometrical simplicity (Figure 20). There are three major differences between the present approach and the one by Jinlian *et al*. [3]. Firstly, in the present approach, the flow in the channel is considered a 2D Stokes viscous incompressible flow, instead of a Darcy flow with an equivalent permeability. This is probably one of the principal differences between both approaches since the Darcy flow in the channel is an approximation of the real 2D flow field. This approximation is the source of the second main difference between the two mathematical formulations. In the Darcy-Darcy formulation of [3], the matching conditions between the channels and the porous media are defined by continuity of pressure and normal fluxes, without defining any condition for the tangential velocities. In the Stokes-Darcy formulation of the present work, the matching conditions are totally defined in terms of the velocities and surface tractions, Eqs. 65, 66 and 68. The other important difference between the two approaches is the numerical technique used to track the fluid front. In the present BEM formulation the position of the moving boundary is directly obtained by the Euler integration of the kinematic condition, Eq.73, after imposing the dynamic condition, which, in this sub-section, is given by the continuity between the liquid and air pressures, i.e., $P_{cap} = 0$ in Eqs.74a and 74b, to be consistent with the work of Jinlian *et al.* [3]. On the other hand, the FAN scheme is used in [3] to track the moving boundary. This scheme is a volume of fluid approximation that does not determine the exact position of the moving boundary, but an average location instead.

Reproduction of the conditions used in [3] requires a constant injection pressure of $500\ kPa$ and an air pressure of $100\ kPa$. In both approaches, after the void is formed, the air is assumed to obey the ideal gas law and, for a volume fiber content of $V_f = 0.45$, using

Eqs. 63a and 63b, the main tow permeabilities are $K_1 = 2.63 \times 10^{-11} m^2$ and $K_2 = 1.32 \times 10^{-12} m^2$. In the present example the fluid viscosity is $\mu = 0.1934\, Pa.s$ and the comparison is given in terms of T^* and A^*, where T^* is the time normalized with respect to the total filling time (total time is $0.130 \times 10^{-1} s$ for CV/FAN and $0.117 \times 10^{-1} s$ for BEM) and A^* stands for the area of the void over the cross section area of the weft. Symmetry conditions are prescribed along the half-height of the warps.

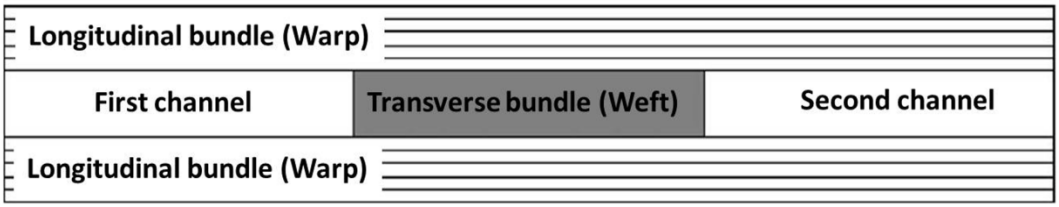

Figure 20 Mode I of the RUC configuration used in Jinlian et al.
Source: Jinlian et al [3]

Filling of the first channel.

Comparison of the time evolution of the filling process is presented in Figure 21, showing some similarities and discrepancies among both approaches. In the first instants of filling of the BEM simulation (Figure 21a), taking the maximum fluid front position in the channel and the minimum in the warp, the channel flow is ahead of the flow in the warp by a distance equivalent to 8.48% of the RUC's length. As the filling progresses, this separation increases due to the difference in flow resistance between both media, as it can be appreciated in the Figure 21b, where the distance between both flows is 19.50% of the RUC's length. The first important dissimilarity between the BEM and the CV/FAN approaches can be identified after comparing the Figure 21b to Figure 21c, which have the same fluid front position in the channel. The normalized time for the CV/FAN simulation is $T^* = 3.62 \times 10^{-3}$, whereas for the BEM simulation is $T^* = 1.13 \times 10^{-3}$. Considering the total filling times ($0.130 \times 10^{-1} s$ for CV/FAN and $0.117 \times 10^{-1} s$ for BEM), this means that the modeling of the free fluid in the channel as a darcian fluid with an equivalent permeability could lead to underestimated fluid front velocities in comparison with the real Stokes flow.

Impregnation of tows until flow reaches the second channel.

The BEM code predicts an arrival time of the channel fluid front to the weft of $T^* = 3.02 \times 10^{-3}$ (Figure 21d), which is only a small fraction of the total filling time. After this time, the fluid front velocity decreases in nearly two orders of magnitude as the fluid impregnates the weft, as can be inferred from the time evolution reported in Figure 21d, Figure 21e, Figure 21g and Figure 21h (BEM), and Figure 21f and Figure 21i (CV/FAN). After the flow has reached the weft, one of the main differences between both simulations occurs at the warps, where the average fluid front position predicted by the BEM approach is always behind the CV/FAN one (Figure 21e vs. Figure 21f and Figure 21h vs. Figure 21i). There are two main reasons for such a difference, due to the two main simplifications considered in the CV/FAN approach. Firstly, in the early instants of filling, the slip condition between the channel and porous medium in BEM, not considered in CV/FAN, results in a delay of the porous medium flow with respect to the channel flow for BEM (Figure 21a and Figure 21b), which causes the delay in the subsequent instants. Besides, and probably more significant, the simplified weighted-averaged displacement of the moving front in the CV/FAN approach instead of the direct time integration of the kinematic condition used in the BEM approach, results in a faster fluid front motion in the porous region for CV/FAN, with an almost straight shaped interface at the warp instead of the resulting concave shaped interface predicted by BEM. It is important to highlight that the form of the fluid front in the weft is clearly concave for both approaches.

During the weft impregnation, the normalized time, T^*, for any fluid front position is longer in BEM than in CV/FAN. For instance, in the instant corresponding to Figure 21e and Figure 21f, 12.2% of the filling time has elapsed in the BEM simulation, while in CV/FAN, 9.53%. When the flow reaches the other edge of the weft, as it is depicted in Figure 21h (BEM) and Figure 21i (CV/FAN), the BEM code predicts an arrival time equivalent to 75.7% of the total filling time, which is 15.74% larger than the value predicted by CV/FAN. Besides, it is relevant to mention that the minimum position of the fluid front in the weft is much farther away from the right edge of the weft in the BEM simulation than in the CV/FAN one, leading to the formation of a larger void in the BEM simulation.

Filtration from the warp towards the second channel and void formation.

When the fluid percolates from the warps towards the second channel, the fronts coming from both warps encounter each other and an air void is trapped inside the weft, as it can be seen in Figure 21j, where the normalized time is $T^* = 8.36 \times 10^{-1}$ according to the BEM code. Once these fluid fronts merge one another, the trapped air is compressed until the equilibrium is attained, Figure 21k (BEM) and Figure 21l (CV/FAN). In this process of void compressibility, the BEM code predicts that the bubble is predominantly compacted toward the right edge of the weft (Figure 21k) and not in both directions, as it is predicted by CV/FAN (Figure 21l); this induces a final position of the void in the BEM solution that is very close to the right extreme of the weft, which is coherent with other experimental and numerical researches [3], [4], [25], [170], [171]. The BEM simulation predicts a larger void than the one predicted by CV/FAN; the final void size is equivalent to 3.3% of the area of weft cross section for CV/FAN, whereas to 10.5% for BEM. With respect to the bubble shape, the CV/FAN approach predicts a triangular shaped bubble, whereas the BEM one, an elliptical shaped bubble.

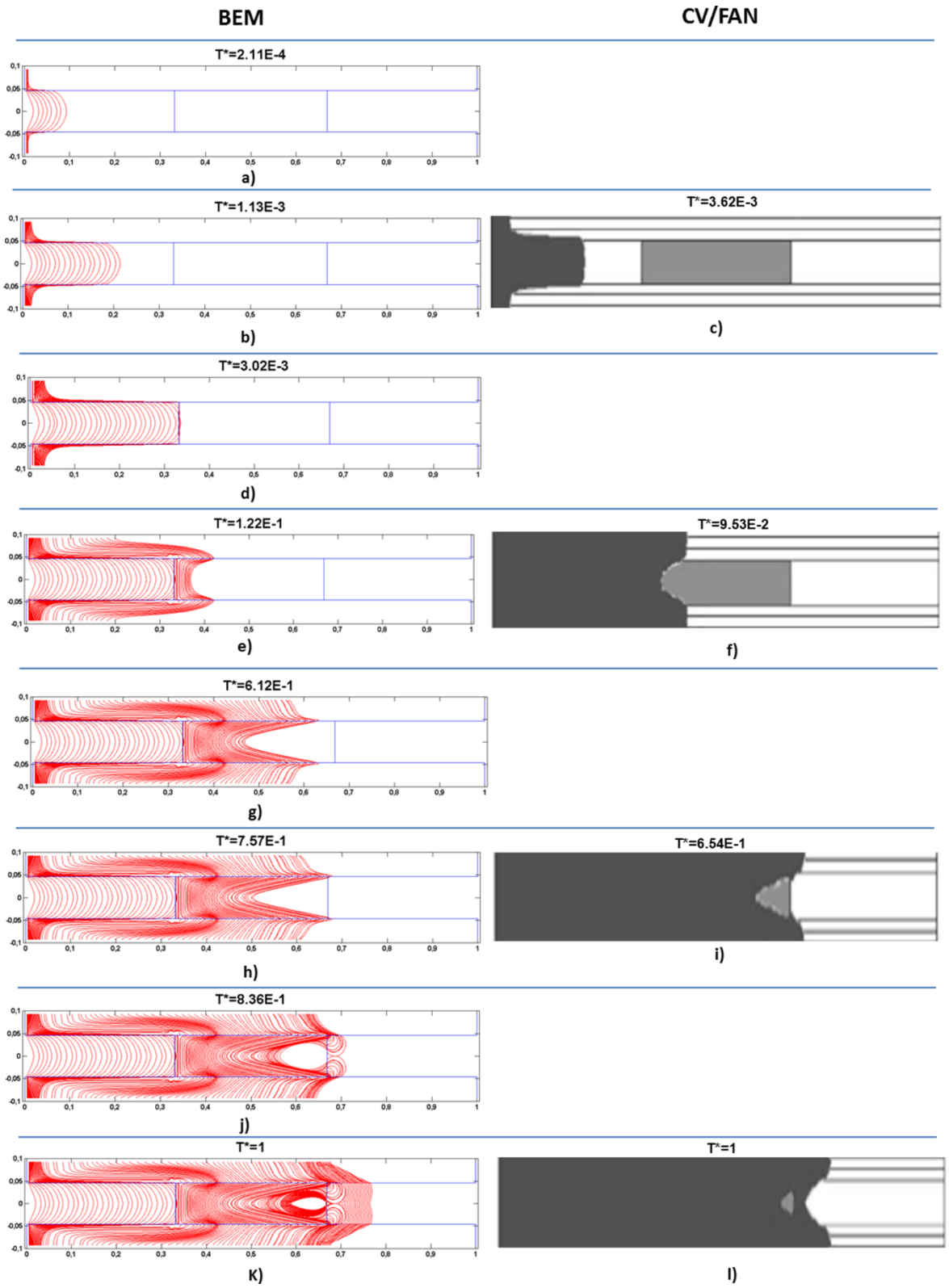

Figure 21 Comparison of filling instants between BEM and CV/FAN simulations.

Variation in void size with the anisotropy ratio, K_1/K_2.

As it was pointed out by Jinlian *et al* [3], the anisotropy ratio of permeability (K_1/K_2) has a relevant influence on the final void size, with larger voids as K_1/K_2 increases. In the Table 5, it is reported the comparison between the void size predicted by the two approaches for three of the anisotropy ratios considered by Jinlian *et al* [3]. As expected, the voids predicted by BEM are larger than those ones predicted by CV/FAN for all cases, due to the reason commented above, however it is worth noting that the BEM approach is in agreement with the CV/FAN one in the sense that it predicts an increase of the void size with the increase of the anisotropy ratio, K_1/K_2.

Table 5 Variation of the final void size with the anisotropy degree, K_1/K_2

Anisotropy degree	Area of void/Area of tow´s cross section (CV/FAN)	Area of void/Area of tow´s cross section (BEM)
10	0.5%	1.3%
20	3.3%	10.5 %
30	5.8%	16.6%

Times of the filling stages.

To finish the present sub-section, Figure 22 represents the filling process of the RUC predicted by BEM divided into four stages with their corresponding fraction of time: filling of the first channel, impregnation of tows until the flow reaches the second channel, filtration from the warps towards the second channel until void formation, and compression of void until the equilibrium. The time taking place in each stage is reported as a percentage of the total filling time. As expected, the longest process corresponds to the impregnation of the tows until the flow reaches the second channel, and the shortest, to the filling of the first channel. It is worth noting that the void compression until the equilibrium takes more time than its formation once the flow is infiltrated from the warps towards the second channel.

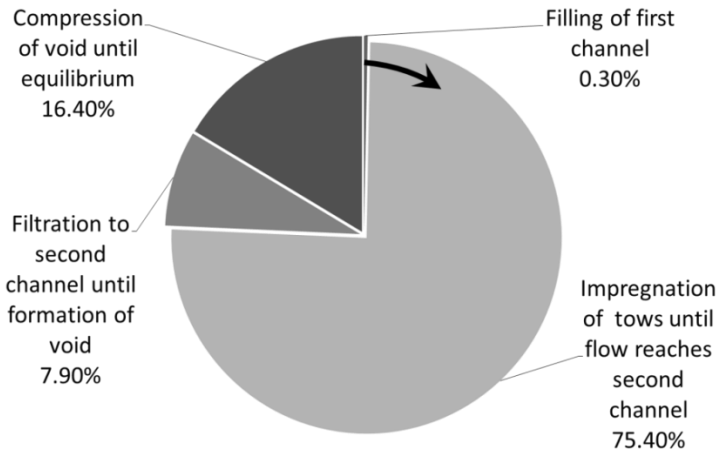

Figure 22 Stages of the filling of the RUC.

3.4.3 Influence of processing, geometric and material variables on the void formation.

Problem statement and results of RUC filling.

The viscous effects in the RUC impregnation are associated to the prescribed inlet conditions (pressure or flow rate), while the capillary effects to the surface tension and contact angle. The modified capillary number is used in the literature to relate both types of effects:

$$C_a^* = \langle u_f \rangle^f / R_{fluid} \quad (92),$$

with $\langle u_f \rangle^f$ as the pore velocity and $R_{fluid} = \lambda . cos(\theta)/\mu$ as the fluid penetrativity, which depends on the contact angle (θ), surface tension (λ) and viscosity (μ). Some authors have used the superficial velocity for computing C_a^* instead of the pore velocity [44], [81], but others agree that the last one is more consistent with the phenomenon of partial saturation of the RUC because of the inclusion of a geometry-dependent property, that is, the porosity [75], [89], [172]. When the filling problem is analyzed in a macroscopic framework, the pore velocity is defined as the average velocity inside the RUC with respect to the porous volume of the RUC, namely, $\langle u_f \rangle^f = \left(\int_{V_p} u_f . dV_p \right) / V_p$, with u_f as the pointwise velocity of the liquid inside the RUC and V_p as the porous volume of the RUC. On the other hand, in the filling of RUC's at mesoscopic scale, $\langle u_f \rangle^f$ is given by the average inlet pore velocity

of the RUC conceived as a single pore unit, as it was considered in the works of DeValve and Pitchumani [80] and Schell at el. [81]. Therefore, $\langle u_f \rangle^f$ is computed here as:

$$\langle u_f \rangle^f = Q/A_p \tag{93},$$

with Q given as the total inlet flow rate and A_p as an equivalent inlet porous area of the unit-width RUC, given by $A_p = H_{ch} + H_p \varepsilon_t$, where H_{ch} is the height of the channel and $H_p = H - H_{ch}$ is the height of the longitudinal tow (warp); see Figure 23 where the half-height of the tows is represented. The areal porosity of the tow is taken equal to the volumetric porosity, ε_t.

In the present section, a constant inlet flow rate is assumed in order to maintain a constant value of C_a^* during the filling process. However, the prescribed flow rate is a defective boundary condition in the sense that the inlet flow rates at the channel $\left(Q^{(s)}\right)$ and at the porous media $\left(Q^{(d)}\right)$ are unknown a priori [173], [174], but the total flow rate, $Q = Q^{(s)} + Q^{(d)}$, is known instead (See Figure 23). To deal with this indeterminacy, it is imposed a uniform inlet pressure that changes in time during the filling process in order to keep constant the total flow rate. In this way, the inlet boundary condition prescribed at the warps is uniform pressure, i.e., $p^{(d)} = \bar{p}_{in}(t)$, and, at the channel, the conditions are uniform normal surface tractions together with zero vertical velocity, i.e., $\hat{n}_i \sigma_{ij} \hat{n}_j = -\bar{p}_{in}(t)$, $u_2 = 0$, with the value of the inlet pressure, $\bar{p}_{in}(t)$, as an unknown function of the time to be determined. To complete the problem, the balance of fluxes at the inlet is taken into account:

$$\begin{aligned} Q &= Q^{(s)} + Q^{(d)} \\ &= \int_{A_p^{(s)}} u_1^{(s)} dA + \int_{A_p^{(d)}} u_1^{(d)} dA = \int_{A_p^{(s)}} u_1^{(s)} dA + \int_{A_p^{(d)}} -(K_1/\varepsilon_t \mu).(dp/dx_1)^{(d)} dA \end{aligned} \tag{94},$$

where Q is the total inlet flow rate, $Q^{(s)}$ is the inlet flow rate of the channel, $Q^{(d)}$is the inlet flow rate of the warp, $A_p^{(s)}$ is the inlet area of the channel, $A_p^{(d)}$ is the inlet porous area of the warp, $u_1^{(s)}$ is the inlet velocity in the channel, $u_1^{(d)}$ is the inlet pore velocity of the warp and $(dp/dx_1)^{(d)}$ is the pressure gradient in the horizontal direction at the inlet of the warp.

The flow rates appearing in Eq. 94 can be expressed numerically in terms of the values of $u_1^{(s)}$ and $(dp/x_1)^{(d)}$ in the nodes of the quadratic isoparametric elements. In general, the flow rate entering a quadratic element "*j*" can be approximated as follows:

For Stokes domain:

$$Q^{(j)} = \left(\int_{-1}^{1} L_i(\zeta)\,.\,|J|d\zeta\right)^{(j)} \left(u_1^{(s)}\right)_i^{(j)}, i = 1,2,3 \text{ (Sum on "}i\text{")} \quad (95a),$$

For Darcy domain:

$$Q^{(j)} = \left(-(K_1/\mu)\int_{-1}^{1} L_i(\zeta)\,.\,|J|d\zeta\right)^{(j)} \left((dp/dx_1)_i^{(d)}\right)^{(j)}, i = 1,2,3 \text{ (Sum on "}i\text{")} \quad (95b),$$

where $\left(u_1^{(s)}\right)_i^{(j)}$ and $\left((dp/dx_1)_i^{(d)}\right)^{(j)}$ represent the horizontal velocity in the channel inlet and the pressure gradient in the warp inlet for the node "i" of the element "*j*". Therefore, the total inlet flow rate is $Q = \sum_{j=1}^{N_{elem}} Q^{(j)}$, where N_{elem} stands for the total number of elements of the inlet. After grouping the common nodes, this rate can be expressed in terms of the horizontal velocity for the channel and of the pressure gradient in x-direction for the warps. On that basis, the form of the matrix system corresponding to Eq.94 is the next:

$$Q = \left(\overrightarrow{S^{(s)}}\right)_{1\times N_{inl}^{(s)}} \left(\overrightarrow{u_1^{(s)}}\right)_{N_{inl}^{(s)}\times 1} + \left(\overrightarrow{S^{(d)}}\right)_{1\times N_{inl}^{(d)}} \left(\overrightarrow{(dp/dx_1)^{(d)}}\right)_{N_{inl}^{(d)}\times 1} \quad (96),$$

where $\overrightarrow{S^{(s)}}$ is a row vector for the Stokes domain in terms of integrals of interpolation functions, while $\overrightarrow{S^{(d)}}$ is a row vector for the Darcy domain in terms of integrals of interpolation functions, K_1 and μ; on the other hand, $N_{inl}^{(s)}$ is the number of nodes at the channel inlet boundary, $N_{inl}^{(d)}$ is the number of nodes at the warp inlet boundary, $\overrightarrow{u_1^{(s)}}$ is a column vector containing the inlet velocities at the nodes of the Stokes domain and $\overrightarrow{(dp/dx_1)^{(d)}}$ is a column vector containing the pressure gradients in x-direction at the nodes of the Darcy domain. Considering the Eq. 96, a well-posed but probably still ill-conditioned problem is obtained at each time instant.

In this section, several simulations of the RUC filling process are carried out at constant flow regime in order to study the influence of geometric, material and processing variables on the void formation. The RUC geometry is the same as the one represented in Figure 20 and it can be characterized by the total height and length of the RUC, H and L, respectively, and by the height and width of the weft, H_{ch} and w, respectively, as shown in Figure 23.

Additionally, two non-dimensional ratios are defined as $b_1 = w/L$ and $b_2 = H_{ch}/H$, where b_1 is modified here by changing the width of the weft, while $b_2 = 0.5$ for all simulations. Values of $H = 0.8 \times 10^{-3} m$, $L = 3.0 \times 10^{-3} m$ and $H_{ch} = 0.4 \times 10^{-3} m$ are considered for the RUC and the liquid has a viscosity of $\mu = 0.1\, Pa.s$ and a density of $\rho = 1000\ Kg/m^3$. The selected data are representative of the geometry of highly compacted fibrous reinforcements and the properties of liquids used in Liquid Composite Molding (LCM). Considering a hexagonal array of fibers in the tows, the tow porosity, ε_t, can be computed as follows:

$$\varepsilon_t = 1 - 3\pi {R_f}^2 / \left(6\sqrt{3}\left(R_f + d\right)^2\right) \quad (97),$$

whereas the RUC or global porosity, ε_{RUC}, defined as the total porous volume (porous volume of the warps and weft plus the volume of the channels) divided by the total volume of the RUC, can be calculated as:

$$\varepsilon_{RUC} = (1 - b_1)(1 - b_2) + (1 + b_1 b_2 - b_2)\varepsilon_t \quad (98).$$

The parameters that characterize the void formed are also represented in Figure 23. The void content is expressed as the area of the bubble over the area of the weft, its location, as the ratio "l_{edge}/w", with l_{edge} as the distance from the bubble tip to the rear (right) edge of the weft, and its shape, as the aspect ratio of the equivalent ellipse, "a/b". Three different modified capillary numbers, C_a^*, are taking into account and for each one of them it is studied the influence on the void characterization of the following variables: tow porosity (ε_t), ratio between the weft width and the RUC length (b_1), RUC porosity (ε_{RUC}) and fluid penetrativity (R_{fluid}).

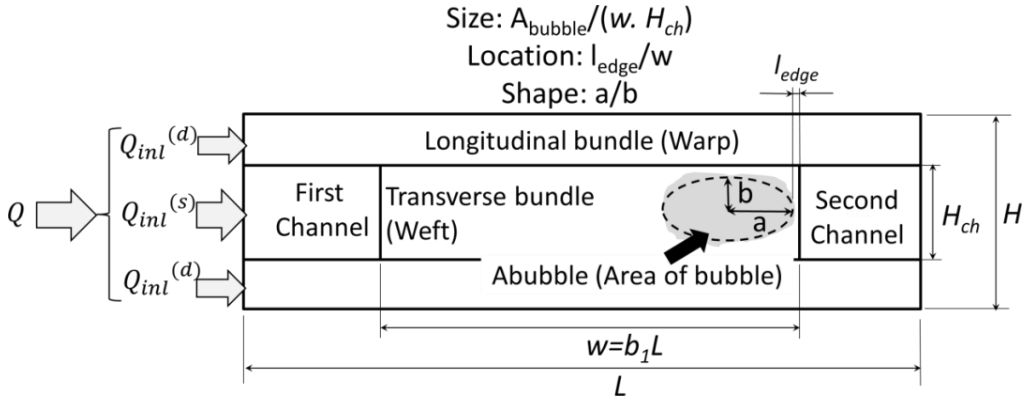

Figure 23 Scheme of the problem of filling of the RUC at constant flow rate.

To carry out the parametric study, a reference case is defined, and it is denoted as *Serie 1*. Some parameters are fixed and others are determined from the fixed ones (computed parameters). The fixed parameters are: radius of fiber (R_f), half-distance between fibers (d), length and height of the RUC (L and H, respectively), width and height of the weft (w and H_{ch}, respectively), surface tension (λ) and contact angle (θ); the computed parameters are: tow porosity (ε_t), main tow permeabilities $(K_1\ and\ K_2)$, slip coefficient (γ), RUC porosity (ε_{RUC}) and fluid penetrativity (R_{fluid}). The corresponding values for the reference case, *Serie 1*, are given in Table 6.

Three additional cases, *Series 2, 3* and *4*, are taken into account by changing one or two of the fixed parameters shown in Table 6, in such a way that in *Serie 2*, the parameter d is changed to $2.5\,\mu m$, resulting in the modification of the next parameters: $\varepsilon_t = 0.42$, $K_1 = 3.31 \times 10^{-12} m^2$, $K_2 = 7.37 \times 10^{-13} m^2$ and $\gamma = 1.54$. In *Serie 3* the width of the transverse tow (weft) is increased, leading to $b_1 = 0.7$, while in *Serie 4*, λ and θ are changed to $30\,mN/m$ and 20 degrees, respectively, bringing about a change in the fluid penetrativity, $R_{fluid} = 2.82 \times 10^{-1}\ m/s$. In each one of the series, the following modified capillary numbers are considered: $C_a^* = 6.03 \times 10^{-2}, C_a^* = 6.27 \times 10^{-1}$ and $C_a^* = 1.21$.

From the comparison between the results of these series, the effect of the different parameters on the void size, shape and location are analyzed. The plots of RUC filling of the mentioned series are shown in Figure 24a-l. In all series considered, no void formation is observed inside the RUC when $C_a^* = 6.03 \times 10^{-2}$, i.e., at the lower inlet flow rate, as it can be observed in Figure 24a to Figure 24d. The results of the simulations of the parametric study are summarized in Table 7.

Table 6 Simulation data for the reference case *(Serie 1)* in Stokes-Darcy formulation

Fixed parameters					
Radius of the fibers, R_f (μm)	Half-distance between fibers,d (μm)	Ratio among the width of transverse tow and length of RUC (b_1)	Ratio among the height of transverse tow and height of RUC (b_2)	Surface tension, λ (mN/m)	Contact angle, θ (degrees)
10	5	0.5	0.5	15	30

Computed parameters					
Porosity of the tow for hexagonal array, ε_t	Porosity of the RUC, ε_{RUC}	K_1 (m^2)	K_2 (m^2)	Slip coefficient, γ	Fluid penetrativity, R_{fluid}(m/s)
0.6	0.70	1.98E-11	4.14E-12	1.29	1.30E-1

Table 7 Void characterization of all simulations of parametric study Stokes-Darcy (Note: for C_a^*=6.03×10^{-2} no void formation was obtained)

Modified capillary number, C_a^*	Series	Void size: $A_{bubble}/(w.H_{ch})$	Void shape: a/b	Void location: l_{edge}/w
$C_a^* = 6.27 \times 10^{-1}$	1	1,54E-02	1,98	6,67E-04
	2	1,25E-02	2,03	6,67E-04
	3	9,94E-03	1,84	1,90E-03
	4	1,11E-02	2,06	4,00E-03
$C_a^* = 1.21$	1	2,45E-02	1,11	6,00E-03
	2	1,39E-02	2,05	1,33E-04
	3	1,06E-02	1,80	9,52E-04
	4	1,55E-02	1,41	3,33E-03

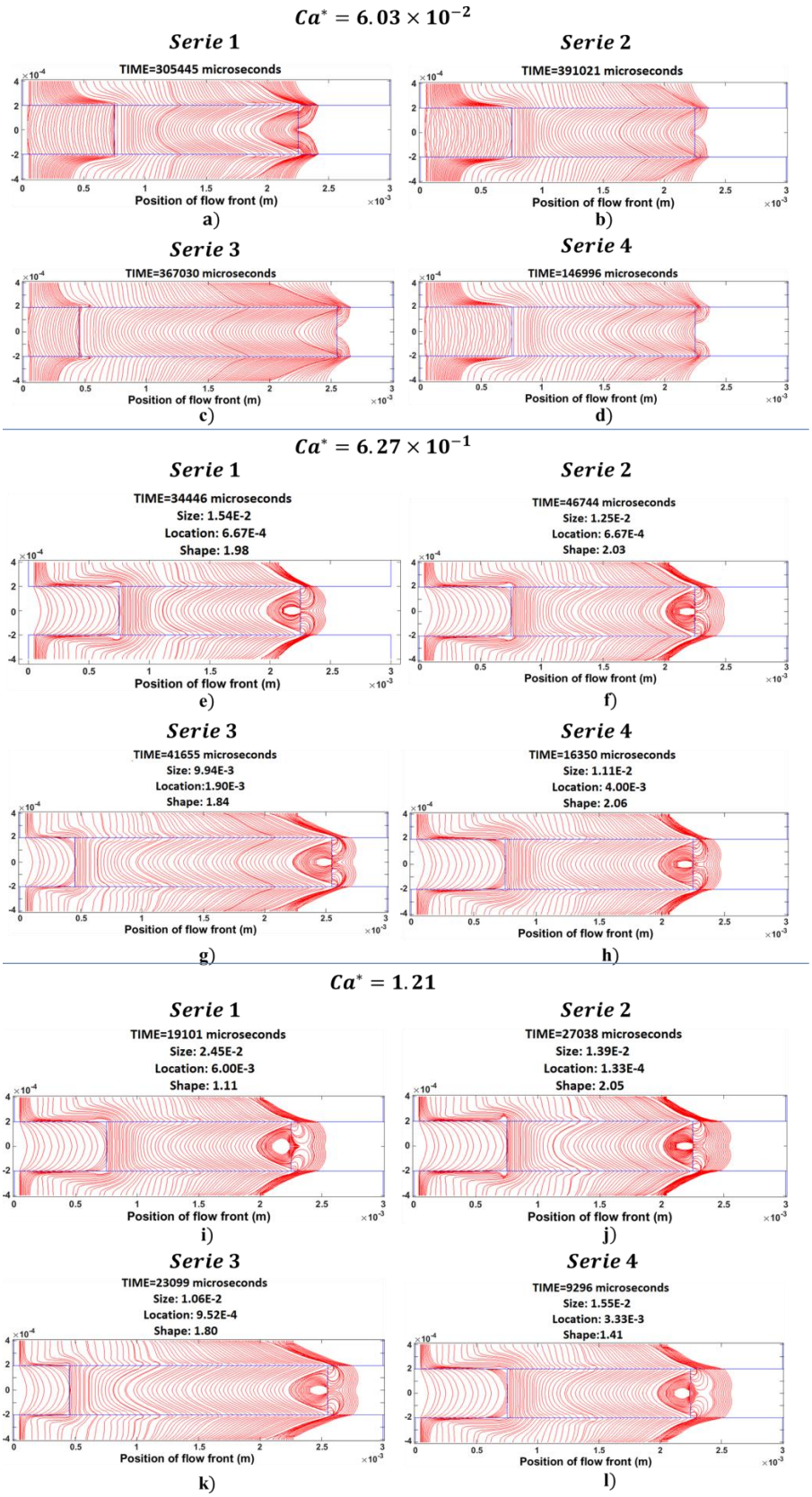

Figure 24 Simulations for the parametric study using Stokes-Darcy.

Influence of parameters on the void size.

The semi-log plot of $Void\ Content\ vs.\ C_a^*$ is shown in Figure 25a, where it can be observed that for a given Serie, the void content increases as C_a^* increases, which can be confirmed in other experimental works. For instance, according to the experimental results in [44], [77], [175], there exists an optimal value of the modified capillary number, $C_{a,opt}^*$, where the void content is the lowest and, from that optimal point onward, the microvoids (voids formed in the bundles) are larger as C_a^* is higher (Figure 25b,c), validating the present results. Besides, the values represented in Figure 25a fit well to logarithmic curves, as it can be confirmed by the R^2 value of the fit curves, and this behavior is in agreement with other numerical and experimental researches [25], [44], [75], [77], [81], see for instance Figure 25b,c. However, it is important to mention that, according to [80], [81], [175], the behavior of the microvoid size with C_a^* is not necessarily monotonic increasing for all values of C_a^* greater than $C_{a,opt}^*$ because it is possible to obtain a value of C_a^* from which the void compression is the most relevant process and the microvoid size reduces with C_a^*. This is out of the scope of the present work, but could be addressed in future researches using the numerical code developed here to run simulations at higher modified capillary numbers, C_a^*.

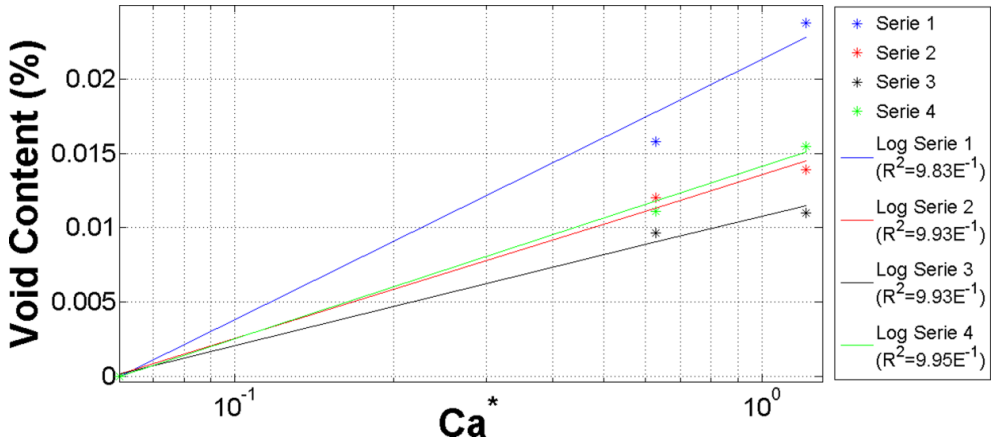

a)

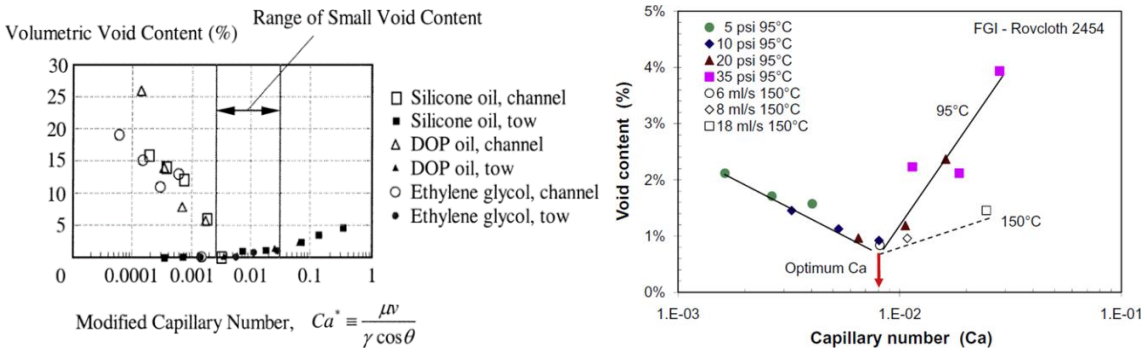

b) **c)**

Figure 25 Plot of Void Content vs. C_a^*. a) BEM simulations (Author), b) Experimental results of Kang, Lee & Hahn [25] **c) Experimental results of Leclerc & Ruiz** [77]

The largest void contents correspond to *Serie 1* and the smallest ones, to *Serie 3*, as can be seen in Table 7 for both cases of C_a^* where void formation occurs. The difference between these series is the width of the weft, expressed as the ratio b_1 (See Figure 23), i.e., the void is smaller as the weft is wider. It is important to remind that the void content, as expressed here, represents the fraction of the weft area that is not saturated and that is considered ineffective to support mechanical loads. Bearing this in mind, it can be concluded that the increment of the width of the weft is beneficial for the mechanical performance of the composite not only because it implies a higher global fiber volume content, but also because it promotes a lower void content during the processing at constant flow rate regime. The reduction of the void size with the increase of the weft width is due to the higher inlet pressures that are required for the wider weft cases since the fluid front travels a longer distance before reaching the right edge of the weft, resulting in a higher pressure field for a given value of Q, which induces a higher saturation of the weft when the fluid percolates from the warps towards the channels, and a larger void compression. This can be seen by comparing the zones of void formation of the *Series 1* and *3* for $C_a^* = 1.21$, which are represented in Figure 26a and Figure 26c, respectively. In these figures, as well as in Figure 26b that corresponds to the zone of void formation for *Serie 2* and $C_a^* = 1.21$, three fluid fronts are highlighted in different colors, namely: 1) when the flow starts the migration towards the channel (green), 2) when the fluid fronts encounter one another (blue) and 3) when the partial equilibrium is reached in the bubble (violet). For the instant corresponding to fluid front 1 *(green)*, the unsaturated area of the weft for the *Serie 3*

(Figure 26c) is greater than for *Serie 1* (Figure 26a), but when the filling evolves from 1 *(green)* to 2 *(blue)*, the reduction in the void size is 17.3% for *Serie 1* and 49.5% for *Serie 3*, and this leads to a smaller bubble for the wider weft, *Serie 3*, when the fluid fronts encounter one another. The compression of the air, expressed as the reduction of the void volume and that takes places between the fluid fronts 2 *(blue)* and 3 *(violet)*, is: 59.0% for *Serie 1* and 65.8% for *Serie 3*. Accordingly, the causes of the difference between the void size of *Series 1* and *3* are: 1) the flow inside the weft advances more in *Serie 3* than in *Serie 1* in the time elapsed between the onset of liquid migration towards the channel *(green)* and the merging of the fluid fronts *(blue)*, 2) the void compression until the partial equilibrium *(blue to violet)* is larger for *Serie 3* than for *Serie 1*, as it becomes evident when compared the equilibrium pressures of the bubble of both series, which are shown in Figure 26a and Figure 26c.

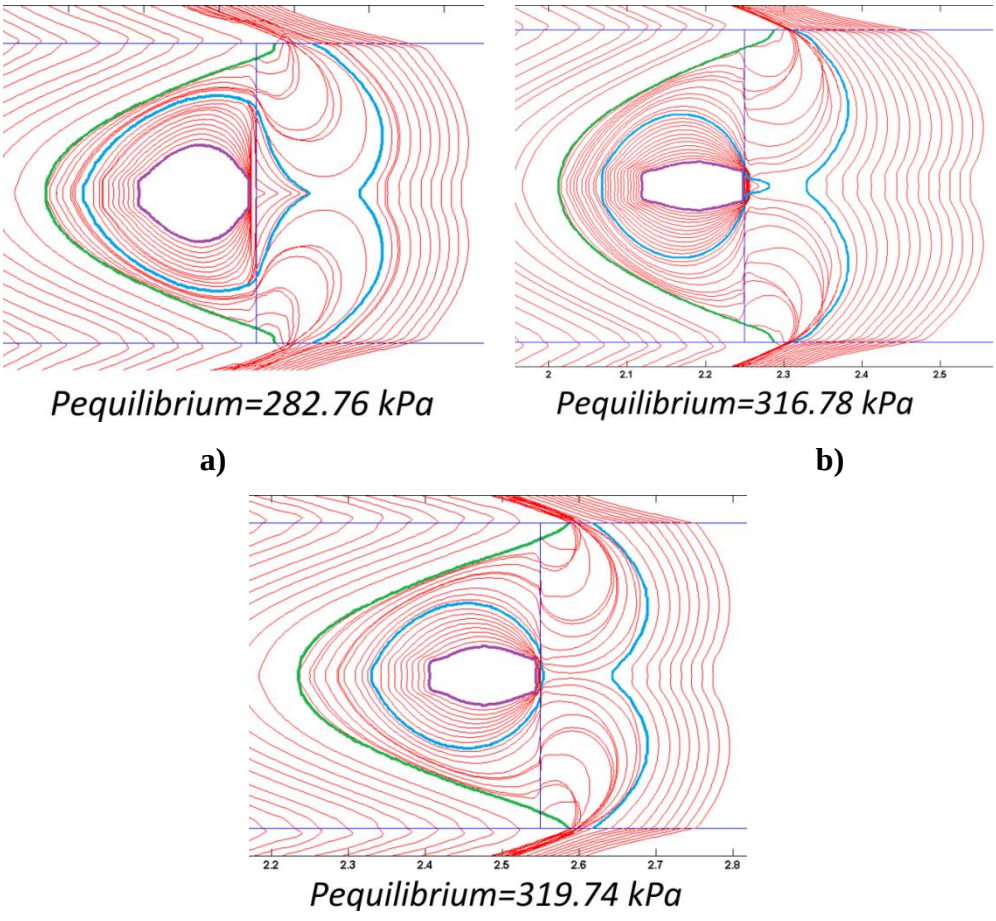

Figure 26 Detail of zones of void formation for C_a^*=1.21. a) Serie 1, b) Serie 2, c) Serie 3.

To determine the influence of the tow porosity, ε_t, *Serie 1* ($\varepsilon_t = 0.60$) and *Serie 2* ($\varepsilon_t = 0.42$) are compared one another. As can be noticed from Table 7, the reduction of the tow porosity from $\varepsilon_t = 0.60$ to $\varepsilon_t = 0.42$ causes the decrease on the void size, as it is also observed when compared Figure 26a and 26b. This is a consequence of several things: 1) the reduction of the anisotropy ratio, K_1/K_2, when the tow porosity, ε_t, decreases, 2) the higher saturation of the weft for $\varepsilon_t = 0.42$ when the fluid percolates from the warps towards the channel, 3) the lowering in the magnitude of the permeability as the porosity is reduced, and the concurrent increase of the inlet pressure in order to keep a constant inlet flow rate, which results in a higher void compression after the bubble is formed due to the higher values of the liquid pressure surrounding the bubble. In order to explain these causes, Figure 26a and Figure 26b are compared. When the flow starts the migration towards the channel *(green line)*, the unsaturated area of the weft is larger in the case of $\varepsilon_t = 0.60$, which boosts the formation of a larger initial void. A possible explanation for this is that the anisotropic ratio, K_1/K_2, is larger for $\varepsilon_t = 0.60$; considering that the advancement of the fluid front at the warp-weft interface is ruled by both K_1 and K_2, whereas the advancement of the fluid front at the symmetric plane of the weft is almost exclusively ruled by K_2, the increase of K_1/K_2 causes a larger separation between both fluid fronts during the whole filling for $\varepsilon_t = 0.60$; this in turn leads to a larger unsaturated zone for $\varepsilon_t = 0.60$. This corroborates the results obtained in Table 5, where the void size increases as K_1/K_2 is higher. On the other hand, the filled area in the weft between 1 *(green)* and 2 *(blue)* is larger for $\varepsilon_t = 0.42$. To explain this, it is important to take account that the change of ε_t has a double effect on the fluid motion in fibrous reinforcements: as ε_t is lower, the permeability decreases and this causes the flow to move slower; but, on the other hand, the reduction of ε_t increases the radial capillary pressure in the weft, whereby the fluid front velocity increases. In the present case, the second effect, added to the fact that the filtration velocity from the warps into the channel is lower for $\varepsilon_t = 0.42$ due to the lower transverse permeability, K_2, causes a greater reduction in the unsaturated area between the fluid fronts 1 *(green)* and 2 *(blue)* for $\varepsilon_t = 0.42$, leading to a smaller initial void in the instant when channel fluid fronts merge one another. Finally, once the bubble has been formed, the bubble compression is bigger for $\varepsilon_t = 0.42$ by two reasons: 1) higher fluid pressures are obtained for the lower porosity at the same value of C_a^*, 2) the higher

capillary pressures obtained for $\varepsilon_t = 0.42$ also produces a higher wicking effect inward to the bubble, which benefits the reduction of the void size. As expected, a higher equilibrium pressure of the bubble is obtained for the lower porosity, $\varepsilon_t = 0.42$.

It is important to mention that the behavior of the void size with ε_t obtained here is not in accordance with the results reported in [81], where the increment of ε_t generates smaller bubbles, but there is a relevant difference between the RUC geometry of that work and the one contemplated here. In that work, Schell and Deleglise [81] consider that the weft perimeter is totally surrounded by the free fluid, whereas, in the present work, a free fluid channel is not taken into account between the warps and the weft, emulating in this way a highly compacted preform. This suggests that the influence ε_t on the final void size depends on the level of compaction of the RUC, but shall be confirmed in further researches.

By comparing *Series 1* and *4* in Table 7 for both values of C_a^*, it can be concluded that the increment of R_{fluid} reduces the final void content. This confirms the importance to use low viscosity and highly compatible liquids (liquids with high surface tension and low contact angle with fibers) in LCM processes. On the other hand, according to Eq.98, the RUC porosity, ε_{RUC}, is modified by changing ε_t and/or b_1. Therefore, as can be concluded from results of Table 7, the reduction of ε_{RUC}, by increasing b_1 or by decreasing ε_t, causes a lower final void content.

Influence of parameters on the void shape.

According to Figure 24e-l, the void geometry can be almost circular, oval or cylindrical, depending on the *Serie* considered and on the value of C_a^*. These kinds of void geometries have been previously visualized in experimental works using optical microscopy (OM) and image analysis [170], [176], [177], which proves that the present results are coherent with the real void shapes obtained in LCM processes. It is important to mention that, in general, the void aspect ratio can have a significant influence on some mechanical properties of the composite, as the interlaminar shear strength [178], [179], fracture toughness [127], out-plane modulus [117], among others, being therefore interesting to address some conclusions about the influence of the parameters studied here on this ratio.

Comparison between *Series 1* and *2* for both cases of C_a^* (See Table 7) shows an increment of the void aspect ratio when ε_t decreases, being more significant for $C_a^* = 1.21$, as can be also seen in Figure 26a and Figure 26b. On the other hand, by comparing *Series 1* and *3*, it can be concluded that the increase of b_1 results in the increase of the void aspect ratio for $C_a^* = 1.21$ (as seen in Figure 26a and Figure 26c), whereas a contrary behavior is obtained for $C_a^* = 6.27 \times 10^{-1}$. From the above results follow that a reduction on the RUC porosity, ε_{RUC}, due to a decrease of ε_t, causes an increment of the void aspect ratio for both values of C_a^*, whereas the increase in the void aspect ratio due to reduction in ε_{RUC}, in virtue of the increase of b_1, is only observed for $C_a^* = 1.21$. Finally, it can be inferred by comparison of *Series 1* and *4*, for both values of C_a^*, that an increment on R_{fluid} results in a higher void aspect ratio, but this increment is more notorious for $C_a^* = 1.21$. In general, the comparison of all *Series* reveals that the void aspect ratio is more sensitivity to the variations of the parameters studied here for the larger capillary number, $C_a^* = 1.21$.

According to Table 7, for cases with $\varepsilon_t = 0.60$ (*Series 1,3 and 4*), the aspect ratio of the void reduces with the increment of C_a^*. On the other hand, for $\varepsilon_t = 0.42$ (*Serie 2*), a reverse behavior is observed, i.e., the increase of C_a^* results in the increase of the void aspect ratio, although this increase is not significant. It is worth noting that the shape of the void is closely related to the void size (See Figure 26a-c); as the void size is smaller its aspect ratio tends to increase because the bubble undergoes a greater compression in the vertical than in the horizontal direction. This result is in agreement with previous experimental results, where the reduction of the void's height with the void content is also reported, see [117].

Influence of parameters on the void location.

According to Table 7, the void location, expressed as "l_{edge}/w" (See Figure 23), is not considerably affected by the parameters studied here. In general, the final void is always located at the rear (right) edge of the weft, which is in agreement with other results [3], [4].

3.4.4 Analysis of capillary-driven and pressure-driven flow fields

Inlet pressure history.

During the filling of the first channel at the lowest capillary number, $C_a^* = 6.03 \times 10^{-2}$ (Figure 27b and Figure 28a), before the front reaches the weft, the flow is driven by the surface tractions of the moving front. Figure 27b presents the detailed behavior of the

almost constant pressure region of the inlet pressure history shown in Figure 27a. At these times, the inlet pressures correspond to small negative values, while the pressures at the fluid front in the channel (see Figure 28a) are given by larger negative values due to the curvature of the moving interface (surface tension effect). The difference between the pressures at the fluid front and at the inlet induces negative pressure gradients in the direction of the fluid motion. A similar behavior occurs during these times at the warps, where the fluid motion is driven by the capillary pressure (compare inlet pressures of Figure 27b to fluid front pressures of upper part of Figure 28a). When the channel flow arrives to the low permeable weft, the inlet pressure increases significantly due to the high resistance encountered, reaching a maximum value of $8.806 \times 10^4 Pa$ at the end of the simulation (see Figure 27a). In this case, in both the warps and wefts, the flow is driven by the inlet pressure rather than by the capillary pressure of the fluid front (compare inlet pressures of Figure 27a after flow reaches the weft to the capillary pressures in the warps and wefts appearing in Figure 28b).

The evolution of the moving front for the largest capillary number, $C_a^* = 1.21$, shows significant differences with respect to the previous case. In Figure 29a,b, it is reported the variation of the inlet pressure with time to keep a total inlet flux of $Q = 5 \times 10^{-5}\ m^3/s$, which corresponds to $C_a^* = 1.21$. Figure 29b shows the zoom of the inlet pressure evolution in the time during the filling of the first channel, until the moving front reaches the weft. In this case, the pressure of the moving front in the channel resulting from the surface tension effect (Figure 30a) is smaller than the inlet pressure (Figure 29b), and consequently, in contrast with the previous case, the flow in the channel during this period is pressure-driven instead of capillary-driven. As observed, the shape of the fluid front in the channel changes from concave in the case of capillary-driven flow (i.e., low C_a^*, see Figure 28a) to convex in the pressure-driven flow (i.e., high C_a^*, see Figure 30a). On the other hand, for $C_a^* = 1.21$, the flow in the warp, before the weft is impregnated, is primarily driven by the capillary pressure, as it was the case of the low C_a^*, with negative capillary pressures of order of $\mathcal{O}(3)$ in the fluid front (see upper part of Figure 30a), while the inlet pressures are positive and of the order $\mathcal{O}(2)$ (see Figure 29b). As in the case of low C_a^*, after the fluid front in the channel has reached the weft, an important increment of the inlet pressure is noticed (see Figure 29a) and the flows in both warps and weft are driven by the imposed inlet pressure

(magnitudes of negative capillary pressures are smaller than the inlet pressure), which in turn achieves a maximum value of $2.865 \times 10^6\ Pa$; compare pressures of Figure 29a after flow reaches the weft to pressures of Figure 30b.

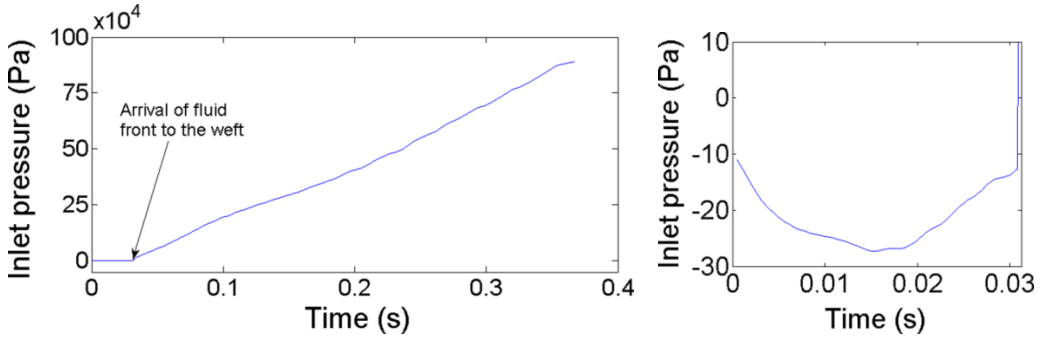

a) **b)**

Figure 27 Inlet pressure vs.Time for C_a^*=6.03×10^{-2} . a) Total filling, b) Before the flow reaches the weft.

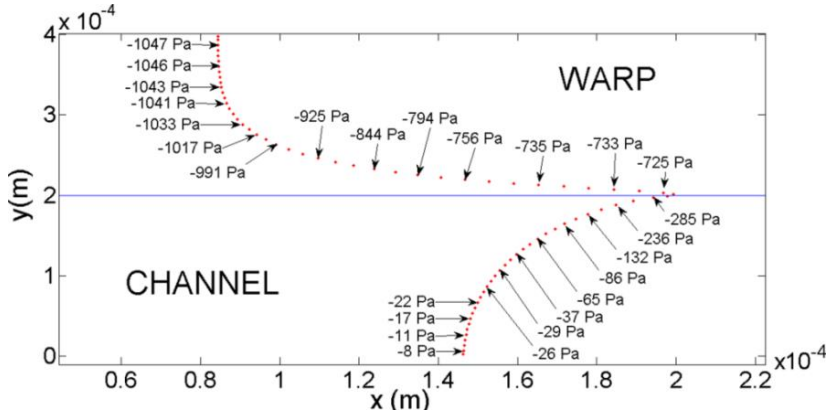

a)

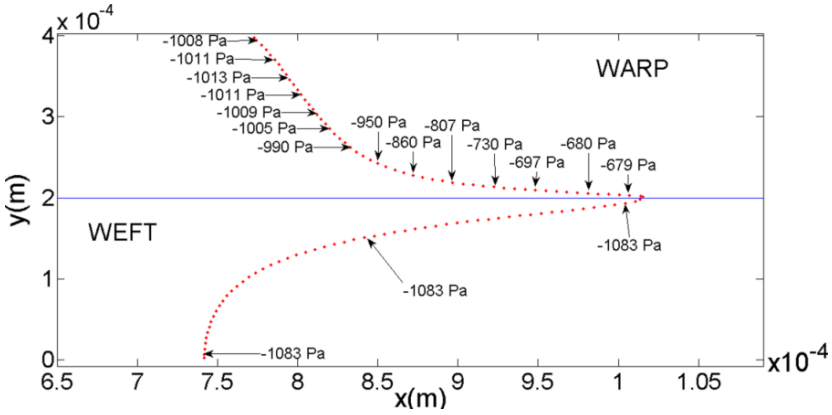

b)

Figure 28 Capillary pressure at the flow front for C_a^*=6.03×10^{-2}, a) Before flow reaches the weft, b) After flow reaches the weft.

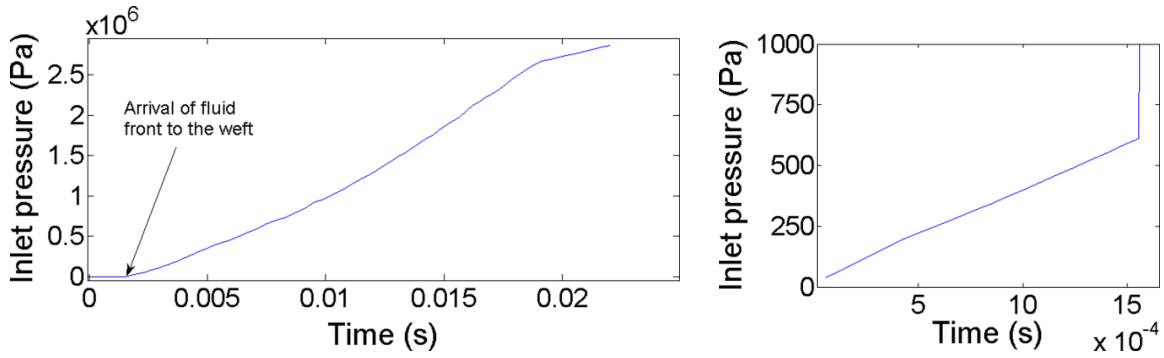

a) **b)**

Figure 29 Inlet pressure vs. Time for C_a^*=1.21. a) Total filling, b) Before flow reaches the weft.

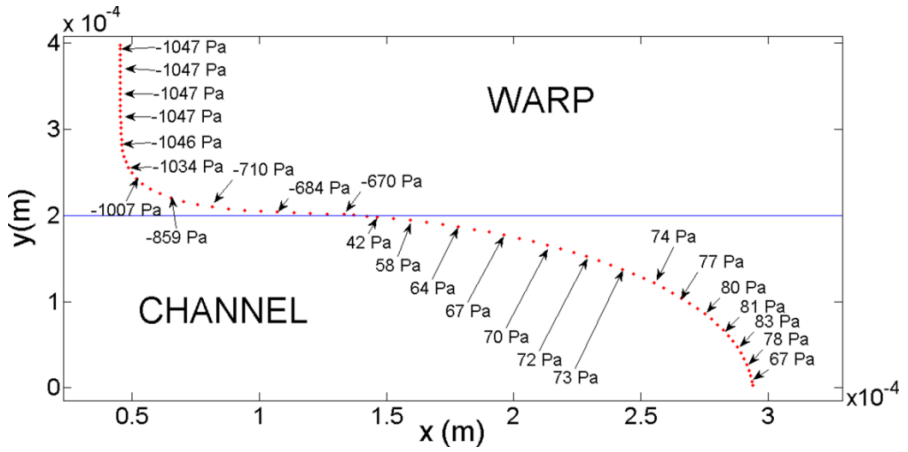

a)

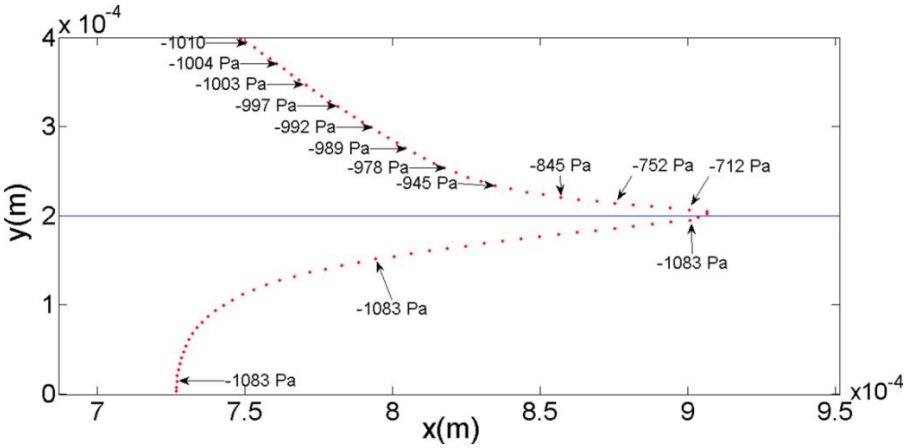

b)

Figure 30 Capillary pressure at the flow front for C_a^*=1.21. a) Before flow reaches the weft, b) After flow reaches the weft.

Inlet velocity profiles in the channel and warps

The inlet velocity profiles in the channel and warps are reported in Figure 31 in the case of low C_a^* for several time instants, corresponding to three profiles when the fluid front is still in the channel without reaching the weft, one profile when the front arrives to the weft and another profile when the front is impregnating the weft. On the other hand, Figure 32 shows the inlet velocity profiles for the case of high C_a^* at five different time instants, two corresponding to instants when the fluid front is still in the channel, one instant when the flow arrives at the weft and two when the fluid front is inside the weft. It is important to realize that in the case of $C_a^* = 1.21$ (Figure 32), all velocity profiles in the channel are convex-shaped, different to the convolute-shaped profiles obtained at the beginning of the filling in the case of low C_a^* (Figure 31). This happens because in the case of $C_a^* = 1.21$, the fluid motion in the channel is always pressure-driven, while in the other case, $C_a^* = 6.03 \times 10^{-2}$, it is capillary-driven before the fluid front reaches the weft, as explained before.

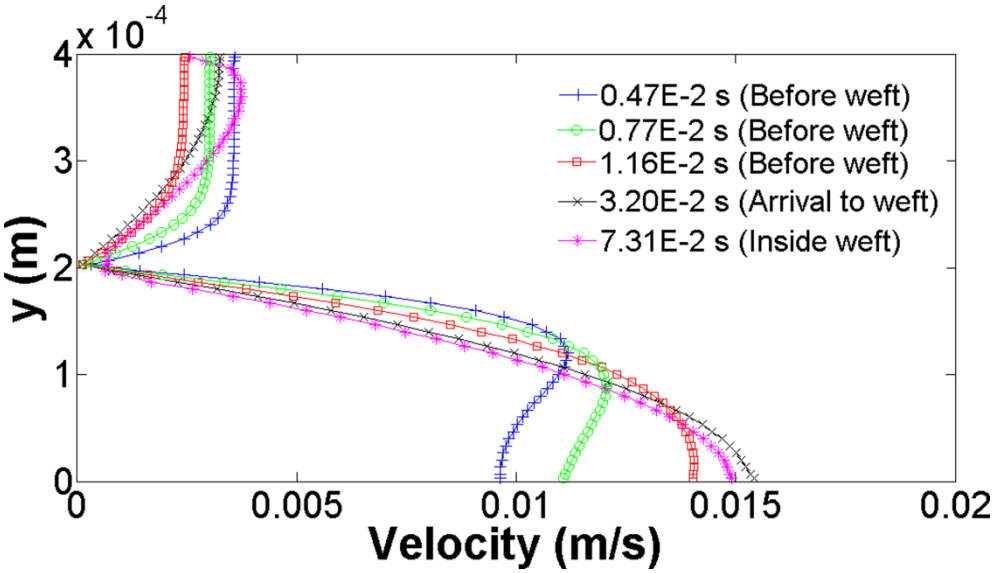

Figure 31 Inlet velocity profiles for $C_a^*=6.03\times10^{-2}$ at several time instants.

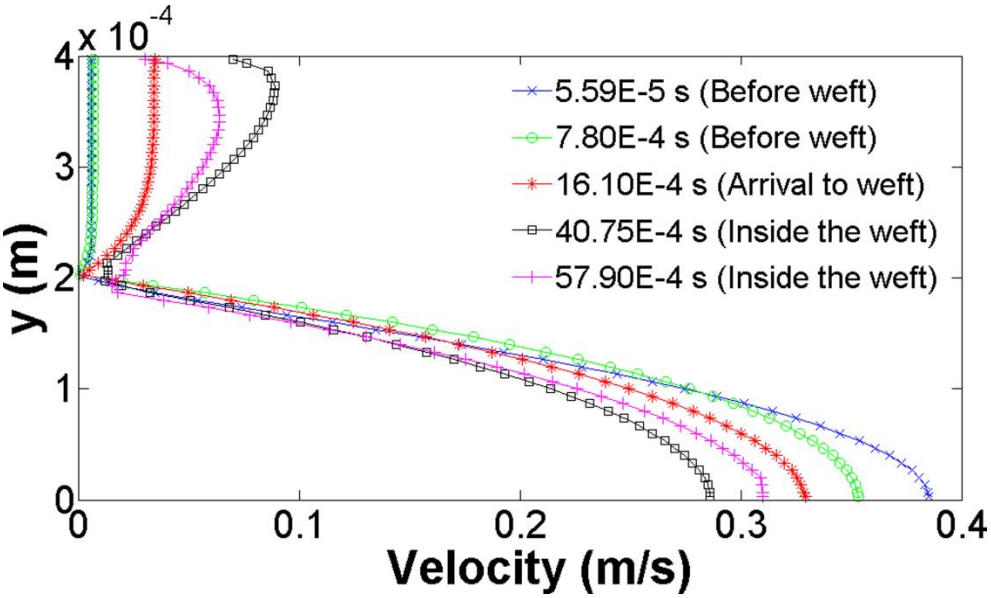

Figure 32 Inlet velocity profiles for C_a^*=1.21 at several time instants.

Inlet flow rates distribution

Figure 33 reports the time evolution of the inlet flow rates in the channel and warps, with a resulting total inlet flow rate of $Q = 2.5 \times 10^{-6}\ m^3/s$, which corresponds to $C_a^* = 6.03 \times 10^{-2}$. As it can be observed, during the filling process of the first channel, the inlet flow rate in the channel increases monotonically, whereas the one in the warp decreases. At the time when the fluid front arrives to the weft, there is a sudden decrease in the channel flow rate and a concurrent increase in the warp flow rate, after which, there is a slight increase in the channel flow rate and an equivalent decrease in the warp flow rate, with the channel flow rate always larger than the warp one. On the other hand, Figure 34 presents the time evolution of the inlet flow rate at the channel and warps, with a corresponding total inlet flux of $Q = 5 \times 10^{-5}\ m^3/s$ ($C_a^* = 1.21$). The general behavior is similar to the case of the low capillary number in the sense that the channel flow rate is always above the warps one and an abrupt change occurs in both rates when the fluid front arrives to the weft (Figure 33 and Figure 34), but, in the case of $C_a^* = 1.21$, the channel and warp fluxes remains almost constant before the flow reaches the weft (Figure 34) instead of the monotonous variation observed for the low capillary number situation (Figure 33).

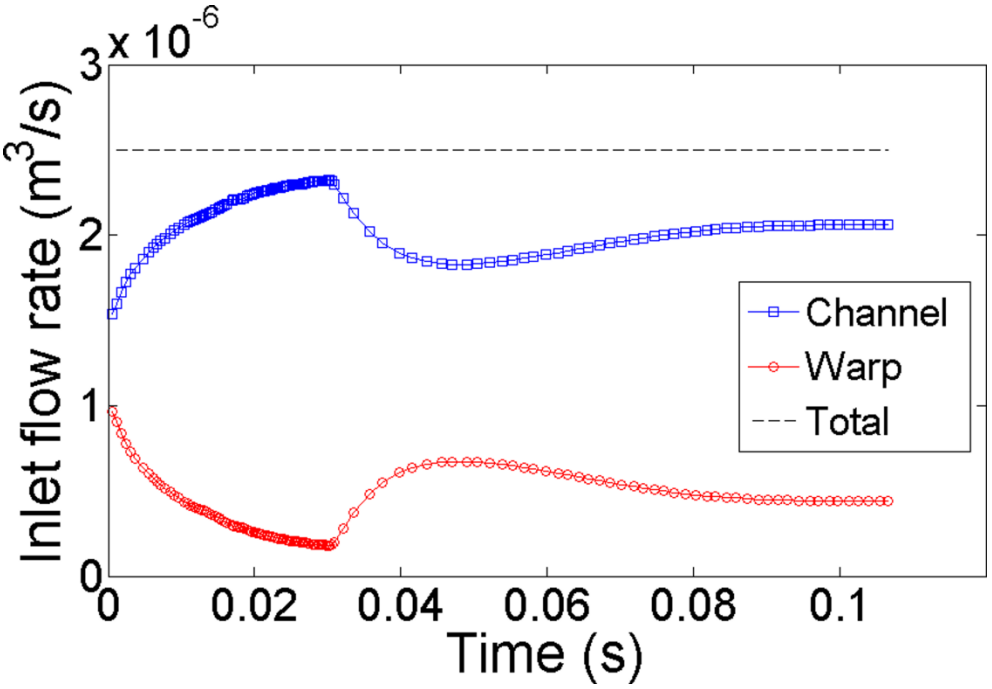

Figure 33 Inlet flow rate distribution in the time for $C_a^*=6.03\times10^{-2}$.

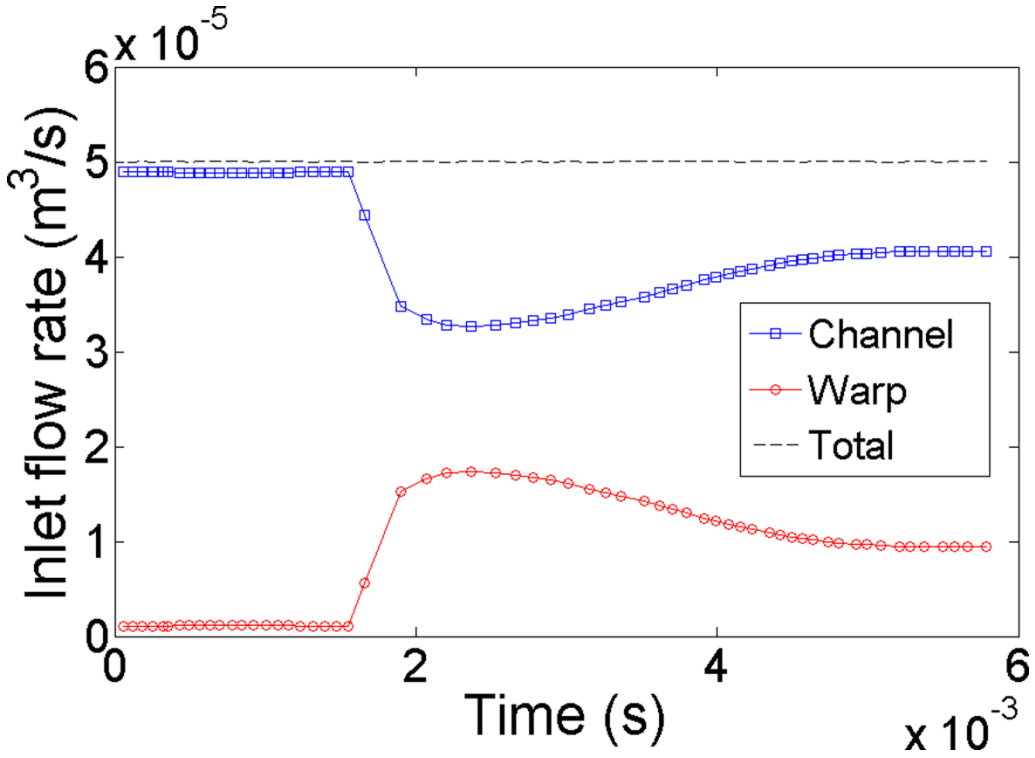

Figure 34 Inlet flow rate distribution in the time for $C_a^*=1.21$.

Velocity fields.

The velocity fields for $C_a^* = 6.03 \times 10^{-2}$ in two filling instants are represented in Figure 35 and Figure 36, where some graphics are off-scale for sake of clarity. In the first instant, Figure 35, the flow has not reached the weft, and two domains are partially saturated: the first channel and the warp (Figure 35a). Three detailed zones are considered for each domain, which are clearly identified in Figure 35b for the channel and Figure 35c for the warp. The details for the channel, Figure 35d, Figure 35e and Figure 35f, show that the change in the velocity direction from the inlet to the fluid front is more pronounced as the points are closer to the interface with the warp. For instance, in the Figure 35f, the horizontal component of the velocity vectors is larger than the vertical one for all points, whereas in the Figure 35d, which corresponds to the zone near the interface with the warp, the vertical component is zero at the inlet, but it becomes very important as the points approximate to the fluid front, where it is also observed that the magnitude of the velocity is greater with respect to the inlet velocities. A similar behavior can be observed for the warp, see Figure 35g to Figure 35i, i.e., both the magnitude and the direction of the velocity vectors change more from the inlet to the fluid front in the zone near the interface with the channel. In this first case, the mass exchange between both domains, channel and warp, takes place from the channel towards the warp (Figure 35j).

The second case is presented in Figure 36, where the fluid front is impregnating the warp and the weft, while the channel is totally filled with liquid (Figure 36a). The identification of the details of the channel, warp and weft is shown in Figure 36b, Figure 36c and Figure 36d, respectively. For the channel, according to Figure 36e to Figure 36i, a substantial amount of fluid entering the channel displaces towards the transition zone channel-warp-weft, which originates an important change in the velocity direction in all zones of the filled channel. The significant increase in the magnitudes of the velocity in points close to or lying on the interface channel-warp, Figure 36e, is an indication of the considerable amount of fluid coming from the inferior zones, Figure 36h and Figure 36i. For the warp domain, the velocity is practically horizontal in the neighborhood of the symmetric boundary (Figure 36j and Figure 36l), but the velocity direction is altered as the points are closer to the interfaces with the channel and with the weft due to the mass transfer (Figure 36j and Figure 36k) and to the fluid front (Figure 36m); in the detail 1 of the warp (Figure 36j), it is

also appreciated that the magnitude of the velocity is lower as the points are closer to the interface with the channel. For the weft, in a similar fashion as for the warp, the velocity is almost horizontal in the neighborhood of the symmetric boundary, and its direction varies considerably in points nearby to the interface with the warp and to the fluid front (Figure 36n and Figure 36o). For the interface channel-warp, Figure 36p, the mass transfer takes place from the warp towards the channel only in points near the inlet, however, the mass transfer is reversed in one point along this interface and the percolation of fluid from the channel towards the warp increases until the transition point channel-warp-weft, where the mass exchange reaches its maximum. The net mass transfer in the channel-warp interface occurs from the channel into warp. After the transition point channel-warp-weft is reached, Figure 36p, the mass transfer from the weft into warp decreases until it is reversed, in such a way that in the fluid front the mass transfer from the warp into the weft reaches its maximum.

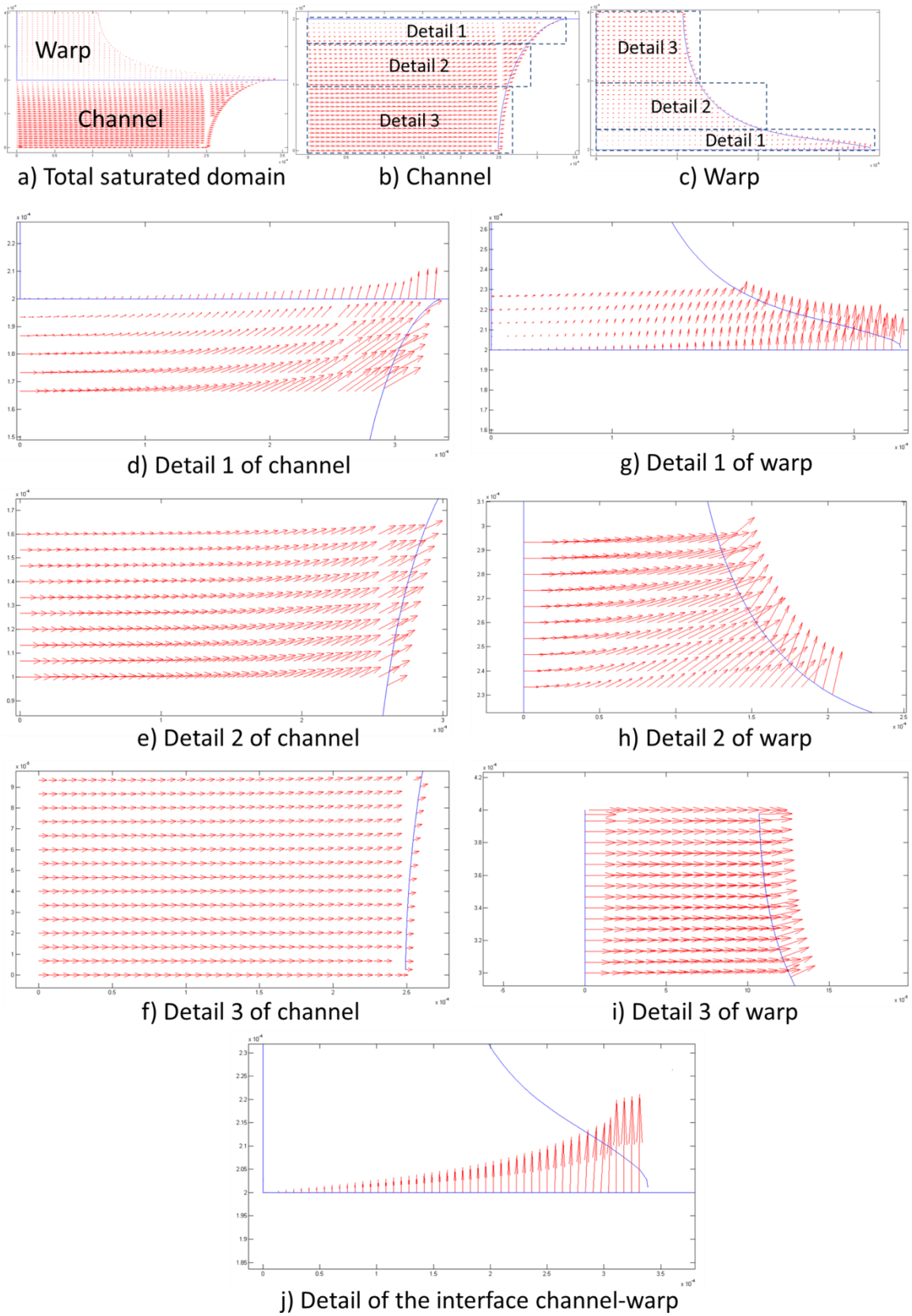

Figure 35 Velocity field for $C_a^*=6.03\times10^{-2}$ before the flow reaches the weft.

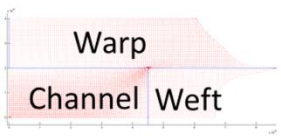

a) Total saturated domain

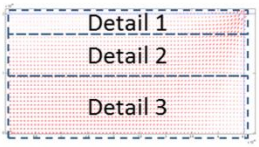

b) Channel

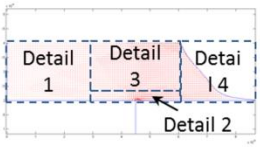

c) Warp

d) Weft

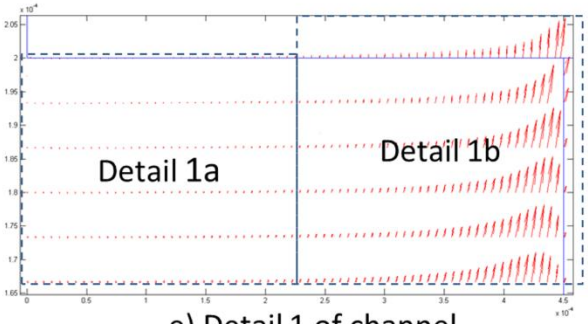

e) Detail 1 of channel

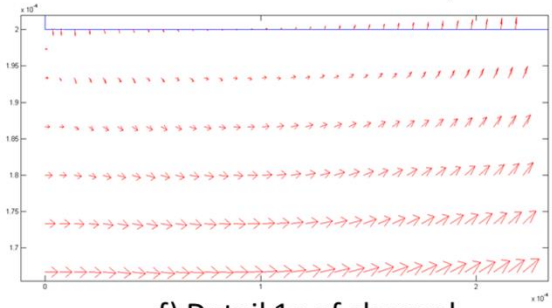

f) Detail 1a of channel

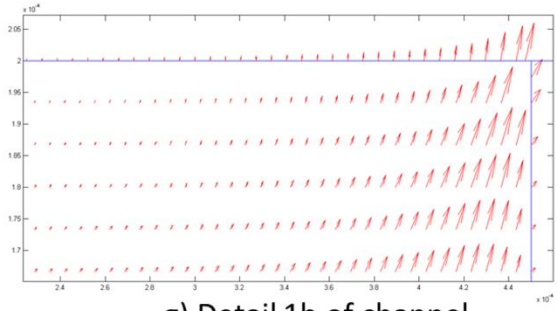

g) Detail 1b of channel

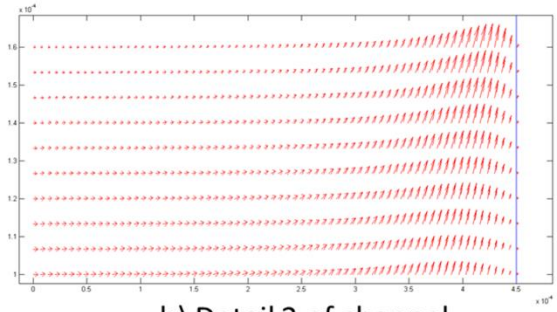

h) Detail 2 of channel

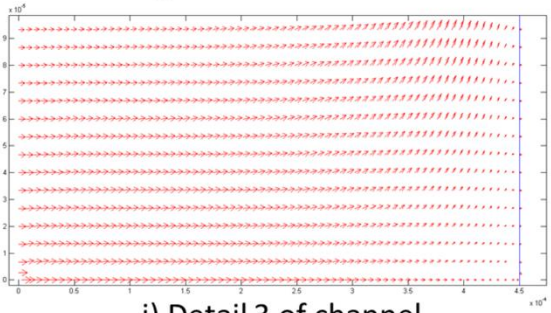

i) Detail 3 of channel

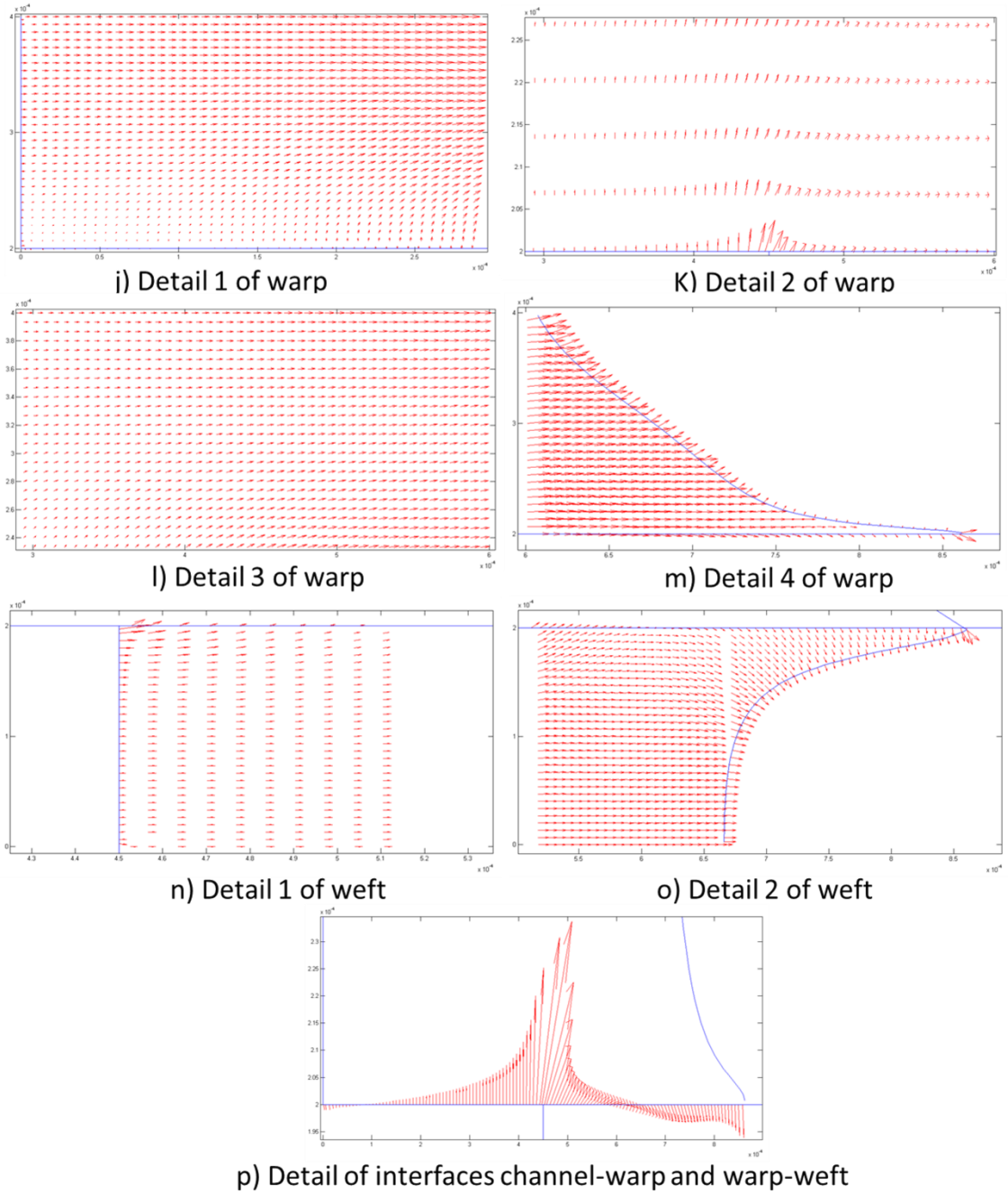

Figure 36 Velocity field for C_a^*=6.03×10^{-2} after the flow reaches the weft

The velocity fields for $C_a^* = 1.21$ for two filling instants are represented in Figure 37 and Figure 38. For the first case, Figure 37, in the same way as for $C_a^* = 6.03 \times 10^{-2}$, three detailed zones are considered for each domain, which are clearly identified in Figure 37b for the channel and Figure 37c for the warp. As in the case of the lowest capillary number, $C_a^* = 6.03 \times 10^{-2}$, the change of the velocity direction from the inlet to the fluid front is

more notorious as the points are closer to the interface with the warp (Compare Figure 37d, Figure 37e and Figure 37f), but an important difference can be identified between the velocity vectors in the channel fluid front of the present case, $C_a^* = 1.21$, and the ones of the case of $C_a^* = 6.03 \times 10^{-2}$: in the present case the normal component of the channel fluid front velocity is considerably greater than the tangential component for all points (See Figure 37d, Figure 37e and Figure 37f) in such a way that the advancement of the fluid front is almost totally determined by the magnitude of the velocity; on the other hand, for $C_a^* = 6.03 \times 10^{-2}$, the tangential component of the channel fluid front velocity is relevant in some points (Figure 35d, Figure 35e and Figure 35f) and this component does not contribute to the fluid front advancement according to the kinematic condition, Eq. 73.

According to Figure 37g to Figure 37i, in the warp, both the magnitude and the direction of the velocity vectors change more from the inlet to the fluid front in the zone nearby to or along the interface channel-warp; in this interface, the largest velocities are obtained near the fluid front (Figure 37g). As in the case of $C_a^* = 6.03 \times 10^{-2}$, the mass exchange between both domains, channel and warp, takes place from the channel towards the warp (Figure 37j), but, in this case of $C_a^* = 1.21$, the tangential component of the interfacial velocity is more important (Figure 37j) than for $C_a^* = 6.03 \times 10^{-2}$ where it is negligible in all points (Figure 35j).

The second filling instant for $C_a^* = 1.21$ is presented in Figure 38, where it can be appreciated that the general behavior of the velocity field is very similar to the second case of $C_a^* = 6.03 \times 10^{-2}$ (Figure 36), even though the velocity vectors are not the same.

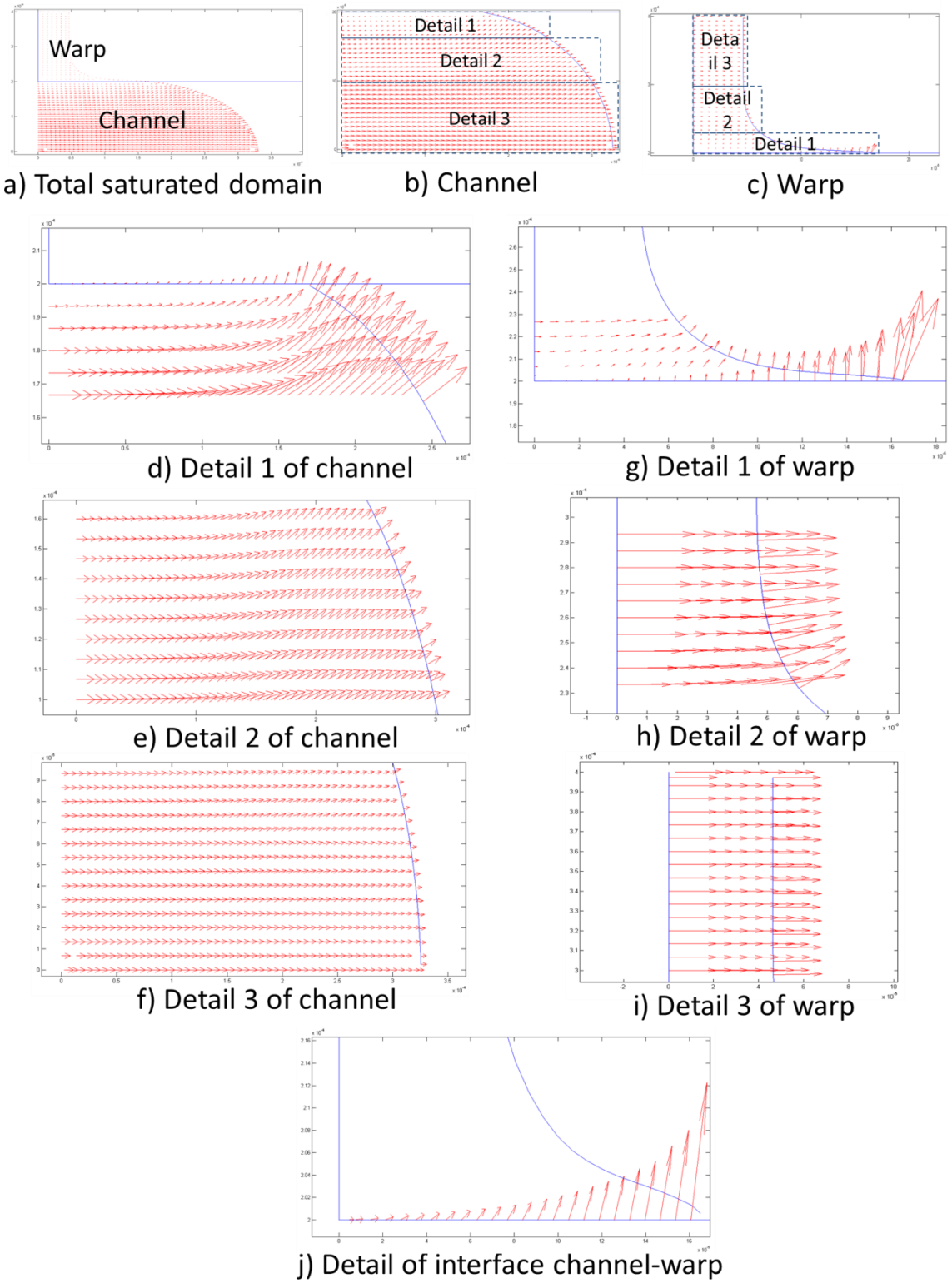

Figure 37 Velocity field for C_a^*=1.21 before the flow reaches de the weft

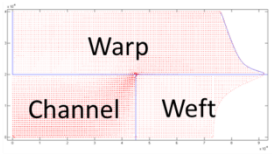

a) Total saturated domain

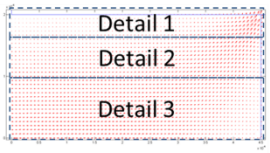

b) Channel

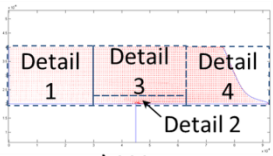

c) Warp

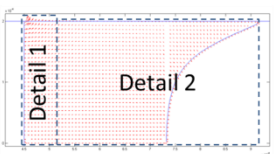

d) Weft

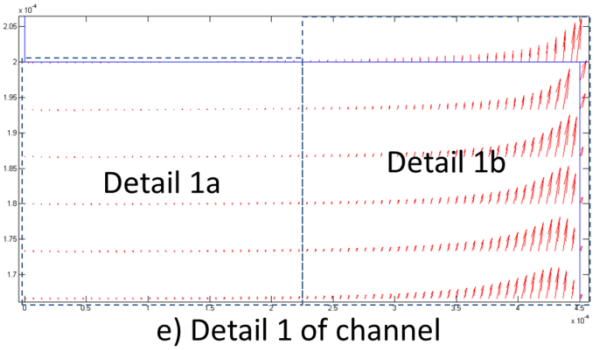

e) Detail 1 of channel

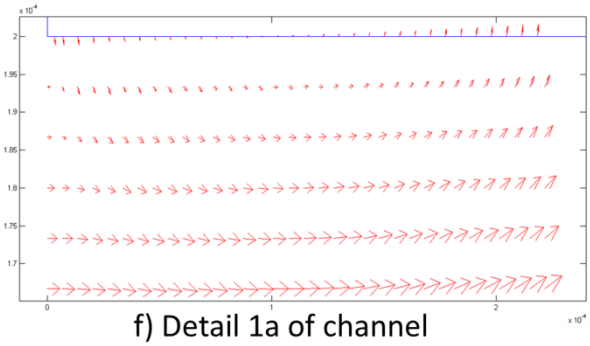

f) Detail 1a of channel

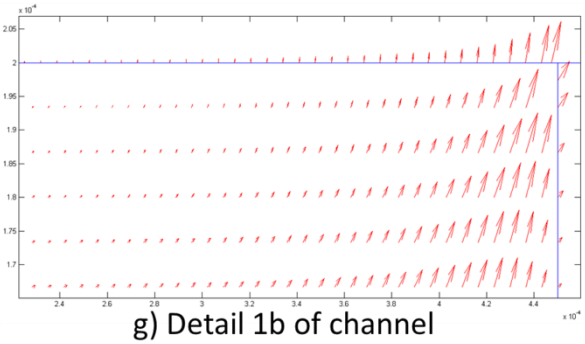

g) Detail 1b of channel

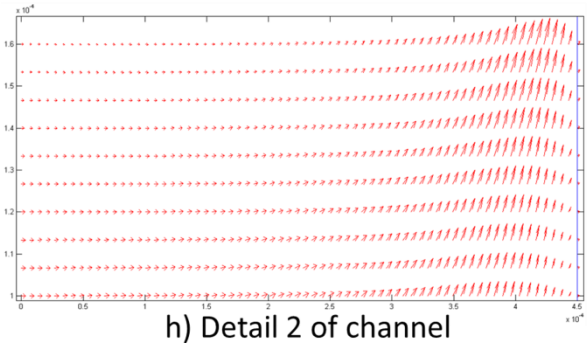

h) Detail 2 of channel

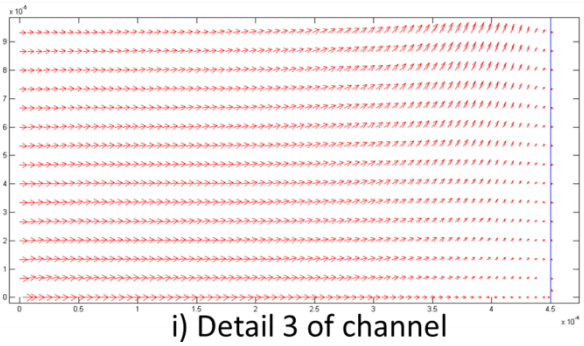

i) Detail 3 of channel

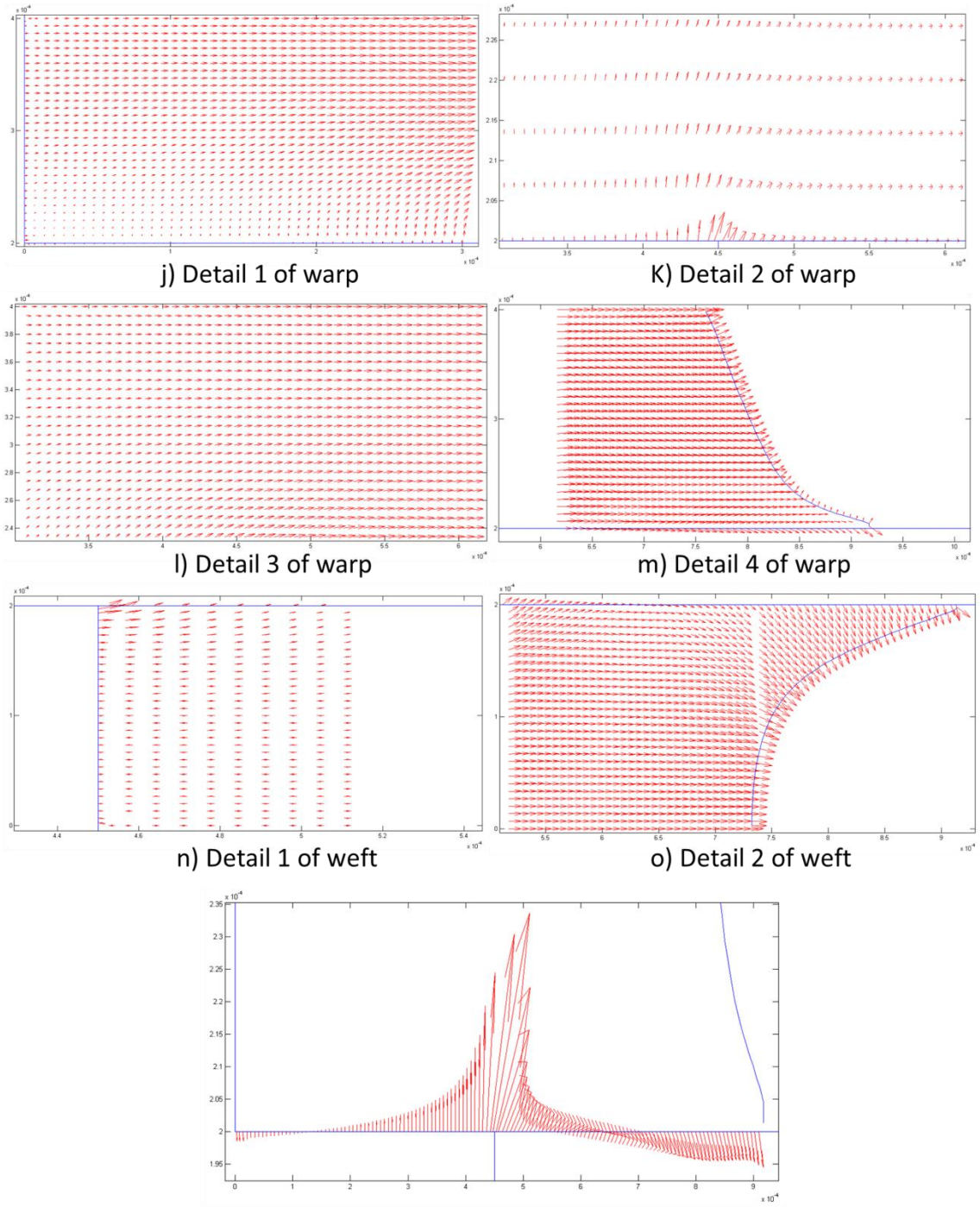

Figure 38 Velocity field for C_a^*=1.21 after the flow reaches de the weft

3.5 Conclusions

In this chapter, the BEM method has been implemented for the simulation of void formation in dual-scale fibrous reinforcements using a Stokes-Darcy formulation.

Comparison of the BEM numerical results with the analytical solution of a simple coupled problem free fluid-porous media was carried out, showing good agreement between them. In general, the developed BEM code converges to the analytical solution as the mesh is finer and the accuracy is acceptable for the kind of problem treated here.

Two types of RUC filling problems were considered. The first one consisted on the simulation of the simultaneous filling of the channels and tows at constant pressure regime. The main objective of this simulation was to compare the present BEM results with those ones previously reported in the literature using a CV/FAN approach. Several differences between both results were identified: the filling times at the instants before the fluid front reaches the weft are overestimated by the CV/FAN scheme, due to the approximation of the channel flow as a Darcian flow with an equivalent permeability. On the other hand, when the fluid front is impregnating the weft the filling times are underestimated by the CV/FAN approach, with a predicted almost straight shaped fluid front in the warps instead of the concave shaped one obtained by BEM. These differences were attributed to the slip matching condition considered in the BEM approach, not taken into account in the CV/FAN, and to the differences between the tracking techniques used to update the position of the moving boundary. Both approaches predicted that the void size increases as K_1/K_2 is higher, but larger voids were obtained with the BEM approach.

The second case consisted on a parametric study of a filling process at constant flow rate, in order to determine the influence of processing, geometric and material parameters on the size, shape and location of the voids formed by mechanical air entrapment. According to the results, it can be concluded that the driving forces of the fluid motion depend on the magnitude of the capillary number, C_a^*, and on the location of the fluid front. At $C_a^* = 6.03 \times 10^{-2}$, and when the fluid front has not reached the weft, the flow is capillary-driven in both the warps and the channel, however, at $C_a^* = 1.21$, the capillary pressure is the principal driving force for the flow in the warps, whereas the inlet pressure is the major force driving the flow in the channel. When the fluid front is impregnating the weft, the inlet pressure is the main driving force for the two capillary numbers. Besides, the value of C_a^* also determines whether the void is formed or not, in such a way that for $C_a^* = 1.21$ and $C_a^* = 6.27 \times 10^{-1}$ the numerical simulation predicted void formation, contrarily to the case of $C_a^* = 6.03 \times 10^{-2}$ where no void formation was obtained.

A summary of the major conclusions of the present parametric study can be outlined as:

- The void size is greater as C_a^* is higher for given values of ε_t, b_1, ε_{RUC} and R_{fluid}.
- The void location is not significantly affected by any of the parameters considered here. In general, void is always formed at the right edge of the weft.
- For a constant C_a^*, the reduction of the RUC porosity, ε_{RUC}, in virtue of the increment of b_1 or of the reduction of ε_t, as well as the increment of the fluid penetrativity, R_{fluid}, lead to the formation of smaller voids.
- The relationship between the considered parameters and the void shape depends on C_a^*. For both $C_a^* = 6.27 \times 10^{-1}$ and $C_a^* = 1.21$, the increase of R_{fluid} leads to a higher aspect ratio. In general, the void aspect ratio tends to increase as the void is smaller since the void undergoes a greater compression in the vertical than in the horizontal direction.

Generally speaking, the velocity fields for $C_a^* = 6.03 \times 10^{-2}$ and $C_a^* = 1.21$ have some similarities and differences among them. When the fluid is still impregnating the first channel, for both values of C_a^*, the velocity directions in the warp and channel are more affected as the points are closer to the interface warp-channel, in which the mass transfer occurs from the channel towards the warp in all points belonging to it. While the tangential velocity at the fluid front for $C_a^* = 6.03 \times 10^{-2}$ is relevant, it is virtually negligible for $C_a^* = 1.21$. Regarding the tangential velocity at the interface channel-warp, a contrary behavior was obtained, namely, it is important for $C_a^* = 1.21$, whereas insignificant for $C_a^* = 6.03 \times 10^{-2}$. On the other hand, when the fluid front is impregnating the weft and the first channel is totally filled of liquid, the velocity vectors are not exactly the same for both values of C_a^*, but the behavior of the velocity fields is similar in several aspects: 1) the global mass transfer reaches its maximum in the neighborhood of the transition channel-warp-weft, 2) the mass transfer at the interface channel-warp takes place from the warp towards the channel in points close to the inlet, but it is reversed in a certain point along this interface, in such a way that the net mass transfer occurs from the channel towards the warp, 3) the mass transfer iat the interface warp-weft takes place from the weft towards the warp in the transition channel-warp-weft, it decreases along this interface and then it is reversed, in such a way that in the neighborhood of the fluid front, the mass transfer from the warp towards the weft reaches its maximum.

4. VOID FORMATION IN DUAL-SCALE FIBROUS REINFORCEMENTS BASED ON THE STOKES-BRINKMAN FORMULATION[♠]

4.1 Introduction

Under the following assumptions: the solid phase is stationary, the fluid is newtonian and incompressible, the inertial effects can be neglected, a quasi-static approach can be considered and the tow porosity is constant inside the RUC, the momentum equation in the porous media (tows or bundles) can be simplified into the Brinkman equation. Additionally, it is important to remind that Darcy equation can be achieved as long as two length-scale restrictions are satisfied, namely, $(L_{RUC}/L)^2 \ll 1$ and $L_{RUC} \gg L_f$, where L, L_{RUC} and L_f are the characteristic lengths of the volume averaged quantities, of the RUC and of the fluid phase, respectively. The averages implicit in the Brinkman equation can be viewed as averages over an ensemble of different scales of the porous medium that interpolate between the Stokes and Darcy equations. On small length scales, the pressure gradient balances the Laplacian of the velocity and the flow is essentially viscous, Stokes flow, while over larger length scales, the velocity is slowly varying and the pressure gradient balances the average velocity as it does in Darcy's law (for more details see Durlofsky and Brady [180]).

Krotkiewski et al [181], using a direct numerical simulation of the flow field in homogeneous two dimensional porous media having characteristic length L and macroscopic permeability K, found that the Stokes solution is dominant for $K/L^2 \geq 10$, Darcy law is representative of the flow field if $K/L^2 \leq 10^{-4}$, while for $10^{-4} \leq K/L^2 \leq 10$, the Brinkman approximation should be used to account for the transition between both flow regimes, Stokes and Darcy. According to these authors, the use of the Brinkman law is necessary in dual-scale porous media when the ratio between the effective saturated permeability, $K_{eff,sat}$, and the permeability of the porous media (tows in this case), K_t, is lower than the unity. However, this ratio is not the unique criterion to establish whether the Brinkman or the Darcy approximation is more convenient and the matching conditions of the coupled problem play a major role in the selection of the momentum equation for the

[♠] **The results of the present chapter were published in: Iván David Patiño Arcila, Henry Power, César Nieto Londoño, Whady Felipe Flórez Escobar, *"Stokes-Brinkman formulation for prediction of void formation in dual-scale fibrous reinforcements: a BEM/DR-BEM simulation". Published in: Germany. Computational Mechanics, ISSN: 1432-0924, v.59, First On-line, p.1 - 23,2017***

porous medium. If the Brinkman equation is used, the matching conditions on the interface channels-tows can be put explicitly in terms of the components of the vectors of velocity and traction because the order of this equation is the same as the order of the Stokes equation; on the other hand, if the Darcy law is employed, a slip condition for the tangential velocities shall be considered along the interface channel-tows [157], [159], which implies the use of a dimensionless slip coefficient, γ, which, in turn, involves experimental tests or models for its estimation that are still matter of controversy.

In the Stokes-Brinkman approach the continuity of the velocity field is always considered and two types of conditions could be employed for the tractions: continuous [182] and jump stress [183], [184]. The continuity of stress was initially used by [182], [185], however a jump stress matching condition was proposed later in [183] based on the non-local form of the volume-averaged momentum equation for the analysis of the interface region between the channel and the porous medium. By means of experiments, Ochoa-Tapia and Whitaker [184] found that for unidirectional flow in parallel domains, the jump stress tensor has the form $T_{ij} = \beta\delta_{ij}$, where β is a jump stress coefficient ranging between -1 and 1.47 [20]. However, Phillipe Angot [186] demonstrated mathematically that well-posedness of the Stokes-Brinkman problem is only possible when $\beta \geq 0$. The theoretical estimation of the value of β was developed in [187], [188], where it was established that β depends on the porosity of the porous medium in the inter-region channel-tow, ε_{ct}. The physical meaning of β at the micro-scale is still debatable, but some works have demonstrated that this coefficient is related to the excess quantities for ε_{ct} and for the ratio ε_{ct}/K_t along the interface between the free fluid and the porous medium, and that these quantities vary with the position of the interface region and lead to changes in the viscosity and in the drag force (friction) [189]. In a work focused in the prediction of the effective saturated permeability, $K_{eff,sat}$, of dual-scale fibrous reinforcements [20], it was taken $\beta = 0.7$ for all simulations, concluding that the type of matching condition used for the tractions (continuity or jump) has a strong influence on the boundary layer thickness in the porous medium for unidirectional flow in parallel domains, but a non-significant influence on $K_{eff,sat}$, which is dependent on the pore geometry. In this point, it is relevant to mention that the study of the pore geometry dependency of the effective saturated permeability, $K_{eff,sat}$, could be a complicated and computationally expensive task, but some recent

efforts have been addressed to reduce the computational cost without compromising the accuracy. For instance, a multiscale framework relating $K_{eff,sat}$ with some microstructural attributes extracted by X-Ray tomography was proposed in [190], where several computational techniques were efficiently combined (Level Set, Graph Theory and Lattice Boltzman/Finite Element) to determine the tortuosity, porosity and homogenized effective permeability at the specimen scale. The particular problem solved in [20] by FEM is also considered here for validation of the numerical technique implemented.

The Brinkman equation includes an effective viscosity term, μ_{eff}, to consider the viscous diffusion not deemed in the Darcy's law. In order to explain the meaning of this term, it is necessary to consider that the volume averaging method allows describing the porous medium flow in terms of averages of the local quantities by means of the Darcy-Brinkman equation, which is given by Eq. 99c considering $\mu_{eff} = \mu$, where μ is the real fluid viscosity. The expression $\mu_{eff} = \mu$ is valid provided that a non-slip condition on the interfaces between the fluid and solid phases of the porous medium is considered, as done in the traditional volume-averaging method. However, the non-coincidence between μ_{eff} and μ has been demonstrated in several experimental, numerical and theoretical works, suggesting that the non-slip condition is not necessarily valid in all cases. For instance, Givler and Altobelli [191] experimentally found that μ_{eff} is 7.5 times the value of μ for high-porous open cell foams and moderate Reynolds numbers, whereas Starov and Zhdanov [192] studied the dependency of μ_{eff} on the porosity and particle size in porous media composed of equally sized spherical particles, finding that μ_{eff} can be lower or larger than μ. On the other hand, the numerical flow simulations conducted by [193] in 3D regular arrays of cubes showed that $\mu_{eff} < \mu$, whereas those ones executed by [194] indicated that $\mu_{eff} > \mu$ in order to match the Brinkman equation with the numerical solutions in the boundary layer developed in the porous medium domain when it is in contact with a free-fluid domain. A very illustrative theoretical work was published by [195], where it was demonstrated that the effective viscosity, μ_{eff}, is different to the fluid viscosity, μ, when a slip condition at the fluid-solid interface of the porous medium is considered. Using an up-scaling procedure, a boundary-value problem to compute μ_{eff} was obtained in that work, achieving important conclusions. In general, the effective viscosity is

different to the fluid viscosity, i.e, $\mu_{eff} \neq \mu$, because it is a term that 'absorbs' the microscale variations of the velocity gradient when a variationless velocity gradient model is used at macroscopic scale. Furthermore, as the prescribed slip coefficient at the fluid-solid interface increases, the boundary layer thickness decreases and a non-slip condition tends to be reached, in such a way that in the limit when the slip coefficient tends to infinity, $\mu_{eff} = \mu$.

The estimation of the effective viscosity term, μ_{eff}, in the Brinkman equation is known to depend on the geometry of the porous medium and the interface matching condition. For an array of cylinders, an acceptable approximation for μ_{eff} is to assume that $\mu_{eff} = \mu$ when the continuous stress condition is used, while $\mu_{eff} = \mu/\varepsilon_t$ is a better approximation when the jump stress condition is employed [20], [196], [197], where ε_t represents the tow porosity.

In the present section, simulations of RUC fillings of dual-scale fibrous reinforcements are carried out using BEM-based techniques. For the channel domain, pure BEM for Stokes is applied, whereas for the porous domain, three approaches are implemented: pure BEM for Darcy, pure BEM for isotropic Brinkman (BEM-ISO) and DR-BEM for Brinkman. Firstly, the last two approaches are validated by comparison with a benchmark analytical solution used previously in the literature to assess the robustness of FEM-based numerical solutions of flow problems in dual-scale porous media [20], [85]. Additionally, the solutions of simple isotropic problems using these two approaches are compared one another in order to determine which of the following strategies is better to deal with the more complex free-boundary problems: 1) to use an only-boundary integral formulation for the Brinkman equation, which implies fundamental solutions for anisotropic domains that entail numerical complexity, or 2) to use a boundary-domain integral formulation for the Brinkman equation in terms of the Stokes fundamental solutions, where the domain integral is transformed into a boundary integral using the Dual Reciprocity Boundary Element Method (DR-BEM). To the best of the author's knowledge, the comparison between these two strategies has not been done yet in any other work.

The developed BEM numerical schemes are then used to simulate the simultaneous filling of channels and tows inside the RUC at constant pressure regime with the purpose of analyzing the influence of the matching conditions, at several capillary ratios (C_{cap}), on the

void formation. This type of filling problem has been previously considered in the literature using different formulations and numerical techniques. For instance, Gourichon et al. [5] studied the influence of the RUC porosity in the formation of voids using a Darcy-Darcy formulation and the FEM/CV conforming method. On the other hand, Schell et al [81] studied the influence of the tow porosity, ε_t, on the final void content using the same formulation and numerical technique as [5], while the problem of unidirectional filling considering circular tows and radial coordinates was tackled in [22] using a Stokes-Brinkman formulation and the Finite Volume method, where it was studied the effect of the filling velocity, resin viscosity, inter-tow dimension and intra-tow dimension on the shape of the fluid front. Considering the mentioned works and some other publications in the composites area solving Stokes-Brinkman by domain-meshing techniques [20], [23], [24], [85], [96], it is important to emphasize the main advantages of the BEM approach employed here: firstly, the use of BEM-based techniques does not imply any mesh discretization of the problem domain, and, secondly, the tracking technique used here (*Appendix C*) assures a higher order accuracy of the shape of the fluid front regarding other techniques like the Volume of Fluid (VOF) [36], [111] or the Level Set Method [46], [50], [58].

From the viewpoint of the physical analysis, the principal contributions of this chapter are summarized as follows:

- The study of the influence of two types of Stokes-Brinkman matching conditions, continuous stress and jump stress, on the void formation process is carried out. Other works have analyzed the influence of these conditions on the effective saturated permeability, $K_{ff,sat}$ [20], [85], but not on the size, shape and location of the voids formed by mechanical entrapment of air.
- The processes of the void formation using Stokes-Brinkman and Stokes-Darcy formulations are compared each other in this chapter, which has not been presented before to the best of the author's knowledge.
- The influence of the RUC compaction on the void formation is also investigated here and the results are compared with previous works.

In this chapter, it is considered a 2D RUC geometry emulating a longitudinal plane of a cross ply fabric (Figure 39). The unidirectional filling of 3D RUC's of fabrics has been

recently considered by superposition of 2D simulations at several longitudinal planes of the RUC, showing good agreement with experimental results [80]. Therefore, it can be inferred that the parametric study of the 2D geometry represented in the Figure 39 can be useful to understand the influence of some factors on the void formation in cross ply fabrics using the Stokes- Brinkman formulation.

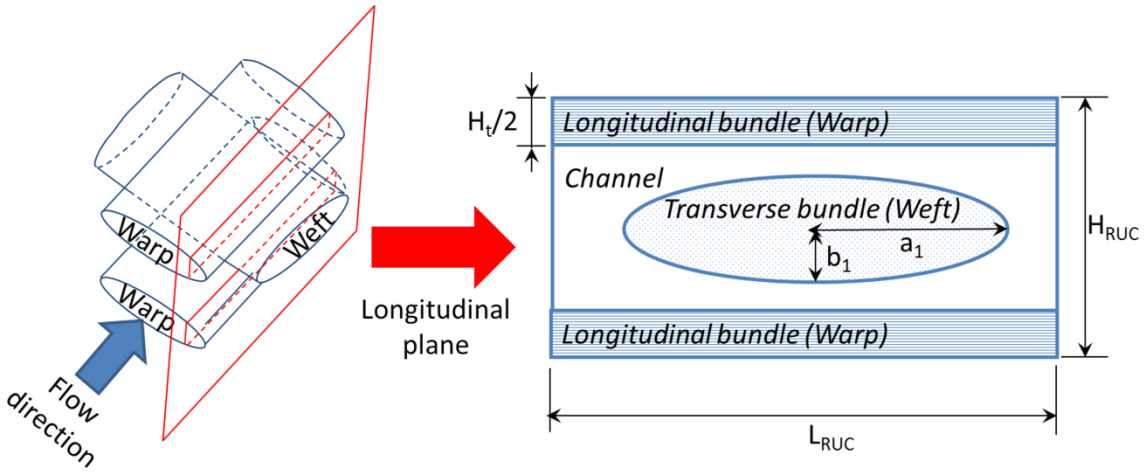

Figure 39 Scheme of RUC for the problem of simultaneous filling using the Stokes-Brinkman formulation.

4.2 Governing equations, matching conditions and boundary conditions

In the Stokes-Brinkman formulation, the governing equations are the following (volume-averaged symbols are omitted):

Mass conservation (For all domains):

$$\frac{\partial u_i}{\partial x_i} = 0 \tag{99a}$$

Momentum for the Stokes domain (Channels flow):

$$\mu\left(\frac{\partial^2 u_i}{\partial x_j x_j}\right) - \frac{\partial p}{\partial x_i} = 0 \tag{99b}$$

Momentum for the Brinkman domain (Porous media flow):

$$\mu_{eff}\frac{\partial^2 u_i}{\partial x_j \partial x_j} - \frac{\partial p}{\partial x_i} = \frac{\mu}{K_i}u_i \tag{99c}$$

Here u_i, p, μ, μ_{eff} and K_i represent the velocity vector, pressure, liquid viscosity, effective viscosity and main permeabilities, respectively. The next non-dimensional variables are defined for the length, velocity, time and pressure [198], [199]:

For all domains:

$$\hat{x}_i = x_i/L^* \tag{100a}$$

$$\hat{u}_i = u_i/U_{max} \tag{100b}$$

$$\hat{t} = t/(L^*/U_{max}) \tag{100c}$$

For the Stokes domain (Channels flow):

$$\hat{p} = \frac{p}{\mu.U_{max}/L^*} \tag{100d}$$

For the Brinkman domain (Porous media flow):

$$\hat{p} = \frac{p}{\mu_{eff}.U_{max}/L^*} \tag{100d}$$

where L^* and U_{max} are the characteristic length and the maximum velocity of the problem, respectively. In terms of these characteristic values, the non-dimensional form of Eqs. 99a-c is the following:

$$\frac{\partial \hat{u}_i}{\partial \hat{x}_i} = 0 \tag{101a}$$

$$\frac{\partial^2 \hat{u}_i}{\partial \hat{x}_j \hat{x}_j} - \frac{\partial \hat{p}}{\partial \hat{x}_i} = 0 \tag{101b}$$

$$\frac{\partial^2 \hat{u}_i}{\partial \hat{x}_j \partial \hat{x}_j} - \frac{\partial \hat{p}}{\partial \hat{x}_i} = \chi_i^2 \hat{u}_i \tag{101c},$$

where $\chi_i^2 = 1/Da_i^* = (L^*)^2\mu/\left(K_i.\mu_{eff}\right)$ is the inverse of the Darcian number, Da_i^*, in the principal direction "i".

The non-dimensional matching conditions for the Stokes-Brinkman problem are as follows [186]:

- Continuity of velocities:

$$\hat{u}_i^{(s)} = \hat{u}_i^{(b)} \tag{102}$$

- Normal and tangential component of the jump of stress:

$$\left(\hat{t}_i^{(s)} + \left(\mu_{eff}/\mu\right)\hat{t}_i^{(b)}\right)\hat{n}_i = -\frac{L^*}{\sqrt{K_n}}\beta_n \hat{u}_i^{(s)}\hat{n}_i \tag{103a}$$

$$\left(\hat{t}_i^{(s)} + \left(\mu_{eff}/\mu\right)\hat{t}_i^{(b)}\right)\hat{\tau}_i = -\frac{L^*}{\sqrt{K_\tau}}\beta_\tau \hat{u}_i^{(s)}\hat{\tau}_i \tag{103b}$$

where "s" and "b" represent the Stokes and Brinkman domain, respectively, whereas $\hat{t}_i^{(s)} = (L^*/(\mu U_{max}))\sigma_{ij}\hat{n}_j$ and $\hat{t}_i^{(b)} = \left(L^*/\left(\mu_{eff}U_{max}\right)\right)\sigma_{ij}\hat{n}_j$ are defined as the dimensionless traction vectors, with σ_{ij} as the Newtonian stress tensor. Here K_n and K_τ are the effective permeabilities in the normal and tangential direction at the interface channel-

tows, respectively, with the effective permeability in any orientation, ϕ_i, given by Eq.29. On the other hand, β_n and β_τ are the normal and tangential jump coefficients. It is very important to mention that some authors consider that the minus sign of the right hand side term of Eqs. 103a,b is implicit in the stress jump coefficients, β_n and β_τ [20], [85].

In the present chapter, the RUC filling is carried out at constant inlet pressure for all cases. Therefore, the non-dimensional inlet boundary conditions are as follows:

At the Stokes domain:

$$\hat{t}_1^{(s)} = -\overline{p_{in}} L^* / (\mu U_{max})\, \widehat{n_1^{(s)}},\ \hat{u}_2^{(s)} = 0 \tag{104a}$$

At the Brinkman domain:

$$\hat{t}_1^{(b)} = -\overline{p_{in}} L^* / \left(\mu_{eff} U_{max}\right) \widehat{n_1^{(b)}},\ \hat{u}_2^{(b)} = 0 \tag{104b}$$

where $\overline{p_{in}}$ represents the prescribed inlet pressure. No-flux condition, $\hat{u}_i \hat{n}_i = 0$, and zero traction in the tangential direction, $\hat{t}_i \hat{\tau}_i = 0$, are used in boundaries where symmetry is specified. At the fluid fronts, kinematic and dynamic boundary conditions are defined. The former condition is equivalent to Eq.73 in non-dimensional form, whereas the dynamic condition accounts for the discontinuities of normal stress due to the capillary pressure, P_{cap}; these conditions have the next form:

Kinematic condition (For all domains):

$$d\hat{x}_i / d\hat{t} = \hat{u}_n \hat{n}_i = \left(\hat{u}_j . \hat{n}_j\right) \hat{n}_i \tag{105a}$$

Dynamic condition (At the Stokes domain):

$$\hat{t}_i^{(s)} = L^* \left(P_{cap} - P_{air}\right) / (\mu U_{max})\, \hat{n}_i \tag{105b}$$

Dynamic condition (At the Brinkman domain):

$$\hat{t}_i^{(b)} = L^* \left(P_{cap} - P_{air}\right) / \left(\mu_{eff} U_{max}\right) \hat{n}_i \tag{105c}$$

where $\hat{n}_i$ is the outwardly oriented normal vector of the fluid front, P_{air} is the air pressure in the fluid front and $\hat{u}_n$ is the dimensionless normal pore velocity, defined as the dimensionless normal Darcy velocity divided by the tow porosity, ε_t [75], [130]. The same mathematical model used in Chapter 3 for the calculation of P_{cap} in the channel and tows, Eqs. 76 to 80, can be applied in the present case. The main permeabilities of the tows, K_1 and K_2, can be also computed using the Gebart model [135], which was previously presented in Chapter 3, Eqs. 63 and 64.

The Stokes-Darcy formulation is also considered in the present chapter only for comparison purposes with the Stokes-Brinkman formulation. In dimensionless form, the Darcy equation is as follows:

$$\hat{u}_i = -K_i^* \left(\frac{\partial \hat{p}}{\partial \hat{x}_i}\right) \tag{106},$$

where $K_i^* = K_i/(L^*)^2$ is the non-dimensional permeability in the principal direction "i" and $\hat{p} = p/(\mu.U_{max}/L^*)$ is the non-dimensional pressure, while $\hat{x}_i$ and $\hat{u}_i$ were defined in Eqs. 100a and 100b, respectively. The matching and boundary conditions for the Stokes-Darcy formulation shown in Chapter 3, Eqs. 65 to 70, are applicable in this case in non-dimensional form.

4.3 Integral equation formulations and numerical techniques

Three numerical approaches are considered to deal with the governing equations presented in Section 4.2. For the Stokes-Brinkman problem, both pure BEM for isotropic porous domains and DR-BEM for isotropic and anisotropic porous domains are implemented. For the Stokes-Darcy problem of this chapter, the pure BEM formulation presented in Chapter 3, Eqs. 81 to 85, is applied as well.

The integral formulation for the isotropic Brinkman equation has the same form as for the Stokes equation, Eq. 81, with fundamental solutions given by [200], [201]:

$$U_i^j(\xi, y) = \frac{1}{4\pi}\left[A_1(z)\delta_{ij} + A_2(z)\frac{(y_i-\xi_i)(y_j-\xi_j)}{r^2}\right] \tag{107a}$$

$$K_{ij}(\xi, y) = -\frac{1}{2\pi}\left[\frac{(y_j-\xi_j)\widehat{n_i}}{r^2}D_1(z) + \frac{(y_k-\xi_k)\widehat{n_k}}{r^2}D_2(z)\delta_{ij} + \frac{(y_i-\xi_i)\widehat{n_j}}{r^2}D_2(z) + \frac{(y_i-\xi_i)(y_j-\xi_j)(y_k-\xi_k)\widehat{n_k}}{r^4}D_3(z)\right] \tag{107b},$$

where:

$z = \chi r$

$A_1(z) = 2[K_0(z) + z^{-1}K_1(z) - z^{-2}]$

$A_2(z) = 2[-K_0(z) - 2z^{-1}K_1(z) + 2z^{-2}]$

$D_1(z) = 2K_2(z) + 1 - 4z^{-2}$

$D_2(z) = 2K_2(z) - zK_1(z) + 4z^{-2}$

$D_3(z) = -8K_2(z) - 2zK_1(z) + 16z^{-2}$,

with $K_0(z), K_1(z)$ and $K_2(z)$ as the modified Bessel functions of second class, of order zero, one and two, respectively. In the kernels corresponding to the fundamental solutions represented in Eqs. 107a and 107b, singularities of order $\mathcal{O}(z^3)$ and $\mathcal{O}(z^4)$ arise, respectively, when $r \to 0$. These singularities cannot be tackled using Rigid Body Motion, but a decomposition method instead. This method is described in [202] and has been implemented successfully by other authors in Stokes-Brinkman problems [200], [201]. In this method, the Brinkman fundamental solutions are decomposed into two parts:

$$U_i^j(\xi, y) = U_i^{j(s)}(\xi, y) + U_i^{j(c)}(\xi, y) \tag{108a}$$

$$K_{ij}(\xi, y) = K_{ij}^{(s)}(\xi, y) + K_{ij}^{(c)}(\xi, y) \tag{108b},$$

where the first right-hand side terms of the Eqs.108a and 108b are the Stokes fundamental solutions for velocity and traction, respectively, and the last ones are complementary terms. The singularities associated to the Stokes fundamental solutions, $U_i^{j(s)}(\xi, y)$ and $K_{ij}^{(s)}(\xi, y)$, are treated as mentioned in Chapter 3, while the Telles transformation [166] is used to deal with the weak singularities of the complementary terms, $U_i^{j(c)}(\xi, y)$ and $K_{ij}^{(c)}(\xi, y)$.

The explicit forms of $U_i^{j(c)}(\xi, y)$ and $K_{ij}^{(c)}(\xi, y)$ are obtained after expanding in power series the modified Bessel functions of second class that appear in the Brinkman fundamental solutions, Eqs. 107a,b, and subtracting the Stokes fundamental solutions, $U_i^{j(s)}(\xi, y)$ and $K_{ij}^{(s)}(\xi, y)$, resulting in:

$$U_i^{j(c)}(\xi, y) = \frac{1}{4\pi}\left\{\delta_{ij}\left[-\left(\gamma_E + \frac{1}{2} + ln\left(\frac{\chi}{2}\right)\right) + 2\sum_{l=1}^{\infty}\frac{z^{2l}}{2^{2l}(l!)^2}\left(\left(\frac{2l+1}{2l+2}\right).\left(\Psi(l+1) - ln(z/2)\right) - \frac{1}{2^2(l+1)^2}\right)\right] - \frac{\hat{x}_i\hat{x}_j}{r^2}\left[\sum_{l=1}^{\infty}\frac{z^{2l}}{2^{2l}(l!)^2}\left(\left(\frac{2l}{l+1}\right)\Psi(l+1) - \frac{1}{(l+1)^2} - \frac{2l}{l+1}ln(z/2)\right)\right]\right\} \tag{109a}$$

$$K_{ij}^{(c)}(\xi, y) = \frac{1}{2\pi}\left\{\frac{\hat{x}_j}{r^2}\hat{n}_i\left[\sum_{l=1}^{\infty}\frac{z^{2l}}{2^{2l-1}(l!)^2}\left(\frac{l}{l+1}\Psi(l+1) - \frac{1}{2(l+1)^2} - \frac{l}{l+1}\ln\left(\frac{z}{2}\right)\right)\right] + \left(\frac{\hat{x}_i}{r^2}\hat{n}_j + \frac{\hat{x}_k\hat{n}_k}{r^2}\delta_{ij}\right)\left[\sum_{l=1}^{\infty}\frac{z^{2l}}{2^{2l}(l!)^2}\left(\frac{l^2+2l}{(l+1)^2} - \frac{2l^2}{l+1}\Psi(l+1)\right)\right] - \frac{\hat{x}_i\hat{x}_j\hat{x}_k\hat{n}_k}{r^4}\left[\sum_{l=1}^{\infty}\frac{z^{2l}}{2^{2l-1}(l!)^2}\left(1 - \frac{2}{(l+1)^2} + \frac{2l(1-l)}{l+1}\left(\Psi(l+1) - ln(z/2)\right)\right)\right]\right\} \tag{109b},$$

where $\Psi(1) = -\gamma_E$ and $\Psi(l+1) = -\gamma_E + \sum_{j=1}^{l}(1/j)$, with $\gamma_E = 0.5772$ .... as the Euler constant. The last pure BEM formulation, referred as *BEM-ISO* in the present work, can be also used in anisotropic porous domains when the flow is unidirectional, taking the equivalent permeability in the flow direction as calculated by Eq.29. Moreover, Kohr and Sekar [203] deduced Green functions for the anisotropic Brinkman equation in the Fourier space, which reduce to the ones employed here when $\chi_1 = \chi_2$ (isotropic domain). An alternative approach for anisotropic Brinkman consists on structure this equation as a Stokes equation with a non-homogeneous term, which is treated using DR-BEM [63]. The integral formulation in that case is as follows:

$$c_{ij}(\xi)u_j(\xi) = \int_S K_{ij}(\xi,y)\,u_j(y)dS_y - \int_S U_i^j(\xi,y)\,t_j(y)dS_y + \int_\Omega U_i^j(\xi,y)\,g_j(y)d\Omega_y \quad (110)$$

In the present DR-BEM implementation, the non-homogeneous term, $g_j(y) = \chi_j^2 u_j(y)$, is approximated using Radial Basis Function (RBF) interpolation given by Augmented Thin Plate Splines (ATPS). The augmented part of a generalized thin plate spline of order n is a polynomial of order $n-1$ that is added to obtain an invertible interpolation matrix [204]. In the present work, $n = 2$ and the form of the ATPS is as follows:

$$f^m(y) = \begin{Bmatrix} r^2\ln(r) & for\ m\ \epsilon\ [1, N_B+N_I] \\ 1 & for\ m = N_B+N_I+1 \\ y_1 & for\ m = N_B+N_I+2 \\ y_2 & for\ m = N_B+N_I+3 \end{Bmatrix} \quad (111),$$

where N_B is the number of boundary points, N_I is the number of interior points and $r(y,z^m) = |y-z^m|$ is the distance between the field points, y, and the trial points, z^m. Accordingly, the non-homogeneous term can be expanded as follows:

$$g_j(y) = \sum_{m=1}^{N_B+N_I+3} \alpha_l^m \delta_{jl} f^m(y),\ j = 1,2;\ l = 1,2 \quad (112),$$

where α_l^m represent the approximation coefficients in the direction "l". The ATPS represented in Eq. 111 requires the addition of orthogonality conditions, as shown in the following equation:

$$\sum_{m=1}^{N_B+N_I} \alpha_l^m = \sum_{m=1}^{N_B+N_I} \alpha_l^m\, y_1^m = \sum_{m=1}^{N_B+N_I} \alpha_l^m\, y_2^m = 0 \quad (113)$$

After substituting Eq.112 into Eq.110, the integral representation takes the following form:

$$c_{ij}(\xi)u_j(\xi) =$$

$$\int_S K_{ij}(\xi,y)\,u_j(y)dS_y - \int_S U_i^j(\xi,y)\,t_j(y)dS_y + \sum_{m=1}^{N_B+N_I+3}\alpha_l^m \int_\Omega U_i^j(\xi,y)\,\delta_{jl}f^m(y)d\Omega_y \quad (114)$$

The transformation of the domain integrals into boundary integrals is accomplished by defining the following auxiliary Stokes field:

$$\frac{\partial \hat{u}_j^{(ml)}}{\partial y_j} = 0 \quad (115a)$$

$$\mu\frac{\partial^2 \hat{u}_j^{(ml)}}{\partial y_k \partial y_k} - \frac{\partial \hat{p}^{(ml)}}{\partial y_j} = f^m(y)\delta_{jl} \quad (115b),$$

with the particular solutions for the ATPS given in [205], [206]. The substitution of the auxiliary field defined in Eqs.115a,b into Eq. 114 and the application of the Green's identities in the domain integral, lead to the following boundary-only integral representation:

$$c_{ij}(\xi)u_j(\xi) =$$

$$\int_S K_{ij}(\xi,y)\,u_j(y)dS_y - \int_S U_i^j(\xi,y)\,t_j(y)dS_y + \sum_{m=1}^{N_B+N_I+3}\alpha_l^m\left(c_{ij}(\xi)\hat{u}_j^{(ml)}(\xi) - \int_S K_{ij}(\xi,y)\,\hat{u}_j^{(ml)}(y)dS_y + \int_S U_i^j(\xi,y)\,\hat{t}_j^{(ml)}(y)dS_y\right) \quad (116),$$

where the coefficients α_l^m are achieved by collocation of N_B boundary nodes and N_I internal nodes according to Eq. 112; in other words, Eq.112 can be written in vector form as $\overrightarrow{g_l} = [F]\overrightarrow{\alpha_l}$, from which $\overrightarrow{\alpha_l} = [F]^{-1}\overrightarrow{g_l}$, with $l = 1,2$.

The treatment of the singularities arising in the kernels K_{ij} and U_i^j, the contour and variables discretization, and the solution of the final matrix system are carried out as done in Chapter 3. In the DR-BEM formulation of the Stokes-Brinkman problem, the coordinate systems of the saturated porous domains (warps and weft in this case) are continuously updated as the fluid front advances, in such way that each coordinate system is located in the corresponding centroid of each saturated domain to avoid the increment of the condition number of the final system as the filling takes place. As in Chapter 3, the technique described in *Appendix C*. is used to track the moving fronts. In this case the magnitude of the time step decreases as the capillary ratio, C_{cap}, increases. The normal vector and curvatures of the moving interface are updated using Eqs. 86 to 89.

4.4 Results and discussion

4.4.1 Validation and comparison of the BEM approaches for Stokes-Brinkman problems

Two problems admitting analytical solutions are considered to validate and compare the Stokes-Brinkman approaches implemented here. The first problem is sketched in Figure 40a and it consists on a pressure-driven, fully developed flow in an isotropic porous medium with no slip and no penetration conditions in the walls. The non-dimensional analytical solution for the velocity profile is given by:

$$\hat{u}_x(\hat{y}) = c_1 e^{\chi\hat{y}} + c_2 e^{-\chi\hat{y}} - \left((1/\chi^2)(\Delta\hat{p}/\Delta\hat{x})\right) \quad (117a)$$

$$c_2 = \left((1/\chi^2)(\Delta\hat{p}/\Delta\hat{x})\right).(e^{\chi} - 1)/(e^{\chi} - e^{-\chi}) \quad (117b)$$

$$c_1 = \left((1/\chi^2)(\Delta\hat{p}/\Delta\hat{x})\right) - c_2 \quad (117c),$$

where $\hat{u}_x$ is the dimensionless horizontal velocity and $\Delta\hat{p}/\Delta\hat{x}$ is the dimensionless pressure gradient. In this case, the characteristic length is taken as $L^* = H$, where H is the total height of the domain (Figure 40a).

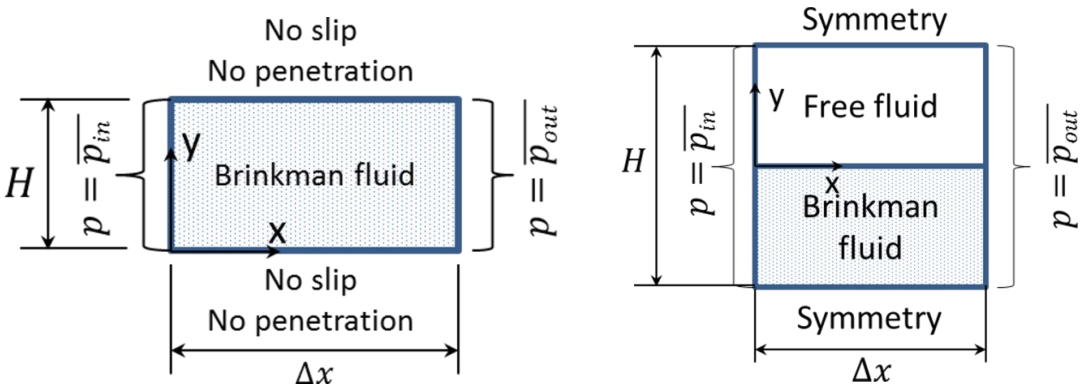

Figure 40 Scheme of problems of Brinkman admitting analytical solutions. a) Only Brinkman. b) Coupled Stokes-Brinkman.

Data to run the simulations of this first problem are summarized in Table 8, in which the mesh-size is reported as $h = e/H$, where e represents the size of one quadratic element. The plots of L^2 *relative error norm vs. Meshsize* are presented in Figure 41a-d, where a power convergence is obtained for both BEM-ISO and DR-BEM. In general, the L^2 relative error norm is greater in BEM-ISO than in DR-BEM for any combination of mesh-size (h) and χ^2. Additionally, BEM-ISO diverges for $\chi^2 = 1 \times 10^3$, which means that this

approach is not suitable for small permeabilities and/or large ratios of μ/μ_{eff}. For both approaches, the accuracy increases as the coefficient χ^2 decreases and, for a determined value of χ^2, the convergence order, n_c, is higher in DR-BEM, which implies another advantage of this scheme with respect to BEM-ISO.

Analytical and numerical results for $h = 5.00 \times 10^{-2}$ are compared in Figure 42, where it is confirmed that BEM-ISO is much less accurate than DR-BEM for high values of χ^2. As expected, the velocity profile tends to flatten as the flow approximates to the darcian regime and this behavior is well predicted by DR-BEM, but not by BEM-ISO.

Table 8 Data to run the simulations of Brinkman problem of Fig 40a

Geometric data		Material data							Processing data		Meshsize			
H (m)	Δx (m)	μ $(Pa.s)$	μ_{eff} $(Pa.s)$	χ^2					$\overline{p_{in}}$ (Pa)	$\overline{p_{out}}$ (Pa)	h			
1×10^{-3}	1×10^{-3}	0.1	0.1	1×10^{3}	1×10^{2}	10	1	0.1	1000	0	2.50×10^{-2}	3.33×10^{-2}	5.00×10^{-2}	1.00×10^{-1}

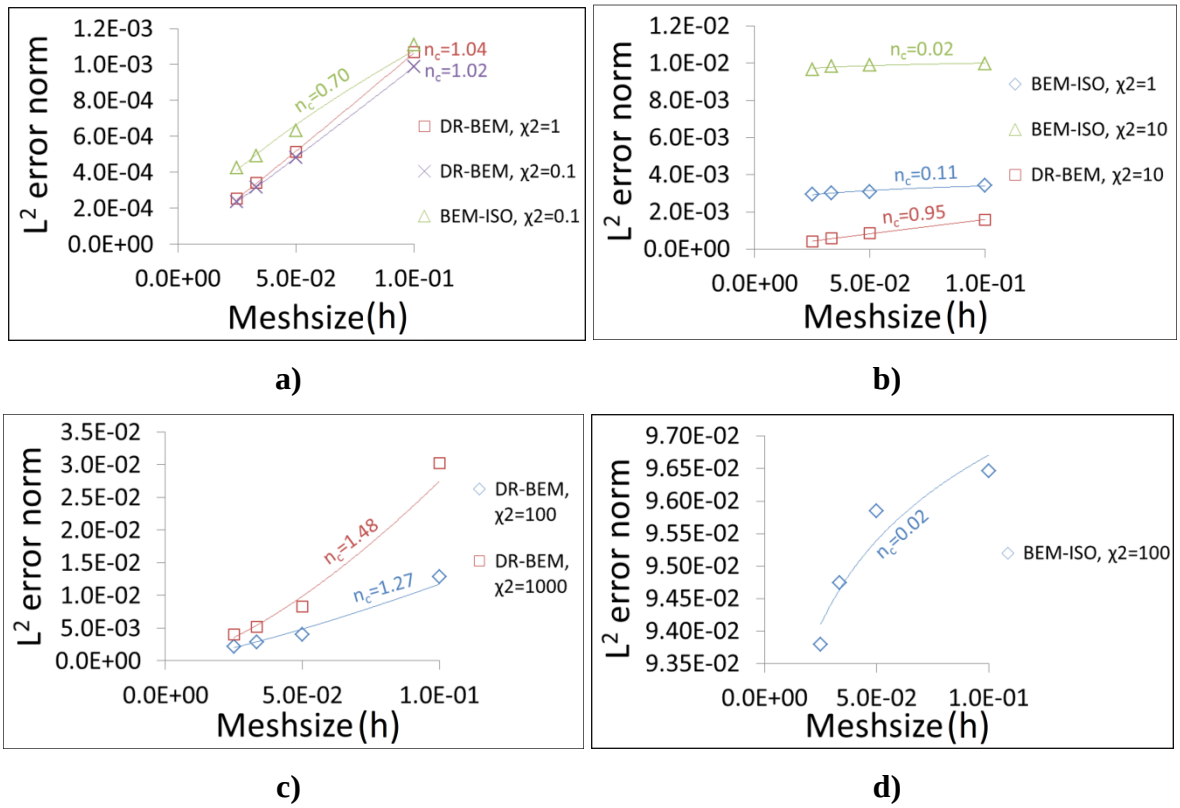

Figure 41 Plot of convergence for Brinkman problem of Fig 40a. a) χ^2=[0.1,1], b) χ^2=[1,10], c) χ^2=[1×10^2,1×10^3] (DR-BEM), d) χ^2=1×10^2 (BEM-ISO).

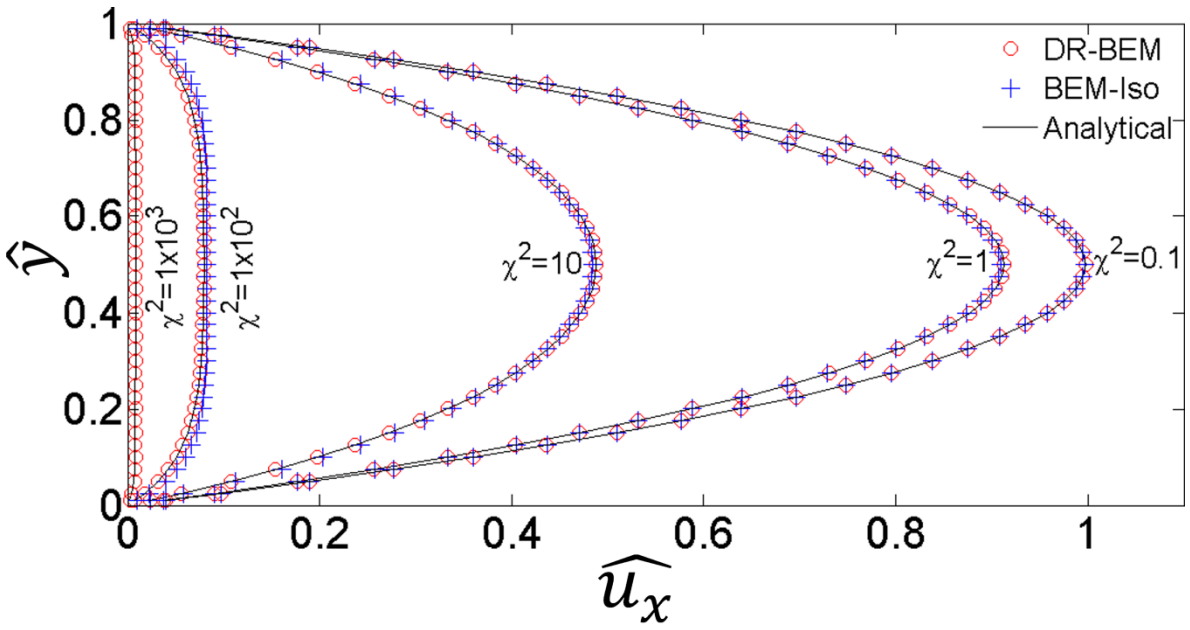

Figure 42 Graphical comparison between analytical and numerical solutions for Brinkman problem of Fig.40a with h=5.00×10^{-2}.

The second problem considered in this section is represented in Figure 40b. It is a coupled Stokes-Brinkman problem that has been used by other authors to validate FEM-based algorithms [20], [85], [96]. In this problem, the inlet and outlet are subjected to pressure boundary conditions and the upper and lower boundaries, to symmetry boundary conditions. Both continuous and jump stress matching conditions at the interface between the two layers are considered. The analytical solution for the velocity profiles is given by Eqs. 118a,b and it is only valid provided that the boundary layer thickness of the Brinkman flow is smaller than the height of the porous medium, in such a way that the solution tends to a Darcy flow in the lower part of the porous medium domain.

Analytical solution for the Stokes domain:

$$\widehat{u_x^s}(\hat{y}) = -\left(\widehat{H}/2\right).\left(\hat{y}-\hat{y}^2/\widehat{H}\right).(\Delta\hat{p}/\Delta\hat{x})^s - \left(\widehat{H}/(2L^*)\right)\sqrt{\phi K_1}/\left(1+\beta\sqrt{\phi}\right)(\Delta\hat{p}/\Delta\hat{x})^s - K_1/\left(L^{*2}\left(1+\beta\sqrt{\phi}\right)\phi\right)(\Delta\hat{p}/\Delta\hat{x})^b \quad (118a)$$

Analytical solution for the Brinkman domain:

$$\widehat{u_x^b}(\hat{y}) = -K_1/\left(L^{*2}\phi\right)(\Delta\hat{p}/\Delta\hat{x})^b - \quad (118b),$$

$$\left\{\left[\left(\widehat{H}/(2L^*)\right)\sqrt{\phi K_1}(\Delta\hat{p}/\Delta\hat{x})^s + K_1/\left(L^{*2}\phi\right)(\Delta\hat{p}/\Delta\hat{x})^b\right]/\left(1+\beta\sqrt{\phi}\right) - K_1/\left(L^{*2}\phi\right)(\Delta\hat{p}/\Delta\hat{x})^b\right\}.e^{\left(\sqrt{\varphi/K_1}\hat{y}L^*\right)}$$

where $\phi = \mu/\mu_{eff}$.

Data to run simulations of this second problem are given in the Table 9.

Table 9 Data to run the simulations of Stokes-Brinkman problem of Fig 40b

Geometric data		Material data								Processing data		Meshsize			
$H\ (m)$	$\Delta x\ (m)$	μ $(Pa.s)$	μ_{eff} $(Pa.s)$	χ^2				β			$\overline{p_{in}}$ (Pa)	$\overline{p_{out}}$ (Pa)	h			
6×10^{-3}	1×10^{-3}	0.1	0.1	1×10^4	1×10^3	1×10^2	18	0	0.5	1	100	0	2.50×10^{-2}	3.33×10^{-2}	5.00×10^{-2}	1.00×10^{-1}

The plots of L^2 *relative error norm vs. Meshsize* are represented in Figure 43a-c for the BEM-ISO approach and Figure 43d-g for the DR-BEM approach. In general, DR-BEM is more accurate than BEM-ISO in all situations. In fact, for $\chi^2 = 1\times10^4$, BEM-ISO does not converge. For BEM-ISO, the convergence order, n_c, increases as β is increased for $\chi^2 = 1\times10^3$ (Figure 43a), but for $\chi^2 = 1\times10^2$ (Figure 43b) and $\chi^2 = 18$ (Figure 43c) an opposite behavior is obtained. In the three plots of convergence of BEM-ISO (Figure 43a-c), it is observed that the L^2 relative error norm diminishes with the increase of β, and, when compared Figure 43b and Figure 43c, it is also worth noting that the L^2 relative error norm is not as sensitive to the parameter χ^2 as it is to the parameter β, for χ^2 between 1×10^2 and 18.

The plots of convergence for DR-BEM are shown in Figure 43d-g. According to Figure 43d to Figure 43f, from $\chi^2 = 1\times10^4$ to $\chi^2 = 1\times10^2$, the order of convergence, n_c, is greater as χ^2 decreases for a constant value of β; on the other hand, a contrary behavior is observed from $\chi^2 = 1\times10^2$ (Figure 43f) to $\chi^2 = 18$ (Figure 43g). If the jump coefficient, β, and the mesh-size, h, are kept constants, the L^2 relative error decreases with the reduction of χ^2, which is reasonable because in the DR-BEM formulation the approximation error of the non-homogeneous term has a stronger influence on the results as χ^2 is larger. Another thing to notice in the plots of convergence of DR-BEM is the reduction of the L^2 relative error norm with the increase of β for $\chi^2 = 1\times10^4$ (Figure

43d) , $\chi^2 = 1 \times 10^3$ (Figure 43e) and $\chi^2 = 1 \times 10^2$ (Figure 43f); for $\chi^2 = 18$ (Figure 43g), an opposite behavior is found. The last aspect to highlight in Figure 43e-g is the reduction of the convergence order with β for $\chi^2 = 1 \times 10^3, \chi^2 = 1 \times 10^2$ and $\chi^2 = 18$.

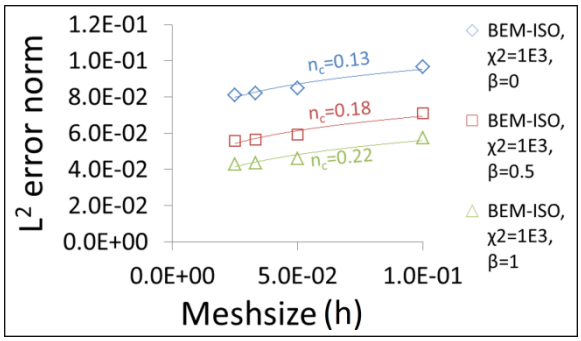

a)

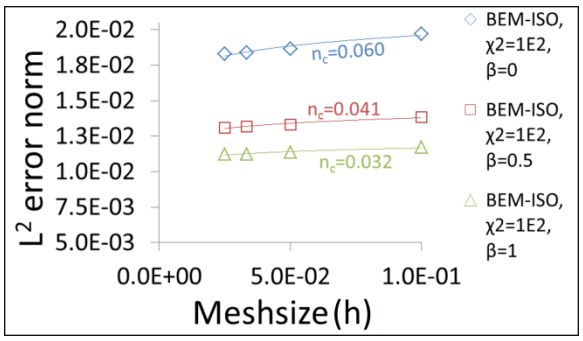

b)

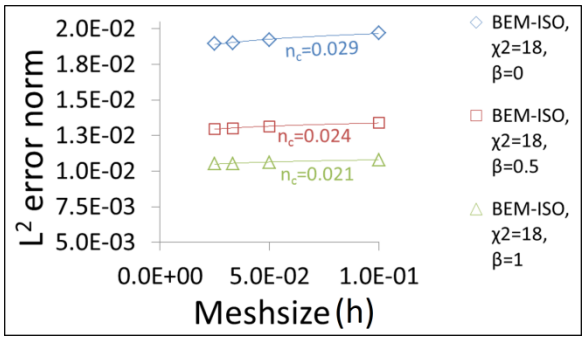

c)

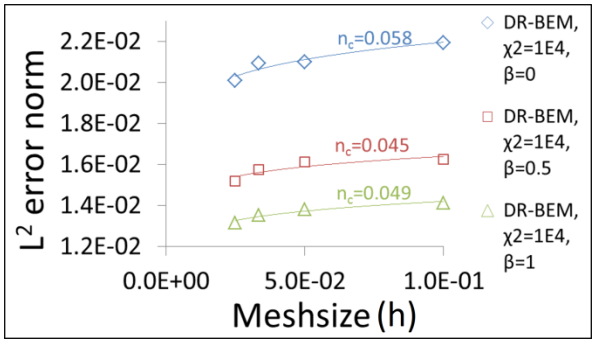

d)

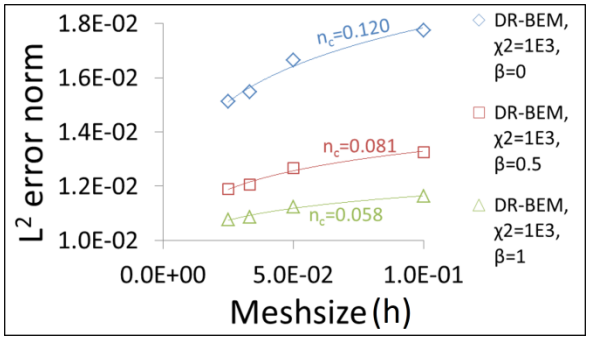

e)

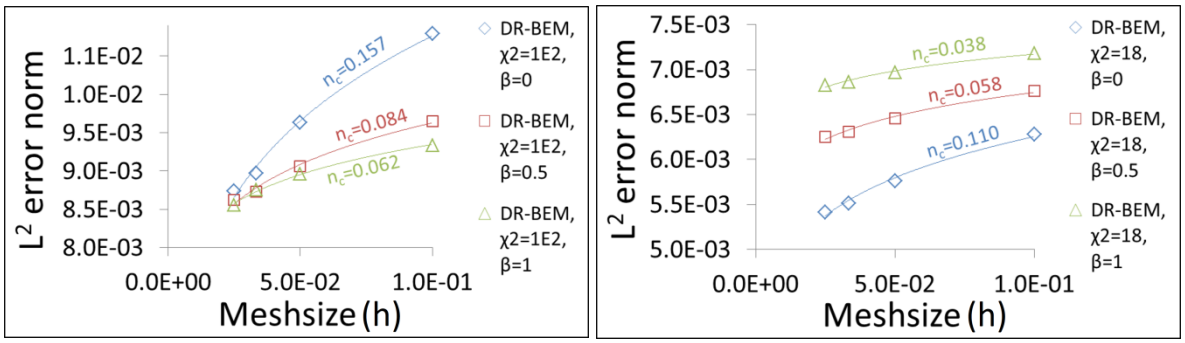

f) **g)**

Figure 43 Plot of convergence for Stokes-Brinkman problem of Fig. 40b. a) χ^2=1×10^3 (BEM-ISO) b) χ^2=1×10^2 (BEM-ISO), c) χ^2=18 (BEM-ISO), d) χ^2=1×10^4 (DR-BEM), e) χ^2=1×10^3 (DR-BEM) , f) χ^2=1×10^2 (DR-BEM), g) χ^2=18 (DR-BEM).

The analytical and numerical results for $h = 5.00 \times 10^{-2}$ are compared in Figure 44a-d, where it is confirmed that the DR-BEM solution is more accurate than the BEM-ISO. In general, the increase of the jump stress coefficient, β, reduces the velocities in the Stokes domain, being this reduction more important as χ^2 decreases (See for example Figure 44d). As expected, for a constant β, the thickness of the boundary layer increases with the reduction of χ^2. On the other hand, the increase of β reduces the boundary layer thickness and this reduction is more notorious as χ^2 decreases. The same conclusions were reached in [85] using a FEM-based method[1], which means that the present approaches are consistent with other results.

It is important to remember that BEM-ISO and DR-BEM are different numerical approaches to obtain the fluid flow solution only in the porous domain. For the coupled Stokes-Brinkman problem of Figure 40b, pure BEM was used to solve the governing equations in the channel domain in all cases. Considering this and having concluded that DR-BEM is more suitable for this particular case, the numerical formulation used in this chapter to solve the subsequent Stokes-Brinkman problems is referred as *BEM/DR-BEM* from now on.

[1] The authors presented the formula of the stress jump condition with the minus sign implicit in the coefficient β. Thus, β assumes a different sign with respect to the one of the present work, but both models are equivalent each other.

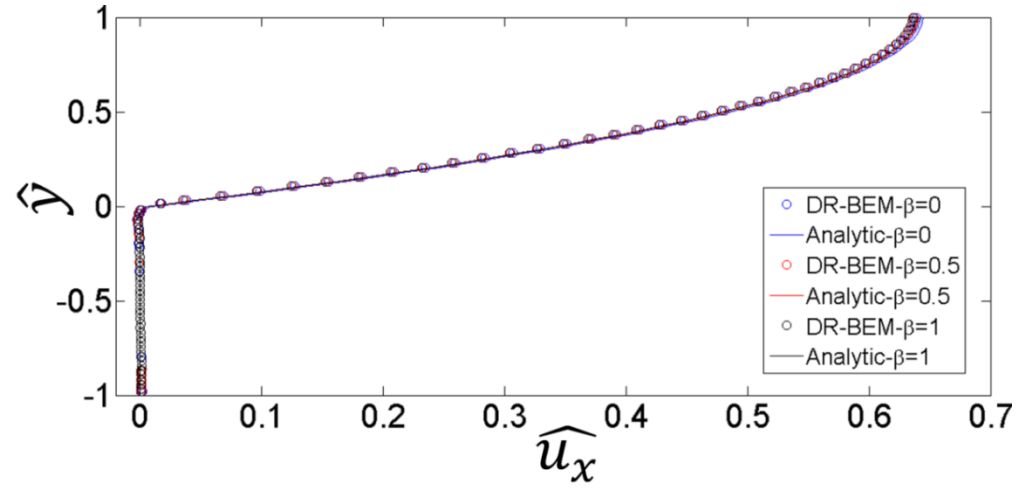
DR-BEM-β=0
Analytic-β=0
DR-BEM-β=0.5
Analytic-β=0.5
DR-BEM-β=1
Analytic-β=1
$\hat{y}$
$\widehat{u_x}$

a)

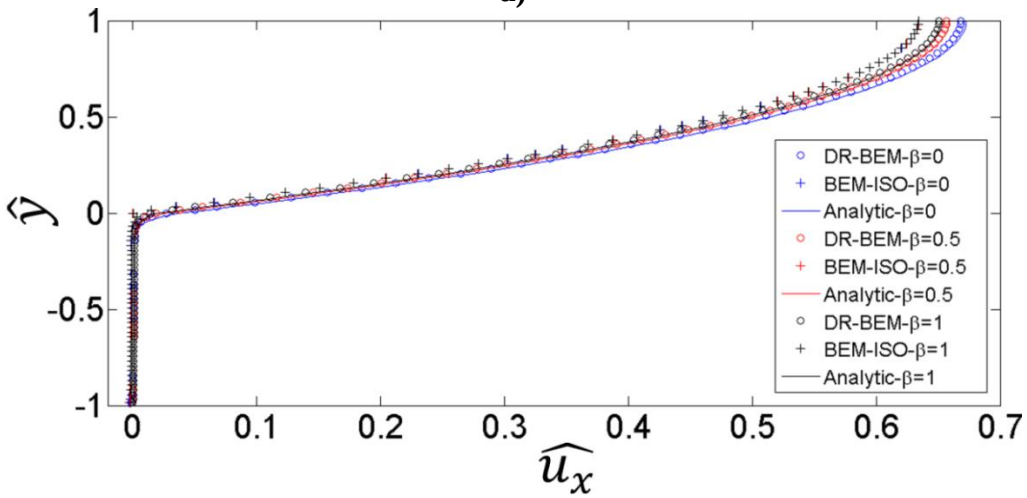
DR-BEM-β=0
BEM-ISO-β=0
Analytic-β=0
DR-BEM-β=0.5
BEM-ISO-β=0.5
Analytic-β=0.5
DR-BEM-β=1
BEM-ISO-β=1
Analytic-β=1
$\hat{y}$
$\widehat{u_x}$

b)

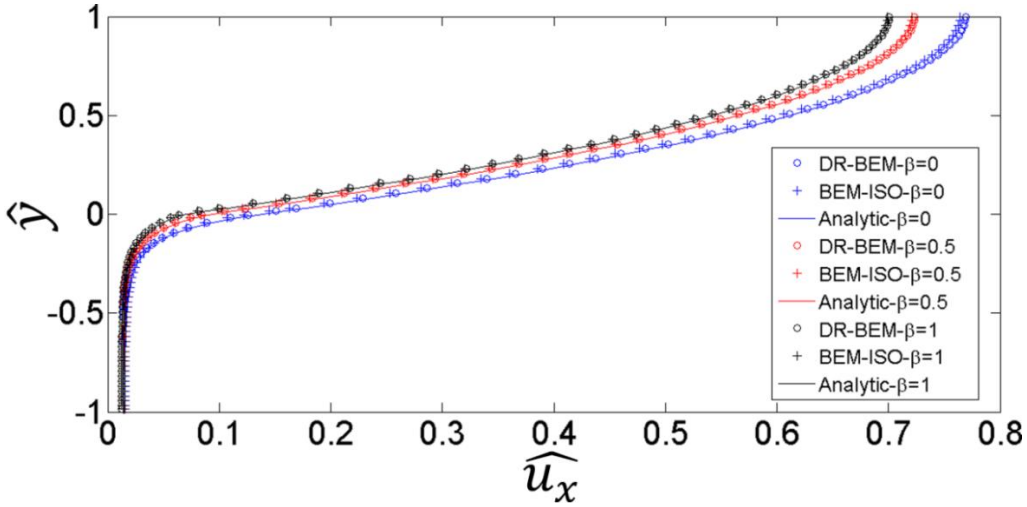
DR-BEM-β=0
BEM-ISO-β=0
Analytic-β=0
DR-BEM-β=0.5
BEM-ISO-β=0.5
Analytic-β=0.5
DR-BEM-β=1
BEM-ISO-β=1
Analytic-β=1
$\hat{y}$
$\widehat{u_x}$

c)

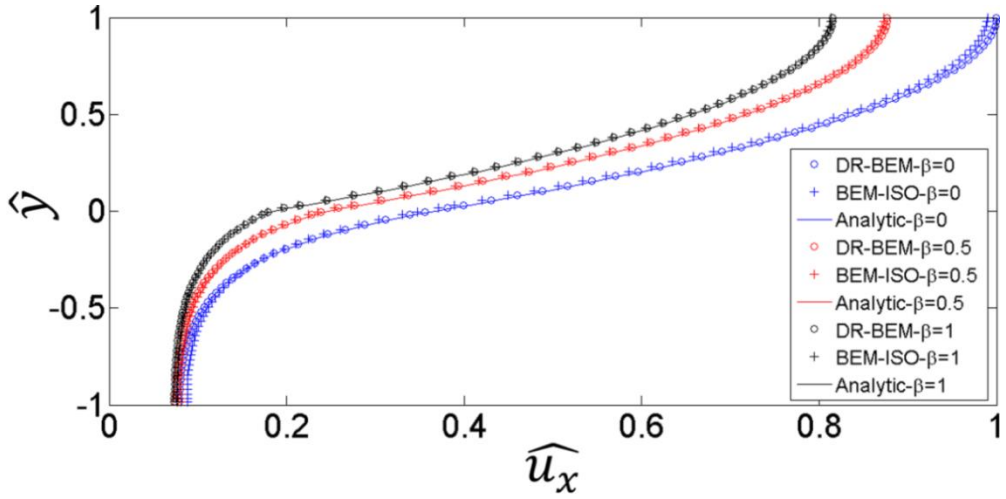

d)

Figure 44 Graphical comparison between analytical and numerical solutions for Stokes-Brinkman problem of Fig. 40b with h=5.00×10^{-2}. a) χ^2=1×10^4, b) χ^2=1×10^3, c) χ^2=1×10^2, d) χ^2=18.

The problem represented in Figure 40b was also solved in [20] using a modified Brinkman approach that reduces to the Stokes flow in the channel domain. In that approach, the stress jump condition is incorporated by a level-set formulation and the numerical solution is obtained by the Finite Element Method (FEM). The authors considered the following parameters in the simulations: $H = 1cm$, $\beta = 0.7$, $\mu_{eff} = \mu/\varepsilon_t$ with $\varepsilon_t = 0.5$, and $K = 10^{-4}cm^2$, where K is the permeability of the porous medium in the flow direction. Considering a characteristic length of $L^* = H$, the inverse Darcian number is $\chi^2 = 5.00 \times 10^3$ in this problem. Four mesh-sizes were evaluated, $h = 0.1cm$, $h = 0.05cm$, $h = 0.01cm$ and $h = 0.005cm$, using a uniform distribution of a regular mesh of square elements over the entire domain, with "h" as the length of the side of one square element, obtaining a total number of elements in each case equal to $0.1/h^2$. In a similar fashion, in the present BEM/DR-BEM scheme, "h" represents the size of one quadratic element of the contour mesh, which leads to $N_E = (3 \times 0.1 + 2 \times 1)/h$, $N_B = 4(0.6/h + 1)$ and $N_L = (0.2/h - 1) \times (1/h - 1)$, with N_E as the number of boundary elements of the whole domain (Stokes and Brinkman), whereas N_B and N_L are the boundary and interior trial points in the Brinkman domain, respectively. The characteristics of the meshes for this particular case and the corresponding L^2 relative error norms of the BEM/DR-BEM solution are presented in Table 10.

Table 10. Characteristics of meshes and L^2 relative error norms of BEM/DR-BEM solution

Element size, h (cm)	*FEM scheme*	*BEM/DR-BEM scheme*			
	Number of uniformly distributed elements	*Number of boundary elements for the whole domain (Stokes+Brinkman)*	*Number of trial points in the boundaries of the Brinkman domain*	*Number of trial points in the interior of the Brinkman domain*	*L^2 relative error norm*
0.1	10	23	28	9	1.01E-01
0.05	40	46	52	57	1.35E-02
0.01	1000	230	244	1881	9.89E-04
0.005	4000	460	484	7761	3.21E-04

According to [207], the application of the Finite Element Method (FEM) to fluid flow problems implies the use of mixed formulations where multiple field variables shall be considered, like the velocity and pressure in the case of an incompressible fluid flow. In such a cases, the discretization scheme of the domain should fulfill three conditions with the purpose to assure the solvability, stability and optimality of the FEM solution, namely, consistency, ellipticity and Inf-Sup condition, being the last one the most difficult to satisfy due to the choice of numerical constants to be introduced in the FEM formulation or to the modification of the original FEM scheme in order to satisfy implicitly such a condition. The statement of the Inf-Sup condition depends on the problem being analyzed; in the case of Stokes-Darcy problems, this condition is detailed in [208]. For both Stokes and Brinkman flows, some distorted FEM meshes could not satisfy the Inf-Sup condition, resulting in spurious pressure modes (for more details see [207]). On the other hand, in the present BEM/DR-BEM formulation for Stokes/Brinkman problems, in both flow fields, spurious pressure modes are not possible due to the unique relationship between the velocity and pressure fundamental solutions in the integral formulation of the problems. However, significant numerical errors and inaccuracy can be found by using very distorted BEM meshes, due to the ill conditioning of the global matrix system and/or the appearance of near-singularities in the numerical integrations. Therefore, in our scheme, it is convenient to avoid a distorted mesh, i.e., a mesh having adjacent elements with very dissimilar sizes, to preserve the accuracy of the solution. As mentioned in *Appendix C.*, since the points at the fluid front are not uniformly spaced just after the fluid front advancement, a remeshing algorithm is implemented with the purpose to obtain a balanced mesh in every time instant and avoid in this way the loss of accuracy in the solution.

The comparison of the present BEM/DR-BEM scheme with the FEM scheme of [20] is shown in Figure 45a,b, where a semi-log plot is adopted in order to distinguish the velocities in the porous domain, which can be several orders of magnitude lower than the velocities in the channel. In the present BEM/DR-BEM scheme, the positions of the interior trial points for the RBF interpolation are determined by an extension of the boundary mesh points into the domain, with exception of the points close to the corners. In both BEM/DR-BEM and FEM schemes, the numerical solution converges satisfactorily to the analytical one, obtaining very accurate solutions for the two finer meshes, $h = 0.01\text{cm}$ and $h = 0.005\text{cm}$; however, a domain mesh is required in the FEM instead of the only boundary discretization used in BEM/DR-BEM, which represents an advantage of the last one. Two main differences between the two numerical schemes can be observed. Firstly, the BEM/DR-BEM shows high accuracy in the Stokes velocity profile, channel flow, for all mesh sizes, while the Brinkman velocity profile is over-predicted for the coarser meshes. On the other hand, the FEM scheme always predicts an accurate velocity profile in the porous medium (Brinkman), but the velocity profile in the channel (Stokes) is under-predicted for the coarser meshes. As commented in [20], the observed behavior in the FEM solution is due to the interpolation scheme used in the level-set formulation. To be more specific, it is necessary to mention that a single equivalent momentum equation for the coupled Stokes-Brinkman domain was considered in [20], which is essentially a Stokes equation modified with permeability and jump stress terms to account for the fluid flow in the porous medium and the stress matching condition in the interface, respectively. Additionally, the domain geometry was defined by a level set function, Φ, where $\Phi = 0$ at the interface, $\Phi > 0$ at the free-fluid domain and $\Phi < 0$ at the porous medium. When $|\Phi| < \varepsilon_{\text{int}}$, with ε_{int} as the half thickness of the diffuse interfacial region, an interpolation functions is defined to express the permeability and jump stress terms as a function of Φ and ε_{int}, and the errors of such interpolation led to greater numerical errors in the Stokes velocity profile than in the Brinkman one, as explained in [20]. On the other hand, the observed behavior of the numerical solution with the mesh size in the BEM/DR-BEM approach is due to the approximation error on the evaluation of the volume integral in the integral representation formula used to represent the Brinkman flow, Eq.110. As mentioned before, in the case of the Stokes flow an exact only-boundary integral formulation is

known, Eq.81, requiring only the discretization of the boundary integral densities, u_i and t_i, without any additional approximation. The discretization of the densities, u_i and t_i, is also required in Eq.110, besides the corresponding approximation of the volume integral. The transformation of the domain integral appearing in Eq.110 into the boundary integrals arising in Eq.116 by DR-BEM involves the interpolation of the non-homogeneous term, $g_j(y)$, using Augmented Thin Plate Splines (ATPS) as shown in Eq.112. In this case, the approximation error of such interpolation, which is greater as the permeability is lower and/or the mesh is coarser, is the principal error source of the Brinkman velocity profiles.

It is worth-mentioning that in the BEM/DR-BEM results no oscillations are present in points close to the interface Stokes-Brinkman for any mesh-size, contrary to the FEM scheme used in [20] where oscillations can be noticed for the coarser meshes (See details of Figure 45a and Figure 45b).

The Stokes-Brinkman simulations of the following sections are conducted using the BEM/DR-BEM scheme with a mesh-size of $h = e/H = 5.00 \times 10^{-2}$, with corresponding L^2 relative error norms of order $O(-2)$ for χ^2 ranging between 10^3 and 10^4 according to the last analyses.

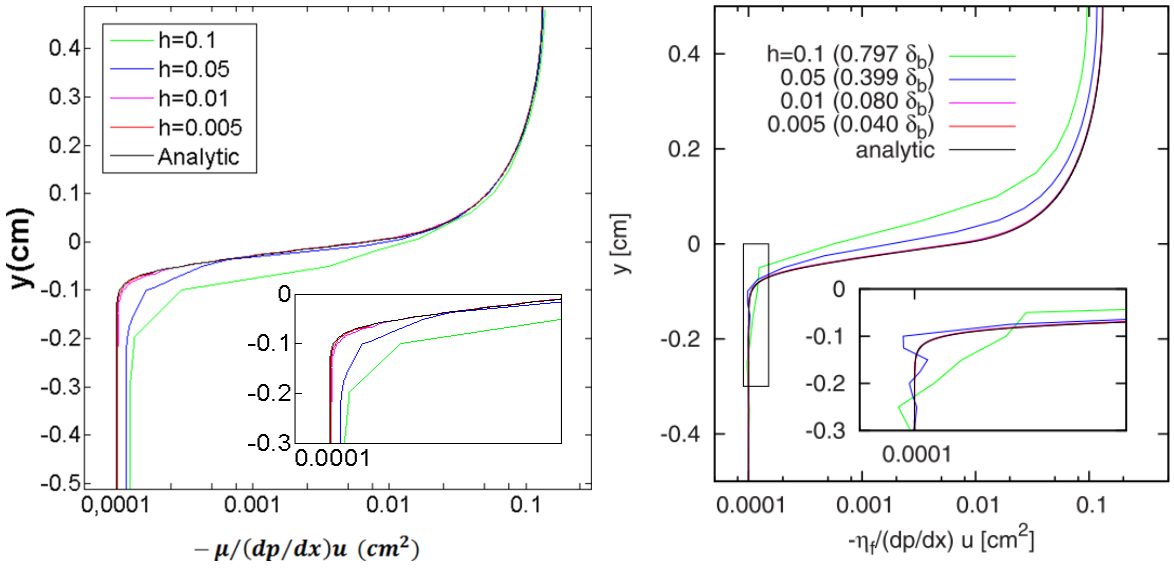

a) **b)**

Figure 45 Velocity profiles for coupled Stokes-Brinkman problem at several mesh sizes. a) BEM/DR-BEM approach (Author). b) FEM approach [20].

4.4.2 Simulation data and void characterization

Simulations considered in the following sections are classified into five different series. *Series 1* to *4* provide different data to be used in the simulations performed with the Stokes-Brinkman formulation, while *Serie* 5 defines the data of the simulations run with the Stokes-Darcy formulation. The parameters of the *Serie 1*, which is taken as the reference case, are presented in Table 11, where the fixed parameters are prescribed values and the computed parameters are determined from the former ones. The geometrical parameters of the RUC considered in this chapter are represented in Figure 39. The jump coefficient, β, of the simulations of *Serie 1* is calculated using the model of Valdés-Parada et al. [187], [188] together with the Larson-Hidgon coefficient in the inter-region channel-tow, γ^* [209] :

$$\beta = \frac{2\varepsilon_{ct}^{3/2}}{3\sqrt{\gamma^*}(1+\varepsilon_{ct})^3} \tag{119a}$$

$$\gamma^* = (2\times 10^{-3})/(1-\varepsilon_{ct})^{2/3} \tag{119b},$$

where the porosity of the inter-region channel-tow, ε_{ct}, is approximated as the porosity of the bundle, ε_t, and it is considered that $\mu_{eff} = \mu/\varepsilon_t$. In simulations of *Serie 2*, the jump coefficient is changed to $\beta = 0.7$, which corresponds to the approximation considered in [20], where $\mu_{eff} = \mu/\varepsilon_t$. For *Serie 3*, the RUC is compacted and the following parameters are changed with respect to *Serie 1*: $H_{RUC} = 1.2\times 10^{-3}m$, $H_t = 4.0\times 10^{-4}m$, $a_1 = 8.4\times 10^{-4}m$ and $b_1 = 2.0\times 10^{-4}m$ (See Figure 39). In *Serie 4*, the continuous stress condition is considered taking $\beta = 0$ and $\mu_{eff} = \mu$. Considering a characteristic length equal to the tow height, i.e., $L^* = H_t$ (See Figure 39), to be consistent with the characteristic lengths of the benchmark problems of Figure 40a,b, the inverse Darcian numbers in the principal directions for the *Series 1* and *2* are $\chi_1^2 = 1.40\times 10^3$ and $\chi_2^2 = 6.80\times 10^3$; for *Serie 3* (compacted domain) the corresponding values are $\chi_1^2 = 9.80\times 10^2$ and $\chi_2^2 = 4.76\times 10^3$, whereas for *Serie 4* (continuous stress case), they are $\chi_1^2 = 2.26\times 10^3$ and $\chi_2^2 = 1.10\times 10^4$. For simulations of *Serie 5,* a Stokes-Darcy approach is taking into account and therefore, the jump stress coefficient, β, is not applicable in such case, but the slip coefficient, γ, which is approximated as $\gamma = 1/\left(\varepsilon_t{}^{1/2}\right)$ [158]. As a constant pressure regime is considered in all simulations, the imbalance

between viscous and capillary forces is quantified by mean of the capillary ratio, $C_{cap} = P_{cap,max}/P_{in}$ [11], where $P_{cap,max}$ and P_{in} stand for the maximum capillary pressure and inlet pressure, respectively. For *Series 1,2,3* and *5*, three different capillary ratios are contemplated: $C_{cap} = 1 \times 10^{-2}, C_{cap} = 1 \times 10^{-1}$ and $C_{cap} = 5 \times 10^{-1}$, whereas for *Serie 3* only the lower value of C_{cap} is taking into account, i.e, $C_{cap} = 1 \times 10^{-2}$. The following results are acquired from each simulation:

- Size, shape and location of voids, expressed as (See Figure 46):

$$Size = A_{void}/((L_{RUC})^2) \quad (120a)$$

$$Size^* = A_{void}/(2A_{RUC}) \quad (120b)$$

$$Shape = a/b \quad (120c)$$

$$Location = l_{void}/(2a_1) \quad (120d),$$

  where A_{void} is the void area, $A_{RUC} = L_{RUC}.H_{RUC}$ is the RUC area, L_{RUC} is the RUC length, "a" and "b" are the semi-major and semi-minor axes of the ellipse circumscribing the void, a_1 is the semi-major axis of the weft, and l_{void} is the distance between the front edge of the weft and rear edge of the void (See Figure 46). When the size of voids of two different domains are compared one another, either "$Size$" or "$Size^*$" could be used indistinctively as long as both A_{RUC} and L_{RUC} remain constant; otherwise, it is convenient to take into account both "$Size$" and "$Size^*$" in the analysis. For example, if the influence of the RUC compaction is going to be study, both variables should be considered since they do not necessarily have the same meaning because A_{RUC} is modified when the RUC is compacted.
- Real, dimensionless and normalized times for several filling instants: The dimensionless time was defined in Eq.100c, while the normalized time is defined as $t^* = t/t_{filling}$, where $t_{filling}$ is the total filling time of the RUC. In the simulations of the following sections, two adjacent RUC's are considered and the filling stops when the partial equilibrium of the bubble formed in the second RUC has been reached.
- RUC's saturation vs. Normalized time.
- Velocity profiles at inlets, fluid fronts and interfaces.
- Compression of the voids, defined by the compressibility ratio:

$$\psi = \frac{V_{void}^{o} - V_{void}^{f}}{V_{void}^{f}} \quad (121),$$

where V_{void}^{o} and V_{void}^{f} stand for the initial and final volume of the void, respectively.

Table 11 Simulation data for the reference case (*Serie 1*) in Stokes-Brinkman formulation

Fixed parameters									
Radius of the fibers, R (μm)	*Half-distance between fibers, d (μm)*	*Length of the RUC, L_{RUC} (m)*	*Height of the RUC, H_{RUC} (m)*	*Height of the warps, H_t (m)*	*Major axis of wefts, a_1 (m)*	*Minor axis of wefts, a_2 (m)*	*Surface tension, σ (mN/m)*	*Contact angle, θ (degrees)*	*Real viscosity, μ (Pa.s)*
20	11	2.3×10^{-3}	1.4×10^{-3}	4.8×10^{-4}	7.0×10^{-4}	2.4×10^{-4}	15	30	0.1
Calculated parameters									
Porosity of the tow for hexagonal array, ε_t		*K_1 (m^2)*		*K_2 (m^2)*	*Jump stress coefficient, β*	*Fluid penetrativity, R_{fluid} (m/s)*		*Effective viscosity, μ_{eff} (Pa.s)*	
0.62		1.02 E-10		2.10E-11	1.24	1.30E-1		0.16	

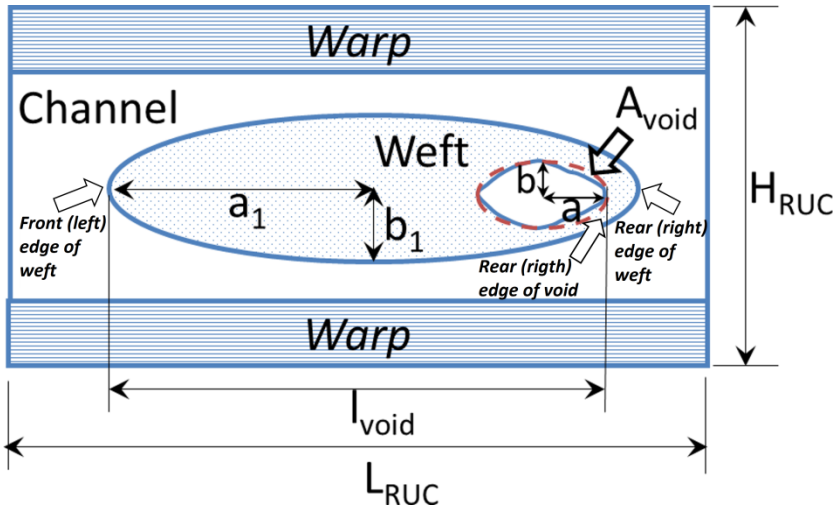

Figure 46 Scheme of void characterization

4.4.3 Comparison between Stokes-Darcy and Stokes-Brinkman approaches

Despite the most of cases in composites processing involve low permeability tows and, therefore, are prone to be modeled by the Darcy approximation, some authors prefer to use the Brinkman equation in its original form [20], [85], [96], since it is possible to impose explicitly the matching conditions at the channel-tow interface in terms of the interfacial

velocity and traction components, considering that the Brinkman and Stokes partial differential equations are of the same order. As expected, several authors have used the Darcy equation to model the flow in the tows [3], [8], [103], but, considering that this is a first order partial differential equation, a slip matching condition for the tangential velocities in the channel-tow interface has to be imposed as shown in Chapter 3 and the value of the slip coefficient, γ, appearing in that condition is not a closed problem. Considering that both approaches, Stokes-Brinkman and Stokes-Darcy, have been used in the literature and are consistent with the problem dealt here, the present section is devoted to compare the results of void formation obtained by both of them, namely, *Serie 1* for Stokes-Brinkman and *Serie 5* for Stokes-Darcy. It is important to mention that a coupled solution system is considered for both approaches, i.e., the equations of the free-fluid and porous medium domains, as well as the matching conditions, are directly included in a single solution system, which could be ill-conditioned as mentioned before. In other works, decoupled strategies have been used for the solution of Stokes-Darcy problems, such as: iterative subdomain methods [210], Lagrange multipliers [211], two-grid method [212], among others. For instance, Mu and Zhu [208], who used the Saffman matching condition for the tangential velocities, proposed and assessed a decoupling FEM methodology based on interface approximations via temporal extrapolation for non-stationary cases. This methodology allows solving two decoupled sub-problems independently by invoking conventional Stokes and Darcy solvers. After analyzing the behavior of the convergence rate and approximation errors with the time step and element size regarding a coupled strategy, it was concluded that the proposed methodology is computationally effective for this kind of problems. In future works, decoupled strategies could be implemented using BEM.

Comparison of the RUC filling process for $C_{cap} = 1 \times 10^{-2}$.

In Figure 47, they are compared several filling instants of the Stokes-Darcy *(S-D)* and Stokes-Brinkman *(S-B)* approaches for $C_{cap} = 1 \times 10^{-2}$; in each instant, the fluid front position along the channel is the same for both approaches, *S-D* and *S-B*, but different evolution times are predicted. First filling instant looks very similar for both approaches (Figure 47a vs. Figure 47b), but *S-D* predicts a slightly greater time than *S-B*. As expected

for $C_{cap} = 1 \times 10^{-2}$, the fluid fronts in the channels exceed the fluid front in the tows and the first weft is surrounded by the liquid. At the filling instant of Figure 47c and Figure 47d, when the liquid at the channel is approximately half the way along the first weft, 6.57% of the total filling time has elapsed according to S-D, whereas *S-B* predicts a value of 5.78%. Additionally, the minimum position of the fluid front in both the warps and the weft is larger for *S-D*. When the channel fluid fronts totally surround the first weft and merge one another, the air is trapped and the void compression occurs. According to Figure 47e and Figure 47f, the fluid fronts in the warps and the weft for *S-D* are ahead with respect to *S-B*, and this causes a smaller initial bubble for *S-D*. Moreover, the real arrival time to this position is longer for *S-B*, but the normalized time is shorter instead. This last feature is common for all the cases analyzed in Figure 47a-h, where the normalized times of the fluid front evolution are always shorter for the *S-B* simulation. In the Figure 47g and Figure 47h, it is important to realize that for both simulations, *S-D* and *S-B*, the maximum position of the channel fluid front is almost 80% of the total length of the domain, while the time has not reached 60% of the total filling time. This is a manifestation of the reduction of the saturation rate regarding the initial one, as it will be confirmed later. When the channel fluid fronts totally surround the second weft, they merge one another again and the second bubble is formed. This bubble undergoes a compression until the partial equilibrium is attained (Figure 47i and Figure 47j). In this case, *S-D* predicts a smaller void and a lower void aspect ratio than *S-B* in both wefts, as it can be confirmed in Table 12 for $C_{cap} = 1 \times 10^{-2}$. In general, the influence of the formulation type, *S-D or S-B*, on the void location is not as significant as the influence on the void size and shape.

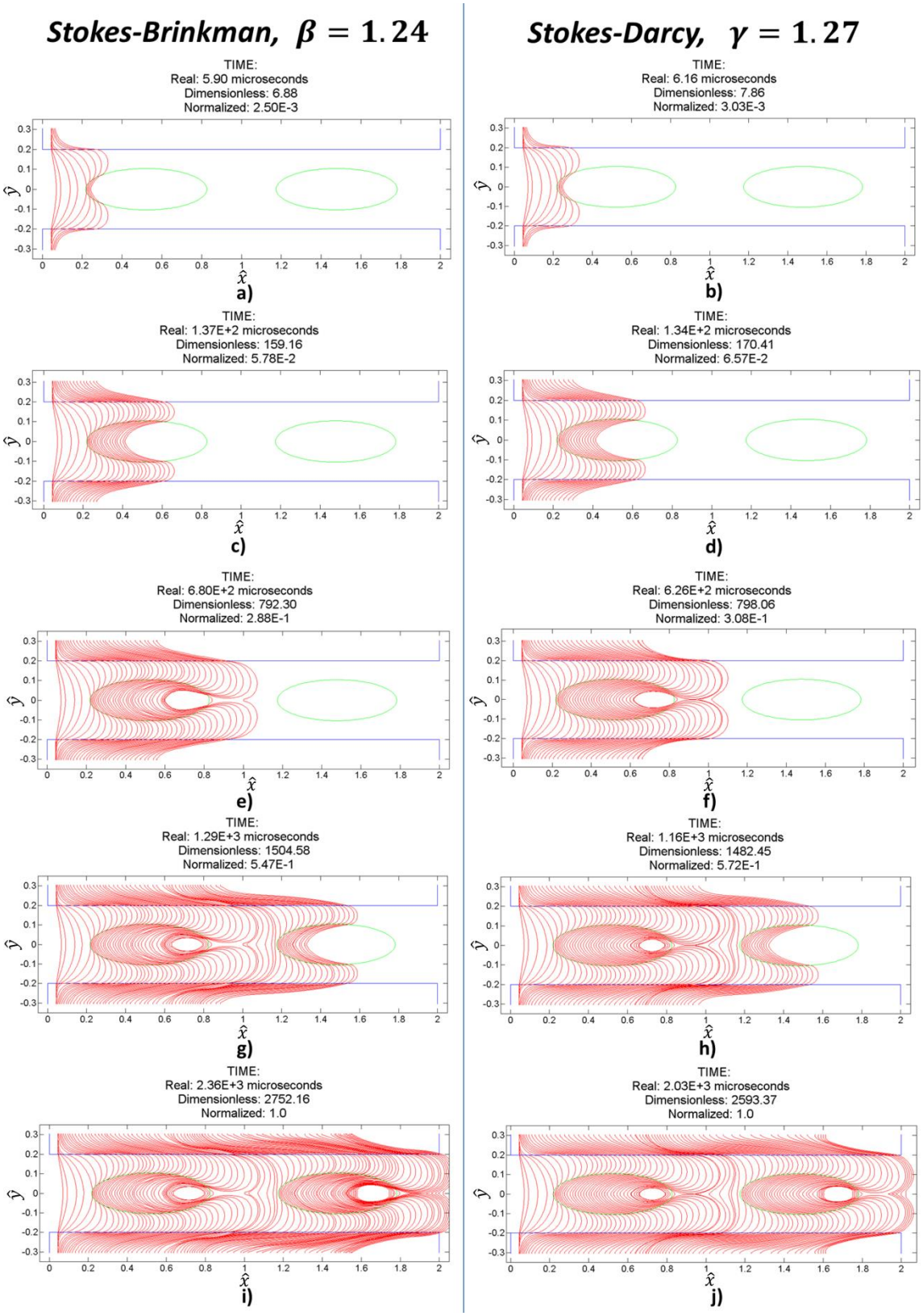

Figure 47 Comparison of void formation between Stokes-Brinkman with β=1.24 and Stokes-Darcy with γ=1.27, for $C_{cap}=1\times10^{-2}$

Void size difference between the first and second weft.

For $C_{cap} = 1 \times 10^{-2}$, the bubble of the first weft is smaller than the one of the second weft for both approaches, *S-B* (Figure 47i) and *S-D* (Figure 47j). To explain this, the details of void formation for *S-D* and *S-B* are shown in the Figure 48a-d, where the fluid fronts corresponding to the instants of flow merging *(blue)* and bubble equilibrium *(violet)* are highlighted in different colors The comparison between these fluid fronts (blue and violet) in each figure is an indication of the void compression. Accordingly, in the first weft (Figure 48a for *S-B* and Figure 48b for *S-D*) the void compression is higher than in the second weft (Figure 48c for *S-B* and Figure 48d for *S-D*) for both approaches, and this is the main cause of the size difference between the final voids; for the first weft the compressibility ratio is $\psi = 0.512$ for *S-B* and $\psi = 0.587$ for *S-D*, whereas, for the second one, it is $\psi = 0.304$ for *S-B* and $\psi = 0.332$ for *S-D*. This is reasonable since higher pressures are reached in the neighborhood of the first bubble because it is closer to the inlet of the RUC.

The RUC fillings for the other two capillary ratios studied here ($C_{cap} = 1 \times 10^{-1}$ and $C_{cap} = 5 \times 10^{-1}$) are presented in Figure 49a-d. In those cases, the relationship between the size of the first and second void is opposite to the one described above $\left(C_{cap} = 1 \times 10^{-2}\right)$, that is, the second void is smaller than the first one. This apparent unexpected behavior is well predicted by both the *S-D* and the *S-B* approach and it is due to the relationship between the capillary and viscous forces, and to the void compression. In general, during the filling of two adjacent RUC's at constant pressure regime, the velocities of the channel fluid fronts surrounding the first weft are greater than those ones surrounding the second weft because the saturated domain is smaller in the first case, which represents a lower flow resistance, and the inlet pressure is kept constant during the whole injection. Considering this and the fact that the capillary forces promote the weft impregnation, the separation between the channel fluid front surrounding the weft and the fluid front inside the weft tends to be inferior for the second weft as the capillary effects are more relevant, i.e., as C_{cap} is larger. Considering that for $C_{cap} = 1 \times 10^{-1}$ and $C_{cap} = 5 \times 10^{-1}$ the capillary effects are more important than for $C_{cap} = 1 \times 10^{-2}$, it is expected a greater fluid infiltration in the second weft than in the first one before the channel fluid fronts merge one

another, leading to a smaller initial void size in the second weft regarding the one in the first weft in the cases of $C_{cap} = 1 \times 10^{-1}$ and $C_{cap} = 5 \times 10^{-1}$. Additionally, the void compression is lower for those cases with respect to the case of $C_{cap} = 1 \times 10^{-2}$ since the inlet pressures are lower as well, and the initial and final void sizes are almost the same for both wefts (See Figure 50a and Figure 50b, corresponding to the case of $C_{cap} = 1 \times 10^{-1}$ for *S-B*). As the initial and final void sizes are very similar for both wefts (low void compressibility), and considering that the initial void size is smaller in the second weft due to the greater infiltration of liquid into this weft before the channel fluid fronts merge each other, it is reasonable to obtain smaller voids in the second weft.

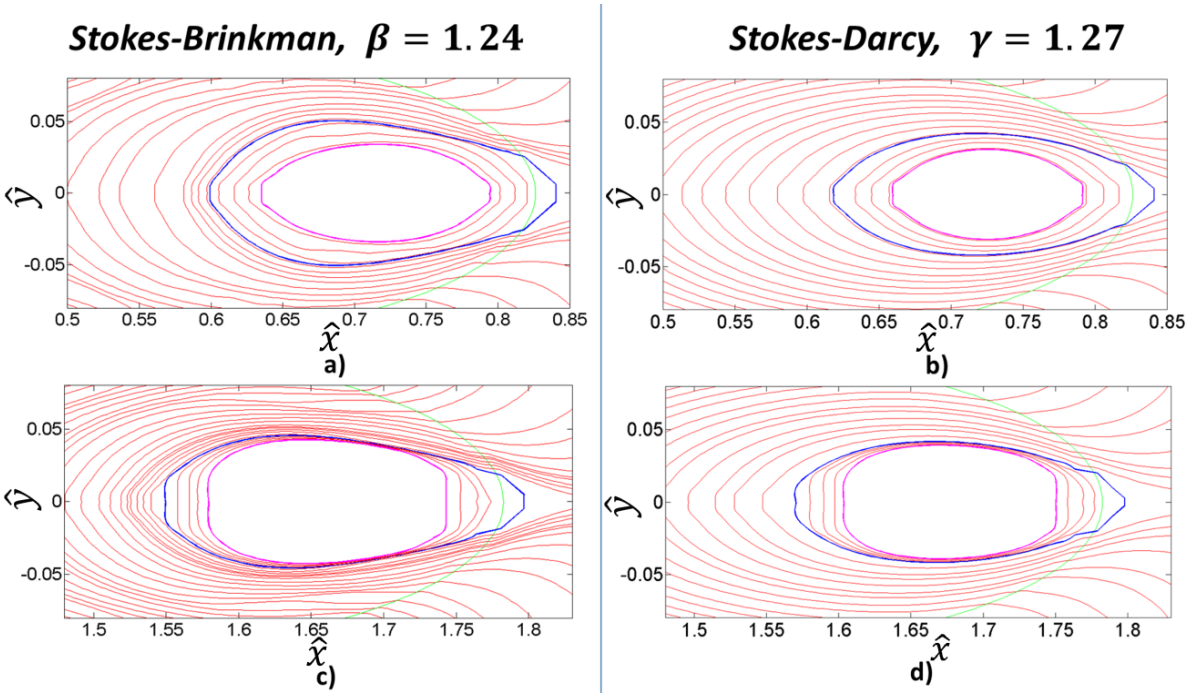

Figure 48 Detail of void formation for Stokes-Darcy and Stokes-Brinkman formulations and $C_{cap}=1\times10^{-2}$. a) First weft (Stokes-Brinkman, β=1.24), b) First weft (Stokes-Darcy, γ=1.27), c) Second weft (Stokes-Brinkman, β=1.24), d) Second weft (Stokes-Darcy, γ=1.27)

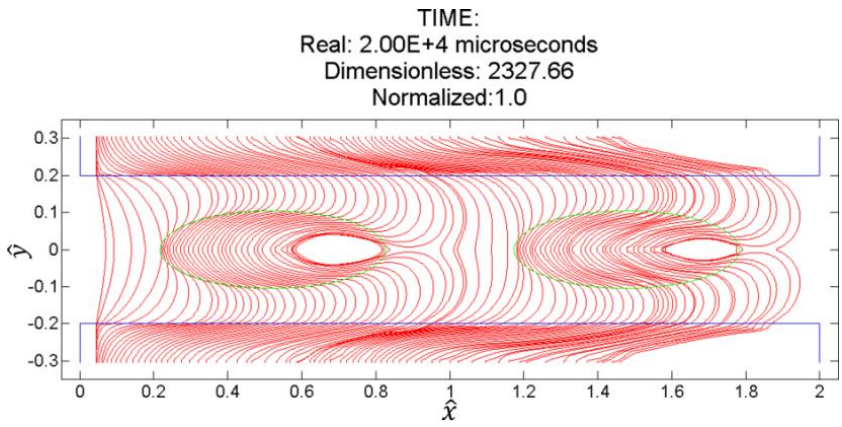
TIME:
Real: 2.00E+4 microseconds
Dimensionless: 2327.66
Normalized:1.0
$\hat{y}$
$\hat{x}$

a)

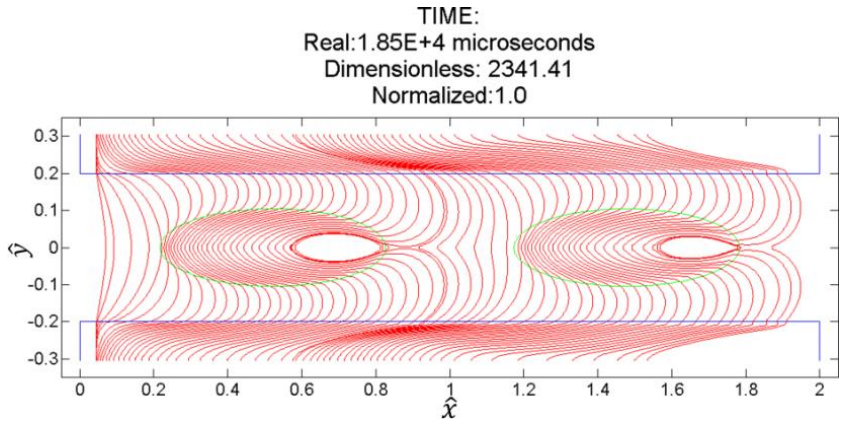
TIME:
Real:1.85E+4 microseconds
Dimensionless: 2341.41
Normalized:1.0
$\hat{y}$
$\hat{x}$

b)

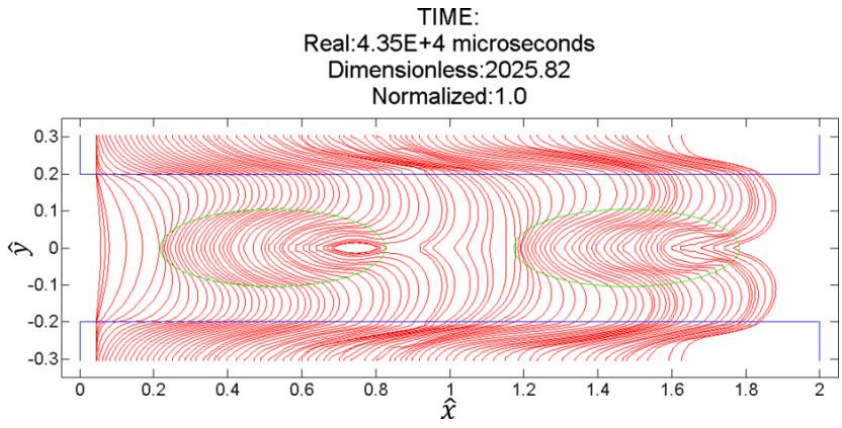
TIME:
Real:4.35E+4 microseconds
Dimensionless:2025.82
Normalized:1.0
$\hat{y}$
$\hat{x}$

c)

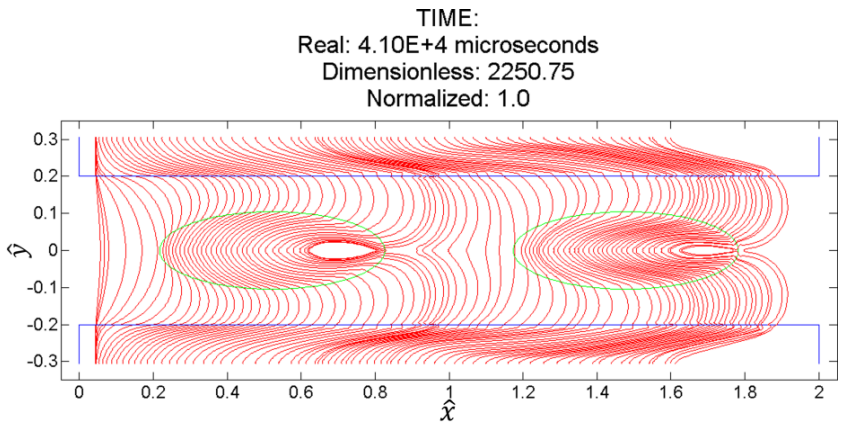

d)

Figure 49 Total fillings of RUC's in S-D and S-B for $C_{cap}=1\times10^{-1}$ and $C_{cap}=5\times10^{-1}$,a) $C_{cap}=1\times10^{-1}$ (Stokes-Brinkman, β=1.24), b) $C_{cap}=1\times10^{-1}$ (Stokes-Darcy, γ=1.27), c) $C_{cap}=5\times10^{-1}$ (Stokes-Brinkman, β=1.24), d) $C_{cap}=5\times10^{-1}$ (Stokes-Darcy, γ=1.27).

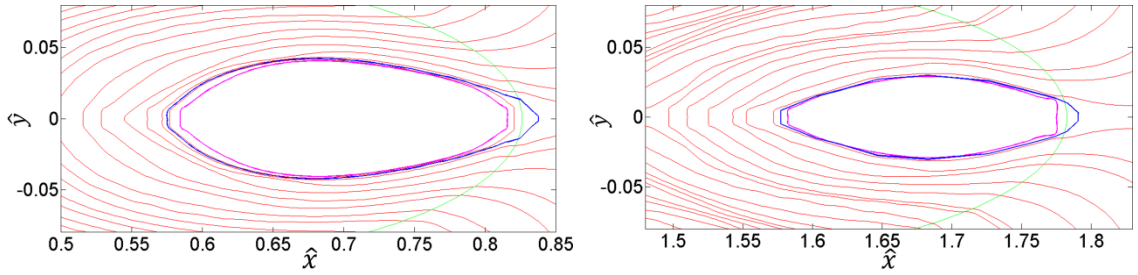

a) **b)**

Figure 50 Detail of void formation for $C_{cap}=1\times10^{-1}$ in Stokes-Brinkman approach with β=1.24 . a) First weft, b) Second weft

Results of void characterization.

The characterization of the final voids is shown in Table 12. Both approaches, *S-D* and *S-B*, predict a similar behavior of the void size and shape with the capillary ratio, C_{cap}. The largest voids of the first weft are obtained for $C_{cap} = 1 \times 10^{-1}$ and the smallest ones for $C_{cap} = 5 \times 10^{-1}$, with the void size corresponding to $C_{cap} = 1 \times 10^{-2}$ in between them. On the other hand, for the second weft, the void is always smaller as C_{cap} is higher, with no void formation, $Size^* = 0$, for $C_{cap} = 5 \times 10^{-1}$ when using the *S-B* approach (See Figure 49c), while the *S-D* predicts the formation of a very small bubble (See Figure 49d). Regarding the void shape, the increase of C_{cap} generates bubbles with a higher aspect ratio for the first and second weft in both approaches, *S-B* and *S-D.*

Table 12 Characterization of final voids for S-B with β=1.24 and S-D with γ=1.27

Approach	Capillary ratio	Void of first weft			Void of second weft		
		$Size^*$	Shape	Location	$Size^*$	Shape	Location
Stokes-Brinkman	1.00E-02	7.58E-03	2.34E+00	9.48E-01	9.87E-03	1.93E+00	9.35E-01
	1.00E-01	1.08E-02	2.84E+00	9.83E-01	6.55E-03	3.32E+00	9.87E-01
	5.00E-01	1.97E-03	4.24E+00	9.65E-01	0.00E+00	NA	NA
Stokes-Darcy	1.00E-02	5.08E-03	2.10E+00	9.32E-01	8.01E-03	1.86E+00	9.46E-01
	1.00E-01	1.07E-02	3.10E+00	9.84E-01	7.34E-03	3.59E+00	9.91E-01
	5.00E-01	4.94E-03	4.17E+00	9.78E-01	2.45E-03	5.21E+00	9.66E-01

Comparison of saturation curves.

The global saturation curves predicted by the *S-D* and *S-B* approaches for the three capillary ratios are compared in Figure 51a, where it can be seen a similar general behavior for all curves. In the Figure 51b, the S-D curve for $C_{cap} = 1 \times 10^{-1}$ is showed to describe the general behavior of the curves of Figure 51a and several filling instants are highlighted using marker points that are numerated from 0 to 5. According to Figure 51b, the highest saturation rate, i.e., the slope of the curve, is reached at the beginning of the injection *(from 0 to 1)*, but when the fluid front arrives to the first weft *(point 1)*, the saturation rate decreases until the merging of the fluid fronts *(from 1 to 2)* due to the flow resistance exerted by the first weft. When the channel fluid fronts have surrounded the first weft and encountered one another, an increase in the saturation rate can be noticed *(point 2)* and this rate is kept almost constant until the arrival of the fluid front to the second weft *(from 2 to 3)*, moment from which the saturation rate progressively decreases again until the second merging of the fluid fronts *(from 3 to 4)* due to the resistance exerted by the second weft. In point *(4)*, saturation rate barely increases, and from *(4)* to the end of simulation (5), saturation rate is essentially constant. The nearly constant saturation rate between *2* and *3*, as well as between *4* and *5*, is expected since no porous obstacles are present in the channel in those intervals, in contrast with what happens in the intervals *from 1 to 2* and *from 3 to 4*, where the saturation rate decreases due to the presence of the first and second weft, respectively.

According to Figure 51a, for $C_{cap} = 1 \times 10^{-2}$ and $C_{cap} = 1 \times 10^{-1}$, the saturation curves of both approaches (*S-D* and *S-B*) are almost similar, but the final saturation is slightly higher for *S-D* (See detail in Figure 51a). The highest differences between the predicted saturation curves of both approaches (*S-D* and *S-B*) are found for $C_{cap} = 5 \times 10^{-1}$, i.e, when the capillary effects are the most important; in this case, the final RUC saturation is barely higher for the *S-B* scheme (See detail in Figure 51a).

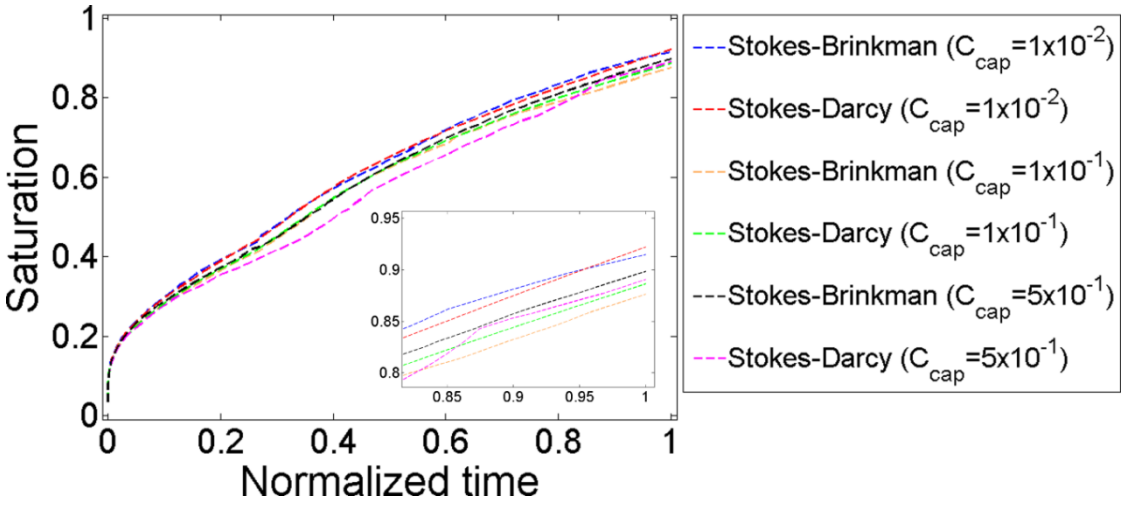

a)

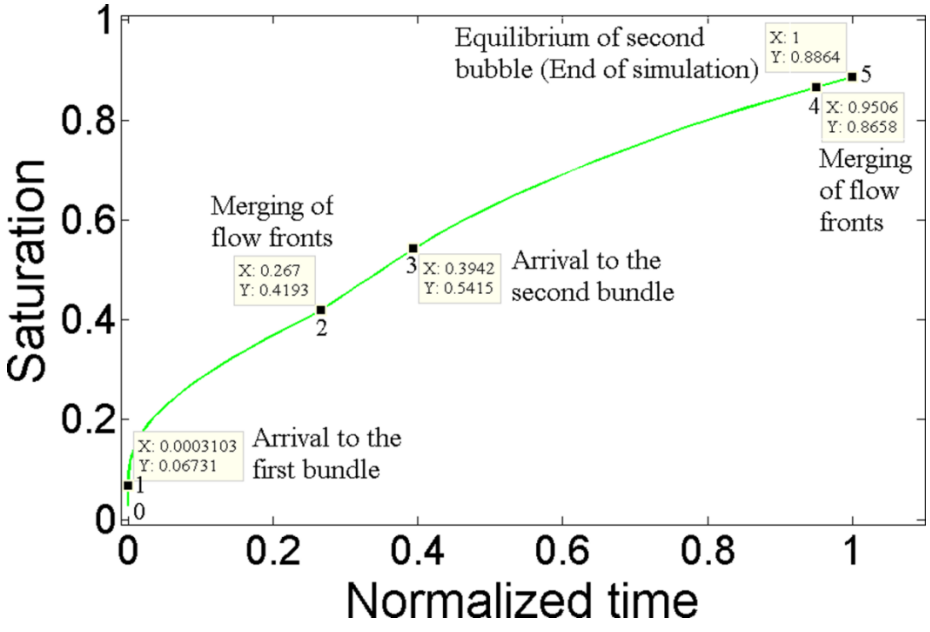

b)

Figure 51 Saturation curves for S-D and S-B formulations.a) Comparisson Stokes-Brinkman with β=1.24 vs. Stokes-Darcy with γ=1.27, b) Stokes-Darcy for C_{cap}=1×10^{-1}

4.4.4 Influence of matching conditions on the void formation for the Stokes-Brinkman approach.

Influence of the jump stress coefficient.

The influence of the jump stress coefficient, β, on the void formation can be studied by comparing results of *Series 1* ($\beta = 1.24$) and *2* ($\beta = 0.70$). For *Serie 2*, the total RUC fillings are shown in Figure 52a-c, where, in the case of $C_{cap} = 1 \times 10^{-2}$ (Figure 52a), the fluid fronts with the same positions in the channel as the ones reported in the first column of Figure 47 for the *Serie 1,* are highlighted in black color. In general, the real, dimensionless and normalized arrival times corresponding to these positions are shorter for $\beta = 0.70$.

As it can observed in the Table 13, the behavior of the void size with C_{cap} in the case of $\beta = 0.70$ is similar to the one previously obtained for $\beta = 1.24$, that is, the void size does not vary monotonically with C_{cap} in the first weft, but it does in the second weft, in which the increase of C_{cap} brings about the reduction of the void size. According to Table 13, when void is formed, smaller voids are obtained in both wefts for $\beta = 0.70$, being this difference less significant for $C_{cap} = 5 \times 10^{-1}$ in the first weft. The total void size, which is the sum of the void size of both wefts, is thereby also lower for $\beta = 0.70$. Although the size of the first bubble is not a monotonic function of C_{cap} for both values of β, the size of the second bubble is a decreasing monotonic function of C_{cap}, and the resulting total void size also decreases with C_{cap}. This last behavior is in agreement with results previously reported in the literature [11], where unidirectional macroscopic simulations were carried out using the software LIMS and it was found that the saturated length corresponding to the arrival of the fluid front to the extreme of a cavity is larger as C_{cap} increases, which, from a mesoscopic viewpoint, can be interpreted as the reduction of the total void size with the increment of C_{cap} for a determined position along the cavity.

In general, the void shapes obtained in this work are physically consistent with some experimental works. For instance, Hamidi el al [170], [213], [214] studied the void morphology in the Resin Transfer Molding process (RTM), obtaining that the bubbles formed inside the bundles can be cigar-shaped, i.e., bubbles with a very high aspect ratio (See Figure 53a, Figure 49d-second weft, Figure 52b-second weft), elliptical bubbles with a

lower aspect ratio tan the previous ones (See Figure 53b, Figure 49a, Figure 49b, Figure 52a, Figure 52b-first weft), and, in less proportion, almost circular bubbles having an aspect ratio close to one (See Figure 53c, Figure 54). According to the results of Table 14, the behavior of the shape of the first and second bubbles with C_{cap} in the case of $\beta = 0.70$ is similar as for $\beta = 1.24$, that is, the aspect ratio increases with C_{cap}. For $C_{cap} = 1 \times 10^{-2}$, the aspect ratio of the first and second bubble does not considerably change with β, while for $C_{cap} = 1 \times 10^{-1}$, a significant reduction of the aspect ratio with β can be noticed for each bubble. In the case of $C_{cap} = 5 \times 10^{-1}$, only the first bubble is formed for both values of β and the aspect ratio increases with β. The BEM/DR-BEM results do not reveal a relevant influence of β and C_{cap} on the location of the void, which is always formed at the rear edge of the weft, in agreement with the experimental research of Hamidi et al. [170], where radial injections in a circular mold were conducted, finding that the most of voids were formed at the rear edge of the wefts corresponding to the flow direction, both inside the tow and in the transition tow-channel. Other numerical works have also predicted the void formation at the extreme of the weft [3], [25], [171].

In summary, it can be concluded that the process of void formation by mechanical entrapment of air is defined by a dynamic balance between the inlet and capillary pressures, which is characterized by the capillary ratio, C_{cap}. The void size and shape are also influenced by the magnitude of C_{cap}, as well as by the value of the jump stress coefficient, β. On the other hand, the void location appears to be independent on both C_{cap} and β, since the voids are always located at the rear edge of the wefts, which is in agreement with previous numerical and experimental works.

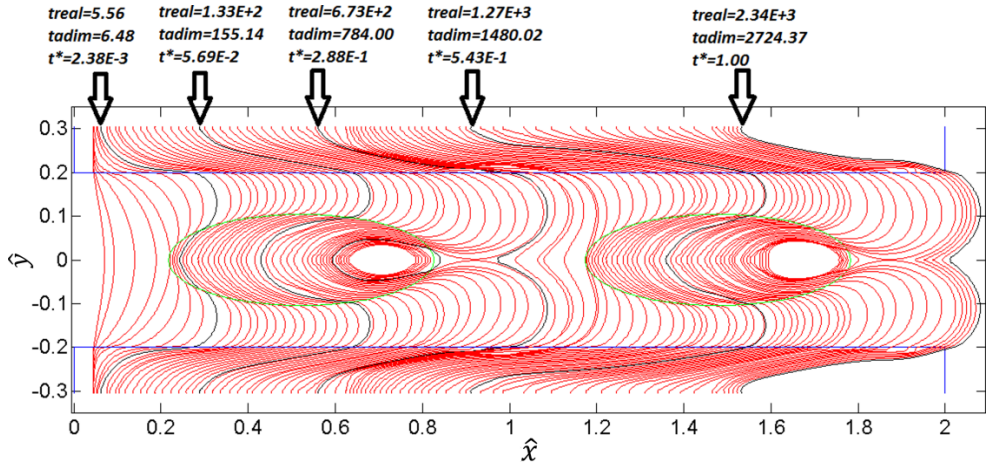

a)

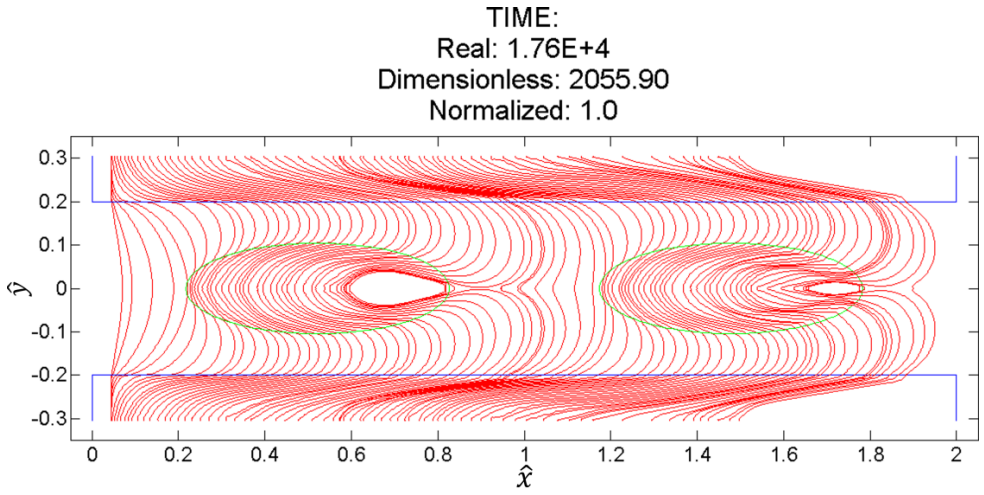

b)

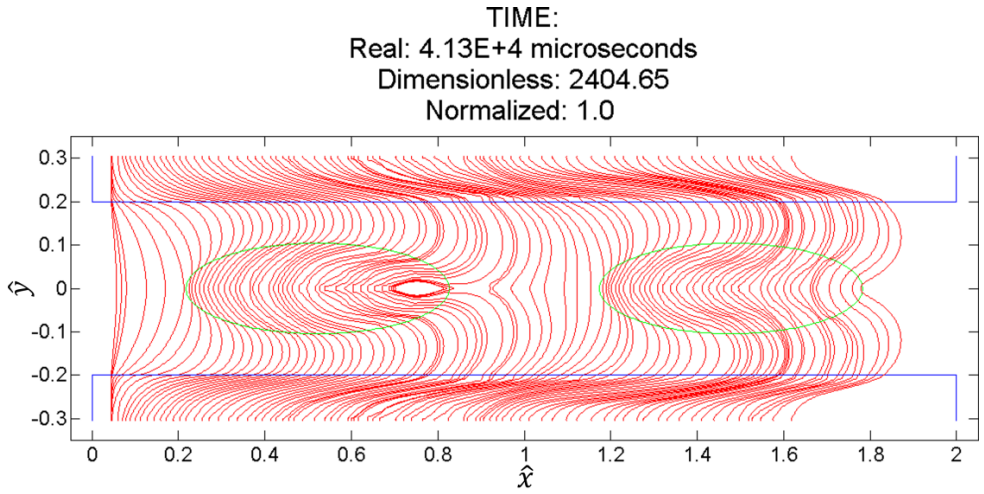

c)

Figure 52 Total fillings of RUC's for Stokes-Brinkman with β=0.7. a) $C_{cap}=1\times10^{-2}$, b) $C_{cap}=1\times10^{-1}$, c) $C_{cap}=5\times10^{-1}$

Table 13 Influence of β and C_{cap} on the void size

Capillary ratio	Void size					
	First weft		Second weft		Total	
	β=1.24	β=0.70	β=1.24	β=0.70	β=1.24	β=0.70
1.00E-02	7.582E-03	6.573E-03	9.866E-03	8.796E-03	1.745E-02	1.537E-02
1.00E-01	1.077E-02	1.039E-02	6.548E-03	2.150E-03	1.732E-02	1.254E-02
5.00E-01	1.973E-03	1.927E-03	0.000E+00	0.000E+00	1.973E-03	1.927E-03

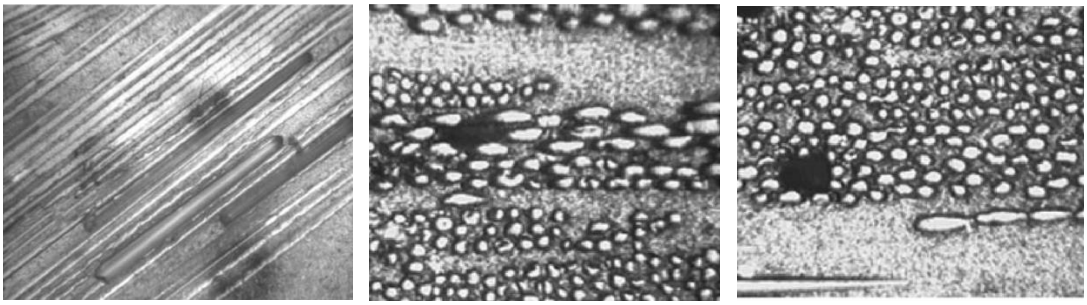

a) **b)** **c)**

Figure 53 Optical microscopic images of voids formed inside bundles, a) Cigar-shaped bubbles, b) Elliptical bubbles, c) Almost circular bubbles. Source: Hamidi et al [170]

Table 14 Influence of β and C_{cap} on the void shape.

Capillary ratio	Void aspect ratio			
	First weft		Second weft	
	β=1.24	β=0.70	β=1.24	β=0.70
1.00E-02	2.34	2.22	1.93	1.90
1.00E-01	2.84	3.19	3.32	4.18
5.00E-01	4.24	3.48	NA	NA

Comparison of void size between continuous-stress and jump-stress simulations.

The influence of the type of interface condition on the void formation for $C_{cap} = 1 \times 10^{-2}$ is studied by comparing results of *Serie 2* (stress jump condition, $\beta = 0.7$) and *Serie 4* (continuous stress condition, $\beta = 0$). The total RUC filling for the continuous stress condition is represented in Figure 54, where the fluid fronts having the same positions in the channels as those ones shown in Figure 52a are highlighted with the corresponding black arrows. The comparison between both simulations (Figure 52a vs. Figure 54) indicates that, for a same fluid front position in the channel, the positions of the fluid front

in the warps and wefts are more advanced in the continuous-stress case ($\beta = 0$), and consequently, the initial size of the first and second bubbles, corresponding to the instants when the channel fluid front completely encloses the first and second weft, respectively, is smaller in the continuous stress condition. The initial and final void size for the first weft in the jump-stress condition, Figure 52a, are $Size^* = 1.52 \times 10^{-2}$ and $Size^* = 6.57 \times 10^{-3}$, respectively; on the other hand, these values for the continuous-stress condition, Figure 54, are $Size^* = 6.30 \times 10^{-3}$ and $Size^* = 2.69 \times 10^{-3}$. Thus, the compressibility ratio is $\psi = 0.567$ for the jump-stress case and $\psi = 0.573$ for the continuous stress case. Accordingly, the void compression does not have a relevant influence in the difference between the final void sizes of these two cases (continuous-stress and jump-stress) since it is almost the same, and the principal cause of this difference is the initial void size, which is smaller in the case of $\beta = 0$, leading to a smaller final void size in such a case. A similar behavior can be appreciated for the void size in the second weft, namely, the initial void is smaller in the continuous-stress case and the compressibility ratio is almost the same for both cases (continuous-stress and jump-stress); the difference between the final void sizes of these two cases for the second weft is even higher than for the first weft, in such a way that for the jump-stress condition, the final void size is $Size^* = 8.80 \times 10^{-3}$ and for the continuous-stress condition is $Size^* = 2.02 \times 10^{-4}$.

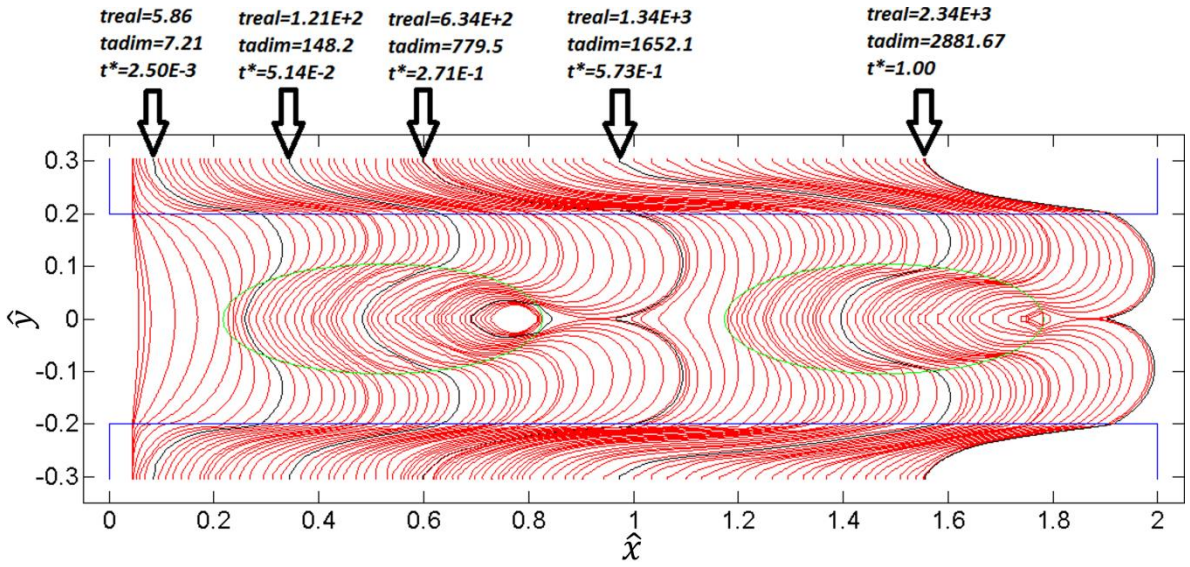

Figure 54 Total filling of the RUC for the continuous-stress condition and $C_{cap}=1\times10^{-2}$

Comparison of saturation curves between continuous-stress and jump-stress simulations.

Saturation curves are very important since they allow describing quantitatively how the behavior of the saturated volume is in the time or in the space, and they can be useful for comparing two or more filling processes at several filling instants. The saturation curves for the continuous (C-S) and jump stress (J-S) filling processes are compared in Figure 55. For any value of the normalized time, $t^* = t/t_{filling}$, the saturation is higher in the C-S simulation, but the general behavior of both curves is very similar to the one presented in Figure 51b. In both curves, the same representative filling instants shown in Figure 51b are indicated with arrows. The saturation difference between the C-S and J-S simulations for any filling instant i can be written as:

$$ds = s_i^{cont} - s_i^{jump} \tag{122}$$

where s_i^{cont} and s_i^{jump} stand for the RUC saturation at the instant *"i"* in C-S and J-S, respectively. The absolute change of the saturation difference, ds, between two filling instants, *i* and *j*, is represented as follows:

$$\begin{aligned}\Delta(ds)_{i-j} &= \left(s_j^{cont} - s_j^{jump}\right) - \left(s_i^{cont} - s_i^{jump}\right) \\ &= \left(s_j^{cont} - s_i^{cont}\right) - \left(s_j^{jump} - s_i^{jump}\right)\end{aligned} \tag{123a}$$

$$\Delta(ds)_{i-j} = \frac{\left(\Delta V_{channels}^{ij}+\Delta V_{warps}^{ij}+\Delta V_{weft1}^{ij}+\Delta V_{weft2}^{ij}\right)^{cont}-\left(\Delta V_{channels}^{ij}+\Delta V_{warps}^{ij}+\Delta V_{weft1}^{ij}+\Delta V_{weft2}^{ij}\right)^{jump}}{V_{RUC}} \tag{123b}$$

where $\Delta V_{channels}^{ij}$ is the change of the saturated volume in the channels between instants *i* and *j*, ΔV_{warps}^{ij} is the change of the saturated volume in the warps, ΔV_{weft1}^{ij} is the change of saturated volume in the first weft and ΔV_{weft2}^{ij} is the change of saturated volume in the second weft. It is very important to take into account that ds is not referred to the saturation difference for a determined value of the normalized time, t^*, but to the saturation difference for the filling instants highlighted in Figure 55, which do not necessarily have the same normalized times in both curves.

In the first filling instant *(point 1)*, when the flow reaches the first weft, the RUC saturation is very similar for both simulations, C-S and J-S, because it is primarily determined by the saturation of the channel, which is almost the same in both cases. So, when the fluid front reaches the first weft, ds is very small, namely, $ds = 0.00774$. During the impregnation of

the first weft *(from 1 to 2)*, ds increases until the merging of the channel fluid fronts *(point 2)*. This happens because $\left(\Delta V_{weft1}^{12}\right)^{cont} > \left(\Delta V_{weft1}^{12}\right)^{jump}$ between the arrival of the fluid front to the first weft and the merging of the channel fluid fronts; in other words, this happens because the first weft saturates more in C-S than in J-S when the fluid surrounds it *(from 1 to 2)*. Therefore, in the flow merging instant *(point 2)*, the saturation difference between C-S and J-S has increased to $ds = 0.0242$.

The change of the saturated volume of the first weft between the flow merging instant and the arrival of the fluid front to the second weft *(from 2 to 3)*, can be expressed as $\Delta V_{weft1}^{23} = V_{void1}^{(2)} - V_{void1}^{(3)}$, where $V_{void1}^{(2)}$ is the initial volume of the bubble *(void volume at instant 2)* and $V_{void1}^{(3)}$ is the volume of the bubble at the instant when fluid front reaches the second weft *(void volume at instant 3)*. From the definition of the compressibility ratio, ψ, in Eq.121, it is obtained that $\Delta V_{weft1}^{23} = \psi^{(2-3)} V_{void1}^{2}$, where $\psi^{(2-3)}$ is the compression of the void between instants 2 and 3. According to results presented above, the compression of the void is very similar in the C-S and J-S simulations, so, it can inferred that $\left(\Delta V_{weft1}^{23}\right)^{jump} > \left(\Delta V_{weft1}^{23}\right)^{cont}$ because the initial void volume, $V_{void1}^{(2)}$, is greater for the J-S simulation. Accordingly, if $\left(\Delta V_{weft1}^{23}\right)^{jump} > \left(\Delta V_{weft1}^{23}\right)^{cont}$, and considering that $(\Delta V_{channels}^{23})^{cont} \approx (\Delta V_{channels}^{23})^{jump}$ and $\left(\Delta V_{warps}^{23}\right)^{cont} \approx \left(\Delta V_{warps}^{23}\right)^{jump}$ according to the simulation results, it is achieved that $\Delta(ds)_{2-3} < 0$ according to Eq.123b, which means a lower saturation difference between C-S and J-S, ds, at the moment when the flow reaches the second weft *(point 3)* than the one previously obtained at the moment of the fluid front merging *(point 2)*. So, when the fluid front arrives to second weft *(point 3)*, $ds = 0.0195$, which is lower than the difference obtained for the instant *2*.

The behavior of ds between the arrival of the fluid front to the second weft and the second merging of the channel fluid fronts *(from to 3 to 4)*, considering that $(\Delta V_{channels}^{34})^{cont} \approx (\Delta V_{channels}^{34})^{jump}$ and $\left(\Delta V_{warps}^{34}\right)^{cont} \approx \left(\Delta V_{warps}^{34}\right)^{jump}$ according to the simulation results, is determined by the following differences (See Eq. 123b): $d_{weft1}^{34} = \left(\Delta V_{weft1}^{34}\right)^{jump} - \left(\Delta V_{weft1}^{34}\right)^{cont}$ and $d_{weft2}^{34} = \left(\Delta V_{weft2}^{34}\right)^{cont} - \left(\Delta V_{weft2}^{34}\right)^{jump}$. Accordingly, if $d_{weft2}^{34} > d_{weft1}^{34}$, ds should increase. Considering that the change of saturation associated to the

compression of the void in the first weft is larger for J-S, i.e., $d^{34}_{weft1} > 0$, as it was previously demonstrated, it is a necessary but not sufficient condition that $d^{34}_{weft2} > 0$ in order to obtain an increment in ds. This condition is satisfied in this case due to the larger infiltration occurring in the second weft for the C-S condition, as it was mentioned before. Additionally, considering that the change of the saturated volume in the first weft due to the void compression, ΔV^{34}_{weft1}, is negligible with respect to the change of the saturated volume in the second weft, ΔV^{34}_{weft2}, in both C-S and J-S, the behavior of ds between the instants *3* and *4* is primarily determined by the change of the saturation in the second weft, which is larger for the C-S condition $\left(d^{34}_{weft2} > 0\right)$, leading to an increment of ds *(See instant 4)*. Hence, when the channel flows merge again each other *(Point 4)*, $ds = 0.0257$, which is a higher saturation difference between C-S and J-S than the one obtained when the flow arrives to the second weft *(Point 3)*, $ds = 0.0195$. At the end of the simulation, the RUC saturation is $s = 0.928$ for C-S and $s = 0.904$ for J-S (*See filling instant 5*).

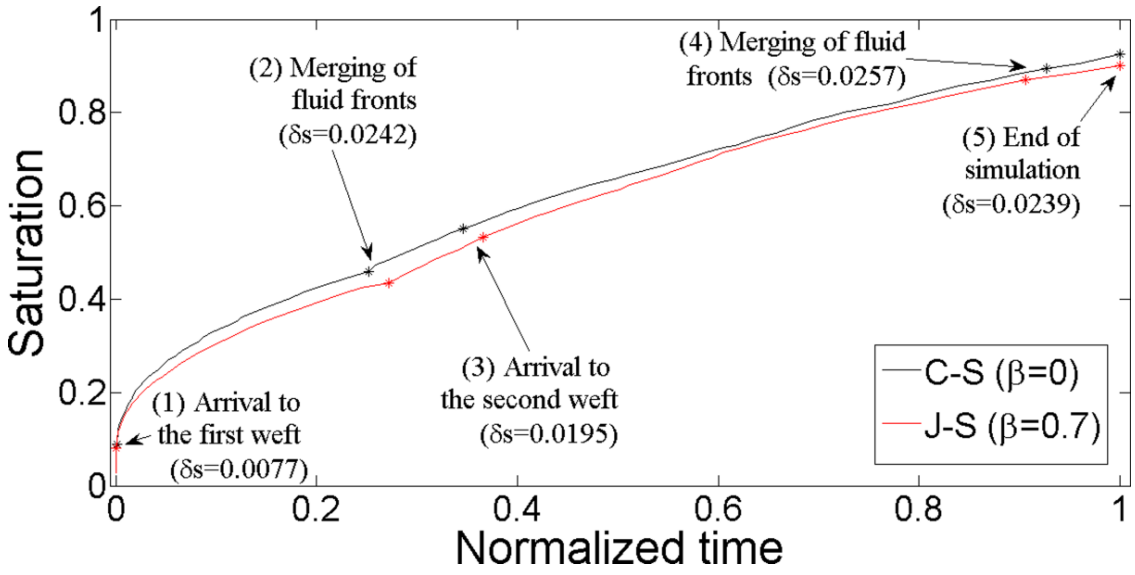

Figure 55 . Comparison of saturation curves for continuous and jump stress conditions and $C_{cap}=1\times10^{-2}$

Comparison of interfacial velocities between continuous-stress and jump-stress simulations.

The change of the matching condition can also modify the velocity along the interface channels-tows. The velocity vectors along this interface for the J-S and C-S conditions are shown in the Figure 56a-f, corresponding to filling instants having the same fluid front position in the channel. As it is logic, the velocities of the channel domain are greater than those ones of the tows domains, warp and weft (Figure 56a,b). Along the interface channel-warp, in both C-S (Figure 56d) and J-S (Figure 56c), the magnitude of the velocity increases from the inlet towards the fluid front and the net mass transfer occurs from the channel towards the warp. In the interface channel-weft, in the neighborhood of the left extreme of the weft, both C-S (Figure 56f) and J-S (Figure 56e) simulations predict a mass transfer taking place primarily from the weft into the channel; then, the mass transfer direction is reversed and it reaches its peaks in points close to the fluid front. The total mass transfer from the channel towards the weft is considerably larger than the mass transfer in the contrary direction for both simulations, C-S and J-S.

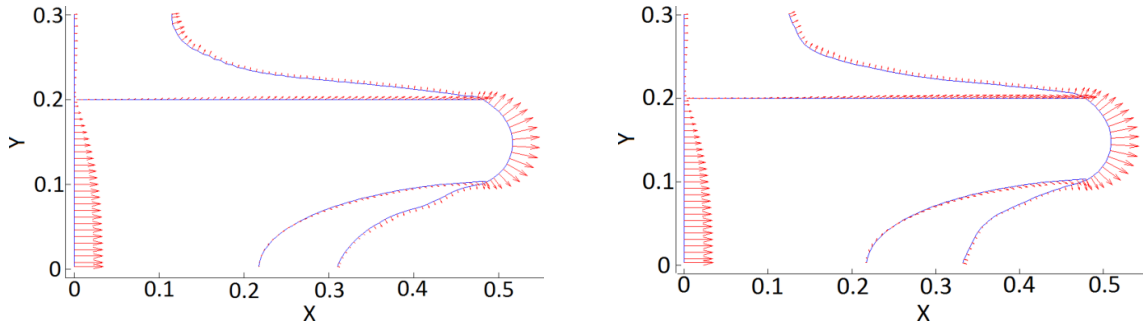

a) **b)**

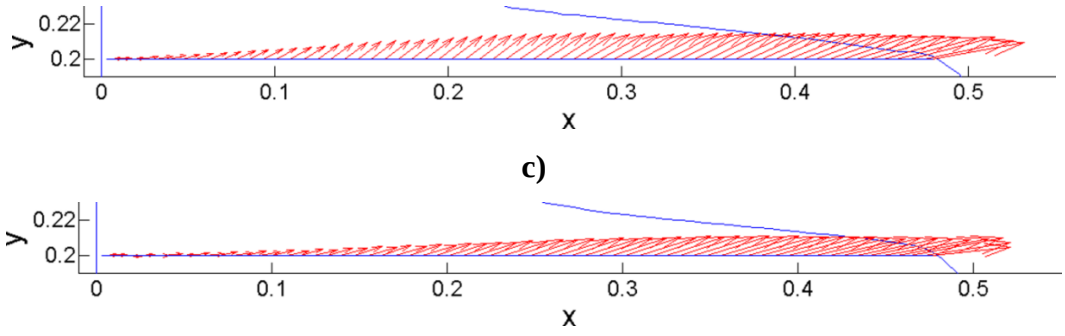

c)

d)

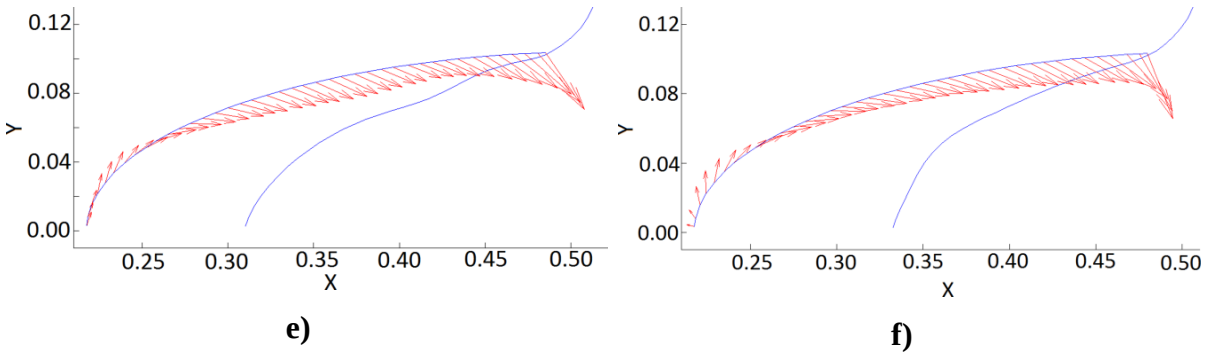

Figure 56 Velocity vectors for jump-stress and continuous-stress conditions along the interface channel-tows. a) Velocity vectors for jump-stress, b) Velocity vectors for continuous-stress, c) Velocity vectors for interface channel-warp (Jump-stress), d) Velocity vectors for interface channel-warp (Continuous-stress), e) Velocity vectors for interface channel-weft (Jump-stress), f) Velocity vectors for interface channel-weft (Continuous-stress).

The comparison between the velocity profiles along the interface channel-warps is shown in Figure 57a, in which it can be observed that the normal velocity is inferior to the tangential velocity in all positions along the interface for both C-S and J-S conditions. For any position along the interface, the C-S tangential velocity is greater than the J-S tangential velocity, while the difference between the normal velocities of C-S and J-S depends on the position along the interface, but, in general, it not so significant, which is in agreement with the relatively small difference between the warp saturations of C-S and J-S during the filling process of the first weft (from point 1 to 2 in Figure 55).

On the other hand, the velocity profiles for the interface channel-weft are shown in Figure 57b, where it can be observed that for both C-S and J-S, in points near to the left extreme of the weft (corresponding to the left extreme of the plot), negative normal velocities are obtained (which correspond to the mass transfer from the weft towards the channel, see Figure 56f and Figure 56e), and there is an increment of the tangential velocity that is more notorious in the C-S simulation, being this increment the main cause by which the tangential velocities in C-S remain above the tangential velocities in J-S for all positions along the interface. For the C-S simulation, once the direction of the mass transfer is reversed (positive normal velocities), the normal velocity undergoes an increment along all interface positions until the fluid front (the fluid front corresponds to the right extreme of the plot), whereas the tangential velocity increases until certain point nearby the fluid front and then decreases. On the other hand, for the J-S simulation, once the mass transfer

direction changes, the normal and tangential velocities increase first and then they are subjected to a small reduction and subsequent increment until a certain point nearby the fluid front; this increment is kept for the normal velocity, but the tangential velocity decreases instead. In the neighborhood of the fluid front, the increment of the normal velocity and the decrease of the tangential one are more notorious for the C-S simulation. According to Figure 57b, the mass transfer from the channel into the weft is greater for C-S, which is in agreement with the previous analysis of Figure 55, where a higher saturation of the first weft between instants 1 and 2 was obtained for C-S.

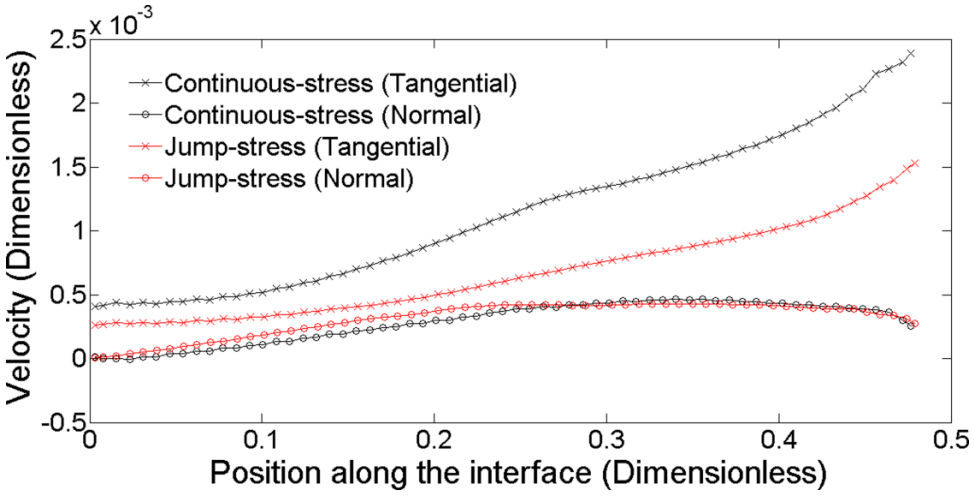

a)

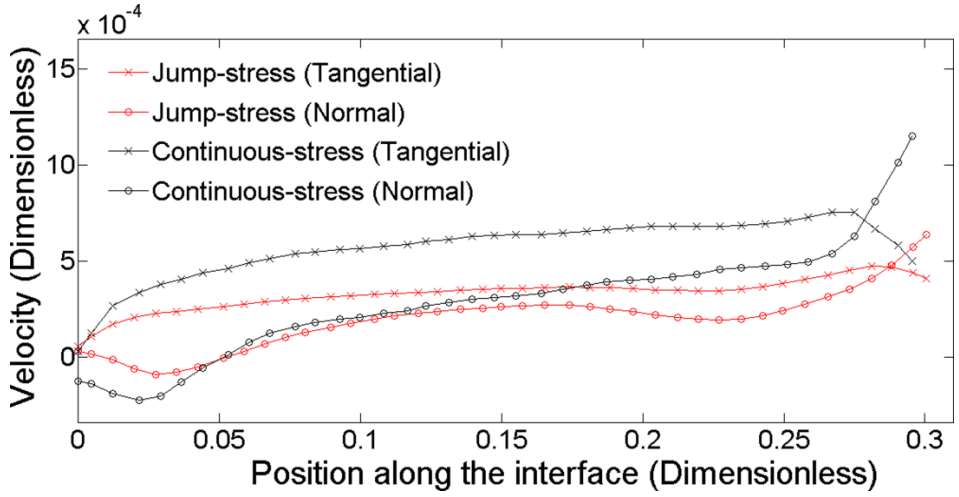

b)

Figure 57 Interfacial velocity profiles for continuous-stress and jump-stress conditions. a) Velocity profiles for interface channel-warp, b) Velocity profiles for interface channel-weft

4.4.5 Influence of RUC compaction on void formation

Statement of problem of void compaction.

A typical compaction curve of fibrous reinforcements is shown in Figure 58 [128], [215], [216]. Three zones can be distinguished in this curve and the fiber volume fractions delimiting these zones (V_{fo}, V_{f1}, V_{f2}) depend on the RUC architecture, fiber material and ply stacking. In the first zone, the dominant phenomenon is the nesting, which causes changes in the inter-tow space, in the aspect ratio of the tows and, probably, the shearing deformation of the tows. In the second zone, in addition to the nesting, the tow fibers could undergo an axial deformation, changing their aspect ratio. The third zone is dominated by the bending deformation of the tows, where a breakage of fibers can occur. In the present work, it is only considered the nesting of the RUC expressed as the reduction of the inter-tow distance and the change of the aspect ratio of the tows, and it is considered that the tows are always in contact with the liquid of the channels.

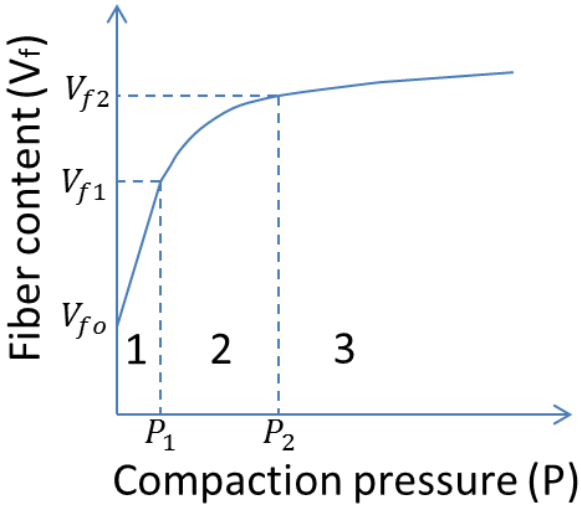

Figure 58 Typical compaction curve of fibrous reinforcements

Influence of RUC compaction on the RUC filling process.

For $C_{cap} = 1 \times 10^{-2}$, the comparison between the first column of Figure 47 and the Figure 59a allows establishing the influence of the RUC compaction in the filling times and in the fluid front shapes considering the same fluid front positions in the channel, which are highlighted with black color in Figure 59a. In the following analysis, *R-D* stands for the reference domain considered in Figure 47 and *C-D* stands for the compacted domain of Figure 59a. For the first filling instant (Figure 47a and first fluid front highlighted in Figure

59a), the real, non-dimensional and normalized times are longer in *C-D*. This is reasonable because after the fluid front reaches the first weft, the fluid front velocity in the channels decreases due to the mass transfer from the channels towards the first weft, and in the compacted domain, *C-D*, this event takes place first because the left extreme of the first weft is closer to the RUC inlet. For the second filling instant (Figure 47c and second fluid front highlighted in Figure 59a), the times are still longer in *C-D*, in which $2.35 \times 10^2\ \mu s$ have elapsed to this position, whereas $1.37 \times 10^2\ \mu s$ is the time elapsed for *R-D*. In the filling that occurs between the second and third instants, with the third filling instant corresponding to Figure 47e and the third fluid front highlighted in Figure 59a, the fluid front in the first weft advances more in the *C-D* simulation because the weft is more flattened in the compacted domain, and, in consequence, the initial void is smaller for *C-D*. The initial void size for *R-D* is $Size = 1.87 \times 10^{-2}$, which corresponds to $Size^* = 1.54 \times 10^{-2}$, whereas, for C-D, this value is $Size = 1.28 \times 10^{-2}$ ($Size^* = 1.32 \times 10^{-2}$) . After the void compression, the final void size is still smaller for the *C-D* simulation, in which $Size = 5.10 \times 10^{-3}$ ($Size^* = 4.88 \times 10^{-3}$) in contrast to the final void size for the R-D simulation, $Size = 9.23 \times 10^{-3}$ ($Size^* = 7.58 \times 10^{-3}$).

The real and normalized times in the third and fourth fluid front positions are still greater for *C-D* (compare Figure 47e to the third fluid front highlighted in Figure 59a, and Figure 47g to fourth highlighted position of Figure 59a). In the fourth fluid front, 70.7% of the total filling time has elapsed for *C-D* and 54.7% for *R-D*, which means that the fluid front in the channels is decelerating more in *R-D* than in *C-D*. From the fourth fluid front to the instant when channel fluid fronts have totally surrounded the second weft, the change of saturation in the weft is higher for *C-D*, which leads to the generation of a smaller initial void in the compacted domain. The initial void size is $Size = 1.73 \times 10^{-2}$ ($Size^* = 1.42 \times 10^{-2}$) for *R-D* and $Size = 1.04 \times 10^{-2}$ ($Size^* = 9.98 \times 10^{-3}$) for *C-D*. In *R-D* the compressibility ratio of the bubble is $\psi = 0.304$ and the final void size is $Size = 1.20 \times 10^{-2}$ ($Size^* = 9.87 \times 10^{-3}$); on the other hand, the compression of the bubble is larger for *C-D*, $\psi = 0.476$, and the final void is thereby smaller, $Size = 5.46 \times 10^{-3}$ ($Size^* = 5.23 \times 10^{-3}$). The total filling time is longer in *C-D* than in *R-D*, i.e., the RUC impregnation process is slower in the compacted domain.

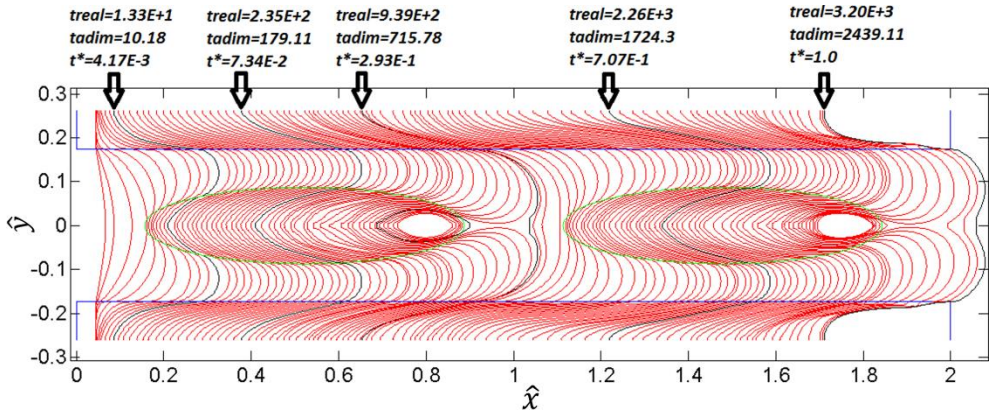

a)

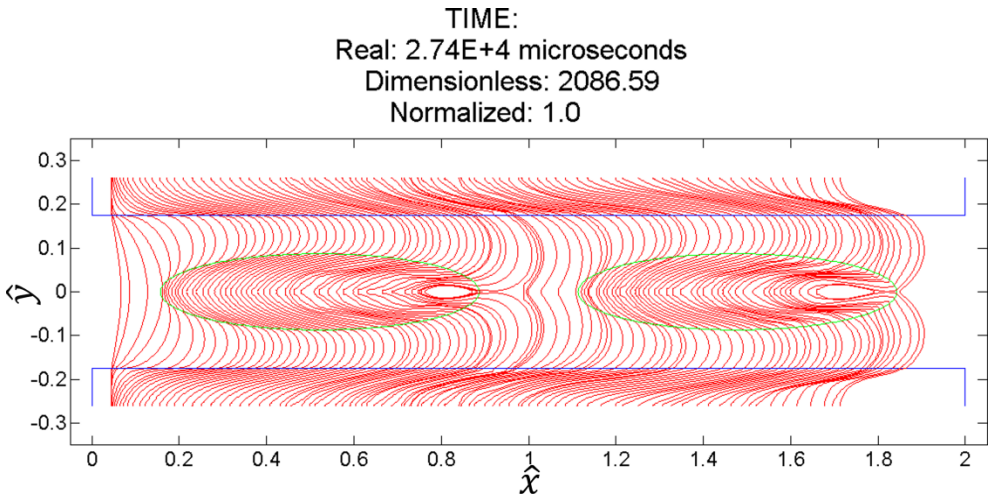

b)

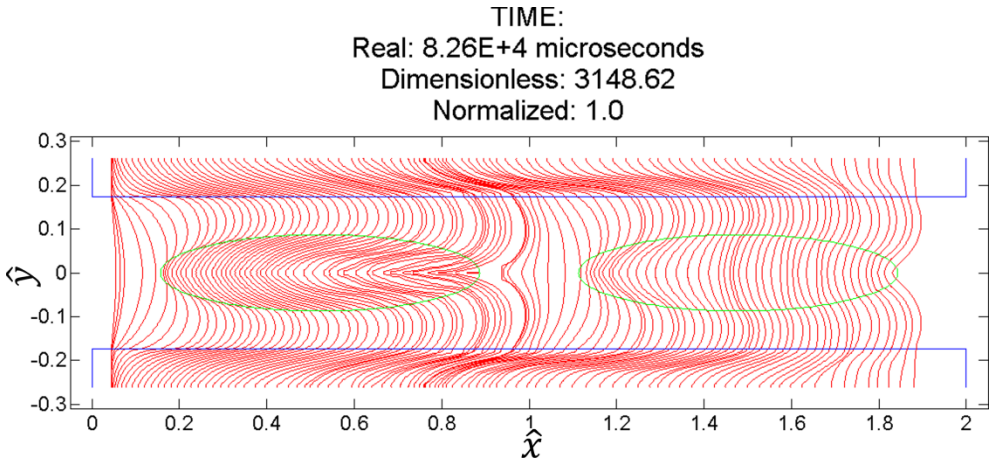

c)

Figure 59 Total fillings of compacted RUC's for Stokes-Brinkman with β=1.24. a) $C_{cap}=1\times10^{-2}$, b) $C_{cap}=1\times10^{-1}$, c) $C_{cap}=5\times10^{-1}$

The influence of the inter-tow space on the fluid front positions has been studied in [22], where a geometry consisting on two concentric domains, namely, a channel surrounding a tow, was considered. As it is shown in Figure 60a, in which the half distance between the tows, *h*, is represented from $r = 1.5mm$ upwards, Yang et al.[22] found that the reduction of the inter-tow distance, i.e., the compaction of the RUC, reduces the difference between the maximum position of the fluid front at the channel and the minimum position of the fluid front at the tow for a certain filling instant. In Figure 60b the minimum fluid front positions at the warps of *R-D* and *C-D* for the filling instants analyzed here are compared. As observed, these positions are always larger for *C-D*. Bearing in mind that the maximum position of the channel fluid front is the same in both simulations, *R-D* and *C-D*, in each filling instant, this implies a smaller difference between the minimum fluid front position at the warps and the maximum fluid front position at the channel for the compacted domain (*C-D*) in each filling instant. This is in agreement with the results presented in Figure 60a taking into account that the inter-tow dimensions of the compacted domain, *C-D*, are smaller than those ones of the reference domain, *R-D*.

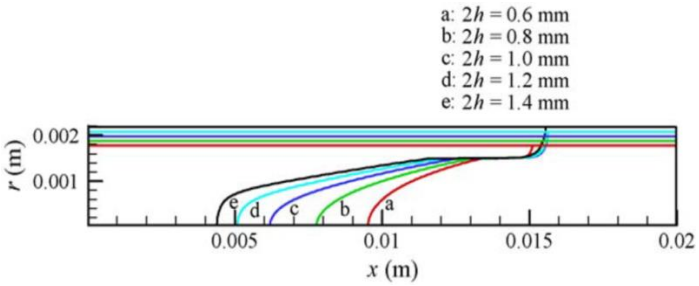

a)

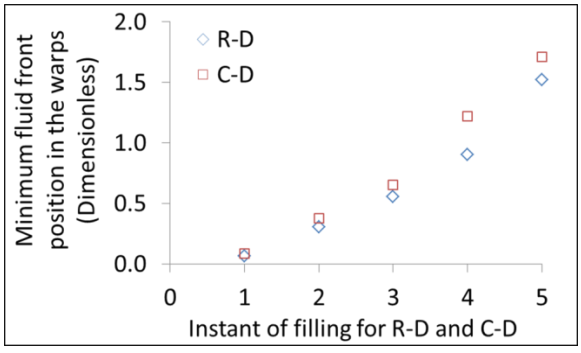

b)

Figure 60 Influence of RUC compaction on fluid front positions. a) Influence of inter-tow distance on fluid front positions according to Yang et al [22] b) Comparison between the minimum fluid front positions in the warps of C-D and R-D (Author)

Influence of the RUC compaction on the voids characteristics.

The influence of the RUC compaction on the void characteristics can be determined by comparing results of Serie *1* and *3*. According to Table 15, for a constant value of C_{cap}, smaller voids are obtained for the compacted domain (*C-D*) in both wefts. From an experimental viewpoint, the influence of the compaction of fibrous reinforcements on the void content is still debatable. To make reference to experimental works, it is important to consider that the RUC compaction leads to the increase of the global fiber volume content, V_f. Bearing this in mind, whereas an increase of the void content with V_f was obtained in hemp fiber reinforced polyethylene terephthalate composites by Madsen el al. [217], which is not in agreement with the present results, Shah et.al [218] found a reduction of the void content with V_f for flax reinforced and jute reinforced unsaturated polyester composites, coinciding with the present results.

According to Table 15, for the first weft, the void size decreases with the increment of C_{cap} for the compacted domain (*C-D*), whereas the relationship between the void size and C_{cap} is not monotonic for the reference domain (*R-D*) as commented before. The void size of the second weft and the total void size have the same behavior with C_{cap} for *C-D* and *R-D*, i.e., they decrease as C_{cap} increases.

The void shapes obtained in Figure 59a-c are also physically consistent with the ones observed in Hamidi el al [170], [213], [214], see Figure 53a-c. According to Table 16, for the first weft and $C_{cap} = 1 \times 10^{-2}$, the void aspect ratio is barely smaller for *C-D*, while for $C_{cap} = 1 \times 10^{-1}$ and $C_{cap} = 5 \times 10^{-1}$ the increase of the void aspect ratio with the RUC compaction is important. For the second weft, the RUC compaction causes the increase of the void aspect ratio for both $C_{cap} = 1 \times 10^{-2}$ and $C_{cap} = 1 \times 10^{-1}$. No void formation is obtained in the second weft for $C_{cap} = 5 \times 10^{-1}$ in both cases (*R-D* and *C-D*), while the bubble formed in the first weft for *C-D* and $C_{cap} = 5 \times 10^{-1}$ is very small as can be appreciated in Figure 59c. The location of the final void, when formed, is not considerably affected by the RUC compaction.

Table 15 Influence of compaction and C_{cap} on the void size.

Capillary ratio	Void size					
	First weft		Second weft		Total	
	R-D	*C-D*	*R-D*	*C-D*	*R-D*	*C-D*
1.00E-02	7.582E-03	4.883E-03	9.866E-03	5.230E-03	1.745E-02	1.011E-02
1.00E-01	1.077E-02	2.134E-03	6.548E-03	2.572E-03	1.732E-02	4.707E-03
5.00E-01	1.973E-03	3.338E-05	0.000E+00	0.0000E+00	1.973E-03	3.338E-05

Table 16 Influence of compaction and C_{cap} on the void shape.

Capillary ratio	Void aspect ratio			
	First weft		Second weft	
	R-D	C-D	R-D	C-D
1.00E-02	2.34	2.24	1.93	2.33
1.00E-01	2.84	3.80	3.32	4.41
5.00E-01	4.24	13.35	NA	NA

4.5 Conclusions

In this chapter, BEM techniques have been implemented for the simulation of void formation in fibrous reinforcements using a Stokes-Brinkman formulation. Firstly, in order to define which numerical approach was more appropriate to deal with the Brinkman equation, pure BEM (referred here as BEM-ISO) or DR-BEM, two problems with analytical solutions were solved numerically using both approaches and the solutions were compared each other, obtaining that DR-BEM is more accurate, has better convergence orders and is even suitable for darcian regimes where the pure BEM approach diverges. Both numerical solutions, pure BEM and DR-BEM, predicted the increase of the error with χ^2 and, for the Stokes-Brinkman problem admitting analytical solution, they also predicted the reduction of the Stokes velocity and of the boundary layer thickness with the increase of β and χ^2, which is in agreement with other results [85]. For $\chi^2 = [1 \times 10^4, 1 \times 10^3, 1 \times 10^2]$, the DR-BEM solution is more accurate as β increases and the convergence order reduces with χ^2. Having demonstrated the superior performance of DR-BEM for the solution of the Brinkman equation and considering that pure BEM is always employed for the channel domain, the present numerical formulation was name as BEM/DR-BEM.

The numerical solution obtained with the present BEM/DR-BEM formulation for the Stokes-Brinkman problem was compared with the FEM solution of [20], finding that both ones converge satisfactorily to the analytical solution, with more notorious errors in the Brinkman domain than in the Stokes domain in BEM/DR-BEM, contrarily to the FEM solution where the errors in the Stokes domain are greater. Conversely to the FEM approach, no numerical oscillations in the boundary layer were gotten with the present BEM/DR-BEM formulation.

The problem of void formation during the filling of two adjacent RUC's, for three different capillary ratios, $C_{cap} = [1 \times 10^{-2}, 1 \times 10^{-1}, 5 \times 10^{-1}]$, was tackled using two formulations: Stokes-Darcy (S-D) and Stokes-Brinkman (S-B), which predicted the same general behavior of the void size and shape with C_{cap}. Accordingly, for the first weft, the change of void size with C_{cap} is not monotonous, since the largest voids were obtained for $C_{cap} = 1 \times 10^{-1}$ and the smallest ones, for $C_{cap} = 5 \times 10^{-1}$, whereas for the second weft, the void is smaller as C_{cap} is higher; regarding the void shape, the aspect ratio increases with C_{cap} for both wefts. On the other hand, for a same value of C_{cap}, similar saturation curves were obtained with S-D and S-B, with exception of the case where the capillary effects are more relevant, i.e., $C_{cap} = 5 \times 10^{-1}$. In the case where capillary effects are not significant, i.e., $C_{cap} = 1 \times 10^{-2}$, S-D predicted smaller voids and lower aspect ratios than S-B for both wefts.

According to the BEM/DR-BEM results, void size and shape are also influenced by the matching conditions Stokes-Brinkman. When using the jump stress condition (J-S), the smallest voids at both wefts were obtained for the lowest value of the jump stress coefficient, $\beta = 0.7$, for all values of C_{cap}, with exception of the second weft when $C_{cap} = 5 \times 10^{-1}$, where no void formation was obtained; regarding the void shape, a single relationship between the coefficient β and the void aspect ratio was not reached for all values of C_{cap} and both wefts. The general behavior of the void size and aspect ratio with C_{cap} in both wefts, which was described above, did not change with β, as well as the decreasing behavior of the total void content with C_{cap}. On the other hand, for $C_{cap} = 1 \times 10^{-2}$, the lowest void content was obtained for the continuous-stress case (C-S), and this is coherent with the larger saturation obtained in C-S with respect to J-S for all filling

instants, despite both saturations curves, C-S and J-S, showed a similar general behavior. According to the BEM/DR-BEM results, for the specific filling instant where interfacial velocities were analyzed, the net mass transfer takes place from the channel towards the warps and from the channel towards the weft in both C-S and J-S, with the net mass transfer channel-warps in C-S barely superior to the one in J-S, and the net mass-transfer channel-weft in C-S considerably greater than the one in J-S. Along the interface channel-warp the tangential velocities are larger than the normal ones for both C-S and J-S, with the C-S tangential velocities greater than the J-S ones. For the interface channel-weft, this last conclusion is also valid, namely, tangential velocities are greater in C-S.

The BEM/DR-BEM results also showed that the RUC compaction generates smaller voids for both wefts and all values of C_{cap}, with exception of the second weft when $C_{cap} = 5 \times 10^{-1}$, where no void formation was obtained in both the original domain (R-D) and the compacted domain (C-D). Moreover, the impregnation process of the C-D is slower than the one of the R-D. The RUC compaction also modifies the general behavior of the void size with C_{cap} in the first weft regarding the original domain (R-D), since a decreasing relationship is obtained, i.e., the void is smaller as C_{cap} increases. On the other hand, BEM/DR-BEM results also revealed that the RUC compaction causes the increase of the void aspect ratio in the first weft for $C_{cap} = 1 \times 10^{-1}$ and $C_{cap} = 5 \times 10^{-1}$, and in the second weft, for $C_{cap} = 1 \times 10^{-2}$ and $C_{cap} = 1 \times 10^{-1}$.

5. DYNAMIC VOID EVOLUTION IN DUAL-SCALE FIBROUS REINFORCEMENTS USING THE STOKES-DARCY FORMULATION[♠]

5.1 Introduction

In dual-scale fibrous reinforcements, once the voids are formed, several processes can take place in such voids, like compression, displacement, migration and splitting. The physical assumptions and governing laws of each process depend on the zone where the bubble is located. For channel voids (macrovoids or inter-tow voids), Lundstromg [86] supposes a spherical bubble that experiences a compression governed by the ideal gas law, where the capillary pressure needs to be considered and the void shape does not change when compressed. On the other hand, the displacement of macrovoids along the channels has been studied in both numerical [4], [78], [79], [95], [96] and experimental works [4], [89], [219], [220], where it has been mentioned that this process is mainly governed by drag and adhesion forces. The former type of forces makes reference to the pressure difference between both extremes of the bubble, while the second one, to the interfacial adhesion between the bubbles and the walls of the domain, which, in the present case, represent the contour of the tows. According to Kang and Koelling [89] if the void is smaller than the inter-tow space (channel) it tends to be spherical to minimize the free surface energy and it moves easily until it reaches a constriction, where a minimum pressure gradient is required to induce the movement according to [221], [222]. On the other hand, if the frontal section of the bubble is equal to the inter-tow space, the bubble tends to be cylindrical as its volume increases [89]. The bubble length has a double effect in its mobility [86], [89], [222]: as the bubble is larger, the pressure difference is higher, promoting the bubble's motion, but the contact surface with the tows increases, as well as the interfacial forces, which make more difficult the bubble's motion. Strictly speaking, the motion of macrovoids along the channels depends mainly on the pressure difference, the frontal area, perimeter and length of the bubble, the surface tension at the liquid-gas interface, the liquid viscosity, the advancing and receding contact angles and the architecture of the channels [221], [222].

[♠] **The results of the present chapter are intended to be published in: Iván David Patiño Arcila, Henry Power, César Nieto Londoño, Whady Felipe Flórez Escobar, *"Boundary Element Method for the dynamic evolution of intra-tow voids in fibrous reinforcements using a Stokes-Darcy approach"*, to be submitted *(In preparation)*.**

Since some of these parameters are difficult to determine experimentally, some phenomenological models have been proposed to relate the average liquid velocity, $\langle u_g \rangle^g$, which can be straightforwardly measured, and the void velocity [4], [79], [222], $\langle u^v \rangle$, with the piecewise function proposed by Lee et al [4], [79] as one of the most cited in the literature. In that model, a critical liquid velocity for the onset of void mobilization, $\langle u_g^{crit} \rangle^g$, is proposed, in such a way that the void motion can be neglected below this critical value.

The bubbles formed inside the tows (microvoids or intra-tow voids), which are the principal focus of the present chapter, can also undergo several processes. The microvoid compression takes place by the overall effect of the pressure of the liquid surrounding the tow, the air pressure at the fluid front, which in turns depends on the initial air pressure, bubble volume and air dissolution, and the capillary pressure. According to Park and Lee [79], the process of microvoids compression in dual-scale fibrous reinforcements is considerably more delayed than the corresponding macrovoids compression due to the dissimilar permeabilities of the tows and channels; in general, almost any void process occurring inside the tows is more delayed than the corresponding process occurring in the channels, as it is also appreciated here in Section 5.3.1. As it was mentioned in [79], and confirmed in this work, the compression of the bubble inside the tow takes place provided that the air pressure at the fluid front is lower than the average liquid pressure surrounding the tow plus the magnitude of the capillary pressure, otherwise, the bubble moves inside the tow without changing its volume and could migrate towards the channels.

The conditions that lead to the void migration from the tow towards the channel have been studied in different numerical and experimental works. For instance, Lundstrom et al. [223] introduced the concept of critical bubble volume according to which the bubble compresses until a critical value where it is able to migrate into the channels as a result of the high pressure, and then it is transported along the channels. This concept was brought up later in the experimental work of Guorichon et al. [175] to explain the reduction of the microvoid content with the modified capillary number, C_a^*, in constant flow rate injections, after reaching a certain value of the inlet pressure; this value of pressure was identified as the critical pressure for the onset of void migration, P_c; for pressures below this value, no void migration is obtained. The concept of critical pressure was used in the development of a

numerical model to predict the dynamic void content in macroscopic simulations in Liquid Composites Molding processes (LCM) [5], [84], where the FEM/CV conforming technique was used to solve the governing equations. The critical pressure, P_c, was taken as an input parameter that modifies the equivalent fiber volume fraction appearing in the calculation of the fill factor of the Control Volumes (CV's), in such a way that when the pressure is greater than P_c in the CV, the equivalent fiber volume fraction is set to its initial value in order to consider the void elimination out of the tow. According to Yamaleev and Mohan [224], the increase of the liquid pressure not only favors the reduction of the void content because of the void compression, but also because it promotes the air dissolution into the liquid by molecular diffusion.

The void migration model presented in [79] suggests that the pressure gradient, $\Delta P/\Delta x$, is the same in the macropore (inter-tow space) and in the micropore (intra-tow porous space), and that the void migration is related with this pressure gradient and, consequently, with the average liquid velocity, $\langle u_g \rangle^g$. On the other hand, Lundstrom et al. [78] used the Monte Carlo method to solve the bubble transport equations and the Level Set Method to track the fluid front, finding that the wettability of the fibers favors the motion of the microvoids from the tows towards the channels and that the gas diffusion is the principal mechanism of microvoids elimination in points far upstream of the fluid front.

In the present chapter the Boundary Element Method (BEM) is applied in the problem of the dynamic evolution of voids formed in dual-scale fibrous reinforcements using a Stokes-Darcy formulation. The processes of compression, displacement, migration and splitting of intra-tow voids are analyzed at the mesoscopic level, i.e, considering the filling in a Representative Unitary Cell (RUC). It is assumed that the channel is fully filled of liquid before any infiltration can take place inside the tows, as it has been assumed in other works devoted to the filling simulations in LCM processes [8], [13], [14], [102], [225], [226]. This assumption is valid provided that the channel viscous velocity is considerably larger than the tow capillary velocity at the fluid front, which is more realistic when the channel is significantly more permeable than the tows and the injection pressure or flow rate are high enough to neglect the capillary effects at the macroscopic fluid front. This is a common particular case in real applications of LCM processes. The principal contributions of the present chapter can be summarized as follows:

- The simulation of void motion at both macroscopic and mesoscopic scales has been tackled by several numerical techniques: FEM/CV conforming [5], [79], [84], Monte Carlo Method [78], FEM/CV non-conforming [41], among others. The works using FEM/CV techniques require the domain discretization, whereas the present BEM approach only requires the use of a mesh along the contour of the problem. Additionally, as mentioned before, the tracking of the fluid front in FEM/CV techniques is carried out by assigning a fill factor to each control volume (CV) and using interface capturing schemes to approximate the shape of the fluid front. On the other hand, the numerical technique used to track the fluid front in [78] is the Level Set Method, where specific solvers for hyperbolic equations are required to find a signed distance function; additionally, a domain mesh is required and the accuracy of the fluid front position depends on the refinement of that mesh, in whose points the extended velocities need to be calculated [108]. The present numerical scheme to track the fluid front, see *Appendix C*, is much simpler, computational cheaper and assures a higher order accuracy of the fluid front shape since the fluid front position is directly obtained from the velocity field of the moving interface.
- To the best of the author's knowledge, the migration of the bubbles from the tows towards the channel at the mesoscopic scale has not been directly simulated, but considered in macroscopic simulations by stochastic approaches [78], phenomenological models involving experimental tests [4], [79], or experimental parameters, like the critical pressure, that account for the void migration in macroscopic simulations and are introduced as input parameters in the numerical codes [5], [84]. In the present chapter, the migration and splitting of intra-tow bubbles is simulated at the mesoscopic scale using BEM, and the influence of the average pressure $\left(\langle P_g \rangle^g\right)$, pressure gradient $(\Delta P/\Delta x)$ and surface tension (λ) on those processes is studied as well. Additionally, the behavior of the source term associated to the void migration is also analyzed, as well as the behavior of the ratio between the average void migration velocity, $\langle u_{air} \rangle$, and the average liquid velocity in the channel, $\langle u_g \rangle^g$. This ratio is important because it relates a variable that is difficult to measure, namely, the void migration velocity, with a straightforwardly measurable variable, namely, the average liquid velocity in the channel.

- In the composites area, when it is assumed that the channels are totally filled with liquid before the infiltration of the tows takes place, most of authors suppose a uniform pressure for the liquid in the channels in the mesoscopic simulations [8], [13], [14], [102], [225], [226]. This assumption is not physically consistent with the fact that the fluid in the channels is actually moving. Additionally, the processes of displacement at constant volume, migration and subsequent splitting of the intra-tow bubbles are not possible under this assumption since the fluid front moves towards the center of the tows, no matter the direction of the fluid velocity in the channels, causing that the bubbles remain trapped or disappear depending on the air entrapment parameter considered [11]. Some experimental and numerical researches have confirmed that the bubbles are not necessarily located at the center of tows and can even migrate towards the channel depending on the liquid pressure gradient and the internal pressure of the void [3], [25], [171], [175], [220], [227]. In the present chapter, the channel and tows are modeled using the Stokes and Darcy equations, respectively, a pressure gradient is considered along the RUC length and the matching conditions between the tows and the channels determine the filling of the former ones. In this way, descentered bubbles are formed inside the tows and the displacement, migration and splitting of those bubbles are possible, which is more consistent with the experimental researches.

5.2 Mathematical model and numerical techniques

The governing equations and matching conditions for the Stokes-Darcy formulation, which were presented in Eqs. 61-62 and 65-68, are applicable in this case. On the other hand, the boundary conditions can be classified into three types in the present case (See Figure 61):

- *Inlet and outlet conditions at the Stokes domain (channel or gap):*

$$t_1^{inl} = -p_{in}.\widehat{n_1},\ u_2 = 0 \tag{124a}$$

$$t_1^{out} = -p_{out}.\widehat{n_1},\ u_2 = 0 \tag{124b},$$

where t_1^{inl} and t_1^{out} are the inlet and outlet surface tractions in the horizontal direction, while p_{in} and p_{out} stand for the prescribed inlet and outlet pressures of the RUC.

- *No penetration conditions at the Darcy domains (tows):*

$$\partial p/\partial \hat{n} = 0 \tag{125}$$

- *Free-surface conditions at the both domains*: these conditions are applied at the moving boundaries between the liquid and air phases, which correspond to the fluid fronts inside the tows and to the bubble front in the channel when the void migration is present. Kinematic and dynamic conditions shown in Eqs.73 and 74a-b, respectively, are applied. Capillary pressures in the fluid fronts in the tows and in the bubble front in the channel when migration occurs, are computed as it was exposed in Chapter 3.

The Gebart's model [135] is also applied in this case for the calculation of the main tow permeabilities, K_1 and K_2, see Eqs.63a,b and 64a-c.

The integral equation formulations and all numerical considerations exposed in Section 3.3 are applicable as well to this particular problem.

5.3 Results

5.3.1 Stokes-Darcy approach for filling of tows assuming fully filled channels

Description of the problem.

The RUC geometry and boundary conditions considered here are shown in Figure 61, where three domains can be clearly differentiated: longitudinal tows (warps), transverse tow (weft) and channel. In dual-scale porous media, subscript "t" is commonly used to represent the tow domain, whereas "g" is employed to represent the channel domain since this is also referred in the literature as the gap domain [6], [8], [10]. The channels are totally filled with liquid while the tows impregnation occurs, and pressure boundary conditions are prescribed at the inlet and outlet of the RUC, generating a pressure gradient along the RUC length, which is the principal difference with previous works that have assumed fully filled channels, in which a uniform channel pressure has been considered instead [8], [13], [14], [102], [225], [226]. In this chapter, a full compressibility is deemed for the air inside the weft and the total saturation is thus not possible. For the warps, on the contrary, the air compression is not taken into account because it is considered that the air can displace towards the adjacent RUC in the flow direction considering that, when the problem is conceived at the macroscopic frame (filling of cavities), this adjacent RUC is less saturated than the analyzed RUC. Contrary to other works, the vacuum pressure, P_{vac}, is considered

here since it is usually applied in LCM processes and considerably facilitates the void compression.

The BEM code employed here was previously validated in Chapter 3 with the analytical solution of a coupled problem Stokes-Darcy developed in *Appendix B.*

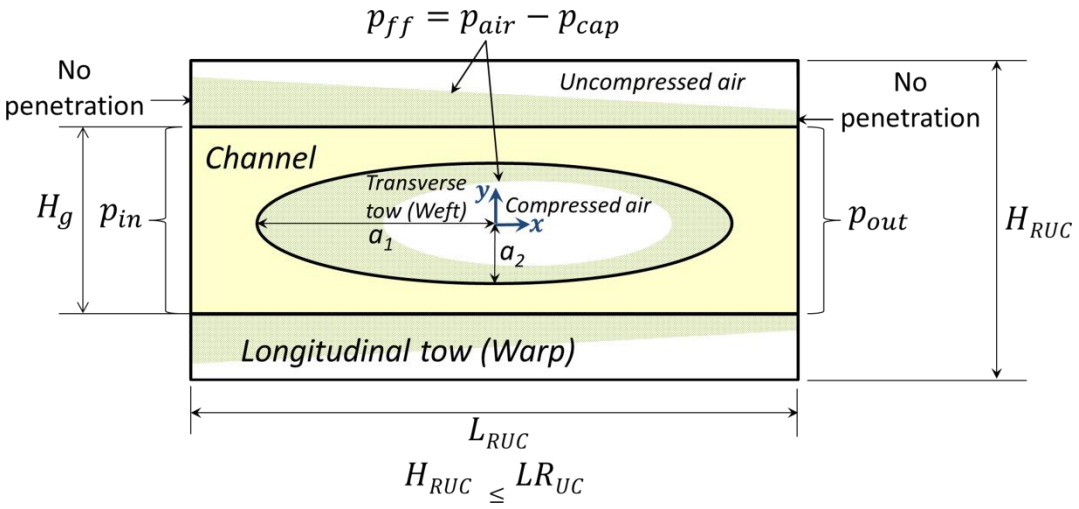

Figure 61 Scheme of the mesoscopic problem assuming full-filled channels

Simulation data.

To illustrate the principal differences between the classical approach, where the channel flow is not modeled and a uniform pressure is supposed in the channel, and the present approach, where the channel flow is modeled by the Stokes equation and it is prescribed a pressure gradient along the RUC, two BEM simulations are compared each other (Figure 62a-c and Figure 63a-k). In both simulations, for each instant of filling, they are shown the normalized time, i.e., the ratio between the real time and the total time of simulation (t/t_{sim}), the warps saturation (S_{warps}), weft saturation (S_{weft}) and total tows saturation (S_t); the x and y coordinates are reported in non-dimensional form as $x^* = x/L_{RUC}$ and $y^* = y/L_{RUC}$. The geometric and material inputs of both simulation are the same and they are shown in Table 17, where H_{RUC}, L_{RUC}, H_g, a_1, a_2, μ, K_1, K_2, λ, θ, R_f and ε_t stand for the height of the RUC, length of the RUC, height of the channel or gap, semi-major axis of the weft, semi-minor axis of the weft, liquid viscosity, major permeability, minor permeability, surface tension, contact angle, fiber radius and tow porosity. In Table 17 it is

also observed that in the classical approach (Figure 62a-c) a uniform channel pressure of $\langle P_g \rangle^g = 122\ kPa$ is prescribed, while in the present one (Figure 63a-k), inlet and outlet pressures of $p_{in} = 125.5\ kPa$ and $p_{out} = 118.5\ kPa$ are considered, which originate a pressure gradient along the RUC of $\Delta P/\Delta x = 5.83 \times 10^3\ kPa/m$, with a corresponding average pressure of $\langle P_g \rangle^g = 122\ kPa$, coinciding with the average pressure of the other approach. For the classical approach, Figure 62a-c, the air pressure is the atmospheric and it remains constant during the whole filling due to the full air dissolution assumption; in the current approach, Figure 63a-k, a vacuum pressure of $P_{vac} = -75\ KPa$ is taken into account and it remains constant in the warps due to the above exposed reasons, but changes in the weft in virtue of the air compression.

Table 17 Simulations data for comparison between the classical and the present approach for tows filling assuming full filled channels

Geometric and material data											
H_{RUC} (m)	L_{RUC} (m)	H_g (m)	a_1 (m)	a_2 (m)	μ (Pa.s)	K_1 (m^2)	K_2 (m^2)	λ (mN/m)	θ	R_f (μm)	ε_t
4.50 E-04	1.20 E-03	3.00 E-04	5.00 E-04	1.00 E-04	0.1	2.07 E-13	1.08 E-14	15	30°	20	0.15
Processing data											
Classical approach	Present Stokes-Darcy approach										
$\langle P_g \rangle^g$ (kPa)	p_{in} (kPa)		p_{out} (kPa)		$\Delta P/\Delta x$ (kPa/m)		$\langle P_g \rangle^g$ (kPa)		P_{vac} (kPa)		
122	125.5		118.5		5.83×10^3		122		-75		

Simulation of filling with the classical approach.

Several filling instants of the simulation with the classical approach are shown in the Figure 62a-c. As it is observed, the fluid front moves uniformly in the warps and the weft, towards the edges and towards the center of the RUC, respectively, which is logic since the pressure is the same in all points of the interface channel-tows. In this case, the warps saturate first (Figure 62b) and then, the total saturation is reached once the weft is completely filled (Figure 62c). Thus, according to this approach, the air in the weft escapes as the filling takes place (full air dissolution) and this leads to the total saturation of the RUC. However, this is an ideal case that does not necessarily correspond to the real process. The real

behavior of the air inside the bundles is still an open problem. According to the experimental research of Neacsu et al [228], this behavior ranges between the two extreme scenarios compared in this section: full air compressibility and full air dissolution. To consider the effects of air compressibility and air dissolution at the same time, experimental tests are required in order to determine a lumped function for the fraction of escaped air [163], [228], and this is out of the scope of the present work. However, as shown later, the assumption of full air compressibility allows considering the processes of bubble migration and splitting (which are not present in the situation of full air dissolution), coinciding with other experimental results that have reported the presence of those processes in the processing of composites by Liquid Composites Molding, LCM [175], [220], [223], [229].

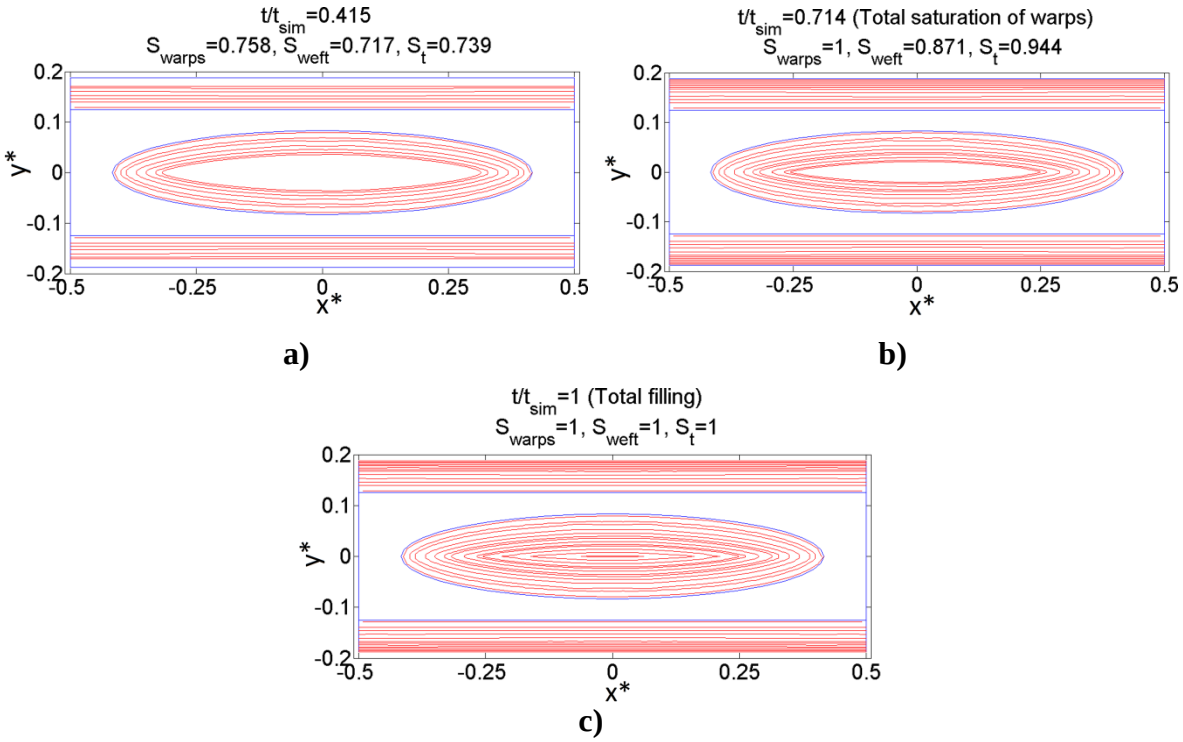

a) **b)**

c)

Figure 62 Instants of tow filling with the traditional approach. a) Warps and weft unsaturated, b) Total saturation of warps, c) Total saturation of the RUC

Simulation of filling with the current Stokes-Darcy approach.

For the current Stokes-Darcy approach, assuming full air compression in the weft, several instants of filling are represented in the Figure 63a-k. In the classical approach, under the assumption of full air dissolution, the void formation is not possible (Figure 62a-c), but, in the present case, three stages can be clearly identified in the dynamic void evolution in

Figure 63a-k: compression, displacement and migration. In the first stage (compression), conversely to the other approach, the fluid fronts in the warps are not parallel to the superior and inferior edges of the RUC, and the fluid front in the weft is slightly decentered, as it can be noticed by comparing the datatips of the Figure 63a among them. This phenomenon is logic because the inlet pressure is higher than the outlet pressure to be consistent with the flow direction in the channel; for larger pressure gradients, this phenomenon is more notorious. The filling of the warps occurs at a time instant equivalent to 2.7% of the total time of the simulation, but the permeation of the weft still remains in this time (Figure 63b). When the pressure of the trapped air inside the weft has reached the value of the average pressure of the liquid surrounding the weft plus the magnitude of capillary pressure, the air compression stops and the onset of void mobilization takes place (green line in Figure 63c). From this time instant until the onset of void migration, the change of the weft saturation, S_{weft}, is negligible and an equilibrium saturation, S_t^{eq}, is achieved, because the bubble moves towards the right extreme of the weft, changing its shape, without changing its volume (Figure 63d to Figure 63g). The details of Figure 63d and Figure 63f are shown in Figure 63e and Figure 63g, respectively, and are off-scale for visualization purposes; in these details the void displacement is represented by green lines. Small changes of S_{weft} during this process of void displacement are caused by numerical errors in the tracking of the fluid front, but they can be neglected. It is important to notice that, according to the BEM results, the compression of the void until the equilibrium saturation, S_t^{eq}, is reached (Figure 63a to Figure 63c) takes less time than the motion of the void towards the right edge of the weft (Figure 63d to Figure 63g). The first phenomenon lasts 13.3% of the total simulation time, whereas the second one takes almost the remaining time, namely, 86.7%.

As it can be observed in Figure 63f, when the flow reaches the right extreme of the weft, the normalized time is $t/t_{sim} = 1 - 2.80 \times 10^{-5}$, which is almost the unity because the time elapsed from this point until the end of the simulation, which corresponds to the partial migration of the bubble from the weft towards the channel, is much shorter than the times of the other two phenomena undergone before by the bubble (compression and displacement at constant volume), given that the order of magnitude of the velocities in the channel is considerably larger than the order of magnitude of the velocities inside the tows

due to the dissimilar permeabilities of these domains. The process of void migration can be seen in Figure 63h to Figure 63k. This process is governed by the difference between the capillary forces on the bubble surface and the pressure forces of the compressed air. The capillary forces depend on the surface tension, λ, and on the curvature of the bubble surface, κ, while the air pressure, P_{air}, decreases as the bubble expands in the channel. As observed in Figure 63k, the bubble tends to be ovoid-shaped in this case. The influence of the average pressure, pressure gradient and surface tension on the migration and splitting of the bubble is analyzed in the Section 5.3.2.

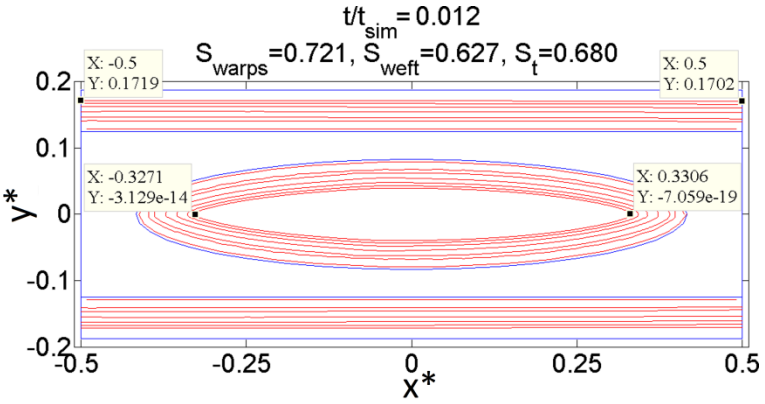

a)

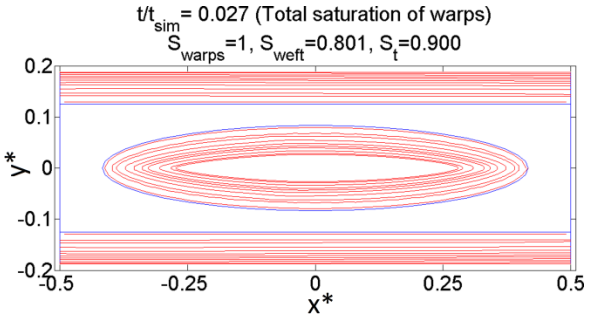

b)

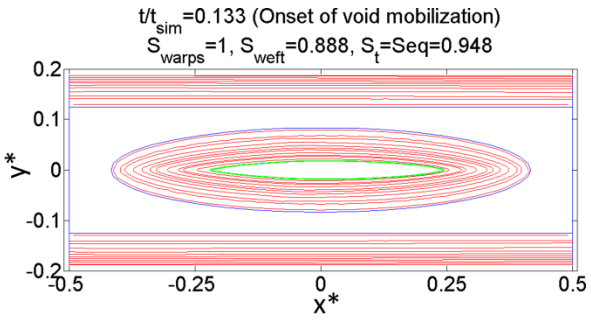

c)

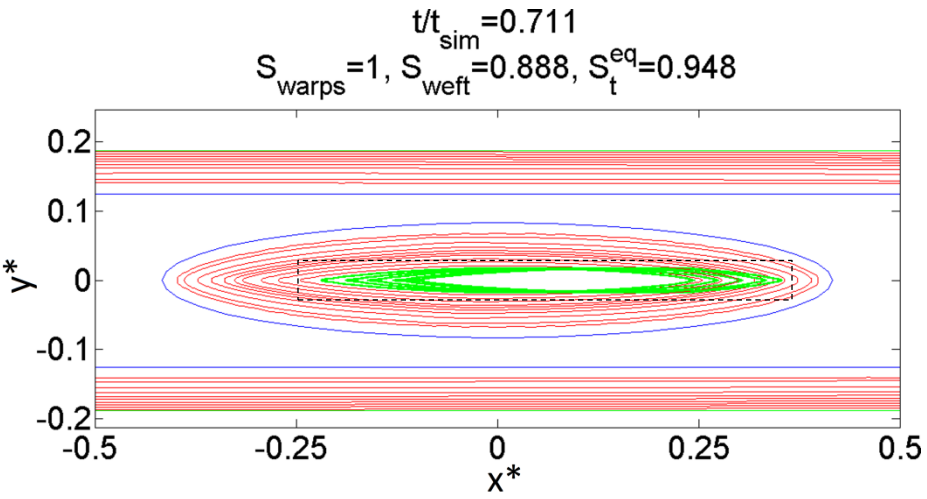
t/t_sim=0.711
S_warps=1, S_weft=0.888, S_t^eq=0.948
0.2
0.1
0
-0.1
-0.2
y*
-0.5
-0.25
0
0.25
0.5
x*

d)

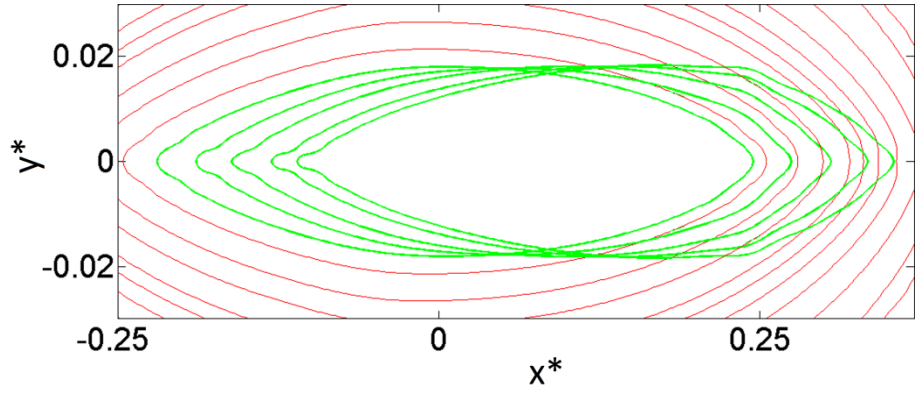
0.02
0
-0.02
y*
-0.25
0
0.25
x*

e)

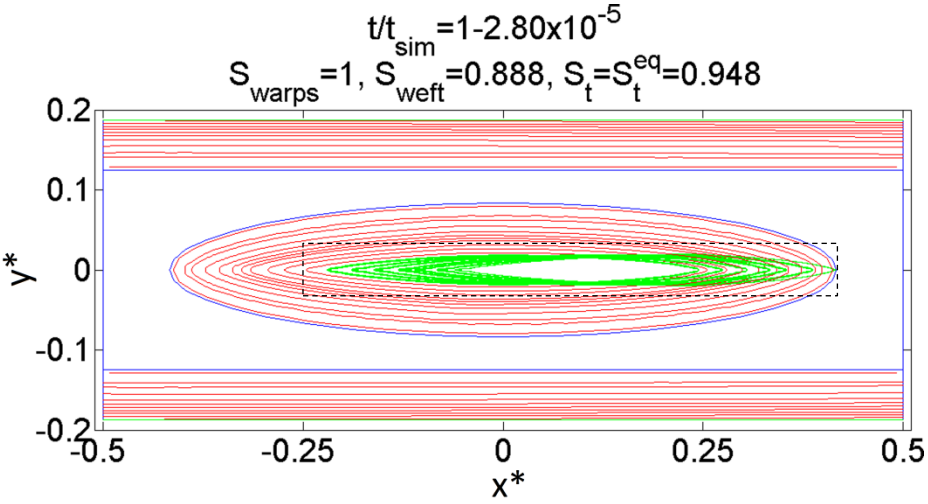
t/t_sim=1-2.80x10^-5
S_warps=1, S_weft=0.888, S_t=S_t^eq=0.948
0.2
0.1
0
-0.1
-0.2
y*
-0.5
-0.25
0
0.25
0.5
x*

f)

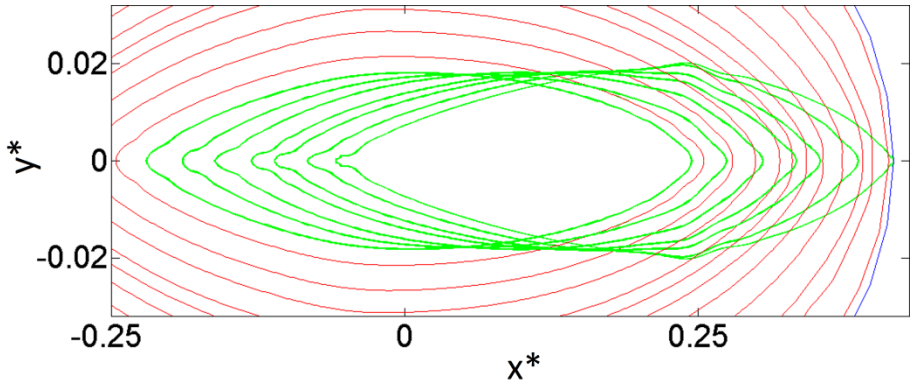
0.02
0
-0.02
y*
-0.25
0
0.25
x*

g)

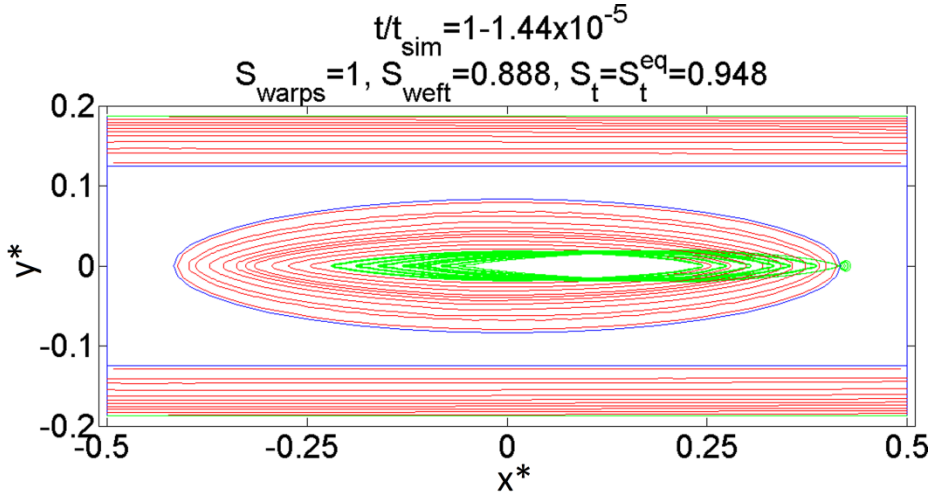
t/t_sim=1-1.44x10^-5
S_warps=1, S_weft=0.888, S_t=S_t^eq=0.948
0.2
0.1
0
-0.1
-0.2
y*
-0.5
-0.25
0
0.25
0.5
x*

h)

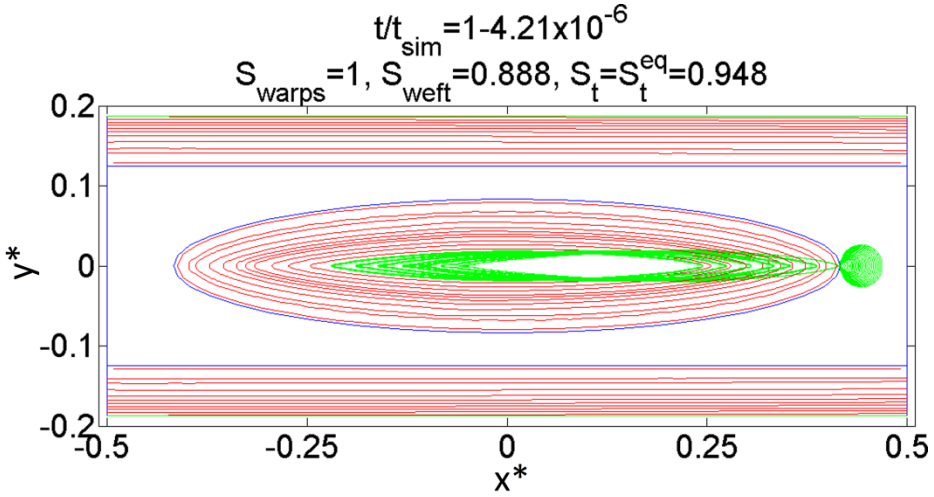
t/t_sim=1-4.21x10^-6
S_warps=1, S_weft=0.888, S_t=S_t^eq=0.948
0.2
0.1
0
-0.1
-0.2
y*
-0.5
-0.25
0
0.25
0.5
x*

i)

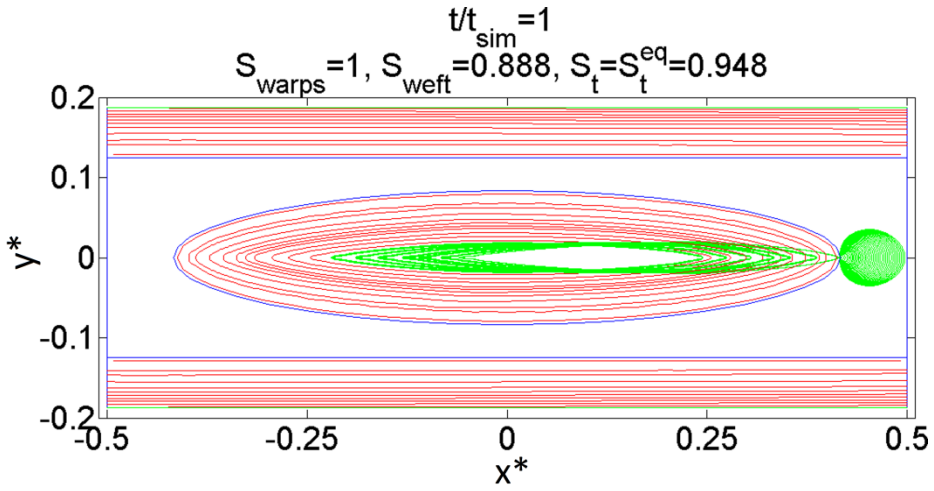

j)

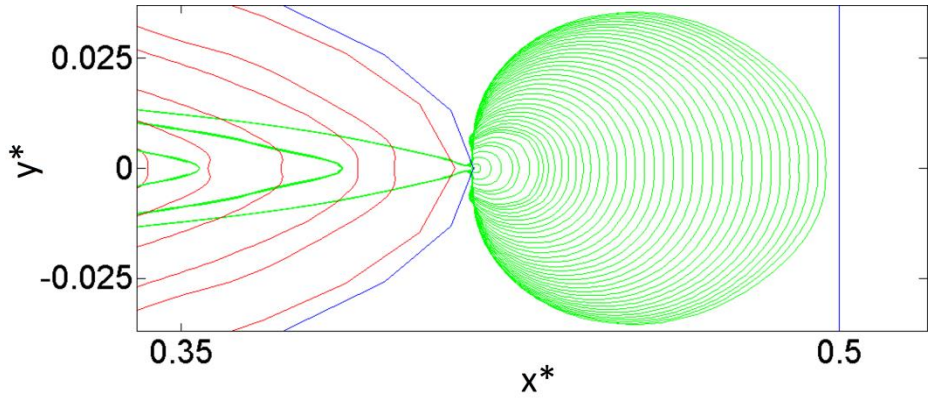

k)

Figure 63 Instants of tows filling with the current Stokes-Darcy approach assuming full air compressibility. a) Warps and weft unsaturated, b) Total saturation of warps, c) Instant of end of compression and onset of void mobilization, d) Motion towards right extreme of the weft, e) Detail of Figure 63d, f) Arrival of bubble to right extreme of the weft and onset of void migration, g) Detail of Figure 63f, h) Stage 1 of void migration, i) Stage 2 of void migration, j) Stage 3 of void migration (until bubble is in the neighborhood of the RUC's edge), k) Detail of void migration

Velocity fields and streamlines when the bubble is compressing.

The velocity fields and streamlines when the bubble is compressing inside the weft and the warps are totally saturated, that is, there is not mass transfer from the channels into the warps, are shown in the Figure 64a-h, where some figures are off-scale for visualization purposes. Several features can be identified in the Figure 64a-c for the channel domain. Firstly, the velocity vectors at the interface with the weft are almost tangential to such interface (See Figure 64b and Figure 64c), which means that the magnitude of the normal

penetration velocity into the weft is very small in comparison with the tangential velocity. It is also important to highlight the increment in the magnitude of the velocity with the reduction of the inter-tow space (Figure 64a-c) because this indicates that the effect of this reduction in the velocity field is more relevant than the effect of the liquid absorption into the tows that reduces the velocity magnitude along the RUC. Regarding the streamlines, the BEM code predicts that the inferior ones (nearby the lower edge of Figure 64a) tend to concentrate in the symmetric boundary as the inter-tow space reduces. In general, when a streamline traverse the whole RUC, it ends in a lower vertical position with respect to its starting vertical position and this is more notorious as the streamlines are closer to the symmetric boundary.

On the other hand, for the weft domain (Figure 64d-h) it can be appreciated that the velocity in the interface channel-weft is essentially normal to the interface; this means that the tangential Darcy velocity appearing in Eq. 66, $u_i^{(d)}$, is negligible in this particular case. It is also worth noting, by comparing the magnitudes of the velocity vectors along the interface channel-weft (Figure 64d), that the mass transfer is greater as the inter-tow space is lower, in such a way that the normal velocities at the interface channel-weft are larger in points close to the center of the weft, whereas they are smaller in the neighborhoods of the right and left edges of the weft. The mass transfer in the left half of the weft is barely greater than the mass transfer in the right half, but this difference is enough to generate a decentered bubble, as it was shown in the Figure 63a. As it can be appreciated in Figure 64h, most of the streamlines whose starting point has a horizontal position beyond the horizontal limits defined by the fluid front, converge in the right and left extremes of such a fluid front, and the starting points of these streamlines coincide with the points of low mass transfer, as it can be noticed by comparing Figure 64d and Figure 64h.

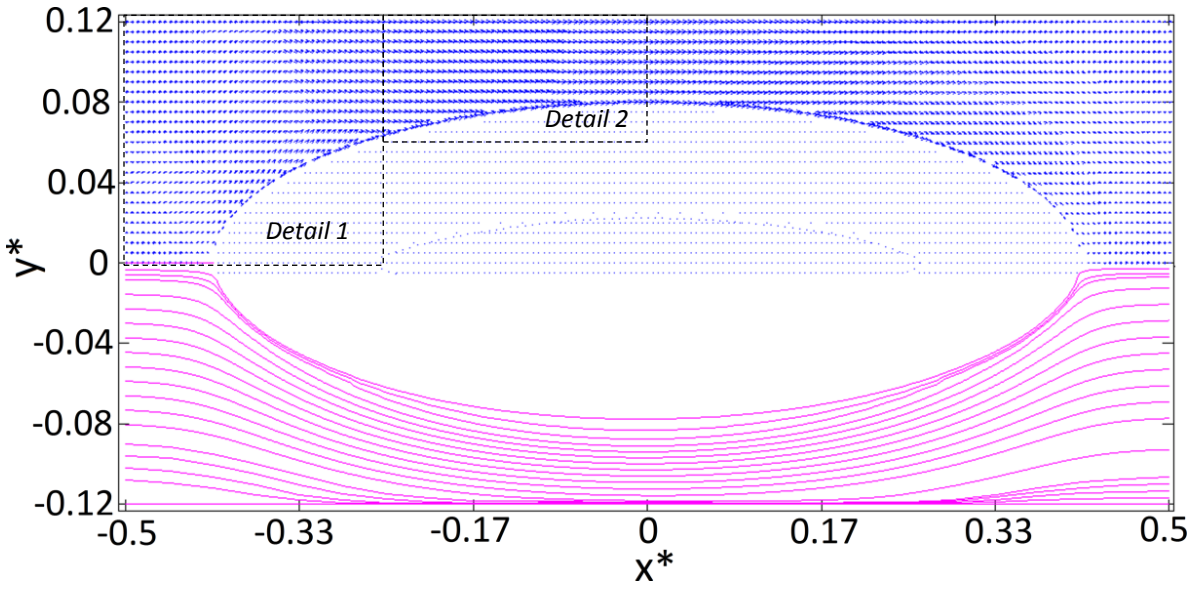
Detail 2
Detail 1
0.12
0.08
0.04
0
-0.04
-0.08
-0.12
y*
-0.5
-0.33
-0.17
0
0.17
0.33
0.5
x*

a)

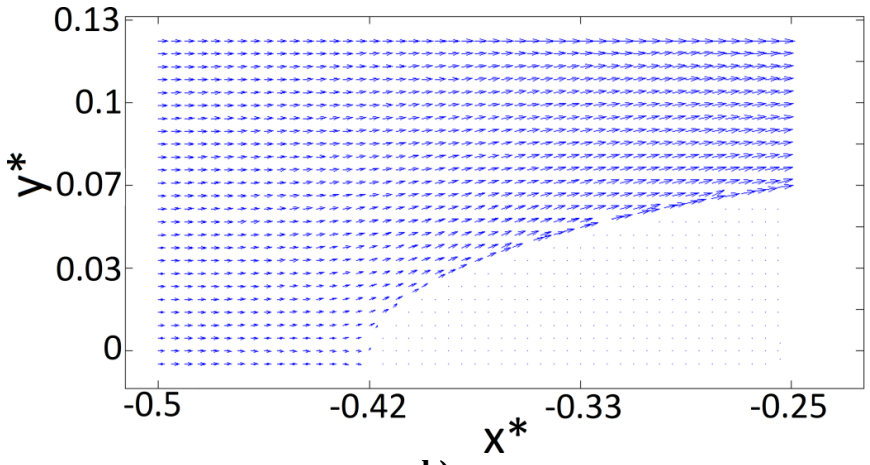
0.13
0.1
0.07
0.03
0
y*
-0.5
-0.42
-0.33
-0.25
x*

b)

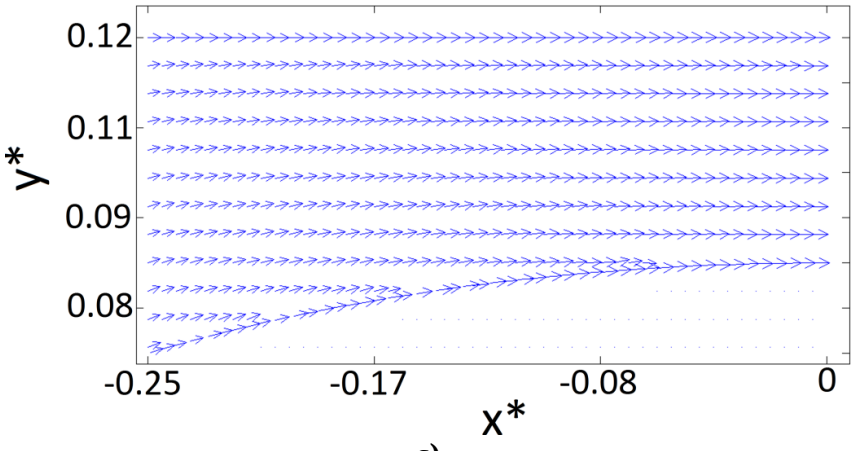
0.12
0.11
0.09
0.08
y*
-0.25
-0.17
-0.08
0
x*

c)

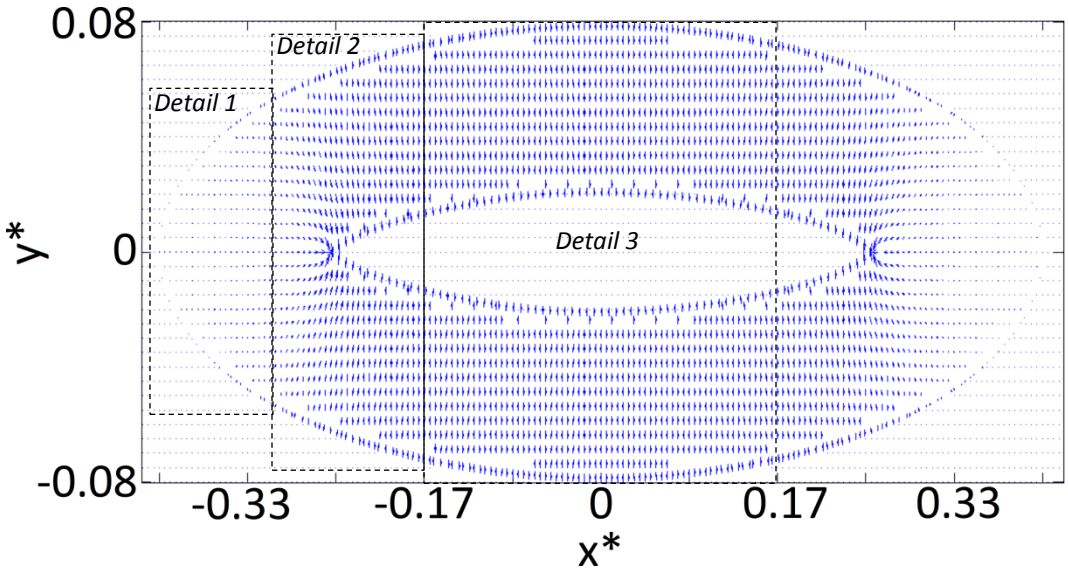
0.08
0
-0.08
y*
Detail 1
Detail 2
Detail 3
-0.33
-0.17
0
0.17
0.33
x*

d)

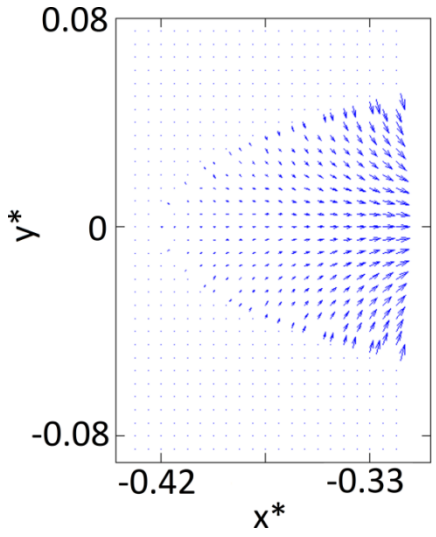
0.08
0
-0.08
y*
-0.42
-0.33
x*

e)

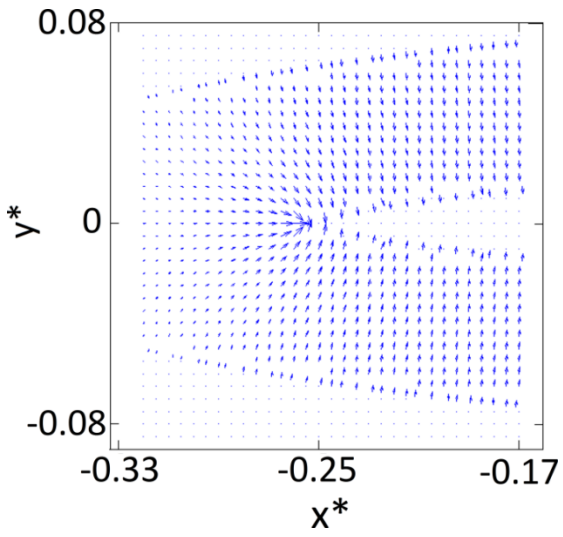
0.08
0
-0.08
y*
-0.33
-0.25
-0.17
x*

f)

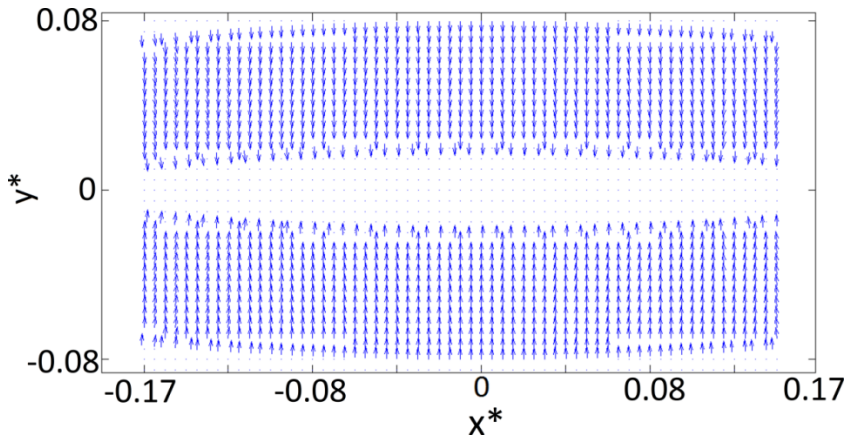
0.08
0
-0.08
y*
-0.17
-0.08
0
0.08
0.17
x*

g)

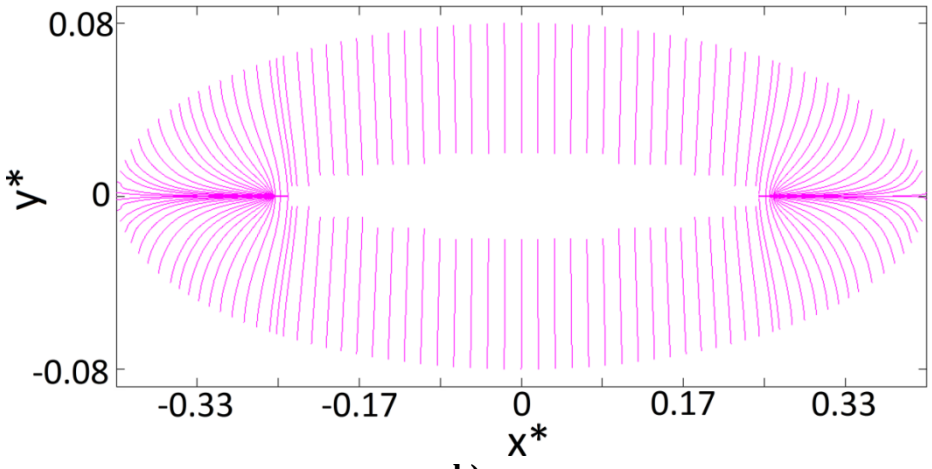

h)

Figure 64 Velocity field and streamlines when bubble is compressing. a) Velocity field and streamlines for the channel domain, b) Detail 1 of Fig. 64a, c) Detail 2 of Fig. 64a, d) Velocity field for the weft domain, e) Detail 1 of Fig. 64d, f) Detail 2 of Fig. 64d, g) Detail 3 of Fig. 64d, h) Streamlines for the weft domain

Velocity fields and streamlines when the bubble is migrating.

The velocity fields and streamlines when the bubble migration occurs are represented in Figure 65a-g. For the channel domain (Figure 65a,b), it can be appreciated that the highest velocities are obtained in the region of bubble migration, which means that the average air migration velocity, $\langle u_{air} \rangle$, is greater than the average liquid velocity in the channel, $\langle u_g \rangle^g$, for this particular case. However, this is not always the situation as it is shown later in Section 5.3.2. As observed in Figure 65a, the streamlines starting in the inlet boundary (violet lines) encounter with those ones starting in the contour of the partially escaped bubble (red lines) and this causes the accumulation of the former ones in the right inferior zone of the RUC. In the Figure 65a, likewise to the formerly commented case of void compression in the weft (Figure 64a), a high density of streamlines can be observed in the symmetric boundary of the RUC when the inter-tow distance is the smallest, namely, in the half of the RUC. On the other hand, for the weft domain (Figure 65c-f), the velocity magnitudes are larger in points whose horizontal position is between the horizontal limits defined by the fluid front, as in the last case analyzed (Figure 64d-g). In this case, the most of streamlines starting in the zone of low mass transfer at the channel-weft interface, where the normal velocities are smaller, converge in the left extreme of the fluid front (See Figure 65c). According to Figure 65g, in the right extreme of the weft, some streamlines are very

short since the interface channel-weft, where the streamlines start, is adjacent to the fluid front, where the streamlines finish.

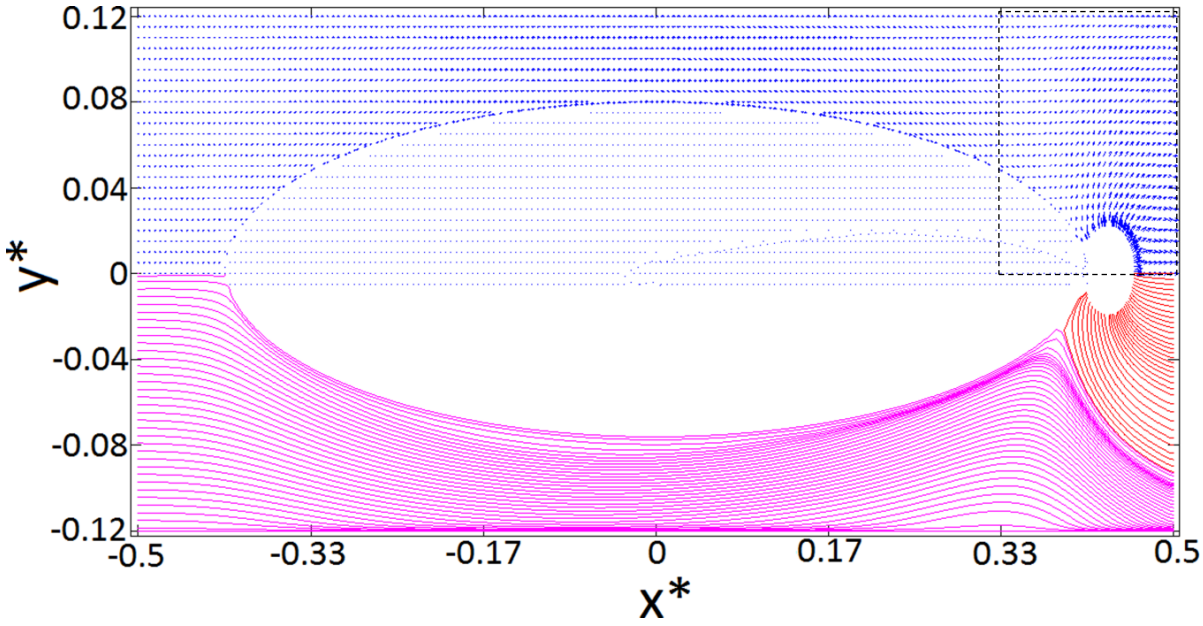

a)

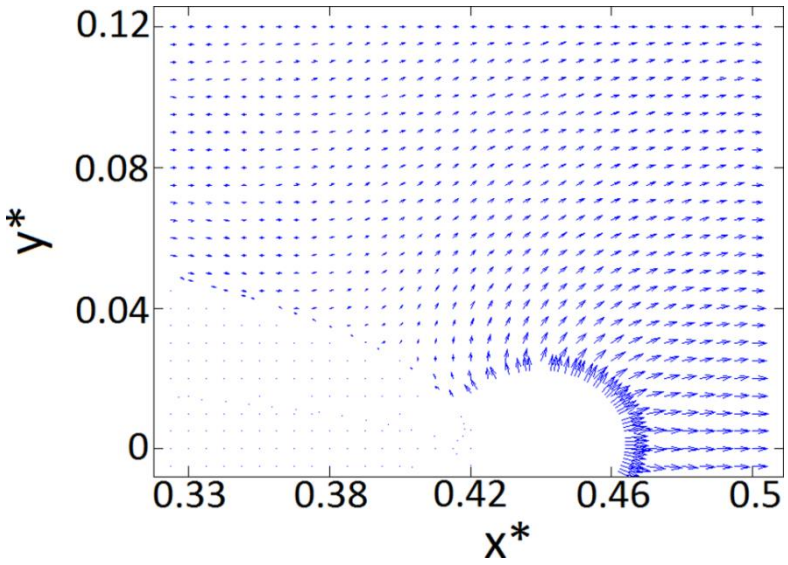

b)

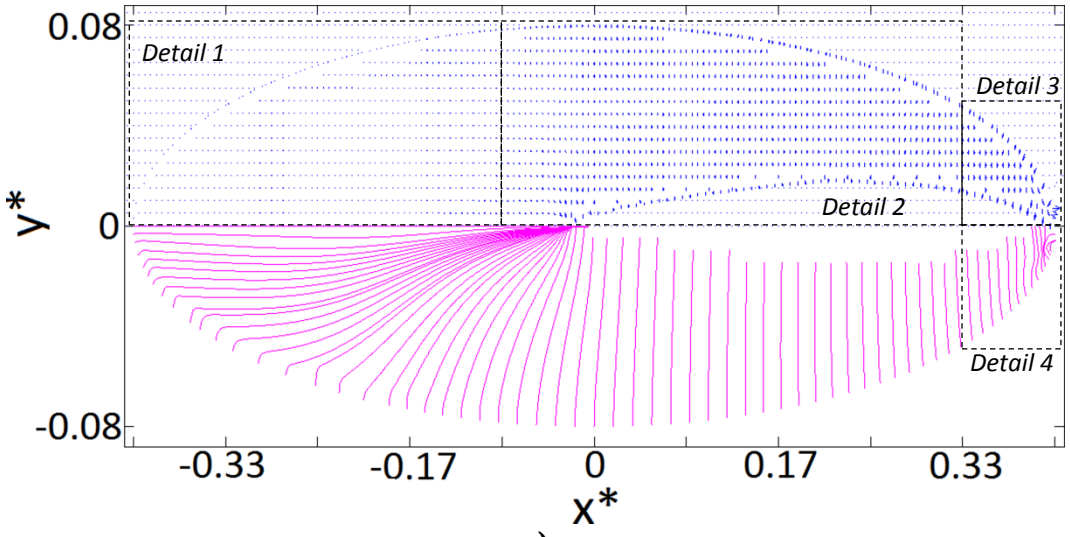
Detail 1
Detail 2
Detail 3
Detail 4
0.08
0
-0.08
y*
-0.33
-0.17
0
0.17
0.33
x*

c)

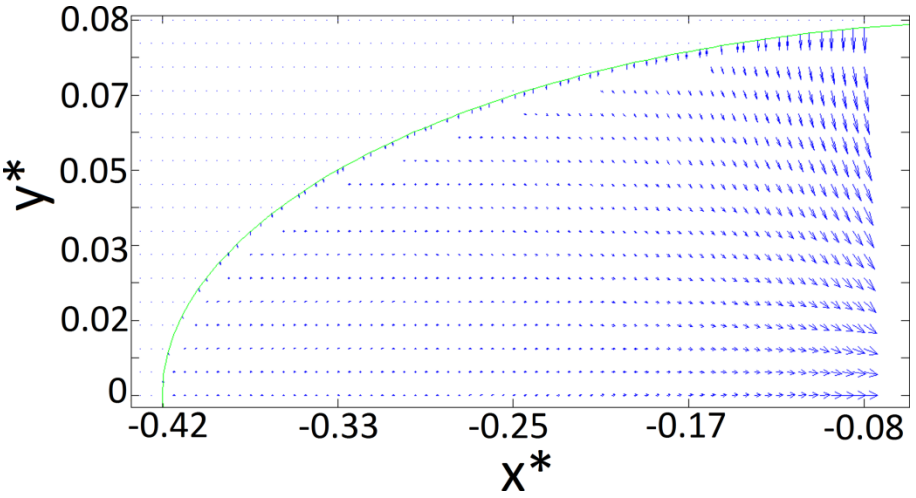
0.08
0.07
0.05
0.03
0.02
0
y*
-0.42
-0.33
-0.25
-0.17
-0.08
x*

d)

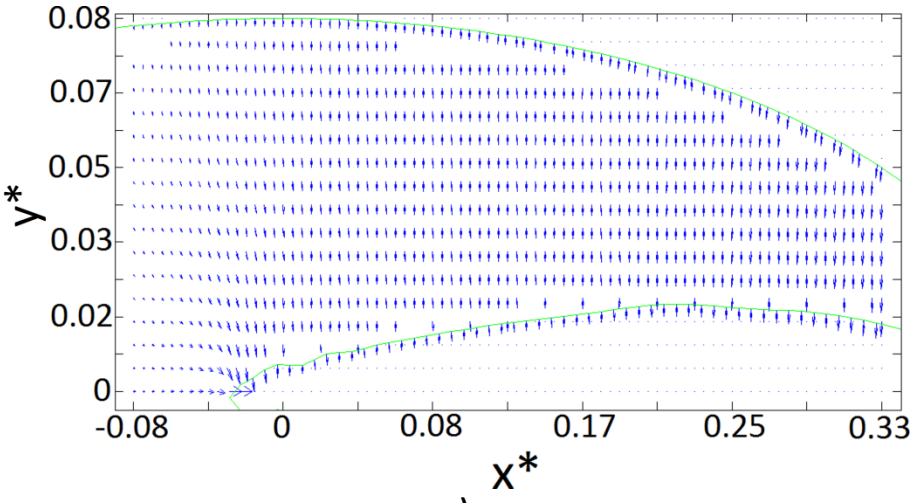
0.08
0.07
0.05
0.03
0.02
0
y*
-0.08
0
0.08
0.17
0.25
0.33
x*

e)

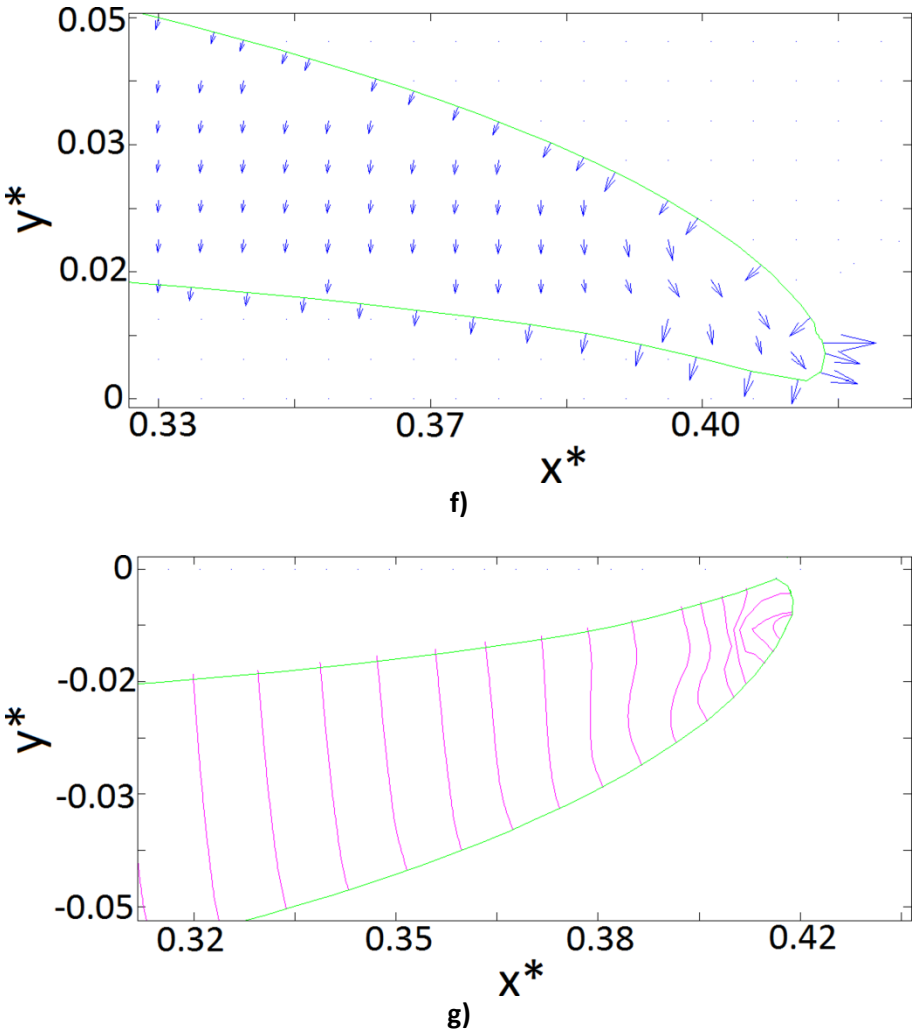

Figure 65 Velocity field and streamlines when bubble is partially escaping. a) Velocity field and streamlines for the channel domain, b) Detail of Fig. 65a, c) Velocity field and streamlines for the weft domain, d) Detail 1 of Fig. 65c, e) Detail 2 of Fig. 65c, f) Detail 3 of Fig. 65c, g) Detail 4 of Fig. 65c

5.3.2 Dynamic evolution of intra-tow void

Definition of the problem.

Two mechanism of transport of intra-tow voids are notable in dual-scale fibrous reinforcements: molecular diffusion and migration [230]. The first mechanism has been modeled by introducing an air entrapment parameter that takes into account the fraction of escaped air through the liquid [11]. The second mechanism is the mechanical migration of voids occurring from the tows towards the channels, which is the situation studied here.

The intra-tow void migration in dual scale fibrous reinforcements has been studied in [4], [5], [78], [79], [84], [175], [220]–[222], [230], [231]; there are several aspects that can be identified in those works and are the key to address the present analysis. Firstly, the void migration strongly depends on the balance between the interfacial and pressure forces on the bubble surface [221], [222], [230], [231]. The modification of the interfacial forces can be carried out by changing the surface tension of the liquid, λ; on the other hand, the air pressure inside the bubble, P_{air}, in the onset of void migration is the same as the pressure when the bubble reaches the equilibrium saturation, S_t^{eq}, thereby depending on the history of void compression, which in turn depends on the average pressure, $\langle P_g \rangle^g$, pressure gradient, $\Delta P/\Delta x$, and fluid penetrativity, $R_{fluid} = \lambda.cos(\theta)/\mu$. This last variable, R_{fluid}, relates the capillary and viscous forces intervening in the impregnation of the tows. It is important to mention that the air pressure inside the bubble decreases or increases obeying the ideal gas law, depending on the bubble expansion or compression, thereby changing the importance of the interfacial forces with respect to the pressure ones as the bubble evolves.

Another common aspect that has been considered in [4], [78], [79], [219], [222] is the relationship between the void velocity and the channel liquid velocity, being this last one directly related with the pressure gradient. For voids moving freely along the channels, some phenomenological models relating both velocities have been proposed [4], [79], [219], but, to the best of the author's knowledge, not too much effort has been focused in studying the relationship between the void migration velocity and the channel liquid velocity when the void moves from the tows towards channel. This relationship is concisely studied as part of the present analysis. Additionally, the effect of the change of the pressure gradient (which modifies the average liquid velocity) on the void migration is studied as well.

The third factor found in some researches is referred to the existence of a critical pressure for the void elimination, P_c [5], [84], [175]. The concept of critical pressure, P_c, was considered in [5], where the influence of this pressure on the saturation curves in macroscopic simulations was studied. To explain better this concept, one plot of [5] is extracted in Figure 66, where some saturation curves of constant flow rate injections in unidireccional cavities are represented. As it is observed in some curves, the unsaturated volume stabilizes at determined time instant, in which the critical pressure for void

elimination is reached. As the inlet flow rate is higher, the critical pressure, P_c, is reached faster; when P_c is achieved, the premise in [5] is that the air entrapment and air elimination rates are the same, generating a constant unsaturated volume until the cavity is totally filled, which happens when $t/t_{inj} = 1$ in Figure 66; from that moment onwards the unsaturated volume decreases due to the compression of the existing voids, until the equilibrium is attained in the voids. The concept of critical pressure for void elimination was also implemented in [81] in mesoscopic simulations and experimentally confirmed by [84]. In the present simulations, it is evaluated if the change of the average pressure in the channel, $\langle P_g \rangle^g$, could favor the void migration from the weft towards the channel to verify the concept of critical pressure.

In this Section 5.3.2, several cases are considered to analyze the influence of the aforementioned variables in the process of void migration.

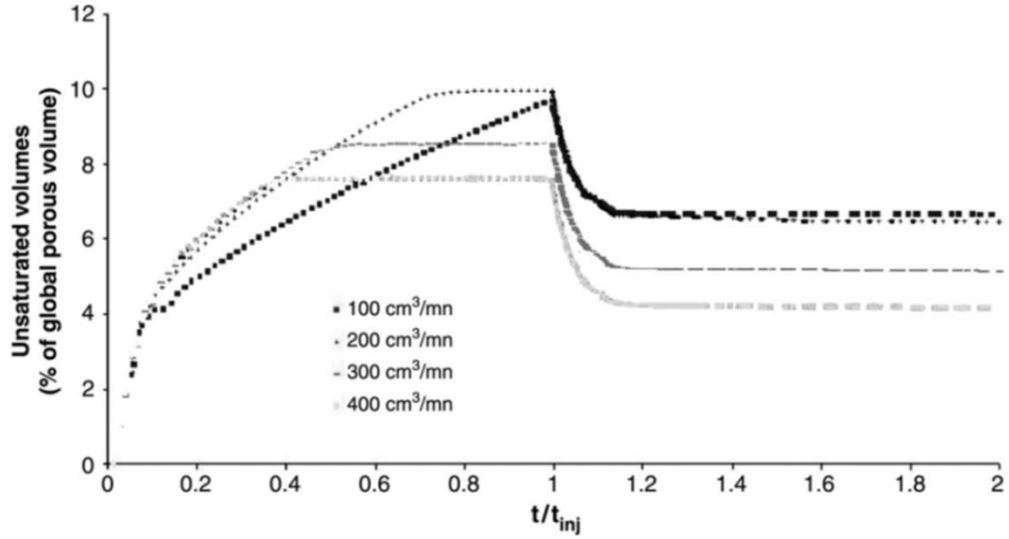

Figure 66 Plot of Unsaturated Volume vs. $\mathbf{t/t_{inj}}$ for several inlet flow rates. Source: Guorichon et al [5]

Case 1 of reference.

The geometric data $(H_{RUC}, L_{RUC}, H_g, a_1, a_2, R_f, \varepsilon_t, K_1, K_2)$ of the simulation of this *Case 1* are given in Table 17. The material and processing data are the following: $\mu = 0.1\ Pa.s$, $\lambda = 12mN/m$, $\theta = 30°$, $p_{in} = 105.5\ kPa$, $p_{out} = 98.5\ kPa$, $\langle P_g \rangle^g = 102kPa$ and $\Delta P/\Delta x = 5.83 \times 10^3\ kPa/m$. In the Figure 67a-e, it is detailed the bubble front evolution when the partial migration of air occurs, where it is observed that the bubble is ovoid-shaped at the end of the simulation (Figure 67e) like the one obtained in Figure 63k. In each

time instant, it is reported the ratio between the average air migration velocity, $\langle u_{air} \rangle$, and the intrinsic phase volume-averaged gap velocity (referred in this chapter as the average liquid velocity for sake of simplicity), $\langle u_g \rangle^g$, which is defined as follows:

$$r_1 = \frac{\langle u_{air} \rangle}{\langle u_g \rangle^g} = \frac{\left(\int_{\Gamma_{air}} u_{air}.d\Gamma_{air}\right)/\Gamma_{air}}{\left(\int_{A_g} (u_1)_g.dA_g\right)/A_g} \quad (126),$$

where $(u_1)_g$ is the pointswise horizontal liquid velocity in the gap or channel domain, A_g is the total area of the channel domain, Γ_{air} is the bubble front in the channel, i.e., the air-liquid interface in the channel, and $u_{air} = u_i^{air}.\hat{n}_i^{air}$ is the pointwise air migration velocity, with $\hat{n}_i^{air}$ and u_i^{air} as the "i" components of the normal vector and of the air velocity, respectively, at the interface Γ_{air}. Additionally, in Figure 67a-e, they are reported the air pressure, P_{air}, and the normalized air migration rate defined as $\langle S_g^v \rangle_{norm} = \langle S_g^v \rangle / \langle S_g^v \rangle_{max}$, where $\langle S_g^v \rangle$ is the source term that appears in the void convection equation, Eq.129 [4], [79] and $\langle S_g^v \rangle_{max}$ is the maximum value of $\langle S_g^v \rangle$ during the whole simulation. In this case, $\langle S_g^v \rangle$ accounts for the rate of air added from the tow into the channel per unit of RUC volume, as follows:

$$\langle S_g^v \rangle = (1/V_{RUC}) \int_{A_{gt}^v} (u_i^v)_{gt}.(\hat{n}_i^v)_{gt} dA_{gt}^v \quad (127),$$

where V_{RUC} is the total volume of the RUC and A_{gt}^v is the area of the portion of the channel-tow interface where air migration occurs, while $(u_i^v)_{gt}$ and $(\hat{n}_i^v)_{gt}$ are the "i" components of the air velocity and normal vector, respectively, at the channel-tow interface. Considering mass conservation on the domain corresponding to the migrating bubble, the source term, $\langle S_g^v \rangle$, can be computed here as follows:

$$\langle S_g^v \rangle = (1/V_{RUC}) \int_{\Gamma_{air}} u_{air}.d\Gamma_{air} \quad (128),$$

To understand better the meaning of $\langle S_g^v \rangle$, it is necessary to consider Eq. 129, which is a macroscopic, convective-type equation that has been used by several authors to model the air content in the gaps or channels, $\langle \varphi_g \rangle$ [4], [79]. In this equation, $\langle u_i^v \rangle$ is the volume-averaged void velocity in the channel, which, according to experimental works [4], [89], [219], is closely related to the average liquid velocity in the channel, $\langle u_g \rangle^g$, as shown in Figure 68, where it is observed that after the average liquid velocity, $\langle u_g \rangle^g$, reaches a critical value, i.e., $\langle u_g \rangle^g \geq \langle u_g^{crit} \rangle^g$, voids start moving faster along the channels than the

liquid. On the other hand, in Eq. 129, $\langle S_g^v \rangle$ is a source term that takes into account the contributions of air into the channel or gap domain, which can be made by the initial air content of the liquid, the evaporation of chemical volatile gases and/or the migration of air from the tows towards the channel, being the last one the contribution analyzed here.

$$\frac{\partial \langle \varphi_g \rangle}{\partial t} + \frac{\partial}{\partial x_i}\left(\langle u_i^v \rangle \langle \varphi_g \rangle\right) = \langle S_g^v \rangle \tag{129}$$

Summarizing, the source term, $\langle S_g^v \rangle$, indicates the amount of air passing from the tow toward the channel (Eq.127), while the ratio r_1 represents how fast this air migration happens with respect to the average liquid velocity (Eq.126). In Figure 67a-e, the reported results of P_{air}, r_1 and $\langle S_g^v \rangle_{norm}$ in each figure correspond to the last bubble front.

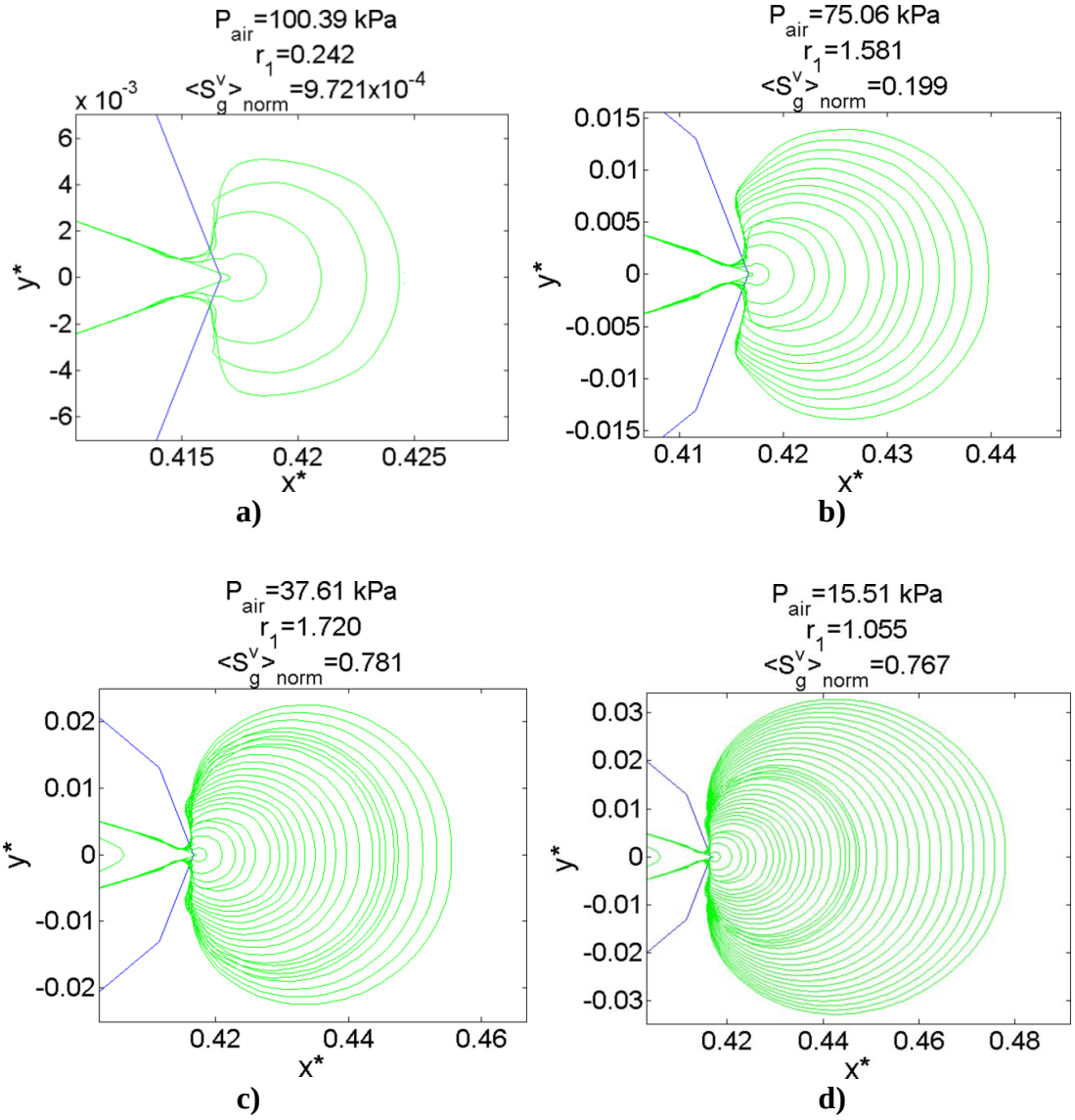

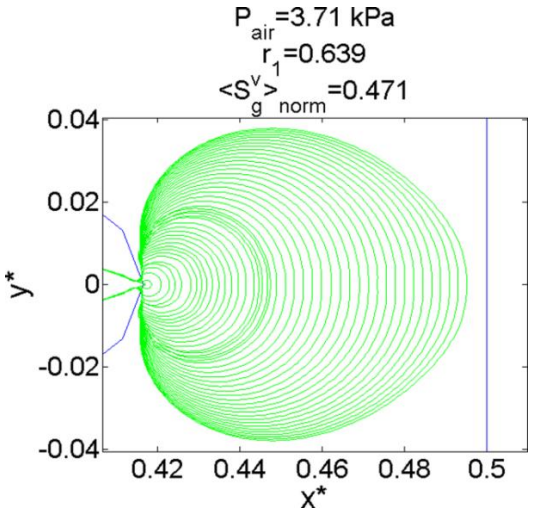

e)

Figure 67 Instants of air migration from the tows towards the channel for the Case 1 (Reported values of P_{air}, r_1 and $\langle S_g^v \rangle_{norm}$ in each figure correspond to the last bubble front). a) t/t_{total} =0.112, b) t/t_{total} =0.476, c) t/t_{total} =0.765, d) t/t_{total} =0.922, e) t/t_{total} =1.0

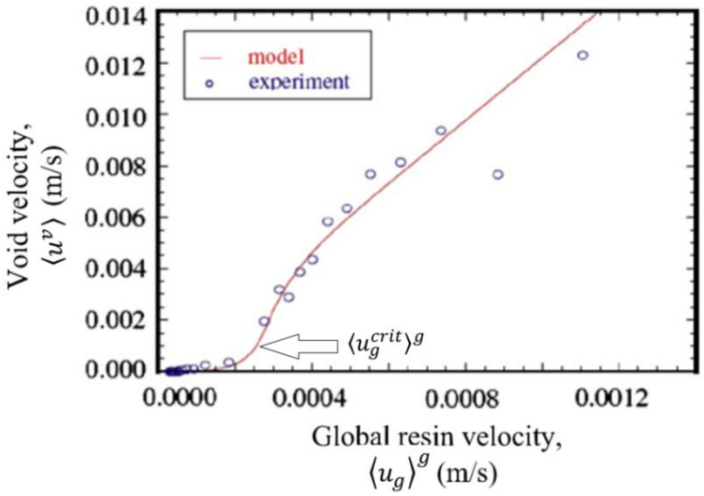

Figure 68 Relationship between the void velocity in channel, $\langle u_v \rangle$ and the resin velocity, $\langle u_g \rangle^g$. Source: Park et al. [79]

Having clarified the meaning of r_1 and $\langle S_g^v \rangle_{norm}$, the evolution of these quantities in the normalized time, t/t_{total}, is represented in the Figure 69a and Figure 69b, respectively, where the initial time instant corresponds to the onset of void migration and t_{total} is the total time of simulation of the void evolution in the channel. According to Figure 69a, the ratio r_1 is initially less than one, which means that void migrates at a lower average velocity

than the average liquid velocity in the channels. However, r_1 increases so that the air migration velocity becomes faster than the liquid velocity after $t/t_{total} = 0.231$, approximately. Then, the increment of r_1 continues until $t/t_{total} = 0.399$; in this time instant, $\langle u_{air} \rangle$ is 1.581 times greater than $\langle u_g \rangle^g$. The behavior of r_1 between $t/t_{total} = 0.399$ and $t/t_{total} = 0.751$ can be characterized by having a zone where r_1 is almost constant, another one where an oscillation is noticed and a peak point where r_1 reaches its maximum value. In this peak point, $\langle u_{air} \rangle$ is 1.718 times greater than $\langle u_g \rangle^g$. After this point, r_1 decreases with the time and it becomes less than one again in $t/t_{total} = 0.935$, approximately. At the end of the simulation, $\langle u_{air} \rangle$ is 0.639 times the value of $\langle u_g \rangle^g$.

On the other hand, the Figure 69b represents the behavior of the normalized void migration rate, $\langle S_g^v \rangle_{norm}$, with the normalized time, t/t_{total}. At the beginning of the simulation, $\langle S_g^v \rangle_{norm}$ slightly increases until $t/t_{total} = 0.133$. From $t/t_{total} = 0.133$ to $t/t_{total} = 0.564$, three well-differentiated zones of almost constant increment of $\langle S_g^v \rangle_{norm}$ can be observed. After $t/t_{total} = 0.564$, the increment of $\langle S_g^v \rangle_{norm}$ is more pronounced until it reaches practically the maximum value in $t/t_{total} = 0.828$, remaining essentially constant until $t/t_{total} = 0.86$. Thereupon, $\langle S_g^v \rangle_{norm}$ decreases until the end of the simulation.

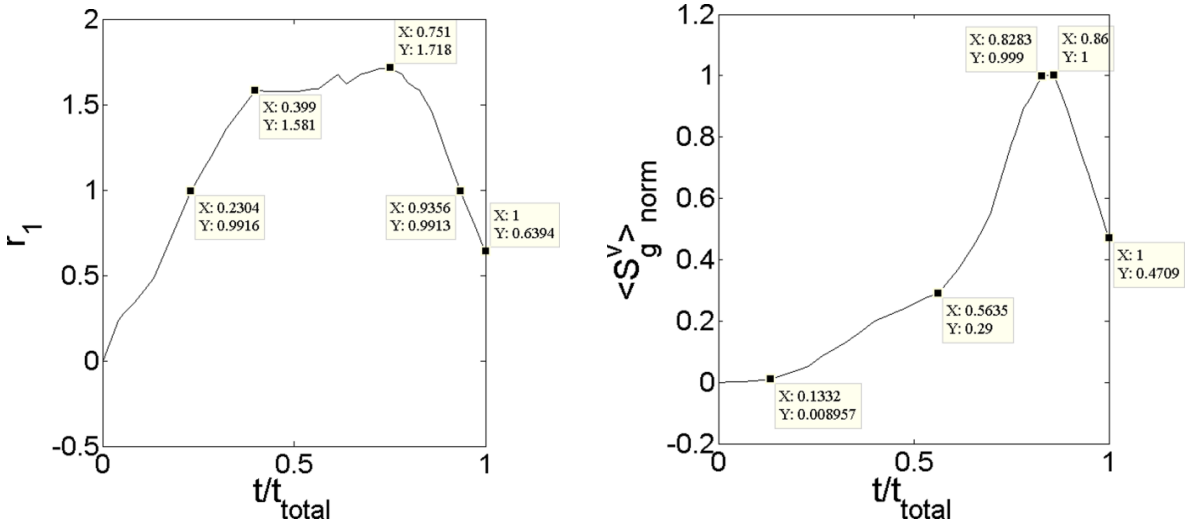

a) **b)**

Figure 69 Behavior of r_1 and $\langle S_g^v \rangle_{norm}$ in the time for the Case 1. a) Plot r_1 vs. t/t_{total} for Case 1, b) Plot of $\langle S_g^v \rangle_{norm}$ vs. t/t_{total} for Case 1

Two important things are worth noting in the curves of Figure 69a,b. If the ratios r_1 of Figure 69a are compared to the ratios $\langle u^v \rangle / \langle u_g \rangle^g$ obtained from Figure 68, it can be concluded that the ratio between the void velocity and the average liquid velocity in the channel is considerably higher when the voids move freely along the channels, i.e., after the critical velocity, $\langle u_g^{crit} \rangle^g$, has been reached (Figure 68), than when they migrate from the tows towards the channel (Figure 69a). In other words, it can be asserted that, for a certain liquid velocity, the process of void migration from the tows towards the channel is considerably slower than the process of void motion freely along the channels, which is agreement with the results obtained by Lundstrom et al [78].

The second aspect to be noticed in Figure 69a and Figure 69b is that the reduction of r_1 and $\langle S_g^v \rangle_{norm}$ with t/t_{total} at the end of these curves poses the question whether it is possible or not to obtain negative values of r_1 and $\langle S_g^v \rangle_{norm}$ under other conditions, which would denote a contraction of the bubble. To tackle this issue, the surface tension of the liquid is modified to $\lambda = 16\, mN/m$ and another simulation is run in the *Case 2* keeping constant the other data.

Case 2: Increase of the surface tension of the liquid, λ

For the case where the liquid has a surface tension of $\lambda = 16\, mN/m$ several instants of the void evolution are shown in the Figure 70a-d. As in Figure 67a-d, the reported values of P_{air}, r_1 and $\langle S_g^v \rangle_{norm}$ in each figure correspond to the last bubble front. A bubble expansion can be noticed in the Figure 70a, where the last front of the bubble corresponds to the normalized time $t/t_{total} = 0.325$, in which the air pressure is $P_{air} = 41.65\, kPa$, while $r_1 = 1.546$ and $\langle S_g^v \rangle_{norm} = 1$, that is, the void migration rate reaches its peak in this point. From the beginning of the air migration until this instant, the air pressure continuously reduces because of the expansion of the void. Then, in the first four bubble fronts of the Figure 70b *(green lines)*, the bubble is still expanding in almost all directions, but, in the fifth bubble front *(red line)*, an important contraction in some points of the bubble contour can be appreciated. The time where this localized contraction occurs is $t/t_{total} = 0.423$, with corresponding values of $P_{air} = 8.46\, kPa$, $r_1 = 0.323$ and $\langle S_g^v \rangle_{norm} = 0.240$, which means that the void is migrating at a lower velocity with respect to the average liquid

velocity and it is still increasing in volume, but this expansion is decelerating. The bubble continues expanding, each time slower, until $t/t_{total} = 0.504$ (See Figure 71a,b). The bubble evolution from $t/t_{total} = 0.504$ until $t/t_{total} = 0.692$ is shown in Figure 70c, where, for a better understanding, the void evolution is represented from the darker to the lighter line. The values of the P_{air}, r_1 and $\langle S_g^v \rangle_{norm}$ for the bubble fronts of this figure are: $P_{air} = [6.38, 8.49, 13.51, 25.84, 41.02]$, $r_1 = [0, -0.036, -0.179, -0.338, 0]$, $\langle S_g^v \rangle_{norm} = [0, -0.018, -0.125, -0.246, 0]$. The increment of the air pressure in these instants indicates that the bubble is compressing, but the zero values of r_1 and $\langle S_g^v \rangle_{norm}$ corresponding to the last instant (lighter line in Figure 70c), where $t/t_{total} = 0.692$, indicate that the bubble will undergo an expansion just after this time. It is important to mention that the negative values of r_1 and $\langle S_g^v \rangle_{norm}$ in the three intermediate instants of Figure 70c mean that the net air flow rate has been reversed, thereby going from the channel towards the tows (bubble contraction). In the last part of the simulation, which is shown in Figure 70d and where the bubble evolution is also represented from the darker to the lighter line, one cycle of expansion and another of contraction take place, and, contrary to the bubble observed in Figure 67e, the final bubble tends to be long drop-shaped. The last analysis allows concluding that when the interfacial forces on the bubble surface are relevant with respect to the pressure ones, the surface tension of the injected liquid has an important influence on the dynamic evolution (expansion and compression cycles) and shape of the intra-tow voids that migrate from the tows towards the channel.

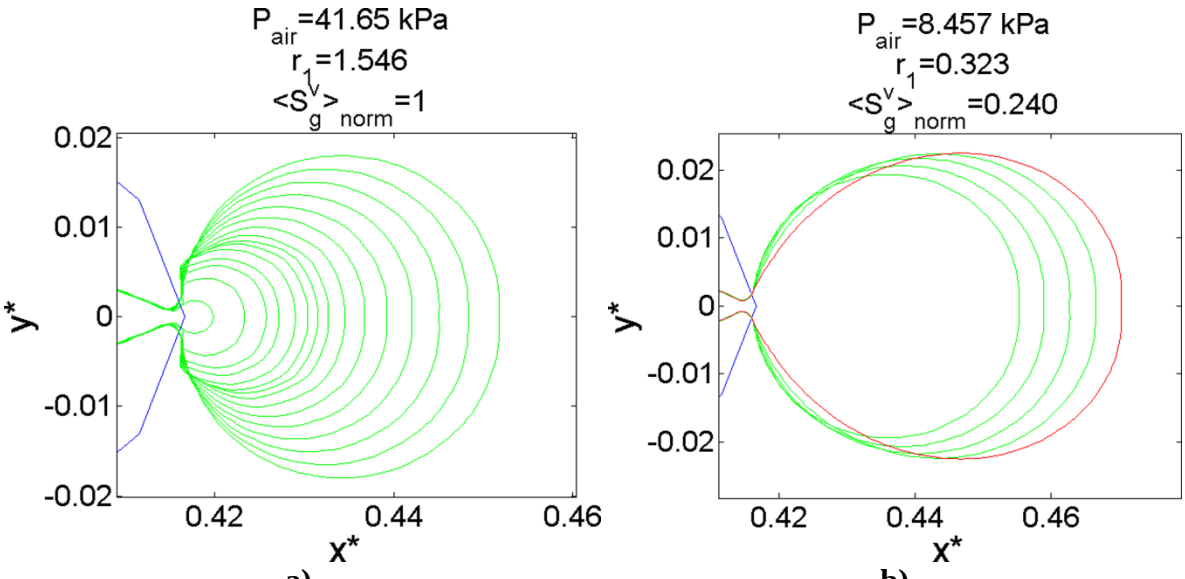

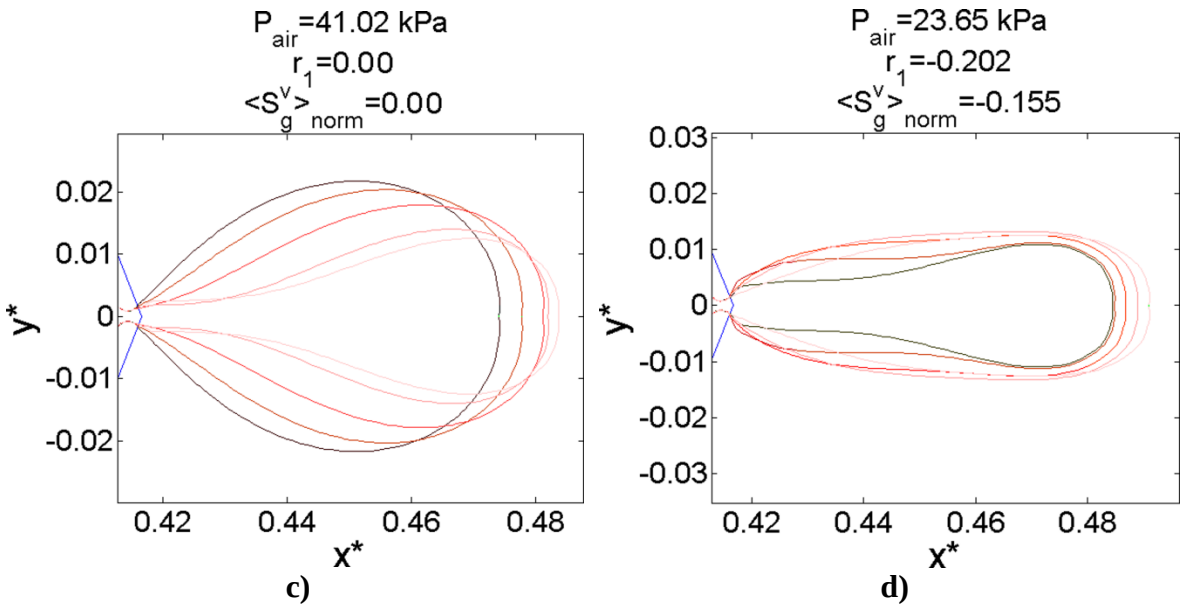

Figure 70 Instants of air migration from the tows towards the channel for Case 2, λ=16mN/m (Reported values of P_{air}, r_1 and $\langle S_g^v \rangle_{norm}$ in each figure correspond to the last bubble front). a) From t/t_{total} =0 to t/t_{total} =0.325, b) From t/t_{total} =0.363 to t/t_{total} =0.423, c) From t/t_{total} =0.504 to t/t_{total} =0.692, d) From t/t_{total} =0.764 to t/t_{total} =1.0

The plots of r_1 $vs.\, t/t_{total}$ and $\langle S_g^v \rangle_{norm}$ $vs.\, t/t_{total}$ for the simulation of the Figure 70 are represented in Figure 71a and Figure 71b, respectively. The general behavior of these curves until $t/t_{total} = 0.504$ is very similar to the behavior obtained for the curves of Figure 69a and Figure 69b, respectively. Afterwards, r_1 and $\langle S_g^v \rangle_{norm}$ can assume negative values, which means that the void is compressing. Then, these quantities become positive again, from $t/t_{total} = 0.692$ to $t/t_{total} = 0.929$, which indicates one cycle of bubble expansion, and finally, they are negatives again, from $t/t_{total} = 0.929$ to the end of the simulation, corresponding to a cycle of bubble contraction. The Figure 71a shows that $\langle u_{air} \rangle$ can exceed $\langle u_g \rangle^g$ only in some time instants of the first cycle of bubble expansion; the maximum value of $\langle u_{air} \rangle$ is 1.696 times the value of $\langle u_g \rangle^g$. It is important to remark that during the bubble contraction cycles of Figure 71a, the magnitude of the average air velocity, $|\langle u_{air} \rangle|$, always remains lower than the liquid velocity, $\langle u_g \rangle^g$. On the other hand, Figure 71b has the same cycles of bubble expansion and contraction as Figure 71a and the slopes appearing in that figure account for the acceleration or deceleration of the bubble expansion or contraction. Several zones can be distinguished in Figure 71b. For the first cycle of bubble expansion, the maximum increments of the void expansion rate

(acceleration) arise between $t/t_{total} = 0.235$ and $t/t_{total} = 0.325$, and the maximum decelerations ensue immediately after, between $t/t_{total} = 0.325$ and $t/t_{total} = 0.416$, approximately. In the first cycle of bubble contraction, the increment of the void compression rate takes place between $t/t_{total} = 0.504$ and $t/t_{total} = 0.634$, whereas this rate diminishes between $t/t_{total} = 0.634$ and $t/t_{total} = 0.692$. In this last time instant, as it was abovementioned in the analysis of Figure 70, the second cycle of bubble expansion starts and it is characterized by a pronounced acceleration and the subsequent deceleration. Then the void compression takes place again in $t/t_{total} = 0.929$ until the end of the simulation.

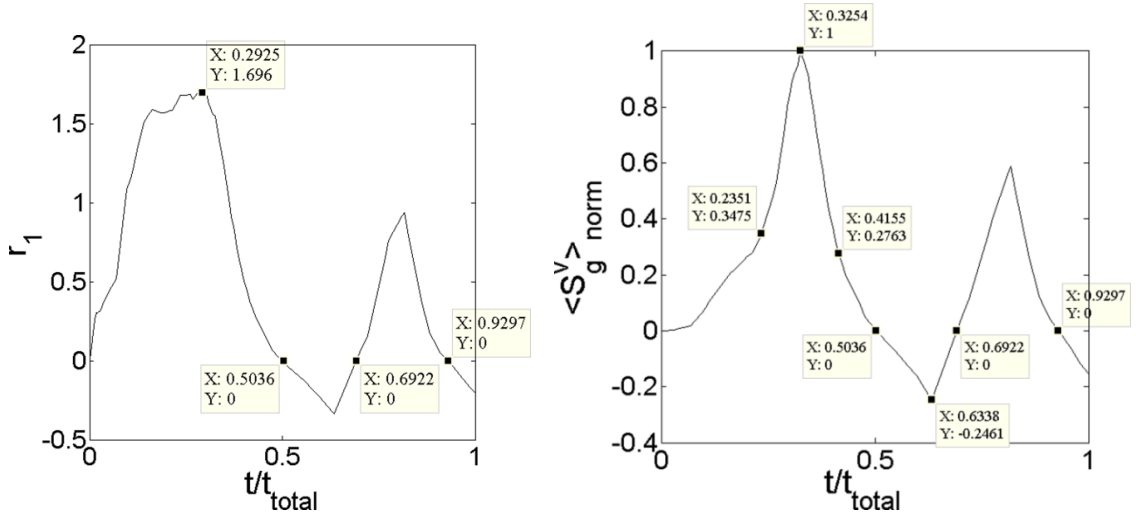

a) **b)**

Figure 71 Behavior of r_1 and $\langle S_g^v \rangle_{norm}$ in the time for the Case 2, λ=16 mN/m. a) Plot r_1 vs. t/t_{total} , b) Plot of $\langle S_g^v \rangle_{norm}$ vs. t/t_{total}

Case 3: Void migration is not possible

As it was aforementioned, most of authors have found that the void migration is highly dependent on the balance between the interfacial and pressure forces. If the last simulation, *Case 2*, is run with a surface tension of $\lambda = 20mN/m$, BEM results predict that the air pressure of the trapped bubble is not high enough to induce the partial void migration. This phenomenon is represented in Figure 72, where the small initial domain that is intentionally generated to assess if there is or not void migration corresponds to the outer bubble front, and the arrows represent the direction of the bubble motion. As it can be observed, as the simulation develops, the bubble front gets back and the initial domain shrinks, which can

be interpreted as the impossibility of the trapped bubble to migrate from the tow towards the channel. It can be concluded that the surface tension, λ, has two opposite effects in the impregnation of dual-scale fibrous reinforcements: it promotes the infiltration of the tows because as λ is greater, the capillary pressure is also greater, but, conversely, an increment of λ causes a greater opposition to the void migration.

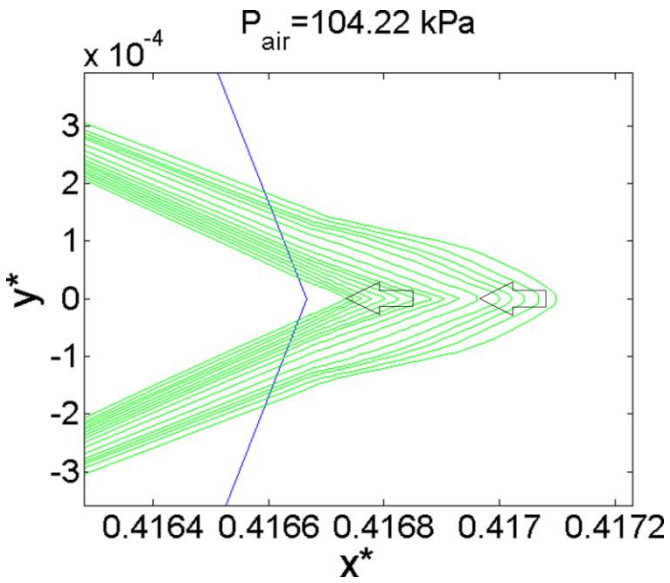

Figure 72 Representation of not void migration for λ=20mN/m, $\langle P_g \rangle^g$=102kPa and ΔP/Δx=5.83×10^3 kPa/m

Case 4: Modification of the pressure gradient, $\Delta P/\Delta x$.

Several authors coincide that the increment of the pressure gradient could favor the intra-tow void migration [78], [86], [220]–[222], [230]. In a recent experimental work, Vilá et al. [220] used the X-ray computed tomography to study the void transport in vacuum assisted infiltration processes, finding that the intra-tow voids are more prone to migrate as the pressure gradient is high enough to overcome the capillary forces; they also observed that very small voids can still remain trapped inside the tow once the larger void has been removed.

In the present case, it is evaluated if the increment of the pressure gradient induces the void migration for the case considered in Figure 72, where the liquid surface tension is $\lambda = 20\text{mN/m}$ and no void migration is possible. Accordingly, the pressure gradient is increased from $\Delta P/\Delta x = 5.83 \times 10^3\ kPa/m$ to $\Delta P/\Delta x = 1.08 \times 10^4\ kPa/m$ and the

average pressure is kept constant in $\langle P_g \rangle^g = 102kPa$, by prescribing $p_{in} = 108.5\ kPa$ and $p_{out} = 95.5\ kPa$; the initial domain of this simulation corresponds to the arrival of the bubble to the edge of the weft (just before a possible void migration occurs).

According to Figure 73a, when the pressure gradient increases as done here, the bubble trapped inside the tow barely compresses (see black arrow), thereby leading to a small increment in the air pressure from $104.22\ kPa$ to $107.11\ kPa$. In Figure 73a the *red line* is the front of the bubble that is not able to migrate when the original pressure gradient is hold, namely, when $\Delta P/\Delta x = 5.83 \times 10^3\ kPa/m$, while the *green line* is the front corresponding to the small compression undergone by the bubble when the pressure gradient is increased to $\Delta P/\Delta x = 1.08 \times 10^4\ kPa/m$. Then, once the small contraction of the void takes place, the bubble displaces again towards the right extreme of the weft and the void expansion in the channel is possible in this case, as it can be confirmed in Figure 73b and Figure 73c. Additionally, the bubble experiences a contraction until its splitting (breaking), which occurs before it arrives to the right edge of the RUC, as it can be appreciated in Figure 73d, where the bubble evolution is represented from the darker to the lighter line. Considering that the increment of the pressure gradient along the RUC induces a higher average liquid velocity in the channel, $\langle u_g \rangle^g$, it can be concluded that, at the macroscopic scale, the increment of $\langle u_g \rangle^g$ could promote the void elimination, which is in agreement with previous works [78], [86], [220]–[222], [230].

After the void splitting, the simulation continues using the same parameters. The results of Figure 74a-h show a process of stepwise void elimination, where several stages of compression-displacement-migration-splitting occur successively, leading to a smaller void inside the weft. In this case, two of these stages are presented and the graphical comparison between the initial and the final bubble inside the weft after three splittings is presented in Figure 74i, where it can be noticed a small reduction in the void size. This indicates that, according to the present BEM results, the void elimination from the tows towards the channels in dual-scale fibrous reinforcements can be considered a slow pulsating process, but further experimental and numerical works shall be done to confirm this conclusion.

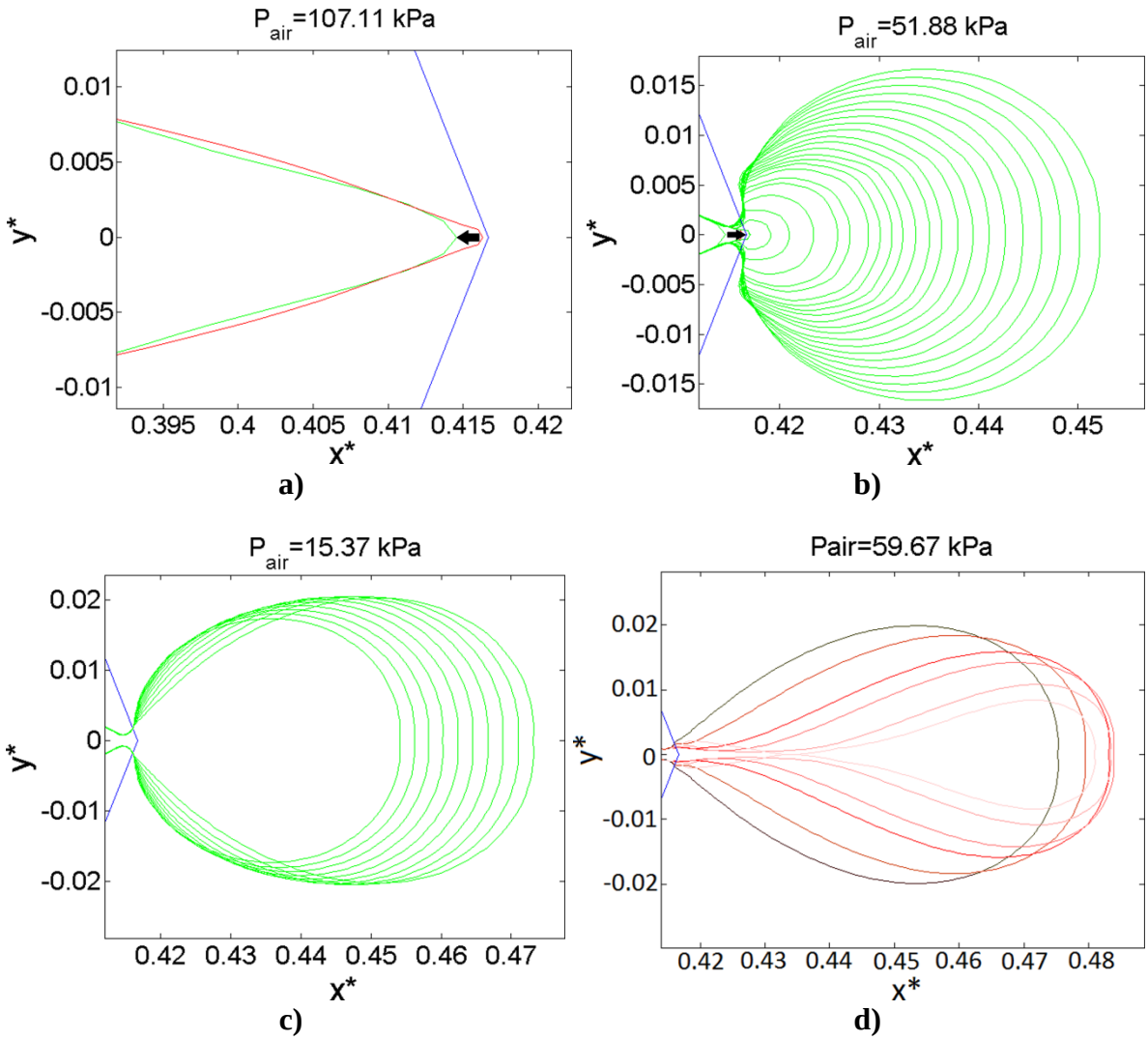

Figure 73 Effect of increment of the pressure gradient, ΔP/Δx, on the void migration. a) Small compression of the bubble, b) Displacement and expansion of the bubble, c) Expansion of the bubble, d) Contraction and splitting of the bubble (From darker to lighter line).

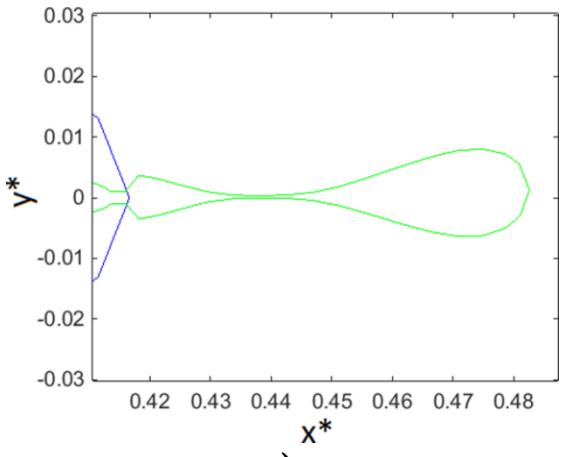
0.03
0.02
0.01
0
-0.01
-0.02
-0.03
y*
0.42 0.43 0.44 0.45 0.46 0.47 0.48
x*

a)

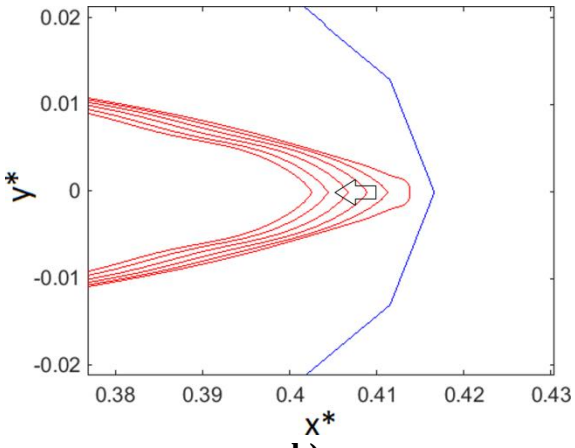
0.02
0.01
0
-0.01
-0.02
y*
0.38 0.39 0.4 0.41 0.42 0.43
x*

b)

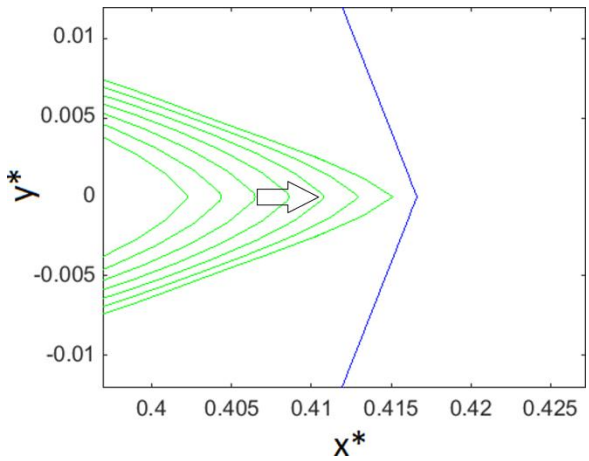
0.01
0.005
0
-0.005
-0.01
y*
0.4 0.405 0.41 0.415 0.42 0.425
x*

c)

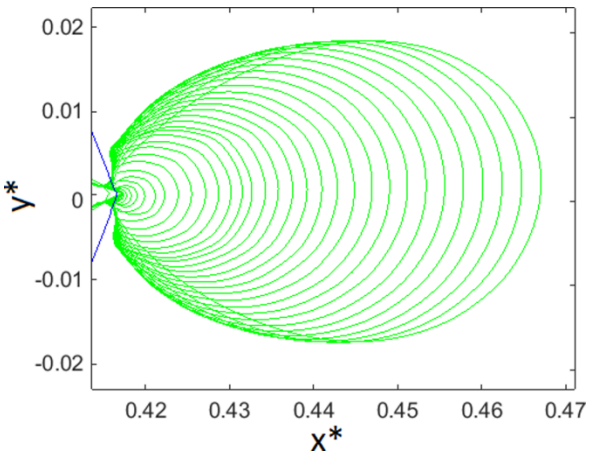
0.02
0.01
0
-0.01
-0.02
y*
0.42 0.43 0.44 0.45 0.46 0.47
x*

d)

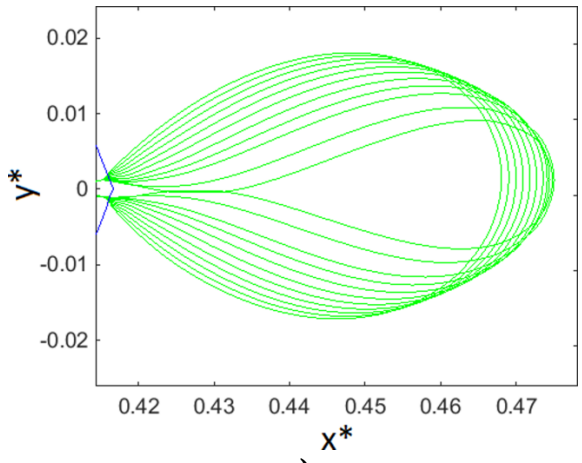
0.02
0.01
0
-0.01
-0.02
y*
0.42 0.43 0.44 0.45 0.46 0.47
x*

e)

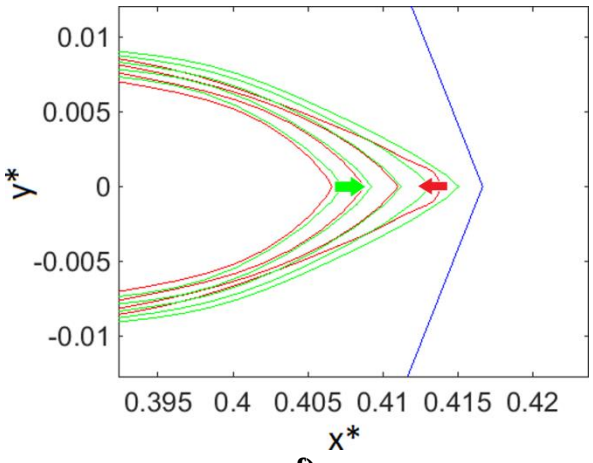
0.01
0.005
0
-0.005
-0.01
y*
0.395 0.4 0.405 0.41 0.415 0.42
x*

f)

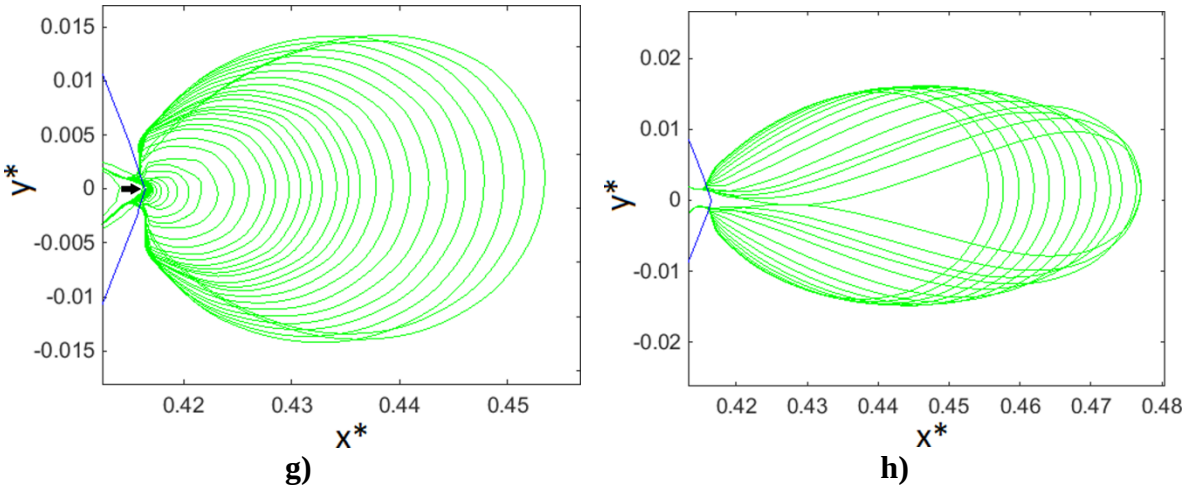

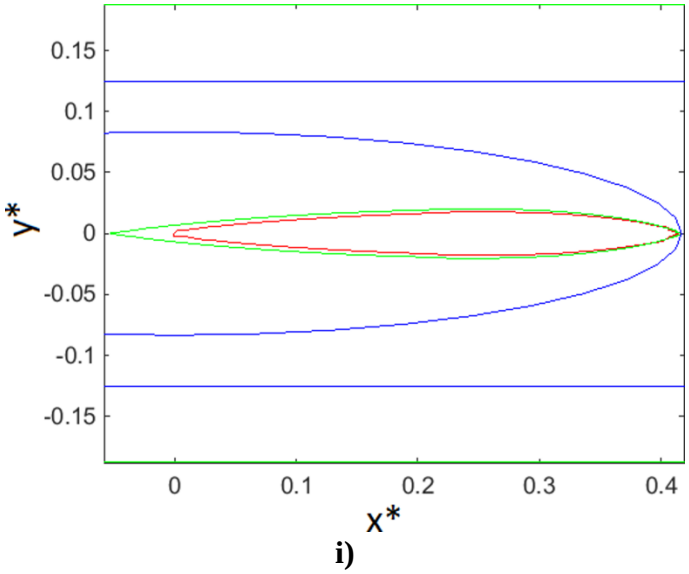

i)

Figure 74 Process of stepwise void elimination. a) Initial splitting, b) Second stage of compression, c) Second stage of mobilization towards the right extreme of the weft, d) Second stage of void migration, e) Second migration and subsequent splitting, f) Third stage of compression (red lines and red arrow) and subsequent mobilization towards the right extreme of the weft (green lines and green arrow), g) Third stage of void migration, h) Third migration and subsequent splitting, i) Comparison between the initial (green line) and the final (red line) bubble inside the weft after three splittings.

Case 5: Modification of the average pressure, $\langle P_g \rangle^g$

In this last case, it is evaluated if the increase of the average pressure, $\langle P_g \rangle^g$, can lead to the migration of the bubble considering the same surface tension as in *Case 3* ($\lambda = 20\text{mN/m}$), where void migration is not possible (see Figure 72). A simulation with initial domain corresponding to the arrival of the bubble to the right edge of the weft is performed,

considering a higher average channel pressure of $\langle P_g \rangle^g = 242kPa$, which is obtained by prescribing $p_{in} = 245.5\ kPa$ and $p_{out} = 238.5\ kPa$; notice that the pressure gradient of *Case 3*, $\Delta P/\Delta x = 5.83 \times 10^3\ kPa/m$, is kept constant. The first effect of this change, contrary to the *Case 4* (which corresponds to the increment of the pressure gradient with respect to the *Case 3*), is an important compression experienced by the void (Figure 75a), which leads to an important increment of the air pressure, from $104.22\ kPa$ to $244.37\ kPa$, in such a way that when the compressed void displaces towards the right extreme of the weft (Figure 75b), the pressure allows surpassing the interfacial forces and the void migration occurs for the same pressure gradient and surface tension of the *Case 3*, as shown in Figure 75c. In this case, a continuous bubble expansion is maintained until the bubble is near the right edge of the RUC. This result confirms that the increment of $\langle P_g \rangle^g$ above a determined value, which is called by some authors the critical pressure [5], [81], [84], could lead to the migration of the voids formed inside the tow.

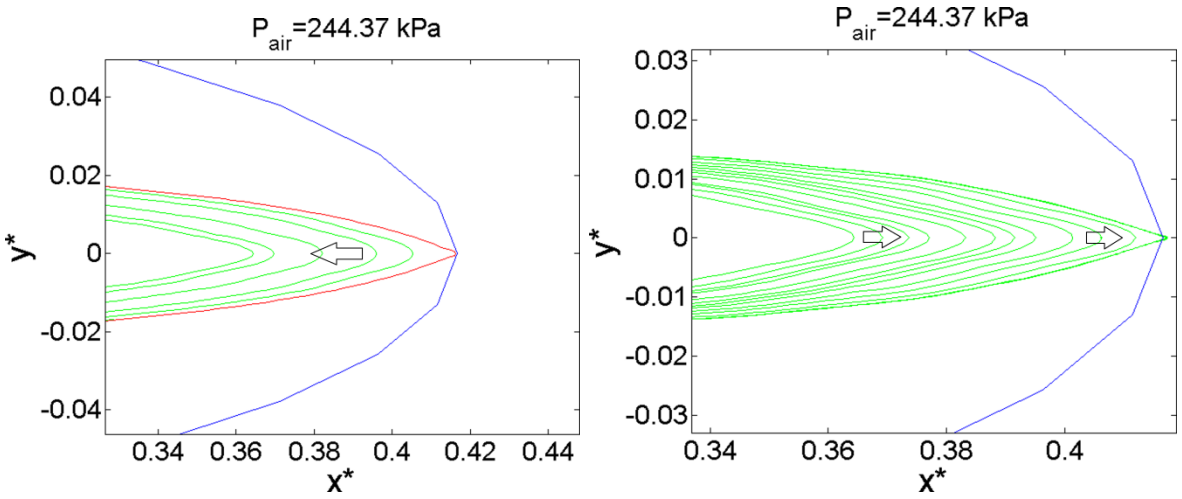

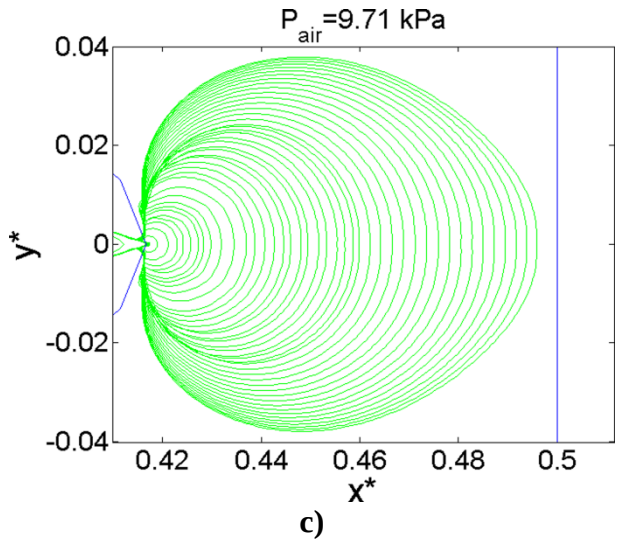

c)

Figure 75 Effect of increment of average pressure, $\langle P_g \rangle^g$, on the void migration. a) Bubble contraction, b) Bubble displacement, c) Migration of the bubble

5.4 Conclusions

In this chapter, the BEM method has been implemented for the simulation of the dynamic evolution of intra-tow voids in dual-scale fibrous reinforcements at mesoscopic scale, using a Stokes-Darcy formulation. As in other works, the assumption of fully filled channels was considered, but, instead of considering a constant channel pressure, a pressure gradient was prescribed along the RUC length to be consistent with the fluid motion. This simple modification allowed contemplating some bubble processes not taken into account in the traditional approach, namely, displacement at constant volume, migration and splitting (breaking). According to the BEM results, the processes occurring inside the tows, compression and displacement, are much slower than those ones occurring in the channel, migration and splitting, which is coherent with the larger velocities obtained in the channel regarding the velocities inside the tows; moreover, for the RUC geometry and the cases deemed here, the BEM code predicts that the process of void displacement inside the tow takes more time than the void compression. The analysis of the velocity field and streamlines allowed concluding that, at the interface channel-weft, for the cases considered here, the tangential Darcy velocity is negligible and the mass transfer from the channel towards the weft is not uniform along this interface, being greater in points whose horizontal position is between the horizontal limits defined by the fluid front inside the tows, and considerably decreasing in points with horizontal positions beyond these limits.

The streamlines corresponding to the zones of low mass transfer tend to converge in the horizontal extremes of the fluid front.

Two numerical parameters were taken into account to quantify the process of void migration: the ratio between the average void migration velocity and the average channel liquid velocity, r_1, and the normalized air migration rate, $\langle S_g^v \rangle_{norm}$. In general, the void migration velocity is not constant during the whole migration process. The behavior of r_1 in the time showed that the bubble can migrate at both a lower and a higher velocity with respect to the average liquid velocity. It is even possible to obtain negative values of r_1, where the parameter $\langle S_g^v \rangle_{norm}$ is also negative, corresponding to the bubble contraction. Moreover, from the comparison with other works, it was obtained that, for a determined liquid velocity, the void migration from the tows towards the channel is considerably slower than the void migration along the channels.

From the behavior of $\langle S_g^v \rangle_{norm}$ in the time, it can be concluded that the void in the channel can be subjected to several cycles of expansion and contraction, with corresponding accelerations (increase in the expansion or contraction rates) and decelerations (decrease in the expansion or contraction rates), before the void splitting occurs. According to the BEM results, this splitting is product of a process in which the air pressure drops as a consequence of the bubble expansion until the interfacial forces on the bubble surface become significant to modify the shape of the bubble, which can lead to its breaking. Once the void splitting happens, the air inside the tow is compressed again until the equilibrium is achieved and the resulting bubble could migrate towards the channel until another splitting occurs. This allows concluding that, in general, the bubble inside the tow cannot be totally removed in a single step and the intra-tow void elimination is a slow pulsating process instead, where partial portions of air are removed; however, this conclusion needs to be confirmed with further experimental works.

The influence of the surface tension, pressure gradient and average pressure in the process of void migration was also studied here. Even though the surface tension favors the tow impregnation due to the increase of the capillary pressure, it also opposes to the void migration due to the increase of the surface tractions in the bubble surface; on the other hand, the increase of the pressure gradient (which leads to the increase of the average liquid

velocity in the channel) and of the average pressure promotes the void migration, which is in agreement with other numerical and experimental results at macroscopic scale.

6. MULTISCALE FILLING SIMULATIONS IN DUAL-SCALE FIBROUS REINFORCEMENTS[♠]

6.1 Introduction

In dual-scale fibrous reinforcements, the channels formed between the tows are considerably more permeable than the tows, leading to a non-uniform saturation of the preform as the filling takes place. At the mesoscopic level, the differences between the flow in the channels and the flow in the tows depend on the relationship between the viscous and capillary forces; these differences significantly affect the pressure and velocity fields at the macroscopic level. For instance, in unidirectional injections, the reduction of the pressure is linear along the mold length in single-scale fibrous reinforcements, whereas this reduction is almost parabolic for the partially saturated zone in dual-scale fibrous reinforcements due to the presence of a sink term, S_g, in the mass conservation equation [83]. On the other hand, in unidirectional constant flow rate injections, the increment of the inlet pressure with the time is linear for single-scale fibrous reinforcements, whereas a pressure drooping occurs for dual-scale fibrous reinforcements [83], [225].

The simulations of filling of dual-scale fibrous reinforcements can be classified into two main categories: mesoscopic simulations and macroscopic simulations. The mesoscopic simulations consists on the filling of the Representative Unitary Cell (RUC) and can be carried out to: 1) determine the effective properties of the porous medium, such as the effective unsaturated and saturated permeabilities, and the constitutive relationships of these properties [138]–[140], 2) compute the coupling terms between the mesoscopic and macroscopic governing equations in order to deduce lumped functions for such a terms, in terms of volume-averaged quantities [10], [12], [225], [232].

On the other hand, the macroscopic simulations make mention to those ones carried out in cavities, where the porous medium is initially dry and then a liquid passes throughout it, driven by positive pressure, gravity and/or capillary pressure. During the filling of the cavity, the dual-scale fibrous reinforcement is not uniformly impregnated as the fluid front progresses because of the dissimilar permeabilities of the channels and the tows, which

[♠] **The results of the present chapter are intended to be published in: Iván David Patiño Arcila, Henry Power, César Nieto Londoño, Whady Felipe Flórez Escobar, "Multiscale filling simulations in dual-scale fibrous reinforcements using Boundary Element Techniques" to be submitted *(In preparation).***

originates partial saturation effects. Two strategies can be considered to determine the influence of such effects in the macroscopic variables: in the first one, simultaneous and iterative-corrected simulations are conducted at both scales (macroscopic and mesoscopic) [8], [14], [94], whereas in the second one, which is less rigorous but computational cheaper, functions for the effective properties or for the coupling terms are obtained by running several mesoscopic simulations of the RUC filling, and those functions are then used in the macroscopic equations [12], [13], [101], [102], [138]–[140], [225], [232]. This second strategy, in turns, can be divided into two approaches. In the first approach, some constitutive relationships permeability-saturation and capillary pressure-saturation are obtained at the mesoscopic scale and then the Richards' equation is solved using these constitutive equations [138]–[140]. In the second approach, which is used in the present work, a sink function, S_g, is obtained by running several simulations at the mesoscopic scale and this function is used afterwards in the solution of a Poisson type equation, which is obtained from the mass conservation equation considering the sink function, S_g, and the Darcy law with an equivalent channel permeability, K_g [12], [13], [101], [102], [225], [232].

In the present chapter the Boundary Element Method (BEM) is applied to the problem of impregnation of dual-scale fibrous reinforcements used in the processing of composite materials, based on the Stokes-Darcy (at the mesoscopic scale) and equivalent Darcy (at the macroscopic scale) formulations. A new methodology is presented for the calculation of the sink function, S_g, and the influence of several parameters on the effective unsaturated permeability, K_{eff}, is studied as well. The principal contributions of this chapter attend some drawbacks identified in similar works and they are summarized as follows:

- As in the other problems analyzed along this work, the problem of multiscale filling of dual-scale fibrous reinforcements has been tackled mostly using domain mesh techniques. For instance, the Finite Element/Control Volume (FEM/CV) conforming method was used in [13] introducing 'slave' elements into the original nodes of the FEM mesh, with the purpose to simulate the delayed saturation of the tows as the macroscopic fluid front progresses. On the other hand, Park et al [79] used a modified FEM/CV method to predict the change of the void content and saturation along the mold length; in this work, the mesh in the neighborhood of the fluid front was refined in

adaptive manner by using floating imaginary nodes that were placed in the contour of the FEM elements taking into account the value of the fill factor [233]; a smoother fluid front was achieved regarding the traditional FEM/CV methods, but at the expense of the increase of the computational cost. The change of the saturation at both mesoscopic (tows) and macroscopic (cavity) levels and the drooping of pressure in constant flow rate injections were studied in [225] using FEM to solve the governing equations and the Nodal Saturation Method to track the fluid front [234]. The FEM/CV conforming method was also used in coupled multiscale simulations of partially saturated flow for isothermal [14], non-isothermal [8] and reactive [94] conditions, where two FEM meshes and the corresponding CV meshes were required since the mesoscopic (filling of tows) and macroscopic (filling of cavity) simulations were run simultaneously, implying a high computational cost. As important contribution, in the present work, the use of BEM techniques implies the reduction of the mesh in one dimension, which is convenient when dealing with moving boundary problems, and the tracking technique of *Appendix C* assures a higher order accuracy of the fluid front shape by reasons mentioned in other chapters. Additionally, only one contour mesh is required for each scale of simulation because a lumped strategy is used. Some works that make use of BEM techniques have also dealt with simulations of partially saturated flow in porous media [15]–[18], but the partial saturation effects were taken into account by using experimental constitutive laws for the permeability and the capillary pressure in soils-water systems, which is not our case because of the non-existence of such constitutive equations for woven reinforced preforms. In [139], [140], constitutive equations permeability-saturation and capillary pressure-saturation were obtained for non-woven reinforcements by running several FEM simulations at the microscopic scale, but these equations are not applicable in this case where woven reinforcements are considered.

- The second contribution of the present chapter is referred to the problem of how to take into account the partial saturation of the RUC's in the behavior of some macroscopic variables during the filling of the cavity. As it was mentioned before, there are mainly two numerical strategies to tackle this problem: 1) to carry out simultaneous and iterative-corrected simulations at both mesoscopic and macroscopic scales, 2) to conduct several simulations at the mesoscopic scale in order to deduce lumped

functions to be used at the macroscopic scale. The second strategy is employed in the present work because it implies less computational cost, but it is introduced an important modification in the methodology to obtain the sink function, S_g, which is related to the prescription of a pressure gradient along the RUC instead of considering an uniform pressure in the channels, as it was exposed in Chapter 5. When it is assumed that the channels are totally filled with liquid before any infiltration into the tows can take place, most of authors have supposed that the saturation rate inside the RUC, $\dot{S}_t$, is a function only of the uniform pressure of the liquid contained in the channels, $\langle P_g \rangle^g$, and of the total saturation, S_t [13], [225], [232], [235]. This classical methodology has several weaknesses due to its simplifications: 1) the impregnation in the tows takes place towards the center of them, no matter the magnitude or direction of the channel fluid velocity, which is not in accordance with other researches where the void location is not necessarily symmetric with respect to the centroid of the tow [3], [25], [171], [175], [220], [227], 2) the air compressibility and partial air dissolution are not taken into account, but a the full air dissolution instead, thereby leading to a constant air pressure in the fluid front during the whole filling of the tows, which does not reproduce the real situation of Liquid Composites Molding (LCM) processes [11], [92], 3) the capillary pressure is assumed constant during the whole RUC filling and the model to compute this pressure is employed indistinctively for the warps and the wefts, 4) the vacuum pressure is not considered as an initial condition for the air pressure, which is not coherent with some applications of composites manufacturing where the vacuum pressure is recognized as a relevant processing parameter [223], [236]–[238], 5) the prescription of a constant pressure in the channels of the RUC is not physically consistent with the fact that the fluid is actually moving, 6) the processes of void displacement, migration and subsequent splitting, which have been reported in experimental researches [89], [175], [219], [220], [227], are not possible using this simplified methodology as it was shown in Chapter 5. Consequently, the classical methodology to compute S_g is refuted in the present work in favor of the prescription of a pressure gradient along the RUC length, $\Delta P/\Delta x$, at it was done in Chapter 5, and, by mass conservation in the channel domain, the rate of saturation of the tows, $\dot{S}_t$, is established in terms of the difference between the inlet and outlet flow rates of the

RUC, which can be directly accomplished from the BEM simulation. The proposed methodology is more robust than the classical one because it tackles the aforementioned drawbacks as follows: 1) decentered voids are obtained in the transverse tow (weft) due to the prescription a pressure gradient, as shown in Chapter 5, 2) air compressibility and partial air dissolution are considered simultaneously in the boundary condition of the fluid front at the mesoscopic scale by means of the air entrapment parameter, λ, proposed in [11], 3) the flow-direction dependent model for the capillary pressure obtained in Chapter 3 is used here, 4) the vacuum pressure, P_{vac}, is taken into account as an independent variable of the function S_g, 5) there exists a velocity field in the channel that is consistent with the flow direction as shown in Chapter 5, 6) the displacement, migration and splitting of voids is possible under the assumption of full air compressibility, as shown in Chapter 5. Using the proposed methodology, a sink function, S_g, is obtained after running a considerable amount of mesosocopic simulations (RUC fillings), and, once the function S_g is known, macroscopic unidirectional simulations are run using the Dual Reciprocity Boundary Element Method (DR-BEM); the macroscopic simulations are performed to assess the coherence of the present methodology with a previous work [83] by comparing the pressure profiles, and to analyze the behavior of the global saturation in the space and the time under both constant pressure and constant flow rate regimes. The DR-BEM code is validated with an analytical solution at constant pressure regime [101].

- Finally, the curves of the effective unsaturated permeability, K_{eff}, against tow saturation, S_t, are obtained from the mesoscopic simulations, and the influence of the tow aspect ratio, a_1/a_2, and tow porosity, ε_t, on those curves is studied. The relationship between K_{eff} and S_t is important when the Richards' equations needs to be solved. To the best of the author's knowledge, there is not another work devoted to the study of the behavior of the curves of $K_{eff}\ vs. S_t$ with a_1/a_2 and ε_t in dual-scale fibrous reinforcements, but some works have studied the effective saturated permeability instead [20], [85] and these results are compared to the present ones in the limit when the total saturation is close to one, $S_t \to 1$.

6.2 Governing equations, boundary conditions and matching conditions

At the mesoscopic scale (filling of RUC's), the Stokes-Darcy formulation is used and the governing equations and matching conditions of Chapter 3, as well as the boundary conditions of Chapter 5, can be applied here. At the macroscopic scale, an equivalent Darcy approach is used, in which the channels of the fibrous reinforcement are conceived as a porous network having an equivalent permeability, K_g, and a sink term, S_g, accounting for the liquid absorption into the tows per unit RUC volume, needs to be considered in the continuity equation [6], [10]. Accordingly, for the channel domain, the following equations are valid:

$$\frac{\partial}{\partial x_i}\langle u_{i_g}\rangle = -S_g \tag{130a}$$

$$\langle u_{i_g}\rangle = -\frac{K_{i_g}}{\mu}\cdot\frac{\partial}{\partial x_i}\langle P_g\rangle^g \tag{130b},$$

where "g" represents the gaps between the tows (channels), in such a way that $\langle u_{i_g}\rangle$ and $\langle P_g\rangle^g$ stand for *i* component of the phase volume-averaged velocity and the intrinsic phase volume-averaged pressure in the channels, respectively, while K_{i_g} represents the equivalent channel or gap permeability in the principal direction *i* assuming impermeable tows. On the other hand, S_g is defined as follows:

$$S_g = \frac{1}{V_{RUC}}\int_{A_{gt}} u_{i_{gt}}\,.\,\hat{n}_{i_{gt}}\,dA_{gt} \tag{131},$$

where A_{gt}, $u_{i_{gt}}$ and $\hat{n}_{i_{gt}}$ stand for the area, velocity and normal vector at the interface channel-tow, which is represented by subscript "gt".

For the particular case of unidirectional filling at the macroscopic scale, which is considered here, the non-dimensionalization of the macroscopic variables depends on the injection regime, as follows (volume-averaged symbols are omitted for sake of simplicity):

For both constant pressure and constant flow rate regimes:

$$\hat{x} = x/L \tag{132a}$$

$$\hat{L}_{ff} = L_{ff}/L \tag{132b},$$

For a constant pressure regime only:

$$\hat{t} = t/\left(L^2\mu/\left(\left|P_{inj} - P_{vac}\right|K_g\right)\right) \tag{133a}$$

$$\hat{p} = p/\left|P_{inj} - P_{vac}\right| \tag{133b}$$

$$\widehat{u_1} = u_1/\left(\left(\left|P_{inj} - P_{vac}\right|K_g\right)/(L\mu)\right) \tag{133c}$$

For a constant flow rate regime only:

$$\hat{t} = t/\left(LA/Q_{inj}\right) \tag{134a}$$

$$\hat{p} = p/\left(Q_{inj}L\mu/\left(A.K_g\right)\right) \tag{134b}$$

$$\widehat{u_1} = u_1/\left(Q_{inj}/A\right) \tag{134c},$$

where x, L_{ff}, t, p and u_1 are the horizontal coordinate, fluid front position along the cavity, time, pressure and horizontal velocity, respectively, whereas $\hat{x}$, $\hat{L}_{ff}$, $\hat{t}$, $\hat{p}$ and $\widehat{u_1}$ are the corresponding non dimensional variables; on the other hand, L, μ, P_{inj}, P_{vac}, K_g, A and Q_{inj} stand for the length of the mold, liquid viscosity, injection pressure, vacuum pressure, equivalent gap permeability, cross section area of the mold and injection flow rate, respectively.

6.3 Integral equation formulations and numerical techniques.

At the mesoscopic scale (filling of RUC's), the integral equation formulations and all numerical considerations exposed in Section 3.3 are applicable to this particular problem. At the macroscopic scale, for unidirectional injections, the combination of the mass conservation, Eq.130a, and momentum conservation, Eq.130b, leads to a Poisson type equation, whose integral formulation is given by:

$$c(\xi)p(\xi) = \int_S\ p^*(\xi,y)\,q(y)dS_y - \int_S\ q^*(\xi,y)\,p(y)dS_y - \int_\Omega\ b(y)p^*(\xi,y)\,d\Omega_y \tag{135},$$

where the fundamental solutions, p^* and q^*, have the same form as the ones presented in Section 3.3, considering $K_1 = K_2 = K_g$, where K_g is the effective gap permeability in the fluid direction as found in Section 6.5.3. The non-homogeneous term of Eq.135 is given as: $b = \left(\mu/K_g\right)S_g$, where S_g is the lumped function for the sink term, which is deduced in the Section 6.5.2.

The domain integral of the Eq.135 can be transformed into boundary integrals using the Dual Reciprocity Boundary Element Method (DR-BEM) [63]. Firstly, the non-homogenous term, b, is approximated using Radial Basis Function (RBF) interpolation with Augmented Thin Plate Splines (ATPS) of order $n = 2$ (See Eqs. 111), as follows:

$$b(y) = \sum_{m=1}^{N_B+N_I+3} \alpha^m f^m(y) \tag{136}$$

where α^m represent the approximation coefficients, with the orthogonality conditions given by:

$$\sum_{m=1}^{N_B+N_I} \alpha^m = \sum_{m=1}^{N_B+N_I} \alpha^m \, y_1^m = \sum_{m=1}^{N_B+N_I} \alpha^m \, y_2^m = 0 \tag{137}$$

After substituting Eq.136 into Eq.135, the integral representation takes the following form:

$$c(\xi)p(\xi) = \int_S \; p^*(\xi,y)\, q(y) dS_y - \int_S \; q^*(\xi,y)\, p(y) dS_y - \sum_{m=1}^{N_B+N_I+3} \alpha^m \int_\Omega \; p^*(\xi,y)\, f^m(y) d\Omega_y \tag{138}$$

The transformation of the domain integral into a boundary integral is accomplished by defining the following auxiliary pressure field:

$$\frac{\partial^2 \hat{p}^m}{\partial y_k \partial y_k} = f^m(y) \tag{139},$$

with the particular solutions for the ATPS given in [239].

The substitution of Eqs.139 into Eq. 138 and the application of Green's identities in the domain integral lead to the following boundary-only integral representation:

$$c(\xi)p(\xi) = \int_S \; p^*(\xi,y)\, q(y) dS_y - \int_S \; q^*(\xi,y)\, p(y) dS_y - \sum_{m=1}^{N_B+N_I+3} \alpha^m \left(c(\xi)\hat{p}^m(\xi) - \int_S \; p^*(\xi,y)\, \hat{q}^m(y) dS_y + \int_S \; q^*(\xi,y)\, \hat{p}^m(y) dS_y \right) \tag{140},$$

where the coefficients α^m are obtained from the inverse of the matrix $[F]$, which, in turns, is obtained by collocation of N_B boundary nodes and N_I internal nodes according to Eq. 136. In vector form, Eq.136 is $\vec{b} = [F]\vec{\alpha}$, from which $\vec{\alpha} = [F]^{-1}\vec{b}$.

In the macroscopic problem, the boundary and the physical variables are discretized using quadratic isoparametric interpolation and discontinuous shape functions with a collocation factor of $\alpha_{dis} = 2/3$ are used in the corners [165]. To compute the regular integrals, standard Gaussian interpolation is used. The singularities of the integrals of the DLP are treated using the Rigid Body Motion principle [149], [150] and the singular integrals of the SLP, using the Telles transformation [166]. The final system at macroscopic scale can be written as:

$$[H]^{(d)}_{(N_B+N_I)\times(N_B+N_I)}\vec{p} - [G]^{(d)}_{(N_B+N_I)\times N_B}\vec{q} = [M]_{(N_B+N_I)\times(N_B+N_I+3)}.\vec{b} \quad (141),$$

where the matrix $[M]$ is as follows:

$$[M]_{(N_B+N_I)\times(N_B+N_I+3)} = \left([H]^{(d)}_{(N_B+N_I)\times(N_B+N_I)}\widehat{[p]}_{(N_B+N_I)\times(N_B+N_I+3)} - [G]^{(d)}_{(N_B+N_I)\times N_B}\widehat{[q]}_{N_B\times(N_B+N_I+3)}\right)[F^{-1}]_{(N_B+N_I+3)\times(N_B+N_I+3)} \quad (142),$$

with $\widehat{[p]}$ and $\widehat{[q]}$ as the matrices corresponding to the evaluation of the particular solutions in all field points, whereas $[F^{-1}]$ is the inverse of the matrix $[F]$. As it is shown in Section 6.5.2, the sink function, S_g, obtained here is non-linear, and thereby the system defined by Eq. 141 is solved using fixed point Picard iteration.

At the macroscopic scale, the fluid front tracking is also carried out by using the technique described in *Appendix C*.

6.4 Methodology for calculation of the sink function, S_g

Description of the problem.

The sink term, S_g, defined in the Eq.131, is the coupling term between the flow in the channels and the flow in the tows, and it can be characterized in terms of some volume-averaged variables of the RUC; once the function for S_g has been obtained, it can be used in the Eq.130a. According to Simacek and Advani [13], S_g can be taken as a function of the volume-averaged pressure, $\langle P_g\rangle^g$, and the saturation of the tows, S_t. The sink function, S_g, was implemented in macroscopic filling simulations in [101], [102], [235] using FEM/CV conforming, but neither capillary nor air compressibility and dissolution effects were considered. One of the most outstanding works to establish a function for S_g was developed in [12], [232], where the next general equation was deduced:

$$S_g = \left(f_1\left(\langle P_g\rangle^g\right)/\mu\right)\left\{e^{A_2(1-S_t)^{A_3}} - 1\right\} \quad (143),$$

where $f_1\left(\langle P_g\rangle^g\right) = \varepsilon_t\left(1-\varepsilon_g\right)A_1\left(\langle P_g\rangle^g\right)$, $A_1\left(\langle P_g\rangle^g\right) = (A_1^*/\beta^*)\langle P_g\rangle^g$ and the coefficients A_1^*, A_2, A_3 and β^* are determined after running several simulations of filling of the tows assuming a constant liquid pressure in the channels, $\langle P_g\rangle^g$.

A different methodology to calculate the function S_g is proposed in the present work, where both the air compressibility and air dissolution are considered. When the air dissolution is

present, it is possible to reach the total tow saturation, $S_t = 1$, otherwise, an equilibrium saturation, S_t^{eq}, is reached instead, as mentioned in Chapter 5. The RUC geometry and type of boundary conditions for the determination of the sink function, S_g, are shown in Figure 61. As mentioned before, the air compression is considered for the weft and the total tow saturation is thus not possible when the air dissolution is neglected. For the warps, on the contrary, the air compression is not taken into account and the total saturation is possible in all cases.

Scale constraints.

As it is well-known from the volume-averaging method [130], several scale constraints shall be complied in order to simplify the general volume-averaged momentum equation, which is quite complex as shown in Chapter 2, into the simpler Darcy's law, Eq.130b, which is used here for the channel domain at the macroscopic scale. Additionally, the LCM processes implies another scale restrictions. Therefore, both the RUC geometry and the prescribed inlet and outlet pressures used for the determination of S_g in the mesoscopic simulations, as well as the physical conditions of the macroscopic problem (filling of cavity), need to be in accordance with these scale restrictions. First of all, applying the constraints of [130] on the channel or gap phase, "g", the Darcy's simplification is possible provided that the following equation is valid for the phase volume-averaged pressure gradient, $\langle \partial P_g / \partial x_i \rangle$:

$$\langle \partial P_g / \partial x_i \rangle = \varepsilon_g \left(\partial \langle P_g \rangle^g / \partial x_i \right) + (1/V_{RUC}) \int_{A_{gt}} \widetilde{P_g} \cdot \hat{n}_{gt} dA \qquad (144),$$

where P_g stands for the pointwise pressure in the channel domain, whereas $\widetilde{P_g} = P_g - \langle P_g \rangle^g$ is defined as the local variation of the pressure and $\varepsilon_g = V_g / V_{RUC}$ is the gap porosity, with V_g as the volume of the channel or gap phase. The Eq. 144, in turns, is valid under the next scale restrictions:

$$L_g \ll L_{RUC} \qquad (145a)$$

$$(L_{RUC})^2 \ll L_{\varepsilon g} L_{p1g} \qquad (145b),$$

where L_{RUC} and L_g are the characteristic length-scales of the RUC and of the channel or gap phase, respectively. On the other hand, $L_{\varepsilon g}$ and L_{p1g} are the characteristic length-scales defined by the estimates $\nabla \varepsilon_g = \mathcal{O}\left(\Delta \varepsilon_g / L_{\varepsilon g}\right)$ and $\nabla \nabla \langle P_g \rangle^g = \mathcal{O}\left(\nabla \langle P_g \rangle^g / L_{p1g}\right)$,

respectively, where Δ stands for the absolute change of the variable, while ∇ and $\nabla\nabla$ represent the first and second derivative, respectively. On the other hand, the symbol $\mathcal{O}$ is used to denote the order of magnitude. The constraint of Eq. 145a is satisfied in this case because the average inter-tow distance, which can be taken as the characteristic length-scale of the channels, L_g, is chosen smaller than the RUC length, L_{RUC}. In a similar fashion, the constraint of Eq.145b is also satisfied here because a homogeneous porous medium at macroscopic scale is considered, leading to $L_{\varepsilon g} \to \infty$ [130]. For heterogeneous porous media, the fulfillment of Eq.145b depends on the gradient of the gap porosity, $\nabla\varepsilon_g$, and on the relationship between the first and second derivatives of the volume-averaged pressure, which can be defined by the ratio $r_g = \nabla\langle P_g\rangle^g / \nabla\nabla\langle P_g\rangle^g$. According to [130], when $\nabla\varepsilon_g$ is very large, $L_{\varepsilon g} \approx L_{RUC}$, in which case, considering an order of magnitude of $\mathcal{O}(-3)$ for L_{RUC}, the minimum allowable order of magnitude of L_{p1g}, in order to comply the Eq.145b, would be $\mathcal{O}(-2)$, i.e., $r_g > 10^{-2}$ to fulfill Eq.145b. The filling of heterogeneous dual-scale porous media is not tackled in this work, but it could be considered in forthcoming investigations under the scale restrictions mentioned here.

In LCM processes, the assumption of full-filled channels is more realistic as the viscous forces exceeds the capillary ones, which can be valid when: 1) the tows permeabilities, K_1 and K_2, are very small regarding the gap permeability, K_g, and 2) the inlet injection pressure, P_{inj}, is at least one order of magnitude larger than the typical capillary pressures in these processes, which usually have an order of $\mathcal{O}(3)$ [75], [140], [145], [228]. The first condition is fulfilled in this chapter since K_1 and K_2 have an order of $\mathcal{O}(-13)$ and $\mathcal{O}(-14)$, respectively, while the gap permeability has an order of $\mathcal{O}(-8)$ as shown in Section 6.5.3. To satisfy the second condition, a minimum injection pressure of order $\mathcal{O}(4)$ is considered in the macroscopic simulations.

On the other hand, according to Park et. al [83], the pressure profiles for unidirectional injections in dual-scale fibrous reinforcements can be divided into three categories, as it is shown in the Figure 76a-c. For the fully saturated zone, $S_t = 1$, the pressure profile is linear, while the non-linear part of this profile in the partially saturated zone, $S_t < 1$, can be approximated by quasi-parabolic curves that could be concave (Figure 76a), convex (Figure 76b) or both ones (Figure 76c), depending on the importance of the sink term, S_g, in such a

way that as S_g is greater, the profile tends to be slightly concave as reported in [240], [241], while a convex profile is liable to be obtained as S_g is lower [242]. Taking into account the possible forms of this profile and considering a minimum order for the injection pressure, P_{inj}, of $\mathcal{O}(4)$, and a maximum order for the length scale of the macroscopic problem (length of the mold), L, of $\mathcal{O}(0)$, it is expected a minimum order for the pressure gradient of around $\mathcal{O}(3)$. As the order of L_{RUC} is $\mathcal{O}(-3)$ in the present work, the minimum order for the change of pressure along the RUC length, Δp, could be taken here as $\mathcal{O}(0)$.

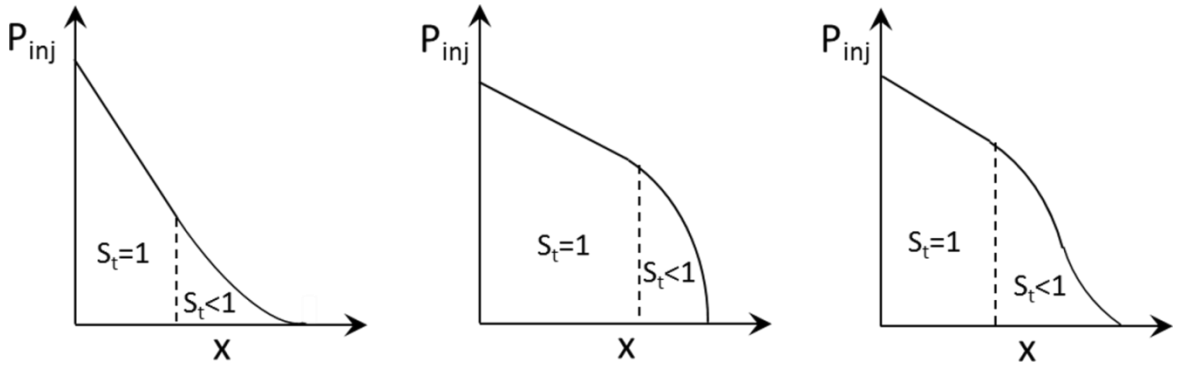

Figure 76 Typical pressure profiles in unidirectional injections for dual-scale fibrous reinforcements. a) Linear-Concave, b) Linear-Convex, c) Linear-Convex-Concave. Source: Park et al [83]

On the other hand, the maximum order for the pressure gradient is determined by considering a mesoscopic scale restriction for the local velocity variation in the channel phase, $\widetilde{u_g}$, which establishes that:

$$\langle|\widetilde{u_g}|\rangle^g \ll \langle u_g\rangle^g \quad (146),$$

where $\widetilde{u_g} = u_g - \langle u_g\rangle^g$.

In some researches about LCM processes, the maximum order of the volume-averaged velocity in the channel, $\langle u_g\rangle^g$, has been taken as $\mathcal{O}(-1)$ [77], [80], [81] and the maximum order of the resin viscosity is $\mathcal{O}(-1)$. Consequently, taking into account these orders of magnitude and that the gap permeability, K_g, is of order $\mathcal{O}(-8)$ for the RUC geometry considered in this work, the maximum order for the pressure gradient according to the Darcy's law is $\mathcal{O}(6)$, which corresponds to a pressure change along the RUC length, Δp, of

order $\mathcal{O}(3)$. However, the consideration of an order $\mathcal{O}(-1)$ as the upper limit for $\langle u_g \rangle^g$, could lead to high Reynolds numbers and this is not consistent with the Stokes approximation for the channels. Consequently, in the present chapter, the starting point for the maximum order of Δp in the RUC is $\mathcal{O}(3)$ (which corresponds to a channel velocity, $\langle u_g \rangle^g$, of order $\mathcal{O}(-1)$), but it is necessary to check that the gap Reynolds number, R_{eg}, remains small according to the following definition:

$$R_{eg} = \rho \langle u_g \rangle^g L_g / \mu \tag{147},$$

where ρ, μ and L_g stand for the liquid density, liquid viscosity and characteristic length of the gap phase.

Calculation of the sink function, S_g

Taking into account the last constraints, a pressure gradient is imposed along the RUC and the sink term, S_g, is computed by applying the principle of mass conservation in the gap or channel domain. Accordingly, for a unitary width RUC, the equation to compute S_g is as follows:

$$S_g = \frac{(\bar{u}_{in} - \bar{u}_{out}) H_g}{H_{RUC} \cdot L_{RUC}} \tag{148},$$

where the mean inlet and outlet velocities of the RUC , $\bar{u}_{in}$ and $\bar{u}_{out}$, are defined by:

$$\bar{u}_{in} = \left(\int_{-H_g/2}^{H_g/2} u_{in} \, dy \right) / H_g \tag{149a}$$

$$\bar{u}_{out} = \left(\int_{-H_g/2}^{H_g/2} u_{out} \, dy \right) / H_g \tag{149b},$$

where u_{in} and u_{out} are the pointwise inlet and outlet velocities obtained from the BEM simulations.

The total saturation of the tows, S_t, is defined as:

$$S_t = V_{liq} / V_{pt} = V_{liq} / \left(\sum V_{pt}^{(i)} \right) = \left(\sum s^{(i)} V_{pt}^{(i)} \right) / \left(\sum V_{pt}^{(i)} \right) \tag{150},$$

where V_{liq} is the total volume of liquid inside the tows (including warps and weft), V_{pt} is the total porous volume of the tows, $V_{pt}^{(i)}$ is the porous volume of the tow "i" and $s^{(i)} = V_{liq}^{i} / V_{pt}^{(i)}$ is the saturation of the tow "i", with V_{liq}^{i} as the volume of liquid inside the tow "i". From now on, considering that the channels are totally filled of liquid in the RUC, S_t is referred as the total saturation.

The saturation rate can be found by taking the time derivative of Eq. 150:

$$\dot{S}_t = \left(\sum \dot{s}^{(i)} V_{pt}^{(i)}\right) / \left(\sum V_{pt}^{(i)}\right) \tag{151}$$

By mass conservation, the following is valid:

$$\left(\sum \dot{s}^{(i)} V_{pt}^{(i)}\right) = (\bar{u}_{in} - \bar{u}_{out}) H_g \tag{152}$$

Solving for the term "$(\bar{u}_{in} - \bar{u}_{out})H_g$" in the Eq.148, substituting into Eq.152 and then substituting the resulting expression into the Eq.151, it is obtained the next relationship between the total saturation rate, $\dot{S}_t$, and the sink term, S_g:

$$\dot{S}_t = \left[H_{RUC}.L_{RUC} / \left(\sum V_{pt}^{(i)}\right)\right] S_g \tag{153}$$

Taking into account that $\varepsilon_g = V_g / V_{RUC}$ and considering the same porosity, ε_t, for all tows, the following expression can be written:

$$\varepsilon_g = 1 - \left(\sum V_t^{(i)}\right) / (H_{RUC}.L_{RUC}) = 1 - \left(\frac{1}{\varepsilon_t}\right) \frac{\left(\sum V_{pt}^{(i)}\right)}{H_{RUC}.L_{RUC}} \tag{154},$$

where $V_t^{(i)}$ is the volume of the tow "i", with $V_{pt}^{(i)} = \varepsilon_t V_t^{(i)}$.

Solving for $\left(\sum V_{pt}^{(i)}\right) / (H_{RUC}.L_{RUC})$ in the Eq.154 and substituting into Eq.153, the following relationship is obtained for the sink term, S_g:

$$S_g = \varepsilon_t \dot{S}_t \left(1 - \varepsilon_g\right) \tag{155}$$

The last equation is useful since it allows establishing the relationship between volume-averaged quantities and the sink term, S_g, once the relationship between those quantities and the saturation rate, $\dot{S}_t$, has been obtained.

6.5 Results and discussion

6.5.1 Analysis of saturation in mesoscopic simulations

In this section, the behavior of the total saturation, S_t, in the time is obtained using BEM and the classical methodology, and the results are compared with those previously reported in [12], [225]. Then, the influence of the total saturation (S_t), volume-averaged pressure $\left(\langle P_g \rangle^g\right)$ and pressure gradient $(\Delta P / \Delta x)$ in the inlet and outlet velocity profiles of the channel, u_{in} and u_{out}, and in the phase-intrinsic volume-averaged gap velocity, $\langle u_g \rangle^g$, is

analyzed using the proposed methodology. Both $\langle P_g \rangle^g$, $\langle u_g \rangle^g$ and $\langle u_g \rangle$ are computed using the BEM results in the boundary and interior points of the channel domain. In the case of the phase-intrinsic volume-averaged pressure, $\langle P_g \rangle^g$, BEM results indicate that it is very similar to the average of the inlet and outlet pressures.

Saturation curves using the classical methodology.

Firstly, some filling simulations of the RUC represented in Figure 61 are run using BEM and the classical methodology used in [12], [13], [101], [102], [225], [232], namely, a uniform pressure is supposed in the channel as the boundary condition of the tows and it is only simulated the filling of such a tows. Additionally, the air compressibility, partial air dissolution and vacuum pressure are not considered, and it is supposed full air dissolution. Data to run the simulations using such methodology are shown in the Table 18, where the channel pressures, $\langle P_g \rangle^g$, coincide with the ones used in [12], [225]. It is defined the normalized time as follows:

$$\tau = t/t_{fill} \tag{156},$$

where t_{fill} is the total filling time, which is obtained from the BEM simulations and reported in Table 19.

The RUC geometries considered in Wang and Grove [225] and Tan [12] are represented in Figure 77a and Figure 77b, respectively, while the RUC geometry of this work is displayed again in Figure 77c. Using the BEM results, the curves of $S_t \, vs. \tau$ for all values of $\langle P_g \rangle^g$ were obtained as shown in the Figure 77f. When these curves are compared to the curves of the Figure 77d and Figure 77e, which correspond to the saturation curves obtained by Wang and Grove [225] and Tan [12], respectively, some similarities can be identified. First of all, the results converge into a single master curve in all figures. Secondly, despite the curves are not exactly the same, a similar general behavior of the saturation rate is observed: it is very large at the beginning of the injection and decreases as the filling takes place. The agreement of the current BEM results with the results of [12], [225] suggests that the present code is reliable enough to tackle the other problems of the present chapter. The saturation curves obtained by the proposed methodology will be presented in Section 6.5.2.

Table 18 Data of simulations of tows filling with the classical methodology

Processing data							
Number of simulation	1	2	3	4	5	6	7
Channel pressure, $\langle P_g \rangle^g$ (Pa)	100	300	500	1000	5000	10000	50000

Geometric and material data											
Total height of the RUC, H_{RUC} (m)	Length of the RUC, L_{RUC} (m)	Total height of the channel, H_g (m)	Major axis of the weft, a_1 (m)	Minor axis of the weft, a_2 (m)	Viscosity, μ (Pa.s)	Major permeability, K_1 (m^2)	Minor permeability, K_2 (m^2)	Surface tension, λ (mN/m)	Contact angle, θ	Fiber radius, R_f (μm)	Tow porosity, ε_t
4,50 E-04	1,20 E-03	3,00 E-04	5,00 E-04	1,00 E-04	0,1	2,07 E-13	1,08 E-14	15	30°	20	0,15

Table 19 Filling times obtained from BEM simulations with the classical methodology

Number of simulation	1	2	3	4	5	6	7
Filling time (s)	23,54	21,14	19,18	15,59	6,22	3,55	0,80

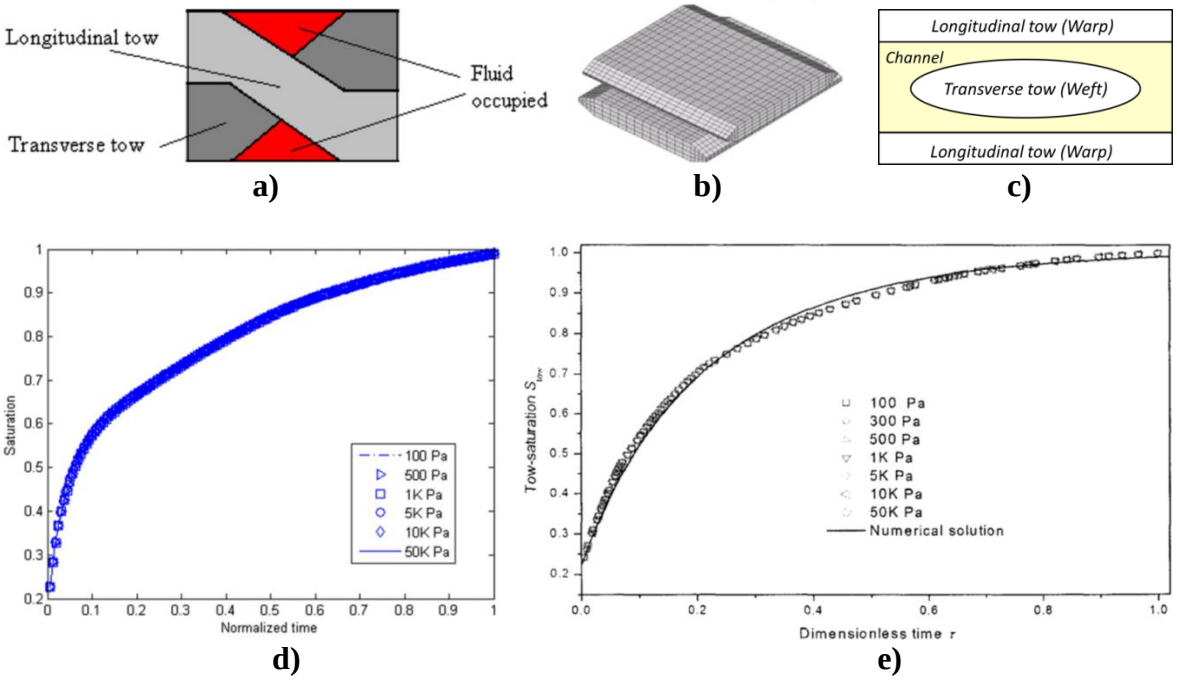

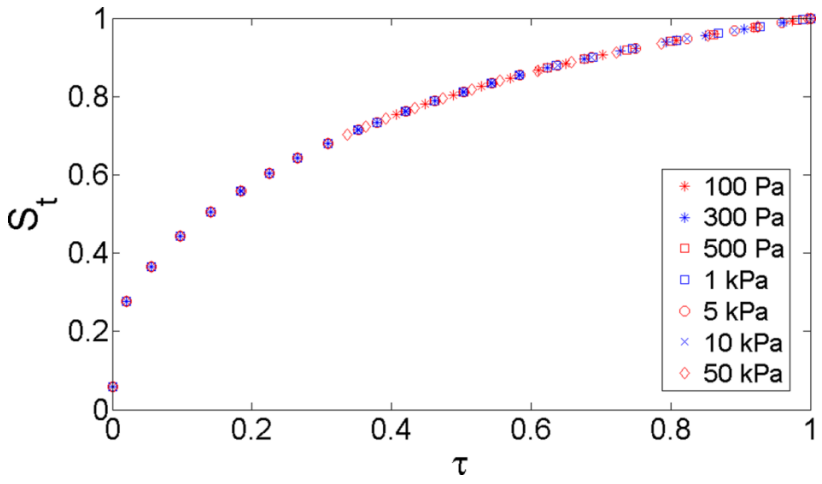

f)

Figure 77 Comparison of saturation curves obtained by the classical methodology. a) RUC geometry of Wang and Grove [225]**, b) RUC geometry of Tan [12], c) RUC geometry of this work, d) Saturation curve of Wang and Grove** [225]**, e) Saturation curve of [12], f) Curve S_t vs. τ of this work**

Influence of saturation, volume-averaged pressure and pressure gradient on the channel velocity field using the proposed methodology.

In this part, several simulations of filling of the RUC represented in Figure 61 are carried out using the proposed methodology, namely, a pressure gradient is prescribed along the RUC length, the channel domain is modeled as a Stokes flow and the matching conditions Stokes-Darcy are considered. Additionally, full air compressibility is deemed as in the simulation of Figure 63. The geometric and material data of Table 18 are taken into account.

The influence of the pressure gradient $(\Delta P/\Delta x)$, average pressure $\left(\langle P_g \rangle^g\right)$ and total saturation (S_t) on the horizontal channel velocities is represented in Figure 78 to Figure 83, where the velocities are normalized with the maximum velocity in each case for comparison purposes, i.e., $u^* = u/u_{max}$, but they are referred in the following analysis as 'velocities' instead of 'normalized velocities' for sake of simplicity. For the simulations corresponding to Figure 78, Figure 79 and Figure 80, an average pressure of $\langle P_g \rangle^g = 62\ kPa$ and a pressure gradient of $\Delta P/\Delta x = 5.83 \times 10^3\ kPa/m^3$ are considered. The inlet velocity profiles of the channel domain for several values of total saturation, S_t, are represented in the Figure 78, where it is observed that for a fixed vertical position,

$y^* = y/L_{RUC}$, the inlet velocity, u_{in}^*, reduces with the increase of S_t, and this reduction is more significant as the saturation is lower. On the other hand, in the Figure 79 the inlet and outlet velocity profiles of the channel domain for several values of S_t are compared each other, and it can be noticed that, for a fixed vertical position, y^*, and saturation, S_t, the inlet velocity, u_{in}^*, is greater than the outlet velocity, u_{out}^*. It is also worth noting that the difference between the inlet and outlet velocity profiles is lower as the saturation, S_t, is higher, which is in agreement with the reduction of the saturation rate, $\dot{S}_t$, with the increase of S_t, because the decrease of $\dot{S}_t$ means a lower liquid absorption into the bundles and a concurrent lower difference between the inlet and outlet velocity profiles by mass conservation. When S_t is close to one, the difference between u_{in}^* and u_{out}^* for a fixed vertical position is very small, see velocity profiles for $S_t = 0.939$ in Figure 79.

The Figure 80 shows that the volume-averaged gap velocity in the horizontal direction (flow direction in this case), $\left(\langle u_g \rangle^g\right)^*$, does not change significantly with the saturation, S_t, and thereby it can be taken the average value of this velocity for the whole simulation. In other words, the velocity field in the channel at the mesoscopic scale is clearly affected by the saturation, S_t, but the volume-averaged gap velocity in the flow direction, which is a macroscopic variable, is not considerably influenced by S_t. As the present problem is symmetric with respect to the "x" axis (See Figure 61), the volume-averaged gap velocity in the vertical direction is always zero, not requiring any analysis.

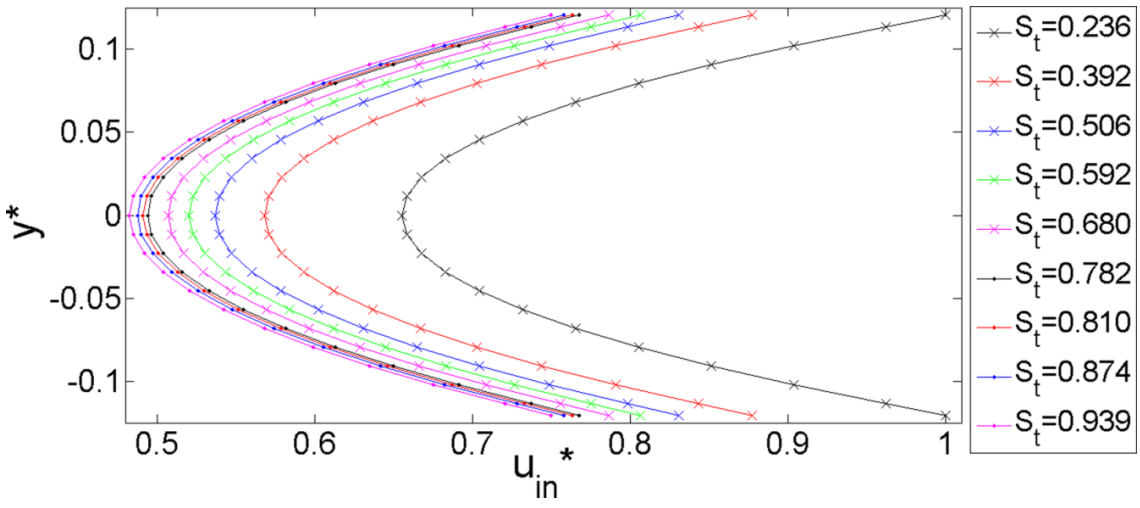

Figure 78 Influence of the total saturation, S_t, on the inlet velocity profile

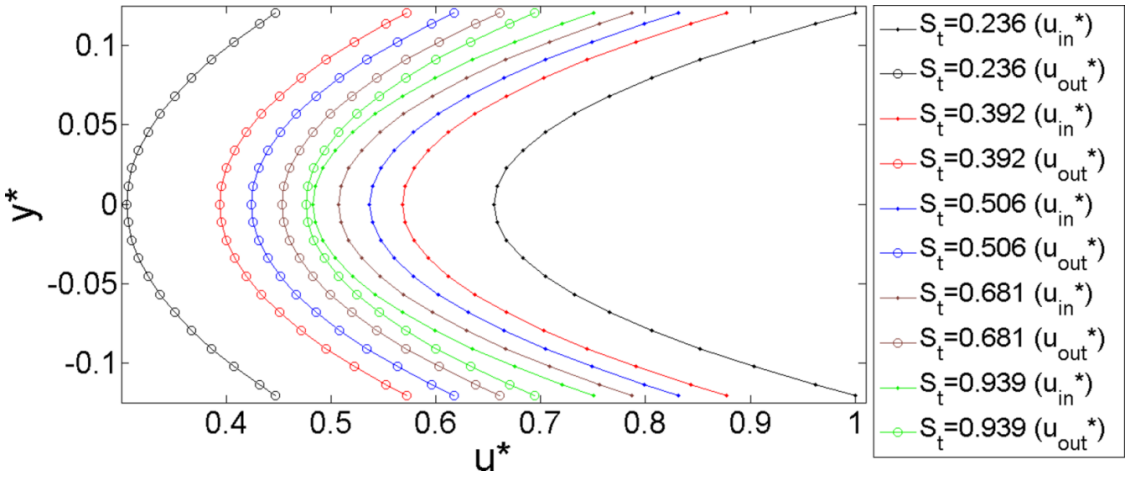

Figure 79 Difference between the inlet and outlet velocities for several values of S_t

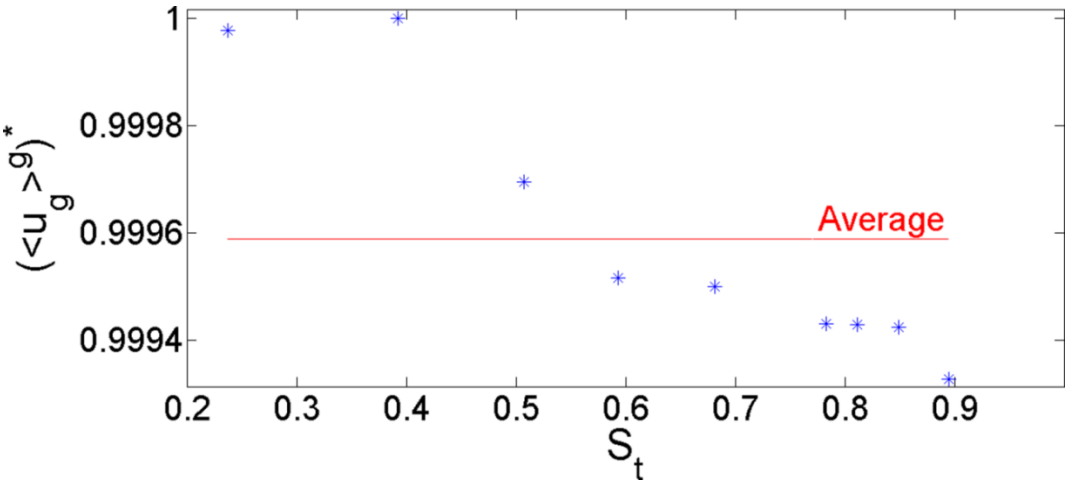

Figure 80 Influence of S_t on $(\langle u_g \rangle^g)^*$

To establish the influence of $\langle P_g \rangle^g$ on the inlet and outlet velocities, some velocity profiles are plotted in Figure 81a-c for two values of the average pressure, $\langle P_g \rangle^g = [22, 122]\ kPa$, three levels of total saturation, $S_t = [0.235, 0.554, 0.893]$, and a single pressure gradient, $\Delta P/\Delta x = 5.83 \times 10^3\ kPa/m$. For $S_t = 0.235$ and $S_t = 0.554$ (Figure 81a,b), it can be noticed that the increment of $\langle P_g \rangle^g$ causes the increase of the inlet velocities and the reduction of the outlet ones, and this effect is more notorious for the lowest saturation, $S_t = 0.235$, than for the intermediate one, $S_t = 0.554$. On the other hand, for $S_t = 0.893$ (Figure 81c) it is not possible to establish a monotonic relationship between $\langle P_g \rangle^g$ and the inlet and outlet velocities for all vertical positions of the profiles, y^*. In this figure, it is important to notice some vertical positions where the outlet velocity, u^*_{out}, is greater

than the inlet velocity, u_{in}^{*}, for the case of $\langle P_g \rangle^g = 122kPa$, but the total inlet flow rate is still greater than the total outlet flow rate, which is in accordance with the mass conservation principle. Figure 81a-c confirm that the difference between the inlet and outlet velocities is greater as the total saturation, S_t, is lower, and this conclusion is corroborated for all values of $\langle P_g \rangle^g$ considered in the present chapter. According to the Figure 82 the influence of $\langle P_g \rangle^g$on $\left(\langle u_g \rangle^g\right)^*$ is negligible as long as the pressure gradient is constant. On the other hand, Figure 83 shows that the volume-average gap velocity, $\left(\langle u_g \rangle^g\right)^*$, increases with the pressure gradient, $\Delta P/\Delta x$.

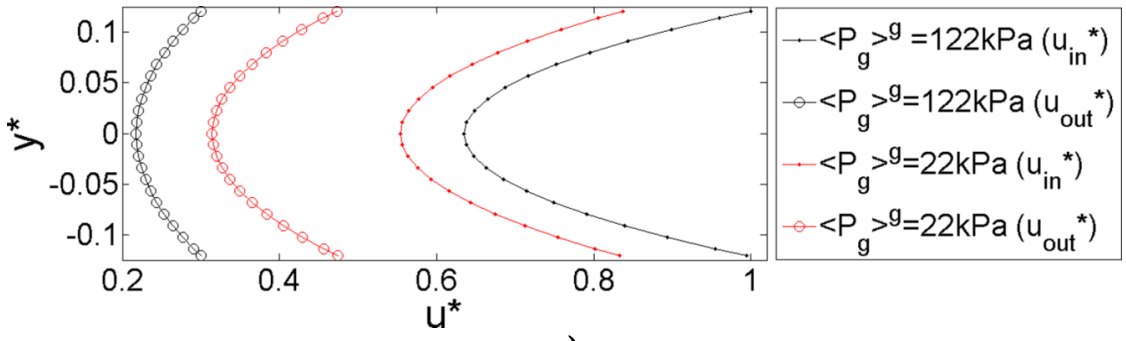

a)

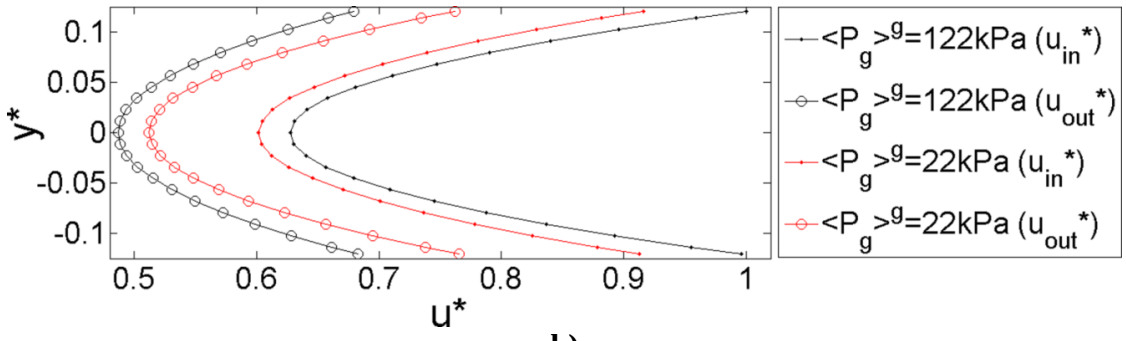

b)

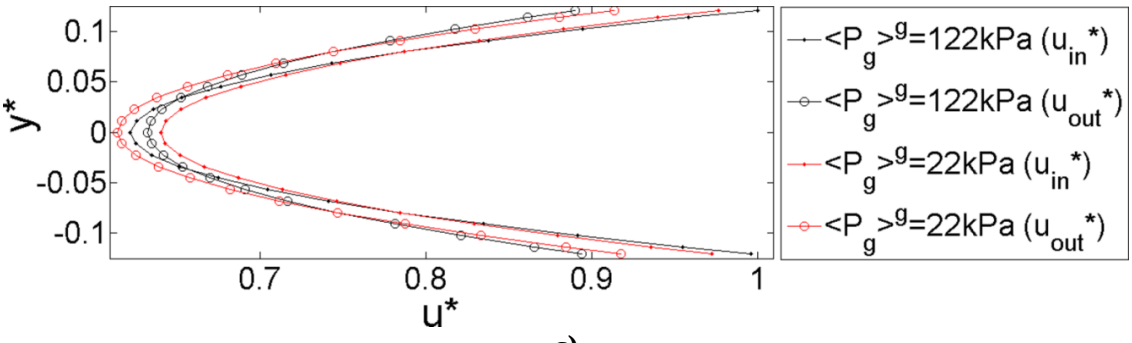

c)

Figure 81 Influence of $\langle P_g \rangle^g$ on the inlet and outlet velocities. a) Low saturation (S_t=0.235), b) Medium saturation (S_t=0.554), c) High saturation (S_t=0.893).

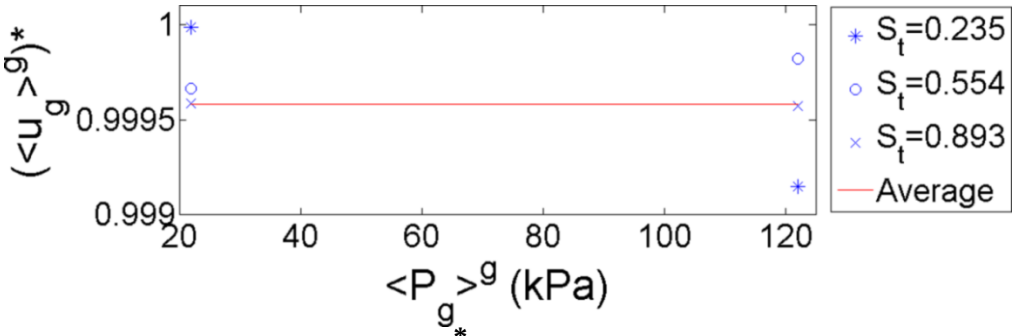

Figure 82 Influence of $\langle P_g \rangle^g$ on $(\langle u_g \rangle^g)^*$ for several values of S_t and $\Delta P/\Delta x = 5.83 \times 10^3$ kPa/m

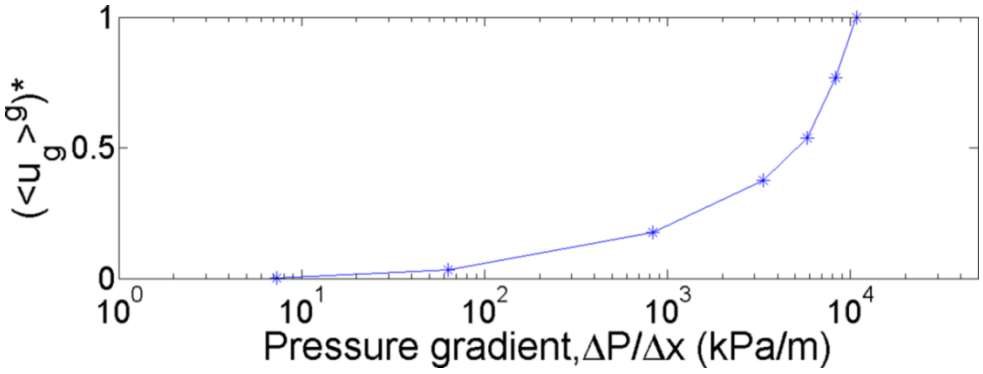

Figure 83 Influence of the pressure gradient on $(\langle u_g \rangle^g)^*$

To conclude this section, the fulfillment of the constraint of Eq. 146 is verified considering the horizontal velocities in the channel obtained by BEM in the instants represented in Figure 63a-j. The ratio $\langle|\widetilde{u_g}|\rangle^g / \langle u_g \rangle^g$ for each one of these instants is computed, obtaining the results summarized in the Table 20, where it is observed that the restriction of Eq.146 is satisfied in all instants. For all simulations considered in this chapter, Eq.146 is fulfilled.

Table 20 Ratio $\langle|\tilde{u}_g|\rangle^g / \langle u_g \rangle^g$ for filling instants of Fig. 63a-j.

Time instant, t/t_{sim}	Description	$\langle|\widetilde{u_g}|\rangle^g / \langle u_g \rangle^g$
0.012	Warps and weft saturation	0.475
0.027	Total saturation of warps	0.488
0.133	Onset of void mobilization	0.495
0.711	Void displacement at constant volume	0.513
1-2.80x10^{-5}	Onset of void migration	0.524
1-1.44x10^{-5}	Void migration (1)	0.567
1-4.21 x10^{-6}	Void migration (2)	0.601
1	Void migration (3)	0.613

6.5.2 Calculation of the sink function

Statement of the problem and simulation data.

As it is mentioned in [11], there are two limits for an air bubble that is trapped inside a tow: full air dissolution and full air compressibility. Both extreme situations were compared in Chapter 5, Figure 62a-c and Figure 63a-k. According to [163], the behaviour of the air entrapped inside the tow can be considered as a weighted average between both limits and the pressure at the fluid front can be described by the following equation:

$$P_{ff} = (1-\lambda)P_{ff}^{lower} + \lambda P_{ff}^{upper} \quad (157),$$

where P_{ff}, P_{ff}^{lower} and P_{ff}^{upper} stand for the fluid front pressure, and lower and upper bounds of the fluid front pressure, respectively, whereas λ is the air entrapment parameter, ranging between 0 and 1, that allows considering the air dissolution. The values of p_{ff}^{lower} and p_{ff}^{upper} are given by the following equations assuming an ideal gas:

$$P_{ff}^{lower} = P_{vac} - P_{cap} \quad (158a)$$

$$P_{ff}^{upper} = min\left(P_{vac}/\left(1-S_{weft}\right), P_{liquid}\right) - P_{cap} \quad (158b),$$

with P_{vac}, P_{cap} and P_{liquid} as the vacuum pressure, capillary pressure and average pressure of the liquid surrounding the tow, which shall be taken as absolute pressures in Eqs. 157 and 158a,b. When $\lambda = 0$ the case of full air dissolution is obtained (Figure 62a-c), while for $\lambda = 1$ the case of full air compressibility is reached (Figure 63a-k).

In the present work, the air entrapment parameter, λ, is taken into account in the deduction of the sink function, S_g, with the purpose to consider the combined effect of air compression and partial air dissolution. Both λ and P_{vac} are prescribed values, while P_{cap} is computed according to the models mentioned in Chapter 3. On the other hand, P_{liquid} is given by the BEM simulation. The deduction of the sink function, S_g, is developed by running several series of simulations as shown in the Table 21. For each serie of this table, five air entrapment parameters are considered, namely, $\lambda = 1$ (full air compressibility), $\lambda = 0.75$, $\lambda = 0.50$, $\lambda = 0.25$ and $\lambda = 0$ (full air dissolution), obtaining in this way a total of 280 simulations, i.e., five simulations for each serie. The geometric and material data that are kept constants in the simulations are shown in Table 18, with exception of the viscosity that is changed in the last four series of Table 21. When these geometric and

material data are maintained constant, the filling of the RUC of Figure 61 depends on the fluid front pressure, P_{ff}, average pressure, $\langle P_g \rangle^g$, pressure gradient, $\Delta P/\Delta x$, and the fluid viscosity, μ. As P_{cap} is not considered here as an input parameter of the function S_g, but as a computed parameter instead, the function S_g obtained here is not valid when the microstructure and/or porosity of tows, as well as the capillary properties, change. In such a case, another function S_g shall be obtained using the same methodology exposed here.

It is important to mention that the process of void migration (See Figure 63h-k) is not explicitly considered here in the deduction of S_g. However, the change of the weft saturation, S_{weft}, during this process is very small since the void expansion in the channel is considerably faster than the void compression inside the weft, as it was concluded in Chapter 5. Therefore, if the warps are totally filled during the void migration process, which is the present case, S_g can be considered almost constant as this migration occurs, but, if the void splitting (breaking) arises, this approximation is not valid anymore and the functions obtained here do not apply in such a case.

Table 21 Series of simulations for the determination of the sink function, S_g

Serie of simulations	Inlet pressure, p_{in} (kPa)	Outlet pressure, p_{out} (kPa)	Vacuum pressure, P_{vac} (kPa)	Average pressure, $\langle P_g \rangle^g$ (kPa)	Pressure gradient, $\Delta P/\Delta x$ (kPa/m)	Viscosity, μ (Pa.s)
1	5.500	-1.500	-75	2	5.83E+03	0.1
2	25.500	18.500	-75	22	5.83E+03	0.1
3	45.500	38.500	-75	42	5.83E+03	0.1
4	65.500	58.500	-75	62	5.83E+03	0.1
5	85.500	78.500	-75	82	5.83E+03	0.1
6	105.500	98.500	-75	102	5.83E+03	0.1
7	125.500	118.500	-75	122	5.83E+03	0.1
8	165.500	158.500	-75	162	5.83E+03	0.1
9	205.500	198.500	-75	202	5.83E+03	0.1
10	245.500	238.500	-75	242	5.83E+03	0.1
11	2.500	1.500	-75	2	8.33E+02	0.1
12	22.500	21.500	-75	22	8.33E+02	0.1
13	42.500	41.500	-75	42	8.33E+02	0.1
14	62.500	61.500	-75	62	8.33E+02	0.1
15	82.500	81.500	-75	82	8.33E+02	0.1

16	102.500	101.500	-75	102	8.33E+02	0.1
17	122.500	121.500	-75	122	8.33E+02	0.1
18	2.038	1.962	-75	2	6.33E+01	0.1
19	22.038	21.962	-75	22	6.33E+01	0.1
20	42.038	41.962	-75	42	6.33E+01	0.1
21	62.038	61.962	-75	62	6.33E+01	0.1
22	82.038	81.962	-75	82	6.33E+01	0.1
23	102.038	101.962	-75	102	6.33E+01	0.1
24	122.038	121.962	-75	122	6.33E+01	0.1
25	2.004	1.996	-75	2	7.33E+00	0.1
26	22.004	21.996	-75	22	7.33E+00	0.1
27	42.004	41.996	-75	42	7.33E+00	0.1
28	62.004	61.996	-75	62	7.33E+00	0.1
29	82.004	81.996	-75	82	7.33E+00	0.1
30	102.004	101.996	-75	102	7.33E+00	0.1
31	122.004	121.996	-75	122	7.33E+00	0.1
32	125.500	118.500	-50	122	5.83E+03	0.1
33	125.500	118.500	-25	122	5.83E+03	0.1
34	125.500	118.500	0	122	5.83E+03	0.1
35	5.500	-1.500	-50	2	5.83E+03	0.1
36	5.500	-1.500	-25	2	5.83E+03	0.1
37	5.500	-1.500	0	2	5.83E+03	0.1
38	25.500	18.500	-50	22	5.83E+03	0.1
39	25.500	18.500	-25	22	5.83E+03	0.1
40	25.500	18.500	0	22	5.83E+03	0.1
41	65.500	58.500	-50	62	5.83E+03	0.1
42	65.500	58.500	-25	62	5.83E+03	0.1
43	65.500	58.500	0	62	5.83E+03	0.1
44	105.500	98.500	-50	102	5.83E+03	0.1
45	105.500	98.500	-25	102	5.83E+03	0.1
46	105.500	98.500	0	102	5.83E+03	0.1
47	165.500	158.500	-50	162	5.83E+03	0.1
48	165.500	158.500	-25	162	5.83E+03	0.1
49	165.500	158.500	0	162	5.83E+03	0.1
50	245.500	238.500	-50	242	5.83E+03	0.1
51	245.500	238.500	-25	242	5.83E+03	0.1
52	245.500	238.500	0	242	5.83E+03	0.1
53	125.500	118.500	-75	122	5.83E+03	0.01
54	125.500	118.500	-75	122	5.83E+03	0.05
55	125.500	118.500	-75	122	5.83E+03	0.2
56	125.500	118.500	-75	122	5.83E+03	0.3

Influence of average pressure and pressure gradient on the saturation curves.

Firstly, to study how the pressure gradient affects the behavior of the total saturation, S_t, several curves of $S_t\ vs.\ t^*$ are shown in Figure 84, where $t^* = t/t_{max}$ is the normalized time, i.e., the ratio between the real time, t, and the maximum time considered in the simulations of Figure 84, t_{max}. The case of full air compressibility is taken into account and it is prescribed a vacuum pressure of $P_{vac} = -75kPa$, which can be considered as a conventional value in LCM processes [236]. The curves of Figure 84 correspond to some simulations from series 1 to 31 of Table 21 considering $\lambda = 1$. In each curve, the time instant from which the total tow saturation, S_t, remains essentially constant can be identified. This time instant corresponds to the onset of the void mobilization in the case of full air compressibility (See Figure 63c). According to the BEM code, from this time instant to the arrival of the bubble to the right extreme of the weft (See Figure 63c to Figure 63f), the change of the void volume is negligible and the total saturation remains essentially constant as long as the warps are fully saturated. This phenomenon has also been mentioned in [79]. Taking this in mind, only some results are reported in Figure 84 once the point of equilibrium saturation has been reached in each curve. As it can be observed, all simulations having the same average pressure, $\langle P_g \rangle^g$, tend to converge into a single curve, no matter the value of the pressure gradient, $\Delta P/\Delta x$. The same conclusion can be obtained for the other values of the air entrapment parameter, λ, where the total saturation is possible.

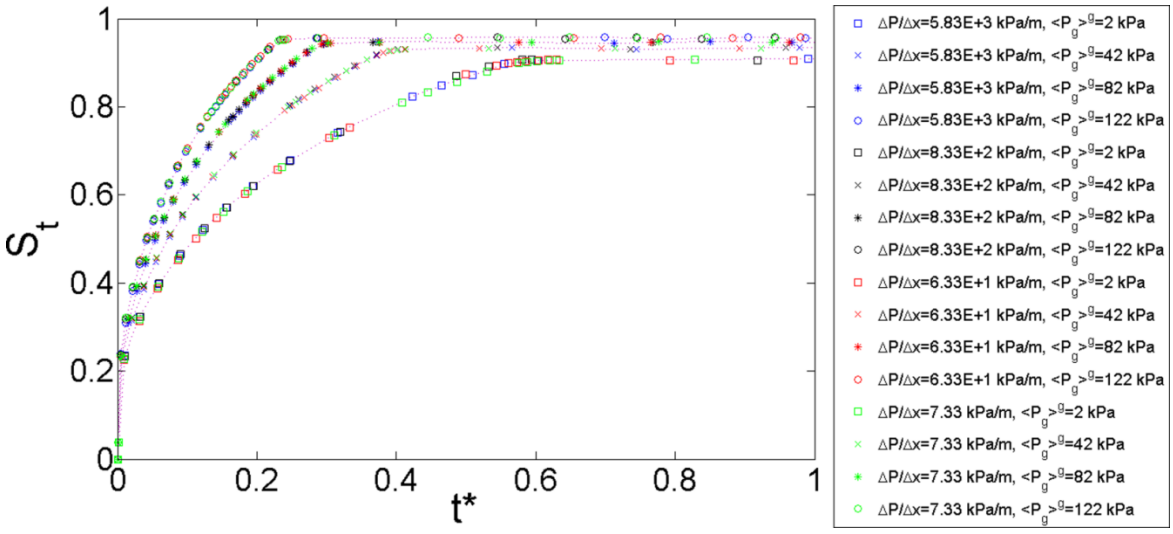

Figure 84 Influence of $\langle P_g \rangle^g$ and $\Delta P/\Delta x$ on the saturation curve S_t vs. t^*

Equilibrium time and equilibrium saturation.

In order to unify the equilibrium times of the saturation curves, the following normalized time is defined for each curve:

$$\tau = t/t_{eq} \qquad (159),$$

where t_{eq} represents the equilibrium time in which no net mass transfer from the channels into the tows is present, i.e., the time when the equilibrium saturation is reached. When $\lambda < 1$, the equilibrium time is the one when all tows are fully saturated, thereby coinciding with t_{fill} (See Eq. 156); on the other hand, when $\lambda = 1$ (full air compressibility), it is time corresponding to the onset of void mobilization inside the weft (Figure 63c). For $\lambda < 1$, the equilibrium saturation is $S_t^{eq} = 1$, while for $\lambda = 1$ the value of S_t^{eq} is not known a priori and shall be determined using the results of the BEM simulations.

The curves of $S_t\ vs.\ \tau$ for several combinations of $\langle P_g \rangle^g$, λ and P_{vac}, taking $\lambda < 1$, are shown in the Figure 85a. The BEM results indicate that these curves tend to converge into a single master curve for any combination of $\langle P_g \rangle^g$, λ and P_{vac}, enhancing in this way the conclusion obtained with the classical methodology that establishes the invariance of the curves of $S_t\ vs.\ \tau$ under $\langle P_g \rangle^g$, see Figure 77d-f. However, this behavior is not observed for $\lambda = 1$ according to the curves presented in Figure 85b, and the principal reason is that the equilibrium saturation, S_t^{eq}, depends on the average pressure, $\langle P_g \rangle^g$, in such a way that as $\langle P_g \rangle^g$ increases, S_t^{eq} also increases (Figure 85b). This poses the necessity to obtain a function for S_t^{eq} in the case of $\lambda = 1$ and this problem is tackled in the next lines.

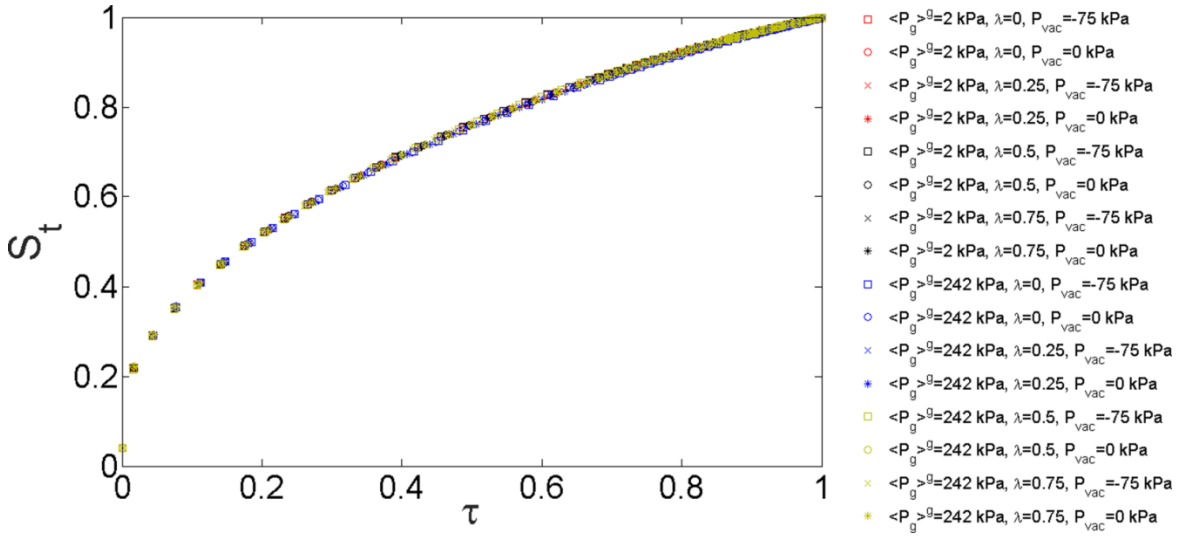

a)

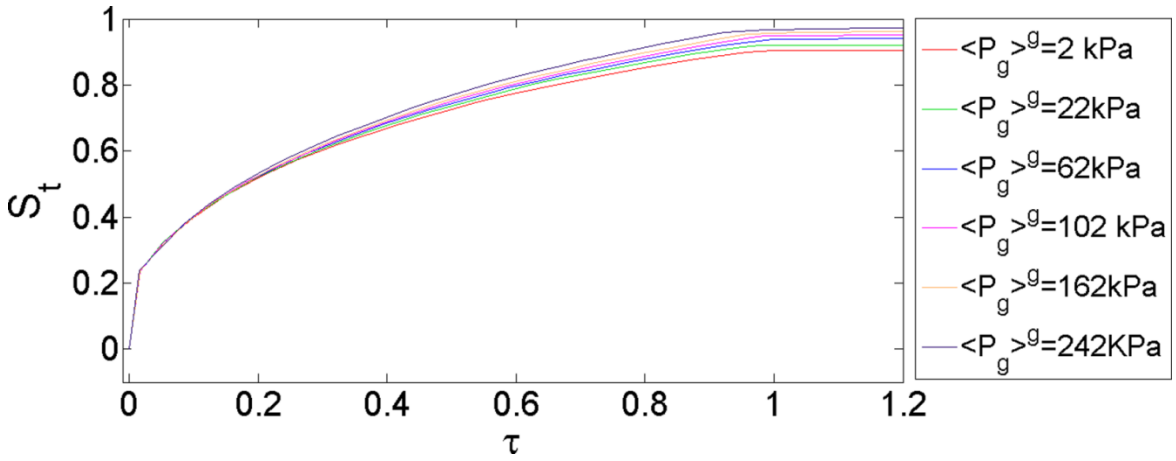

b)

Figure 85 Plots of S_t vs τ using the proposed methodology, a) For λ<1 (Partial or total air dissolution), b) λ=1 (Full air compressibility)

From the Figure 84, it is clear that the equilibrium time, t_{eq}, depends on $\langle P_g \rangle^g$ when $\lambda = 1$ and is not sensible to the values of $\Delta P/\Delta x$ considered in this work, but nothing can be concluded regarding the influence of the vacuum pressure, P_{vac}, because this pressure was taken constant in the simulations of that figure, i.e., $P_{vac} = -75kPa$. With the purpose to determine the influence of the vacuum pressure, P_{vac}, on t_{eq}, four simulations of the Table 21 are initially considered, namely, 7 and 32 to 34 with $\lambda = 1$, corresponding to an average pressure of $\langle P_g \rangle^g = 122kPa$ and vacuum pressures of $P_{vac} = [-75, -50, -25, 0]kPa$, respectively. In the Figure 86, it is observed that as the vacuum is higher, the equilibrium saturation, S_t^{eq}, is reached more quickly, i.e., t_{eq} is shorter, which is reasonable since the vacuum pressure is applied in LCM processes to promote the impregnation of the tows. In that figure, the equilibrium time is reported as $t_{eq}/t_{eq,patm}$, where $t_{eq,patm}$ stands for the equilibrium time when the initial air pressure is the atmospheric one, namely, $P_{vac} = 0$ kPa. In Figure 86, it is also worth noting that S_t^{eq} decreases as the vacuum is lower. Accordingly, results of Figure 86 confirm the importance of the vacuum pressure, P_{vac}, in the processing of composite materials because when the filling of the RUC is conducted considering that the initial air pressure is the atmospheric one, $P_{vac} = 0\,kPa$, the equilibrium saturation is $S_t^{eq} = 0.8355$, but, on the other hand, when a vacuum pressure of $P_{vac} = -75kPa$ is applied, an equilibrium saturation of $S_t^{eq} = 0.9582$ is reached, which

means a smaller void inside the weft. Additionally, the equilibrium time for the case with $P_{vac} = -75kPa$ is 61.90% the equilibrium time obtained for $P_{vac} = 0\,kPa$, which represents another advantage of the application of vacuum.

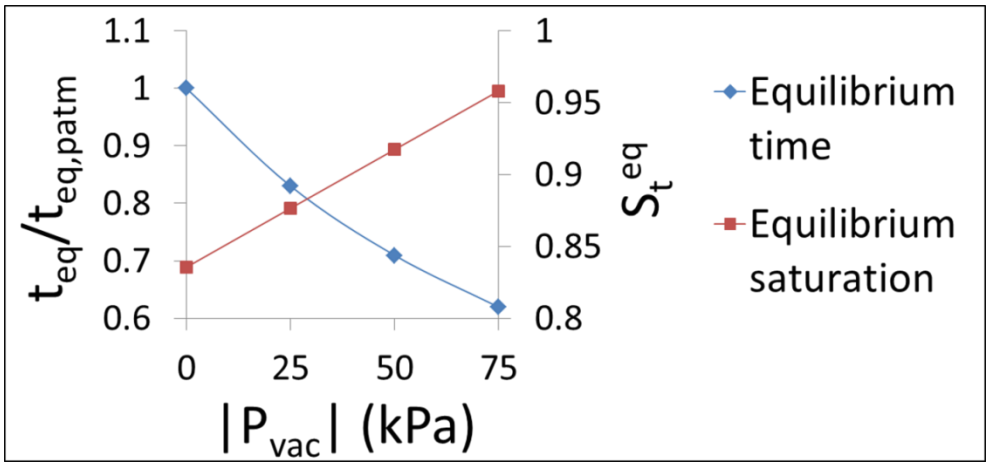

Figure 86 Influence of vacuum pressure on the equilibrium time and equilibrium saturation

From the above analysis, it is therefore obvious that both t_{eq} and S_t^{eq} depend on $\langle P_g \rangle^g$ (Figure 84) and P_{vac} (Figure 86) for the case of $\lambda = 1$. Now, in order to define how the combination of $\langle P_g \rangle^g$ and P_{vac} affects the behavior of t_{eq} and S_t^{eq}, some results of the series 35 to 56 of Table 21 with $\lambda = 1$ are considered. In the Figure 87, the equilibrium time, t_{eq}, is represented as a function of the variable $T' = \mu/\left|P_{vac} - \langle P_g \rangle^g\right|$, and it can be noticed that all points tend to coincide into a single curve; this means that t_{eq} can be conceived as a function of the difference between P_{vac} and $\langle P_g \rangle^g$, and of the viscosity, μ, in such a way that for all combinations of P_{vac}, $\langle P_g \rangle^g$ and μ leading to a same value of T', similar values of t_{eq} are expected. The same conclusion is reached for the cases with $\lambda < 1$. This conclusion is applicable for the orders of magnitude of $\langle P_g \rangle^g$, P_{vac}, μ and $\Delta P/\Delta x$ considered here, but not necessarily extensible to other orders of magnitude of these variables. As it is shown in Figure 87, a linear type curve fits well to data; so, the function for t_{eq} has the next form:

$$t_{eq} = B_1 T' \qquad (160),$$

where $B_1 = 5.37096 \times 10^7$ in this case. In the linear regression model of the Figure 87, the fit curve is forced to pass by the origin because for a zero viscosity fluid, $t_{eq} \to 0$.

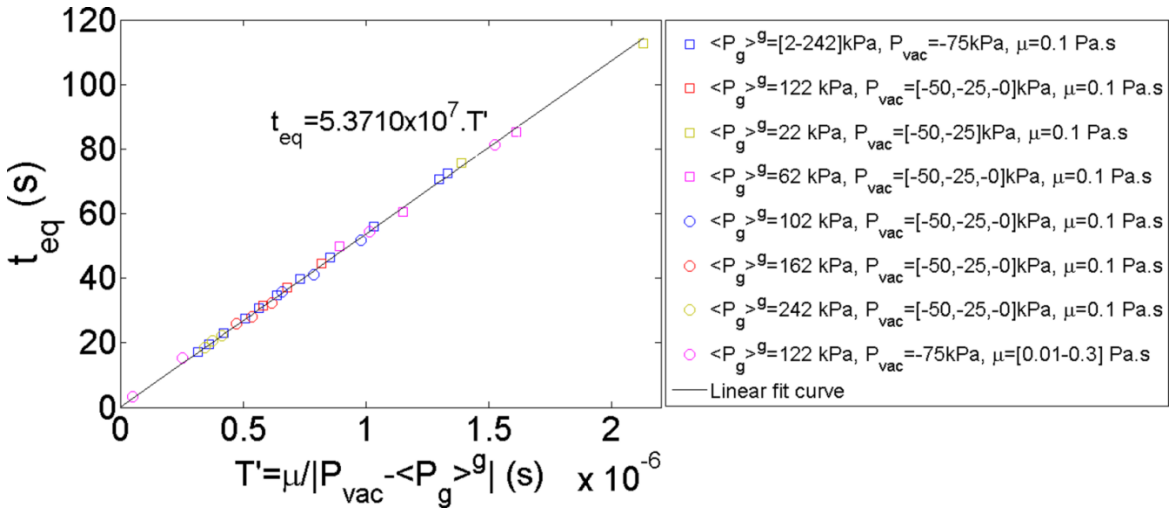

Figure 87 Plot of t_{eq} vs. $T'=\mu/|P_{vac}-\langle P_g\rangle^g|$

On the other hand, the starting point for the determination of a function for S_t^{eq} is the curve of S_t^{eq} vs. $|P_{vac}|$ of Figure 86 (red line). According to this curve, the relationship between S_t^{eq} and $|P_{vac}|$ is linear when $\langle P_g\rangle^g$ remains constant. To verify this relationship, several curves of S_t^{eq} vs. $|P_{vac}|$ for different values of $\langle P_g\rangle^g$ are presented in Figure 88a, where it can be observed that the linear relationship is kept, but the slope, "m", and intercept, "b", of the linear fitting curves vary with $\langle P_g\rangle^g$. Accordingly, in Figure 88b and Figure 88c, "m" and "b" are put in terms of $\langle P_g\rangle^g$. For the slope, m, the better fitting curve is of exponential type (Figure 88b), whereas for the intercept, b, which corresponds to the equilibrium saturation when the initial air pressure is the atmospheric one ($P_{vac} = 0\ kPa$), a second order polynomial fitting is acceptable (Figure 88c). Accordingly, the general regression equation for S_t^{eq} obtained from the simulations is as follows:

$$S_t^{eq} = \left(B_2 e^{B_3\langle P_g\rangle^g}\right)|P_{vac}| + \left(B_4\left(\langle P_g\rangle^g\right)^2 + B_5\left(\langle P_g\rangle^g\right) + B_6\right) \qquad (161)$$

For this particular problem, the fitting coefficients are: $B_2 = 3.072721 \times 10^{-6}$, $B_3 = -4.695990 \times 10^{-6}$, $B_4 = -4.018033 \times 10^{-12}$, $B_5 = 1.953801 \times 10^{-6}$ and $B_6 = 6.589545 \times 10^{-1}$. In the Figure 88d, the regression curve of $S_t^{eq}\ vs.\langle P_g\rangle^g$ is compared with the results of the BEM simulations considering a vacuum pressure of $P_{vac} = -75kPa$; some simulation results presented in such figure were not used in the deduction of the regression model. The L^2 relative error norm of the regression model is $L^2 = 9.64 \times 10^{-3}$,

which allows concluding that the model is reliable enough to describe the behavior of S_t^{eq} in terms of $\langle P_g \rangle^g$ and P_{vac} when $\lambda = 1$ (full air compressibility).

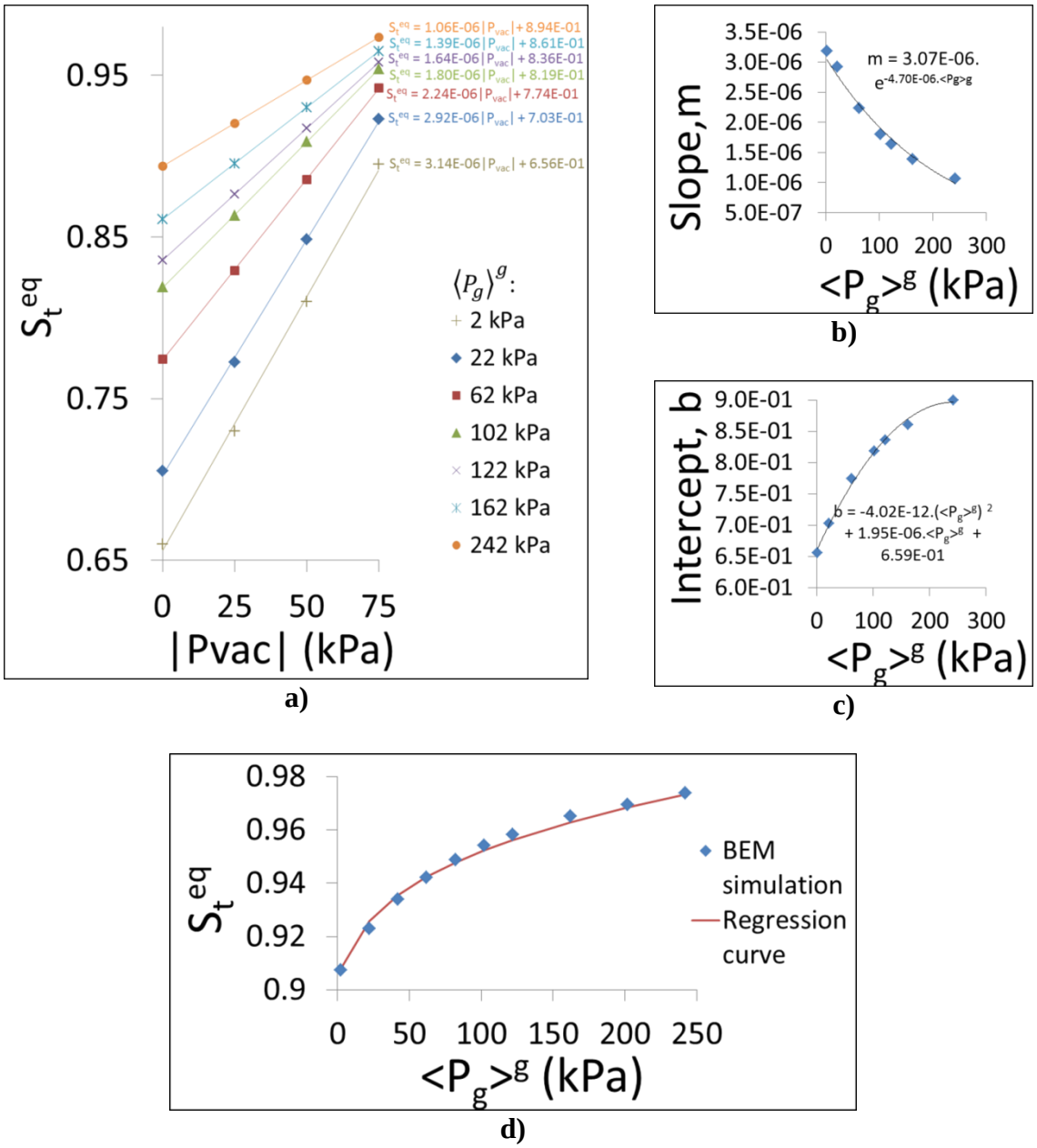

Figure 88 Plots of the regression model for S_t^{eq}. a) Plots of S_t^{eq} vs. $|P_{vac}|$ for several values of $\langle P_g \rangle^g$, b) Plot of slope, m, vs $\langle P_g \rangle^g$, c) Plot of intercept ,b, vs $\langle P_g \rangle^g$, d) Verification of the regression model of S_t^{eq} vs $\langle P_g \rangle^g$ with P_{vac}=-75kPa

Determination of the sink function, S_g.

Two procedures can be implemented for the determination of the sink term, S_g. In the first one, the saturation rate, $\dot{S}_t$, is computed from the plot of $S_t\ vs\ t$ taking the numerical derivatives and then, the Eq.155 is used to calculate S_g considering the tow and gap porosities, ε_t and ε_g, respectively, where ε_g can be computed as (See Figure 61):

$$\varepsilon_g = 1 - \frac{(H_{RUC} - H_g)L_{RUC} + \pi a_1 a_2}{H_{RUC}.L_{RUC}} \qquad (162),$$

corresponding to a value of $\varepsilon_g = 0.376$ in this case. This indirect procedure for the calculation of S_g has been previously used in [12], [225], [232]. On the other hand, in the second procedure, S_g is acquired directly from the mass transfer from the channel towards the tows, which can be estimated once the velocity fields along the interfaces channels-tows are known from the BEM solution. The comparison among the results of both procedures, direct and indirect, considering $\lambda = 1$, is shown in the Figure 89, where the plots of $S_g\ vs. S_t$ for several combinations of $\langle P_g \rangle^g$ and P_{vac} are presented. Considering all marked points of the Figure 89, the average relative difference between the results of both procedures, defined here as $L_1 = (1/N_{point})\left(\sum_{i=1}^{N_{point}} \left|(s_g^{ind})_i - (s_g^{dir})_i\right| / (s_g^{dir})_i\right)$, where N_{point}, $(s_g^{ind})_i$ and $(s_g^{dir})_i$ are the number of points, sink term computed at point "i" by the indirect procedure and sink term computed at point "i" by the direct procedure, respectively, is $L_1 = 0.0593$, obtaining an acceptable coincidence.

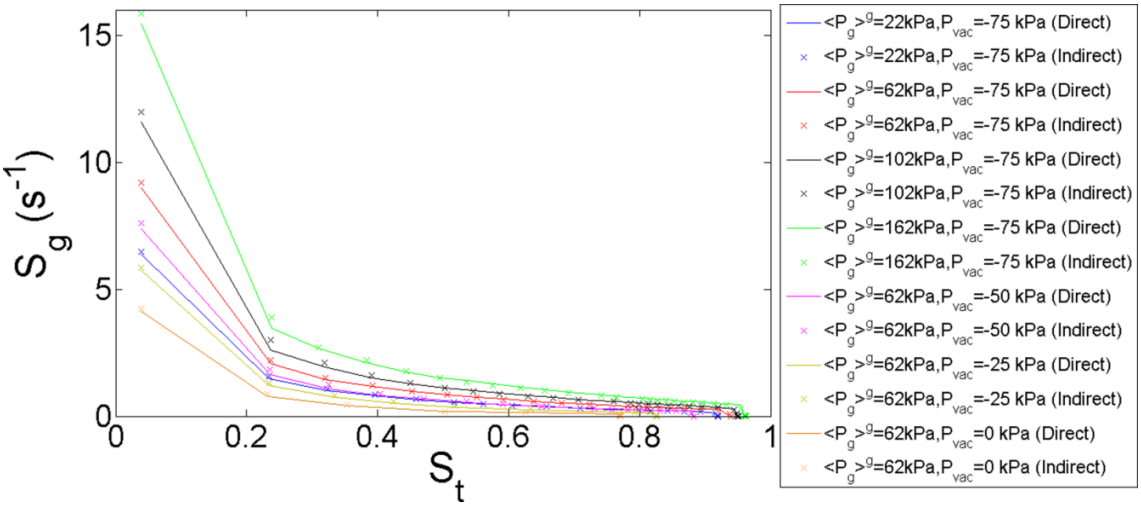

Figure 89 Comparison between direct and indirect procedures for the calculation of S_g.

On the other hand, using the results of FEM simulations, a three parameter regression function for the sink term, S_g, has been adopted in [12], [225], [232]. The form of this function was presented in Eq. 143. This function cannot be used here in its original form, but it is the starting point to purpose another lumped function. Firstly, it is convenient to remember that when $\lambda < 1$ the total tow saturation is possible and the Eq.143 does not need to be modified initially, however, in the case of full air compressibility, $\lambda = 1$, the total tow saturation is not possible and Eq.143 is thereby modified with the purpose to set S_g to zero when the equilibrium saturation, S_t^{eq}, is reached. Accordingly, Eq.143 is rewritten as Eq.163, which can be used for any value of λ, considering that $S_t^{eq} = 1$ when $\lambda < 1$:

$$\langle S_g \rangle = \left(f_1\left(\langle P_g \rangle^g\right)/\mu\right)\left\{e^{A_2\left(S_t^{eq} - S_t\right)^{A_3}} - 1\right\} \tag{163}$$

Secondly, in order to evaluate the convenience of the model of Eq.163, some regression curves of this model for the BEM results, computing S_g by the direct method, are considered (Figure 90a and Figure 90b). The case of full air compressibility, $\lambda = 1$, considering $\langle P_g \rangle^g = 202kPa$ and $P_{vac} = -75kPa$, is represented in Figure 90a, whereas a second case corresponding to partial air dissolution with $\lambda = 0.5$, $\langle P_g \rangle^g = 162kPa$ and $P_{vac} = -25kPa$, is represented in Figure 90b. In both cases, some important differences between the fit model and the BEM results can be noticed and these differences are reflected in the relatively high value of the sum of squared errors, SSE, which is presented in each figure. Similar differences between FEM numerical results and the fit curves defined by Eq.143 were found in the work of Wang and Grove [225], as it is shown in the Figure 90c, which corresponds to a curve of $dS_t/d\tau \; vs. S_t$ that has the same form as the curve $S_g \; vs. S_t$ because $dS_t/d\tau$ and S_g are related by a constant (see Eq. 155). With the objective to improve this fitting model, a potential type function is added to Eq.163 with an additional free parameter, A_4, as it is specified in the Eq. 164. The fitting curves of the improved model for the two cases previously considered are presented in the Figure 90d and Figure 90e, where it can be observed a better correlation with the BEM results. The value of SSE in the improved model is $SSE = 0.326$ for the first case (Figure 90d) and $SSE = 0.110$ for the second one (Figure 90e), whereas, for the original model, these values are $SSE = 13.07$ (Figure 90a) and $SSE = 13.97$ (Figure 90b), respectively, showing that the proposed model is better.

$$\langle S_g \rangle = \left(f_1\left(\langle P_g \rangle^g\right)/\mu\right)\left\{e^{A_2\left(S_t^{eq}-S_t\right)^{A_3}} - 1 + \left(S_t^{eq} - S_t\right)^{A_4}\right\} \quad (164)$$

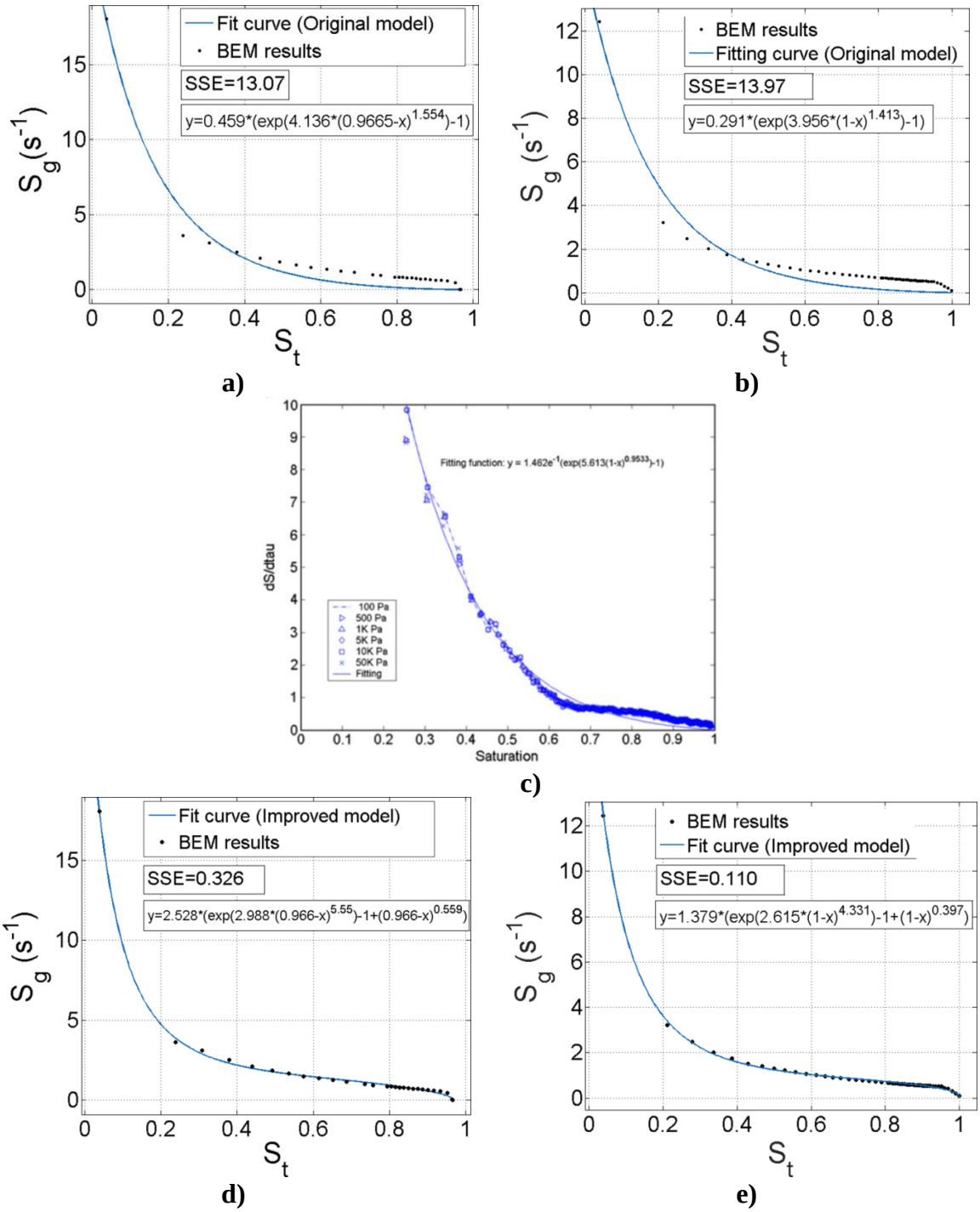

Figure 90 Comparison between fitting models of the sink term, S_g. a) Original fit model for λ=1, $\langle P_g \rangle^g$=202kPa and P_{vac}=-75kPa, b) Original fit model for λ=0.5, $\langle P_g \rangle^g$=162kPa and P_{vac}=-25kPa, c) Original fit model in the work of Wang and Grove [225], d) Improved fit model for λ=1, $\langle P_g \rangle^g$=202kPa and P_{vac}=-75kPa, e) Improved fit model for λ=0.5, $\langle P_g \rangle^g$=162kPa and P_{vac}=-25kPa.

As it was shown in Section 6.4, in the original model, Eq.143, f_1 is a linear function of $\langle P_g \rangle^g$ such that $f_1\left(\langle P_g \rangle^g\right) = \varepsilon_t\left(1-\varepsilon_g\right)A_1\left(\langle P_g \rangle^g\right)$, where $A_1\left(\langle P_g \rangle^g\right) = (A_1^*/\beta^*)\langle P_g \rangle^g$. In general, the present model is more complex since it is not considered a uniform pressure in the gaps and other parameters are taken into account. Accordingly, the dependency of the fitting coefficients of Eq. 164 on $\langle P_g \rangle^g$, P_{vac} and λ cannot be disregarded a priori and a more general form of the Eq.164 can be written as:

$$\langle S_g \rangle = \left(f_1\left(\langle P_g \rangle^g, P_{vac}, \lambda\right)/\mu\right)\left\{e^{A_2\left(\langle P_g \rangle^g, P_{vac}, \lambda\right).\left(S_t^{eq}-S_t\right)^{A_3\left(\langle P_g \rangle^g, P_{vac}, \lambda\right)}} - 1 + \left(S_t^{eq} - S_t\right)^{A_4\left(\langle P_g \rangle^g, P_{vac}, \lambda\right)}\right\} \quad (165)$$

Initially, the form of the fitting parameters of the Eq. 165 in terms of $\langle P_g \rangle^g$ and P_{vac} for the case of full air compressibility, $\lambda = 1$, is obtained. Using a similar methodology to the one exposed in Section 6.4, the function f_1 can be written as: $f_1\left(\langle P_g \rangle^g, P_{vac}, \lambda = 1\right) = \varepsilon_t\left(1-\varepsilon_g\right).A_1\left(\langle P_g \rangle^g, P_{vac}, \lambda = 1\right)$. To establish a function for A_1, A_2, A_3 and A_4, the plots of these fitting parameters against $\langle P_g \rangle^g$ and P_{vac} are taken into account; these plots are represented in the Figure 91a-i. The fitting parameters for each combination of $\langle P_g \rangle^g$ and P_{vac} were obtained using the curve fitting tool of MATLAB.

As it can be observed in the Figure 91a, the linear relationship between A_1 and $\langle P_g \rangle^g$ still remains when the vacuum pressure, P_{vac}, is constant. Additionally, the fit curves are nearly parallel each other, as it can be confirmed by comparing the slopes of the regression equations; the average slope of these curves is $m_1^{av} = 2.89 \times 10^{-6}$. On the other hand, according to Figure 91b, the intercept of the fitting curves, b_1, changes almost linearly with $|P_{vac}|$, and the slope of the linear fitting curve for the plot of b_1 vs $|P_{vac}|$ is $m_1^* = 2.94 \times 10^{-6}$. As m_1^{av} and m_1^* are similar, it is reasonable to suppose that A_1 is approximately a linear function of $\left|P_{vac} - \langle P_g \rangle^g\right|$. This assumption can be confirmed in Figure 91c, where all combinations of $\langle P_g \rangle^g$ and P_{vac} tend to converge into a single curve when the abscissa values are $\left|P_{vac} - \langle P_g \rangle^g\right|$. A similar analysis can be done for the coefficients of the fitting curves of the parameter A_3 (Figure 91g); according to Figure 91h, the parameter A_3 can be also conceived as a linear function of $\left|P_{vac} - \langle P_g \rangle^g\right|$, despite the points are sparser with respect to the fitting curve in this case than for the parameter A_1 (Figure 91c). The

parameter A_4 varies in logarithmic manner with $\left|P_{vac} - \langle P_g \rangle^g\right|$, as it is shown in the Figure 91i. On the other hand, the fitting parameter A_2 varies in almost linear manner with $\langle P_g \rangle^g$ for all values of P_{vac} (Figure 91d), but it is not a single function of $\left|P_{vac} - \langle P_g \rangle^g\right|$ according to the BEM results and deserves another treatment. Accordingly, the coefficients of the regression curves for $A_2\ vs.\langle P_g \rangle^g$, which are represented as m_2 and b_2, are put in terms of $|P_{vac}|$ in the Figure 91e and Figure 91f. For both coefficients, m_2 and b_2, a linear variation with $|P_{vac}|$ can be noticed. Consequently, as a result of all conclusions achieved for the parameters A_1, A_2, A_3 and A_4, the Eq. 165 can be rewritten as:

$$\langle S_g \rangle = \left(f_1\left(\left|P_{vac} - \langle P_g \rangle^g\right|\right)/\mu\right)\left\{e^{A_2\left(\langle P_g \rangle^g, P_{vac}\right).\left(S_t^{eq} - S_t\right)^{A_3\left(|P_{vac} - \langle P_g \rangle^g|\right)}} - 1 + \left(S_t^{eq} - S_t\right)^{A_4\left(|P_{vac} - \langle P_g \rangle^g|\right)}\right\} \quad (166),$$

where:

$$f_1\left(\left|P_{vac} - \langle P_g \rangle^g\right|\right) = \varepsilon_t\left(1 - \varepsilon_g\right)A_1\left(\left|P_{vac} - \langle P_g \rangle^g\right|\right) = \varepsilon_t\left(1 - \varepsilon_g\right)\left(\alpha_1\left|P_{vac} - \langle P_g \rangle^g\right| + \beta_1\right) \quad (167a),$$

$$A_2\left(\langle P_g \rangle^g, P_{vac}\right) = m_2(|P_{vac}|).\, ln\left(\langle P_g \rangle^g\right) + b_2(|P_{vac}|) \quad (167b)$$

$$m_2(|P_{vac}|) = \alpha_2^{(1)}|P_{vac}| + \alpha_2^{(2)} \quad (167c)$$

$$b_2(|P_{vac}|) = \beta_2^{(1)}|P_{vac}| + \beta_2^{(2)} \quad (167d)$$

$$A_3\left(\left|P_{vac} - \langle P_g \rangle^g\right|\right) = \alpha_3\left|P_{vac} - \langle P_g \rangle^g\right| + \beta_3 \quad (167e)$$

$$A_4\left(\left|P_{vac} - \langle P_g \rangle^g\right|\right) = \alpha_4.\, ln\left(\left|P_{vac} - \langle P_g \rangle^g\right|\right) + \beta_4 \quad (167f)$$

and the fitting coefficients are shown in the Table 22.

The above-mentioned procedure is repeated for the other values of λ considered in this work. According to the BEM results, the functions for A_1, A_2, A_3 and A_4 has the same form as for the last case of $\lambda = 1$, Eq.167a-f, with fitting coefficients also given in the Table 22. For $\lambda < 1$, the relationship between the fitting parameters shown in Table 22 and the air entrapment parameter, λ, can be approximated by a linear regression. Therefore, for $\lambda < 1$, each fitting coefficient of Table 22, which can be represented in general form as ψ, can be written as follows:

$$\psi = m_\psi.\lambda + b_\psi \quad (168),$$

where m_ψ and b_ψ are the slope and intercept of the linear fitting curves, while $\psi = \left[\alpha_1, \beta_1, \alpha_2^{(1)}, \alpha_2^{(2)}, \beta_2^{(1)}, \beta_2^{(2)}, \alpha_3, \beta_3, \alpha_4, \beta_4\right]$. The values of m_ψ and b_ψ for each fitting coefficient are shown in the Table 23.

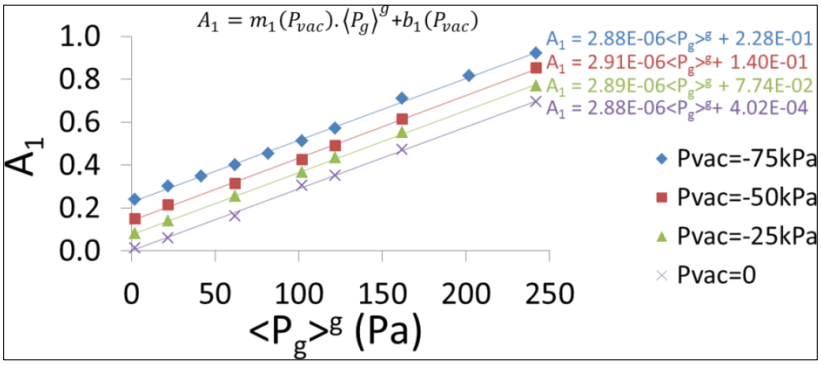

a)

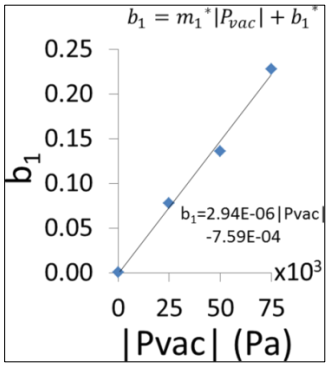

b)

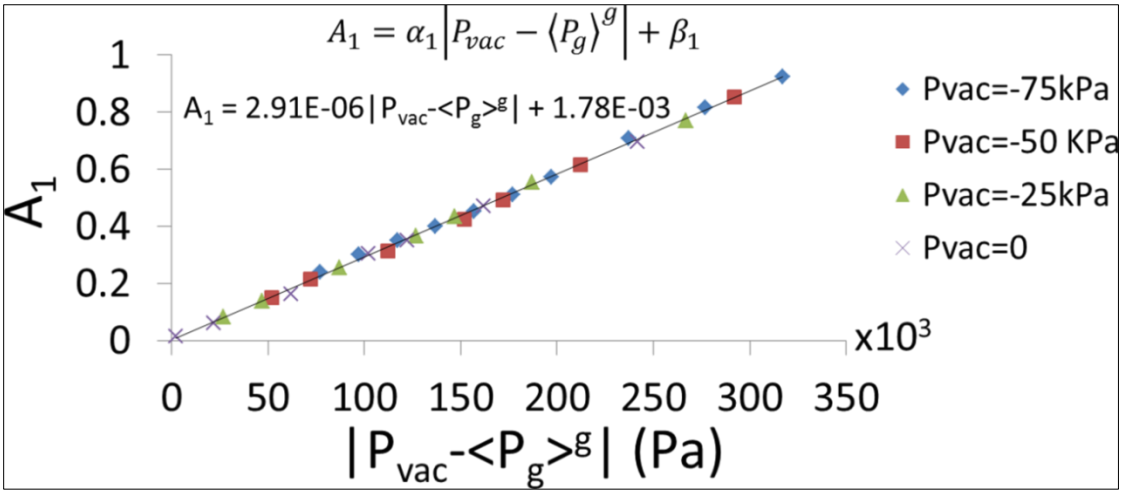

c)

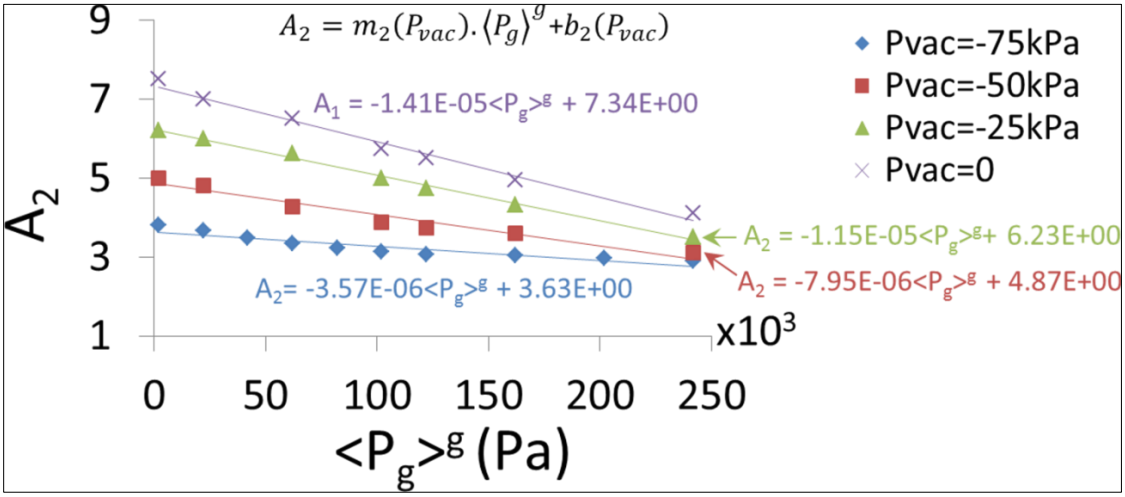

d)

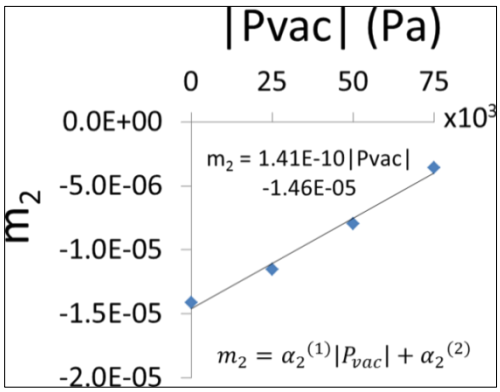
|Pvac| (Pa)
0
25
50
75
0.0E+00
-5.0E-06
-1.0E-05
-1.5E-05
-2.0E-05
x10³
m₂
m₂ = 1.41E-10|Pvac| -1.46E-05
m₂ = α₂⁽¹⁾|P_vac| + α₂⁽²⁾

e)

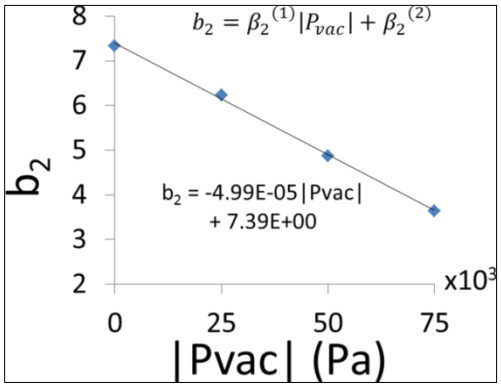
b₂ = β₂⁽¹⁾|P_vac| + β₂⁽²⁾
8
7
6
5
4
3
2
b₂
b₂ = -4.99E-05|Pvac| + 7.39E+00
x10³
0
25
50
75
|Pvac| (Pa)

f)

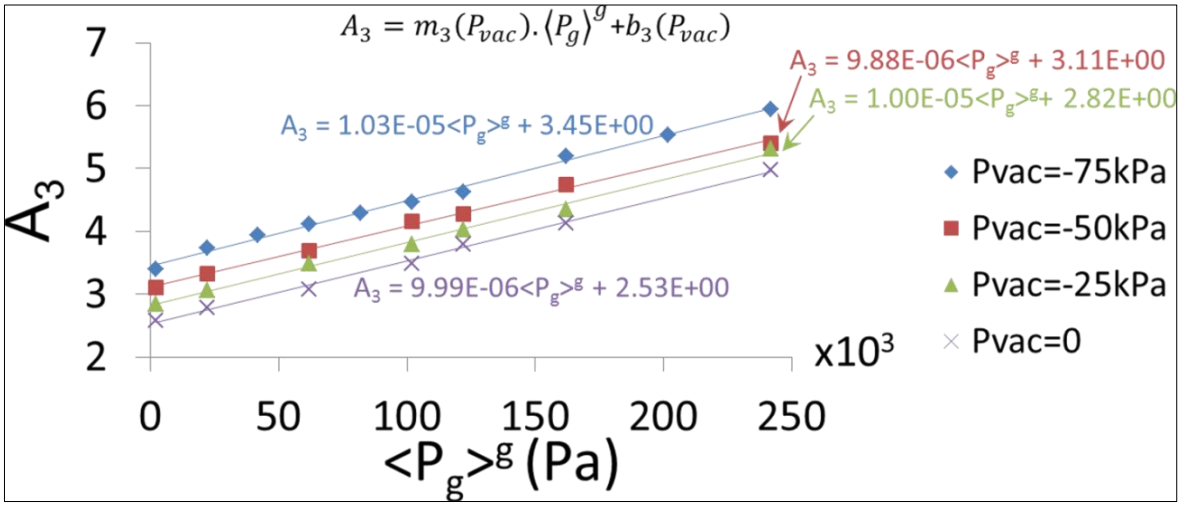
A₃ = m₃(P_vac).⟨P_g⟩^g + b₃(P_vac)
A₃ = 9.88E-06<P_g>^g + 3.11E+00
A₃ = 1.00E-05<P_g>^g + 2.82E+00
A₃ = 1.03E-05<P_g>^g + 3.45E+00
A₃ = 9.99E-06<P_g>^g + 2.53E+00
Pvac=-75kPa
Pvac=-50kPa
Pvac=-25kPa
Pvac=0
A₃
7
6
5
4
3
2
x10³
0
50
100
150
200
250
<P_g>^g (Pa)

g)

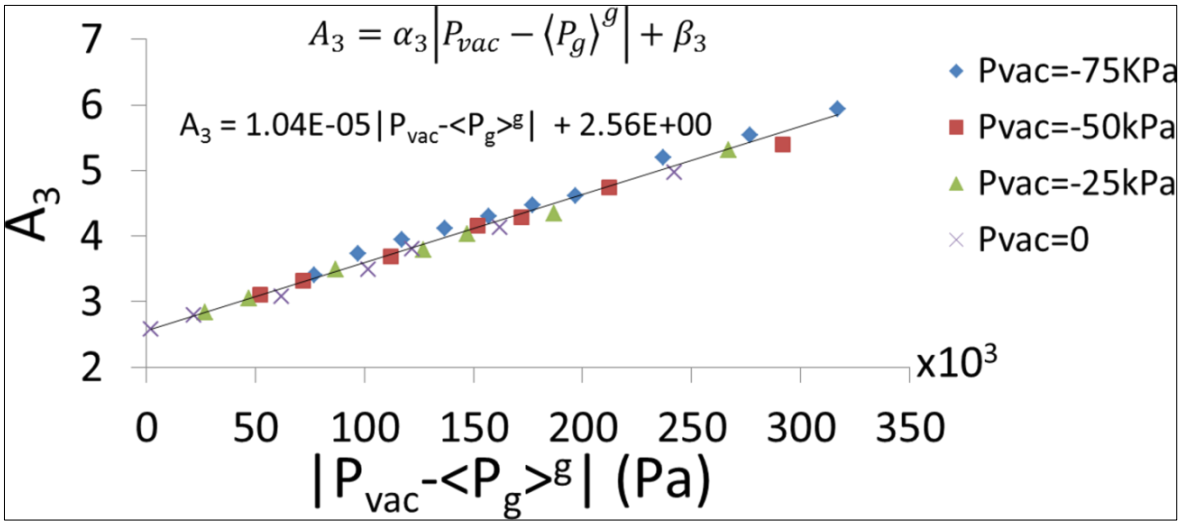
A₃ = α₃|P_vac − ⟨P_g⟩^g| + β₃
A₃ = 1.04E-05|P_vac-<P_g>^g| + 2.56E+00
Pvac=-75KPa
Pvac=-50kPa
Pvac=-25kPa
Pvac=0
A₃
7
6
5
4
3
2
x10³
0
50
100
150
200
250
300
350
|P_vac-<P_g>^g| (Pa)

h)

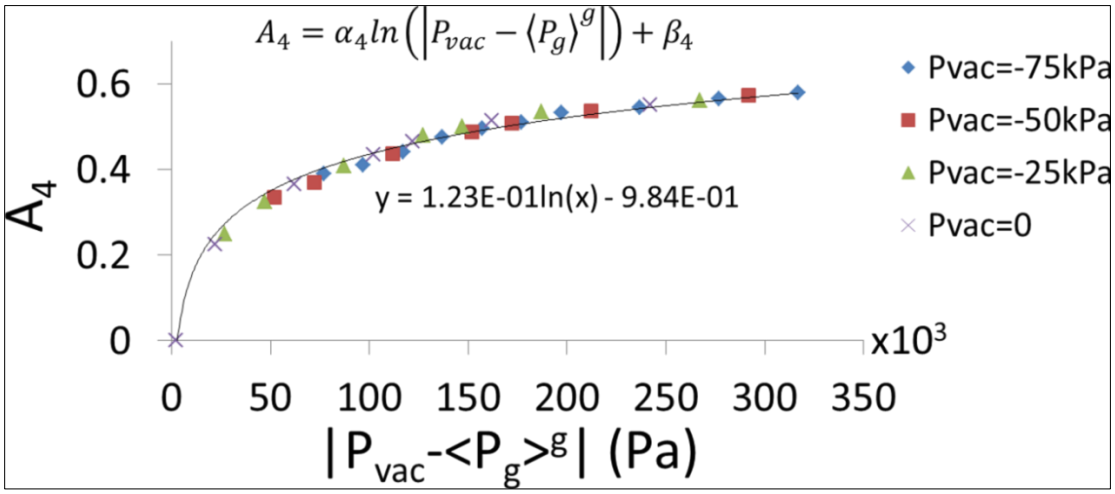

i)

Figure 91 Plots to find the fitting coefficients of the sink function, S_g, for λ=1. a) A_1 vs $\langle P_g\rangle^g$ for several values of P_{vac}, b) b_1 vs $|P_{vac}|$, c) A_1 vs $|P_{vac}-\langle P_g\rangle^g|$, d) A_2 vs $\langle P_g\rangle^g$ for several values of P_{vac}, e) m_2 vs $|P_{vac}|$, f) b_2 vs $|P_{vac}|$, g) A_3 vs $\langle P_g\rangle^g$ for several values of P_{vac}, h) A_3 vs $|P_{vac}-\langle P_g\rangle^g|$, i) A_4 vs $|P_{vac}-\langle P_g\rangle^g|$

Table 22 Fitting coefficients of the regression model for S_g

Air entrapment parameter, λ	α_1	β_1	$\alpha_2^{(1)}$	$\alpha_2^{(2)}$	$\beta_2^{(1)}$	$\beta_2^{(2)}$	α_3	β_3	α_4	β_4
1	2.905 E-06	1.779 E-03	1.407 E-10	-1.457 E-05	-4.992 E-05	7.390 E+00	1.038 E-05	2.558 E+00	1.233 E-01	-9.840 E-01
0.75	3.445 E-06	8.251 E-05	-3.369 E-13	-2.737 E-07	-2.184 E-06	2.682 E+00	1.716 E-07	5.804 E+00	-1.398 E-02	6.568 E-01
0.50	3.323 E-06	1.041 E-04	-1.495 E-12	-7.106 E-08	-2.079 E-06	2.629 E+00	6.072 E-07	5.205 E+00	-8.270 E-03	5.531 E-01
0.25	3.279 E-06	1.283 E-04	-3.218 E-12	9.362 E-08	-2.234 E-06	2.608 E+00	9.452 E-07	4.80 E+00	-1.781 E-03	4.682 E-01
0	3.160 E-06	1.454 E-04	-4.326 E-12	2.425 E-07	-1.602 E-06	2.585 E+00	1.407 E-06	4.558 E+00	3.332 E-03	3.859 E-01

Table 23 Values of m_ψ and b_ψ for the fitting coefficients when λ<1.

ψ	m_ψ	b_ψ
α_1	3.6058E-07	3.1667E-06
β_1	-8.5157E-05	1.4701E-04
$\alpha_2^{(1)}$	5.4765E-12	-4.3976E-12
$\alpha_2^{(2)}$	-6.8480E-07	2.5475E-07
$\beta_2^{(1)}$	-6.3742E-07	-1.7859E-06
$\beta_2^{(2)}$	1.2495E-01	2.5792E+00
α_3	-1.6180E-06	1.3896E-06
β_3	1.6567E+00	4.4709E+00
α_4	-2.3373E-02	3.5894E-03
β_4	3.5911E-01	3.8131E-01

6.5.3 Calculation of effective unsaturated permeability and gap permeability from BEM simulations.

As it was aforementioned, the macroscopic modeling of dual-scale porous media can be tackled in different manners. One of these is based on the Richards' equation, where it is necessary to know a relationship between the effective unsaturated permeability, K_{eff}, also called the total permeability by Ashari [139], [140], and the total saturation, S_t. From the results of the BEM simulations, the curves of $K_{eff}\ vs\ S_t$ can be obtained by computing the value of K_{eff} in each time instant as follows:

$$K_{eff} = \langle u_l \rangle \mu / (\Delta P / \Delta x) \quad (169),$$

where $\langle u_l \rangle$ is the phase volume-averaged horizontal velocity in the liquid phase, l, obtained from the BEM simulation. In this case, the liquid phase includes both the channel and the saturated volume of the tows.

The second approach for dealing with dual-scale porous media at the macroscopic scale is the equivalent Darcy approach, which requires the calculation of the gap permeability, K_g, to model the flow in the channels as a Darcy flow. The gap permeability, K_g, was suggested in [10] and accounts for the easiness of impregnation of the channels considering that the tows are impermeable. Accordingly, this property is only dependent on the RUC architecture and can be determined in this case by setting the normal permeability of the tows, K_n, to zero and using the following equation:

$$K_g = \langle u_g \rangle \mu / (\Delta P / \Delta x) \quad (170),$$

where $\langle u_g \rangle$ is the phase volume-averaged horizontal velocity in the channel or gap domain. It is important to remind that both $\langle u_l \rangle$ and $\langle u_g \rangle$ are referred to the total volume of the RUC.

Series 1, 4, 7, 11, 14, 17, 18, 21 and 24 of Table 21 for $\lambda = 1$, where $\varepsilon_t = 0.15$, and the equivalent simulations with $\varepsilon_t = 0.46$, are initially considered to compute K_g and K_{eff}, and the results are shown in Figure 92a for K_g and Figure 92b,c for K_{eff}. As shown in Figure 92a, which corresponds to the plots of $K_g\ vs. \langle P_g \rangle^g$ for three values of $\Delta P / \Delta x$, the standard deviation of the results is negligible for K_g, $SD = 6.82 \times 10^{-14}$, which demonstrates the coherence of the BEM results with the premise that K_g should remain constant, independent on the value of $\Delta P / \Delta x$ and $\langle P_g \rangle^g$, as long as the RUC geometry is

not altered. Therefore, the gap permeability can be reported here as the average value shown in Figure 92a, i.e., $K_g = 1.35 \times 10^{-8}\, m^2$, which is employed in the macroscopic simulations of the next section. It is very important to notice that this value of K_g confirms the principal assumption of the present chapter: the equivalent permeability of the gap or channel is several orders of magnitude larger than the permeability of the tows.

The curves of $K_{eff}\ vs\ S_t$ for two values of tow porosity, $\varepsilon_t = 0.15$ and $\varepsilon_t = 0.46$, are presented in Figure 92b and Figure 92c, respectively, where it is observed that these curves are not dependent either on the pressure gradient, $\Delta P/\Delta x$, and on the average pressure, $\langle P_g \rangle^g$. To the best of the author's knowledge, there is not another work devoted to the study of the behavior of the effective unsaturated permeability, K_{eff}, with the saturation, S_t, in cross-ply or woven fibrous reinforcements, but some works dealing with non-woven fibrous reinforcements have also found the non-dependency of the curves of $K_{eff}\ vs\ S_t$ on the processing parameters. For instance, Landeryou et al. [138] carried out some experiments in samples at different flow rates and found that the relationship between the unsaturated permeability and the saturation does not depend on the flow rate. Afterwards, Ashari [139], [140] run some FEM simulations to study the influence of the saturation, fiber diameter and fiber content on the unsaturated permeability of non-woven reinforcements, not finding any influence of the applied pressure.

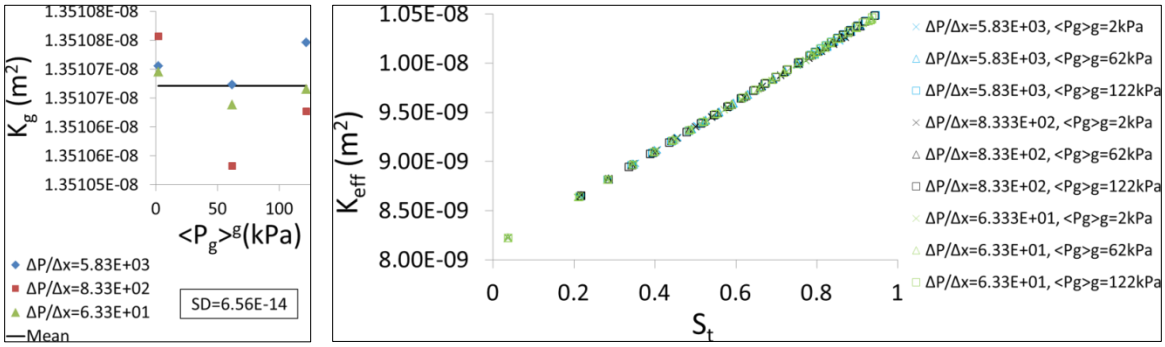

a) **b)**

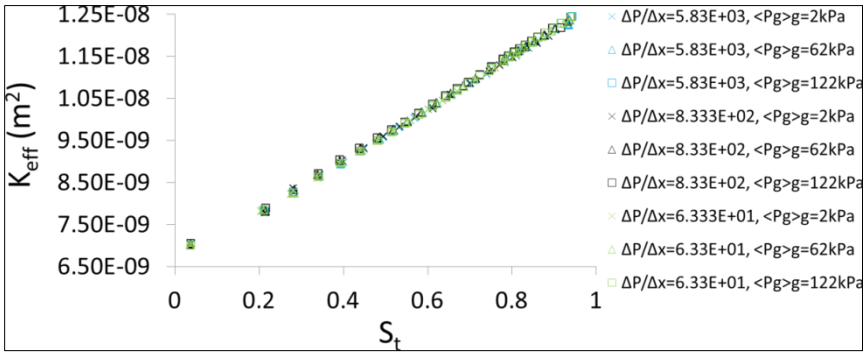

c)

Figure 92 Influence of $\langle P_g \rangle^g$ and $\Delta P/\Delta x$ on K_g and K_{eff}. a) Plot of K_g vs. $\langle P_g \rangle^g$ for several values of $\Delta P/\Delta x$, b) Curves K_{eff} vs S_t for several values of $\Delta P/\Delta x$ and $\langle P_g \rangle^g$, ε_t=0.15, c) Curves K_{eff} vs S_t for several values of $\Delta P/\Delta x$ and $\langle P_g \rangle^g$, ε_t=0.46.

The influence of the tow porosity, ε_t, and the geometry of the weft on K_g and K_{eff} is studied as well in this section. For this purpose, some additional simulations were run considering the data of the *Serie 7* of Table 21 with $\lambda = 1$ (p_{in}=125.5 kPa, p_{out}=118.5 kPa, P_{vac}=-75 kPa, $\langle P_g \rangle^g$=122 kPa, $\Delta P/\Delta x$=5.83×10^3 kPa/m, μ =0.1 Pa.s) and modifying some geometrical parameters of the Table 18 (ε_t, K_1, K_2, a_1, a_2, ε_g), as it is shown in the Table 24. The influence of the tow porosity, ε_t, on the curves of K_{eff} *vs* S_t can be appreciated in the Figure 93, where it can be noticed that when the tows are almost unsaturated, namely, $S_t \to 0$, BEM results predict that K_{eff} is lower as ε_t increases, but, as the warps and wefts are permeated by the liquid (S_t increases), the differences between the unsaturated permeabilites reduce and all curves tend to converge into a single point, which, in the present case, corresponds approximately to $S_t = 0.44$ and $K_{eff} = 9.22 \times 10^{-9} m^2$. After this point, the behavior of K_{eff} with ε_t is reversed, that is, K_{eff} is larger as ε_t increases, and the differences between the unsaturated permeabilities increases with S_t (the curves diverge each other). This behavior is maintained until the total saturation is almost reached, namely, $S_t \to 1$. Accordingly, the BEM results suggest that the variation of K_{eff} with the tow porosity, ε_t, in dual-scale porous media depends on the saturation, S_t.

Table 24 Additional simulations to study the influence of ε_t and the weft geometry on K_g and K_{eff}

Number of simulation	Geometrical parameters modified	Values of parameters modified
1	Porosity-Permeability tensor	$\varepsilon_t = 0.25, K_1 = 1.69 \times 10^{-12} m^2$, $K_2 = 3.06 \times 10^{-13}\ m^2$
2	Porosity-Permeability tensor	$\varepsilon_t = 0.37, K_1 = 7.72 \times 10^{-12} m^2$, $K_2 = 1.70 \times 10^{-12}\ m^2$
3	Porosity-Permeability tensor	$\varepsilon_t = 0.46, K_1 = 2.09 \times 10^{-11} m^2$, $K_2 = 4.64 \times 10^{-12}\ m^2$
4	Aspect ratio of weft	$a_1 = 4.17 \times 10^{-4} m,\ a_2 = 1.20 \times 10^{-4} m,$ $a_1/a_2 = 3.47, \varepsilon_g = 0.376$
5	Aspect ratio of weft	$a_1 = 5.50 \times 10^{-4} m,\ a_2 = 9.00 \times 10^{-5} m,$ $a_1/a_2 = 6.11, \varepsilon_g = 0.376$
6	Gap porosity	$a_1 = 5.86 \times 10^{-4} m,\ a_2 = 1.17 \times 10^{-4} m,$ $a_1/a_2 = 5.00, z = 0.268$
7	Gap porosity	$a_1 = 3.91 \times 10^{-4} m,\ a_2 = 7.82 \times 10^{-5} m,$ $a_1/a_2 = 5.00, \varepsilon_g = 0.489$

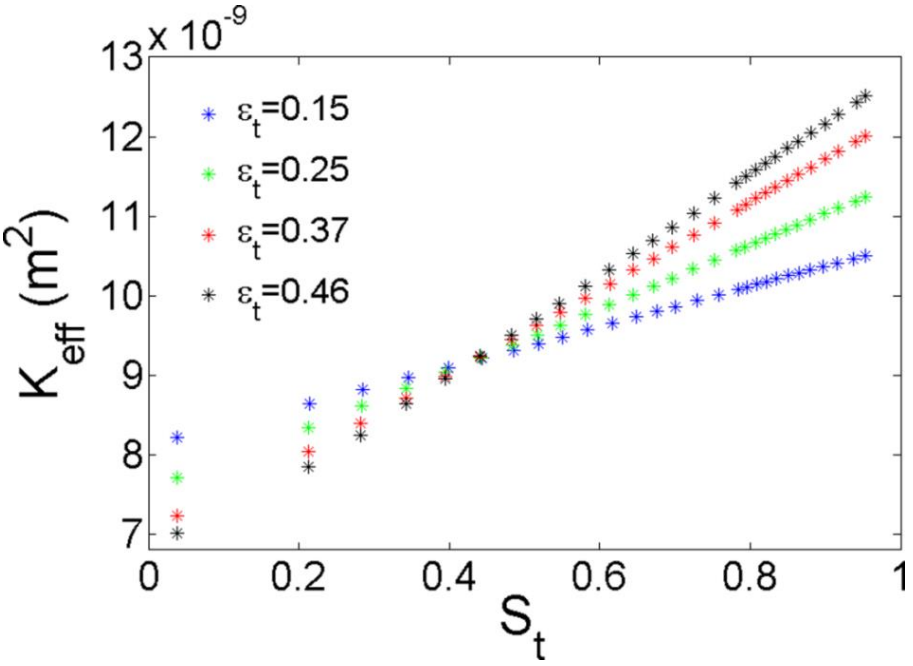

Figure 93 Influence of the tow porosity, ε_t, on the curve of K_{eff} vs S_t

A possible explanation for the variation of the curves of $K_{eff}\ vs. S_t$ with the tow porosity, ε_t, can be constructed by taking into account the phase volume-averaged horizontal

velocity of the liquid phase, $\langle u_l \rangle$, which appears in Eq. 169. In the unit-width RUC of Figure 61, this velocity can be expressed as:

$$\langle u_l \rangle = \left(\int_{A_g} u_g . dA_g + \int_{A_{tows}^{sat}} \langle u_l^{tows} \rangle^l . dA_{tows}^{sat} \right) / A_{RUC} \quad (171),$$

where u_g is the pointwise horizontal velocity of the liquid in the channel or gap domain, A_g is the area of the channel domain, $\langle u_l^{tows} \rangle^l$ is the intrinsic-phase volume-averaged horizontal velocity of the liquid in the tows, A_{tows}^{sat} is the saturated area of the tows and A_{RUC} is the total area of the RUC. Eq. 171 can be also written in terms of the phase volume-averaged velocity in the channel domain, $\langle u_g \rangle$, as follows:

$$\langle u_l \rangle = \langle u_g \rangle + \left(\int_{A_{tows}^{sat}} \langle u_l^{tows} \rangle^l . dA_{tows}^{sat} \right) / A_{RUC} \quad (172),$$

According to Eq. 172, for a determined RUC geometry, $\langle u_l \rangle$ only depends on the velocity field in the channel domain and the velocity field in the saturated volume of the tows. The change of these velocity fields will determine whether $\langle u_l \rangle$ augments or diminishes, and thus, will also regulate the value of K_{eff} according to Eq. 169. However, the construction of an explanation for the behavior of the curves of $K_{eff}\ vs. S_t$ with ε_t by comparing velocity fields could be very complicated and other variables are going to be introduced to justify such a behavior.

Firstly, by mass conservation in the channel domain and considering a unit-width RUC, the rate of liquid that is absorbed by the warps and the weft, $\dot{Q}_{abs}$, can be expressed as:

$$\dot{Q}_{abs} = \left(\int_{-H_g/2}^{H_g/2} u_{in}\, dy \right) - \left(\int_{-H_g/2}^{H_g/2} u_{out}\, dy \right) \quad (173)$$

The Eq. 173 is divided by H_g and Eqs. 149a,b are substituted into the resulting expression to obtain the following equation:

$$\dot{Q}_{abs}/H_g = \bar{u}_{in} - \bar{u}_{out} \quad (174),$$

where the right hand side terms are the mean inlet and outlet velocities of the RUC.

Now, the following expression for the non-dimensional velocity at mesoscopic scale is introduced:

$$\hat{u} = u\mu/(\Delta p L_{RUC}) \quad (175),$$

whereby the phase volume-averaged horizontal velocity of the liquid phase, $\langle u_l \rangle$, can be written as $\langle u_l \rangle = \widehat{\langle u_l \rangle} \Delta p L_{RUC}/\mu$, and, considering that $\Delta x = L_{RUC}$ in this case, the

effective unsaturated permeability defined in Eq.169 can be expressed as $K_{eff} = \widehat{\langle u_l \rangle}(L_{RUC})^2$.

Taking into account Eq. 175, the non-dimensional form of Eqs.172 and 174 is as follows:

$$\widehat{\langle u_l \rangle} = \widehat{\langle u_g \rangle} + \left(\int_{A_{tows}^{sat}} \widehat{\langle u_l^{tows} \rangle^l} . dA_{tows}^{sat} \right) / A_{RUC} \tag{176}$$

$$\Delta\hat{\bar{u}} = \frac{\dot{Q}_{abs} . \mu}{\Delta p L_{RUC} H_g} \tag{177},$$

where the variable $\Delta\hat{\bar{u}} = \widehat{\bar{u}_{in}} - \widehat{\bar{u}_{out}}$ stands for the difference between the non-dimensional mean inlet and outlet velocities.

Considering the definition of the sink term, Eq.131, it is obtained that $\dot{Q}_{abs} = S_g . V_{RUC}$, and the Eq.177 can be written as follows:

$$\Delta\hat{\bar{u}} = \frac{S_g . V_{RUC} . \mu}{\Delta p L_{RUC} H_g} \tag{178}$$

Then, Eq. 155 is substituted into Eq.178 to obtain the next expression:

$$\Delta\hat{\bar{u}} = \frac{\varepsilon_t \dot{S}_t (1 - \varepsilon_g) V_{RUC} . \mu}{\Delta p L_{RUC} H_g} \tag{179},$$

which clearly shows that the difference between the non-dimensional mean velocities at the inlet and outlet of the RUC, $\Delta\hat{\bar{u}}$, is an indication of the amount of liquid absorbed by the tows, expressed here as the total saturation rate, $\dot{S}_t$. This was also analyzed in the Section 6.5.1, where it was remarked that the inlet and outlet velocity profiles are farther away from each other as the saturation rate, $\dot{S}_t$, is higher (Figure 79). According to Eq. 179, if the viscosity (μ), pressure difference (Δp) and RUC geometry $\left(L_{RUC}, V_{RUC}, H_g, \varepsilon_g\right)$ do not change, as in the present analysis, the value of $\Delta\hat{\bar{u}}$ can be only modified by changing ε_t and $\dot{S}_t$, and the value of $\dot{S}_t$, in turns, decreases as the total saturation, S_t, increases. Consequently, it can be concluded that if ε_t is kept constant, the increment of S_t causes the reduction of $\Delta\hat{\bar{u}}$, as it is confirmed in Table 25.

On the other hand, the tow porosity, ε_t, has a well-defined influence on $\Delta\hat{\bar{u}}$, $\widehat{\langle u_g \rangle}$ and $\widehat{\langle u_l \rangle}$ for a constant value of S_t. As it can be observed in Table 25, $\Delta\hat{\bar{u}}$ increases and $\widehat{\langle u_g \rangle}$ decreases as ε_t increases for both saturation levels, $S_t = 0.039$ and $S_t = 0.953$.

For $S_t = 0.039$, considering that the saturated area of the tows, A_{tows}^{sat}, is very small and according to the Eq. 176, it can be asserted that $\widehat{\langle u_l \rangle}$ is almost exclusively dependent on $\widehat{\langle u_g \rangle}$. Accordingly, the reduction of $\widehat{\langle u_g \rangle}$ as ε_t increases leads to the reduction of $\widehat{\langle u_l \rangle}$ as

well, as it can be appreciated in Table 25, and hence, to the reduction of K_{eff} with ε_t considering that $K_{eff} = \langle\widehat{u_l}\rangle(L_{RUC})^2$. As the RUC filling evolves, S_t increases, $\dot{S}_t$ decreases and A_{tows}^{sat} increases. Additionally, as ε_t is higher, the magnitude of $\langle\widehat{u_l^{tows}}\rangle^l$ is greater because the tow permeabilities, K_1 and K_2, are greater as well, and, additionally, A_{tows}^{sat} is larger for a same saturation level, S_t, considering that the inter-fibers spaces inside the tows are larger too. Therefore, the second right-hand side term of the Eq.176 is more important as the total saturation, S_t, and the tow porosity, ε_t, increase, in such a way that in the situation of nearly total saturation, $S_t = 0.953$, $\langle\widehat{u_l}\rangle$ increases with the tow porosity, ε_t (See Table 25), leading to the increment of K_{eff} with ε_t, in spite of $\langle\widehat{u_g}\rangle$ still decreases with the increment of ε_t.

The decrease of the saturated effective permeability with the fiber content of the tows, ϕ_t, in dual-scale fibrous reinforcements has been reported in [20], which is in agreement with the present results since it is equivalent to say that K_{eff} increases with ε_t when $S_t \to 1$, as obtained here, considering that the fiber content of the tow is defined as $\phi_t = 1 - \varepsilon_t$.

Table 25 Influence of the tow porosity, ε_t, on $\langle\hat{u}_l\rangle$ for two levels of total saturation, S_t.

Total tow saturation, S_t	Tow porosity, ε_t.	$\Delta\hat{\bar{u}}$ (Dimensionless)	$\widehat{\langle u_g\rangle}$ (Dimensionless)	$\langle\widehat{u_l}\rangle$ (Dimensionless)
0.039	0.15	2.009×10^{-4}	5.682×10^{-3}	5.708×10^{-3}
	0.25	1.198×10^{-3}	5.339×10^{-3}	5.351×10^{-3}
	0.37	5.943×10^{-3}	5.001×10^{-3}	5.021×10^{-3}
	0.46	9.203×10^{-2}	4.849×10^{-3}	4.869×10^{-3}
0.953	0.15	9.899×10^{-5}	5.680×10^{-3}	7.295×10^{-3}
	0.25	3.585×10^{-4}	5.335×10^{-3}	7.806×10^{-3}
	0.37	4.628×10^{-4}	4.998×10^{-3}	8.235×10^{-3}
	0.46	5.527×10^{-4}	4.845×10^{-3}	8.587×10^{-3}

The influence of the weft geometry on K_{eff} and K_g can be studied by considering *Serie 7* of Table 21 with $\lambda = 1$ and simulations 4 to 7 of Table 24. The plot of $K_g \; vs. \; a_1/a_2$ for a constant value of $\varepsilon_g = 0.376$, with a_1/a_2 as the aspect ratio of the weft (See Figure 61), can be appreciated in the Figure 94a, according to which K_g increases as a_1/a_2 increases provided that ε_g remains constant. On the other hand, according to Figure 94b, if the weft aspect ratio is kept constant, $a_1/a_2 = 5$, K_g is greater as ε_g increases.

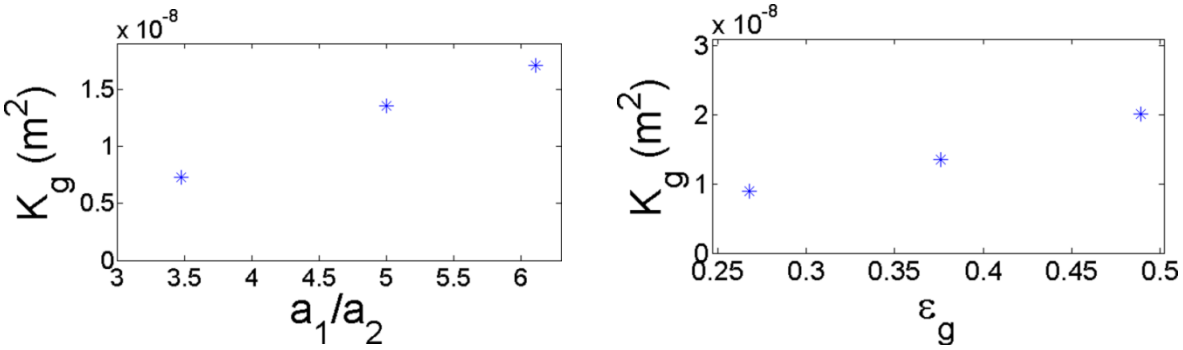

a) b)

Figure 94 Influence of weft geometry on the gap permeability, K_g. a) Influence of aspect ratio of the weft on the gap permeability, b) Influence of the gap porosity on the gap permeability

The curves of $K_{eff}\ vs. S_t$ for the three values of a_1/a_2 considered in Table 24 and $\varepsilon_g = 0.376$ are represented in the Figure 95a, where it is noticed that the increase of a_1/a_2 leads to the increase of K_{eff} for any value of S_t. In the limit when the RUC is nearly saturated, $S_t \to 1$, this is in agreement with the results reported in [20] for the effective saturated permeability of dual-scale fibrous reinforcements. On the other hand, the curves of $K_{eff}\ vs. S_t$ for the three values of ε_g considered in Table 24 and $a_1/a_2 = 5$ are shown in the Figure 95b, where it can be appreciated that the increase of the gap porosity, ε_g, brings about an increase of K_{eff} for any value of S_t.

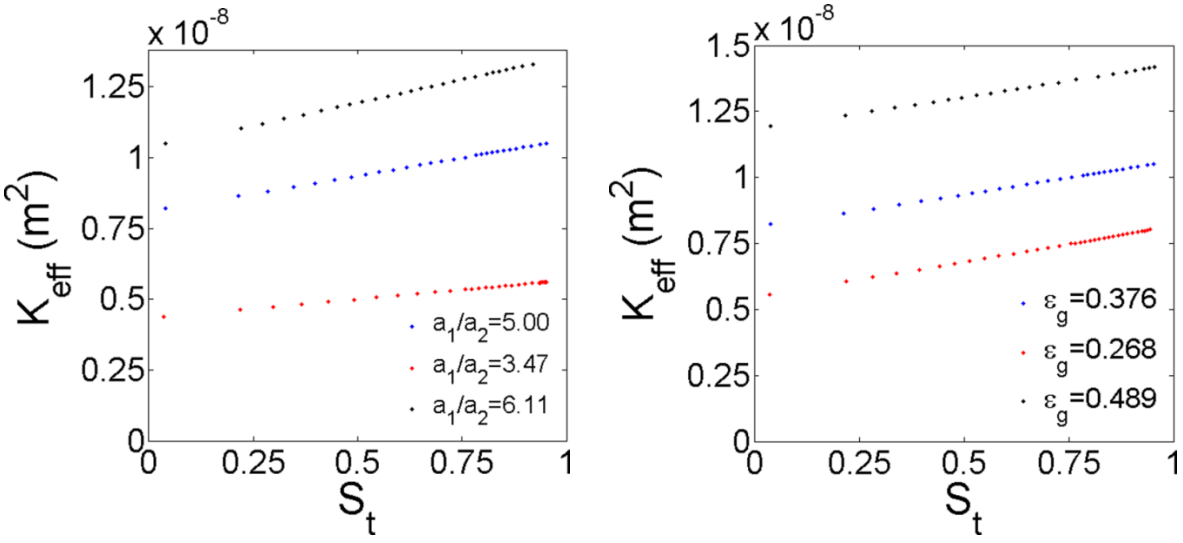

a) b)

Figure 95 Influence of weft geometry on the effective permeability, K_{eff}. a) Influence of the weft aspect ratio on the curve of K_{eff} vs S_t, b) Influence of the gap porosity on the curve of K_{eff} vs S_t

6.5.4 Macroscopic unidirectional simulations

Assessment of accuracy of DR-BEM scheme.

In this section, the DR-BEM scheme presented in Section 6.3 is used to simulate the unidirectional filling of dual-scale fibrous reinforcements at macroscopic scale. Firstly, this numerical scheme is validated with the analytical solution proposed in [101] for unidirectional filling of molds at constant pressure regime. The problem is represented in Figure 96, where a dual-scale fibrous reinforcement is positioned into a cavity and the liquid is injected in unidirectional form at constant inlet pressure, p_{in} . Three zones can be clearly differentiated in the Figure 96: fully saturated zone, partially saturated zone and the dry zone, and the variables L, L_{ff} and L_{us} stand for the mold length, position of the macroscopic fluid front and length of the partially saturated zone, respectively. In the analytical solution presented by [101], the non-dimensional position of the macroscopic fluid front, $\hat{L}_{ff}$, and the non-dimensional length of the partially saturated region, $\hat{L}_{us}$, are predicted as follows:

Non-dimensional position of the macroscopic fluid front, $\hat{L}_{ff}$:

$$\hat{L}_{ff} = \frac{1}{\psi_1} cosh^{-1}\left(\frac{\psi_1^2 \hat{t}}{\varepsilon_g} + 1\right), 0 \le \hat{t} \le \widehat{t_s} \tag{180a}$$

$$\hat{L}_{ff} = \frac{-\sqrt{(\varepsilon_{RUC})^2 - (\varepsilon_g)^2} + \sqrt{(\varepsilon_{RUC})^2 - (\varepsilon_g)^2 + 2\varepsilon_{RUC}\psi_1^2(\hat{t} - \widehat{t_s})}}{\psi_1 \varepsilon_{RUC}} + \frac{1}{\psi_1} cosh^{-1}\left(\frac{\varepsilon_{RUC}}{\varepsilon_g}\right), \widehat{t_s} \le \hat{t} \le \widehat{t_{fill}} \tag{180b}$$

$$\widehat{t_s} = 1/\psi_2 \tag{180c}$$

Non-dimensional length of the partially saturated region, $\hat{L}_{us}$:

$$\hat{L}_{us} = \frac{1}{\psi_1} cosh^{-1}\left(\frac{\varepsilon_{RUC}}{\varepsilon_g}\right) \tag{181},$$

where $\widehat{t_s}$ and $\widehat{t_{fill}}$ are the dimensionless times (see Eq.133a) when the total saturation is reached at the inlet of the mold and when the fluid front arrives to the end of the mold, respectively, while ε_{RUC}, ψ_1 and ψ_2 are the bulk porosity of the RUC and two model parameters, respectively, defined as:

$$\varepsilon_{RUC} = \frac{\sum V_{pt}^{(i)} + V_g}{V_{RUC}} = \frac{\varepsilon_t \sum V_t^{(i)} + V_g}{V_{RUC}} = \varepsilon_t + \varepsilon_g(1 - \varepsilon_t) \tag{182}$$

$$\psi_1 = \sqrt{\frac{a(1-\varepsilon_g)L^2 K_t}{h_t^2 K_g}} \tag{183a}$$

$$\psi_2 = \frac{\psi_1^2}{(1-\varepsilon_g)\varepsilon_t} \quad (183b),$$

where V_g, $V_t^{(i)}$, $V_{pt}^{(i)}$ and V_{RUC} were defined in Section 6.4. On the other hand, in the calculation of ψ_1 and ψ_2 (Eq's. 183a and 183b) three parameters of the tows are considered, namely, K_t, h_t and ε_t, with K_t as the transverse permeability and h_t as the height of the tow. The details of the calculation of the fitting parameter "a" appearing in Eq. 183a can be found in [101]. A linear pressure dependent function for the sink term, S_g, is considered in [101], as shown in the following equations:

$$S_g = c\langle P_g \rangle^g \quad (184a)$$

$$c = \frac{aK_t}{h_t^2 \varepsilon_t \mu} \quad (184b)$$

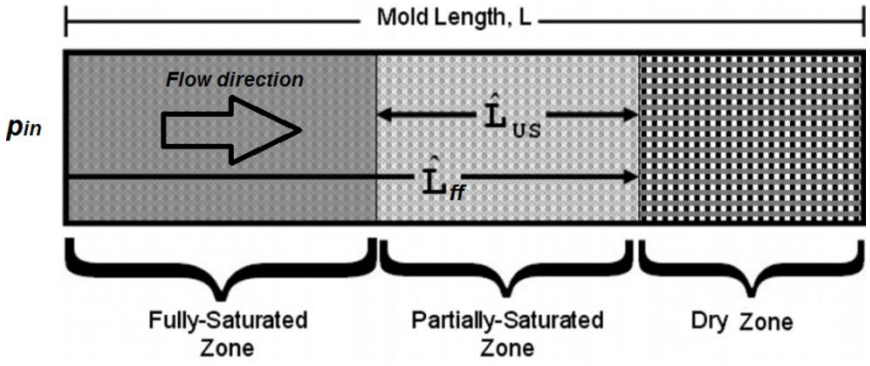

Figure 96 Scheme of unidirectional filling of dual-scale fibrous reinforcements in molds. Source: Zhou, Alms and Advani [101]

The fixed and computed parameters used in the present validation are summarized in the Table 26. The comparison of the analytical and numerical results is carried out on the basis of the L^2 relative error norm and the relative error, E, which are defined as follows:

$$L_2 = \sqrt{\sum_i \left(\hat{L}_{ff,anal}^{(i)} - \hat{L}_{ff,drbem}^{(i)}\right)^2 / \sum_i \left(\hat{L}_{ff,anal}^{(i)}\right)^2} \quad (185a)$$

$$E = \sqrt{\left|\hat{L}_{us,anal} - \hat{L}_{us,drbem}\right| / \hat{L}_{us,anal}} \quad (185b),$$

where $\hat{L}_{ff,anal}^{(i)}$ and $\hat{L}_{ff,drbem}^{(i)}$ are the analytical and DR-BEM solutions of the non-dimensional fluid front position along the mold at the time instant "i", whereas $\hat{L}_{us,anal}$ and $\hat{L}_{us,drbem}$ represent the analytical and DR-BEM solutions of the non-dimensional length of the partially saturated region, $\hat{L}_{us}$.

Table 26 Data for comparison between the analytical and DR-BEM results of macroscopic unidirectional simulations.

Fixed parameters							
Radius of the fiber, R_f (μm)	Half distance between fibers, d (μm)	Height of the tow, h_t (m)	Gap porosity, ε_g	Gap permeability, K_g (m^2)	Inlet pressure, p_{in} (kPa)	Length of the mold, L (m)	Fluid viscosity, μ (Pa.s)
54	2.92	2×10^{-3}	0.268	1×10^{-10}	100	0.1	0.1

Computed parameters								
Tow porosity, ε_t	Transverse tow permeability, K_t (m^2)	Bulk porosity of the RUC, ε_{RUC}	a	ψ_1	ψ_2	c	$\hat{t}_s$	$\hat{L}_{us}$
0.18	4.97×10^{-13}	0.40	0.272	1.578	18.779	1.878×10^{-6}	0.0533	0.607

The plots of L^2 *relative error norm vs Meshsize* for several values of the constant of Courant-Friedrich-Levy, CFL, which is used in the advancement of the moving interface during the mold filling, are presented in the Figure 97a, where the meshsize is reported as $h = e/L$, with e as the size of one quadratic element and L as the length of the mold. Details about the fluid flow advancement using the *CFL* condition can be found in *Appendix C.* The results allow concluding that the DR-BEM scheme is accurate enough to conduct macroscopic unidirectional simulations of dual-scale fibrous reinforcements. Additionally, the small relative errors, E, between the analytical and the numerical solutions of the non-dimensional length of the partially saturated region, $\hat{L}_{us}$, which are shown in the Figure 97b, confirms the accuracy of the present DR-BEM scheme.

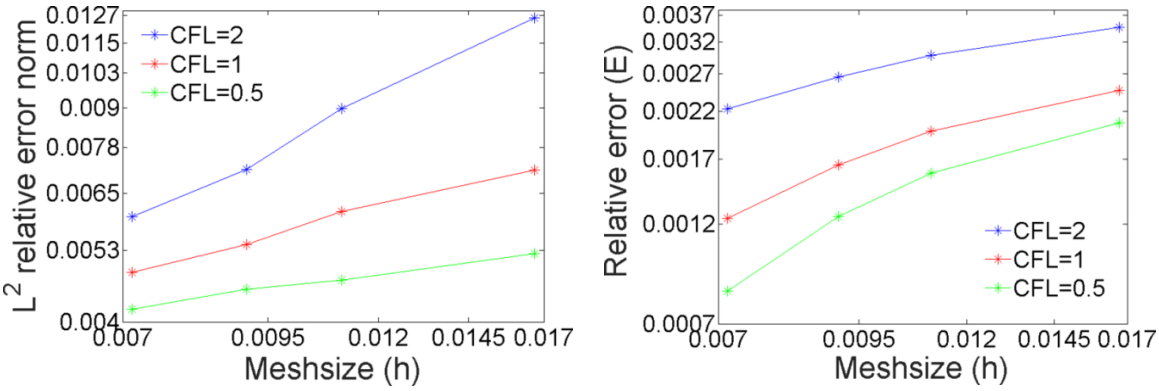

a) **b)**

Figure 97 Plots of convergence for the solution of macroscopic unidirectional filling using the present DR-BEM scheme, a) L^2 relative error norm vs Mesh-size for the fluid front positions, b) Relative error, E, vs. Mesh-size for the length of the partially saturated region.

The graphical comparison between the analytical and the DR-BEM results of the time evolution of the fluid front position is shown in the Figure 98 for $h = 1.11 \times 10^{-2}$ and $\mathrm{CFL} = 1$, which are the parameters employed in the forthcoming simulations.

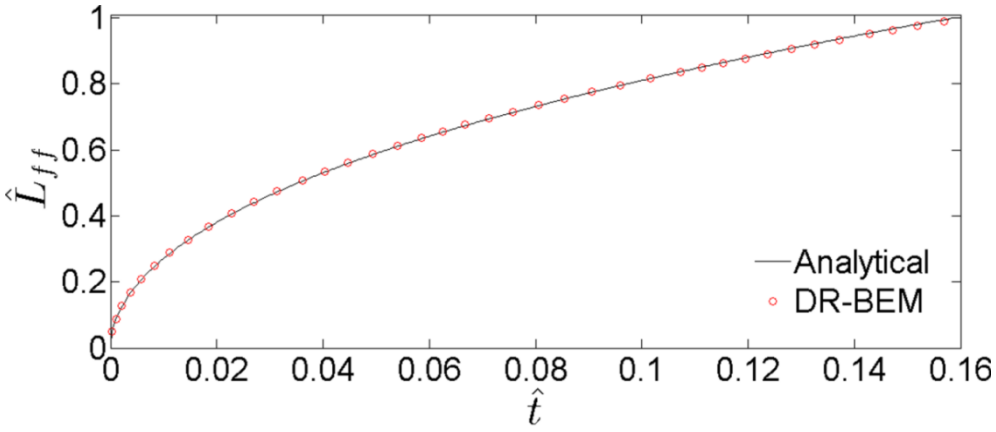

Figure 98 Comparison between the analytical and DR-BEM non-dimensional fluid front positions for macroscopic unidirectional injections at constant pressure.

Series of simulations.

After having validated the DR-BEM scheme used here, this scheme is employed for unidirectional macroscopic simulations using the lumped function for S_g deduced in Section 6.5.2 and the gap permeability, $K_g = 1.35 \times 10^{-8}\, m^2$, obtained in the Section 6.5.3. The material parameters of the following simulations are the same as in Table 18 (μ=0.1 Pa.s, λ=15 mN/m, $\theta = 30°$) and the geometric characteristics of the RUC used in Section 6.5.2 to obtain the function S_g shall be kept unaltered; on the other hand, the geometric data of the mold, as well as the processing data of the different series of simulations are presented in the Table 27. In *Serie 1*, it is considered a constant pressure regime with two inlet pressures, i.e., $P_{inj} = [10{,}100]\, kPa$, a single vacuum pressure of $P_{vac} = 0\, kPa$ and three cases of air dissolution, namely, full air dissolution, $\lambda = 0$, partial air dissolution with $\lambda = 0.75$ and no air dissolution (full air compressibility), $\lambda = 1$. On the other hand, *Serie 2* also corresponds to constant pressure injections, but in this case two vacuum pressures are considered, i.e., $P_{vac} = [0, -75]\, kPa$, while the inlet pressure is kept constant in $P_{inj} = 50\, kPa$ and the air entrapment parameters are the same as in *Serie 1*, namely, $\lambda = [0, 0.75, 1]$. In *Serie 3*, a constant flow rate regime is considered with inlet flow rates of $Q_{inj} = [5 \times 10^{-6}, 1 \times 10^{-5}]\, m^3/s$, a single vacuum pressure of $P_{vac} = 0\, kPa$ and the same air entrapment parameters considered in the other two series.

Table 27 Data of macroscopic unidirectional simulations considering the lumped function for the sink term, S_g

Geometric parameters of the mold		
Length of the mold, L (m)	*Width of the mold, b (mm)*	*Thickness of the mold, t_h (mm)*
0.3	30	3
Parameters of the Serie 1		
Inlet pressure, P_{inj} (kPa)	*Vacuum pressure, P_{vac} (kPa)*	*Air entrapment parameters, λ*
10 100	0	0 0.75 1
Parameters of the Serie 2		
Inlet pressure, P_{inj} (kPa)	*Vacuum pressure, P_{vac} (kPa)*	*Air entrapment parameters, λ*
50	0 -75	0 0.75 1
Parameters of the Serie 3		
Inlet flow rate, Q_{inj} (m^3/s)	*Vacuum pressure, P_{vac} (kPa)*	*Air entrapment parameters, λ*
5×10^{-6} 1×10^{-5}	0	0 0.75 1

Results of Serie 1: Change of inlet pressure, P_{inj}

In the Figure 99a, several curves of $S_t\ vs.\hat{x}$ of the *Serie 1*, with $\hat{x}$ as the non-dimensional horizontal position along the mold, are presented for seven fluid front positions, $\hat{L}_{ff}$, which correspond to the intersection of the curves with the abscissa axis. According to this figure, each pair of curves corresponding to the same fluid front position and having the same air entrapment parameter, λ, are almost identical, independent on the injection pressure, P_{inj} (see the matching between the cross-type and the point-type markers for the blue and red curves in Figure 99a). The dimensionless times, $\hat{t}$, of each one of these pairs of curves are very similar each other and the average value of $\hat{t}$ is reported for each pair in Figure 99a. Considering this, for a determined fluid front position, the curves of $S_t\ vs\hat{x}$ having the same value of λ can be represented as a single curve independent on P_{inj}, provided that $\lambda < 1$ (Figure 99b). On the other hand, in the case of full air compressibility, $\lambda = 1$, the curves are not the same for different values of P_{inj} because the equilibrium saturation, S_t^{eq}, depends on P_{inj} (Figure 99b). Bearing this in mind, the curves of the *Serie 1* are compared each other in the Figure 99b, where several aspects, some of them denoting the physical consistency of the obtained sink function, S_g, are worth noting. Firstly, the difference between the saturation curves is larger as the unidirectional injection evolves, in such a way that the influence of λ is very small at the beginning of the injection, but it becomes more important as the filling takes place. Additionally, for a determined fluid front position, the global saturation (area under the curve) is higher as the air entrapment parameter, λ, decreases, and, for the two cases of full air compressibility, $\lambda = 1$, as the inlet pressure

increases; this is the expected macroscopic behaviour during the filling of molds because λ accounts for the resistance exerted by the air on the fluid fronts inside the tows and, in the cases with $\lambda = 1$, because the equilibrium saturation, S_t^{eq}, is greater for the higher inlet pressure, $P_{inj} = 100\ kPa$; therefore, the reduction of λ and, in the cases with $\lambda = 1$, the increase of P_{inj} promote the tow impregnation, which contributes to the global saturation for all fluid front positions.

According to the dimensionless times of Figure 99b, for a constant inlet pressure, P_{inj}, the increase of the air entrapment parameter from $\lambda = 0.75$ to $\lambda = 1$ (full air compressibility) can both increase or decrease the velocity of the fluid front, which is understandable considering that the change of λ can have a double effect on the fluid front advancement: as λ is lower, the liquid absorption through the tows is promoted as mentioned before, which retards the impregnation in the channels, but, on the other hand, as the tows saturate faster, the saturation rate also decreases faster, which promotes the impregnation in the channels. For the cases when air dissolution is considered, $\lambda < 1$, the first effect prevails, since longer values of $\hat{t}$ were obtained for $\lambda = 0$ than for $\lambda = 0.75$ in all fluid front positions.

If the results of $\lambda = 0$ and $\lambda = 0.75$ in Figure 99b are compared one another, it can be noticed that the total saturation at the inlet is achieved at a lower fluid front position in the former case, whereas the comparison of the results for the cases with $\lambda = 1$ (full air compressibility) and different injection pressures, shows that the fluid front position corresponding to the instant when the equilibrium saturation, S_t^{eq}, is reached at the inlet is lower for the inferior pressure, $P_{inj} = 10\ kPa$.

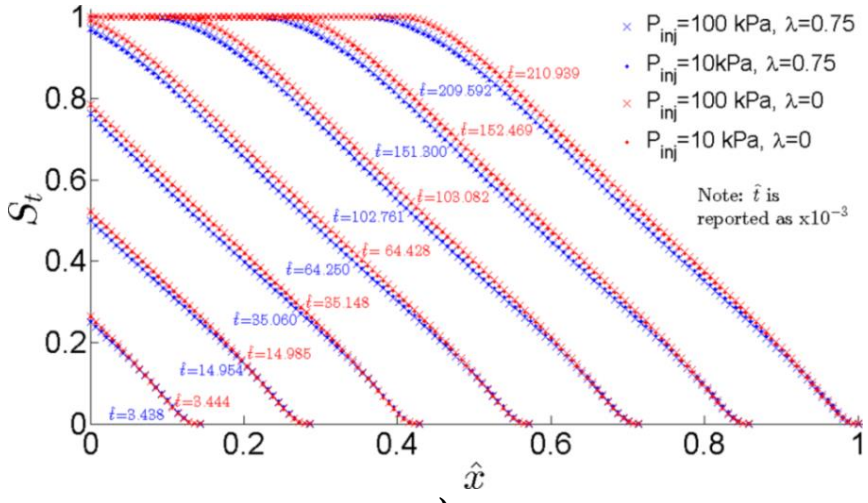

a)

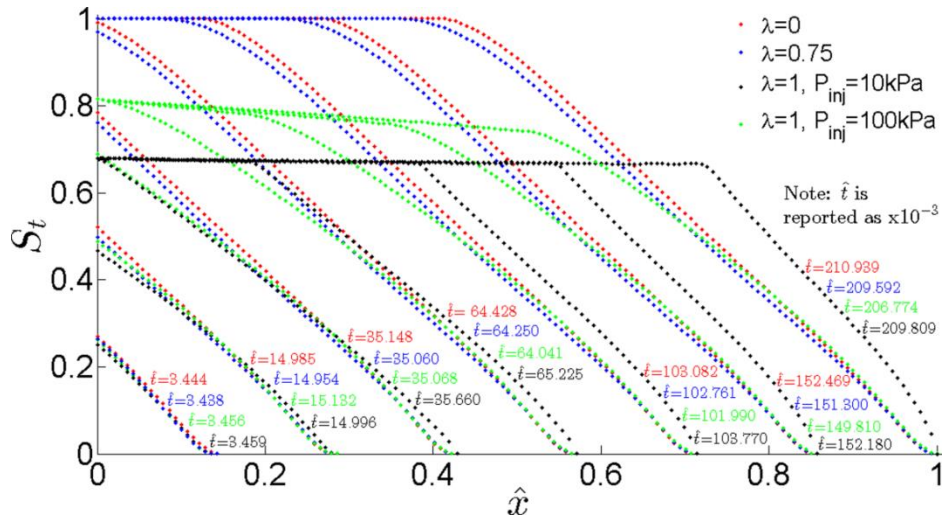

b)

Figure 99 Curves of saturation for *Serie 1*, a) Coincidence of curves having the same air entrapment parameter, λ, when λ<1 , b) Influence of the air entrapment parameter, λ, and injection pressure, P_{inj}

Results of Serie 2: Change of vacuum pressure, P_{vac}

For *Serie 2*, the independency of the curves of $S_t\ vs.\hat{x}$ on the vacuum pressure, P_{vac}, considering $\lambda < 1$, can be appreciated in the Figure 100a, where it is observed that the dimensionless times, $\hat{t}$, for $\lambda = 0$ are longer in all fluid front positions, as in *Serie 1*. On the other hand, according to the results presented in Figure 100b, for each fluid front position, the domain is less saturated (global saturation is lower) as the air entrapment parameter, λ, increases and, for the two cases of $\lambda = 1$, as the magnitude of the vacuum pressure,$|P_{vac}|$, decreases, being this more notorious as the injection evolves. On the other hand, for a constant value of $|P_{vac}|$, the increase of the fluid front velocity (decrease of $\hat{t}$) with λ during the whole injection is only valid when the air dissolution is considered, i.e., for $\lambda < 1$ (compare the values of $\hat{t}$ for $\lambda = 0$ and $\lambda = 0.75$ in each fluid front position). In a similar fashion as *Serie 1*, for $\lambda < 1$, the fluid front position corresponding to the instant when the total saturation is reached at the inlet is lower for the case of full air dissolution, $\lambda = 0$. Moreover, for the cases of $\lambda = 1$, the fluid front position corresponding to the instant when S_t^{eq} is reached at the inlet is lower for the inferior vacuum, $|P_{vac}| = 0kPa$.

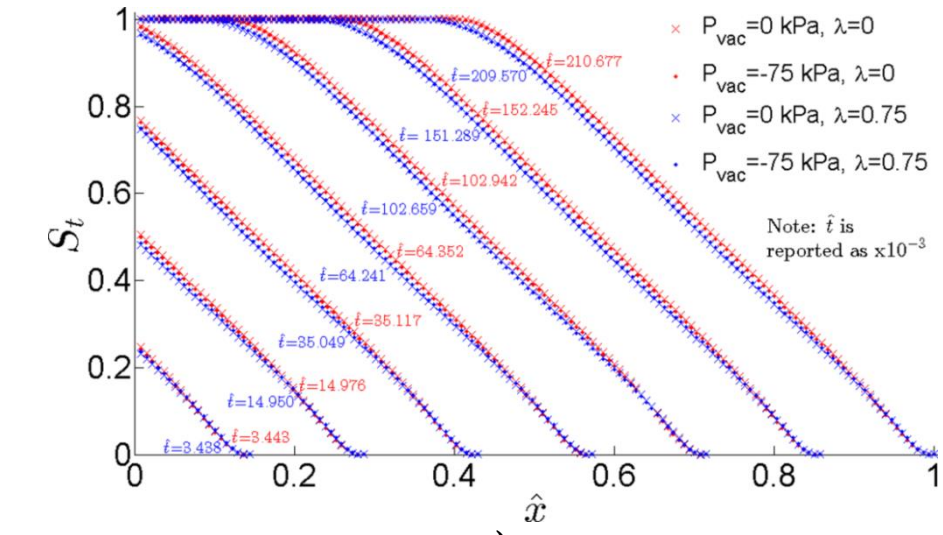

a)

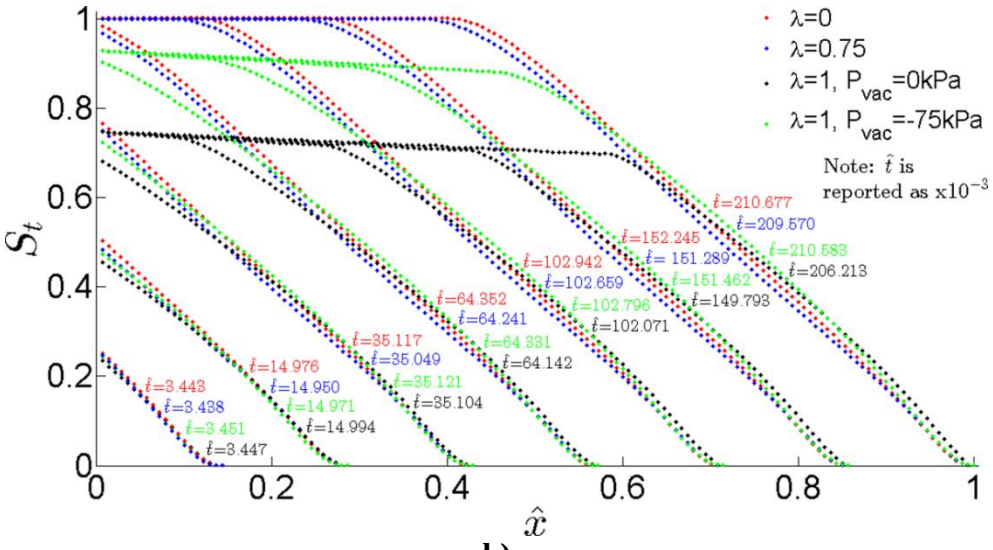

b)

Figure 100 Curves of saturation for *Serie 2*, a) Coincidence of curves having the same air entrapment parameter, λ, when λ<1, b) Influence of the air entrapment parameter, λ, and vacuum pressure, P_{vac}

Results of Serie 3: Change of inlet flow rate, Q_{inj}

Similar conclusions as those ones obtained in *Serie 1* and *2* can be addressed for *Serie 3*, but some differences can be also identified. Likewise to the other series, the curves of $S_t \; vs. \hat{x}$ are independent on the processing parameter (injection or inlet flow rate, Q_{inj}, in this case) when $\lambda < 1$, and the dimensionless times, $\hat{t}$, are longer for $\lambda = 0$ in all fluid front positions (See Figure 101a). According to Figure 101b, for each fluid front position, the

domain is less saturated as the air entrapment parameter, λ, increases and, for the two cases of $\lambda = 1$, as the inlet flow rate decreases, obtaining a more notorious difference between the saturation curves as the injection develops. Conversely to constant pressure injections (Figure 99b and Figure 100b), the behaviour of the global saturation with λ is directly related to the behaviour of $\hat{t}$ with λ in constant flow rate injections (Figure 101b), because the time elapsed from the beginning of the injection to any fluid front position is directly proportional to the volume of fluid injected; as the global saturation decreases with λ at any fluid front position, the injected volume and, consequently, the injection time also decrease with λ, as shown in Figure 101b. This means that, for a constant inlet flow rate injection, the fluid front velocity always increases with λ.

There is an important difference between the curves corresponding to $\lambda = 1$ of the constant inlet pressure regime (Figure 99b and Figure 100b) and those ones of the constant inlet flow rate regime (Figure 101b): in the first ones, the saturation at the inlet reaches an equilibrium saturation, S_t^{eq}, which depends on the injection pressure, P_{inj}, and on the vacuum pressure, P_{vac}, whereas, in the second ones, the saturation at the inlet increases continuously because the injection pressure also increases to maintain a constant flow rate. Additionally, for some curves of $S_t \; vs. \hat{x}$ (Figure 99b, Figure 100b and Figure 101b), it is worth noting that there are two well-differentiated curve portions separated by a break point in which the change of the slope is significant. In the first portion (from the inlet to the break point), the slope is almost constant. For the cases of full air compressibility, $\lambda = 1$, this slope is more pronounced for the constant flow rate regime (Figure 101b) than for the constant pressure ones (Figure 99b and Figure 100b). This general behaviour of the curves of Figure 101b for $\lambda = 1$ is very similar to the one recently obtained in [92], where a constant flow rate regime and the air compressibility were also considered, which demonstrates the coherence of the present DR-BEM results. It is important to highlight that in the cases of $\lambda = 1$ for the constant flow rate regime, Figure 101b, if the unidirectional injection continues indefinitely, the total saturation at the inlet is not going to be reached, and $P_{inj} \to \infty$ as $S_t \to 1$ at the inlet.

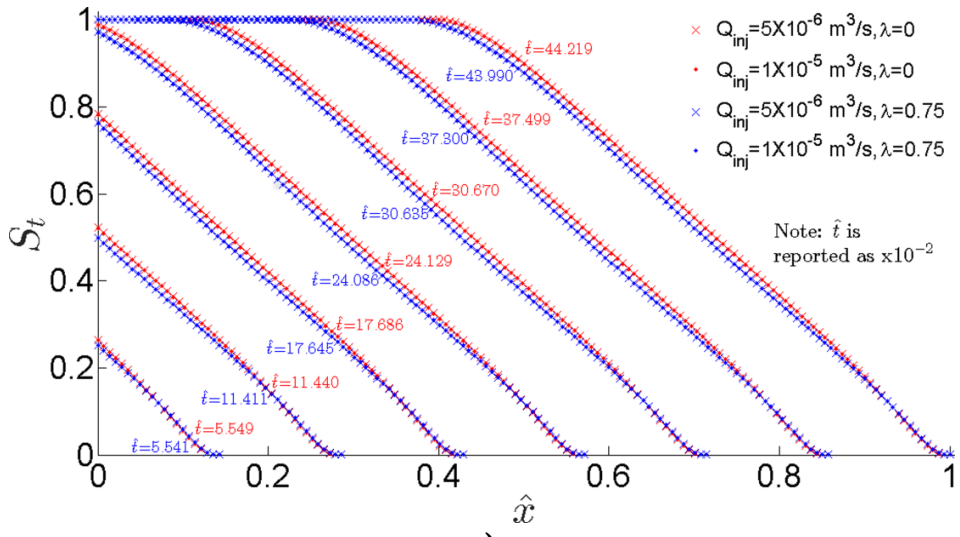

a)

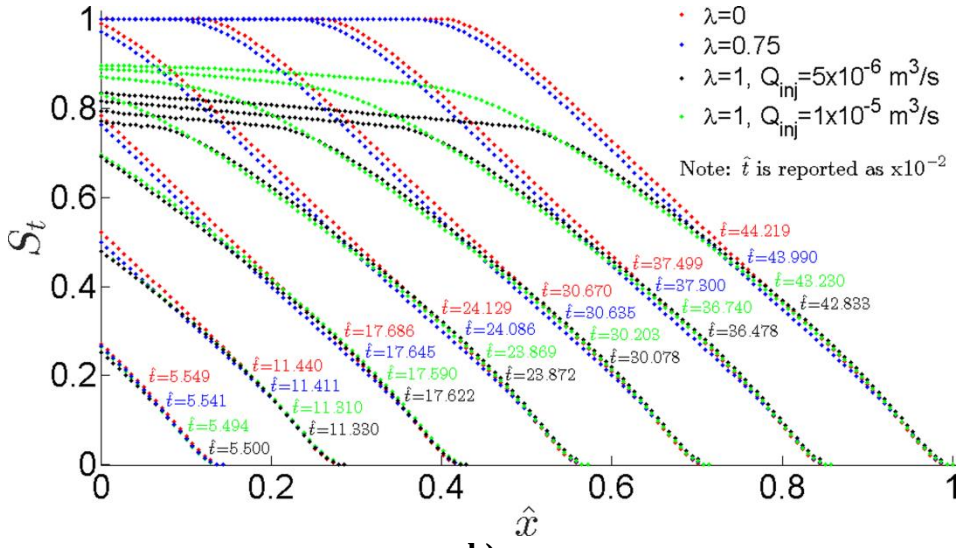

b)

Figure 101 Curves of saturation for *Serie 3*, a) Coincidence of curves having the same air entrapment parameter when λ<1, b) Influence of the air entrapment parameter, λ, and injection flow rate, Q_{inj}

Pressure profiles.

The assessment of the macroscopic simulations using the function S_g obtained in the Section 6.5.2 can be also carried out by comparing the form of the numerical pressure profiles with the profiles presented in the Figure 76. According to [83], the flow rates from the channels towards the tows in the partially saturated region determine whether the pressure profile is convex or concave, and these flow rates, in turns, depends on the saturation degree, S_t. As in the present work the saturation degree, S_t, in the fluid front is

zero due to the assumption of fully filled channels, and the change of S_t in the partially saturated region close to the fluid front is not pronounced (See Figure 99b, Figure 100b and Figure 101b), high values of S_g are expected in that region, which, according to [83], leads to a slightly concave pressure profile, as shown in Figure 76a. The pressure profiles corresponding to the curves of the Figure 99a (constant pressure) and Figure 101a (constant flow rate), with $\lambda = 0$, are depicted in Figure 102a and Figure 102b, respectively, and mark points are added to some profiles to indicate the longitudinal position until which the reinforcement is fully saturated, i.e., the length of the fully saturated zone; some dotted lines are also shown indicating the projection of the linear part of these profiles. As it can be observed for each one of these profiles (Figure 102a,b), the change of the pressure from the inlet until the mark point is linear, but from the mark point until the fluid front, the curve is slightly concave, coinciding with the results reported in [83], [240], [241].

The slope of the pressure profiles in the fully saturated region for the constant flow rate regime (Figure 102b) is another parameter to verify the DR-BEM results. As $S_g = 0$ in this region (no mass transfer from the channel towards the tows), according to Eqs.130a-b and considering that the volume-averaged horizontal velocity is $\langle u_g \rangle = Q_{inj}/A$, the slope of the pressure profile in the fully saturated region shall be the same for all fluid front positions where this region is present and equal to $m_{linear} = \left(p_{sat} - P_{inj}(t)\right)/x_{sat} = -Q_{inj}\mu/\left(AK_g\right)$, where the point (x_{sat}, p_{sat}) is the coordinate corresponding to the threshold of the fully saturated region in each pressure profile (this threshold is represented in non-dimensional form by the mark points of Figure 102a,b). Taking into account the Eq.134b, the non-dimensional slope shall be $\hat{m}_{linear} = -1$, which is in agreement with the slopes obtained in Figure 102b. It is important to notice that $\hat{p}_{sat}$ is practically constant during the whole injection for the constant flow rate regime (Figure 102b), whereas it decreases as the injection develops for the constant pressure regime (Figure 102a).

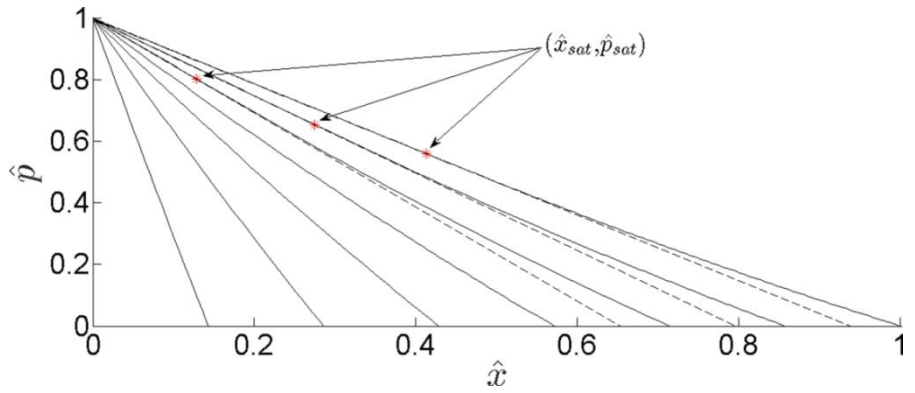

a)

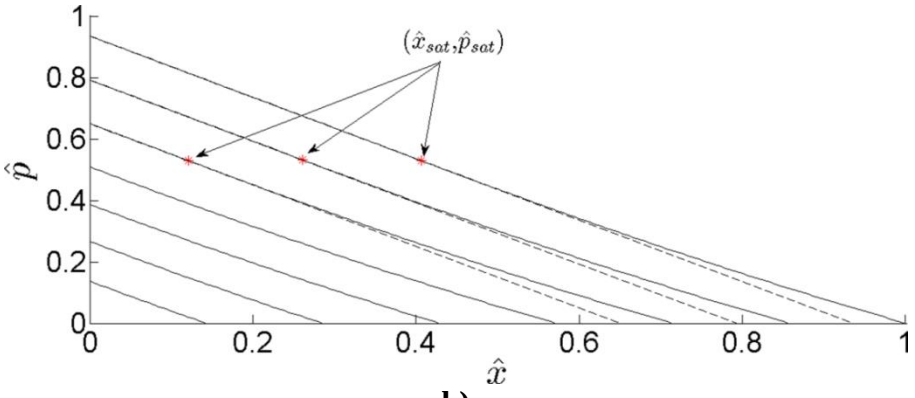

b)

Figure 102 Pressure profiles for unidirectional fillings of dual-scale fibrous reinforcements, a) Constant pressure regime (Figure 99a, λ=0), b) Constant flow rate regime (Figure 101a, λ=0)

6.6 Conclusions

In the present chapter, multiscale filling simulations of dual-scale fibrous reinforcements were carried out using Boundary Element Techniques. At the mesoscopic scale, a Stokes-Darcy BEM approach, previously validated in Chapter 3, was employed for the simulation of the tows filling assuming fully filled channels, whereas, at the macroscopic scale, an Equivalent Darcy DR-BEM approach was satisfactorily validated with the analytical solution obtained in [101] and then used to simulate the unidirectional filling of cavities at both constant pressure and constant flow rate regimes using the sink functions, S_g, obtained here by running several mesoscopic simulations.

At the mesoscopic scale, two methodologies were considered for the tows filling. The classical methodology, consisting on the prescription of a uniform pressure in the channels, was used to obtain the saturation curves of the RUC's, $S_t \; vs \; \tau$, finding a good agreement

with previous works that have implemented this methodology [12], [225]. On the other hand, the proposed methodology, consisting on the prescription of a pressure gradient along the flow direction and the modeling of the channels flow using the Stokes equation, was used to analyze the influence of saturation, volume average-pressure and pressure gradient on the channel velocity field, reaching the following conclusions:

- The inlet and outlet velocity profiles of the RUC are parabolic, which is consistent with the Stokes flow, with the highest velocities reached at the interfaces channel-bundles and the lowest velocity, at the center of the channel.
- The difference between the inlet and outlet velocity profiles is an indication of the saturation rate of the tows. As the saturation of the tows takes place, the saturation rate decreases and this difference reduces since the inlet velocities decrease and the outlet ones increase.
- The velocity field in the channel is affected by the saturation, S_t, in such a way that larger changes of velocities along the RUC length are obtained as S_t decreases, however, the volume-averaged gap velocity in the flow direction, $\langle u_g \rangle^g$, which is a macroscopic variable, remains essentially constant with the change of S_t.
- For a constant pressure gradient, the influence of the average pressure, $\langle P_g \rangle^g$, in the inlet and outlet velocity profiles depends on the saturation, S_t. For low and intermediate values of S_t, the increase of $\langle P_g \rangle^g$ causes the increase of the inlet velocities and the reduction of the outlet ones, being this effect less important as S_t increases; on the other hand, for high values of S_t, a monotonic relationship between $\langle P_g \rangle^g$ and the difference between the inlet and outlet velocities is not necessarily achieved.
- Despite $\langle P_g \rangle^g$ affects the inlet and outlet velocities, the volume-average gap velocity, $\langle u_g \rangle^g$, is not significantly influenced by this macroscopic variable as long as the pressure gradient, $\Delta P/\Delta x$, is constant. On the other hand, if $\Delta P/\Delta x$ increases, $\langle u_g \rangle^g$ increases as well.

The gap permeability, K_g, and the effective unsaturated permeability, K_{eff}, were calculated using the simulations results obtained with the proposed methodology. Both permeabilities are independent on the average pressure, $\langle P_g \rangle^g$, and the pressure gradient, $\Delta P/\Delta x$; in the case of K_{eff}, this conclusion is in agreement with previous works in non-woven

reinforcements [138]–[140]. On the other hand, K_{eff} is directly proportional to the saturation, S_t, and the curves of $K_{eff}\ vs\ S_t$ are influenced by the tow porosity (ε_t), the weft aspect ratio (a_1/a_2), and the gap porosity (ε_g). In the former case, K_{eff} is lower as ε_t increases when the tows are almost unsaturated $(S_t \to 0)$, but, as S_t increases, the differences between the curves of $K_{eff}\ vs\ S_t$ reduces until all curves converge into a single point, from which K_{eff} increases with ε_t for each value of S_t until the tows are fully saturated. On the other hand, the increase of a_1/a_2 keeping constant ε_g, and the increase of ε_g keeping constant a_1/a_2, lead to the increase of K_{eff} for any value of S_t, as well as to the increase of the gap permeability, K_g.

The proposed methodology was also used to determine four-parameter sink functions, S_g, in terms of the saturation, average pressure, vacuum pressure, viscosity and air entrapment parameter, by running several mesoscopic simulations with input data complying certain scale restrictions, and by using fitting equations for the simulation results that are physically consistent with the impregnation process of the tows. The proposed sinks functions fit better to the curves of $S_g\ vs\ S_t$ than sink functions of other works [12], [225]. Once the functions S_g were determined, several macroscopic unidirectional simulations were run using an Equivalent Darcy formulation, with the gap permeability, K_g, previously found. A DR-BEM scheme was used to solve the governing equations, obtaining the following conclusions:

- In both the constant pressure and constant flow rate regime, the influence of the air entrapment parameter, λ, on the saturation curves is more relevant as the injection develops. In general, for each fluid front position along the mold, the global saturation is larger as λ decreases and for the cases of full air compressibility, $\lambda = 1$, as the input processing parameter (inlet pressure, vacuum pressure or flow rate) increases.
- Since in constant flow rate injections the global saturation is directly proportional to the injection time, the reduction of the global saturation with λ for all fluid front positions signifies an increase of the fluid front velocity with λ. On the other hand, for constant pressure injections, the fluid front is faster as λ increases when the air dissolution is present, i.e., $\lambda < 1$; when full air compressibility is considered, i.e., $\lambda = 1$, this behavior is not necessarily kept in all fluid front positions.

- For the cases of full air compressibility, $\lambda = 1$, at constant pressure regime, the equilibrium saturation, S_t^{eq}, is higher as the input processing parameter (inlet pressure or vacuum pressure) increases, and this causes that the fluid front position corresponding to the instant when S_t^{eq} is reached at the inlet is lower as the input processing parameter decreases. On the other hand, at constant flow rate regime, the saturation at the inlet increases continuously because the injection pressure augments to maintain a constant flow rate

The pressure profiles of the macroscopic simulations were obtained for both regimes (constant pressure and constant flow rate), finding that the general behavior of these profiles is in agreement with the profiles commonly found in the literature when the sink term is important in the neighborhood of the fluid front [83], [240], [241]. It was obtained a good agreement between the analytical and numerical slopes of these profiles in the totally saturated zone when the injection is conducted at constant flow rate. Despite the general behavior of the constant-pressure and constant-flow rate profiles are very similar, namely, both are linear in the totally saturated zone and slightly concave in the partially saturated one, two important differences were identified: 1) the magnitude of the slope in the linear zone is constant in the constant flow rate regime, whereas it decreases in the constant pressure one, 2) the pressure corresponding to the threshold of the totally saturated zone, p_{sat}, is practically constant during the whole injection for the constant flow rate regime (Figure 102b), whereas it decreases as the injection develops for the constant pressure regime (Figure 102a).

7. CONCLUDING REMARKS, CONTRIBUTIONS AND FUTURE WORKS.

Summary of problems considered.

In this work, Boundary Element Techniques were implemented in several problems of impregnation of dual-scale fibrous reinforcements used in the processing of composites materials. Three kinds of problems were tackled: 1) simultaneous filling of channels and bundles at mesoscopic scale to study the void formation by mechanical entrapment of air; 2) filling of bundles at mesoscopic scale considering fully filled channels, to study the dynamic evolution of intra-tow voids, to determine sink functions that couple the macroscopic and mesoscopic equations, and to analyse the behaviour of the effective unsaturated permeability under several variables; 3) unidirectional filling of molds at macroscopic scale, to study the behaviour of the global saturation and pressure profiles in time and space when the RUC impregnation is not uniform.

During the development of the above mentioned problems, several issues were overcome: 1) the incorporation of suitable constraints for the time interval based on geometric restrictions and on the modified capillary number (C_a^*) and capillary ratio $\left(C_{cap}\right)$, as well as the implementation of smoothing and remeshing algorithms, in order to track complex fluid front shapes using a simplistic numerical technique, namely, the Direct Euler Integration of the kinematic condition; 2) the solution of coupled problems free fluid-porous media, which are usually ill-conditioned, by using special solvers (Singular Value Decomposition in this case); 3) the treatment of the defective boundary condition that arises in the constant flow rate regime, by considering a physically consistent assumption at the RUC inlet; 4) the deduction of a flow direction-dependent model for the capillary pressure in the porous media in order to avoid using experimental shape factors; 5) the treatment of the numerical errors associated to the calculation of the surface tractions on the channel fluid front, which can have a significant impact on the fluid front advancement when the capillary effects are important; 6) the choice of an appropriate BEM-based numerical scheme to deal with the anisotropic Brinkman equations in coupled problems free fluid-porous media; among others. In the following paragraphs, the main conclusions obtained in this work are summarized and possible future works are identified.

Problem 1: Simultaneous filling of channels and bundles at mesoscopic scale.

For the first type of problem abovementioned, two consistent mathematical formulations were considered: Stokes-Darcy and Stokes-Brinkman. In the former case, a pure BEM scheme was used for both the Stokes and Darcy domains; in the second one, two numerical schemes were compared each other: 1) pure BEM for both the Stokes and Brinkman domains, 2) pure BEM for Stokes and DR-BEM for Brinkman domain (BEM/DR-BEM scheme). Superior accuracy and convergence rates were obtained in BEM/DR-BEM.

All numerical schemes were validated by means of problems admitting analytical solutions. For the validation of the pure BEM scheme used in Stokes-Darcy problems, an analytical solution of a simple case was developed. On the other hand, the validation of the BEM/DR-BEM scheme used in Stokes-Brinkman problems was carried out with a benchmark analytical solution previously employed for the robustness assessment of FEM codes. After evaluating the accuracy and convergence of both numerical schemes, i.e, pure BEM for Stokes-Darcy and BEM/DR-BEM for Stokes-Brinkman, it can be concluded that they are reliable for the solution of coupled problems free fluid-porous media within the limits of the numerical parameters established here, namely, for Stokes-Darcy, anisotropy ratios of permeability, K_1/K_2, and slip coefficients, γ, with orders of magnitude ranging between $\mathcal{O}(-1)$ and $\mathcal{O}(2)$ for the first parameter (K_1/K_2), and between $\mathcal{O}(-2)$ and $\mathcal{O}(0)$ for the second one (γ) ; in the Stokes-Brinkman case, inverse Darcian numbers, χ^2, and jumps stress coefficients, β, with orders of magnitude ranging between $\mathcal{O}(0)$ and $\mathcal{O}(4)$ for the first parameter (χ^2), and having a value of $\mathcal{O}(0)$ for the second one (β).

Problems formerly tackled by other numerical techniques were solved using the present numerical schemes, obtaining important similarities and differences. Pure BEM for Stokes-Darcy was used to solve a pressure-constant, moving-boundary problem previously solved in [3] using a CV/FAN approach. The increase of the void size with the anisotropy ratio of permeability, K_1/K_2, was obtained in both numerical solutions, but differences in the filling times, fluid front shapes and void characterization (size and shape) between both solutions were noticed as well. In both solutions, void remains trapped at the rear edge of the weft, with a smoother void obtained with pure BEM due to the tracking technique of the fluid front. On the other hand, a pressure-driven, fully developed problem, formerly solved by [20] using FEM and a Level Set formulation, was solved here using BEM/DR-BEM for

Stokes-Brinkman. Both FEM and BEM/DR-BEM converged correctly to the analytical solution, but the errors in the Stokes and Brinkman domains were different between both numerical schemes due to the dissimilar interpolation strategies, namely, Level Set interpolation in [20] and Radial Basis Function interpolation here. In both schemes, the reduction of the Stokes velocity and the boundary layer thickness with the increase of β and χ^2 was predicted. Moreover, the boundary layer solution by BEM/DR-BEM was more stable than the one in FEM since no oscillations appeared in the first one.

Parametric studies of simultaneous fillings of RUC's were conducted using both numerical approaches, pure BEM and BEM/DR-BEM, with the purpose to determine the influence of the following aspects on the void formation process: 1) Processing, geometric and material variables, 2) formulation type and corresponding interface matching conditions, 3) injection regime, and 4) RUC compaction. Some results obtained are in agreement with previous experimental, analytical and numerical works, whereas some few results are not. Other results have not been reported yet in other works and pose the necessity of further investigations. According to the simulations of void formation in highly compacted preforms at constant flow rate, the tow porosity, width of transverse tow, fluid penetrativity and RUC porosity have influence on the final void size and shape for different values of the modified capillary number, C_a^*. If the former four parameters are kept constant, numerical results show an increase of the void size with C_a^* in logarithmic manner, which is in agreement with other researches [25], [44], [75], [77], [81]. Other results obtained here that are congruent with previous researches can be highlighted: the void shapes obtained in the parametric studies [170], [176], [177], the increase of the void aspect ratio as the void size decreases [117], the increase of the void size with K_1/K_2 [3] and the location of the void at the rear edge of the weft [3], [4].

The comparison between the processes of void formation using the Stokes-Darcy (S-D) and Stokes-Brinkman (S-B) formulations was carried out considering the filling of two adjacent RUC's (two wefts). Even though the fluid front shapes, filling times and voids characteristics were different between both formulations, the behavior of the size and aspect ratio of voids with the capillary ratio, C_{cap}, in both wefts, was the same; the reduction of the total void size with C_{cap} was predicted by both S-D and S-B, which is in agreement with the experimental work in [11].

According to the BEM/DR-BEM results, the size and aspect ratio of the voids, as well as the saturation curves, are also influenced by the matching conditions Stokes-Brinkman. When void formation occurs, the void size at both wefts, and consequently the total void size, decreases when β decreases, in such a way that the smallest voids are obtained for the continuous-stress condition, $\beta = 0$. On the other hand, the change of the void aspect ratio with β depends on the weft considered and on the capillary ratio, C_{cap}. For the jump stress condition, the behavior of the void size and void aspect ratio with C_{cap} in both wefts, as well as the decreasing behavior of the total void content with C_{cap}, remain unaltered under the jump stress coefficient, β. Regarding the RUC saturation, it can be concluded that its general behavior in the time is consistent with the RUC geometry for the matching conditions evaluated here, with the continuous stress condition predicting larger saturations than the jump-stress one at all filling instants. In addition to the reduction of the total void content with C_{cap}, the shapes and location of the voids obtained with the S-B formulation are also in accordance with results previously reported in the literature [3], [4], [170], [176], [177] .

The BEM/DR-BEM results also showed that the RUC compaction has several effects on the void formation process regarding the original domain. When the RUC is compacted, the impregnation process takes more time, the behavior of the void size with C_{cap} for the first weft is modified, the void size for both wefts and all values of C_{cap} decreases, and the distance between the minimum fluid front position at the warps and the maximum fluid front position at the channel decreases for all filling instants. This last result was also reported in [22].

Problem 2: Filling of bundles at mesoscopic scale considering fully filled channels.

The second kind of problem considered in this work consisted on the simulations of filling of bundles considering fully filled channels at mesoscopic scale. The modelling of the channel fluid flow using the Stokes equation, the consideration of the matching conditions free fluid-porous media and the prescription of a pressure gradient along the flow direction, instead of considering a uniform pressure in the channel, were the principal methodological changes adopted here with respect to other works devoted to this kind of problems [8], [13],

[14], [102], [225], [226]. These simple changes allowed considering some phenomena and parameters that are proper of LCM processes and have been neglected in other works. For instance, the dynamic evolution of intra-tow voids was deemed using the present methodology and the pure BEM scheme for Stokes-Darcy problems. According to the numerical results, the elimination of intra-tow voids from the tows towards the channel is a pulsating process, i.e., a process that occurs in several cycles. Each cycle comprises four void stages: compression and displacement that take place inside the tows, and migration and splitting that occur in the channel and are faster than the former two processes. The numerical results showed that the void compression occurs until the air pressure at the fluid front matches the average liquid pressure surrounding the tow plus the magnitude of the capillary pressure, moment from which the void displacement starts; this confirms the hypothesis of [79]. On the other hand, when the void migrates from the tow towards the channel, it can be subjected to several cycles of expansion and contraction that depend on the evolution of the air pressure and the surface tractions of the bubble. The magnitude of the average velocity of void expansion or contraction is variable and can be lower or higher than the average liquid velocity in the channel domain, but it is considerably inferior to the velocity of the bubbles when they migrate freely along the channels. The void splitting or breaking could arise when the bubble surface deforms enough due to the surface traction effects. According to the numerical results, the increase of the surface tension of the liquid generates a greater opposition to the void migration, whereas the increase of the average liquid velocity and the average pressure in the channel promote the void migration, coinciding with the conclusions reported in [5], [78], [81], [84], [220], [222].

Several simulations of filling of bundles considering fully filled channels were also run to establish lumped functions for the sink term, S_g, that couple the mesoscopic and macroscopic equations, and to determine the influence of the tow saturation and some geometrical variables on the effective unsaturated permeability. The principal contributions of this work to the computation of S_g with respect to other works [12],[225] can be summarized as follows: 1) the inclusion as independent variables of the air entrapment parameter, λ, to consider the air compressibility and air dissolution at the same time, and of the vacuum pressure, P_{vac}, which is a relevant parameter in LCM processes, 2) the consideration of a flow-direction dependent capillary pressure for the porous media, 3) the

statement of a direct methodology to compute the saturation rate in terms of the difference between the inlet and outlet flow rates of the RUC, and 4) the modification of the fitting equation with an additional free parameter to improve the matching with the numerical results.

The simulation results also showed that K_{eff} is directly proportional to the saturation, S_t, and the curves of $K_{eff}\ vs\ S_t$ are influenced by the tow porosity (ε_t), weft aspect ratio (a_1/a_2) and gap porosity (ε_g). Some results obtained here are also in agreement with previous results, such as: the independency of K_{eff} on the processing parameters [138]–[140], the increase of K_{eff} with the tow porosity and with the aspect ratio of the weft when the bundles are totally saturated [20], and the general behavior of the RUC saturation in the time when full air dissolution is considered [12],[225]. Since the channel velocity field needed to be calculated in all filling instants in order to compute S_g and K_{eff}, some interesting conclusions about the influence of the tow saturation, average pressure and pressure gradient on the inlet and outlet velocity profiles and on the volume-averaged horizontal velocity in the channel were obtained. In general, as the tows saturate more, the inlet and outlet velocity profiles get closer each other and consequently the velocity variations along the RUC length decreases; additionally, as S_t is higher, the influence of the average pressure on the velocity profiles is less significant. On the other hand, according to the numerical results, the volume-averaged horizontal velocity in the channel is only affected by the pressure gradient.

Problem 3: Unidirectional filling of molds at macroscopic scale.

The last type of problem considered here was the unidirectional filling of molds at macroscopic scale considering the partial saturation effects arising inside the RUC at mesoscopic scale. A lumped strategy was adopted, i.e., the sink functions for S_g, previously obtained via mesoscopic simulations, were introduced in the macroscopic governing equations, which in turn were solved using the DR-BEM technique and Piccard iteration. The analytical solution of a problem consisting on the unidirectional filling of dual-scale fibrous reinforcements at constant pressure, with the sink term varying as a linear function of the pressure [101], was compared to the DR-BEM solution for validation purposes, obtaining a good accuracy and convergence. On the other hand, both constant

pressure and constant flow rate macroscopic simulations were considered in the parametric study of this problem. Some similarities between both injection regimes (constant pressure and constant flow rate) were found: the influence of the air entrapment parameter, λ, on the saturation curves is more important as the injection develops; the global saturation is higher as λ decreases and, for $\lambda = 1$ (full air compressibility), as the input processing parameters (inlet pressure, vacuum pressure and inlet flow rate) increases. However, some important differences between both regimes can be also mentioned: for constant flow rate injections, the fluid front velocity always increases with λ, whereas for constant pressure ones this is not necessarily valid in all fluid front positions; on the other hand, the saturation at the inlet of the mold continuously increases in constant flow rate injections for $\lambda = 1$, while in constant pressure ones it reaches an equilibrium value instead. The shapes of the pressure profiles obtained in both regimes are in agreement with previous works [83], [240], [241].

Summary of contributions of the present work.

In this part, it is convenient to emphasize the main contributions of the present work regarding previous researches, in light of the objectives initially posed in Section 1.4. These main contributions can be summarized as follows:

Regarding the general objective.

- Implementation for first time of Boundary Element Techniques (BEM) on the processes of formation and dynamic evolution of voids in dual-scale porous media used in the processing of composites materials. As it was mentioned in this work, this implementation entailed several numerical issues, like the solution of ill-conditioned systems, the prescription of defective boundary conditions, the application of constraints for the time step and of smoothing and remeshing algorithms to assure the stability of the fluid front tracking scheme, among others. In addition to the well-known advantages of BEM over domain-mesh techniques in moving boundary problems, which lie in the reduction of the meshing requirements, some benefits of the present numerical scheme with respect to other ones were identified: 1) the fluid front shape is more accurate because it is directly obtained from the kinematic condition, 2) the dynamic condition can be directly imposed on the nodes of the fluid front, 3) neither reconstruction

algorithms nor the solution of a pure advection equation are required to acquire the fluid front position, among others.

Regarding the specific objectives.

- As in previous works, the influence of the modified capillary number (C_a^*), tow porosity, width of transverse tow, fluid penetrativity and RUC porosity on the size, shape and location of voids was studied here as well. However, the use of a Stokes-Darcy formulation in this work allowed considering two important things usually disregarded in other works: 1) the capillary forces associated to the curvature of the moving fluid front in the channel, which can have a relevant influence on the fluid front evolution and consequently, on the void formation process, for small values of C_a^*; 2) the tangential velocities of the porous medium at the interface free fluid-porous medium, which were not neglected a priori in this work by reasons previously argued, allowing in this way to known the complete velocity field at such interface in both the channel and the porous medium domain.
- Analysis of the influence of the stress matching conditions and the formulation type (Stokes-Darcy and Stokes-Brinkman) on the void formation process at several capillary ratios, C_{cap}, which had not been considered before to the best of the author´s knowledge. On the other hand, the influence of the RUC compaction on the void formation process was also analyzed here; previous works only considered the influence of the RUC compaction on the imbalances of the fluid fronts inside the RUC, but not on the formation and final characterization of the voids as done here.
- One simple methodological modification to tackle the problem of tows filling at mesoscopic scale considering fully filled channels was made here. It is based on the prescription of a pressure gradient in the direction of the fluid motion instead of the consideration of an average pressure in the channels. This simple modification, together with the consideration of the air compressibility, led to the following contributions: 1) analysis of the influence of the volume-averaged pressure, pressure gradient and capillary properties on the dynamic evolution of intra-tow voids (compressibility, displacement, migration and splitting) by means of simulations at mesoscopic scale; 2) analysis of the influence of the processing parameters, tow porosity, gap porosity and

weft geometry on the behavior of the effective unsaturated permeability with the saturation in dual-scale fibrous reinforcements.

- Deduction of lumped functions to account for the sink effect in macroscopic simulations. In previous works, lumped sink functions were obtained in terms of the volume-averaged pressure and the saturation only, but, in the present work, two additional parameters that play a major role in the impregnation process of the tows were considered: the vacuum pressure and the air entrapment parameter. The incorporation of the obtained sink functions in the macroscopic governing equations allowed analyzing the influence of these two parameters on the evolution of the global saturation in the space and time, considering the unidirectional filling of cavities at both constant pressure and constant flow rate regimes.
- Development of an analytical solution for a coupled problem free fluid-porous medium, on the basis of the lubrication approximation for the free fluid flow and the EIS transformation for the anisotropic porous medium. This solution can be used later as a benchmark solution for validation of other numerical schemes.
- Deduction of a flow-direction dependent model to compute the capillary pressure, P_{cap}, inside the tows without experimental shape factors. In that way, the dynamic condition of the fluid front inside the tows was prescribed more accurately here than in previous works where a constant value of P_{cap} was considered, even though P_{cap} actually depends on the fluid flow orientation regarding the fibers as it was considered here.

Publications.

- Iván David Patiño Arcila, Henry Power, César Nieto Londoño, Whady Felipe Flórez Escobar, *"Boundary element simulation of void formation in fibrous reinforcements based on the Stokes-Darcy formulation"*. Published in: Switzerland, Computer Methods In Applied Mechanics And Engineering, *ISSN:* 0045-7825 *ed:* North-Holland *v.*304, p.265 - 293 ,2016
- Iván David Patiño Arcila, Henry Power, César Nieto Londoño, Whady Felipe Flórez Escobar, *"Stokes-Brinkman formulation for prediction of void formation in dual-scale fibrous reinforcements: a BEM/DR-BEM simulation"*. Published in: Germany. Computational Mechanics, *ISSN:* 1432-0924, *v.*59, First On-line, p.1 - 23 ,2017

- Iván David Patiño Arcila, Henry Power, César Nieto Londoño, Whady Felipe Flórez Escobar, *"Boundary Element Method for filling of dual scale porous media used in the processing of composites materials"*, in 10th Conference on Boundary Integral Methods, Brighton, United Kingdom, 2015, pp. 1–12.
- Iván David Patiño Arcila, Henry Power, César Nieto Londoño, Whady Felipe Flórez Escobar, *"Boundary Element Method for the dynamic evolution of intra-tow voids in fibrous reinforcements using a Stokes-Darcy approach"*, to be submitted *(In preparation).*
- Iván David Patiño Arcila, Henry Power, César Nieto Londoño, Whady Felipe Flórez Escobar, *"Multiscale filling simulations in dual-scale fibrous reinforcements using Boundary Element Techniques"* to be submitted *(In preparation).*

Future Works.

The statement of future works can be motivated by the following reasons: the necessity of confirming or extending some of the obtained conclusions, the consideration of more complex problems in the area of composites, and the identification of potential applications of the numerical schemes implemented here in other areas.

In the first case, some important aspects deserve a deeper numerical and experimental study, such as: 1) The influence of the tow porosity on the void characteristics considering several RUC geometries and compaction levels, 2) the non-sensitivity of the void location to all parameters studied here considering other RUC geometries, 3) the influence of the RUC compaction on the total void content considering others compaction levels and RUC geometries, 4) the slow stepwise elimination process of intra-tow voids from the tows towards the channel, 5) the behavior of the total void content with C_a^* for larger capillary numbers than the ones considered here, to numerically confirm the reduction of this content once a certain value of C_a^* has been reached, 6) the relationship between the times of the stages involved in the void elimination process taking into account other processing conditions and RUC geometries, 7) the consideration of the void splitting phenomenon on the sink functions calculations, among others.

The numerical codes developed in this work can be considered a first important step to tackle more complex problems of processing of composites manufactured with dual-scale

fibrous reinforcements. One of these problems is the incorporation of non-isothermal and reactive conditions in the filling process at both mesoscopic and macroscopic scales. This problem has been previously considered by [8], [94] using FEM/CV and the classical methodology of prescribing a uniform pressure in the channel to account only for the filling of bundles. This strategy implies the use of two domain meshes at different scales (leading to a very high computational cost), the implementation of tracking techniques that do not reproduce the exact shape of the fluid front and the acceptance of the limitations of the classical methodology that were exposed in this work. These drawbacks can be overcome by incorporating the solution of the energy and species transport equations to the present work, which is part of the ongoing work developed by the author. Considering that continuity, momentum, energy and species equations are coupled altogether, the first developed algorithms for this particular problem have been much more time-demanding than the ones employed in this work, but the obtained results have been satisfactory so far. The consideration of non-newtonian fluids associated to the impregnation of reinforcements with thermoplastic resins or thermosetting resins modified with nanofillers, the simulation of the fabric deformation mechanisms when the impregnation takes place, the consideration of hybrid and/or heterogeneous dual-scale preforms, and the simulation of the mechanical response of dual-scale fibrous reinforcements under the presence of voids, are forthcoming investigations.

Apart from the applications to the composites area, other potential applications of the numerical schemes implemented here to solve coupled problems free fluid-porous media can be identified. As mentioned before, the principal characteristic of those problems is the presence of two domains with very dissimilar permeabilities, which can be found in many applications such as: transport of contaminants in coastal areas and rivers, flooding of dry areas, transport of chemicals from the main blood stream in the arteries through a porous membrane, groundwater infiltration in karst aquifers, flow modeling through oil filters, among others. The simulation of the dynamic response of peatlands under rewetting operations to restore its carbon sink function is another application of particular interest to the author.

Appendix A.

Equivalent Isotropic System (EIS).

The EIS transformation is implemented to transform the pressure field equation of anisotropic Darcy porous media into a simple Laplace equation. This transformation and BEM were previously used in the simulation of single-scale porous media in [50], [58]. The EIS transformation can be conceived as the transformation of an ellipse with main axes equal to $\sqrt{K_1}$ and $\sqrt{K_2}$ into a circle having a radius of $R = \sqrt{K_e}$, with $K_e = \sqrt{K_1 K_2}$ as the equivalent isotropic permeability (Figure A1).

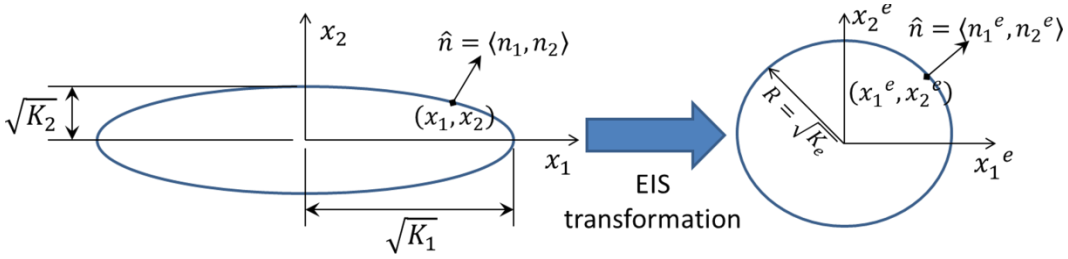

Figure A1 Scheme of EIS transformation

In the original coordinate system, the pressure field equation can be obtained by substituting the Darcy law into the mass conservation equation:

$$K_1 \frac{\partial^2 \mathrm{p}}{\partial {x_1}^2} + K_2 \frac{\partial^2 \mathrm{p}}{\partial {x_2}^2} = 0 \tag{A1}$$

The EIS transformation is defined as follows [59], [144]:

$$\begin{bmatrix} x_1^e \\ x_2^e \end{bmatrix} = \begin{bmatrix} (K_2/K_1)^{1/4} & 0 \\ 0 & (K_1/K_2)^{1/4} \end{bmatrix} \begin{bmatrix} x_1 \\ x_2 \end{bmatrix} \tag{A2}$$

in such a way that the Eq. A1 in the EIS system becomes:

$$K_e \frac{\partial^2 \mathrm{p}}{\partial {x_i^e}} = 0 \tag{A3},$$

whereas the components of the normal vector in the EIS system, $\widehat{n^e} = \langle \widehat{n_1^e}, \widehat{n_2^e} \rangle$, can be computed in terms of the normal components in the original system, $\langle \widehat{n_1}, \widehat{n_2} \rangle$, by using the inverse-transpose of the transformation matrix defined in Eq.A2:

$$\langle \widehat{n_1^e}, \widehat{n_2^e} \rangle = \frac{1}{f^e} \langle (K_1/K_2)^{1/4} \widehat{n_1}, (K_2/K_1)^{1/4} \widehat{n_2} \rangle \tag{A4},$$

where $f^e = \left\| (K_1/K_2)^{1/4} \widehat{n_1}, (K_2/K_1)^{1/4} \widehat{n_2} \right\|$.

Taking into account (A2) and (A4), the normal flux in the EIS system can be expressed as follows:

$$\frac{\partial p}{\partial \widehat{n^e}} = \frac{\partial p}{\partial x_i^e} . \widehat{n_i^e} = \frac{\partial p}{\partial x_i} . \frac{\partial x_i}{x_i^e} \widehat{n_i^e} = \frac{{h_i}^2}{f^e} . \frac{\partial p}{\partial x_i} . \widehat{n_i} \tag{A5}$$

where the scale factors, h_i, are given by:

$$h_1 = (K_1/K_2)^{1/4} \tag{A6}$$

$$h_2 = (K_2/K_1)^{1/4} \tag{A7}$$

If the Eq. A5 is multiplied at both sides by " $-K_e/\mu$ ", the following is achieved:

$$-\frac{K_e}{\mu} \frac{\partial p}{\partial \widehat{n^e}} = -\frac{1}{f^e} . \frac{K_i}{\mu} \frac{\partial p}{\partial x_i} . \widehat{n_i} \tag{A8}$$

After applying the Darcy's law in the right hand side of the Eq.A8 and dividing at both sides by ε_t, the next expression is obtained for the normal pore velocity, u_n, in terms of variables in the EIS system:

$$u_n = -\frac{K_e f^e}{\varepsilon_t \mu} \frac{\partial p}{\partial \widehat{n^e}} \tag{A9}$$

The domain integral formulation in the EIS system can be achieved by applying a similar procedure to the one exposed in Section 2.4, obtaining the following:

$$\int_{\Omega^e} \left(p \frac{\partial^2 p^*}{\partial x_i^{e2}} - p^* \frac{\partial^2 p}{\partial x_i^{e2}} \right) d\Omega^e = \int_{\Omega^e} \frac{\partial}{\partial x_i^e} \left(p \frac{\partial p^*}{\partial x_i^e} - p^* \frac{\partial p}{\partial x_i^e} \right) d\Omega^e \tag{A10}$$

Considering that p and p^* satisfy the original and the singularly forced Laplace equation in the EIS system, respectively, the next equation is obtained:

$$-\int_{\Omega^e} p \delta_2 \left(\overrightarrow{x^e} - \overrightarrow{\xi^e} \right) d\Omega^e = \int_{\Omega^e} \frac{\partial}{\partial x_i^e} \left(p \frac{\partial p^*}{\partial x_i^e} - p^* \frac{\partial p}{\partial x_i^e} \right) d\Omega^e \tag{A11}$$

Taking into account that $d\Omega^e = h_1 h_2 dx_1^e dx_2^e = d\Omega$, the fundamental property of Delta Dirac function applies in the EIS system, i.e, $\int_{\Omega^e} p \delta_2 \left(\overrightarrow{x^e} - \overrightarrow{\xi^e} \right) d\Omega^e = \int_{\Omega} p \delta_2 \left(\vec{x} - \vec{\xi} \right) d\Omega = c\left(\vec{\xi} \right) p\left(\vec{\xi} \right) = c\left(\overrightarrow{\xi^e} \right) p\left(\overrightarrow{\xi^e} \right)$. Thus, the Eq.A11 becomes:

$$-c\left(\overrightarrow{\xi^e} \right) p\left(\overrightarrow{\xi^e} \right) = \int_{\Omega^e} \frac{\partial}{\partial x_i^e} \left(p \frac{\partial p^*}{\partial x_i^e} - p^* \frac{\partial p}{\partial x_i^e} \right) d\Omega^e \tag{A12}$$

Divergence theorem cannot be directly applied in right hand side terms of Eq.A12 since the scale factors, h_i, do not appear. It is necessary first to apply the chain rule and consider that $d\Omega^e = d\Omega$ to accomplish the next expression:

$$-c\left(\overrightarrow{\xi^e} \right) p\left(\overrightarrow{\xi^e} \right) = \int_{\Omega} \frac{\partial}{\partial x_i} \left(p \frac{\partial p^*}{\partial x_i^e} - p^* \frac{\partial p}{\partial x_i^e} \right) \left(\frac{\partial x_i}{\partial x_i^e} \right) d\Omega \tag{A13},$$

Considering Eqs. A2, A6 and A7, the Eq. A13 can be written as:

$$-c(\vec{\xi^e})p(\vec{\xi^e}) = \int_\Omega \frac{\partial}{\partial x_i}\left(p\frac{\partial p^*}{\partial x_i^e} - p^*\frac{\partial p}{\partial x_i^e}\right)h_i d\Omega \tag{A14}$$

As the scale factors, h_i, are constants, (A14) can be rewritten as:

$$-c(\vec{\xi^e})p(\vec{\xi^e}) = \int_\Omega \frac{\partial}{\partial x_i}\left(p\frac{\partial p^*}{\partial x_i^e}h_i - p^*\frac{\partial p}{\partial x_i^e}h_i\right)d\Omega \tag{A15}$$

By applying the divergence theorem in the right hand side integral, the following is obtained:

$$-c(\vec{\xi^e})p(\vec{\xi^e}) = \int_s p\frac{\partial p^*}{\partial x_i^e}h_i\widehat{n_i}\,ds - \int_s p^*\frac{\partial p}{\partial x_i^e}h_i\widehat{n_i}\,ds \tag{A16}$$

Considering that $h_i\widehat{n_i} = \widehat{n_i^e}f^e$ from Eq.A4, the Eq.A16 becomes:

$$c(\vec{\xi^e})p(\vec{\xi^e}) = \int_s p^*\frac{\partial p}{\partial x_i^e}f^e\widehat{n_i^e}\,ds - \int_s p\frac{\partial p^*}{\partial x_i^e}f^e\widehat{n_i^e}\,ds \tag{A17},$$

or equivalently:

$$c(\vec{\xi^e})p(\vec{\xi^e}) = \int_s p^*f^e\frac{\partial p}{\partial \widehat{n^e}}ds - \int_s pf^e\frac{\partial p^*}{\partial \widehat{n^e}}ds \tag{A18},$$

which corresponds to the integral formulation for the anisotropic Darcy equation in the EIS system.

The integral formulation in the original coordinate system can be also obtained directly and it is equivalent to Eq.A18. To demonstrate this, the equation corresponding to the Second Green Identity, Eq.39, is applied in one dimension for both $i = 1$ and $i = 2$ separately; the resulting expressions are multiplied at both sides by K_i, with $i = 1,2$, and added up, to obtain the following:

$$\int_\Omega \left(pK_i\frac{\partial^2 g^*}{\partial x_i^2} - g^*K_i\frac{\partial^2 p}{\partial x_i^2}\right)d\Omega = \int_\Omega \frac{\partial}{\partial x_i}\left(pK_i\frac{\partial g^*}{\partial x_i} - g^*K_i\frac{\partial p}{\partial x_i}\right)d\Omega \tag{A19}$$

Likewise to the last case, the divergence theorem is applied in the right hand side integral. Besides, p is a solution of the original anisotropic Darcy equation, Eq.A1, and the solution of the corresponding singularly forced equation, $K_i(\partial^2 \mathrm{g}^*/\partial {x_i}^2) + \delta_2(\vec{x} - \vec{\xi}) = 0$, is given in [149]:

$$\mathrm{g}^* = \frac{\mathrm{p}^*}{K_e} = -\frac{1}{2\pi K_e}\ln(r^e) \tag{A20}$$

Therefore, the integral formulation in the original system can be written as follows:

$$c(\vec{\xi})p(\vec{\xi}) = \int_s p^*\left(\frac{K_i}{K_e}\right)\frac{\partial p}{\partial x_i}\widehat{n_i}\,ds - \int_s p\left(\frac{K_i}{K_e}\right)\frac{\partial p^*}{\partial x_i}\widehat{n_i}\,ds \tag{A21}$$

Considering that $h_i^2 = K_i/K_e$, the following is obtained:

$$c(\vec{\xi})p(\vec{\xi}) = \int_s \; p^* h_i^2 \frac{\partial p}{\partial x_i} \hat{n}_i \, ds - \int_s \; p h_i^2 \frac{\partial p^*}{\partial x_i} \hat{n}_i \, ds \tag{A22}$$

Applying the inverse of the transformation defined in Eq.A2 and considering the Eq.A5, the following equation is obtained:

$$c(\overrightarrow{\xi^e})p(\overrightarrow{\xi^e}) = \int_s \; p^* f^e \frac{\partial p}{\partial \hat{n}^e} ds - \int_s \; p f^e \frac{\partial p^*}{\partial \hat{n}^e} ds \tag{A23},$$

which is the same Eq.A18 obtained before.

Appendix B.

Development of analytical solution of a coupled Stokes-Darcy problem.

The coupled Stokes-Darcy problem used for the validation of the numerical approach considered in this work consists on a thin rectangular channel coupled with an adjacent rectangular porous channel (Figure 16). The main goal of this solution is the prediction of the pressure and velocities fields in both domains. In the channel, according to the lubrication approximation (thin film flow), the Stokes system of equations is reduced to:

$$\mu \frac{\partial^2 u_1}{\partial x_2^2} = \frac{dp}{dx_1}(x_1) \tag{B1}$$

$$dp/dx_2 = 0 \tag{B2}$$

$$\frac{\partial u_1}{\partial x_1} + \frac{\partial u_2}{\partial x_2} = 0 \tag{B3},$$

while in the porous medium, the problem is described by Darcy's model (Eq. 62a-b). Symmetry conditions are prescribed at the lateral walls ($du_1/dx_2 = 0 \; and \; u_2 = 0$), namely, bottom of the channel and top of the porous medium. At the surface between the two regions, $x_2 = 0$, an unknown tangential velocity coming from the channel, $u_1^-(x_1)$, is considered, and it will be determined from the slip condition, Eq. 66, in terms of the tangential velocity at such surface coming from the porous medium, $u_1^+(x_1)$. Direct integration of (B1) between $x_2 = -h_s$ and $x_2 = 0$, taking into account (B2), and considering the symmetric condition at $x_2 = -h_s$ and that $u_1 = u_1^-$ at $x_2 = 0$, follows:

$$u_1 = \frac{1}{2\mu}.\left(\frac{dp}{dx_1}\right).(x_2^2 + 2h_s x_2) + u_1^-(x_1) \tag{B4}$$

Having an explicit expression for u_1, the value of u_2 can be obtained from the integration of the continuity equation (B3), taking into account the no-flux condition at $x_2 = -h_s$, as:

$$u_2 = -\frac{1}{2\mu}.\left(\frac{d^2p}{dx_1^2}\right).\left(\frac{x_2^3}{3} + h_s x_2^2 - \frac{2}{3}h_s^3\right) - \left(\frac{du_1^-}{dx_1}\right)(x_2 + h_s) \tag{B5},$$

from where it follows that the infiltration velocity towards the porous medium at $x_2 = 0$ is given by:

$$u_2^- = u_2^+ = \frac{h_s^3}{3\mu}.\left(\frac{d^2p}{dx_1^2}\right) - \left(\frac{du_1^-}{dx_1}\right)h_s \tag{B6}$$

To complete the formulation of the lubrication flow in the channel, it is necessary to prescribe inlet and outlet pressures, which are considered as $p = \bar{p}_{in}$ at $x_1 = 0$ and $p = 0$ at $x_1 = l$.

On the other hand, at the porous medium, the pressure and velocity fields are obtained using Eq's 62a-b, which are reduced to the Laplace equation by using the EIS transformation, as it is shown in Appendix A. Pressure boundary conditions are prescribed at the inlet and outlet of the porous medium, with $p = \bar{p}_{in}$ at $x_1 = 0$, i.e., a uniform pressure is considered at the inlet of the two regions, and $p = \bar{p}_{cap}$ at $x_1 = l$, i.e., a capillary pressure is considered at the end of the porous domain; this capillary pressure can have a major role in the impregnation of LCM processes, as it is shown in this work. A harmonic pressure field in the EIS transformed domain that satisfies the inlet and outlet pressure conditions and the no-flux condition at $x_2 = h_d$, is given by:

$$p = a_o x_1^e + b_o + \sum_{n=1}^{\infty} a_n . cosh\left(\lambda_n . ({h_d}^e - x_2^e)\right) . sin(\lambda_n . x_1^e), \quad for\ 0 \le x_2 \le h_d \qquad \text{(B7)},$$

where $a_o = \left(p_{cap} - p_{in}\right)/l^e$, $b_o = p_{in}$ and $\lambda_n = (n\pi)/l^e$, with $n = 1,2,\ldots..$ The coefficients a_n need to be determined from the continuity of surface tractions at the interface between the two media (channel and porous medium). In the above equation superscript "e" stands for the EIS system.

The pressure field in the porous medium can be written in terms of the original space variables as:

$$p = a_o (K_2/K_1)^{\frac{1}{4}} x_1 + b_o + \sum_{n=1}^{\infty} a_n . cosh\left(\lambda_n . (K_1/K_2)^{\frac{1}{4}} (h_d - x_2)\right) . sin\left(\lambda_n . (K_2/K_1)^{\frac{1}{4}} x_1\right), \quad for\ 0 \le x_2 \le h_d \qquad \text{(B8)}$$

Taking the derivative du_1/dx_2 in Eq. (B4) and substituting the resulting expression into the slip condition, Eq. 66, yields:

$$\frac{h_s}{\mu}\left(\frac{dp}{dx_1}\right) = \frac{\gamma\sqrt{2}}{\sqrt{K_1 + K_2}} . (u_1^+ - u_1^-) \qquad \text{(B9)}$$

Taking the x_1 derivative of the above equation and substituting the obtained value of du_1^-/dx_1 into (B6), results in:

$$\left(\frac{d^2 p}{dx_1^2}\right) = \frac{1}{A_1} . \left(u_2^+(x_1) + h_s \frac{du_1^+}{dx_1}\right) \qquad \text{(B10)},$$

where $A_1 = h_s^3/(3\mu) + \sqrt{K_1 + K_2} . h_s^2/\left(\mu\gamma\sqrt{2}\right)$.

Expressing the velocity field in the porous medium, $u^+ = (u_1^+, u_2^+)$, in (B10) by using Darcy law, the Reynolds equation for the pressure field in the channel is obtained:

$$\left(\frac{d^2p}{dx_1^2}\right) = \frac{1}{A_1}.\left(-\frac{K_2}{\mu}\left(\frac{dp}{dx_2}\right)^+ - h_s\frac{K_1}{\mu}\left(\frac{d^2p}{dx_1^2}\right)^+\right) \quad \text{(B11)}$$

In the above equation the pressure p^+ represents the pressure in the surface between the porous medium and the channel, looking from the porous medium side, which is given by evaluating (B8) in $x_2 = 0$. Integrating twice (B11) in the x_1 direction and using the pressure inlet and outlet conditions in the channel, it is found the following expression for the channel pressure field:

$$p = p_{in} - (p_{in}/l)x_1 + \sum_{n=1}^{\infty} a_n.M_n.sin\left(\lambda_n.(K_2/K_1)^{1/4}x_1\right),\ for\ -h_s \le x_2 \le 0 \quad \text{(B12)}$$

Where:

$$M_n = -\frac{1}{A_1}.\left[h_s\frac{K_1}{\mu}cosh\left(\lambda_n.(K_1/K_2)^{1/4}h_d\right) + \frac{K_2}{\mu}\left(\frac{(K_1/K_2)^{3/4}}{\lambda_n}\right)sinh\left(\lambda_n.(K_1/K_2)^{1/4}(h_d)\right)\right]$$

In (B12), the only unknowns are the coefficients of the series, a_n, which are determined by the surface traction condition, Eq. 68, as previously commented:

$$-p^- + 2\mu\left(\frac{\partial u_2}{\partial x_2}\right)^- = -p^+ \quad \text{(B13)}$$

or

$$-p^- - 2\mu\left(\frac{\partial u_1}{\partial x_1}\right)^- = -p^+ \quad \text{(B14)},$$

where the last expression, (B14), was obtained by imposing the equation of continuity in (B13). Taking the x_1 derivative of (B9) to express $(du_1/dx_1)^-$ in terms of the pressure field in the channel and the tangential velocity in the porous medium, u_1^+, and using Darcy law to express u_1^+ in terms of the corresponding pressure gradient, the final equation is:

$$\left(a_o(K_2/K_1)^{1/4} - c_o\right)x_1 - \sum_{n=1}^{\infty} a_n.F_n.sin\left(\lambda_n.(K_2/K_1)^{\frac{1}{4}}x_1\right) = 0 \quad \text{(B15)},$$

with:

$$F_n = M_n\left(1 + \frac{2\sqrt{K_1+K_2}}{\gamma\sqrt{2}}h_s.\lambda_n^2.(K_2/K_1)^{1/2}\right) - cosh\left(\lambda_n.(K_1/K_2)^{\frac{1}{4}}.h_d\right)\left(1 - 2K_1\lambda_n^2.(K_2/K_1)^{\frac{1}{2}}\right),$$

and corresponding Fourier coefficients: $a_n = -2l\left(a_o(K_2/K_1)^{1/4} - c_o\right)/(n\pi F_n)\,(-1)^n$, completing the analytical solution of the problem.

Appendix C.

Tracking of the fluid front.

The Euler integration of the kinematic condition, commonly known as marker particle technique, is a very simple technique to advance the fluid front position, but it could entail some complications. Integrating the kinematic condition defined in Eq.73, the advancement of any evolution point "i" of the moving interface can be computed as (Figure C1):

$$x_{1f}^{(i)} = x_{1o}^{(i)} + u_n^{(i)} \widehat{n_1^{(i)}} \Delta t \tag{C1}$$

$$x_{2f}^{(i)} = x_{2o}^{(i)} + u_n^{(i)} \widehat{n_2^{(i)}} \Delta t \tag{C2},$$

where $\left(x_{1o}^{(i)}, x_{2o}^{(i)}\right)$ and $\left(x_{1f}^{(i)}, x_{2f}^{(i)}\right)$ are the initial and final positions of the evolution point "i", respectively, while $u_n^{(i)}$, Δt, $\widehat{n_1^{(i)}}$ and $\widehat{n_2^{(i)}}$ are the normal velocity, time interval, horizontal component and vertical component of the normal vector.

Several restrictions shall be imposed on the time interval, Δt, in order to keep the numerical stability of the solution, to avoid the crossing of points and to prevent the points to advance beyond the limits of the corresponding domain. Firstly, the numerical stability of the solution can be achieved by applying the CFL condition:

$$\Delta \mathrm{t}_{CFL}^{(k)} \leq \left(\mathrm{C}_{CFL}^{(k)} . \Delta L^{(k)}\right) / u_{n,max}^{(k)} \tag{C3},$$

where $\Delta \mathrm{t}_{CFL}^{(k)}$, $\Delta L^{(k)}$ and $u_{n,max}^{(k)}$ are the CLF time interval, mesh-size and maximum normal velocity corresponding to the domain "k", whereas $\mathrm{C}_{CFL}^{(k)}$ is CFL constant for the domain "k" given in terms of the modified capillary number, C_a^*, for constant flow rate injections, and of the capillary ratio, C_{cap}, for constant pressure injections, as shown in Figs. C2 and C3, where S-D and S-B stand for Stokes-Darcy and Stokes-Brinkman, respectively. The sign "k" refers to any domain that is being impregnated by the fluid front, which in this case could be the channel, the warps and/or the weft (Figure C1). The final CFL time interval is taken as the minimum of all domains "k", i.e., $\Delta t_{CLF} \leq min\left(\Delta \mathrm{t}_{CLF}^{(k)}\right)$.

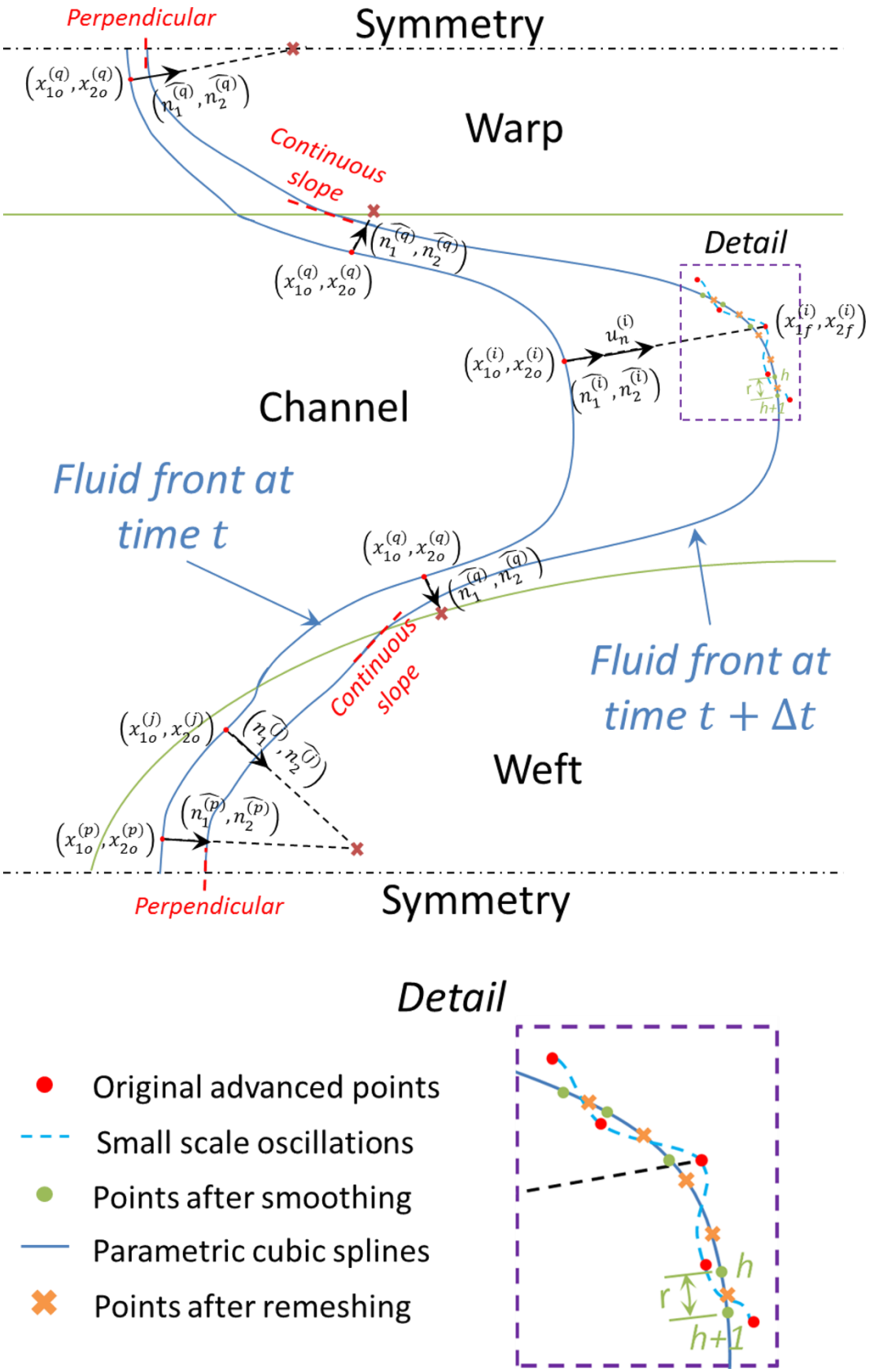

Figure C 1 Scheme of tracking of the fluid front

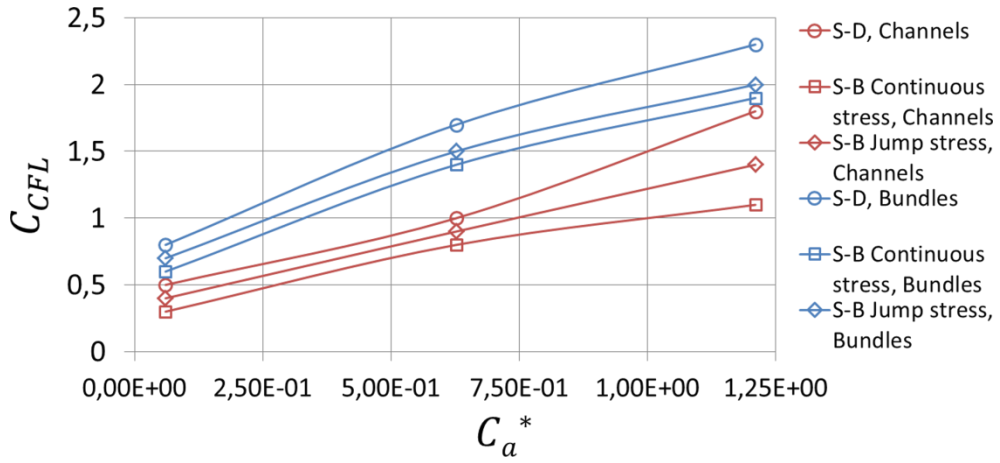

Figure C 2 Plots of C_{CFL} vs. $C_a{}^*$

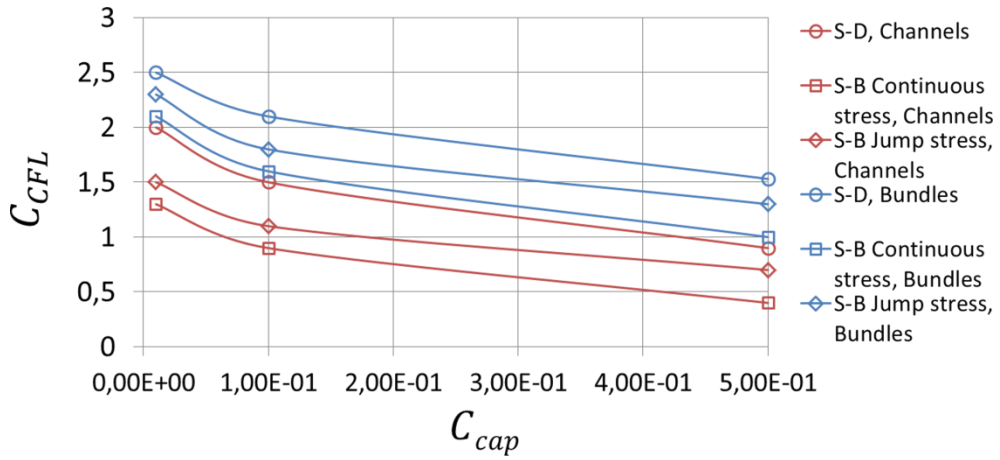

Figure C 3 Plots of C_{CFL} vs. C_{cap}

To avoid the crossing of points and to control the smoothness of the curve, the following restriction is applied for each pair of points "p" and "j" on any moving boundary (Figure C1):

$$\Delta t_{crossing}^{(pj)} \leq \min(\Delta t_p^j, \Delta t_j^p) \quad \text{(C4)},$$

where Δt_p^j is the time taken by the point "p" to intersect the line of movement of the point "j", and, in a similar fashion, Δt_j^p is the time taken by the point "j" to intersect the line of movement of the point "p". The time interval Δt_p^j can be computed as follows:

$$\Delta t_p^j = d_p^j / u_n^{(p)} \quad \text{(C5)},$$

where d_p^j is the distance travelled by point "p" to the intersect line of movement of point "j" as given by:

$$d_p^j = \left[\sum_{m=1}^{2}\left(d_{mp}^j\right)^2\right]^{1/2} \tag{C6}$$

$$d_{mp}^j = \tau_p^j \widehat{n_m^{(p)}} \tag{C7}$$

$$\tau_p^j = \frac{\widehat{n_2^{(j)}}\left(x_{1o}^{(j)} - x_{1o}^{(p)}\right) - \widehat{n_1^{(j)}}\left(x_{2o}^{(j)} - x_{2o}^{(p)}\right)}{\widehat{n_1^{(p)}}\widehat{n_2^{(j)}} - \widehat{n_1^{(j)}}\widehat{n_2^{(p)}}} \tag{C8},$$

where $\widehat{n_m^{(p)}}$ and $x_{mo}^{(p)}$ represent the m component of the normal vector and of the initial position of the evolution point "p", respectively. On the other hand, the time interval Δt_j^p can be computed by interchanging indexes "p" and "j" in equations (C5) to (C8). The restriction for the time interval is given in terms of the minimum value of $\Delta t_{crossing}^{(pj)}$ for the whole pairs of points "p" and "j", as follows: $\Delta t_{crossing} \leq min\left(\Delta t_{crossing}^{(pj)}\right)$.

Another restriction for the time interval considers that any point cannot advance beyond the limits of the domain to which the point belongs (Figure C1); these limits are defined by the interfaces and/or the boundaries, and can be described by parametric curves, $\varphi_m^{(s)}(\nu_s)$, as follows:

$$x_m^{(s)} = \varphi_m^{(s)}(\nu_s),\ m=1,2 \tag{C9},$$

where $x_m^{(s)}$ stands for the "m" coordinate of the curve corresponding to the boundary or interface "s", $\varphi_m^{(s)}$ is the parametric function and ν_s is the independent parameter. The sign "s" represents any interface or boundary, namely, the edges of the RUC, the interfaces channel-warp, interface channel-weft and interfaces warp-weft.

On the other hand, the line of movement of any evolution point "q" can be described as:

$$x_m^{(q)} = x_{mo}^{(q)} + \tau_q \widehat{n_m^{(q)}},\ m=1,2 \tag{C10},$$

where $x_m^{(q)}$ and $x_{mo}^{(q)}$ stand for the "m" coordinate of the line of movement of the point "q" and the "m" component of the initial position of the point "q", respectively, whereas $\tau_q > 0$ is the independent parameter.

The parameters ν_s and τ_q assumes the values $\nu_s = \nu_s^q$ and $\tau_q = \tau_q^s$ in the intersection points between the curves defined by Eqs. (C9) and (C10). Bearing this in mind, the restriction of the time interval for any evolution point "q" is as follows:

$$\Delta t_{limit}^{(q)} \leq \min(\Delta t_q^s) \tag{C11},$$

where Δt_q^s is the time taken by the point "q" to intersect the boundary or interface defined by "*s*", which can be computed as follows:

$$\Delta t_q^s = d_q^s / u_n^{(q)} \tag{C12}$$

$$d_q^s = \left[\sum_{m=1}^{2} \left(d_{mq}^s\right)^2\right]^{1/2} \tag{C13}$$

$$d_{mq}^s = \tau_q^s \widehat{n_m^{(q)}} \tag{C14},$$

where the form of τ_q^s depends on the parametric curve defined in (C9). In the present work, all limits can be described in terms of straight lines and ellipses, where the form of the parametric function, $\varphi_m^{(s)}$, and τ_q^s is as follows:

For straight lines:

$$\varphi_1^{(s)}(\nu_s) = x_{1o}^{(s)} + \nu_s \widehat{n_1^{(s)}} \tag{C15}$$

$$\varphi_2^{(s)}(\nu_s) = x_{2o}^{(s)} + \nu_s \widehat{n_2^{(s)}} \tag{C16}$$

$$\tau_q^s = \frac{\widehat{n_2^{(s)}}\left(x_{1o}^{(s)} - x_{1o}^{(q)}\right) - \widehat{n_1^{(s)}}\left(x_{2o}^{(s)} - x_{2o}^{(q)}\right)}{\widehat{n_1^{(q)}}\widehat{n_2^{(s)}} - \widehat{n_1^{(s)}}\widehat{n_2^{(q)}}} \tag{C17},$$

where $\left(x_{1o}^{(s)}, x_{2o}^{(s)}\right)$ is a known point of the straight line corresponding to the boundary or interface *"s"*, whereas $\widehat{n_1^{(s)}}$ and $\widehat{n_2^{(s)}}$ are the direction cosines.

For ellipses:

$$\varphi_1^{(s)}(\nu_s) = x_{1c}^{(s)} + a_1^{(s)} \cos(\nu_s) \tag{C18}$$

$$\varphi_2^{(s)}(\nu_s) = x_{2c}^{(s)} + a_2^{(s)} \sin(\nu_s) \tag{C19}$$

$$\left(\left(A_2^{(qs)}\right)^2 + \left(B_2^{(qs)}\right)^2\right)\left(\tau_q^s\right)^2 + 2\left(A_1^{(qs)}A_2^{(qs)} + B_1^{(qs)}B_2^{(qs)}\right)\tau_q^s + \left(\left(A_1^{(qs)}\right)^2 + \left(B_1^{(qs)}\right)^2 - 1\right) = 0 \tag{C20}$$

$$A_1^{(qs)} = \left(x_{1o}^{(q)} - x_{1c}^{(s)}\right) / a_1^{(s)} \tag{C21}$$

$$A_2^{(qs)} = \widehat{n_1^{(q)}}/a_1^{(s)} \tag{C22}$$

$$B_1^{(qs)} = \left(x_{2o}^{(q)} - x_{2c}^{(s)}\right)/a_2^{(s)} \tag{C23}$$

$$B_2^{(qs)} = \widehat{n_2^{(q)}}/a_2^{(s)} \tag{C24}$$

where $\left(x_{1c}^{(s)}, x_{2c}^{(s)}\right)$ is the center of the ellipse corresponding to the boundary or interface "s", whereas $a_1^{(s)}$ and $a_2^{(s)}$ are the major and minor semi-axes of the ellipse. The time interval to avoid the advancement of any point beyond the corresponding domain is the minimum value obtained for all evolution points "q", namely, $\Delta t_{limit} \leq \min(\Delta t_{limit}^{(q)})$.Thus, taking into account all constraints above referred, the next expression is achieved for the final time interval, Δt:

$$\Delta t = min\left(\Delta t_{CLF}, \Delta t_{crossing}, \Delta t_{limits}\right) \tag{C25}$$

After defining the suitable Δt and advancing the points of the fluid front according to (C1) and (C2), small-scale oscillations might be present in the resulting interface when the capillary effects are relevant (Figure C1), namely, when C_a^* has an order of magnitude lower or equal than $\mathcal{O}(-2)$, or C_{cap} has an order of magnitude greater or equal than $\mathcal{O}(-1)$. These oscillations, if not suppressed, can be amplified as the fluid front evolves, originating important errors. Therefore, a second-order five-point polynomial fitting is employed here to suppress small-scale oscillations, where the position of each evolution point is corrected taking into account the two adjacent points of each side and using a quadratic fitting curve obtained with the Fitting Toolbox of MATLAB.

Then, parametric cubic splines are fitted to the corrected points (Figure C1), in such a way that for each space interval "r" defined by two adjacent points, "h" and "$h+1$", the next parametric curve is defined:

$$\mathrm{x}_m^{(r)} = \sum_{l=0}^{3} a_{lm}^{(r)} u^l,\ m=1,2,\ u\epsilon[0,1] \tag{C26},$$

where u is the independent parameter, while $r\epsilon[1, N_{points}]$ for closed curves and $r\epsilon[1, N_{points}-1]$ for open curves, with N_{points} as the number of evolution points conforming the moving boundary. The constants $a_{lm}^{(r)}$ are found by forcing the curves defined in (C26) to pass by the evolution points and by forcing the continuity of the first and second derivatives between the curves of adjacent intervals. Additionally, the splines are forced to be perpendicular to the boundaries where the symmetric condition is

prescribed and its slope is maintained continuous in the interfaces considered here: channel-warp, channel-weft and warp-weft. Then, a remeshing algorithm is employed to generate a new set of uniformly spaced points located along the splines, keeping constant the mesh-size defined for each moving boundary (Figure C1).

References

[1] A. W. Chan and R. J. Morgan, "Tow impregnation during Resin Transfer Moulding of bidireccional woven fabrics.," *Polymer Composites*, vol. 14, no. 4, pp. 335–350, 1993.

[2] C. Lekakou, M. Johari, D. Norman, and M. G. Bader, "Measurement techniques and effects on in-plane permeability of woven cloths in resin transfer moulding," *Composites Part A: Applied Science and Manufacturing*, vol. 27, no. 5, pp. 401–408, 1996.

[3] H. Jinlian, L. Yi, and S. Xueming, "Study on void formation in multi-layer woven fabrics," *Composites Part A: Applied Science and Manufacturing*, vol. 35, no. 5, pp. 595–603, 2004.

[4] D. H. Lee, W. Il Lee, and M. K. Kang, "Analysis and minimization of void formation during resin transfer molding process," *Composites Science and Technology*, vol. 66, no. 16, pp. 3281–3289, 2006.

[5] B. Gourichon, C. Binetruy, and P. Krawczak, "A new numerical procedure to predict dynamic void content in liquid composite molding," *Composites Part A: Applied Science and Manufacturing*, vol. 37, no. 11, pp. 1961–1969, 2006.

[6] K. M. Pillai, "Governing equations for unsaturated flow through woven fiber mats. Part 1.Isothermal flows," *Composites Part A: Applied Science and Manufacturing*, vol. 33, pp. 1007–1019, 2002.

[7] K. M. Pillai and M. S. Munagavalasa, "Governing equations for unsaturated flow through woven fiber mats. Part 2. Non-isothermal reactive flows," *Composites Part A: Applied Science and Manufacturing*, vol. 35, no. 4, pp. 403–415, 2004.

[8] H. Tan and K. M. Pillai, "Multiscale modeling of unsaturated flow of dual-scale fiber preform in liquid composite molding II: Non-isothermal flows," *Composites Part A: Applied Science and Manufacturing*, vol. 43, no. 1, pp. 14–28, 2012.

[9] M. S. Munagavalasa and K. M. Pillai, "An estimation of effective thermal conductivity of a fibrous dual-scale porous medium during unsaturated flow," *International Journal of Heat and Mass Transfer*, vol. 49, no. 1–2, pp. 317–328, Jan. 2006.

[10] M. S. Munagavalasa, "Theoretical modelling of unsaturated flow in fibrous dual scale porous media using Volume Averaging Method," PhD Dissertation, College Of Engineering and Applied Science, University of Wisconsin Milwaukee, 2006.

[11] J. M. Lawrence, V. Neacsu, and S. G. Advani, "Modeling the impact of capillary pressure and air entrapment on fiber tow saturation during resin infusion in LCM," *Composites Part A: Applied Science and Manufacturing*, vol. 40, no. 8, pp. 1053–1064, 2009.

[12] H. Tan, "Simulation of flow in dual-scale porous media," PhD Dissertation, College Of Engineering and Applied Science, University of Wisconsin Milwaukee, 2011.

[13] P. Simacek and S. G. Advani, "A numerical model to predict fiber tow saturation during liquid composite molding," *Composites Science and Technology*, vol. 63, no.

12, pp. 1725–1736, 2003.

[14] H. Tan and K. M. Pillai, “Multiscale modeling of unsaturated flow in dual-scale fiber preforms of liquid composite molding I: Isothermal flows,” *Composites Part A: Applied Science and Manufacturing*, vol. 43, no. 1, pp. 29–44, 2012.

[15] B. Natalini, “The boundary element dual-reciprocity method-multidomain approach for 3D potential problems.,” PhD Dissertation, Wessex Institute of Technology, 2005.

[16] B. Natalini and V. Popov, “Boundary element formulation for flow in unsaturated porous media,” *Asociación Argentina de Mecánica Computacional*, vol. XXVI, pp. 1158–1173, 2007.

[17] S. R. Subia and M. S. Ingber, “A 3D boundary element method for steady unsaturated quasi-linear flow in porous media,” *Water Resources Research*, vol. 30, no. 7, pp. 2097–2104, 1994.

[18] B. Natalini and V. Popov, “On the optimal implementation of the boundary element dual reciprocity method—multi-domain approach for 3D problems,” *Engineering Analysis with Boundary Elements*, vol. 31, no. 3, pp. 275–287, Mar. 2007.

[19] M. Piller, D. Casagrande, G. Schena, and M. Santini, “Pore-scale simulation of laminar flow through porous media,” *Journal of Physics: Conference Series*, vol. 501, pp. 1–13, 2014.

[20] W. R. Hwang and S. G. Advani, “Numerical simulations of Stokes–Brinkman equations for permeability prediction of dual scale fibrous porous media,” *Physics of Fluids*, vol. 22, no. 11, pp. 1–14, 2010.

[21] M. Blais, N. Moulin, P. Liotier, and S. Drapier, “Resin-infusion based processes simulation : coupled Stokes-Darcy flows in orthotropic preforms undergoing finite strain,” in *Conference on Computational Methods in manufacturing processes, Keiting, Taiwan*, 2015, pp. 1–3.

[22] J. Yang, Y. Jia, S. Sun, D. Ma, T. Shi, and L. An, “Mesoscopic simulation of the impregnating process of unidirectional fibrous preform in resin transfer molding,” *Materials Science and Engineering A*, vol. 435–436, pp. 515–520, 2006.

[23] D. Shou, L. Ye, Y. Tang, J. Fan, and F. Ding, “Transverse permeability determination of dual-scale fibrous materials,” *International Journal of Heat and Mass Transfer*, vol. 58, pp. 532–539, 2013.

[24] D. Shou, L. Ye, Y. Tang, J. Fan, and F. Ding, “Longitudinal permeability determination of dual-scale fibrous materials,” *Composites Part A*, vol. 68, pp. 42–46, 2015.

[25] M. K. Kang, W. Il Lee, and H. T. Hahn, “Formation of microvoids during resin-transfer molding process,” *Composites Science and Technology*, vol. 60, pp. 2427–2434, 2000.

[26] B. Z. Babu and K. M. Pillai, “Experimental investigation of the effect of fiber-mat architecture on the unsaturated flow in liquid composite molding,” *Journal of composite materials*, vol. 38, pp. 57–79, 2003.

[27] B. Z. Babu, “The effect of fiber mat compression and architecture on the unsaturated

flow in liquid composite molding- Experimental study," MsC Thesis, College of Engineering and Applied Science, University of Wisconsin- Milwaukee, 2002.

[28] J. P. Coulter and S. I. Guceri, "Resin Impregnation During the Manufacturing of Composite Materials Subject to Prescribed Injection Rate," *Journal of Reinforced Plastics and Composites*, vol. 7, no. 3, pp. 200–219, 1988.

[29] R. Gauvin and F. Trochu, "Key issues in Numerical Simulation for Liquid Composite Molding Processes," *Polymer Composites*, vol. 19, no. 3, pp. 233–240, 1998.

[30] K. K. Mohan, R.V. Ngo, N.D Tamma, "On a Pure Finite-Element-Based Methodology for Resin Transfer Mold Filling Simulations," *Polymer Engineering and Science*, vol. 39, no. 1, pp. 26–43, 1999.

[31] A. Shojaei, S. R. Ghaffarian, and S. M. H. Karimian, "Numerical simulation of three-dimensional mold filling process in resin transfer molding using quasi-steady state and partial saturation formulations," *Composites Science and Technology*, vol. 62, no. 6, pp. 861–879, 2002.

[32] A. Shojaei, S. R. Ghaffarian, and S. M. H. Karimian, "Modeling and simulation approaches in the resin transfer molding process: A review," *Polymer Composites*, vol. 24, no. 4, pp. 525–544, 2003.

[33] M. V. Bruschke and S. G. Advani, "A finite element/control volume approach to mold filling in anisotropic porous media," *Polymer Composites*, vol. 11, no. 6, pp. 398–405, 1990.

[34] C. A. Fracchia, J. Castro, and C. L. Tucker, "A finite element/control volume simulation of resin transfer mold filling," in *American Society for Composites Fourth Technical Conference, Lancaster, USA*, 1989, pp. 157–166.

[35] C. D. Rudd, A. C. Long, K. N. Kendall, and C. G. Magin, *Liquid Moulding Technologies.*, 1st ed. Cambridge, England: Woodhead Publishing Limited, 1997.

[36] J. A. García, "Gestión del frente de avance en la modelización numérica del conformado de Transferencia de Resina (RTM).," PhD Dissertation, Department of Mechanical and Materials Engineering, Universitat Politècnica de València, 2000.

[37] S. Liu, B. Bickerton and S. Advani, "Modelling and simulation of RTM Gate control, venting and dry spot prediction," *Composites Part A.*, vol. 27, no. 2, pp. 135–141, 1996.

[38] M. V. Bruschke and S. G. Advani, "RTM: filling simulation of complex three dimensional shell-like structures," *Sampe Quartely*, vol. 23, no. 1, pp. 2–11, 1991.

[39] D. S. Cairns and S. M. Rossell, "Fluid Flow Modeling Of Resin Transfer Molding For Composite Material Wind Turbine," Montana State University,Bozeman, USA, Technical Report SAND2004-0076T, 2004.

[40] F. Trochu, R. Gauvin, and D.-M. Gao, "Numerical Analysis of the Resin Transfer Molding Process by the Finite Element Method," *Advanced in Polymer Technology*, vol. 12, no. 4, pp. 329–342, 1993.

[41] E. Ruiz, V. Achim, S. Soukane, and F. Trochu, "Advanced numerical simulation of liquid composite molding for process analysis and optimization," *Composites Part*

A: Applied Science and Manufacturing, vol. 37, no. 6, pp. 890–902, 2006.

[42] J. Bréard, J. F. Remacle, X.-T. Pham, and F. Trochu, "The effect of the pressure boundary condition on mold filling simulations in liquid composite molding, computer methods in composite materials," *Transactions on Engineering Sciences*, vol. 21, pp. 77–86, 1998.

[43] M. L. Diallo, R. Gauvin, and F. Trochu, "Experimental Analysis and simulation of flow through multilayer fiber reinforcement in LCM," *Polymer Composites*, vol. 19, no. 3, pp. 246–256, 1998.

[44] E. Ruiz, V. Achim, S. Soukane, F. Trochu, and J. Breard, "Optimization of injection flow rate to minimize micro/macro-voids formation in resin transfer molded composites," *Composites Science and Technology*, vol. 66, no. 3–4, pp. 475–486, 2006.

[45] Y.-E. Yoo and W. Il Lee, "Numerical simulation of the resin transfer mold filling process using the boundary element method," *Polymer Composites*, vol. 17, no. 3, pp. 368–374, 1996.

[46] S. Soukane and F. Trochu, "Application of the level set method to the simulation of resin transfer molding," *Composites Science and Technology*, vol. 66, no. 7–8, pp. 1067–1080, 2006.

[47] J. A. García, L. Gascón, E. Cueto, I. Ordeig, and F. Chinesta, "Meshless methods with application to Liquid Composite Molding simulation," *Computer Methods in Applied Mechanics and Engineering*, vol. 198, pp. 2700–2709, 2009.

[48] R. Gantois, A. Cantarel, G. Dusserre, J.-N. Félices, and F. Schmidt, "Numerical Simulation of Resin Transfer Molding Using BEM and Level Set Method," *International Journal of Material Forming*, vol. 3, no. S1, pp. 635–638, 2010.

[49] M.-K. Um and W. Il Lee, "A study on the mold filling process in resin transfer molding," *Polymer Engineering and Science*, vol. 31, no. 11, pp. 765–771, 1991.

[50] R. Gantois, A. Cantarel, and G. Dusserre, "BEM-Based Models to Simulate the Resin Flow at Macroscale and Microscale in LCM Processes," *Polymer Composites*, vol. 34, no. 8, pp. 1235–1244, 2013.

[51] M. Q. Thai, F. Schmidt, G. Dusserre, A. Cantarel, and L. Silva, "BEM computation of 3D Stokes flow including moving front," *International Journal of Material Forming (First On-line)*, pp. 1–14, 2016.

[52] I. D. Patiño, "Simulación por elementos de frontera del proceso de impregnación de preformas reforzantes usadas en RTM," MsC Thesis, Escuela de Ingeniería, Universidad Pontificia Bolivariana, 2013.

[53] J. D. Vanegas and I. D. Patiño, "Filling simulation of the RTM process in isotropic homogeneous/non-homogeneous media using the boundary element method.," *Advanced Composites Materials*, vol. 24, no. 2, pp. 113–139, 2015.

[54] V. R. Voller and S. Peng, "An algorithm for analysis of polymer filling molds," *Polymer Engineering and Science*, vol. 35, no. 22, pp. 1758–1765, 1995.

[55] D. L. Clements, "A boundary integral equation method for the numerical solution of a second order elliptic equation with variable coefficients," *Journal of Australian*

Mathematics Society, vol. 22, no. 02, pp. 218–228, 1980.

[56] D. L. Clements, *Boundary value problems governed by second order elliptic systems*, 1st ed. London, United Kingdom: Pitman Advanced Publishing Program, 1981.

[57] J. A. Sethian, *Level set methods and fast marching methods: evolving interfaces in computational geometry, fluid mechanics, computer vision, and materials science*, 2nd ed. Cambridge, England: Cambridge University Press, 1999.

[58] R. Gantois, A. Cantarel, G. Dusserre, J. N. Félices, and F. Schmidt, "Mold Filling Simulation of Resin Transfer Molding Combining BEM and Level Set Method," *Applied Mechanics and Materials*, vol. 62, pp. 57–65, 2011.

[59] K. L. Adams, W. B. Russel, and L. Rebenfeld, "Radial penetration of a viscous liquid into a planar anisotropic porus medium," *International Journal of Multiphase Flow*, vol. 14, no. 2, pp. 203–215, 1988.

[60] O. E. Lafe, J. A. Ligget, and H. Liu, "BIEM Solutions of combinations of Leakly, Layered, Confined, Unconfined, Nonisotropic aquifiers," *Water Resources Research*, vol. 17, no. 5, pp. 1431–1444, 1981.

[61] G. P. Lennon, "Boundary Element Analysis of Flow in Heterogenous Porous Media," in *ASCE/HYD Specialty Conference . Hydraulic Division, ASCE, Cour d'Alene, USA*, 1984, pp. 177–179.

[62] R. Rangogni, "Numerical solution of the generalized Laplace equation by coupling the boundary element method and the perturbation method," *Applied Mathematical Modelling*, vol. 10, no. 4, pp. 266–270, 1986.

[63] P. W. Partridge, C. A. Brebbia, and L. C. Wrobel, *The Dual Reciprocity Boundary Element Method*, 1st ed. Southampton, England: Computational Mechanics Publication, 1992.

[64] K. El Harrouni, "Dual reciprocity boundary element method for heterogeneous porous media.," in *Boundary Element Technology VII*, Springer Netherlands, 1992, pp. 151–159.

[65] E. Divo, M. Chopra, and A. Kassab, "A generalized boundary element method for groundwater flow in orthotropic heterogeneous media.," *Stormwater Academic Publications*, pp. 1–40, 1997.

[66] A. J. Kassab and E. Divo, "A generalized boundary integral equation for isotropic heat conduction spatially varying thermal conductivity," *Engineering Analysis with Boundary Elements*, vol. 18, no. 4, pp. 273–286, 1997.

[67] W.-T. Ang, D. L. Clements, and N. Vahdati, "A dual-reciprocity boundary element method for a class of elliptic boundary value problems for non-homogeneous anisotropic media," *Engineering Analysis with Boundary Elements*, vol. 27, no. 1, pp. 49–55, 2003.

[68] M. Tanaka, T. Matsumoto, and Y. Suda, "A Dual Reciprocity Boundary Element Method Applied to the Steady-State Heat Conduction Problem of Functionally Gradient Materials. Study on Two-Dimensional Problems.," *Transactions of the Japan Society of Mechanical Engineers A*, vol. 67, no. 662, pp. 1589–1594, 2001.

[69] Y. Zhang and S. Zhu, “On the choice of interpolation functions used in the dual-reciprocity boundary element method.,” *Engineering analysis with Boundary Elements*, vol. 13, pp. 387–396, 1994.

[70] P. W. Partridge, “Towards criteria for selecting approximation functions in the Dual Reciprocity Method,” *Engineering Analysis with Boundary Elements*, vol. 24, no. 7–8, pp. 519–529, 2000.

[71] J. D. Vanegas, I. D. Patiño, and C. A. Vargas, “Boundary element approaches for filling simulations of anisotropic reinforced preforms used in the resin transfer molding process.,” *Journal of Composite Materials*, vol. 48, no. 21, pp. 2603–2629, 2013.

[72] M. A. Martínez, E. Cueto, M. Doblare, and F. Chinesta, “Natural Element Meshless simulation of flows involving short fiber suspensions,” *Journal of Non-newtonian Fluid Mechanics*, vol. 115, no. 1, pp. 51–78, 2003.

[73] D. González, E. Cueto, F. Chinesta, and M. Doblaré, “A natural element updated Lagrangian strategy for free- surface fluid dynamics.,” *Journal of Computer Physics*, vol. 223, pp. 127–150, 2007.

[74] G. W. Lee and K. J. Lee, “Mechanism of void formation in composite processing with woven fabrics,” *Polymer Composites*, vol. 11, no. 7, pp. 563–572, 2003.

[75] F. Lebel, “Controle de la Fabrication des Composites par injection sur renforts,” PhD. Dissertation, Département de Génie Méchanique, Université de Montréal, 2012.

[76] N. Patel and L. J. Lee, “Effects of Fiber Mat Architecture on Void Formation and Removal in Liquid Composite,” *Polymer Composites*, vol. 16, no. 5, pp. 386–399, 1995.

[77] J. S. Leclerc and E. Ruiz, “Porosity reduction using optimized flow velocity in Resin Transfer Molding,” *Composites Part A*, vol. 39, no. 12, pp. 1859–1868, 2008.

[78] T. Lundström, V. Frishfelds, and A. Jakovics, “Bubble formation and motion in non-crimp fabrics with perturbed bundle geometry,” *Composites Part A: Applied Science and Manufacturing*, vol. 41, no. 1, pp. 83–92, 2010.

[79] C. H. Park, A. Lebel, A. Saouab, J. Bréard, and W. Il Lee, “Modeling and simulation of voids and saturation in liquid composite molding processes,” *Composites Part A: Applied Science and Manufacturing*, vol. 42, no. 6, pp. 658–668, 2011.

[80] C. Devalve and R. Pitchumani, “Simulation of void formation in liquid composite molding processes,” *Composites Part A: Applied Science and Manufacturing*, vol. 51, pp. 22–32, 2013.

[81] J. S. U. Schell, M. Deleglise, C. Binetruy, P. Krawczak, and P. Ermanni, “Numerical prediction and experimental characterisation of meso-scale-voids in liquid composite moulding,” *Composites Part A: Applied Science and Manufacturing*, vol. 38, no. 12, pp. 2460–2470, 2007.

[82] C. Ravey, F. Lebel, E. Ruiz, and F. Trochu, “Void minimization and optimization of injection velocity in RTM processing,” in *The 19th International Conference on Composite Materials, Montreal, Canada*, 2013, pp. 1–10.

[83] C. H. Park and W. Il Lee, “Modeling void formation and unsaturated flow in liquid composite molding processes: a survey and review,” *Journal of Reinforced Plastics and Composites*, vol. 30, no. 11, pp. 957–977, 2011.

[84] B. Gourichon, M. Deléglise, C. Binetruy, and P. Krawczak, “Dynamic void content prediction during radial injection in liquid composite molding,” *Composites Part A: Applied Science and Manufacturing*, vol. 39, no. 1, pp. 46–55, 2008.

[85] H. Tan and K. M. Pillai, “Finite element implementation of stress-jump and stress-continuity conditions at porous-medium, clear-fluid interface,” *Computers & Fluids*, vol. 38, no. 6, pp. 1118–1131, 2009.

[86] T. S. Lundström, “Measurement of void collapse during resin transfer moulding,” *Composites Part A: Applied Science and Manufacturing*, vol. 28, no. 3, pp. 201–214, 1997.

[87] M. E. Foley and J. W. Gillespie, “Modeling the Effect of Fiber Diameter and Fiber Bundle Count on Tow Impregnation during Liquid Molding Processes,” *Journal of Composite Materials*, vol. 39, no. 12, pp. 1045–1065, 2005.

[88] V. Neacsu, “Modeling and measurement of microflow of microflow in dual-scale porous media,” PhD Dissertation, Department of Mechanical Engineering, University of Delaware, 2009.

[89] K. Kang and K. Koelling, “Void transport in resin transfer molding,” *Polymer Composites*, vol. 25, no. 4, pp. 417–432, 2004.

[90] V. Frishfelds, T. S. Lundström, and A. Jakovics, “Lattice-gas analysis of fluid front in non-crimp fabrics,” in *19th International Symposium Transport Phenomena, Reykyjavik, Iceland*, 2008, pp. 1–9.

[91] K. M. Pillai and S. G. Advani, “A Model for Unsaturated Flow in Woven Fiber Preforms during Mold Filling in Resin Transfer Molding,” *Journal of Composite Materials*, vol. 32, no. 19, pp. 1753–1783, 1998.

[92] L. Gascón, J. A. García, F. LeBel, E. Ruiz, and F. Trochu, “Numerical prediction of saturation in dual scale fibrous reinforcements during Liquid Composite Molding,” *Composites Part A: Applied Science and Manufacturing*, vol. 77, pp. 275–284, 2015.

[93] L. Gascón, J. A. García, F. Lebel, E. Ruiz, and F. Trochu, “A two-phase flow model to simulate mold filling and saturation in Resin Transfer Molding,” *International Journal Material Forming*, vol. 9, no. 2, pp. 229–239, 2016.

[94] H. Tan and K. M. Pillai, “Multiscale modeling of unsaturated flow in dual-scale fiber preforms of liquid composite molding III: reactive flows,” *Composites Part A: Applied Science and Manufacturing*, vol. 43, no. 1, pp. 29–44, 2012.

[95] V. Frishfelds, T. S. Lundström, and A. Jakovics, “Bubble motion through non-crimp fabrics during composites manufacturing,” *Composites Part A: Applied Science and Manufacturing*, vol. 39, no. 2, pp. 243–251, 2008.

[96] J. J. Gangloff, W. R. Hwang, and S. G. Advani, “Characterization of bubble mobility in channel flow with fibrous porous media walls,” *International Journal of Multiphase Flow*, vol. 60, pp. 76–86, 2014.

[97] C. Di Fratta, F. Klunker, F. Trochu, and P. Ermanni, “Characterization of textile

permeability as a function of fiber volume content with a single unidirectional injection experiment," *Composites Part A: Applied Science and Manufacturing*, vol. 77, pp. 238–247, 2015.

[98] M. W. Tahir, S. Hallström, and M. Åkermo, "Effect of dual scale porosity on the overall permeability of fibrous structures," *Composites Science and Technology*, vol. 103, pp. 56–62, 2014.

[99] T. A. Cender, P. Simacek, and S. G. Advani, "Resin film impregnation in fabric prepregs with dual length scale permeability," *Composites Part A: Applied Science and Manufacturing*, vol. 53, pp. 118–128, 2013.

[100] H. Haji, A. Saouab, and Y. Nawab, "Simulation of coupling filtration and flow in a dual scale fibrous media," *Composites Part A: Applied Science and Manufacturing*, vol. 76, pp. 272–280, 2015.

[101] F. Zhou, J. Alms, and S. G. Advani, "A closed form solution for flow in dual scale fibrous porous media under constant injection pressure conditions," *Composites Science and Technology*, vol. 68, no. 3–4, pp. 699–708, 2008.

[102] F. Zhou, N. Kuentzer, P. Simacek, S. G. Advani, and S. Walsh, "Analytic characterization of the permeability of dual-scale fibrous porous media," *Composites Science and Technology*, vol. 66, no. 15, pp. 2795–2803, 2006.

[103] I. D. Patiño Arcila, H. Power, C. Nieto Londoño, and W. F. Flórez Escobar, "Boundary element simulation of void formation in fibrous reinforcements based on the Stokes–Darcy formulation," *Computer Methods in Applied Mechanics and Engineering*, vol. 304, pp. 265–293, 2016.

[104] I. D. Patiño, H. Power, C. Nieto-Londoño, and W. F. Flórez, "Stokes–Brinkman formulation for prediction of void formation in dual-scale fibrous reinforcements: a BEM/DR-BEM simulation," *Computational Mechanics*, vol. 59, no. 4, pp. 1–23, 2017.

[105] S. Hamaguchi, "Mathematical methods for thin film deposition simulations," *Thin Films*, vol. 22, pp. 81–115, 1996.

[106] Y. Jung, S. J. Kim, and W.-S. Han, "Numerical simulation of RTM process using the extended finite element method combined with the level set method," *Journal of Reinforced Plastics and Composites*, vol. 32, no. 5, pp. 308–317, 2013.

[107] D. Adalsteinsson and J. A. Sethian, "The Fast Construction of Extension Velocities in Level Set Methods," *Journal of Computational Physics*, vol. 148, no. 1, pp. 2–22, 1999.

[108] D. L. Choop, "Another look at velocity extensions in the level set method," *SIAM Journal on Scientific Computing*, vol. 31, no. 5, pp. 3255–3273, 2009.

[109] P. A. Gremaud and C. M. Kuster, "A Study of Numerical Methods for the Level Set Approach," *Applied Numerical Mathematics*, vol. 57, no. 5–7, pp. 837–846, 2005.

[110] J. A. Sethian and P. Smereka, "Level Set Method for fluid interfaces," *Annual Review of Materials Research*, vol. 35, pp. 341–372, 2003.

[111] J. A. García, L. Gascón, and F. Chinesta, "A fixed mesh numerical method for modelling the flow in liquid composites moulding processes using a volume of fluid

technique," *Computer Methods in Applied Mechanics and Engineering*, vol. 192, no. 7–8, pp. 877–893, 2003.

[112] X.-L. Liu, "Isothermal flow simulation of liquid composite molding," *Composites Part A: Applied Science and Manufacturing*, vol. 31, no. 12, pp. 1295–1302, 2000.

[113] I. Sevostianov, V. E. Verijenko, and C. J. von Klemperer, "Mathematical model of cavitation during resin film infusion process," *Composite Structures*, vol. 48, no. 1, pp. 197–203, 2000.

[114] G. Zhan-Sheng, L. Ling, Z. Bo-Ming, and S. Du, "Critical Void Content for Thermoset Composite Laminates," *Journal of Composite Materials*, vol. 43, no. 17, pp. 1775–1790, 2009.

[115] L. Liu, B.-M. Zhang, D.-F. Wang, and Z.-J. Wu, "Effects of cure cycles on void content and mechanical properties of composite laminates," *Composite Structures*, vol. 73, no. 3, pp. 303–309, Jun. 2006.

[116] P.-O. Hagstrand, F. Bonjour, and J. Månson, "The influence of void content on the structural flexural performance of unidirectional glass fibre reinforced polypropylene composites," *Composites Part A: Applied Science and Manufacturing*, vol. 36, no. 5, pp. 705–714, May 2005.

[117] H. Huang and R. Talreja, "Effects of void geometry on elastic properties of unidirectional fiber reinforced composites," *Composites Science and Technology*, vol. 65, no. 13, pp. 1964–1981, Oct. 2005.

[118] C. Dong, "Effects of Process-Induced Voids on the Properties of Fibre Reinforced Composites," *Journal of Materials Science and Technology*, vol. 32, no. 7, pp. 597–604, 2015.

[119] R. Protz, N. Kosmann, M. Gude, W. Hufenbach, K. Schulte, and B. Fiedler, "Voids and their effect on the strain rate dependent material properties and fatigue behaviour of non-crimp fabric composites materials," *Composites Part B: Engineering*, vol. 83, pp. 346–351, 2015.

[120] Y. Li, Q. Li, and H. Ma, "The voids formation mechanisms and their effects on the mechanical properties of flax fiber reinforced epoxy composites," *Composites Part A: Applied Science and Manufacturing*, vol. 72, pp. 40–48, 2015.

[121] M. L. Costa, S. F. de Almeida, and M. C. Rezende, "The influence of porosity on the interlaminar shear strength of carbon/epoxy and carbon/bismaleimide fabric laminates," *Composites Science and Technology*, vol. 61, no. 14, pp. 2101–2108, Nov. 2001.

[122] H. Jeong, "Effects of Voids on the Mechanical Strength and Ultrasonic Attenuation of Laminated Composites," *Journal of Composite Materials*, vol. 31, no. 3, pp. 276–292, 1997.

[123] S. F. de Almeida and Z. D. S. Neto, "Effect of void content on the strength of composite laminates," *Composite Structures*, vol. 28, no. 2, pp. 139–148, Jan. 1994.

[124] M. N. Bureau and J. Denault, "Fatigue resistance of continuous glass fiber/polypropylene composites: Consolidation dependence," *Composites Science and Technology*, vol. 64, no. 12, pp. 1785–1794, 2004.

[125] A. R. Chambers, J. S. Earl, C. A. Squires, and M. A. Suhot, “The effect of voids on the flexural fatigue performance of unidirectional carbon fibre composites developed for wind turbine applications,” *International Journal of Fatigue*, vol. 28, no. 10, pp. 1389–1398, Oct. 2006.

[126] A. Zhang, H. Lu, and D. Zhang, “Effects of voids on residual tensile strength after impact of hygrothermal conditioned CFRP laminates,” *Composite Structures*, vol. 95, pp. 322–327, 2013.

[127] M. Ricotta, M. Quaresimin, and R. Talreja, “Mode I Strain Energy Release Rate in composite laminates in the presence of voids,” *Composites Science and Technology*, vol. 68, no. 13, pp. 2616–2623, Oct. 2008.

[128] A. Miravete, *Materiales compuestos II*, 1st ed. Zaragoza, Spain: INO Reproducciones, 2000.

[129] S. G. Advani and E. M. Sozer, *Process modeling in composites manufacturing*, 2nd ed. Boca Ratón, USA: CRC Press, Taylor and Francis Group, 2011.

[130] S. Whitaker, *The method of volume averaging*, 1st ed. Dordrecht, The Netherlands: Kluwer Academic Publishers, 1999.

[131] T. B. Anderson and A. R. Jackson, “A Fluid Mechanical Description of Fluidized Beds,” *Journal of Chemical Information and Modeling*, vol. 6, no. 4, 1967.

[132] P. Ferland and F. Trochu, “Concurrent methods for permeability measurement in Resin Transfer Molding,” *Polymer Composites*, vol. 17, no. 1, pp. 149–158, 1996.

[133] J. R. Weitzenböck, R. A. Shenoi, and P. A. Wilson, “Radial flow permeability measurement. Part A: theory,” *Composites Part A: Applied Science and Manufacturing*, vol. 30, no. 6, pp. 781–796, 1999.

[134] J. R. Weitzenböck, R. A. Shenoi, and P. A. Wilson, “Radial flow permeability measurement. Part B: application,” *Composites Part A: Applied Science and Manufacturing*, vol. 30, no. 6, pp. 797–813, 1999.

[135] B. R. Gebart, “Permeability of Unidirectional Reinforcements for RTM,” *Journal of Composite Materials*, vol. 26, no. 8, pp. 1100–1133, 1992.

[136] M. T. Van Genuchten, “A closed form equation for predicting the hydraulic condictivity of unsaturated soils.,” *Soil Science Society*, vol. 44, pp. 892–898, 1980.

[137] I. Eames, I. Small, A. Frampton, and A. M. Cottenden, “Experimental and theoretical study of the spread of fluid from a point source on an inclined incontinence bed-pad,” *Proceedings of the Institution of Mechanical Engineers Part H-Journal of Engineering in Medicine*, vol. 217, pp. 263–271, 2003.

[138] M. Landeryou, I. Eames, and A. Cottenden, “Infiltration into inclined fibrous sheets,” *Journal of Fluid Mechanics*, vol. 529, pp. 173–193, 2005.

[139] A. Ashari, “Dual-Scale Modeling of Two-Phase Fluid Transport in Fibrous Porous Media,” PhD. Dissertation, Department of Mechanical Engineering, Virginia Commonwealth University-VCU Scholars Compass, 2010.

[140] A. Ashari and H. Vahedi Tafreshi, “General capillary pressure and relative permeability expressions for through-plane fluid transport in thin fibrous sheets,”

Colloids and Surfaces A: Physicochemical and Engineering Aspects, vol. 346, no. 1–3, pp. 114–122, 2009.

[141] P. Soltani, M. S. Johari, and M. Zarrebini, "Effect of 3D fiber orientation on permeability of realistic fibrous porous networks," *Powder Technology*, vol. 254, pp. 44–56, 2014.

[142] S. Jaganathan, H. Vahedi Tafreshi, and B. Pourdeyhimi, "A realistic approach for modeling permeability of fibrous media: 3-D imaging coupled with CFD simulation," *Chemical Engineering Science*, vol. 63, no. 1, pp. 244–252, 2008.

[143] S. Zobel, B. Maze, H. Vahedi Tafreshi, Q. Wang, and B. Pourdeyhimi, "Simulating permeability of 3-D calendered fibrous structures," *Chemical Engineering Science*, vol. 62, no. 22, pp. 6285–6296, 2007.

[144] T. S. Lundström, R. Stenberg, R. Bergström, H. Partanen, and P. A. Birkeland, "In-plane permeability measurements: a nordic round-robin study," *Composites Part A: Applied Science and Manufacturing*, vol. 31, no. 1, pp. 29–43, 2000.

[145] S. Amico and C. Lekakou, "An experimental study of the permeability and capillary pressure in resin-transfer moulding," *Composites Science and Technology*, vol. 61, no. 13, pp. 1945–1959, Oct. 2001.

[146] L. Skartsis, B. Khomami, and L. Kardos, "The effect of capillary pressure on the impregnation of fibrous media," *SAMPE Journal*, vol. 28, no. 5, pp. 19–24, 1992.

[147] S. C. Amico, "Permeability and capillary pressure in the infiltration of fibrous porous media in RTM," PhD.Dissertation, Department of Mechanical Engineering Science, University of Surrey, 2000.

[148] R. Masoodi and K. M. Pillai, "A General Formula for Capillary Suction-Pressure in Porous Media," *Journal of Porous Media*, vol. 15, no. 8, pp. 775–783, 2012.

[149] C. Posrikidis, *A practical guide to Boundary Element Methods*, 1st ed. London, United Kingdom: Chapman & Hall/ CRC, 2002.

[150] H. Power and L. C. Wrobel, *Boundary Integral Methods in Fluid Mechanics*, 1st ed. Southhampton, United Kingdom: Computational Mechanics Publications, 1995.

[151] Z. Tadmor, E. Broyer, and C. Gudfinge., "Flow Analysis Network (FAN)-A method for solving problems in polymer processing," *Polymer Engineering Science*, vol. 14, pp. 660–665, 1974.

[152] S. Tlupova and R. Cortez, "Boundary integral solutions of coupled Stokes and Darcy flows," *Journal of Computational Physics*, vol. 228, no. 1, pp. 158–179, Jan. 2009.

[153] M. Markov, E. Kazatchenko, A. Mousatov, and E. Pervago, "Permeability of the Fluid-Filled Inclusions in Porous Media," *Transport in Porous Media*, vol. 84, no. 2, pp. 307–317, Nov. 2009.

[154] A. Mikelic, W. Jäger, and W. J. Ager, "On The Interface Boundary Condition of Beavers, Joseph, and Saffman," *SIAM Journal on Applied Mathematics*, vol. 60, no. 4, pp. 1111–1127, 2000.

[155] M. Le Bars and M. Grae Worster, "Interfacial conditions between a pure fluid and a porous medium : implications for binary alloy solidification," *Journal of Fluid*

Mechanics, vol. 550, no. 1, pp. 149 – 173., 2006.

[156] Y. Cao, M. Gunzburger, F. Hua, and X. Wang, "Coupled Stokes-Darcy model with Beavers-Joseph interface boundary condition," *Communications in Mathematical Sciences*, vol. 8, no. 1, pp. 1–25, 2010.

[157] G. S. Beavers, E. M. Sparrow, and R. A. Magnuson, "Experiments on coupled parallel flows in a channel and a bounding porous medium," *Journal of Basic Engineering*, vol. 92D, no. 4, pp. 843 – 848, 1970.

[158] L.-H. Huang, I.-L. Chiang, and C.-H. Song, "A re-investigation of laminar channel flow passing over porous bed.," *Journal of the Chinese Institute of Engineers*, vol. 20, no. 4, pp. 435 – 441, 1997.

[159] P. G. Saffman, "On the boundary condition at the surface of a porous medium," *Studies on Applied Mathematics*, vol. L2, pp. 93–101, 1971.

[160] T. Carraro, C. Goll, A. Marciniak-Czochra, and A. Mikélic, "Pressure jump interface law for the Stokes-Darcy coupling : Confirmation by direct numerical simulations," *Journal of Fluid Mechanics*, vol. 732, pp. 510–536, 2013.

[161] T. Chandrupatla and T. Osler, "The perimeter of an ellipse," *Math. Scientist*, vol. 35, pp. 122–131, 2010.

[162] K. Ahn, J. Seferis, and J. C. Berg, "Simultaneous Measurements of Permeability and Capillary," *Polymer Composites*, vol. 12, no. 3, pp. 146–152, 1997.

[163] V. Neacsu, A. Abu Obaid, and S. G. Advani, "Spontaneous radial capillary impregnation across a bank of aligned micro-cylinders - Part I: Theory and model development," *International Journal of Multiphase Flow*, vol. 32, no. 6, pp. 661–676, 2006.

[164] U. A. Ladyzhenskaya, *The mathematical theory of viscous incompressible flow*, 1st ed. New York, USA: Gordon and Breach, 1963.

[165] X. Zhang and X. Zhang, "Exact integration in the boundary element method for two-dimensional elastostatic problems," *Engineering Analysis with Boundary Elements*, vol. 27, no. 10, pp. 987–997, Dec. 2003.

[166] J. F. Telles, "A self adaptative coordinate transformation for efficient numerical evaluation of general boundary element integrals," *International Journal of Numerical methods in Engineering*, vol. 24, no. 5, pp. 959–973, 1987.

[167] A. Neumaier, "Solving Ill-Conditioned and Singular Linear Systems: A Tutorial on Regularization," *SIAM Review*, vol. 40, no. 3, pp. 636–666, 1998.

[168] A. Rap, L. Elliott, D. B. Ingham, D. Lesnic, and X. Wen, "DRBEM for Cauchy convection-diffusion problems with variable coefficients," *Engineering Analysis with Boundary Elements*, vol. 28, no. 11, pp. 1321–1333, 2004.

[169] N. H. Shuaib, H. Power, and S. Hibberd, "BEM solution of thin film flows on an inclined plane with a bottom outlet," *Engineering Analysis with Boundary Elements*, vol. 33, no. 3, pp. 388–398, Mar. 2009.

[170] Y. K. Hamidi, L. Aktas, and M. C. Altan, "Three-dimensional features of void morphology in resin transfer molded composites," *Composites Science and*

Technology, vol. 65, no. 7–8, pp. 1306–1320, Jun. 2005.

[171] M. A. A. Spaid and F. R. Phelan Jr, "Modeling void formation dynamics in fibrous porous media with the lattice Boltzmann method," *Composites Part A*, vol. 29A, pp. 749–755, 1998.

[172] J. Slade, K. M. Pillai, and S. G. Advani, "Investigation of unsaturated flow in woven, braided and stitched fiber mats during mold-filling in resin transfer molding," *Polymer Composites*, vol. 22, no. 4, pp. 491–505, 2001.

[173] L. Formaggia, J. F. Gerbeau, F. Nobile, and A. Quarteroni, "Numerical Treatment of Defective Boundary Conditions for the Navier-Stokes Equations," *SIAM Journal on Numerical Analysis*, vol. 40, no. 1, pp. 376–401, 2002.

[174] L. Formaggia, A. Veneziani, and C. Vergara, "A new approach to numerical solution of defective boundary problems in incompressible fluid dynamics," *SIAM J. Numer. Anal.*, vol. 46, no. 6, pp. 2769–2794, 2008.

[175] B. Gourichon, C. Binetruy, and P. Krawczak, "Experimental investigation of high fiber tow count fabric unsaturation during RTM," *Composites Science and Technology*, vol. 66, no. 7–8, pp. 976–982, 2006.

[176] M. Kosek and P. Sejak, "Visualization of voids in actual C/C woven composite structure," *Composites Science and Technology*, vol. 69, no. 9, pp. 1465–1469, Jul. 2009.

[177] M. Bodaghi, C. Cristóvão, R. Gomes, and N. C. Correia, "Experimental characterization of voids in high fibre volume fraction composites processed by high injection pressure RTM," *Composites Part A: Applied Science and Manufacturing*, vol. 82, pp. 88–99, 2016.

[178] H. Zhu, D. Li, D. Zhang, B. Wu, and Y. Chen, "Influence of voids on interlaminar shear strength of carbon/epoxy fabric laminates," *Transactions of Nonferrous Metals Society of China*, vol. 19, pp. s470–s475, Sep. 2009.

[179] M. R. Wisnom, T. Reynolds, and N. Gwilliam, "Redution in interlaminar shear strength by discrete and distributed voids," *Composites Science and Technology*, vol. 56, no. 1, pp. 93–101, 1996.

[180] L. Durlofsky and J. F. Brady, "Analysis of the Brinkman equation as a model for flow in porous media," *Physics of Fluids*, vol. 30, no. 11, pp. 3329–3341, 1987.

[181] M. Krotkiewski, I. S. Ligaarden, K.-A. Lie, and D. W. Schmid, "On the Importance of the Stokes-Brinkman Equations for Computing Effective Permeability in Karst Reservoirs," *Communications in Computational Physics*, vol. 10, no. 5, pp. 1315–1332, 2011.

[182] G. Neale and W. Nader, "Practical significance of Brinkman's extension of Darcy's law: coupled parallel flows within a channel and a bounding porous medium," *Canadian Journal of Chemical Engineering*, vol. 52, pp. 475–478, 1974.

[183] J. A. Ochoa-tapia and S. Whitaker, "Momentum transfer at the boundary between a porous medium and a homogeneous fluid I . Theoretical development," *International Journal of Heat and Mass Transfer*, vol. 38, no. 14, pp. 2635–2646, 1995.

[184] J. A. Ochoa-tapia and S. Whitaker, "Momentum transfer at the boundary between a

porous medium and a homogeneous fluid—II. Comparison with experiment," *International Journal of Heat and Mass Transfer*, vol. 38, no. 14, pp. 2647–2655, 1995.

[185] J. Richardson and H. Power, "A BEM analysis of creeping flow past two porous bodies of arbitrary shape," *Engineering Analysis with Boundary Elements*, vol. 17, pp. 193–204, 1996.

[186] P. Angot, "On the well-posed coupling between free fluid and porous viscous flows," *Applied Mathematics Letters*, vol. 24, no. 6, pp. 803–810, 2011.

[187] F. J. Valdés-Parada, B. Goyeau, and J. A. Ochoa-Tapia, "Momentum stress jump condition at the fluid-porous boundary: Prediction of the jump coefficient.," in *Aiche Conference: Transport Processes in Multiphase Systems II, San Francisco, USA*, 2006, pp. 1–8.

[188] F. J. Valdés-Parada, B. Goyeau, and J. A. Ochoa-Tapia, "Jump momentum boundary condition at a fluid-porous dividing surface: Derivation of the closure problem," *Chemical Engineering Science*, vol. 62, no. 15, pp. 4025–4039, 2007.

[189] M. Chandesris and D. Jamet, "Boundary conditions at a fluid–porous interface: An a priori estimation of the stress jump coefficients," *International Journal of Heat and Mass Transfer*, vol. 50, no. 17–18, pp. 3422–3436, Aug. 2007.

[190] W. C. Sun, J. E. Andrade, and W. Rudnicki, "Multiscale method for characterization of porous microstructures and their impact on macroscopic effective permeability," *International Journal for Numerical Methods in Engineering*, pp. 1885–1891, 2011.

[191] R. C. Givler and S. A. Altobelli, "A determination of the effective viscosity for the Brinkman-Forchheimer flow model," *Journal of Fluid Mechanics*, vol. 258, pp. 355–370, 1994.

[192] V. G. Zhdanov and V. M. Starov, "Calculation of the Effective Properties of Porous and Composite Materials," *Colloid J.*, vol. 64, no. 6, pp. 706–715, 2002.

[193] W. P. Breugem, "The effective viscosity of a channel-type porous medium," *Physics of Fluids*, vol. 19, no. 10, pp. 1–16, 2007.

[194] N. Martys, D. P. Bentz, and E. J. Garboczi, "Computer simulation study of the effective viscosity in Brinkman's equation," *Physics of Fluids*, vol. 6, no. 4, pp. 1434–1439, 1994.

[195] F. J. Valdes-Parada, J. A. Ochoa-Tapia, and J. Alvarez-Ramirez, "On the effective viscosity for the Darcy-Brinkman equation," *Physica A: Statistical Mechanics and its Applications*, vol. 385, no. 1, pp. 69–79, 2007.

[196] A. Tamayol, A. Khosla, B. L. Gray, and M. Bahrami, "Creeping flow through ordered arrays of micro-cylinders embedded in a rectangular minichannel," *International Journal of Heat and Mass Transfer*, vol. 55, no. 15–16, pp. 3900–3908, Jul. 2012.

[197] A. Tamayol, J. Yeom, M. Akbari, and M. Bahrami, "Low Reynolds number flows across ordered arrays of micro-cylinders embedded in a rectangular micro/minichannel," *International Journal of Heat and Mass Transfer*, vol. 58, no. 1–2, pp. 420–426, Mar. 2013.

[198] J. Prakash, G. P. Raja Sekhar, and M. Kohr, "Stokes flow of an assemblage of porous particles: stress jump condition," *Zeitschrift für angewandte Mathematik und Physik*, vol. 62, no. 6, pp. 1027–1046, Feb. 2011.

[199] J. Prakash and G. P. Raja Sekhar, "Arbitrary oscillatory Stokes flow past a porous sphere using Brinkman model," *Meccanica*, vol. 47, no. 5, pp. 1079–1095, Nov. 2011.

[200] M. Kohr, W. L. Wendland, and G. P. R. Sekhar, "Boundary integral equations for two-dimensional low Reynolds number flow past a porous body," *Math. Meth. Appl. Sci.*, vol. 32, pp. 922–962, 2009.

[201] E. Ului, "Boundary integral equations for the problem of 2 D Brinkman flow past several voids," *Studia Universitatis Babes-Bolyai Mathematica*, vol. LVI, no. 1, pp. 179–193, 2011.

[202] P. Deuring, "An integral operator related to the Stokes- system on exterior domains," *Math. Meth. in Appl. Sci.*, vol. 13, pp. 323–333, 1990.

[203] M. Kohr, G. P. R. Sekhar, and J. R. Blake, "Green's function of the Brinkman equation in a 2D anisotropic case," *IMA Journal of Applied Mathematics*, vol. 73, no. 2, pp. 374–392, Dec. 2007.

[204] M. A. Goldberg and C. S. Chen, *Discrete Projection Methods for Integral Equations*, 1st ed. Southampton, England: WIT Press, 1997.

[205] W. F. Florez and H. Power, "DRM Mult idomain Mass Conservative Interpolation Approach for the BEM Solution of the Two-Dimensional Navier-Stokes Equations," *Computers and Mathematics with Applications*, vol. 43, pp. 457–472, 2002.

[206] W. F. Florez and H. Power, "Multi-domain mass conservative dual reciprocity method for the solution of the non-Newtonian Stokes equations," *Applied Mathematical Modelling*, vol. 26, no. 3, pp. 397–419, Mar. 2002.

[207] K. J. Bathe, "The inf-sup condition and its evaluation for mixed finite element methods," *Computer and Structures*, vol. 79, no. 2, pp. 243–252, 2001.

[208] M. Mu and X. Zhu, "Decoupled schemes for a non-stationary mixed Stokes-Darcy model," *Mathematics of Computation*, vol. 79, no. 270, pp. 707–731, 2009.

[209] R. E. Larson and J. L. Higdon, "A periodic grain consolidation model of porous media," *Physics of Fluids*, vol. A1, pp. 38–46, 1989.

[210] M. Discacciati, E. Miglio, and A. Quarteroni, "Mathematical and numerical models for coupling surface and groundwater flows," *Applied Numerical Mathematics*, vol. 43, no. 1–2, pp. 57–74, 2002.

[211] W. Layton, F. Schieweck, and I. Yotov, "Coupling fluid flow with porous media flow," *SIAM Journal on Numerical Analysis*, vol. 40, no. 6, pp. 2195–2218, 2002.

[212] M. O. Mu and J. Xu, "A two-grid method of a mixed stokes–darcy model for coupling fluid flow with porous media flow," *SIAM J. NUMER. ANAL*, vol. 45, no. 5, pp. 1801–1813, 2007.

[213] Y. K. Hamidi, L. Aktas, and M. C. Altan, "Effect of packing on void morphology in resin transfer molded E-glass/epoxy composites," *Polymer Composites*, vol. 26, no.

5, pp. 614–627, Oct. 2005.

[214] Y. K. Hamidi, L. Aktas, and M. C. Altan, "Formation of Microscopic Voids in Resin Transfer Molded Composites," *Journal of Engineering Materials and Technology*, vol. 126, no. 4, pp. 420–426, 2004.

[215] B. Chen and T.-W. Chou, "Compaction of woven-fabric preforms in liquid composite molding processes: single-layer deformation," *Composites Science and Technology*, vol. 59, no. 10, pp. 1519–1526, Aug. 1999.

[216] Q. Govignon, S. Bickerton, and P. A. Kelly, "Simulation of the reinforcement compaction and resin flow during the complete resin infusion process," *Composites Part A: Applied Science and Manufacturing*, vol. 41, no. 1, pp. 45–57, 2010.

[217] B. Madsen, A. Thygesen, and H. Lilholt, "Plant fibre composites - porosity and volumetric interaction," *Composites Science and Technology*, vol. 67, no. 7–8, pp. 1584–1600, 2007.

[218] D. U. Shah, P. J. Schubel, P. Licence, and M. J. Clifford, "Determining the minimum, critical and maximum fibre content for twisted yarn reinforced plant fibre composites," *Composites Science and Technology*, vol. 72, no. 15, pp. 1909–1917, 2012.

[219] M. A. Ben Abdelwahed, Y. Wielhorski, L. Bizet, and J. Breard, "Bubble Shape and Transport During LCM Processes: Experimental Modeling in a T-Junction Tube," in *18th International Conference on composites materials, Jeju Island, Korea*, 2011, pp. 1–6.

[220] J. Vilá, F. Sket, F. Wilde, G. Requena, C. González, and J. LLorca, "An in situ investigation of microscopic infusion and void transport during vacuum-assisted infiltration by means of X-ray computed tomography," *Composites Science and Technology*, vol. 119, pp. 12–19, 2015.

[221] N. Patel, V. Rohatgi, and L. J. Lee, "Modeling of void formation and removal in liquid composite molding. Part II: Model development and implementation," *Polymer Composites*, vol. 17, no. 1, pp. 104–114, 1996.

[222] C. Shih and L. J. Lee, "Analysis of void removal in liquid composite molding using microflow models," *Polymer Composites*, vol. 23, no. 1, pp. 120–131, 2002.

[223] T. S. Lundstrom, B. R. Gebart, and C. Y. Lundemo, "Void Formation in RTM," *Journal of Reinforced Plastics and Composites*, vol. 12, no. 12, pp. 1339–1349, 1993.

[224] N. Yamaleev and R. Mohan, "Effect of the phase transition on intra-tow flow behavior and void formation in liquid composite molding," *International Journal of Multiphase Flow*, vol. 32, no. 10–11, pp. 1219–1233, Oct. 2006.

[225] Y. Wang and S. M. Grove, "Modelling microscopic flow in woven fabric reinforcements and its application in dual-scale resin infusion modelling," *Composites Part A: Applied Science and Manufacturing*, vol. 39, no. 5, pp. 843–855, 2008.

[226] N. Kuentzer, P. Simacek, S. G. Advani, and S. Walsh, "Permeability characterization of dual scale fibrous porous media," *Composites Part A: Applied Science and*

Manufacturing, vol. 37, no. 11, pp. 2057–2068, Nov. 2006.

[227] S. W. Eun and W. Lee, "Experimental study of the microvoids formation and transport in the vacuum assisted resin transfer molding process," *Composites Research*, vol. 16, no. 6, pp. 10–15, 2003.

[228] V. Neacsu, A. Abu Obaid, and S. G. Advani, "Spontaneous radial capillary impregnation across a bank of aligned micro-cylinders - Part II: Experimental investigations," *International Journal of Multiphase Flow*, vol. 32, no. 6, pp. 677–691, 2006.

[229] H. J. Barraza, Y. K. Hamidib, L. Aktasb, E. a. O'Rear, and M. C. Altan, "Porosity Reduction in the High-Speed Processing of Glass-Fiber Composites by Resin Transfer Molding (RTM)," *Journal of Composite Materials*, vol. 38, no. 3, pp. 195–226, Feb. 2004.

[230] T. S. Lundström, "Bubble transport through constricted capillary tubes with application to resin transfer molding," *Polymer Composites*, vol. 17, no. 6, pp. 770–779, 1996.

[231] N. Patel, V. Rohatgi, and L. Lee, "Micro scale flow behavior and void formation mechanism during impregnation through a unidirectional stitched fiberglass mat," *Polymer Engineering Science*, vol. 35, no. 10, pp. 837–851, 1995.

[232] H. Tan and K. M. Pillai, "Modeling Unsaturated Flow in Dual-Scale Fiber Mats of Liquid Composite Molding : Some Recent Developments," in *The 10th International Conference on Flow Processes in Composite Materials (FPCM10), Monte Verità, Switzerland*, 2010, pp. 1–5.

[233] M. Kang and W. Il Lee, "A flow-front refinement technique for the numerical simulation of the resin-transfer molding process," *Composites Science and Technology*, vol. 59, pp. 1663–1674, 1999.

[234] M. Lin, T. Hahn, and H. Huh, "A finite element simulation of resin transfer molding based on partial nodal saturation and implicit time integration," *Composites Part A*, vol. 29, pp. 541–550, 1998.

[235] P. Simacek and S. G. Advani, "Modeling resin flow and fiber tow saturation induced by distribution media collapse in VARTM," *Composites Science and Technology*, vol. 67, no. 13, pp. 2757–2769, 2007.

[236] D. Abraham and R. Mcllhagger, "Investigations into various methods of liquid injection to achieve mouldings with minimum void contents and full wet out," *Composites Part A*, vol. 29, pp. 533–539, 1998.

[237] V. R. Kedari, B. I. Farah, and K.-T. Hsiao, "Effects of vacuum pressure, inlet pressure, and mold temperature on the void content, volume fraction of polyester/e-glass fiber composites manufactured with VARTM process," *Journal of Composite Materials*, vol. 45, no. 26, pp. 2727–2742, Sep. 2011.

[238] N. Kuentzer, P. Simacek, S. G. Advani, and S. Walsh, "Correlation of void distribution to VARTM manufacturing techniques," *Composites Part A: Applied Science and Manufacturing*, vol. 38, no. 3, pp. 802–813, 2007.

[239] B. Šarler, J. Perko, D. Gobin, B. Goyeau, and H. Power, "Dual reciprocity boundary

element method solution of natural convection in Darcy–Brinkman porous media," *Engineering Analysis with Boundary Elements*, vol. 28, no. 1, pp. 23–41, 2004.

[240] R. S. Parnas and F. R. Phelan, "The effect of heterogeneous porous media on mold filling in resin transfer molding," *Journal of Chemical Information and Modeling*, vol. 22, no. 2, pp. 53–60, 1991.

[241] Z. Dimitrovova and S. G. Advani, "Mesolevel analysis of the transition region formation and evolution during the Liquid Composite Molding process," *Computers & Structures*, vol. 82, no. 17–19, pp. 1333–1347, 2004.

[242] J. Bréard, Y. Henzel, F. Trochu, and R. Gauvin, "Analysis of dynamic flow through porous media," *Polymer Composites*, vol. 24, no. 3, pp. 390–408, 2003.